PROCEEDINGS OF THE ELECTRON AND LASER BEAM SYMPOSIUM

March 31 - April 2

1965

EDITOR: A. B. EL-KAREH

Preface

Many conferences in this country have included topics which cover a part of the subject matter of this symposium. Nevertheless, it was felt that a meeting entirely devoted to the science and technology of electron, ion and laser beams would be useful. There is considerable interest in the field of high intensity electron beams and related topics. However, a symposium should progress with the times and this year recognition was made of the role that lasers are playing in the field of high intensity radiation. For this reason the title of the symposium was changed to include lasers.

In order to maintain a high standard and a wide coverage, an editorial board was formed consisting of six distinguished scientists from this country and abroad. They were solely responsible for the acceptance of the papers which were presented and for the scope of the conference. The members of the Editorial Board are:

DR. V. E. COSSLETT	CAMBRIDGE UNIVERSITY ENGLAND
PROFESSOR C. FERT	FACULTE DES SCIENCES UNIVERSITE DE TOULOUSE, FRANCE
DR. H. B. LAW	RCA LABORATORIES PRINCETON, NEW JERSEY, U.S.A.
DR. H. MOSS	WESTINGHOUSE ELMIRA, NEW YORK, U.S.A.
DR. S. NAMBA	INSTITUTE OF PHYSICAL AND CHEMICAL RESEARCH TOKYO, JAPAN
DIPL.-PHYS. K. H. STEIGERWALD	K. H. STEIGERWALD GmbH. MUNICH, GERMANY

This meeting was held at the Pennsylvania State University for several reasons. The principal reason is the fact that there are many research laboratories within the University which are directly related to the major topics of the Symposium.

Also, this University has numerous trained staff members experienced in organizing such scientific meetings.

I wish to express my gratitude to Dr. Ernst Weber, President of Brooklyn Polytechnic Institute, New York, for accepting to be our banquet speaker. His speech is included in these proceedings.

I also want to thank Dr. L. L. Marton of the National Bureau of Standards, Dr. H. A. Atwater, Dr. B. R. F. Kendall and Dr. E. W. Mueller of the Pennsylvania State University for acting as moderators during the conference.

The great assistance given by David Schuckers and Derald Cummings is here gratefully acknowledged.

Finally, I cannot possibly close this foreword without thanking Anita Cutchall who, by typing these proceedings in a record time proved beyond doubt that she ranks among the most efficient and accurate typists I have known.

A. B. El-Kareh
Chairman

Electron Physics Laboratory
Electrical Engineering Department
Pennsylvania State University
University Park, Pennsylvania, U. S. A.

TABLE OF CONTENTS

Table of Contents (Cont.)

Table of Contents (Cont.)

THE FEDERAL GOVERNMENT AND ACADEMIC RESPONSIBILITY - PARTNERSHIP OR SUBSIDY

by

Dr. Ernst Weber

President

Polytechnic Institute of Brooklyn

The last 25 years have brought some very fundamental changes to the academic scene, changes that may affect the whole future course of higher education. Those of us who were actively involved in the transition to large scale scientific research and have personally observed the effects upon academia should perhaps recount from time to time what has happened in order to see the present problems in their proper perspective. Though we live in an age of a most astounding pace of change, those who enter now upon academic careers accept the present state as their basis from which to move forward and it is right that this be so. Yet, much fruitless discussion could be saved if issues could be posed within the framework of trends of evolution. We should thus ask first of all:

What has happened to University Research? Rather than deal with the increases in numbers which have been so frequently quoted, let us concentrate upon the change in atmosphere that has taken place. In the 1930's it was the accepted pattern for most senior faculty members to have a small laboratory if they were interested in experimental research, with one or a few graduate students assisting them. Most equipment, even instrumentation was home made, only a few standard commercial instruments were bought because the laboratory allowances were quite small. Indeed, many times the faculty member might have to reach into his own pocket to get small supplies. The total number of doctorate holders in 1940 in the sciences was about 20% of those classified as scientists.[1] Of those classified as engineers, only one in 600 possessed the doctor's degree, indicating that practically all

scientific research in the universities was in the field of the sciences, very little in engineering and that concentrated in a few of the leading schools in the country.

The demonstrated technical capabilities of Germany at the beginning of World War II presented a supreme challenge to the opponents and actually transformed the conflict into a total technological war. This country mobilized its entire scientific and engineering manpower through the Office of Scientific Research and Development (OSRD) under the direction of Vannevar Bush.[2] As President Nathan Pusey of Harvard recently recounted:[3]

> "World War II marked a turning point in the evolution of the university in America. At that moment in time, government as the director of all aspects of the war effort, discovered that it could not carry out its missions without the help of the universities. Initially, it called upon them only for personnel; then, also for the training of specialists. But very quickly it came, in addition, to turn to them for most of the basic and much of the applied research on which the success of the whole complicated war undertaking depended. And so was inaugurated in the early 1940's a relationship new for government and new for universities which has worked a major transformation in our institutions of higher learning and which continues to be of tremendous and growing importance for both parties."

The impact upon universities was, indeed, staggering. The several large centers of war-related research that were organized, such as the Radiation Laboratory at M. I. T., the Radio Research Laboratory at Harvard University, the Applied Physics Laboratory at Johns Hopkins University, and others, recruited faculty from many institutions and grouped them into unique and challenging teams. With financing of the effort hardly a problem, with daring ideas and novel devices being solicited, the imagination and creativity of the groups were fired to the highest level and yielded results far beyond expectations.

So strong was the impression of the value of organized research support, that President Roosevelt only a few months before his death requested Vannevar Bush to examine how the experiences of OSRD as "a unique experiment of team-work and cooperation in coordinating scientific research and in applying existing scientific knowledge to the solution of technical problems paramount in war" could be extended

into peace time effort. In particular, how could questions like these be answered: [4]

> "What can the government do now and in the future to aid research activities by public and private organizations? The proper roles of public and private research, and their interrelation, should be carefully considered."
>
> "Can an effective program be proposed for discovering and developing scientific talent in American youth so that the continuing future of scientific research in this country may be assured on a level comparable to what has been done during the war?"

In these questions we find expressed the whole pattern of postwar developments pertaining to scientific research and the basic explanation of the change in atmosphere that has reverberated so strongly in the universities. V. Bush submitted by mid 1945 as reply[5] the epoch-making report "Science - The Endless Frontier" which culminated in the recommendation to establish a new peace-time agency, which eventually led to the authorization by Congress of the National Science Foundation (NSF) in 1950.

The hiatus between the dissolution of OSRD at the end of the war as promised by V. Bush and the inception of NSF was bridged with foresight and courage by the Navy, first through the Office of Research and Invention and then by the creation of the Office of Naval Research. Military leaders in all services had recognized the invaluable partnership with the academic community during the war and were aware of the critical description of all graduate study and academic research. Though hampered by the lack of flexibility in procurement procedures, all services eventually evolved special offices to deal with universities through contracts and grants in order to retain access to the scientific and engineering manpower that is an essential part of the academic community.

Progress towards Partnership Between the Federal Government and Universities. The sudden exposure of the academic fraternity to the affluence of war-time research and the then ready support of new ideas with equipment and personnel left an imprint that caused many faculty members at the end of the war to look for the best research opportunities. In turn the universities started to build up large research facilities with the aid of the various government agencies in order to provide more attractive settings for the creative faculty members. The total scientific and engineering manpower with advanced training had not been replenished during the war years so that a shortage became evident, leading to intensified bidding for outstanding faculty and rapid growth of a relatively small group of outstanding centers. Thus, in the federal fiscal year 1962 about one third of all research grant and contract moneys from the federal government went to 10 universities which, however, also granted one third of the number of doctor's degrees in those areas.[6] And further, of about four hundred institutions receiving federal research and development (R & D) funds, one hundred accounted for 90 percent of these funds, leaving for the other three fourths only 10 percent.

As a direct consequence of the gap in advanced degrees during the war years, the job opportunities for the graduating classes increased to the point where full-time graduate study became a luxury. This, then required increased stipends and other allowances to attract full-time graduate students.[7] In combination, the NSF fellowship programs, the sponsored research projects and more recently, the NASA traineeships, the National Defense Education Act fellowships have just about sufficed to keep the total output of doctorates in the natural sciences in step with the increase in doctor's degrees in all other fields. Graduate enrollments in the period from 1960 to 1963, averaged over all fields, rose by 31 percent; engineering alone by about 37 percent, so slightly above average; and physical science only by about 20 percent.

Impressed by the urgent need of federal attention to the "problem of scientific progress by basic research, and the making of scientists by graduate education, "the President's Science Advisory Committee"prepared a report[8] in 1960 entitled "Scientific Progress, the Universities, and the Federal Government" in which the interrelation of basic research and graduate study is strongly emphasized. The conclusions reiterate that the existing centers are urgently needed; that graduate education in science and engineering needs expansion; that it is important to attract a larger number of talented students to science and engineering as careers; that constant modernization must be achieved and for that purpose the financing of graduate education should find continued and flexible reinforcement. The report also points to the need for particular encouragement of new fields of research but this should be done whenever practicable in laboratories attached to universities rather than in separate research institutes.

Most interesting are the final recommendations directed to the universities and to government for implementation of the conclusions in terms of a growing partnership designed to reinforce academic freedom and excellence.

There can be no doubt that the fantastic surge in scientific discoveries and engineering utilization of the newly gained knowledge has imposed upon universities an obligation to keep modernizing which is patently beyond the means of any public or private institution.[9] Having demonstrated in World War II the mature leadership of the university faculties in research and development directly applicable to the war effort, basic research and graduate study have become national resources with which the federal government has a primary concern in all its agencies. The crucial issues in this new relationship must be the <u>emphasis upon partnership</u> in its fullest meaning. As the Director of NSF, Dr. Hayworth, phrases[6] it: "This implies the development of increased sensitivity on the part of the government policy-makers and program officers to the total needs of the institutions of higher

education. It also implies a growing degree of understanding on the part of college and university administrators of the way in which federal agencies carry on their business. Scientists and administrators as they develop understanding of and sympathy for the problems on both sides, must carry on a continuing dialogue concerning ways of perfecting government-institutional relationships."

The Issue: Teaching versus Research? We in academic institutions need to face several issues that are brought about by the massive federal aid to basic research but yet must be resolved within the academic community. Uppermost at the present time is the preoccupation of many faculty members with research to the possible detriment of the educational obligation. Though it is apparent that the foundation for this trend was laid during the world war and that this trend has been reinforced by the greater emphasis upon graduate study and the availability of research grants and contracts, the universities have grossly aggravated the situation by rating faculties for promotion in terms of numbers of papers or reports published. This need not even be done overtly, it need only be rumor or occasional confirming action to make the younger and hopefully ambitious faculty member select the course of quickest reward.

The most dramatic exposition was recently given by Dr. John Gardner, President of the Carnegie Foundation for the Advancement of Teaching[10] under the title "Flight from Teaching". He points to the fact that the enormous increase in college population will find fewer teachers with doctoral degrees. Less than half of all those receiving doctor's degrees have entered into or stayed in teaching during the last decade, and it is a fact that the total doctoral output in the sciences and engineering would not suffice to cover the academic demands alone, leaving aside the urgent requirements of industry and government as well as the other sectors of society. The situation is made more serious by the continuous reduction in actual teaching hours per faculty member.[11] Whereas in 1930-31 the

average teaching assignment in 57 mid-west colleges and universities was 19+ contact hours in the sciences and 14 contact hours in the humanities, the average teaching load had dropped to about two thirds of these figures by 1960-61 and in so-called "eminent" universities had decreased to 6 contact hours in the sciences and 8.3 contact hours in the humanities! Certainly one must be careful not to accept these figures at their face values without considering the increased advising load in connection with graduate theses. But even here we need to observe that the Master's theses in many institutions have been made optional so as to reduce this burden and to substitute more liberal allowances for the guidance of research dissertations.

The competition for outstanding faculty has unfortunately led in some instances to disregard of the primary educational function of the university. Research is an integral part of graduate study only if students are actively engaged in the pursuit of research projects as part of their doctoral programs. This is where administrations must be conscious of the proper balance in staff interests and of restoring the appropriate prestige to teaching of students as of at least equal value to other pursuits. This is precisely where the entire academic community must reappraise trends and take corrective action lest the inevitable reaction sets in under pressure from outside that will be difficult to counteract. Neither private nor public institutions can cover today's operational costs and the costs of desirable, pioneering educational developments without large scale support from outside sources encompassing the entire spectrum of society. In turn the academic responsibility to society demands a dedicated effort in educating the most precious natural resource that any nation can have, namely the leadership potential. This demands in turn concentration upon the teaching function which comprises at the graduate level research in the field of competency of the individual teacher or a group of teachers. It certainly permits the freedom of the creative individual to

devote himself entirely to research, as long as he remains in communication with the academic family. It does not condone exclusive emphasis upon research or preference of research activities because of the relatively easy support and recognition.

The Issue: Academic Freedom versus Government Support. If we speak of Academic Freedom broadly we need to recognize that American Universities were founded first and foremost as educational institutions to teach students and not as self-governing, self-sustaining communities of scholars. True, the earliest Italian and French "Studia - generalia" or universities[12] had for all practical purposes complete self-government. In Salerno it was the Masters or Teachers who banded together loosely, taught medicine, and admitted students as early as the 10th and 11th century, becoming a medical school in 1231. In Bologna it was the students from well-to-do families who engaged teachers around 1000 A. D. to teach them the essentials of civil law, becoming a "university" in 1190. A tradition of academic self government and prestige developed that had support from church and state authorities, though temporary conflicts arose when science first came upon the scene.

In this country, however, the early colleges and universities were principally founded on religious grounds. The earliest Institution, Harvard, founded in 1636 was "meant to be the orthodox instrument of the community and its faith",[13] and tolerance was little known. As Professor Mumford Jones[14] emphasizes,

> "From the founding of Harvard College in 1636 to the present day, academic institutions in this country have been directly or indirectly the creatures of government. The picture of a confraternity of scholars spontaneously gathering together and resolving to assure the continuity of knowledge through a system of apprenticeship, whatever is elsewhere true, has virtually no relation to the American

problem. The American people, passionately desiring education for their children, have gone about securing it much as they have gone about securing anything else they wanted for public use - through the creation of legal agencies to get them what they want."

For state universities, legislatures usually set up a Board of Regents; for private universities, charters are secured from state agencies by Incorporators who usually become the Board of Trustees or the Corporation. A college or university legally is in fact a governing board of which, in many cases, if not most, not even the president is a member.

It is against this background that one really would have to argue a code of academic freedom. But even if this legal background did not exist, the term academic freedom has not the same significance in this country as in other parts of the world. The flowering of the German universities in the 18th and 19th century might be attributed to their full implementation of academic freedom which then meant really two complementary elements: freedom of teaching for the faculty or Lehrfreiheit, and freedom of learning for the student, i.e. full mobility or Lernfreiheit. It is the latter that is not accepted wholeheartedly in this country for three reasons according to Mumford Jones:[14] firstly, in the eyes of law, the college stands in loco parentis with respect to the students, particularly if they are minors; secondly, institutions deliberately cultivate parental interest in the life of the college; and thirdly, the students themselves, though they demand freedom, do not especially like the responsibility freedom entails!

If we then add the further facts that abroad practically all universities are organized in terms of "chairs" or life long professorship in specified topics which are grouped into "faculties" that correspond here to divisions or schools; let faculties elect Deans and Deans elect the Rector (somewhat similar to President) for normal periods of one year as the expression of self government; charge little

tuition but are supported by government moneys in the nature of unrestricted grants with little if any detail accountability; we must recognize a very basic difference in environmental settings and therefore interpretation of government relationship. Indeed, the intrinsic suspicion that government support could invite infringement of academic freedom which we nearly accept as natural has little counterpart in the universities where the concept of academic freedom evolved.

More specifically, in our own setting the large scale federal support of higher education through fellowships to students and research funds to institutions has aroused fears that (a) students would select to study in areas in which they could find greatest financial support, (b) faculties would voluntarily select areas for research in which money would readily be available rather than follow their best abilities, (c) faculties could be forced by administrations to work on research projects because of public relations value, (d) institutions could distort their natural educational objectives in order to gain federal support, (e) the supporting agencies through the auditing requirements could force unacademic procedures upon universities. The strongest representations have been made against the large scale support of scientific research by non-science faculties, either because of real concern or because of a feeling of neglect.

Actually, as I have mentioned earlier, the increases in graduate student enrollments in engineering were about the same as, in the physical sciences considerably less than, those for all other fields. Therefore, the federal support program has only served to keep advanced study in science and engineering somewhat in step with the general increase in graduate study. Besides, students always had to select to work with faculty members who could find support for their work no matter where this support came from. With respect to points b, c, and d it is true and always has been so, that faculties and administrations can be swayed by availability of funds to enter into activities for which they are really not prepared or

which are in conflict with their basic objectives. Unfortunately, too many immature graduate programs are undertaken today and yet it would be difficult to establish a policing agency with real powers. Again, it is the responsibility of the academic community as a whole to establish standards, to assist institutions who have real potential and dedication, and to persuade the others to desist from expansions into areas in which they cannot contribute to society. In a democracy one must rely upon voluntary leadership or one loses the essence of freedom that we profess to cherish so much.

It is also true that the requirements of the auditing branches of the federal government have forced changes in accounting and have made university operations more bureaucratic. Some of it is probably of benefit, but the academic community must resist requirements that would make its operations indistinguishable from commercial or industrial establishments as incompatible with the academic climate.

The Issue: The Federal Grant University? The rising costs of university operations and of the needed basic research programs related to graduate study and necessary for maintaining the nation's leadership in science and engineering have been the real source of the increased concern of the federal government with financing higher education. Private institutions all over the nation have been engaged in many large scale fund raising campaigns. Not all of these campaigns have been successful and increasing competition is arising from the public institutions who also find their needs much greater than the states' legislatures are willing to support. It is for this reason that Clark Kerr, President of the far flung University of California foresees a narrowing of the differences between public and private universities[9] and predicts for both that their major support will come from the federal government in the form of large scale grants. As a recent study disclosed, some major universities already list between 30 and

50 percent of their annual budget as contributed by the military and civilian agencies of the federal government.

There would be little excuse for accepting what could be termed the Federal government's monitor role in the substantial broadening of educational programs and opening of new areas of research in colleges and universities were it not for the fact that we are dealing with this national resource of scientific and engineering manpower that is in short supply and must be utilized economically from the nation's point of view. A recent study by a special committee of the National Academy of Sciences[15] under the chairmanship of Dr. J. Killian, Jr. presents recommendations "toward better utilization of scientific and engineering talent" which summarize many of the points discussed here, and emphasize:

> "the importance of carefully thought-out policies and strategies for human resources development and use. We must do more than preach that investment in men is more important than investment in things. We must carry this view into practice."

The report also addresses a series of recommendations particularly to Colleges and Universities, such as

> "Colleges and Universities engaged in scientific and engineering education must accept full responsibility for maintaining a proper balance among the claims of teaching, research, and public service. They should systematically seek the cooperation of the federal government in maintaining the proper balance.
>
> Since the scholar-teacher plays an indispensible role in the cultivation and development of first-rate minds, scientists and engineers who accept faculty membership, should also, with few exceptions, assume an obligation to teach that is as clear and compelling as their commitment to research.

The nation needs not only to further the efforts of its present centers of educational excellence in science, but also develop new ones that are as good as the best it now has."

The proper balance of teaching, research, and public service is, indeed, an academic responsibility that colleges and universities must accept and discharge and that the federal government must accord them as a partnership principle. In turn, colleges and universities must cultivate a true understanding of government ways of doing business to convert into a true partnership what has so often been interpreted as subsidy and if so interpreted, will entail imposition of conditions that could be academically unacceptable. Partnership in itself means a balance of give-and-take that redounds to the benefit of the partners in the performance of their joint obligation: The Education of the Nation's Leadership Potential.

References

1. "Profiles of Manpower in Science and Technology", National Science Foundation, NSF 62-23; Washington, D. C., 1963.
2. "Federal Support of Basic Research in Institutions of Higher Learning", Report by Committee on Science and Public Policy, National Academy of Sciences, Publ. No. 1185, p. 24; Washington, D. C., 1964.
3. Pusey, N. M.,"The University Comes of Age", School and Society, 92, p. 286, 1963.
4. Ref. 2, p. 29.
5. Bush, V., "Science the Endless Frontier: A Report to the President on a Program for Postwar Scientific Research"; Washington, D. C. 1945, reprinted 1960.
6. Hayworth, L. J., "Some Problem Areas in the Relationships Between Government and Universities"; News Report, National Research Council, Natl. Ac. of Sc., XIV, p. 89, Nov.-Dec. 1964; Washington, D. C.

7. Weber, E., "Types of Graduate Subsidy and Their Relation to Educational Values", Jl. Eng. Educ., 44, p. 188, 1953.

8. "Scientific Progress, The Universities, and the Federal Government", Report by the President's Science Advisory Committee; U. S. Government Printing Office; Washington, D. C., Nov. 15, 1960.

9. Kerr, C., "The Uses of the University", Harvard Univ. Press, 1963.

10. Gardner, J. W., "Flight from Teaching", 59th Annual Report, The Carnegie Foundation for the Advancement of Teaching, New York, 1964.

11. Orlans, H., "The Effects of Federal Government in Financing Higher Education", Brookings Institution; Washington, D. C., 1962. See also Science, p. 1625, Dec. 27, 1963.

12. Rashdall, H., "The Universities of Europe in the Middle Ages", 3 vols., 1895, ed. by F. M. Powicke and A. B. Emden, Oxford Univ. P. 1936.

13. Hofstadter, R., and W. P. Metzger, "The Development of Academic Freedom in the United States", Columbia Univ. Press, New York, 1955.

14. Jones, H. M., "The American Concept of Academic Freedom", The American Scholar, 29, No. 1, p. 94, 1959.

15. "Toward Better Utilization of Scientific and Engineering Talent: A Program for Action", Report of the Committee on Utilization of Scientific and Engineering Manpower, National Academy of Sciences; Pub. No. 1191, Washington, D. C., 1964.

A Theoretical Investigation of the Continuous and Characteristic X-ray Emission Intensities from Thin Targets

by

R. Buchanan
Nuclide Corporation
State College, Pennsylvania

Abstract

Expressions for the continuous and characteristic X-ray emission intensities from thin specimens bombarded by a finely focused electron probe are derived. Applying these expressions, the improvement in the resolution of qualitative X-ray microanalysis is evaluated.

Introduction

The X-ray emission intensities from thin (i. e. only a small percentage of incident electrons stopped by target) specimens has recently become of interest because of the combined electron microscope, microanalyzer instruments built by Duncumb[1962], and the author and Nixon[1962] in Cambridge, England. Apart from the obvious advantages of being able to perform both electron microscopy and microanalysis in one instrument, the use of thin specimens in these instruments promises to improve the resolution of the microanalysis by virtually eliminating electron diffusion in the specimen. In this paper a theoretical investigation of both continuous and characteristic X-ray emission intensities from thin specimens is carried out and the resolution of microanalysis using thin specimens predicted.

The Production of X-rays

a. Continuous Radiation

The determination of the energy distribution in the continuous X-ray spectrum is based on the theoretical investigations of Kramers[1923]. He predicted that the continuous X-ray energy emitted per second from a surface element $d\sigma$ of an

infinitely thin target containing A atoms of atomic number N per cm^2 which is bombarded by an electron beam of velocity v, in which s electrons per second pass a cross-section of 1 cm^2 is given by

$$i_\nu \, d\sigma \, d\nu = \frac{32\pi^2 N^2 e^6}{3\sqrt{3}\, c^3 m^2 v^2} \, sA \, d\sigma \, d\nu \qquad (1)$$

for $\nu < \nu_o$, where ν_o is the frequency corresponding to the energy of the incident electrons, e the electron charge in e.s.u., m the electron mass and c the velocity of light.

To evaluate the X-ray output from a thin but finite target, the specimen is considered as a series of infinitely thin slices. In order to relate the electron energy to depth below the surface the Thomson-Whiddington relationship is used;

$$\text{i.e.} \quad V_1^2 - V_x^2 = a_1 x$$

where V_1 is the incident voltage of the beam in electrostatic units of potential, V_x is the voltage of the beam at depth x cm below the surface and a_1 is approximately constant, but varies slightly with incident voltage and target material. A theoretical expression is given for a_1 by Bohr(1913) and this was modified by Kramers to give

$$a_1 = 4\pi e^2 \, ANL$$

where L is a function equal to

$$\log (k \, v^3 \, m / 4\pi \bar{\nu}_i \, e^2)$$

k is a numerical constant equal to 1.1 and $\bar{\nu}_i$ is the mean value of a quantity of the same order of magnitude as the frequency of revolution of the electrons round the nucleus. Kramers has evaluated L for different voltages and materials and found it to vary little from L = 6 for Be, Al, Ca and Ag.

Denoting the energy between ν and $\nu + d\nu$ in the total radiation emitted per incident electron by I_ν it follows from (1) that

$$I_\nu = \int_o^x \frac{32\pi^2}{3\sqrt{3}} \frac{N^2 e^6}{c^3 m^2} \frac{A}{v^2} \, dx \qquad (2)$$

where x is the target thickness in centimeters.

Applying the Einstein relation,

$$eV = h\nu = 1/2 \, m v^2$$

to the Thomson-Whiddington relation,

$$v^2 = \frac{2e}{m} (V_o^2 - a_1 x)^{1/2}$$

by substitution in and integration of equation (2)

$$I_\nu = \frac{32\pi^2}{3\sqrt{3}} \frac{N^2 e^5 A}{c^3 m} \frac{1}{a_1} [V_o - V_x]$$

where V_x is the exit voltage of the electron beam. Replacing a_1 with Kramers' expression

$$I_\nu = \frac{8\pi}{3\sqrt{3}} \frac{N_e^3}{c^3 m L} [V_o - V_x]$$

The total emission intensity per incident electron is

$$I = \int_o^{\nu_o} I_\nu \, d\nu$$

$$= \frac{8\pi}{3\sqrt{3}} \frac{Ne^3}{c^3 m L} [V_o - V_x] V_o \qquad (3)$$

The total quantum intensity from a thin target is

$$n_c = \int_o^{\nu_o} \frac{I_\nu \, d\nu}{h\nu}$$

$$= \frac{8\pi}{3\sqrt{3}} \frac{Ne^3}{c^3 m L h} \ln \nu_o (V_o - V_x) \qquad (4)$$

where h is Planck's constant expressed as erg seconds.

Since no experimental results were available to verify equations (3) and (4), it is interesting to modify equation (3) to comply with thick specimen conditions and compare this with expressions arrived at by other workers for the continuous X-ray emission from thick specimens. Equation (3) becomes

$$I = \frac{8\pi}{3\sqrt{3}} \frac{Ne^3}{c^3 m L} V_o \nu_o$$

since $V_x = 0$. Expressing V_o and ν_o in terms of the electron velocity v, it follows that

$$I = \frac{2\pi}{3\sqrt{3}L} \frac{e^2 m}{c^3 L} N v^4$$

The efficiency of X-ray emission in the continuous is thus

$$\text{Eff.} = 4.34 \times 10^{-4} N \left(\frac{v}{c}\right)^2 \qquad (5)$$

which is twice the expression arrived at by Kramers, but in much better agreement with the formula derived empirically by Beatty(1913). He found that the efficiency of emission from a solid target was given approximately by

$$\text{Eff.} = 4.08 \times 10^{-4} N \left(\frac{v}{c}\right)^2$$

The discrepancy between Beatty's expression and equation (5) can be attributed to the fact that no account has been taken of X-ray absorption or

fluorescence in the specimen, nor of the characteristic radiation. In addition, the effect of back scattered electrons has been neglected.

In the case of a copper target 300 Å thick with V_o = 35 KV and $a_1 = 5.6 \times 10^7$, equation (4) gives the number of quanta emitted per incident electron as 55×10^{-5}.

b. Characteristic Radiation

In an investigation to determine to what extent the characteristic x-radiation from a specimen was due to primary bombardment of the specimen atoms by the incident electrons as opposed to secondary effects, Webster(1927), (1928) was able to show that for electron-opaque targets the ratio

$$Q = \frac{\text{number of direct K ionizations}}{\text{number of continuous spectrum quanta of frequency above } \nu_K}$$

where ν_K is the frequency of the characteristic radiation of the element, is approximately constant for varying electron energies. This fact is true for both thick and thin targets, as the effect of fluorescence is not considered here. This was confirmed by Webster and Hansen(1929) who also pointed out that for thin targets the constancy of Q is subject to wider limits of error.

Stoddard(1934) confirmed that Q was approximately constant over an extended range of excitation potentials. He also pointed out that from the experimental results available, it would appear that Q varies as $Z^{-2.6}$, where Z is the atomic number of the target material.

It follows, then, that the number of K quanta n_K emitted per incident electron is

$$n_K = Qx \text{ (number of continuous quanta of energy } > eV_K)$$

The number of continuous quanta of energy greater than eV_K is given by the integral

$$\int_{\nu_K}^{\nu_o} \frac{I_\nu}{h\nu}\, d\nu$$

therefore

$$n_K = Q \times \int_{\nu_K}^{\nu_o} \frac{I_\nu}{h\nu}\, d\nu$$

$$= Q \times \frac{8\pi}{3\sqrt{3}} \frac{Ne^3}{c^3 m h L} (V_o - V_x) \ln \frac{\nu_o}{\nu_K} \qquad (6)$$

As V_o is increased n_K tends to decrease, since the probability of any single electron penetrating the specimen without causing a K_α quanta to be emitted increases with increasing excitation potential. Increasing V_o, however, increases the current in the probe approximately linearly, so that the total K_α quantum output per unit time increases with increasing beam potential.

For a 300 Å thick copper target at 35 KV, and putting $Q = 3.5$, as evaluated by Stoddard, equation (6) yields a value of 6×10^{-5} quanta per incident electron for n_K. At 100 KV $n_K = 2.7 \times 10^{-5}$.

Castaing[1960] refers to measurements made by himself and Descamps of the K_α emission from thin copper specimens. From the results, he was able to deduce that the ratio of the copper K_α emission from a film of copper ε microns thick to that from a solid copper specimen under the same experimental conditions is given approximately by

$$\frac{I_\varepsilon(Cu)}{I(Cu)} = 0.6\,\varepsilon \qquad (7)$$

for an acceleration voltage of 30 KV.

The quantum efficiency from a solid specimen has been investigated by Duncumb[1957] and he arrived at the expression

$$\eta_K q = 1.04 \times 10^{-9} N Q \omega_\alpha V_K (U-1)^{1.65} \qquad (8)$$

for the number of K_α quanta emitted per incident electron, where N and Q are defined as in the thin specimen formula, ω_α is the fluorescent yield for K_α radiation and U is the ratio $\frac{V_o}{V_K}$. If equation (8) is evaluated at 30 KV for a copper target with the value of 0.395 for ω_α, as determined by Dyson[1956], η_{Kq} is found to be 15×10^{-4} quanta per incident electron.

Substituting this value for η_{Kq} in equation (7), the quantum efficiency for a 300 Å thick copper specimen is found to be 2.7×10^{-5}. Evaluating the quantum efficiency from equation (6) under the same conditions, n_K is found to be 5.4×10^{-5}.

Equation (7) is only approximate, so the discrepancy between the two values of n_K obtained above is considered reasonable. The agreement, however, is sufficient to indicate that equation (6) leads to a value for n_K of the right order of magnitude for copper at 30 KV.

If the quanta emitted per second at 35 KV and 100 KV are denoted by n'_{K_1} and n'_{K_2}, respectively, then the ratio n'_{K_2}/n'_{K_1} is found to be equal to 1.3. By increasing the beam potential from 35 KV to 100 KV, therefore, the number of characteristic quanta emitted per second increases by about one third.

By combining equations (4) and (6) the quantum intensity in the characteristic line can be related to that in the continuous spectrum, thus

$$\frac{n_K}{n_c} = Q \times \frac{\ln \frac{\nu_o}{\nu_K}}{\ln \nu_o}$$

If this ratio is evaluated at 35 KV and 100 KV it is found to increase from 0.109 to 0.189 with increasing beam potential.

Optimum Resolution in the Analysis of Thin Specimens

Smith(1956) has shown that the current i, falling into a probe of Gaussian-optical diameter d_o is given by

$$i = 0.62\, j_c \frac{V_o}{V_e} \alpha^2 \pi \frac{d_o^2}{4} \qquad (9)$$

where $e V_e$ is the most probable energy of electron emission from the cathode, $e V_o$ is the energy of the electron beam and j_c is the current density at the cathode. The fraction 0.62 applies if d_o is defined as the diameter at which the current density in the probe has fallen to one fifth of that on the axis.

The main aberrations which limit the discrimination in the analysis of thin specimens are spherical aberration and diffraction. Smith has considered the optimum conditions for forming a probe in the presence of these two aberrations and he concluded that the minimum probe diameter would be obtained for

$$\alpha = \alpha_{opt.}$$

where

$$\alpha_{opt.} = \frac{1.04}{C_s^{1/4}} \left[\frac{i}{B} + (1.22\lambda)^2 \right]^{1/8}$$

in which

$$B = 0.62\, j_c \frac{V_o}{V_e} \frac{\pi}{4}$$

If $\alpha_{opt.}$ is evaluated for $C_s = 1$ cm, and $V_o = 35$ KV,

$$\alpha_{opt.} = 10^{-2} \text{ radians.}$$

In section b, the number of K_α quanta emitted per incident electron from a

300 Å thick copper target at 35 KV was found to be 6×10^{-5}. If we denote the number of K_α quanta emitted per second under these conditions by n'_K, then

$$n'_K = 3.75 \times 10^{14} \times i$$

where i is the beam current in amperes. If a combined counter and collection efficiency of 0.5% is assumed and if a count rate of 25 counts per second is considered as the acceptable minimum, then the current in the probe to produce this must be 1.3×10^{-11} amperes.

From equation (9) a value for d_o may be found, assuming that

$$j_c = 2 \text{ amperes/cm}^2$$

$$V_e = 0.25 \text{ volt}$$

$$V_o = 35 \text{ KV}$$

$$\alpha = \alpha_{opt.} = 10^{-2} \text{ radians.}$$

The diameter of the X-ray source d is, therefore, obtained by adding in quadrature d_o and the diameters of the discs of confusion due to spherical aberration and diffraction. By so doing, d is found to be equal to 120 Å.

If the discrimination of the system is evaluated at 100 KV, it is found to be 90 Å.

Conclusions

In conclusion it can be said that the resolution of qualitative microanalysis can be improved by using thin specimens. From the theoretical investigation of the X-ray emission from such specimens it appears that the higher the beam potential the better the characteristic emission intensity, and the more favorable the peak to background ratio. The relatively low X-ray yield from thin specimens means that to take advantage of the improved resolution, an X-ray detection system of high

collection efficiency should be used - such as a series of proportional counters. The poor resolution of such detectors may be improved by using a resolving power multiplier, such as that developed by Kendall[1962].

References

1. Beatty, R. T. (1913), Proc. Phys. Soc., 89, p. 314.
2. Buchanan, R. and Nixon, W. C., (1962), Proc. of Third Inter. Symp. on X-Ray Optics and X-Ray Microanalysis, p. 441.
3. Castaing, R. (1960), Advances in Electronics, XIII, Academic Press, N. Y.
4. Duncumb, P. (1957), Ph. D. Thesis, University of Cambridge.
5. Duncumb, P. (1962), Fifth International Congress for Electron Microscopy, Philadelphia, p. KK-4.
6. Dyson, N. A., (1956), Ph. D. Thesis University of Cambridge.
7. Kendall, B. R. F. (1962), R. S. I. Vol. 33, No. 1, p. 30.
8. Kramers, H. A. (1923), Phil. Mag., 46, p. 865.
9. Smith, K. C. A., (1956), Ph. D. Thesis, University of Cambridge.
10. Stoddard, K. B. (1934), Phys. Rev., 46, p. 837.
11. Webster, D. L. (1927), Proc. Nat. Acad. Sci., 13, p. 445.
12. Webster, D. L. (1928), Proc. Nat. Acad. Sci., 14, p. 330.

Scaling of Electron Beam Devices

by

C. S. Bull
The College of Advanced Technology
Birmingham, England

Abstract

Scale models are necessary in engineering practice, but their usefulness depends on finding theoretically how various factors vary under the scaling operations.

In electron beam devices two factors, the cathode temperature and the existence of space charges have made it appear that scaling might be impracticable. It is shown, however, that it is permissible to scale electron beam devices according to the table of scaling factors given in the paper provided the electrode voltages and the cathode temperature are not changed.

Introduction

In engineering applications it is sometimes necessary to make a scale model of a system. If the system is very large and complicated and the theory is known to have approximations of importance, the considerable expense and the risk of costly failure may be avoided if a small scale model be constructed for test prior to the construction of the full size system. On the other hand, a system may be so small that it is not only difficult to construct but also difficult to assess its ideal performance with sufficient accuracy to allow valid conclusions to be drawn. A large scale model will then have advantages.

In electron beam welding the very high power density and its very destructive action, which can be produced by the use of even very modest electron optical systems, are the useful features with which we are concerned. Since the focus is very small and its shape very dependent on the electron optical design, it would be useful if the system could be scaled up, so that more accurate measurements could

be made and the destructive action to some extent limited at the same time.

The simplest scaling operation in valves has been known for very many years, and depends on the use of the assumption that the electron emission velocities are zero. It is then expected that the current densities will vary as $V^{3/2}$ and as x^{-2} where V is the voltage and x the distance between the electrodes. Also for the same voltages applied to scaled systems, the total currents to all electrodes will be the same in both systems.

Langmuir[1] gave a solution to the problem presented by a planar diode in which the thermal emission velocities and space charges are taken into account. It is of forbidding complexity, and has not been applied to devices of general shape. When applied to such problems as the fluctuations or the losses induced in circuits at very high frequencies, the use of Langmuir's methods becomes not only more difficult, but also more limited in its scope. For example, North's[2] method of calculating the fluctuations is applicable only to a range of positive effective anode voltages, and not to negative or retarding voltages.

In face of these difficulties it has been attempted to utilize approximations, but these approximations have been so unsoundly based that under some conditions their use would give less reliable results than rule of thumb methods.

In the study of thermodynamics a carefully drawn set of curves giving the relationship between three variables, such as say U, the internal energy, T, the absolute temperature, and V, the volume, enables all other characteristics of a thermodynamic system to be calculated, at least in principle. Yet the molecules and atoms share energy and have interactions about which we have practically no knowledge. Not only could we not handle it if we had all the information, but also the interactions are by no means of a classical kind, and involve quantum mechanical probability distributions. It appeared, therefore, that for an electron device, in which very many electrons are in motion, it is very likely that there must be

some method akin to thermodynamics with the aid of which the macroscopic performance can be expressed without detailed knowledge of the behavior of individual electrons. It was attempted, therefore, to find a set of variables, which if properly utilized would correspond to the thermodynamic variables, and so make possible general predictions about the action of the valve.

As a result of this search it was found that there are five variables which are either commonly used or can be determined from the characteristic curves. Of these it was found that it is never necessary to utilize all five at once for a knowledge of four would enable the fifth to be calculated. Under some conditions three or perhaps even two variables only were required. The five variables selected were the set

$$i,\ i_s,\ V,\ V_m \text{ and } x\ .$$

where i is the current density at the anode,

i_s is the emission current density at the cathode,

V is the potential at the anode,

V_m is the potential barrier, and

x is the distance between electrodes

It may be thought surprising that the cathode temperature was not included in the set. The following reasoning will substantiate this omission. Space charge effects vary as the emission velocity, which in turn, varies as $T^{1/2}$, where T is the cathode temperature. The total emission, on the other hand, varies exponentially as a function of T. Hence, negligible variations in temperature could be used to bring about appreciable changes in total emission. Therefore, in considering the characteristics of the valve the cathode temperature was regarded as being constant.

It is possible to make thirty differential coefficients between these five variables, taken four at a time, two of the four being held constant. One of these is, of course,

the very well-known conductance

$$g_m = (\partial i/\partial V)_{x, i_s}$$

In the course of the work done to find the relationships between these thirty differential coefficients, it was found that several differential coefficients which might be regarded as scaling characteristics could be formed, such as

$$(\partial i/\partial x) \quad \text{or} \quad (\partial i_s/\partial x)$$

with various pairs of variables held constant.

It was, however, noticed that the potential barrier V_m is closely related to the cathode temperature, being smaller for a given current density the lower the cathode temperature. This suggested that it might be possible to scale the valve if the anode potential V and the barrier potential V_m were held constant, so obtaining the values of differential coefficients

$$(\partial i/\partial x)_{V, V_m} \quad \text{and} \quad (\partial i_s/\partial x)_{V, V_m}$$

from physical information available in the form of equations such as Poisson's equation.

This calculation proved to be possible. It was, however, of wider interest since it was found that the argument could be stated in so general a way that it is applicable to any electron device under a very wide range of circumstances. It was by no means restricted to a planar system or to an assumption that the emission velocities are zero, or that they are the same for all electrons, or that the electrons are emitted in one direction. The only requirement is that the direction and distribution of emission velocities be the same in both the original and the scaled system. Furthermore, there is no need to restrict the scaling to small values, a scaling factor much greater or less than unity being permissible.

The details of the working can be seen in a paper by the author.[3] The results can be expressed by the following table and are, in fact, very simple.

We consider two systems - of which one is k times larger than the other. Positions in these systems can be specified by the radius vector from two arbitrary origins, one in each system. All electrode voltages are to be the same in both systems.

Quantity	Original System		Scaled System
Electron emission velocity	$\underline{v}_o$	=	$\underline{v}_o$
Emission current density over all emitting areas	$i_s(r, \underline{v}_o)$	=	$k^{-2} \cdot i_s(k\underline{r}, \underline{v}_o)$
Current density over all current collecting areas	$i(r, \underline{v}_o)$	=	$k^{-2} \cdot i(k\underline{r}, \underline{v}_o)$
Potential over all boundaries	$V(\underline{r})$	=	$V(k\underline{r})$
Total emission current	$I_s(\underline{r})$	=	$I_s(k\underline{r})$
Total current to any collecting electrode	$I(\underline{r})$	=	$I(k\underline{r})$
Electron path, element length	$\delta s(\underline{r})$	=	$k \cdot \delta s(k\underline{r})$

It will be seen that these scaling conditions can be met even if the cathodes are so hot that the emission velocities are appreciable, provided the two cathodes are at the same temperature, which is of course very easily arranged, being almost unavoidable.

It will also be seen that the test for the scaling conditions, given the same cathode temperature in both systems, is that the total current to each electrode shall be the same in both systems. The velocities are then the same at corresponding points in both systems. The conditions on the current densities ensure that the space charges are fully taken into account.

If we scale up an electron beam, then the intensity and the focus will be reduced

by a factor k^2. This will itself make the beam less destructive and may alone be sufficient to enable more accurate measurements of the size and intensity of the focus to be made. It will also enable the system to be made more accurately, so that electron optical aberrations can be studied in more detail, and possibly removed.

If further, the high tension supply be pulsed so that the duty cycle is say 1% or less, then the total power demanded will be much reduced, and the measurements of intensity and the effects of poor vacuum can be assessed. The only condition for the use of pulsed beams is that the time of flight of the electrons from the cathode to the remotest part of the system shall be considerably shorter than the duration of each pulse. This condition would normally be very easily attained except for exceptionally long beams at relatively low voltage.

References

1. Langmuir, I., The effect of space charge and initial velocities on the potential distribution and thermionic current between parallel plane electrodes, Physical Review, 21, 419 et seq, 1923.
2. North, D. O., Fluctuations in space charge limited currents at moderately high frequencies, R. C. A. Review, 4, 441-472, 5, 106-124, 1940.
3. Bull, C. S., "Space Charge in Planar Diodes", Proc. I. E. E., 97, Part III, 1950.

An Evaluation of Pulsed Laser Welding

by

J. E. Anderson and J. E. Jackson
Union Carbide Corporation, Linde Division
Indianapolis, Indiana

Abstract

The theoretical and experimental studies of pulsed laser welding are sufficiently advanced to present an overall evaluation. In this paper the advantages and limitations of the process are outlined and results are presented of an extensive experimental study of laser welding of wire and sheet as well as a number of specific applications.

Theory reveals two important features of pulsed laser welding. First, the energy input to the workpiece is close to the theoretical minimum to form a given size weld nugget. This greatly reduces the thermal damage to areas adjacent to the weld. Second, the depth of the weld zone that can be achieved with a single pulse is limited by the duration of the laser pulse that can be achieved rather than the laser energy output. Consequently, for lasers that operate in the pulse range from 1 - 10 milliseconds, the depth of the weld zone is below 1/32-inch. This depth limitation can be circumvented under controlled experimental conditions in which a hole is temporarily drilled in the first part of the laser pulse. However, this exception does not seem to be of practical significance in pulsed laser welding at present.

The experimental evaluation was made with a laser containing an energy output varying up to 20 joules and a pulse duration of one to four milliseconds. Similar and dissimilar metal joints were made with a variety of materials including copper, nickel, tantalum, stainless steel, Dumet, Kovar, aluminum, tungsten, titanium and columbium. The joints were evaluated for mechanical strength and electrical resistivity. In addition, the effects of process variables such as energy output and

focusing on the weld joint were examined.

Excellent joints were obtained both with single pulse spot welds such as those joining two wires together and with overlapping spot welds for continuous seams between metal sheets. Dissimilar metal joints could be made providing the metallurgy of the two materials were compatible. Welded joints between materials of widely varying melting points and thermal conductivity were easily achieved. Generally, for fully penetrated welds, the wire diameter was limited to 0.020-inch and below while sheet thickness for seam welds was restricted to below 0.015-inch. This is in agreement with theory. The strength of the joint for fully penetrated welds was equivalent to the parent metal in the annealed condition. The electrical resistivity of the joint was small. The general process requirements as far as accuracy of workpiece position, necessity of shielding reactive metals, and optimum joint orientation are covered in detail in this paper.

The most promising single outlet for pulsed laser welding is the electronics industry. Fusion welds can be made to circuit boards without damage to the substrate. Typical connections such as the leads of flat pack integrated circuits are reproducibly obtained. These studies have shown that although the laser is not a universal device for all joining problems, its unique features are ideal for many specific applications.

Introduction

Although laser welding has been in existence for only a short time, in many respects it has reached a fairly advanced state of development. Specifically, enough is known about the pulsed laser for welding to present an overall evaluation. The theory of the effects of a high intensity pulsed heat source on a metal surface is reasonably well understood. This is backed up by an extensive experimental study of pulsed laser welding of wire and sheet as well as a number of specific applications. Significant advances in laser equipment performance such as in lamp life

are undoubtedly forthcoming. However, it is not believed that this will alter the basic advantages and limitations of the process as they are understood today. This statement does not apply to the continuous laser for welding which will have to be evaluated in its own right when it materializes.

Background and Theory

The distinguishing characteristics of pulsed laser welding stem from the following factors: 1) the source of power for welding is a light beam; 2) it is capable of very high power intensities (radiant power per unit cross sectional area of the beam); and 3) the energy is supplied to the workpiece in short, discrete pulses separated by long cooling periods. The light beam from the laser differs from conventional radiation sources such as the tungsten and arc lamps. Whereas in these other sources the radiation is scattered in all directions, the laser beam is essentially collimated with only small beam divergence. This simplifies the problems of focusing thereby improving the utility of the radiation. In addition, focusing of the collimated beam markedly increases the power intensity above that leaving the laser crystal.

The power intensities possible with a focused laser beam are orders of magnitude higher than those obtained using other heat sources with the only exception of the electron beam. This is illustrated by the comparison of different sources in Table I. The value listed for the laser is not necessarily limiting but, as explained herein, is more than sufficient for any welding operation. It is interesting to note that the argon arc, which is normally considered a very intense heat source, is relatively mild compared to a laser. For a thermal radiation source acting as a black body, a temperature of $115,000^{\circ}K$ would be required to obtain an intensity of 10^9 watts/cm^2. In practice values around 10^4 watts/cm^2 can be achieved with a very intense continuous arc radiation source.

A direct consequence of the high laser intensity is that the welding operation

TABLE I

COMPARISON OF HEAT SOURCES FOR WELDING

Heat Source	Power Intensity (watts/cm^2)
Laser	up to 10^9
Electron Beam	up to 10^9
Electric Arc (Argon - 200 amps)*	1.5×10^4
Oxygen-Acetylene Flame*	10^3
Oxygen-Hydrogen Jet Burner*	3×10^3
Black Body Radiation**	
6,500°K	10^4
11,500°K	10^5
20,500°K	10^6
36,500°K	10^7
65,000°K	10^8
115,000°K	10^9

* Experimentally determined for heat transferred to flat surfaces (ref. 2 and 3)

** Calculated

can be speeded up and the amount of energy required for a particular weld joint reduced appreciably. For a typical laser spot weld on thin stock, the energy required may be about one tenth of that required for the same weld with an electric arc. As a matter of fact the required energy for a laser weld is close to the theoretical minimum required to bring the weld nugget up to the melting point and supply the heat of fusion. With this high melting efficiency, the size of the heat affected zone and the thermal damage to parts adjacent to the weld zone are minimized.

There is a limit to the power intensity that can be tolerated in a welding

operation. If the intensity is increased sufficiently, boiling on the surface of the metal occurs and a jet of vaporized metal is emitted as pictured in Figure 1. Pressure is exerted on the surface by the reaction force of the expelled vaporized metal. The pressure can be estimated by applying the equations for heat conduction, the kinetic theory, and Newton's laws. Using a simplified model, the pressure and temperature were calculated as a function of intensity for iron. The results are plotted in Figure 2. As shown, the pressure on the surface rises very rapidly with increasing intensity once the normal boiling point has been achieved. The pressure can be sufficient to expel liquid metal leaving a hole rather than a weld bead.

As an approximation for operation at atmospheric pressure or above, it can be stated that welding occurs when the power intensity is such that the surface temperature is equal to or is less than the normal boiling point of the metal. For most common metals this is around 10^5 - 10^6 watts/cm^2, well below the maximum for the laser. If the intensity is appreciably greater, drilling rather than welding will occur because of the vaporization pressure. In practice, temperatures higher than the normal boiling point can be tolerated before the pressure is sufficient to expel liquid metal. The exact point where drilling occurs is not known but the steep slope of the pressure curve in Figure 2 indicates it must be reasonably close to the normal boiling point for a laser operating at atmospheric pressure.

If the maximum temperature that can be maintained at the metal surface is close to its boiling point, then this limits the rate of heat conduction into the metal. There is a corresponding limit to the thickness of plate that can be spot welded at full penetration for a given duration of the laser pulse. Using equations given by Adams and Fairbanks,[1] the maximum thickness can be determined as a function of pulse length by assuming that the boiling and melting points are reached at the top and bottom of the plate respectively by the end of the laser pulse. For

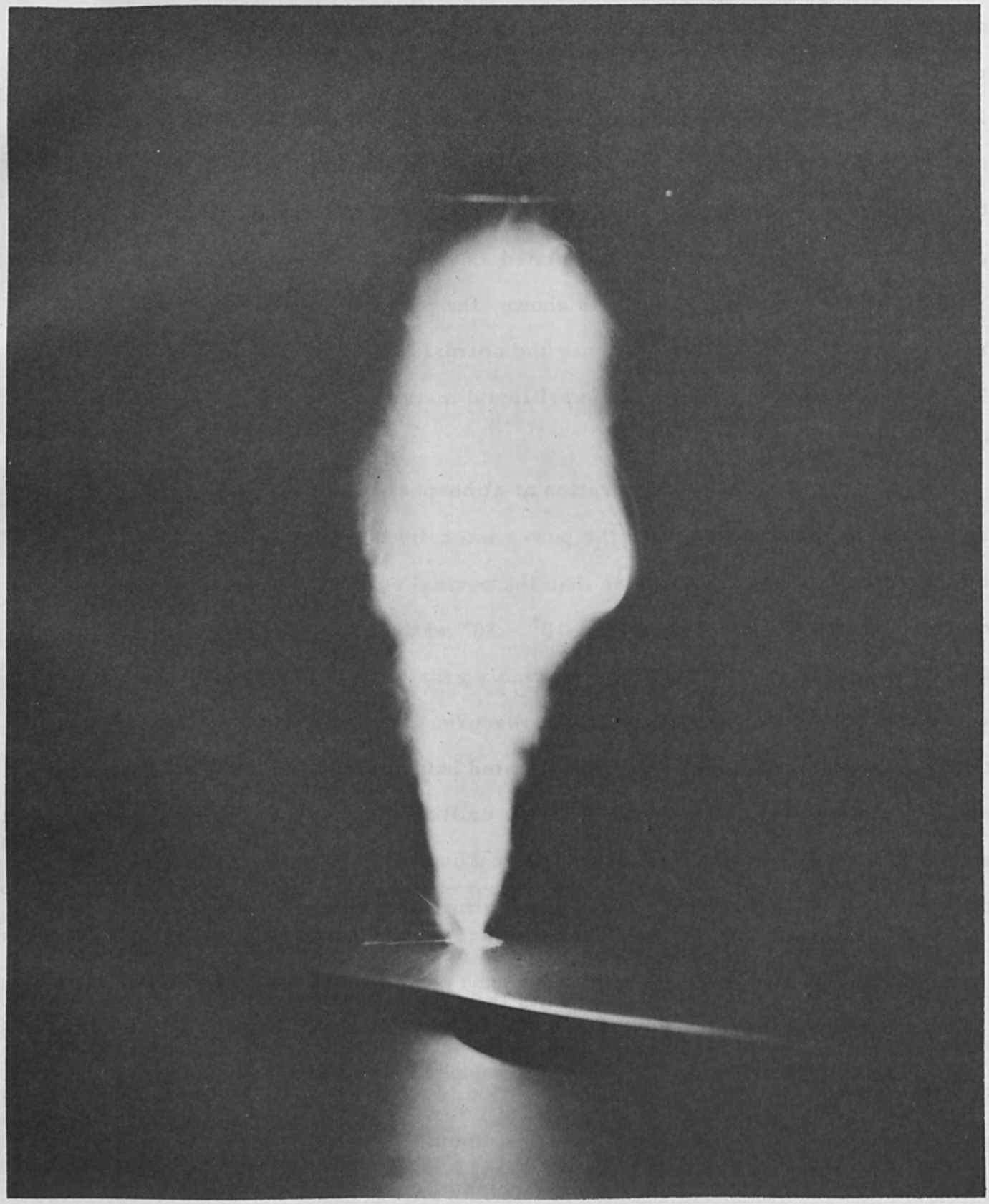

Figure 1 - Vaporized jet of metal obtained by focusing a high intensity laser beam on the metal surface.

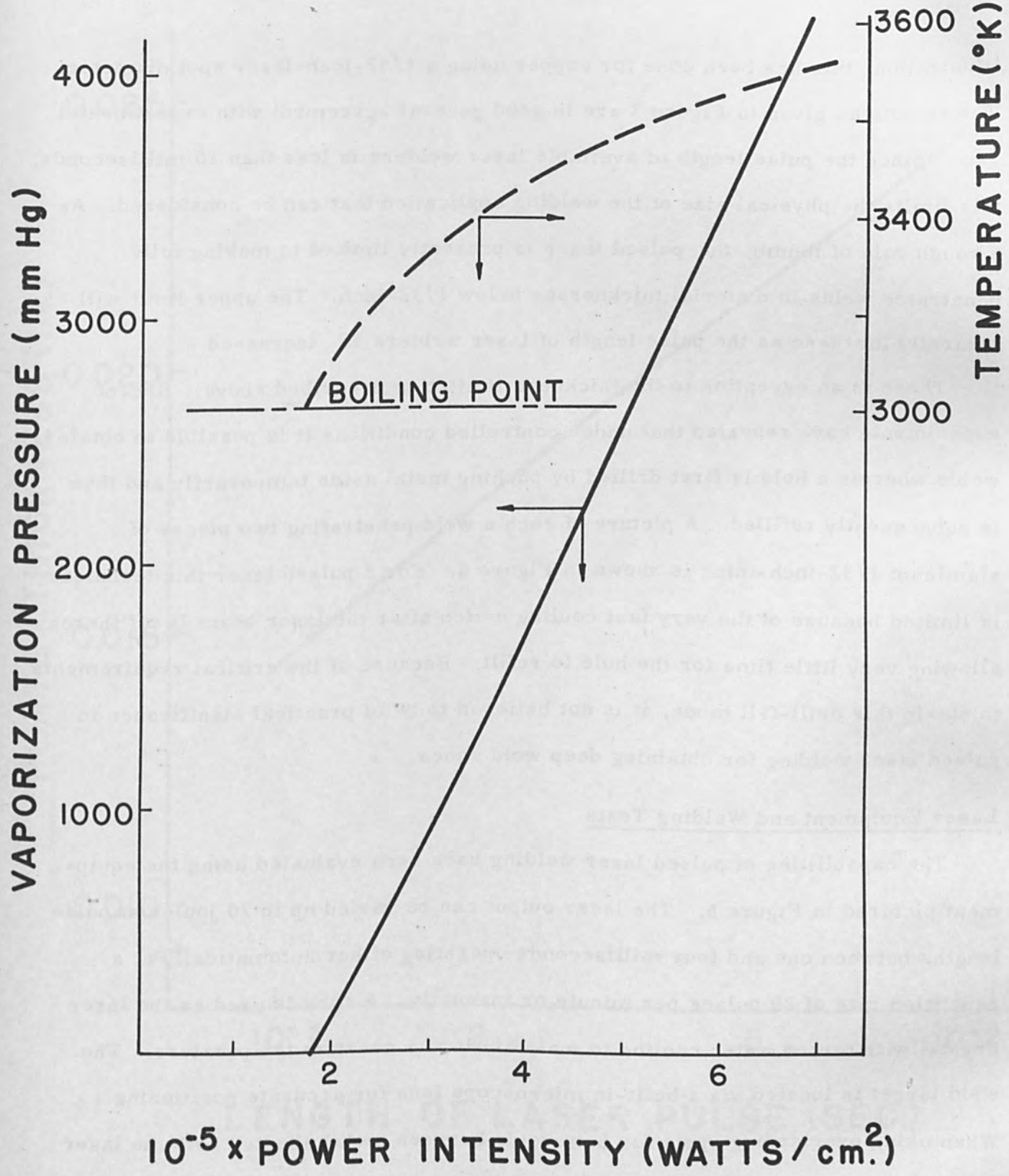

Figure 2 - Pressure and temperature on the surface of iron as a function of the absorbed power intensity for a 1 millisecond pulse.

illustration, this has been done for copper using a 1/32-inch-laser spot diameter. The results as given in Figure 3 are in good general agreement with experimental data. Since the pulse length of available laser welders is less than 10 milliseconds, this limits the physical size of the welding application that can be considered. As a rough rule of thumb, the pulsed laser is presently limited to making fully penetrated welds in material thicknesses below 1/32-inch. The upper limit will naturally increase as the pulse length of laser welders is increased.

There is an exception to the thickness limitation described above. Recent experiments have revealed that under controlled conditions it is possible to obtain welds wherein a hole is first drilled by pushing metal aside temporarily and then is subsequently refilled. A picture of such a weld penetrating two pieces of aluminum 1/32-inch-thick is shown in Figure 4. For a pulsed laser this technique is limited because of the very fast cooling action after the laser beam is off thereby allowing very little time for the hole to refill. Because of the critical requirements to obtain this drill-fill mode, it is not believed to be of practical significance in pulsed laser welding for obtaining deep weld zones.

Laser Equipment and Welding Tests

The capabilities of pulsed laser welding have been evaluated using the equipment pictured in Figure 5. The laser output can be varied up to 20 joules at pulse lengths between one and four milliseconds operating either automatically at a repetition rate of 20 pulses per minute or manually. A ruby is used as the laser crystal with forced water cooling to maintain it at a constant temperature. The weld target is located via a built-in microscope lens for accurate positioning. When using overlapping spots for butt welds between metal sheets, both the laser pulse rate and travel speed of the plate are maintained automatically.

Welds involving different metals and joint designs have been made satisfactorily with the laser. These involve similar and dissimilar metal joints including

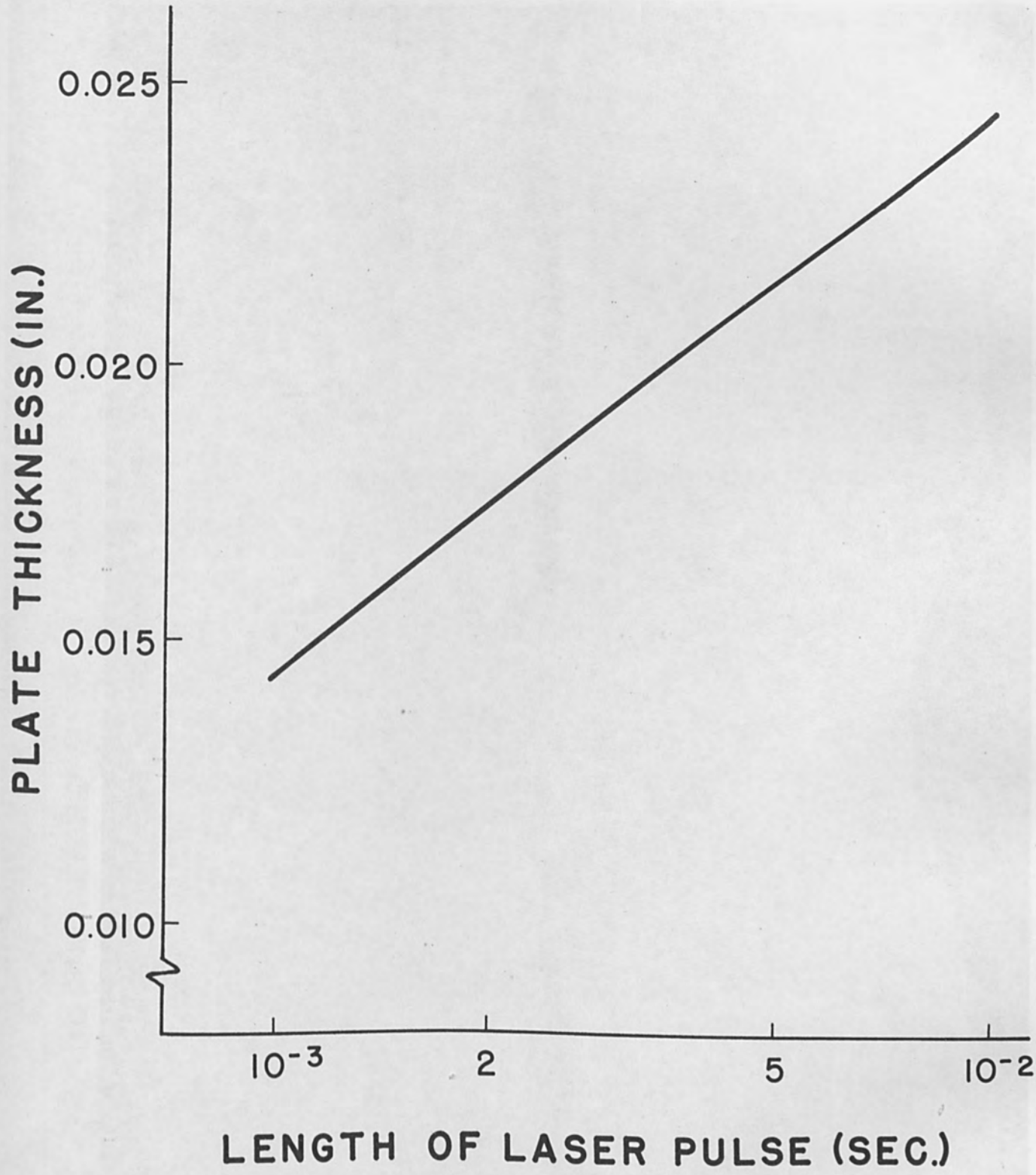

Figure 3 - Maximum sheet thickness of copper that can be welded as a function of pulse length for a 1/32-inch-diameter focused spot.

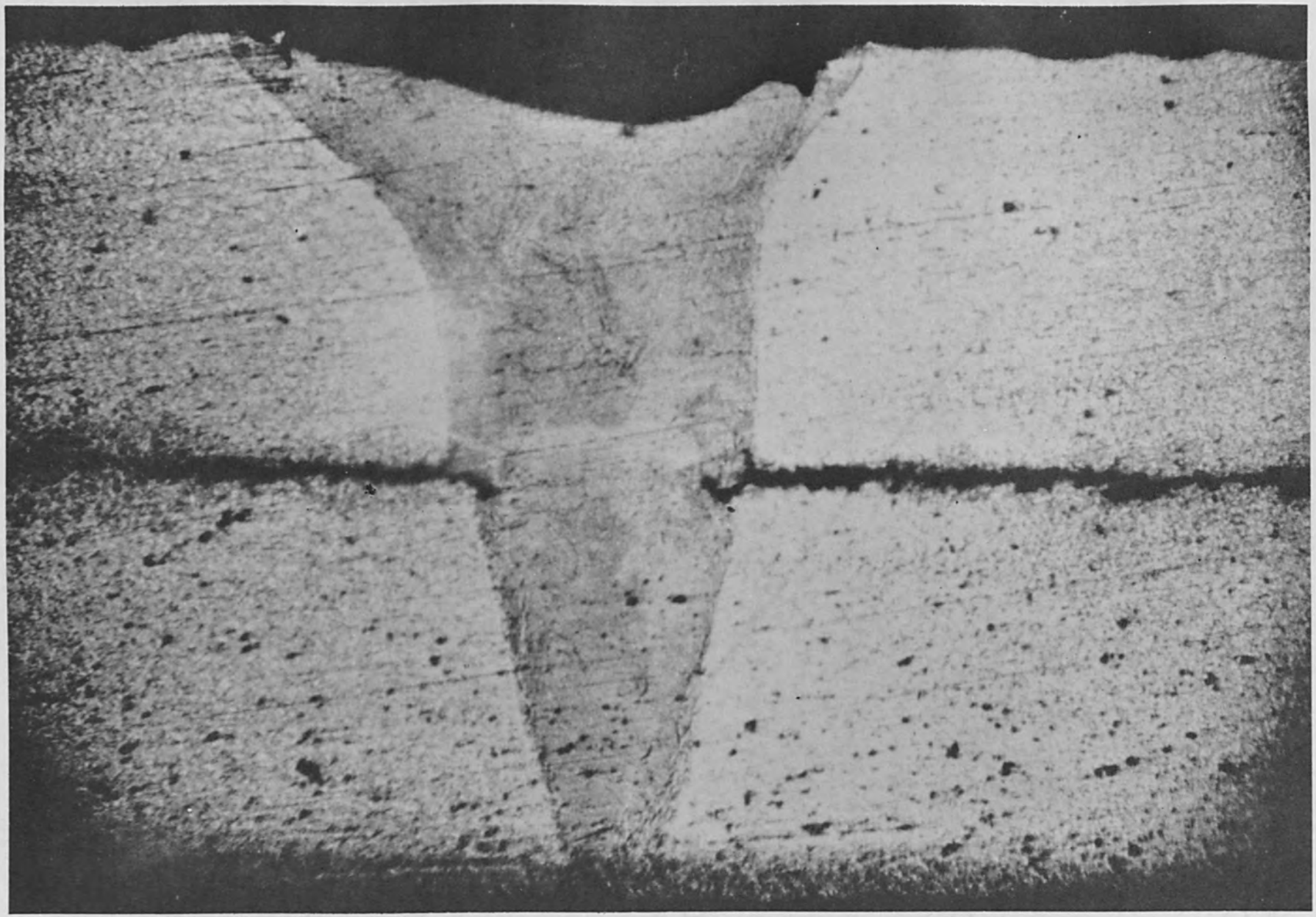

Figure 4 - Laser spot weld between two aluminum sheets, 1/32-inch-thick, using drill-fill technique.

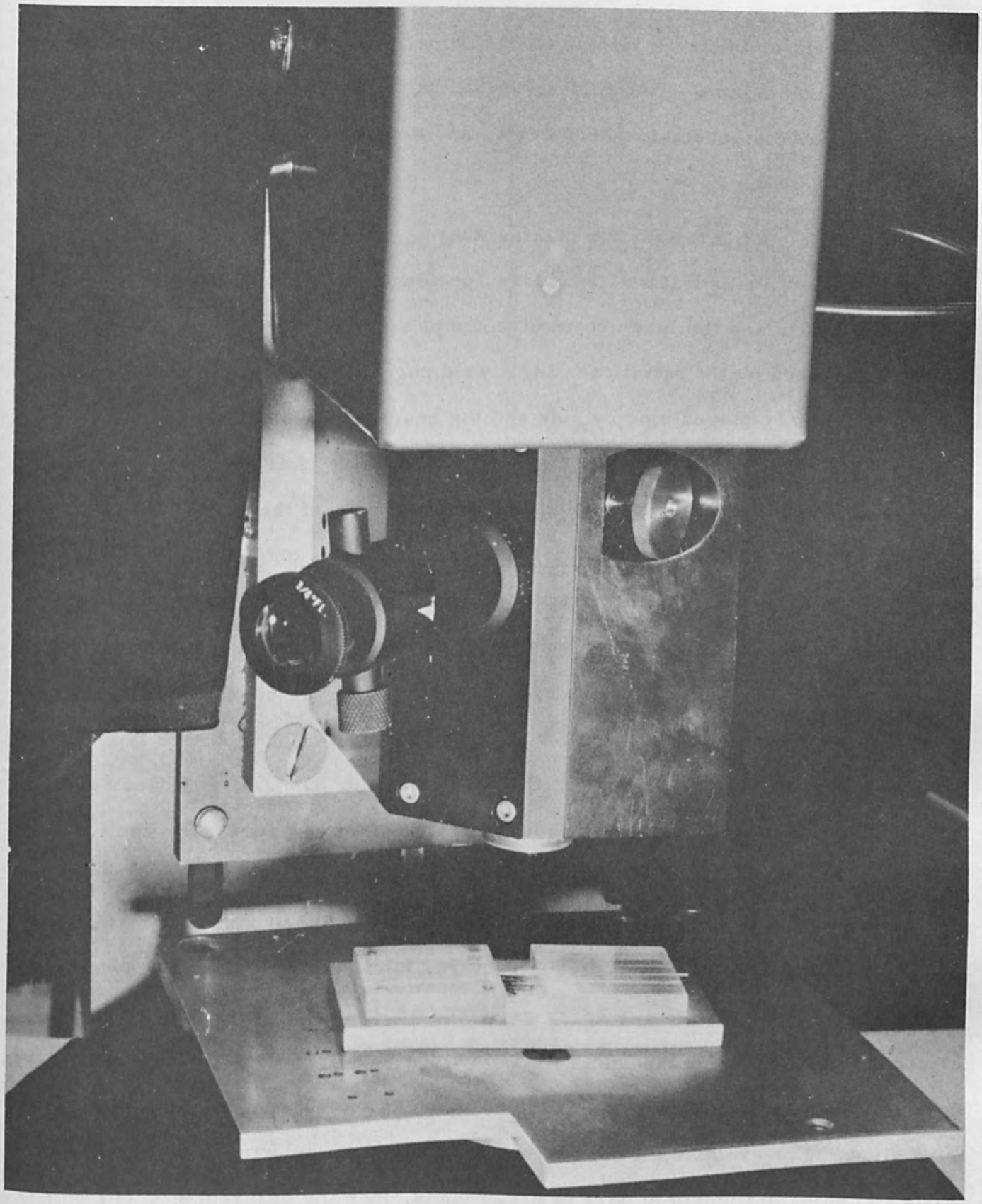

Figure 5 - Laser welder used in this investigation.

copper, nickel, tantalum, stainless steel, Dumet, Kovar, aluminum, tungsten, titanium and columbium. The welds generally fall into the three categories of wire-to-wire welds, sheet-to-sheet welds, and wire-to-sheet welds.

Wire-To-Wire Welds

Four basic configurations for making wire-to-wire welds are shown in Figure 6. With the butt configuration, two wires, preferably with squared off ends, are placed end to end and the laser beam directed at the joint. The energy in the laser beam is absorbed by the metal creating a weld nugget. In the lap joint, the two pieces of wire are placed side by side and the beam directed at the area where they touch. The tee joint is a variation in which the one wire is at right angles to the other while in the cross configuration one wire is on top of the other.

The strength and electrical resistance for wire welds obtained with various materials and joint configurations are given in Table II. The values given in the table were reproducible for many welds. The tensile tests were made by pulling the specimen in the direction of the arrows shown in Figure 6. This method of loading is essentially pure tension for the butt joint, pure shear for the lap, and a combination of tension and shear for the cross and tee. Generally, a laser energy output of 10 joules is required to produce a weld as strong as the wire itself for 0.015-inch diameter wires and about one half as strong as the wire for 0.030-inch diameter wires. These comparisons are based on the soft or annealed form of the wire. Since the weld is a cast microstructure, joints made with hard drawn or severely cold worked wire are never as strong as the wire itself. The values of electrical resistance for the joints were obtained by determining the difference between the resistance of a given weldment plus wire lead and the resistance of the wire alone. For example, if the resistance of the weld and wire is 0.023 ohms while an equivalent length of wire is 0.021 ohms, then the difference, 0.002 ohms, is the joint resistance. In general the weld strength was high and the electrical

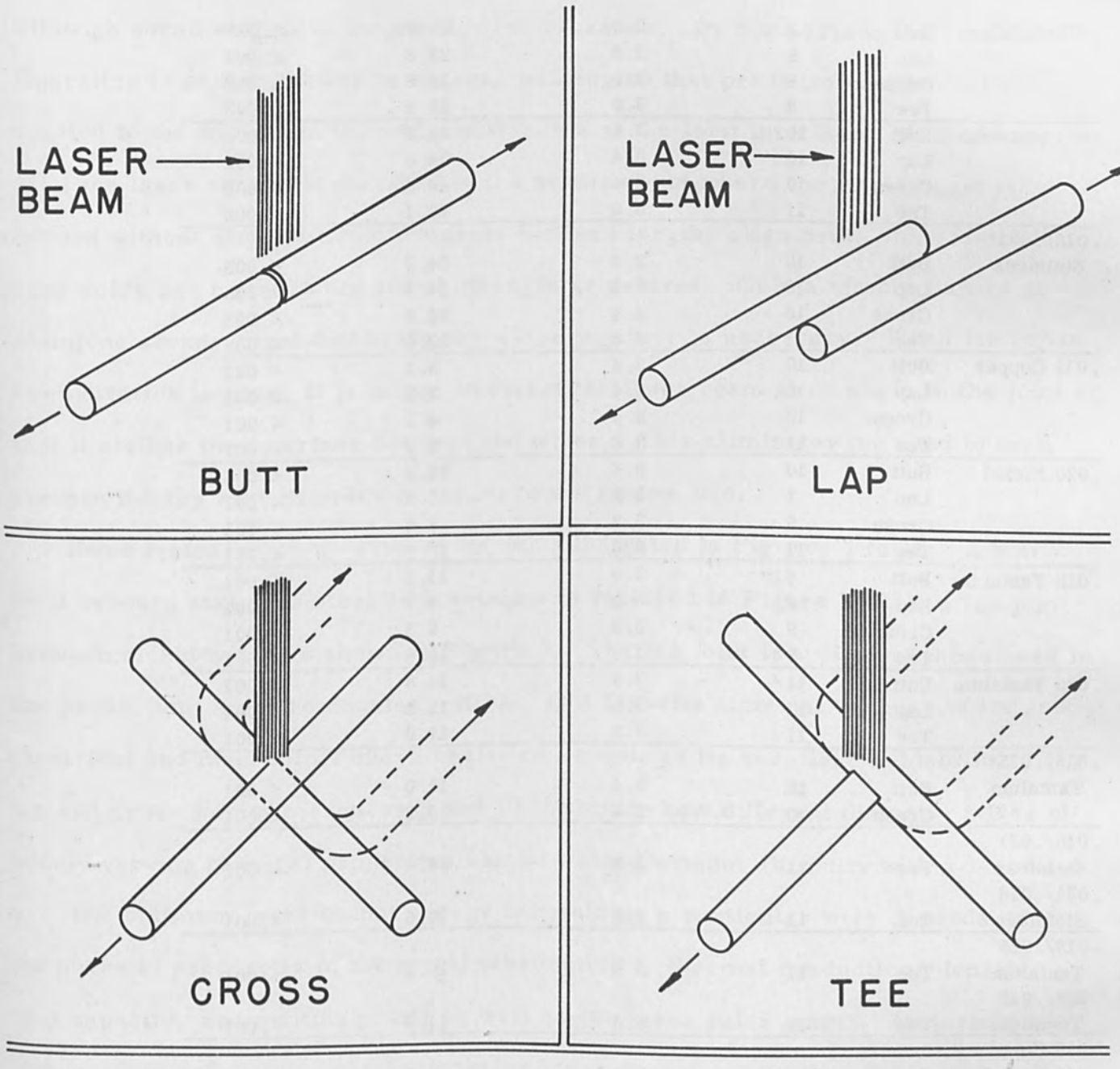

Figure 6 - Basic configurations for wire-to-wire laser spot welds.

TABLE 2

PROPERTIES OF WIRE TO WIRE LASER WELDS

Material	Joint	Laser Output Joules	Pulse Length m sec (Half Power)	Joint Strength Pounds	Joint Resistance ohms
.015 Stainless	Butt	8	3.0	21.3	<.003
	Lap	8	3.0	22.8	<.003
	Cross	8	3.0	25.0	<.003
	Tee	8	3.0	23.2	<.003
.031 Stainless	Butt	10	3.4	31.8	<.002
	Lap	10	3.4	34.6	<.002
	Cross	10	3.4	40.0	<.002
	Tee	11	3.6	40.1	<.002
.015/.031* Stainless	Butt	10	3.4	24.3	<.003
	Lap	10	3.4	24.8	<.003
	Cross	10	3.4	25.6	<.003
	Tee	11	3.6	22.0	<.003
.015 Copper	Butt	10	3.4	5.1	<.001
	Lap	10	3.4	3.2	<.001
	Cross	10	3.4	4.3	<.001
	Tee	11	3.6	3.2	<.001
.020 Nickel	Butt	10	3.4	12.2	<.001
	Lap	7	2.8	7.8	<.001
	Cross	9	3.2	6.8	<.001
	Tee	11	3.6	12.5	<.001
.015 Tantalum	Butt	8	3.0	11.5	<.001
	Lap	8	3.0	8.8	<.001
	Cross	9	3.2	9.3	<.001
	Tee	8	3.0	10.8	<.001
.025 Tantalum	Butt	11	3.5	14.8	<.001
	Lap	11	3.5	12.9	<.001
	Tee	11	3.5	17.0	<.001
.015/.025* Tantalum	Butt	10	3.4	11.0	<.001
	Cross	10	3.4	9.2	<.001
.015/.031 Stainless	Tee	11	3.6	26.4	<.001
.031/.016 Stainless	Tee	11	3.6	19.6	<.001
.015/.025 Tantalum	Tee	11	3.6	19.3	<.001
.025/.015 Tantalum	Tee	11	3.6	11.4	<.001
.015 Copper .015 Tantalum	Butt	10	3.4	3.8	<.001
.015 Copper .015 Tantalum	Tee	10	3.4	4.0	<.001
.015 Copper .015 Tantalum	Lap	10	3.4	5.3	<.001
.015 Copper .015 Tantalum	Cross	10	3.4	4.1	<.001

*When two wire gages are used, the upper number in the size designation is the size of the top member of a cross or cross bar of a tee.

resistance of the joint small.

The preferred joint configuration for laser welding is probably the lap joint although sound welds can be produced in all cases. By comparison the cross configuration is preferable for resistance welding so that pressure can be easily applied to the wires and the weld bead forms at the joint interface. With the lap joint the laser energy is directed to the precise spot where the weld nugget is needed without stringent requirements for lead length, alignment, etc. Multiple spot welds can be made for added strength as desired. Only a simple fixture or clamping arrangement that holds the wires together is necessary. When the cross configuration is used, it is better to direct the laser beam at an angle to the joint so that it strikes the interface between the wires. This eliminates the need to melt through the top wire in order to join it to the bottom one.

Some typical wire-to-wire welds are illustrated in Figures 7 to 10. A butt joint between stainless steel and tantalum is pictured in Figure 7 while a lap joint between nickel wires is shown in Figure 8. The lap joint is typical of those used in the production of micromodules. Nickel is a favorite material because of its good electrical and mechanical characteristics as well as its excellent weldability. The tee and cross joints in Figures 9 and 10 illustrate how different diameter wires of widely varying physical properties can be welded without difficulty with a laser.

The optimum laser output energy for welding a particular wire depends upon the physical properties of the metal (absorptivity, thermal conduction, density, heat capacity, and melting point) as well as the laser pulse length. Materials with high surface reflectivity require greater laser energy output than those with dull rough surfaces because of the fraction of radiant energy absorbed. Also, metals such as copper and silver with high thermal conductivities require a greater output than low conductivity materials like nickel or iron. It is usually easier to make a few test welds to determine the proper settings on the laser welder rather than

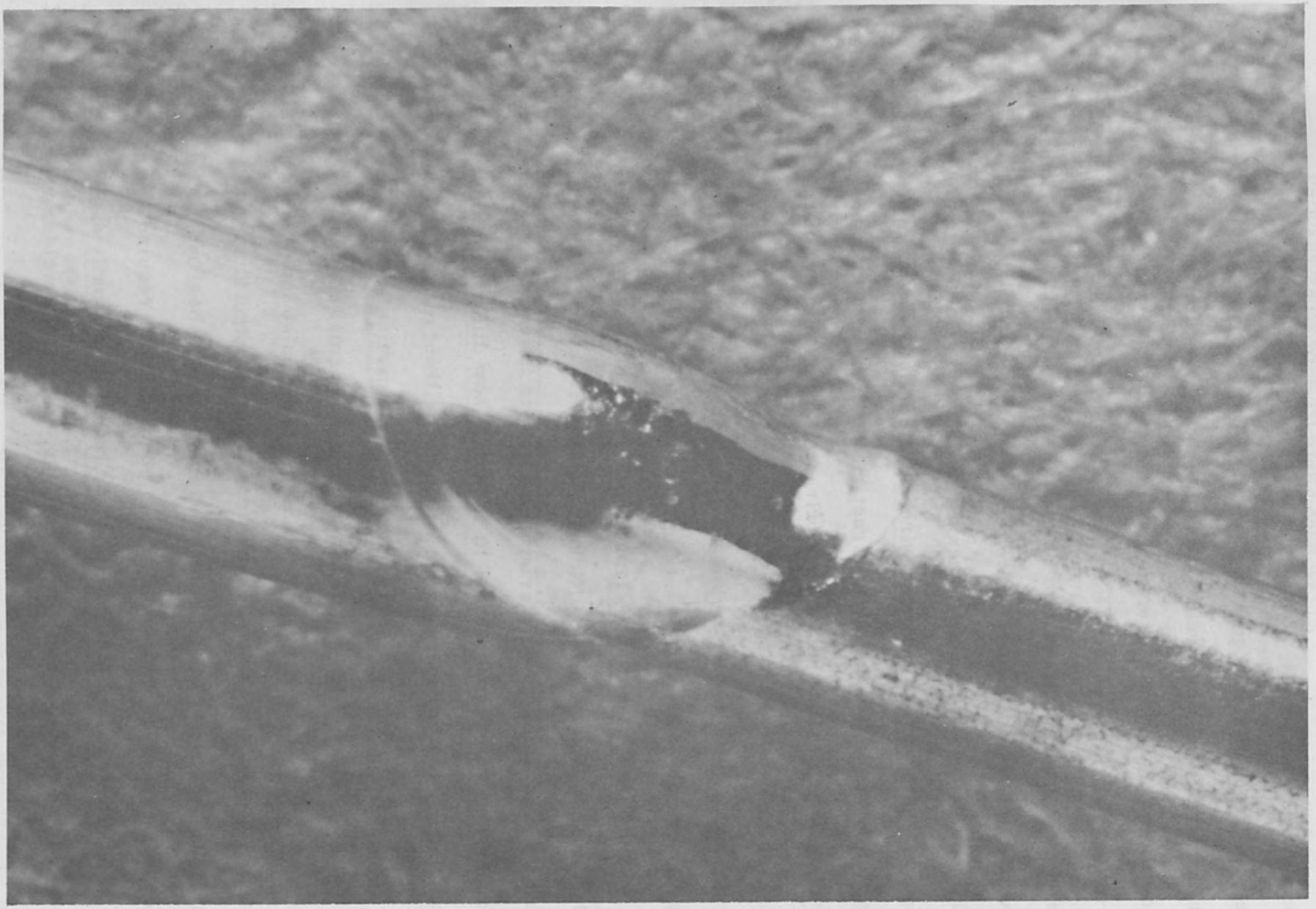

Figure 7 - Butt joint between 0.030-inch-diameter stainless steel and 0.025-inch-diameter tantalum.

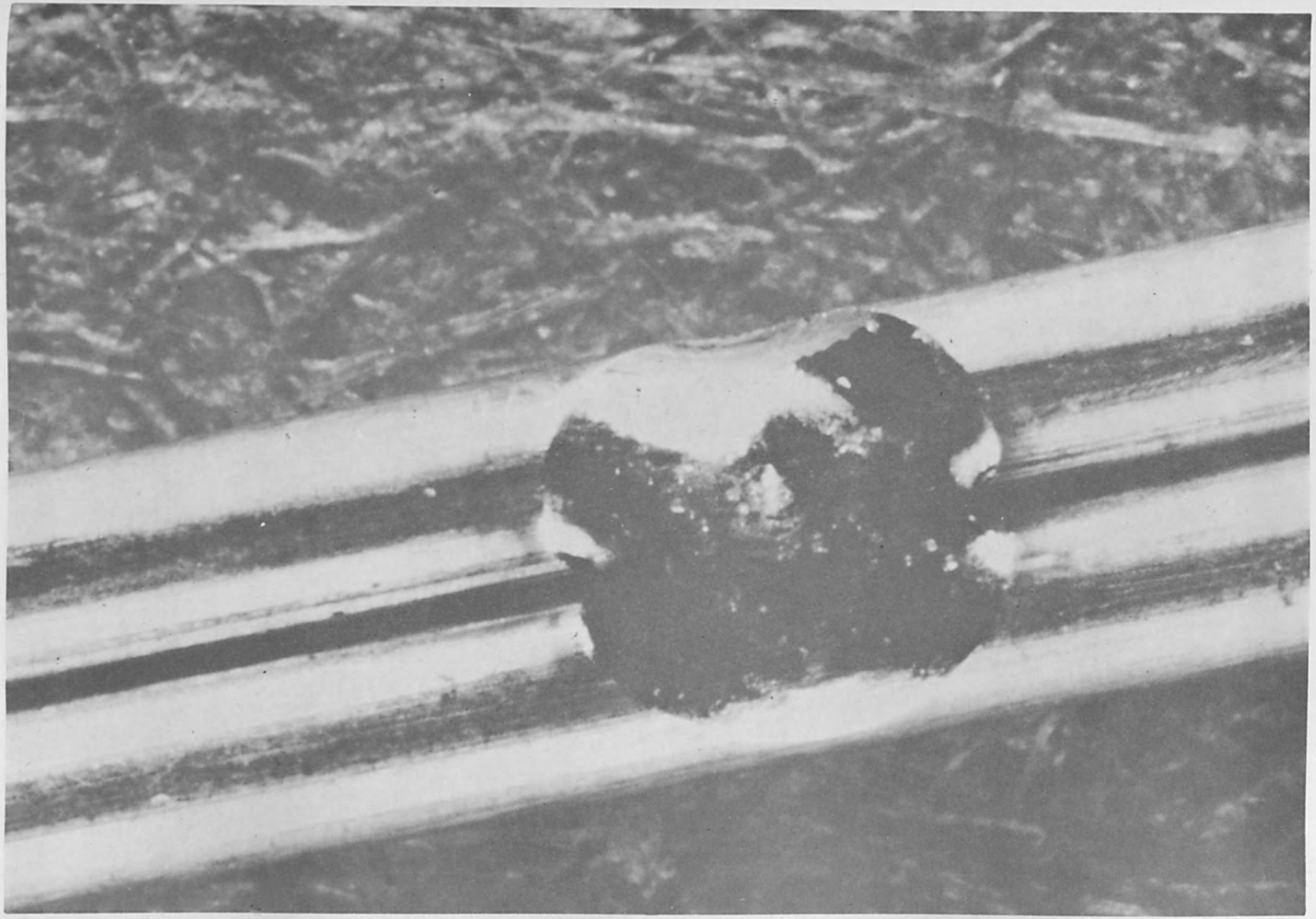

Figure 8 - Lap joint between two 0.020-inch-diameter nickel wires

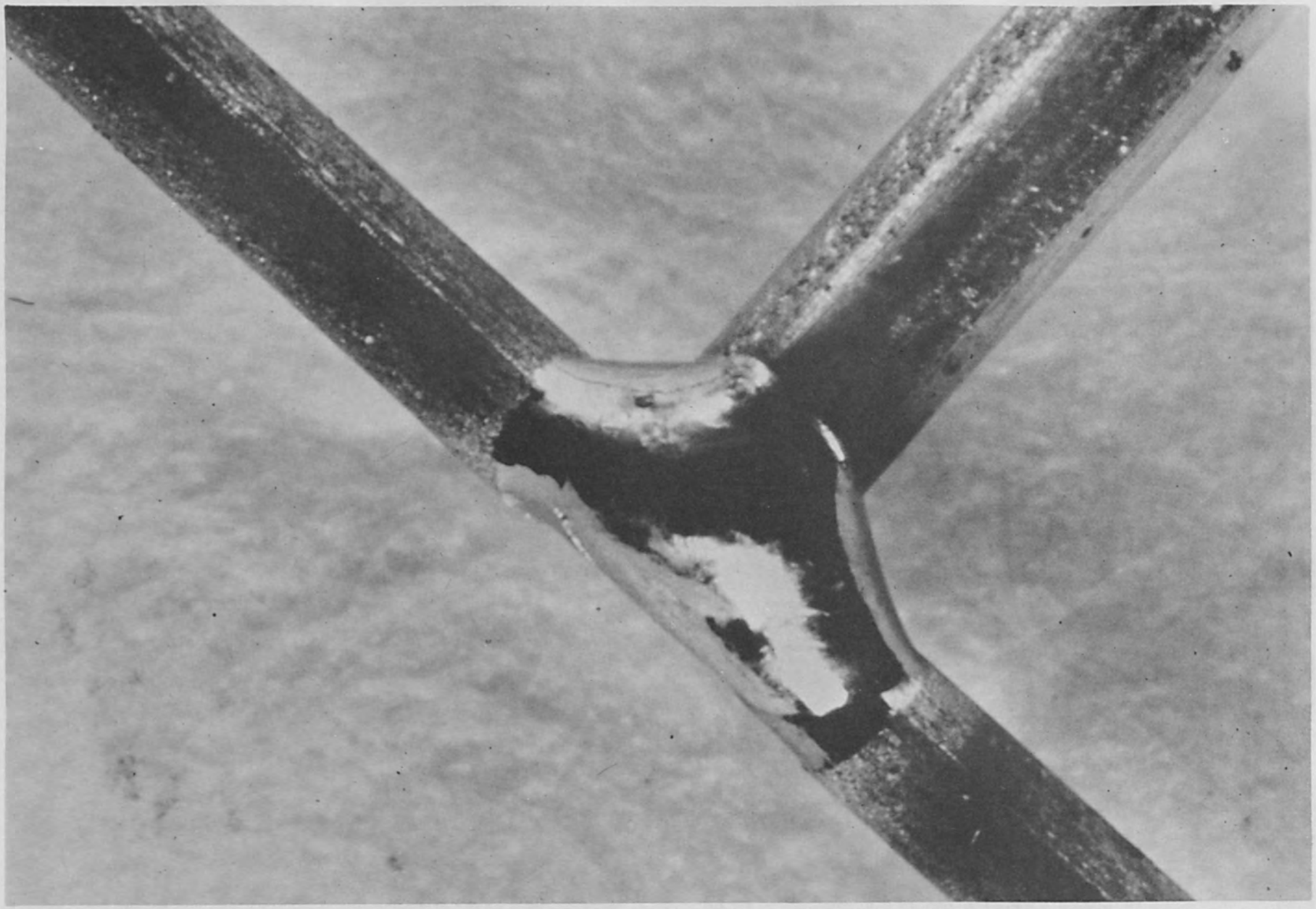

Figure 9 - Tee joint between 0.020-inch-diameter nickel wire and 0.015-inch-diameter tantalum wire.

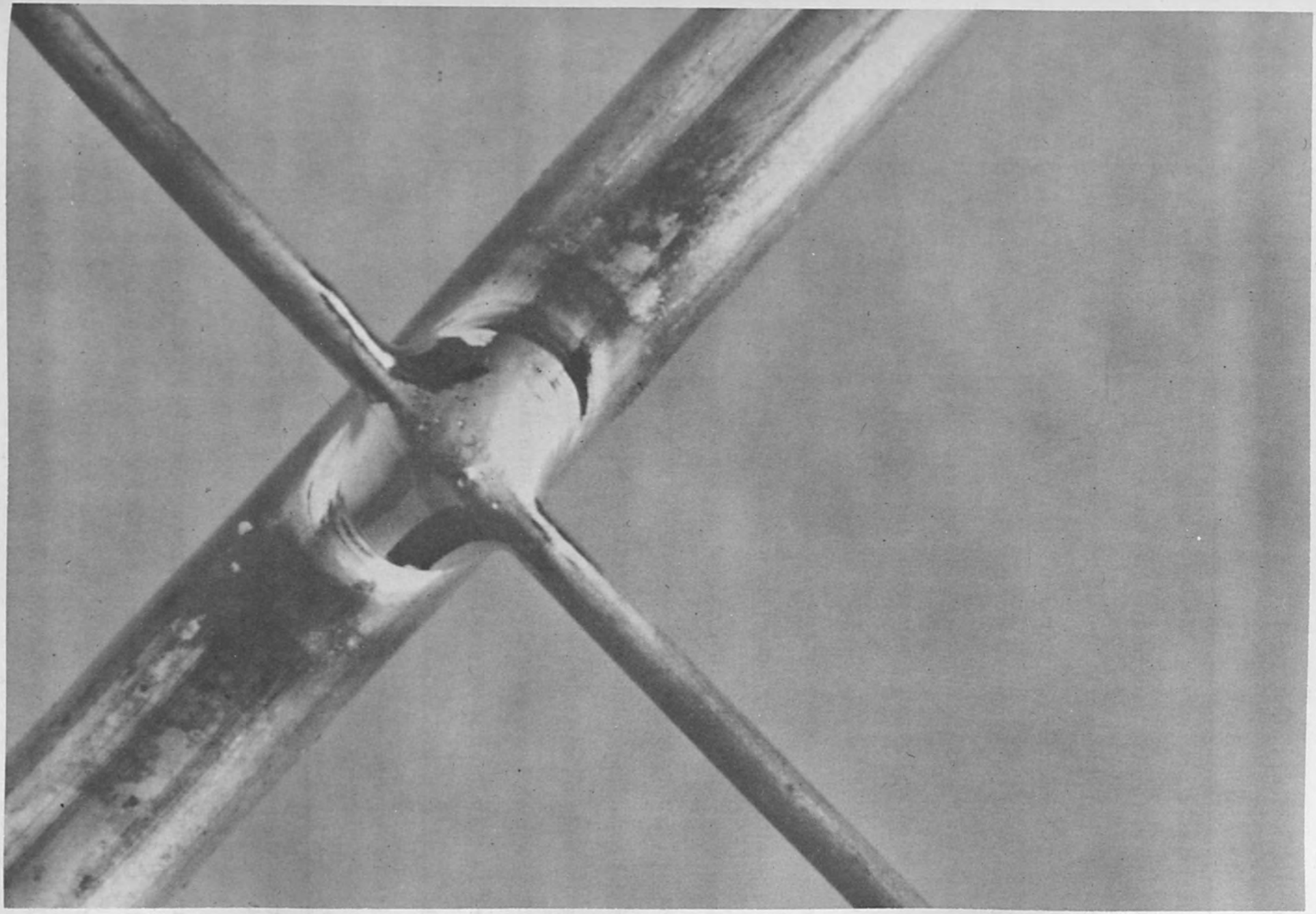

Figure 10 - Cross joint between 0.005-inch-diameter tungsten wire and 0.020-inch-diameter nickel wire.

resort to theoretical calculations. As a guide an approximate correlation, which was derived empirically, is given in Figure 11.

As mentioned previously, the laser output should be controlled to avoid surface boiling which can cause undercutting of the weld and even gouging. In order to avoid boiling the pulse length should be increased as the laser energy output increases. The relationship between laser energy and pulse length is a function of the weld joint and the properties of the material to be welded. The more advanced laser welders automatically provide an increase in pulse length with output. Consequently, when an operator selects a laser output, the machine selects the required pulse length.

The effect of process variations on welding results are illustrated in Figures 12-14. The effect of laser output on joint strength is shown in Figure 12. Around the desired laser output, a 10% change in output produces a 4% change in strength. While the sensitivity of strength-to-output is entirely within acceptable limits, the need for reproducible output in commercial equipment is apparent. The effect of focusing distance on strength is shown in Figure 13. In general one can probably deviate 0.050-inch from a focal length of 2-inch and still obtain acceptable welds. In Figure 14 the effect of wire separation on weld strength for lap welds is given. Although a gap of 0.005-inch can be tolerated for 0.020-inch diameter wires, no separation is recommended.

Sheet-To-Sheet Welds

Configurations for welds between thin gage sheets are shown in Figure 15. The first is a butt joint in which two pieces with square edges are placed side by side while the second is a lap joint in which one sheet is placed on top of the other. Generally the required laser energy output for welding a given thickness of sheet is approximately fifty percent higher than that required for welding the same diameter wire. Thus if 10 joules produces a fully penetrated weld on 0.015-inch diameter

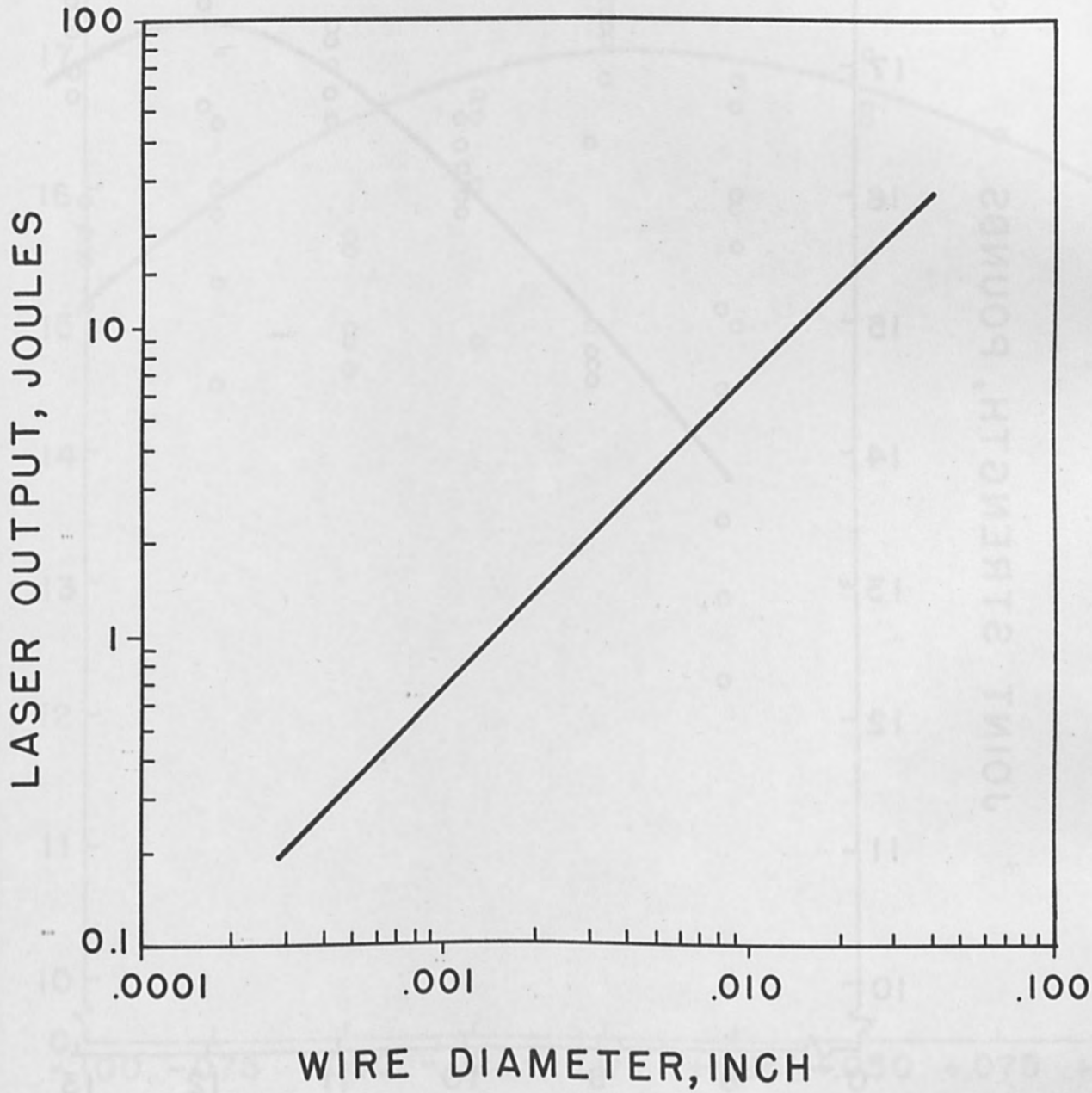

Figure 11 - Approximate laser output required for full strength welds for various wire diameters.

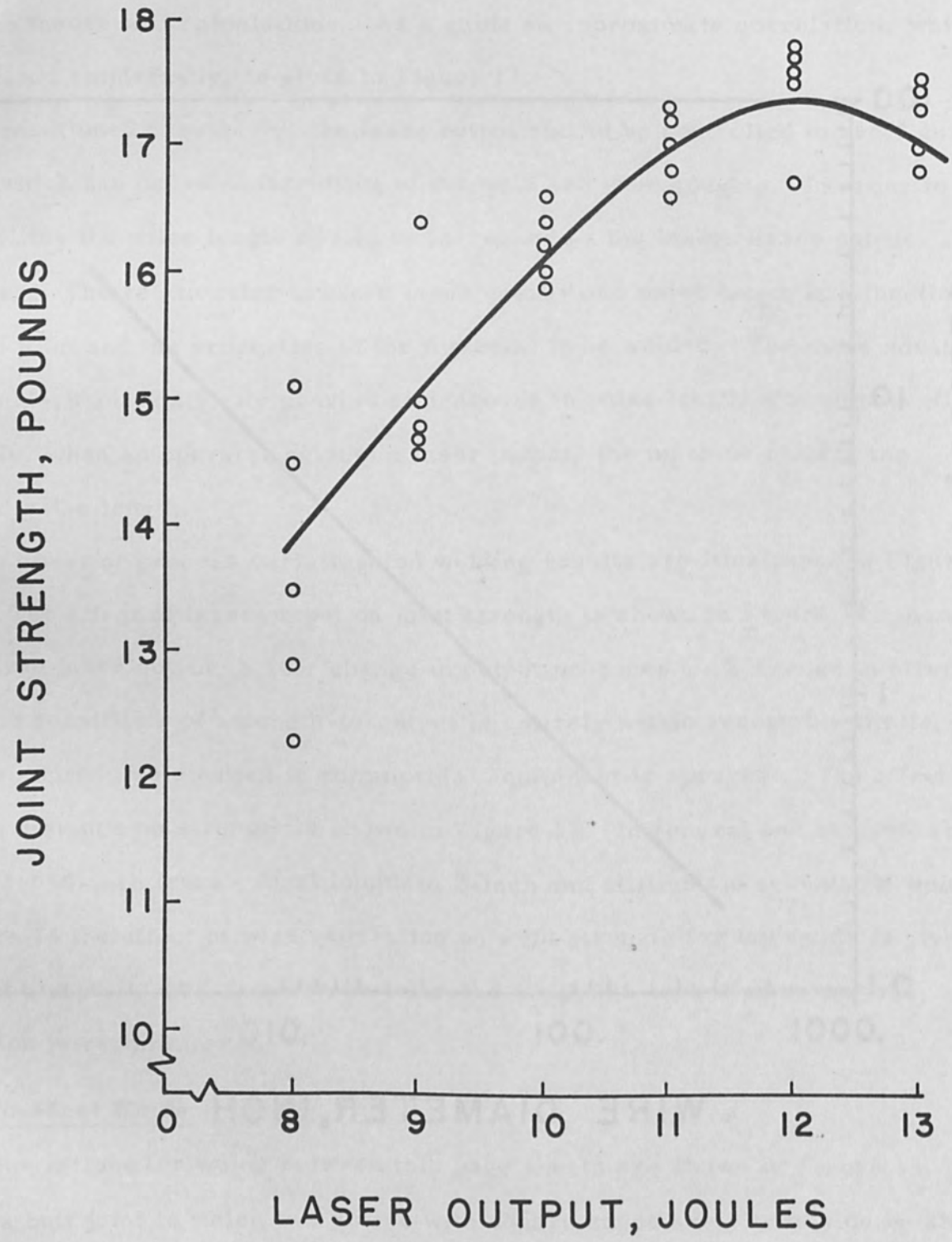

Figure 12 - The effect of laser output on joint strength for a lap weld between 0.020-inch-diameter nickel wires.

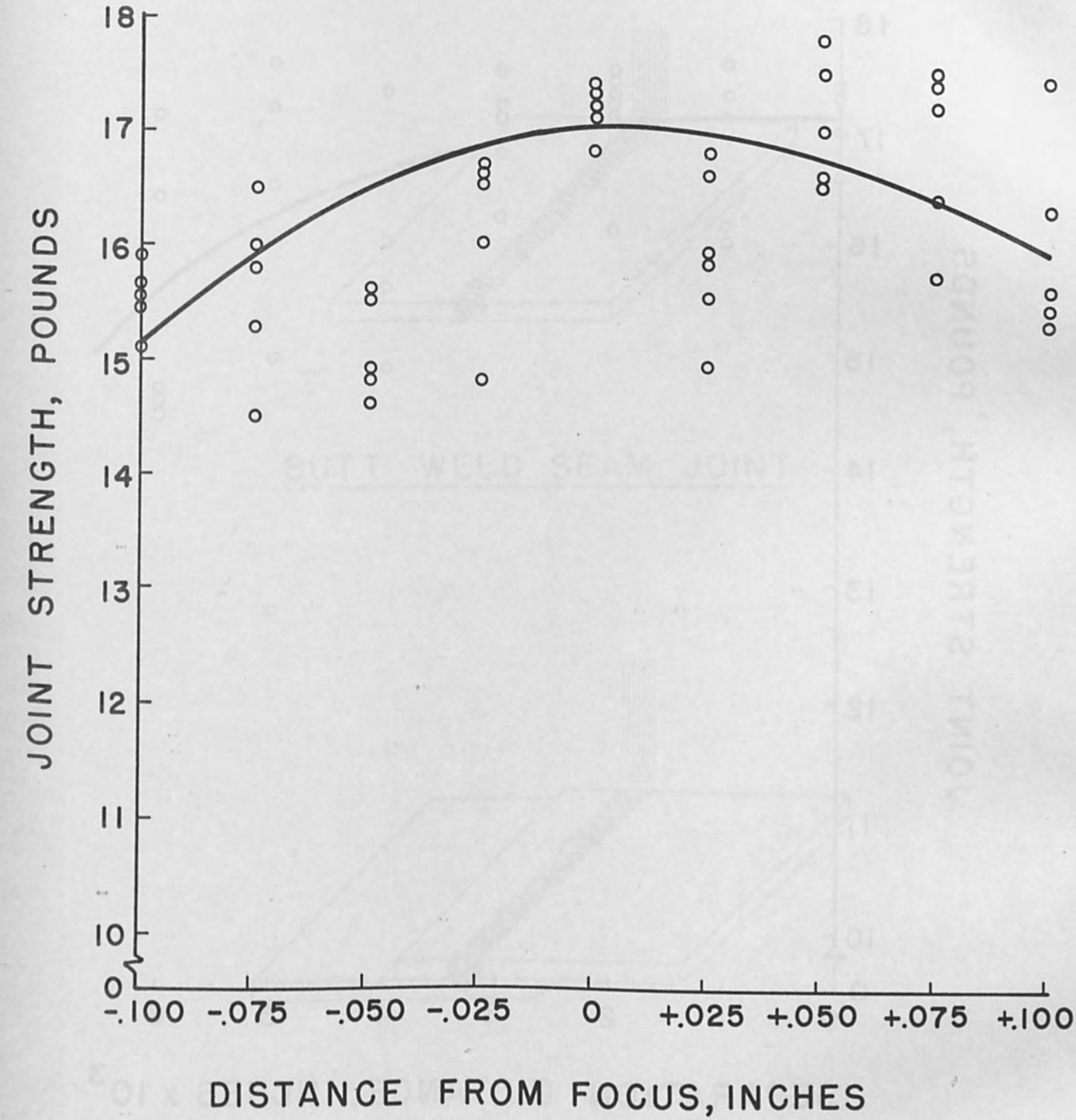

Figure 13 - The effect of distance from optical focal point on joint strength for a lap weld between 0.020-inch-diameter nickel wires.

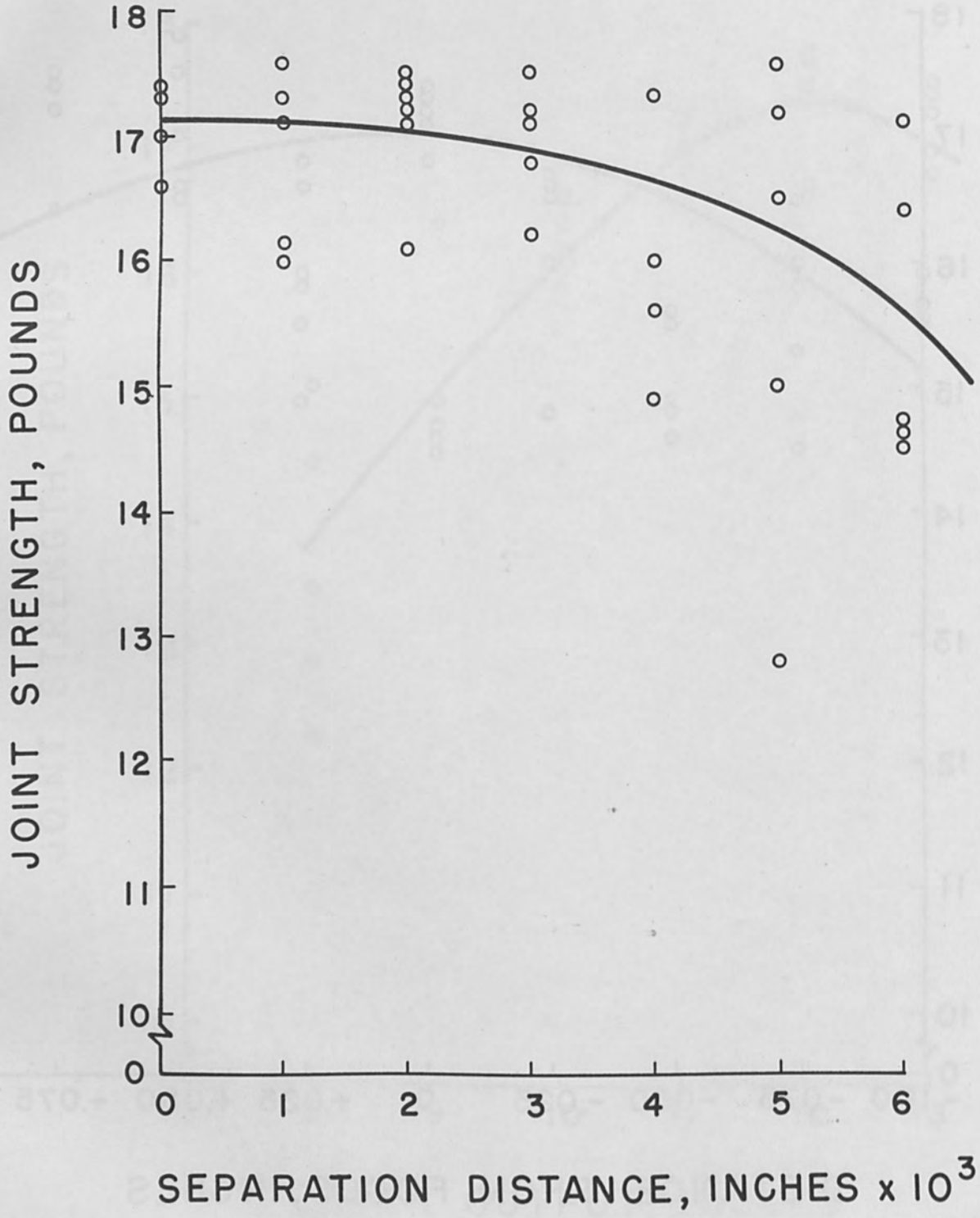

Figure 14 - The effect of joint separation distance on joint strength for a lap weld between 0.020-inch-diameter nickel wires.

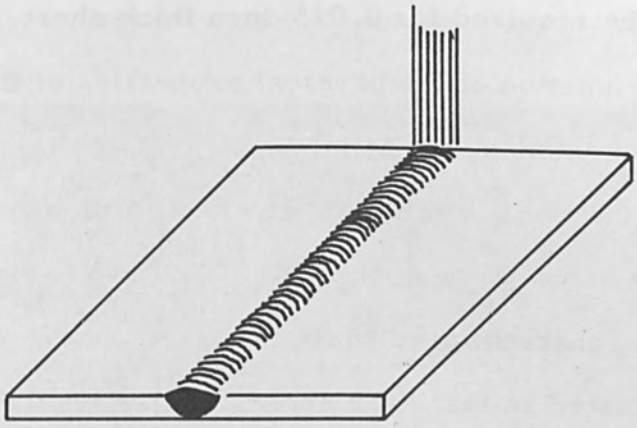

BUTT WELD SEAM JOINT

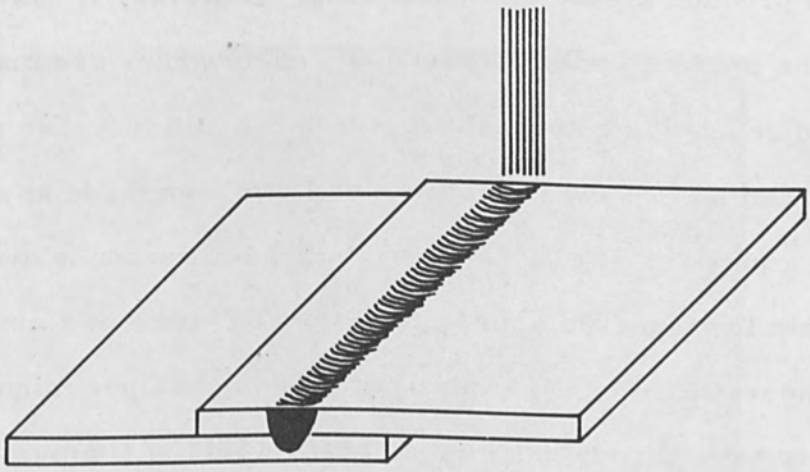

LAP WELDED SEAM JOINT

Figure 15 - Joint configurations for sheet-to-sheet welds.

wire, 15 joules will be required for 0.015-inch thick sheet. As with wire, the precise values are a function of the physical properties of the material as well as the absorptivity of the surface.

A seam weld on 0.010-inch thick Kovar sheet is pictured in Figure 16. This weld was made using overlapping spot welds. The two halves were traversed under the focused spot at a constant speed while the laser was repetitively fired. The travel speed was adjusted so that each spot partially overlapped the previous spot. The net result is a weld that for all practical purposes is a continuous seam. In Figure 17 a lap weld of a piece of tungsten and a piece of aluminum is shown. The spot welds are separated rather than overlapping. Because of the low melting point of the aluminum, the bottom of the weld is larger than the top.

At present seam welds are limited to low welding speeds and consequently to short lengths in practice. With the repetition rate of current lasers, it would take about an hour to produce a weld a few feet long. However, it has been shown that good welds can be produced with the laser and as advances are made in the laser power output and repetition rate, welding speeds should increase many fold. As an example of what can be expected, seam welds have been made at a speed of 1-inch per minute with a pulsed laser that is "on" only 3 milliseconds every 3 seconds. As the repetition rate is increased approaching the "on" time of a continuous laser, the welding speed theoretically should approach 1000-inches per minute.

Tensile tests have been performed on seam welds of titanium, tantalum, stainless steel and nickel. Table III shows the ultimate strength and mode of failure. Photographs of the welds after testing are shown in Figure 18. The strength of the base material is identical to the weld for titanium, tantalum and nickel. The stainless base has an ultimate strength of 200,000 psi. In general the performance is outstanding. The laser output was approximately 5 joules for the 0.005-inch thick material and 10 joules for the 0.010-inch. Usually for seam welds a slightly

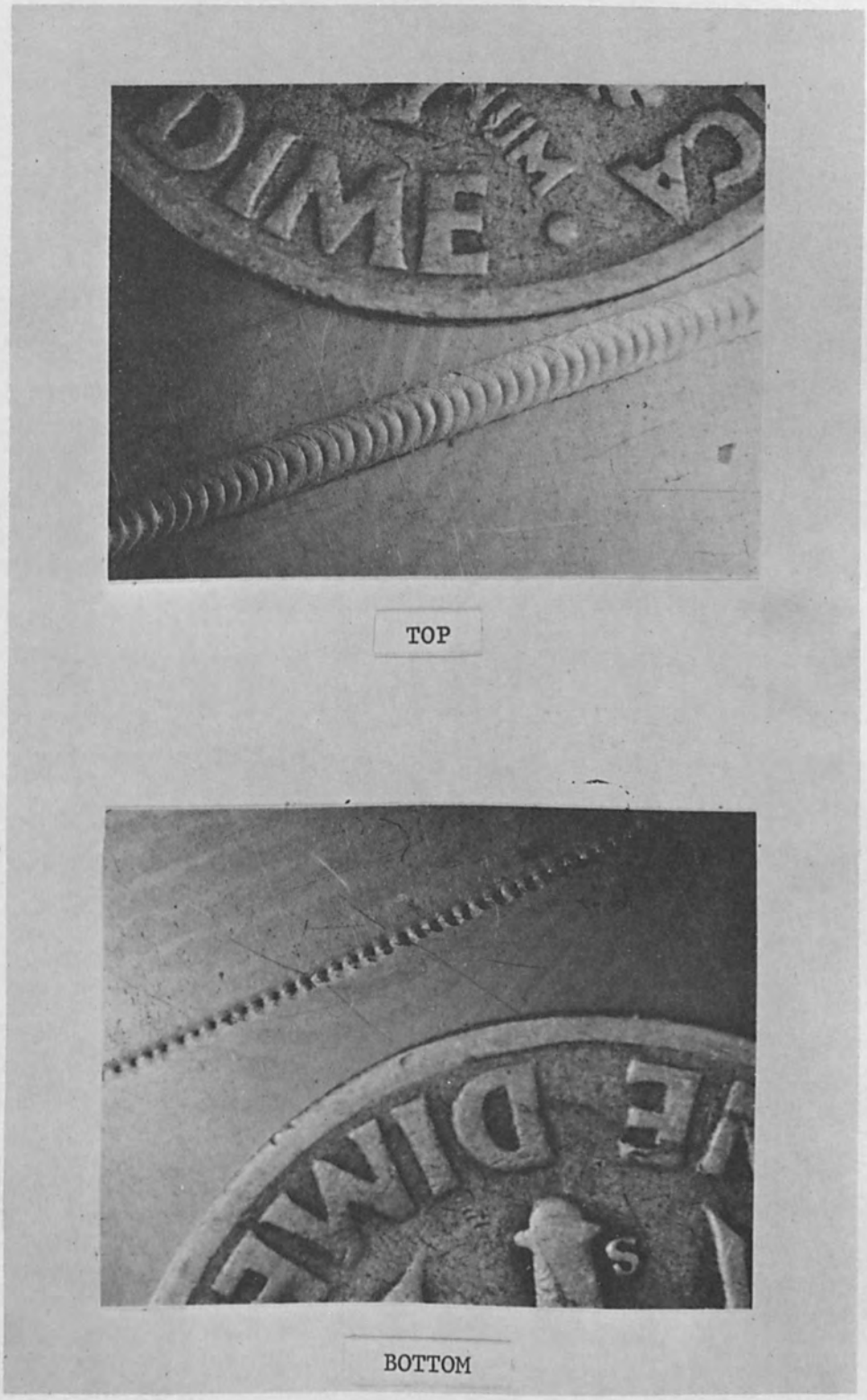

Figure 16 - Butt seam weld between 0.010-inch-thick kovar sheets.

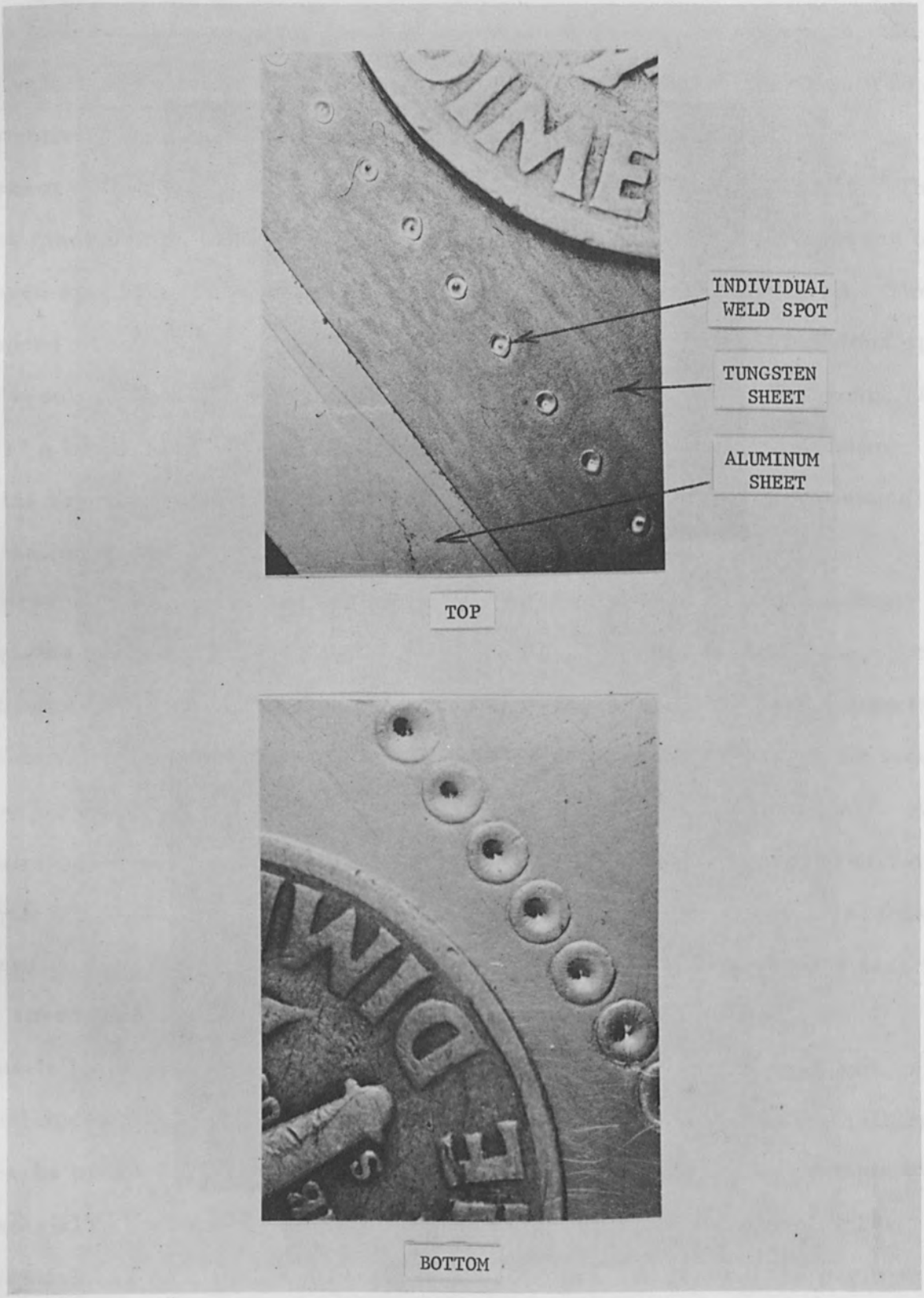

Figure 17 - Lap seam weld of 0.005-inch-thick tungsten sheet on top of 0.005-inch-thick aluminum sheet.

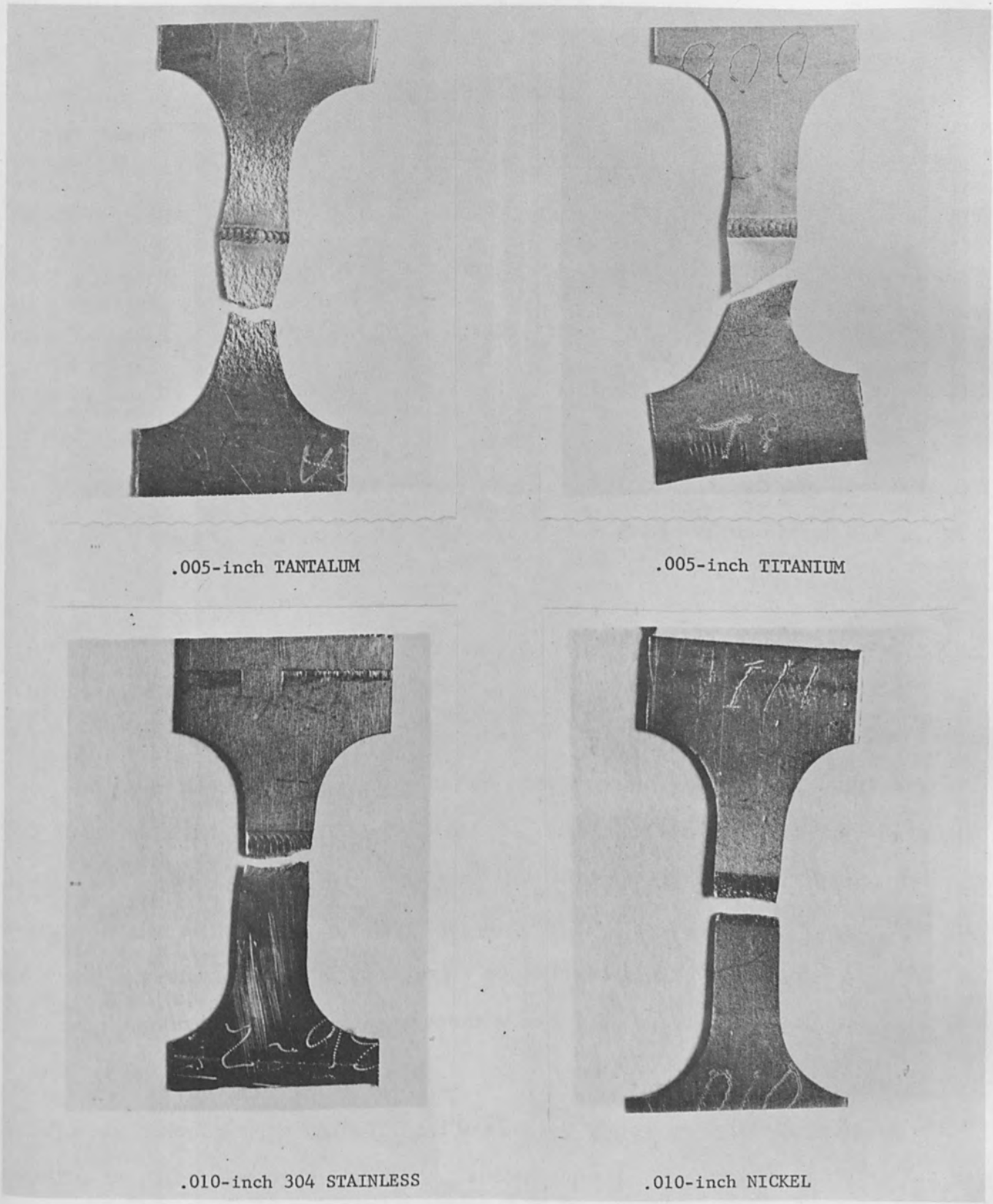

Figure 18 - Photographs of tensile specimens after testing.

TABLE 3

PROPERTIES OF SEAM WELDS

Material	Thickness	Test Width	Load	Stress	Mode of Failure
Titanium	.005-inch	1/8-inch	77 lbs.	123,000 lb/in^2	Broke in base
Tantalum	.005-inch	1/8-inch	29 lbs.	46,000 lb/in^2	Broke in base
Stainless (304)	.010-inch	1/8-inch	221 lbs.	176,000 lb/in^2	Broke in weld
Nickel	.010-inch	1/8-inch	110 lbs.	88,000 lb/in^2	Broke in weld

higher output than that required for full penetration is used so that an underbead 0.010-0.020-inch wide is produced. Then slight misalignment does not produce incomplete penetration.

Wire-To-Sheet Welds

The laser can be used to weld wires to sheet or larger solids. In Figure 19 a nickel wire is shown welded to a large piece of copper. This dramatically illustrates the ability of the laser to weld together pieces of different mass and physical properties. Laser spot welds of leads from a flat pack to a circuit board are pictured in Figure 20. Excellent welds also have been made between wires and film type circuit board material. A design configuration using wires with a slightly flattened end is preferred since it provides a greater contact area with the board and increases the allowable stress on a lead without pealing the coating off the board.

Applications

From an application viewpoint the pulsed laser welder can be looked upon as an unusual welding tool for unusual applications. It is doubtful that it will find utility for routine welding jobs that are adequately handled by more conventional processes. However, there are a number of "unusual welding problems" and the laser should

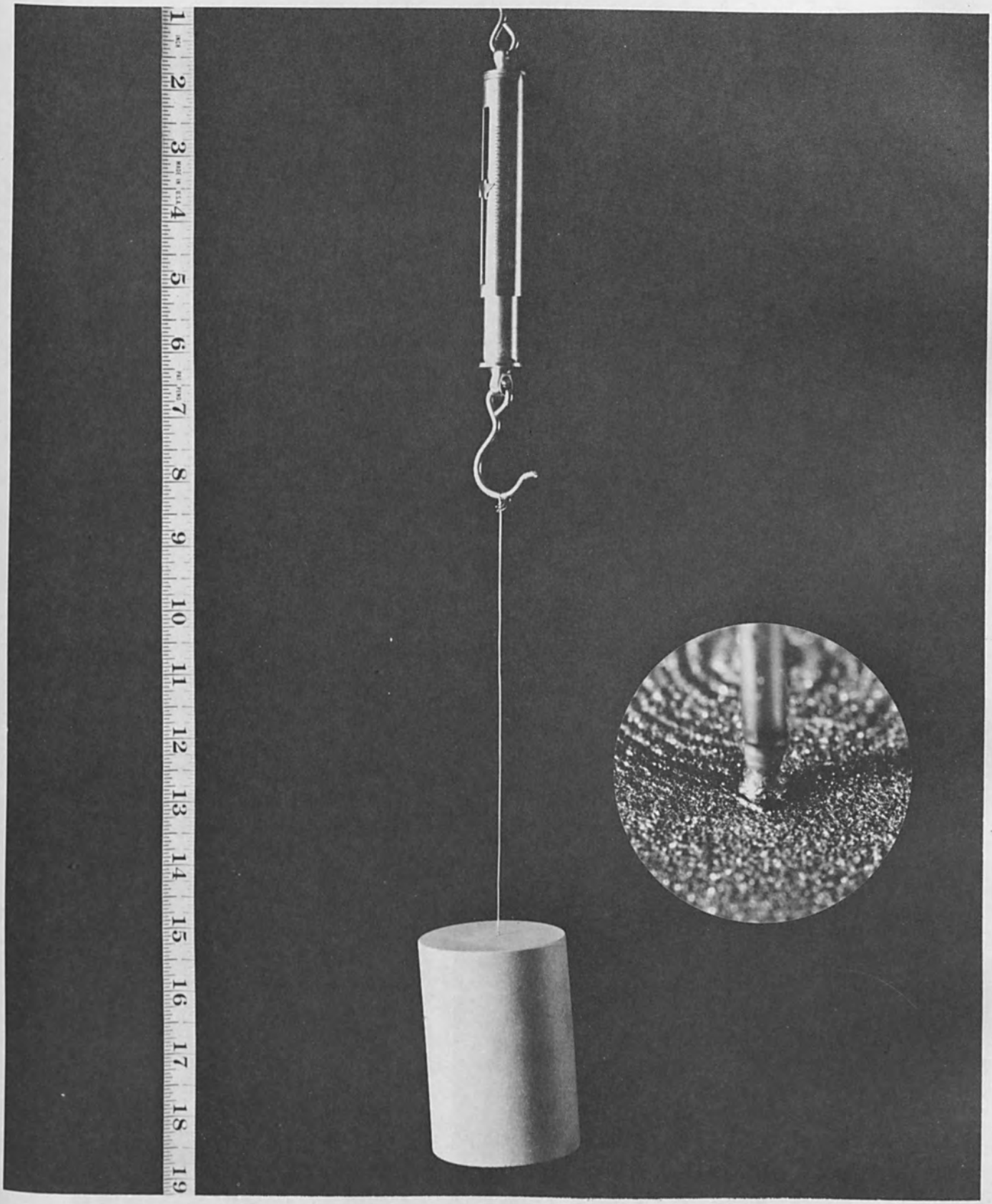

Figure 19 - Laser weld of 0.020-inch-diameter nickel wire to a four pound copper cylinder.

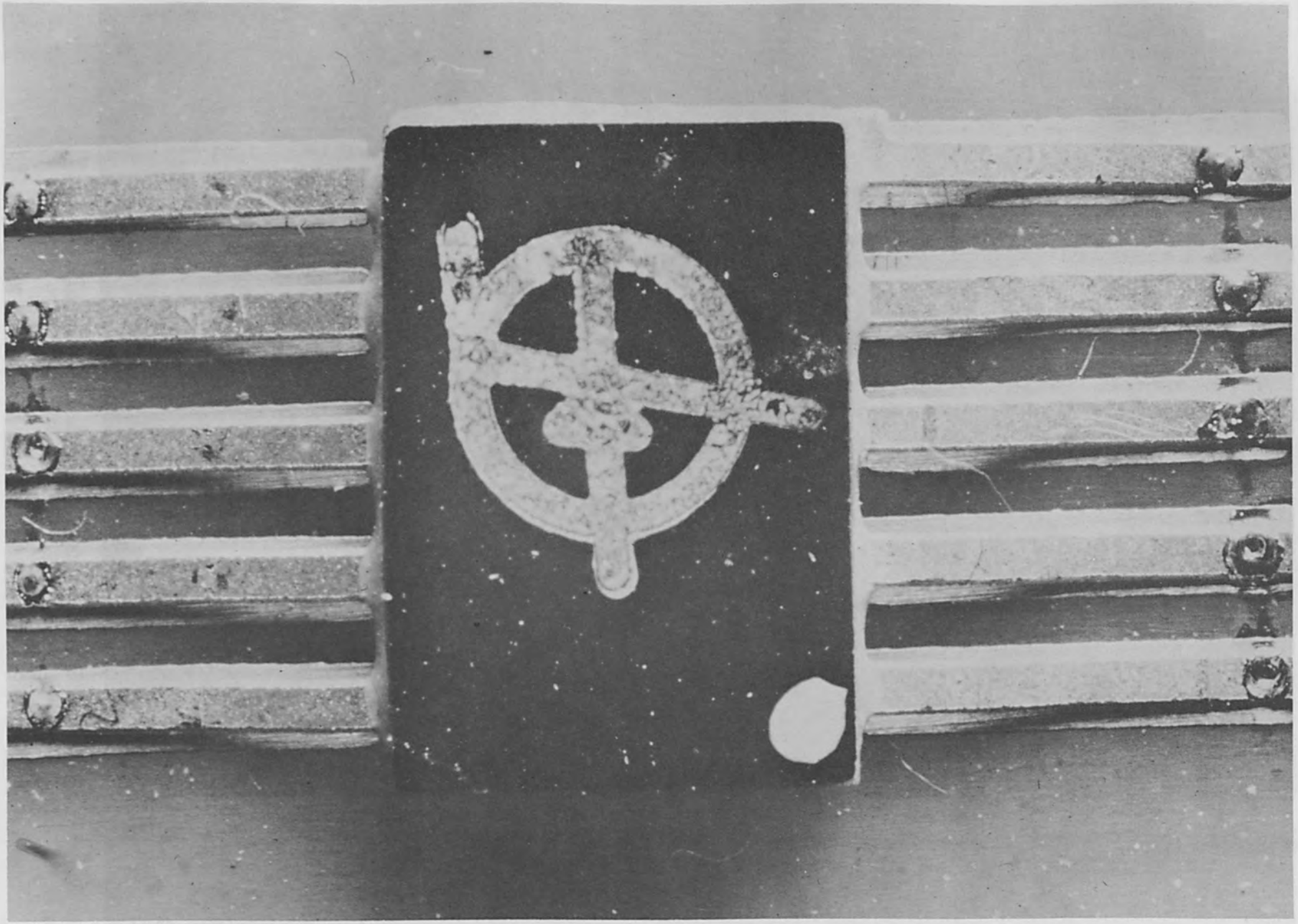

Figure 20 - Spot welds of leads from a flat pack to a circuit board.

prove the answer to many of them.

There are a few guidelines that can be used to determine when laser welding should be considered. In its present state of development an upper limit to the depth of the required weld bead should be about 1/32-inch. Most applications will probably involve welding pieces at thicknesses below 0.020-inch. In addition, the application should take advantage of at least one of the unique features of the laser. For emphasis they are summarized below:

1. The heat input to the workpiece is very small in comparison to other welding processes. This means that the width of the heat affected zone and the thermal damage to parts adjacent to the weld are minimized. The correspondingly fast cooling rates of the weld puddle may have metallurgical advantages for some applications.
2. The high power intensity of the laser can be used to advantage to make difficult welds. These may involve welds between dissimilar metals of widely varying physical properties, between metals of high electrical resistivity, or between parts varying greatly in mass and size.
3. Since the heat source is a light beam, direct contact with the workpiece is not necessary and less accessible joints can be welded provided a direct line of sight is available. Welding through transparent materials as well as in any desired atmosphere is possible.
4. Precision welding can be done with a well defined, focused spot. Spot sizes of the order of a few thousandths of an inch in diameter can be achieved along with accurate positioning.

An example of how the unique features of the laser can be used to advantage:

disconnected wires in a sealed vacuum tube have been joined in practice. The laser beam was first used to create thermal stresses in the wires to bring them closer together. Once they were in contact, they were laser welded. This was accomplished several times without breaking the vacuum seal or damaging parts adjacent to the weld.

The most promising single outlet for pulsed laser welding is the electronics industry. The rapid trend towards miniaturization has led to stringent joining requirements that very often cannot be met adequately by conventional techniques. Welding is preferred over soldering with the demand for higher reliability. The limited accessibility of the joint and the need for precise focusing while avoiding thermal damage to components all suggest laser welding. Connections to thin films, interconnections between integrated circuits, encapsulation, etc. are typical of the problems currently being examined.

Applications in other industries should appear as design engineers become familiar with the capabilities of the laser welder. As new equipment is being designed he can incorporate the laser welding technique into its construction to accomplish joining problems that heretofore were not feasible.

References

1. Adams, Jr., C. M. and R. H. Fairbanks, Sr., "Laser Beam Fusion Welding", Welding Journal, 43, pp 97s-102s (1964).
2. Anderson, J. E. and E. F. Stresino, "Heat Transfer from Flames Impinging on Flat and Cylindrical Surfaces", Journal of Heat Transfer, 85, Series C, pp 49-54 (1963).
3. Nestor, O. H., "Heat Intensity and Current Density Distributions at the Anode of High Current, Inert Gas Arcs", Journal of Applied Physics, 33, pp 1638-1648 (1962).

The Ablation of a Metal by Excited Particles

by

K. W. Arnold
Avco RAD
Wilmington, Massachusetts

Abstract

The measured evaporation rate of material from the cathode of a low current (about 10 amp) d. c vacuum arc cannot be explained by evaporation theory because the cathode spot temperature is too low. A recent hypothesis proposes that evaporation (or ablation) of cathodes occurs rather because they are bombarded with excited atomic or molecular species, which give their energy preferentially to the more loosely bound atoms on the cathode surface: these atoms then escape from the metal and constitute a form of evaporation. To test this hypothesis a carbon arc was operated at low pressure and the ablation rate of the cathode measured both when excited particles were present in the region close to the cathode, and when they were absent. The high ablation rate observed in the former case is strongly consistent with the original assumption that the excited particle flux does ablate the cathode surface.

Introduction

Two of the more interesting problems of the physics of the arc discharge are to explain the mechanism of electron emission at the cathode, and the nature of the evaporation process there. It was during a consideration of these problems that the concept of ablation by excited particles arose; this is the main theme of the paper, but necessary to it are some observations on low current ($i < 10^2$ amp) arc discharges.

These normally belong to one of two categories which are determined by the nature of the cathode spot. It appears that the relevant factor is whether intense

evaporation or thermionic emission of electrons sets in first when the spot temperature is raised. Observations of arcs in air at ordinary pressures show that refractory metals (carbon, silicon, molybdenum, tungsten) support a relatively large, stationary spot having a low current density at the cathode $j_c \sim 10^2 \text{amp/cm}^2$, whilst metals with a low boiling point (copper, mercury, iron) exhibit small mobile spots with j_c of the order of 10^6 amp/cm^2 or more.[1] With the latter the spot appears to be covered with a dense highly luminous layer of cathode vapor, which is not present in the case of refractory cathodes. Arc discharges with refractory cathodes are called "thermionic" arcs, whilst the other type are known as "vapor" or "cold-cathode" arcs.

Electron emission from a thermionic cathode is in good agreement with Richardson's equation:[2] non-refractory metals, however, are completely unable to support the high temperatures requisite for thermionic emission, although this was once thought to apply.[3] Later theories have suggested field emission,[4] thermal ionization of the ambient gas,[5] photo-emission,[6] etc., but the evidence for these mechanisms is not convincing.

A newer theory supposes that electrons are emitted from cold-cathode arc spots by excited atoms.[7] Large concentrations of excited atoms are assumed in the region of dense vapor close to the cathode. Excited atoms, back-scattered to the cathode or produced by the absorption of ultra-violet quanta lose their energy by releasing electrons from the cathode surface rather than by radiation: this is because with the densities near the cathode surface the collision time is shorter than the lifetime of the excited atoms. The electrons then gain sufficient energy in the cathode fall to excite more vapor atoms.

It is clear that this theory could explain electron emission from a cathode spot on a low boiling point metal, and it was thought that although this spot temperature was not high enough for thermionic emission of electrons, it was, nevertheless,

high enough to account for the observed cathode evaporation rate.[8] However, calorimetric measurements show that 40-50% of the arc energy input goes to the cathode, and when the energy loss by thermal conduction into a copper cathode is calculated knowing minimum arcing voltages, it appears that the actual spot temperature may be only 50% or so of the 2500°K necessary to account for the observed evaporation rate if accepted evaporation theory is invoked.[9] The picture is further complicated because the observed evaporation rate is probably considerably lower than the actual evaporation rate, which must really be accounted for.[7]

This paper then is concerned with the evaporation of vapor arc cathodes, and the more general conclusions that can be drawn from the suggested evaporation mechanism.

Ablation by Excited Particles

The main difference between heating a metal to produce vapor, and the production of vapor in a cathode spot is that in the former case heating of the metal is done from underneath and energy communicated to the surface by lattice vibrations, whereas in the latter case there is an energy influx to the spot from above the surface.

Positive ions and fast neutral particles from charge transfer impinge on the spot, both species bringing kinetic energy, and the ions ionization energy as well. Large numbers of vapor atoms also hit the spot, bringing kinetic energy which would for the most part have been brought by positive ions if the vapor atoms had not been interposed. However, many of the vapor atoms are excited, and the spot receives not only quanta but excitation energy directly from atoms hitting the spot before they have an opportunity to radiate. Evaporation energy is also gained if vapor atoms are absorbed back into the lattice.

It was mentioned above that the excited atoms may liberate electrons from the

cathode if the excitation energy exceeds the electronic work function of the cathode; however, the several excited vapor states which are not energetic enough to release electrons still communicate their energy to the spot. But in the spot are lattice atoms at different crystal positions,[9] some only absorbed and some more strongly bound. It is supposed that a lattice atom absorbs (and can re-emit) several small amounts of potential energy from incident species, and moves from its original site through intermediate positions to a final position which corresponds to an energy close to the boundary - from here it ultimately evaporates.[10]

Thus, atoms which are absorbed on the crystal surface may receive enough energy from impinging excited species to cause them to evaporate, atoms in the half-crystal position may be moved to a step, etc. Not only the lower excited states may expend energy in this way, but also higher states which might also have released electrons from the cathode.

It might be thought that an excited atom would rather give its energy to the lattice, causing only an increase in lattice vibrations. This may sometimes happen, but in a different way: the excitation energy may raise an atom to a less strongly bound position on the crystal surface, from where it moves back into its original state after a certain time (if it is not first removed to a higher state). In returning to its original state the binding energy is communicated to the lattice and the process is equivalent to handing the original energy to the lattice after a delay in time. However, in the cathode spot of an arc a high flux of excited particles is experienced, so that the likelihood of an atom once removed to a position of low binding energy returning to its original state is small.

Experimental Confirmation

In order to test the ablative properties of a beam of excited particles, one must first provide an excited particle flux, and then find a way of measuring its effect on a chosen surface. Because of the experimental difficulty of creating a

copious flux of excited particles, it was decided to utilize an arc discharge, and specifically a carbon arc discharge.

It is known that in air at atmospheric pressure the d. c. arc between carbon electrodes is thermionic in nature. As the gas pressure is reduced, a critical point is reached where the cathode spot changes instantaneously to a vapor spot. If the pressure is again increased, the spot reverts to the thermionic mode again. An explanation of these two modes has been given: starting with a vapor spot on a carbon cathode, as the ambient gas pressure is raised a point is reached when a sufficient concentration of N_2 molecules exists to quench the excited carbon vapor close to the cathode spot. This vapor is responsible for electron emission, so that when it is quenched, either the arc must be extinguished or exist in another, i. e. thermionic, mode.[11]

Thus, if a carbon arc is run in air at various ambient pressures, and the ablation rate of the cathode measured for both spot modes close to the critical pressure p_c at which the modes change, it should be possible to detect a much greater ablation rate of the cathode in the so-called vapor spot mode than in the thermionic mode. This is because excited particles exist close to the spot in the vapor mode and could ablate the cathode, whereas they do not exist there in the thermionic mode.

Figure 1 shows the relationship between the cathode ablation rate Q in gms/coulomb and the ambient pressure in torr for a carbon arc. For pressures $p < p_c$ the cathode spot is in the vapor mode, and excited particles exist there, whereas for $p > p_c$ the mode is thermionic. It can be clearly seen that Q is much higher for the vapor mode.

The high values of Q for $p \sim 760$ torr are caused by chemical action between the hot carbon electrodes and the ambient gas, and should not be confused with the phenomena happening at $p \leq p_c$, when carbon is ablated from the cathode as a

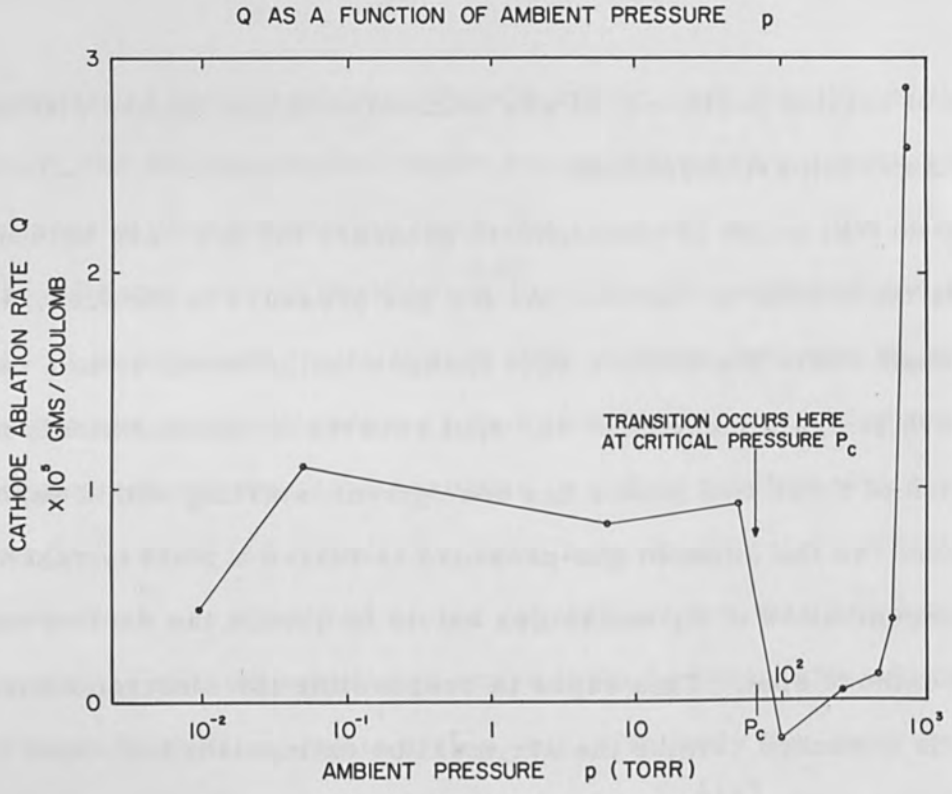

Figure 1

vapor. Similarly the value of Q for $p = 10^2$ torr shows that the cathode actually gained weight during arcing: this is because some carbon vapor from the anode condensed on it during the experiment.

The point of Figure 1 is simply to show that for $p \approx 80$ torr (and with excited particles present) the carbon cathode was ablated at a rate of 10^{-5} gms/coulomb, while for $p \approx 100$ torr (and with no excited particles present) the cathode ablation rate was essentially zero.

Discussion

Certain assumptions have been made in this paper. Firstly, emission of electrons by excited particles is supposed to be the predominant electron emission mechanism at the cathode of a vapor arc.[7] From this it is further supposed that excited states which do not contribute to electron emission can, nevertheless, give their energy to lattice atoms absorbed on the cathode surface, so that these are evaporated or ablated. To test this hypothesis experimentally a carbon arc was

used and the ablation of the cathode measured for the arc spot in the vapor and in the thermionic mode. It is assumed that excited particles exist in the vapor spot region, but do not for the thermionic spot.[11]

There is a good deal of evidence for the validity of these assumptions, however, and it is interesting to note the role played by the excited particle. While certain questions are not yet answered, it does appear that excited particles are responsible for the ablation of vapor arc cathodes, and this process may be significant also in other contexts.

References

1. von Engel, A., Ionized Gases, Clarendon Press, Oxford (1955).
2. de Boer, J. H., Electron Emission, C.U.P. (1935).
3. Stark, J., Phys. Z. 5, 750 (1904).
4. Langmuir, J., Gen. Elect. Rev. 26, 731 (1923).
   Compton, K. T., Phys. Rev. 21, 266 (1923).
5. Slepian, J., Phys. Rev. 27, 407 (1926).
   Weizel, W., et al., Z.f.Phys. 115, 179 (1950).
6. Thomson, J. J., Phil. Mag. 48, 1 (1924).
7. von Engel, A. and A. E. Robson, Proc. Roy. Soc. 242, 217 (1957).
8. von Engel, A. and M. Steenbeck, Elektrische Gasentladungen, Vols. 1 and 2, Springer, Berlin (1932-34).
9. Knacke, O. and I. Stranski, Prog. in Metal Phys. 6, 181 (1956).
10. von Engel, A. and K. W. Arnold, Nature 187, 1101 (1960).
11. von Engel, A. and K. W. Arnold, Proc. Phys. Soc. 79, 1098 (1962).

Electron Beam Simulation of Aerospace Vehicle Heating Rates

by

D. L. Martin and W. W. Woods
The Boeing Company
Seattle, Washington

Abstract

A modified commercial electron beam welder is used as the basis of a system which functions as a simulator of total heat flux for development, test, and calibration of heat rate instruments used in advanced aerospace programs. This equipment has been used to calibrate calorimeters from a few watts/cm^2 to greater than 5000 watts/cm^2. A variety of transient heating rate conditions have been simulated.

Introduction

The development of advanced aero-space vehicles such as supersonic aircraft, missiles, and planetary re-entry vehicles, has emphasized the need for aerodynamic heating rate instrumentation. Where the thermal interchange rate a few years ago was of the order of 1 to 5 watts/cm^2, now measurements of 1000 to 5000 watts/cm^2 are demanded. This drastic increase in levels has rapidly made obsolete the more common laboratory methods of environmental simulation and instrument calibration.

Background

A short summary of a typical instrument and calibration system will illustrate the problems involved. Figure 1 illustrates a common type of heating rate transducer. A thin metal diaphragm is attached at its edge to a thermal sink. Two lead wires attached to the diaphram at its center and at the edge form thermocouple junctions such that a difference in temperature between the junctions produces an emf. An input of uniform thermal power density to the metal diaphragm will

FIGURE 1
HEATING RATE TRANSDUCER

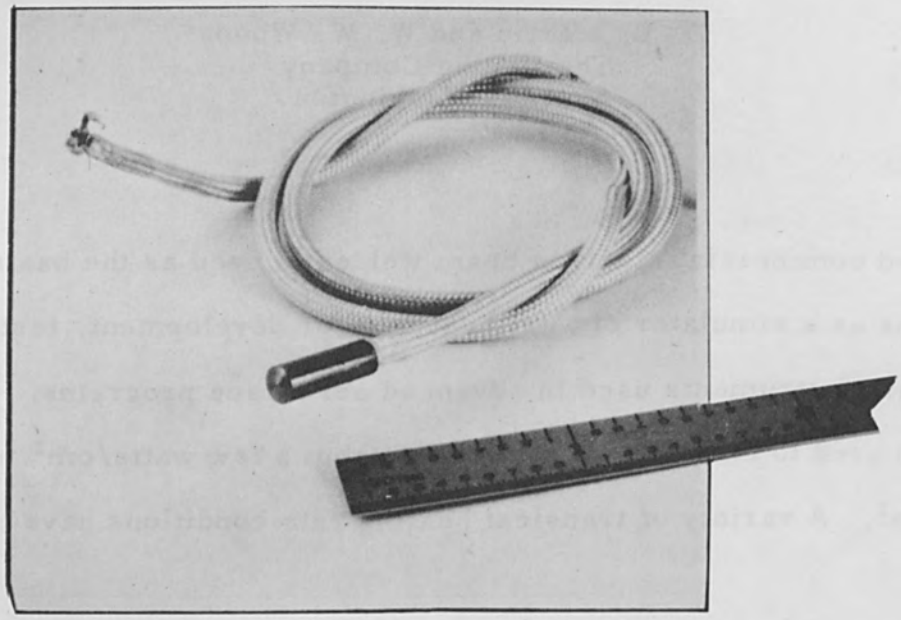

A

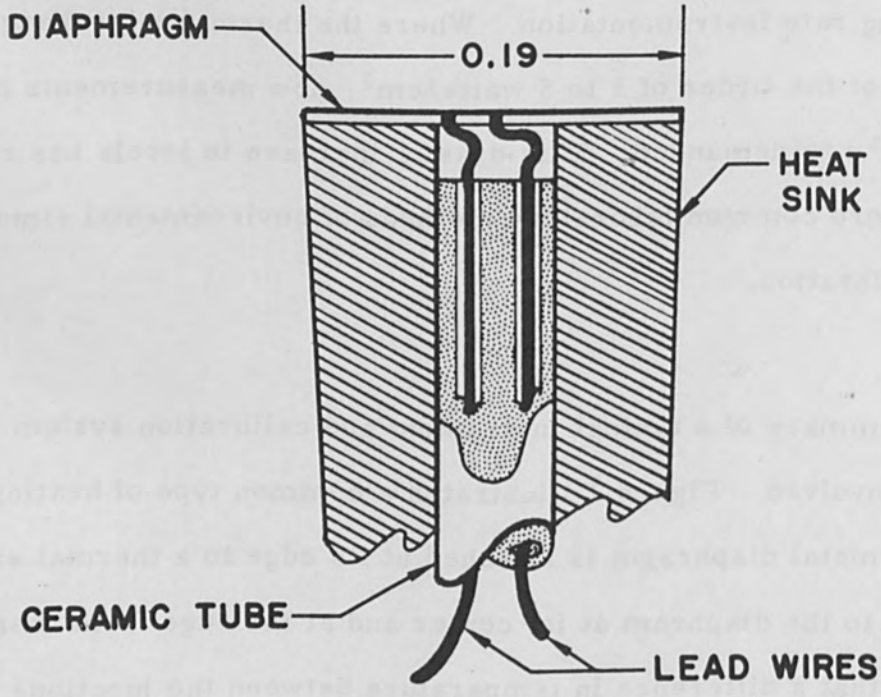

B

produce a thermal gradient across the diaphragm in proportion to the power density input. This gradient is indicated by the emf appearing at the lead wires. This type of instrument is generally installed flush with the surface of the vehicle and is used to sense combined convective and radiative thermal input.

A common method for testing and calibration of this type of sensor is the flat-plate thermal radiation source, or gray body. As shown in Figure 2, this takes the form of a rectangular graphite plate heated to incandescence by the passage of electrical current through it. With a water-cooled protective housing purged by argon gas to exclude oxygen, this type of facility allows close approach of the test instrumentation such that the 180° field of view of the instrument is essentially filled. Blackening of the instrument diaphragm with soot provides a reproducible radiation-absorbing surface, and the radiant power may be measured by comparison to a black body at known temperatures.

This method works well at power densities from approximately 1 to 400 watts/cm^2. At the upper value, however, the radiation source has a quite limited life, as this corresponds to a temperature of $2650^{\circ}C$ ($4800^{\circ}F$), where the vapor pressure of the graphite plate is increasing rapidly. Substitution of lower vapor pressure material such as tungsten does not help materially, as the emittance values are so low that higher temperatures and equivalent vapor pressures are encountered for equivalent power output.

In view of the above considerations, it appeared that a different type of power source was called for. The source must be capable of close control and uniform power density over an appreciable area, and must be amenable to calibration. Electron beam methods appeared to fulfill these requirements most adequately, and several firms had recently marketed welding and melting equipment which could be adapted to the purpose. Accordingly, an electron beam system with a 30 KV, 15 KW, grid-controlled gun was purchased. At the time of purchase, it

FIGURE 2
FLAT PLATE THERMAL RADIATION SOURCE

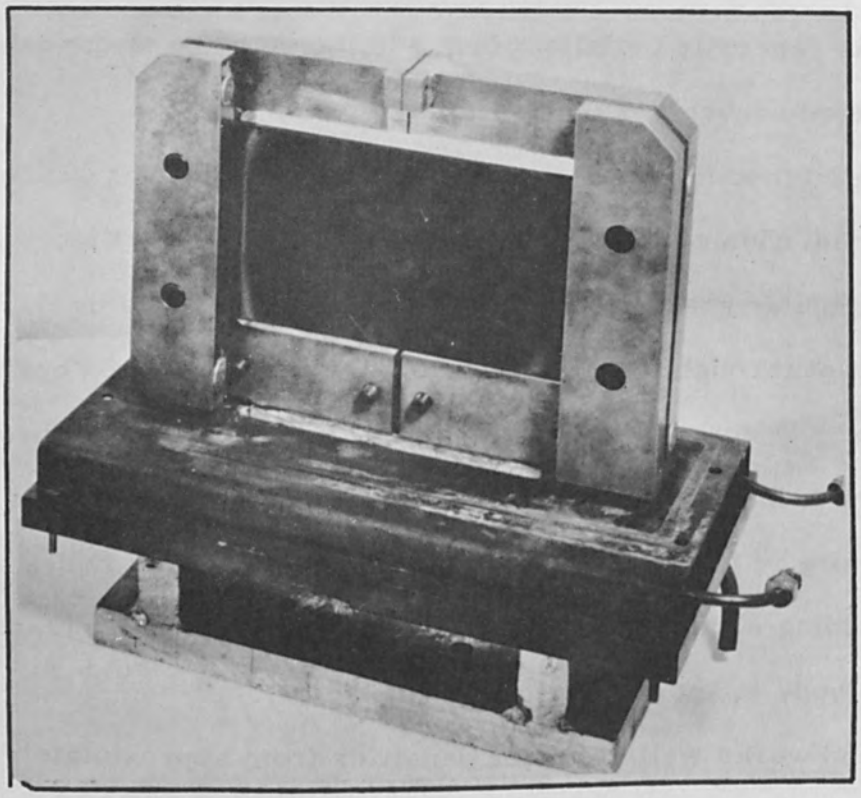

A

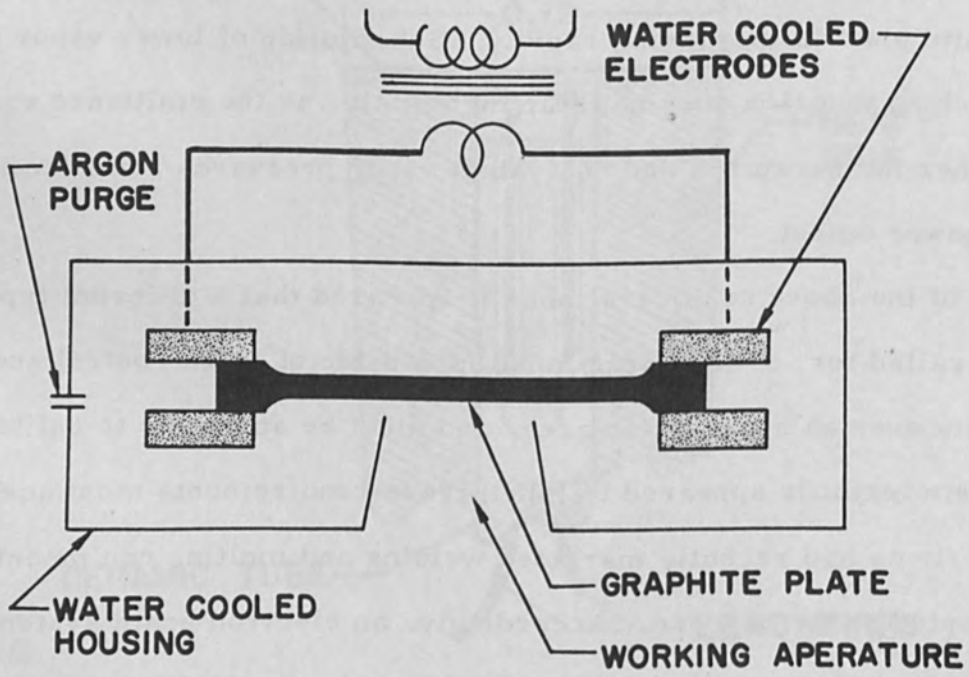

B

was envisioned that considerable modification would probably be necessary to achieve desired performance from standard electron beam equipment.

Initial Work

Initial attempts to obtain uniform illumination involved the use of a stationary, defocussed beam. The focus supply was redesigned and rebuilt to obtain a wider range of focus current, but to no avail. Variations of less than 20% in illumination intensity over a one inch square with any appreciable power density was very difficult to obtain. Very slight changes in the hairpin filament geometry produced large changes in the defocussed spot.

Attempts to determine time constant of developmental instruments by switching the high voltage on and off resulted in minor disaster. The focus current was set for underfocus at operating voltage, and as the cathode voltage swept through the voltage at which the beam would focus (a matter of fractions of a millisecond), a hole would be punched through the thin metal diaphragm of the instrument, effectively destroying the instrument.

The next logical alternative to high voltage switching of a defocussed spot was to utilize a high speed raster scan with the beam deflection system. The deflection coils supplied in the electron beam system were high impedance, television-type coils, housed in a metal can which made operation above 200 cps essentially impossible. Deflection circuitry supplied consisted of manual rheostat controls suitable only for static positioning.

System Modification and Adaptation

A few calculations showed that any attempts to use the provided equipment for sweep rates above 20 KC would be fruitless. Accordingly, a low impedance stator-wound yoke (Figure 3) was constructed, and transistorized sweep amplifiers and oscillators designed and built to drive it. As the backlog of work for this facility was piling up, however, no attempt was made to remove the original beam control

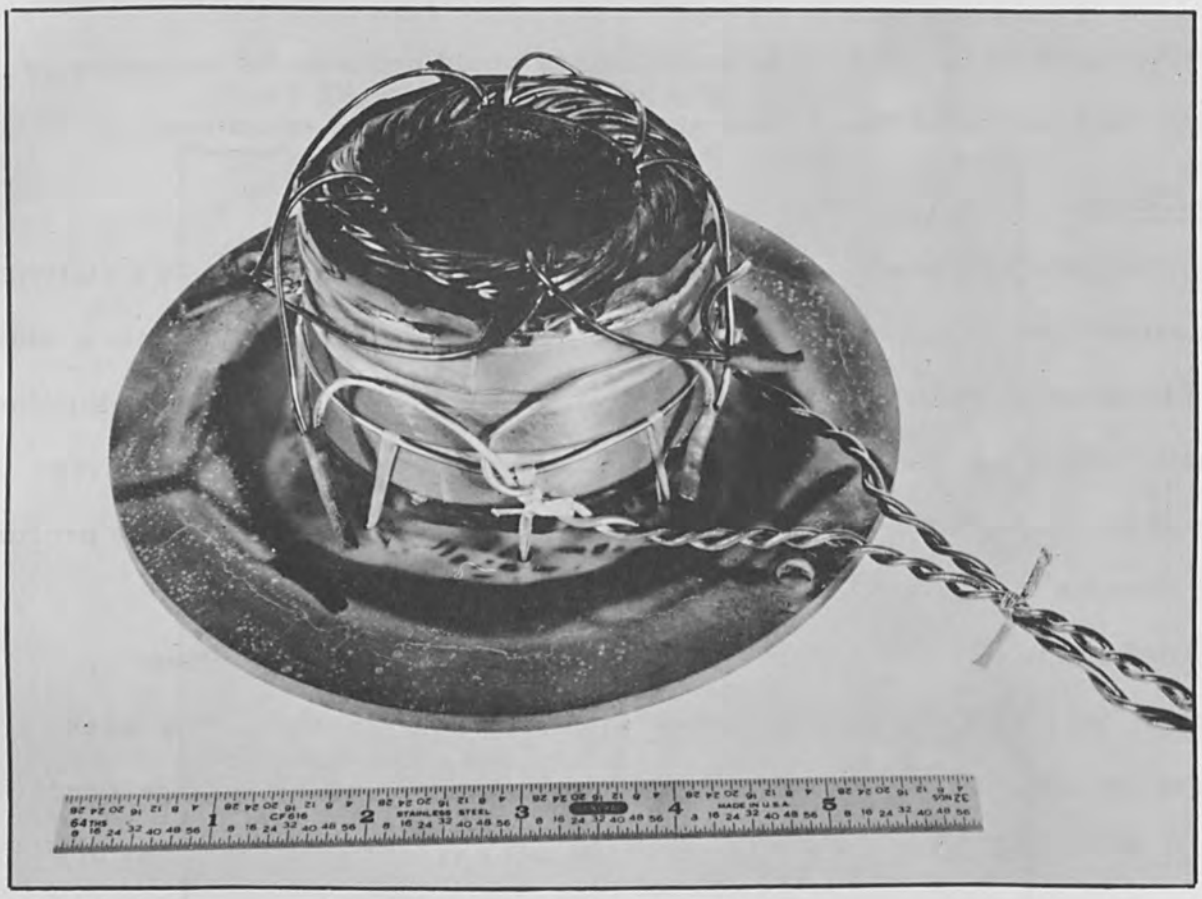

FIGURE 3 DEFLECTION YOKE

equipment, and a mount for the new beam deflection yoke was jury-rigged at the base of the original can, as shown in Figure 4. This arrangement allowed a raster pattern on the work piece of 3 inches square up to sweep rates of 60 KC and 2 inches at 100 KC. The sweep amplifier is limited to ±3 amperes and ±15 volts. Greater sweep sensitivity would be afforded by moving the deflection yoke up to the position of the original device, allowing a longer "throw" and a smaller throat diameter.

The high sweep rates described are mandated by the need for averaging over the time constant of the fastest sensors employed (3 milliseconds or greater). A rolling Lissajous pattern of anharmonic x and y frequencies together with a triangular sweep current wave form insures uniform average illumination. A second input to the amplifier allowed addition of a step input such that the position of the entire pattern could be shifted within 10 microseconds to allow instrument rise time determination.

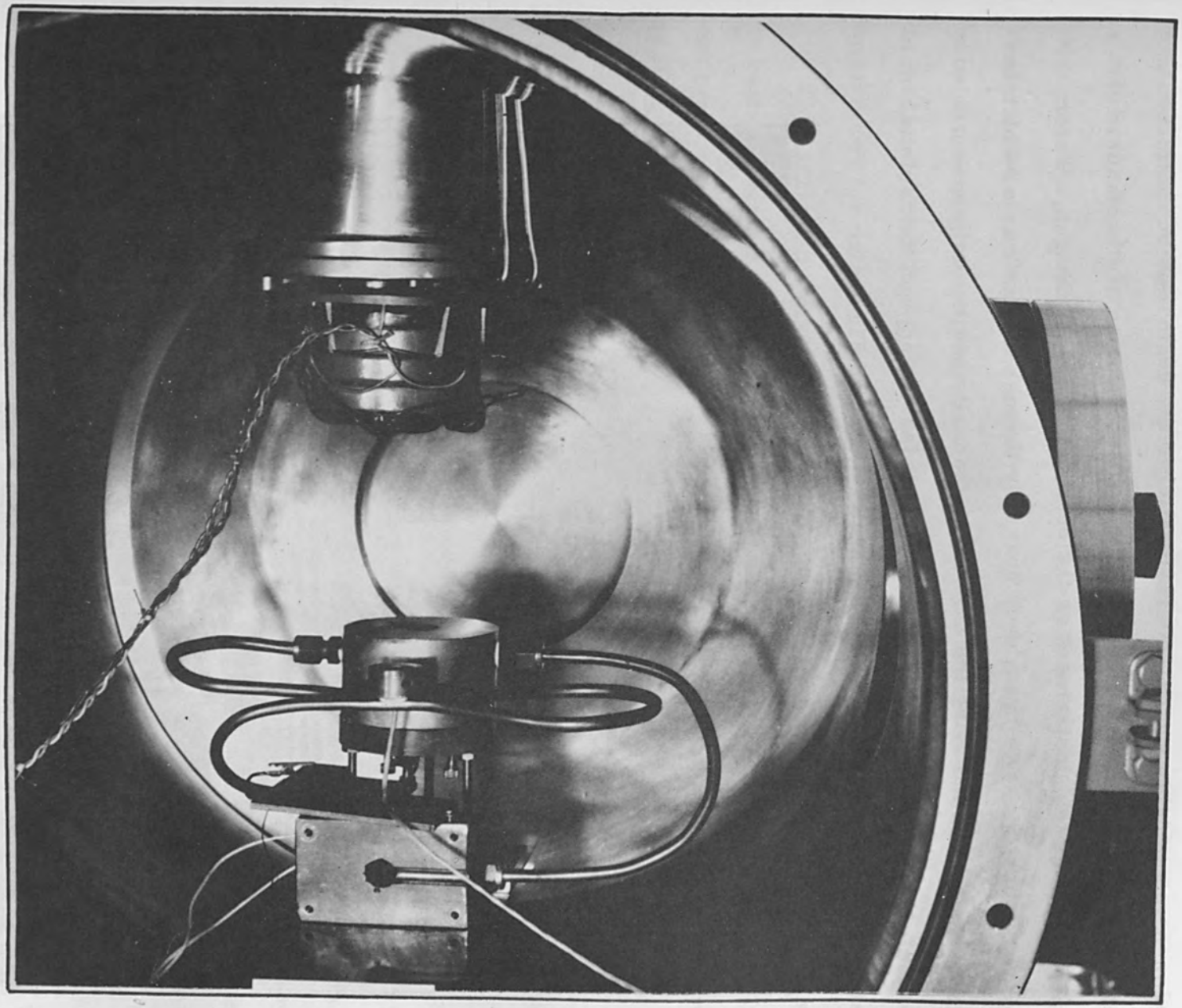

FIGURE 4 GUN-WORK PIECE RELATIONSHIP

Standardization of the raster power density was provided by a slug type calorimeter, shown mounted along with a typical instrument in Figure 4. Both are mounted on a rotary table whose axis is parallel to the beam axis but displaced a few inches. Rotation of the table allows alternate positioning of the standard calorimeter and the test instrument on the beam axis beneath the gun. Water cooling for the heat sinks is brought up coaxially through the table axis, which has a rotary vacuum seal, allowing the table to be manually positioned from outside the chamber. Alignment of the standard and test instruments on the table is facilitated by a split-image optical sight as illustrated in Figure 5.

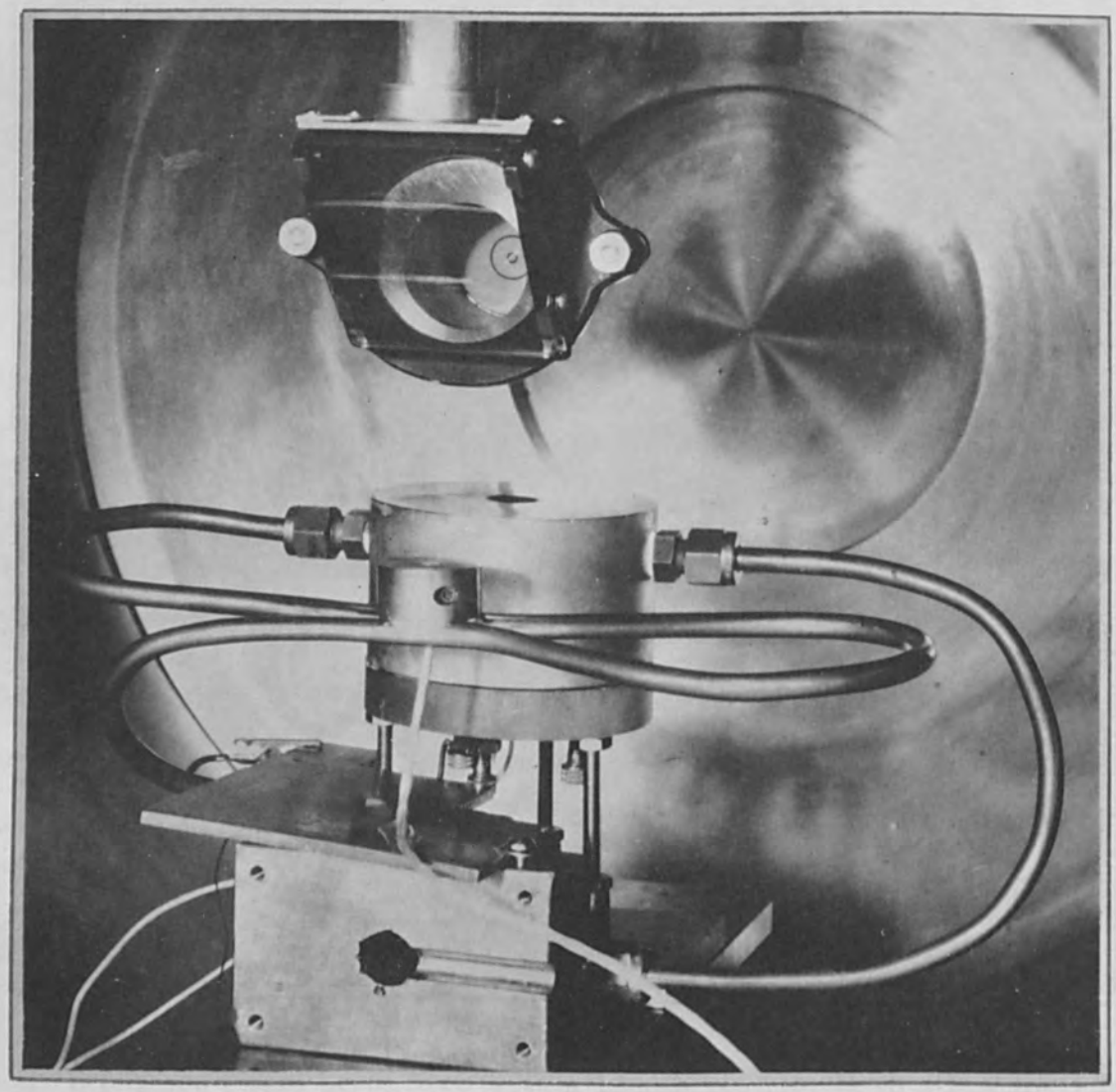

FIGURE 5 OPTICAL ALIGNMENT TOOL

Details of the standard calorimeter are shown in Figure 6. An accurately weighed copper slug with attached thermocouple is mounted on three finely pointed pins for minimum thermal coupling. The pins are electrically grounded to provide a return for beam current. Surrounding the copper slug is a water-cooled jacket with an accurately measured top hole. This hole defines the area of the beam raster to be sampled by the copper slug. Power density is calculated from the rate of rise of slug temperature. The test instrument is swung into position immediately following the standardization measurement, providing minimum opportunity for drift or fluctuation of beam parameters.

This arrangement served well for rough measurements (±5%), but was subject to beam current variations resulting from changes in chamber pressure during calibration runs. Manual control of grid bias voltage to correct this drift proved tedious and not very satisfactory. An automatic beam power controller appeared to be called for.

The controller as it has evolved is pictured in block diagram form in Figure 7. The current provided by the voltmeter bleeder string is used as a measure of beam voltage, and serves as the input to a current amplifier. The amplified current is impressed on an electromagnet which generates a magnetic field proportional to the beam voltage. This field is imposed on a Hall effect transducer which is placed in series with the beam current return lead. The mounting arrangement beneath the power supply control panel is shown in Figure 8. The output signal of the Hall effect transducer is thus proportional to the instantaneous product of beam voltage and beam current. This signal is amplified and compared with a command signal. The difference, or error signal is further amplified and imposed on the electron gun grid to control beam current for the desired power setting. Transfer of the error signal to the 30 KV cathode potential reference is accomplished by modulating a one-megacycle carrier, passing this through a double-tuned air-core isolation

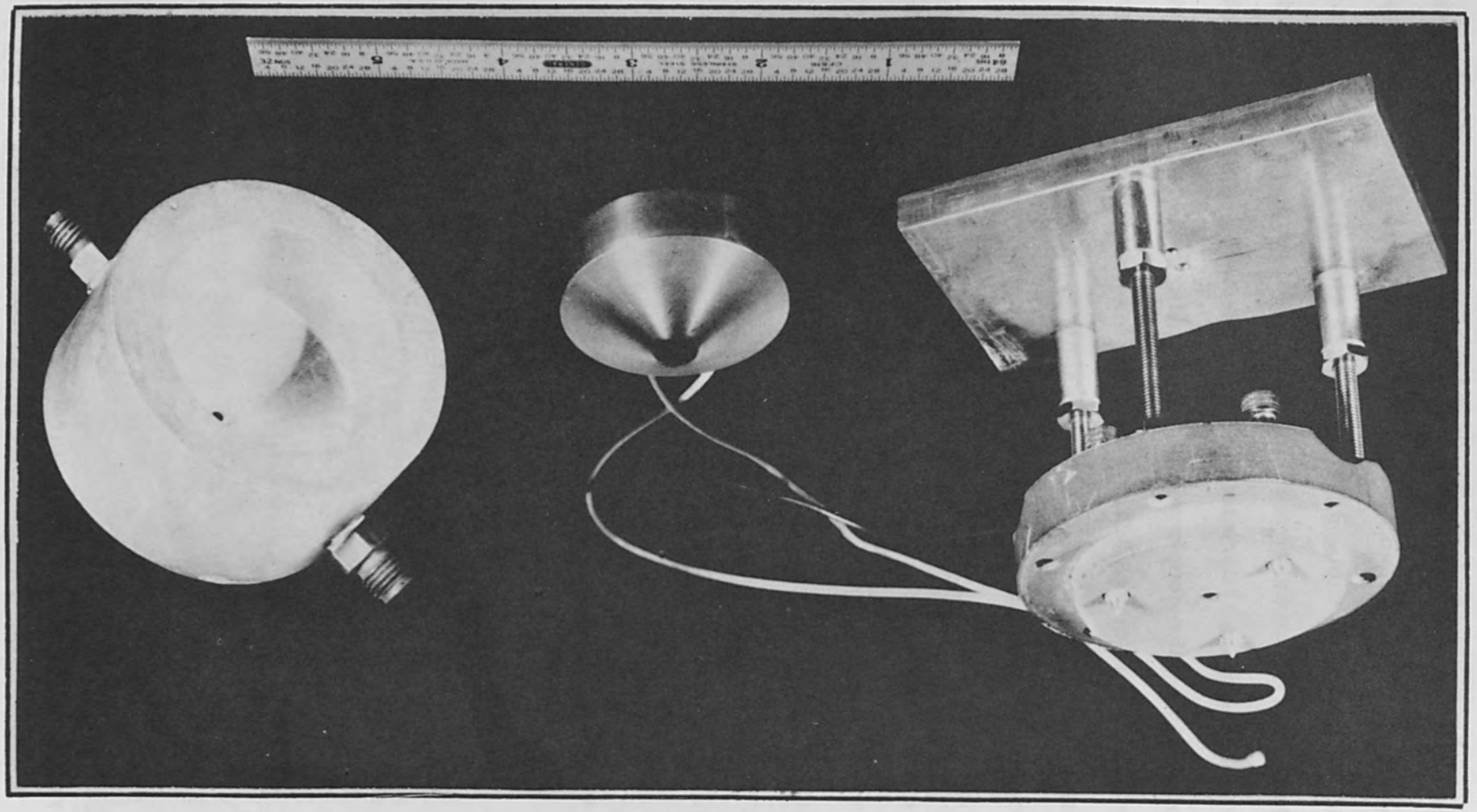

FIGURE 6 STANDARD CALORIMETER DETAILS

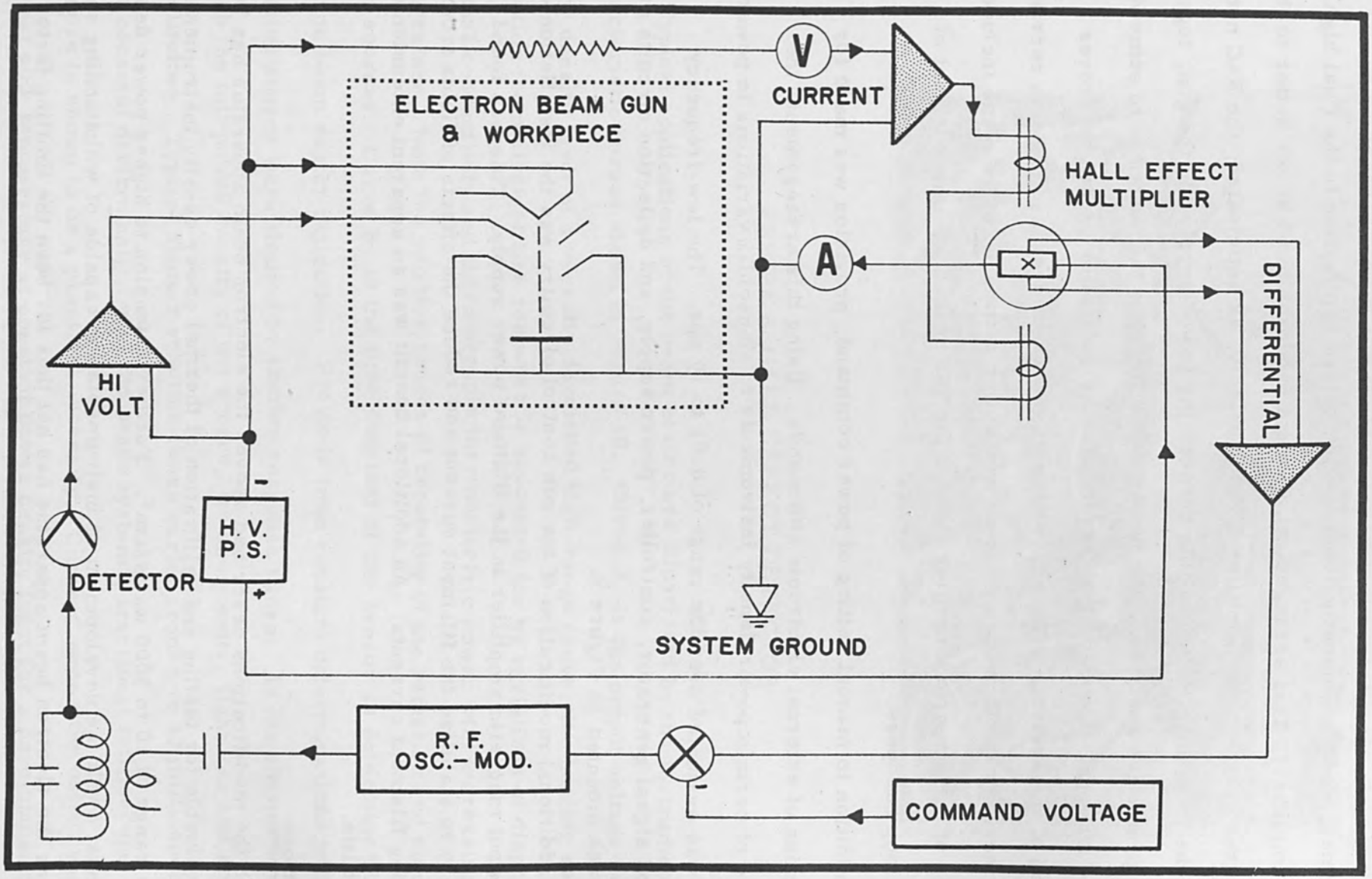

FIGURE 7 BEAM POWER CONTROLLER BLOCK DIAGRAM

transformer, and subsequently demodulating before application to the final high voltage amplifier. This arrangement allows a bandpass to 60 kc or better to the output of the grid voltage amplifier. Unfortunately, as anticipated, the R-C network of the long, high-voltage cable between the power supply and the gun, together with the protective resistor in the power supply reduces the bandpass to somewhat less than 200 cps. Even so, the operation of the controller greatly improves operation of the system. It is interesting to observe a decrease of beam current with an increase in beam voltage at a given power setting. Future plans include mounting of the gun grid amplifier right at the gun header for improvement of control loop bandpass.

In addition to manual setting of power command, provision was made for introduction of external electronic commands. Using this arrangement, the response of certain power density instruments to sinusoidal variations in power density was evaluated over the range of 0.01 to 10 cps. The low-frequency command signal generator, controller, power supply, and deflection circuits are shown rack mounted in Figure 9.

An additional modification of the gun control circuitry was the installation of a d-c output magnetic amplifier in the filament power supply. This was found necessary to stabilize the filament current and reduce the effects of fields from fluctuating filament currents. An additional benefit was an apparent extension of filament life.

Applications

With the modifications described above, the electron beam apparatus has been proven valuable for testing and calibration of thermal power density instrumentation over the range of 10 to 5000 watts/cm^2. Further extension to higher power density levels must await the development of instrumentation capable of withstanding such levels, as the electron beam apparatus has not thus far been the limiting factor.

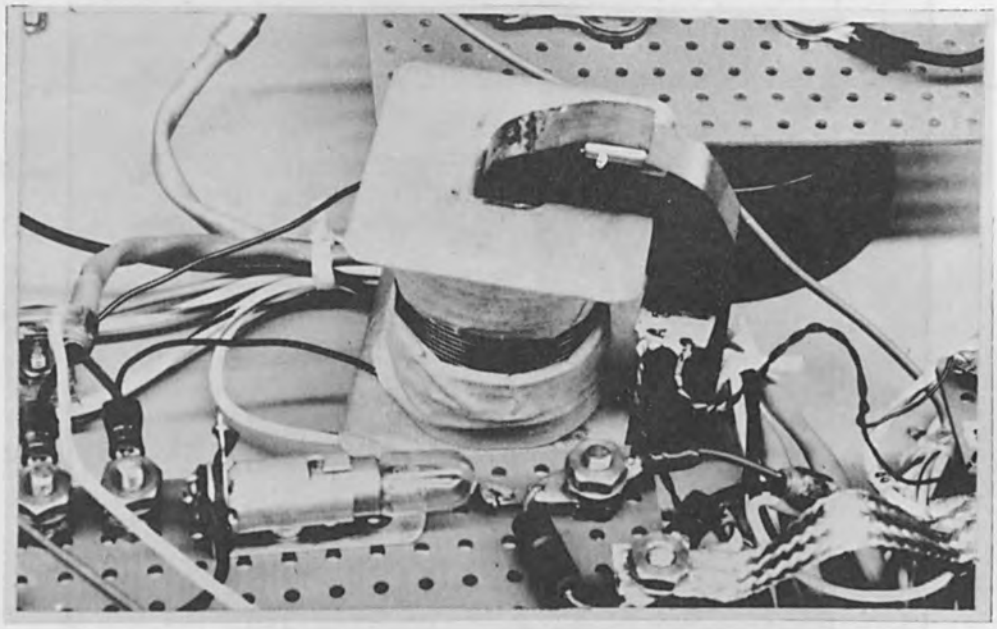

FIGURE 8 HALL EFFECT DETECTOR

Typical applications of the beam heater are illustrated by the instrument characteristic curves shown in Figure 10. Curve A is the output voltage vs. power density input of a recently developed high-range convective heating sensor. Deviation from straight line response is accounted for by variations of diaphragm thermal conductivity and thermocouple thermoelectric power with increasing temperature. Note the relative ranges of capability of the radiation and electron beam sources. Curve B is the time constant of the sensor as determined by step-function beam raster deflection. Previous time constant determinations with the radiation source were limited by shutter response times. As the shutter had to absorb the full power density of the source, its complexity, lightness and speed were limited. Typical shutter reaction times varied from 8 to 40 milliseconds. Time constant determination with the beam system's fractional millisecond response is shown to be a practical necessity. Curve C shows the output voltage vs. heat sink temperature at constant power density input for a developmental

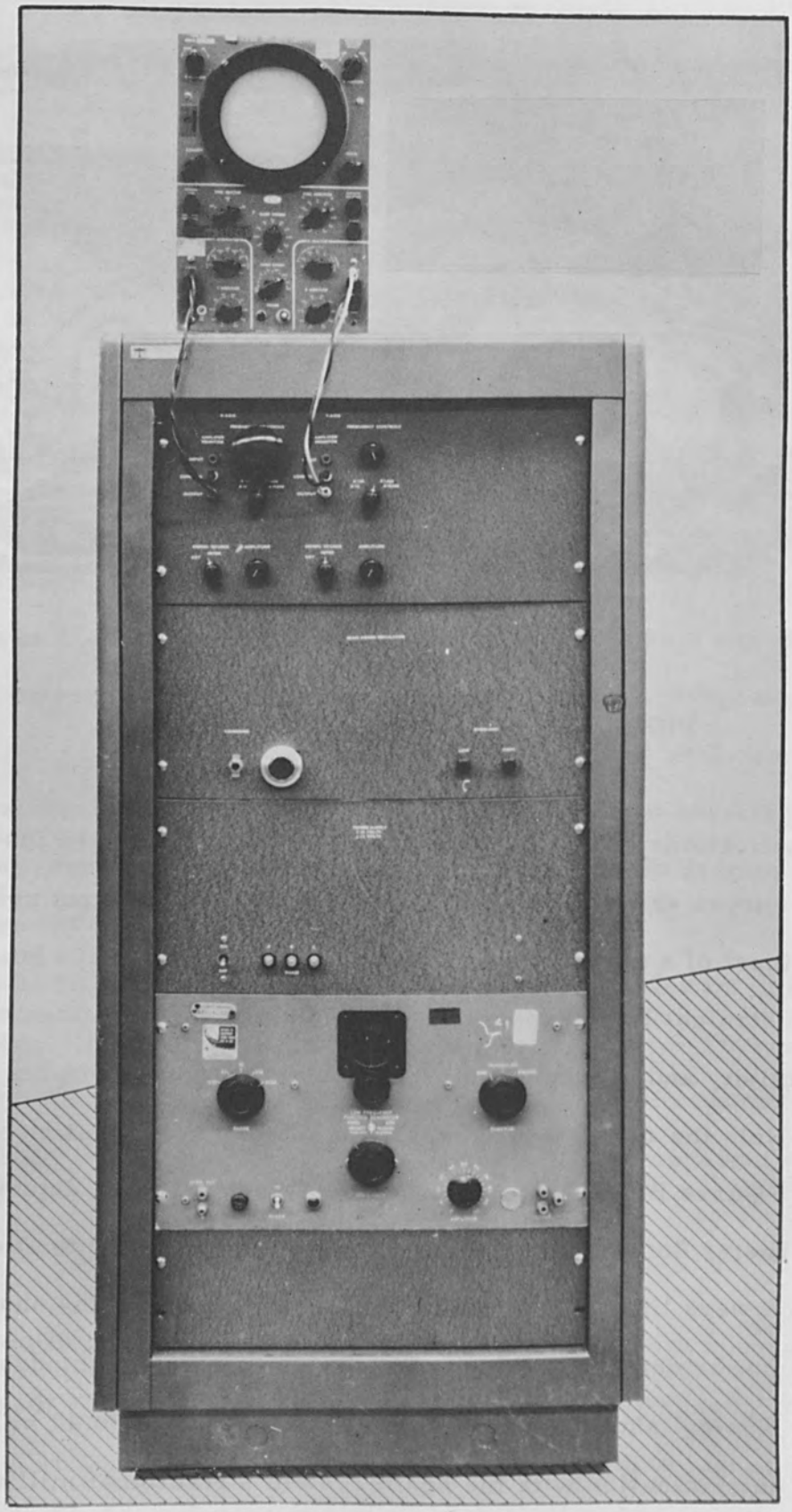

FIGURE 9 BEAM CONTROL CONSOLE

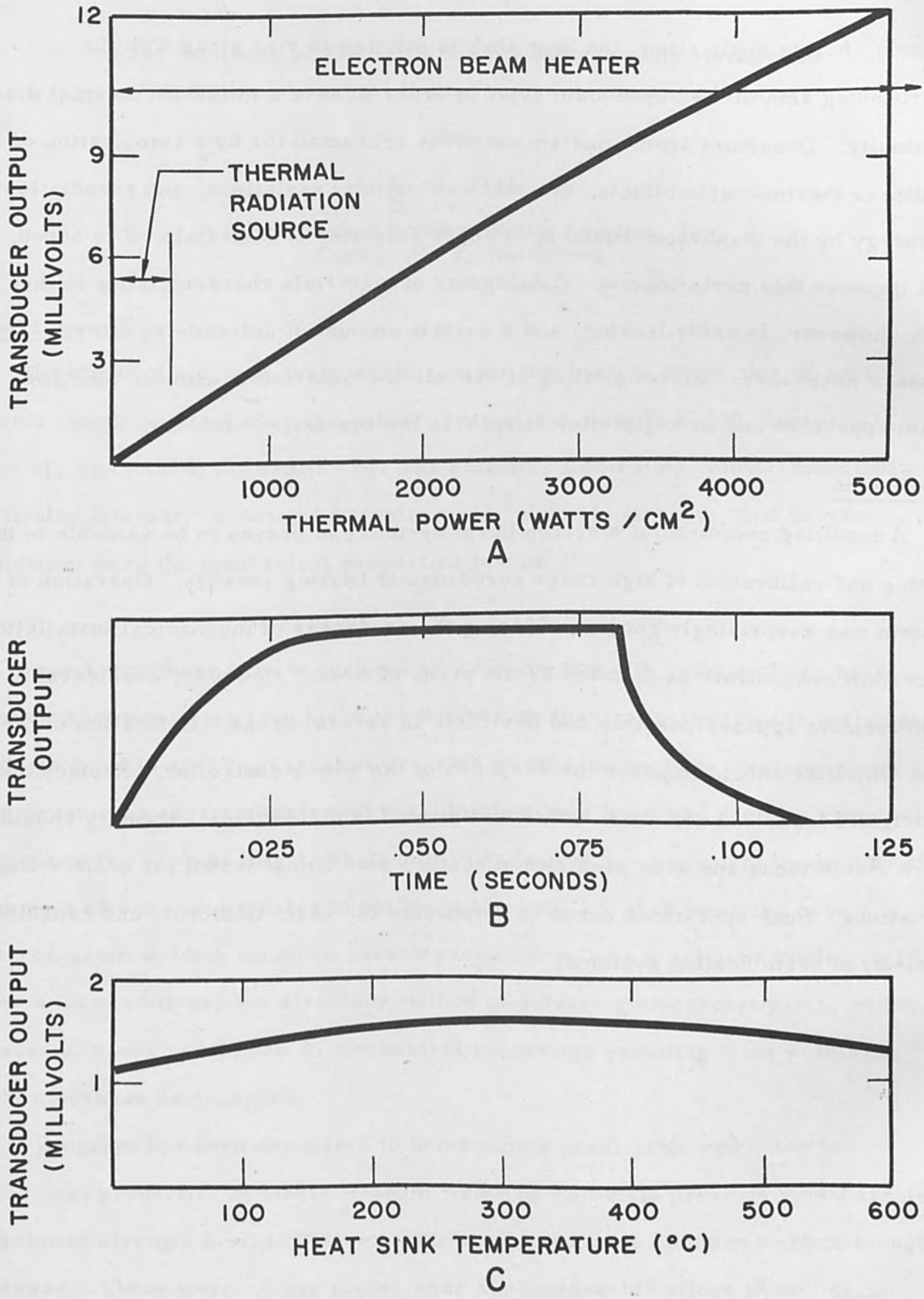

FIGURE 10 SENSOR CHARACTERISTICS

sensor. In this application, the heat sink is allowed to rise along with the surrounding skin of the supersonic craft in order to have a minimum thermal discontinuity. Departure from constant output is accounted for by a combination of nonlinear thermocouple effects, thermal conductivity variations, and reradiation of energy by the diaphragm surface. Proper selection of materials, it is hoped, will improve this performance. Cataloguing of materials characteristics in this area, however, is sadly lacking, and a certain amount of cut-and-try effort appears necessary. Direct plotting of overall characteristics with the electron beam apparatus and an x-y plotter simplifies the evaluation problem.

Conclusion

A modified commercial electron beam system has proven to be valuable in the testing and calibration of high range aerodynamic heating sensors. Operation of the system was surprisingly good considering the crudeness of mechanical installation of certain components as dictated by the press of work. However, considerable improvement appears possible and desirable in several areas. Relocation of the grid amplifier should improve the response of the power controller. Replacement of original focus and deflection yokes and provision of additional circuitry should allow stable focus and wide area sweep raster, both compensated for beam voltage variations. Such operations serve to emphasize the basic flexibility and capability of electron beam heating systems.

The Influence of Electron-Beam Welding on the Mechanical Properties of Several Heat-Treated Aerospace Materials

by

R. E. Fish
Rocketdyne
A Division of North American Aviation, Inc.
Canoga Park, California

Abstract

The effect of electron beam welding on the mechanical properties of heat treated aluminum alloy 6061-T6, nickel base alloys Inconel X-750, Inconel 718, Rene'41, and AlS14130 carbon steel was studied. Controlled reinforcement was of particular interest. Short-time tensile yield, ultimate strength, and percent elongation were the mechanical properties tested.

When a weldment is to be utilized at optimum strength, post-welding heat treatment is mandatory to achieve the desired mechanical properties in materials which respond to such heat treatment. This would also apply to electron-beam welding, but the assumption is that the minimum heat input and deep, narrow welds common to the process might result in less reduction in mechanical properties of materials already heat treated to optimum strength. If such were the case, electron-beam welding would be advantageous not only as a primary joining tool under such conditions, but also as a method of salvaging discrepant parts, which, because of gross reductions in mechanical properties resulting from welding, might otherwise be scrapped.

A program has been conducted to determine a predictable reduction in mechanical properties of electron-beam welds in materials previously heat treated to optimum strength levels. The materials selected were common to rocket-engine hardware. These were: three nickel-base age-hardenable alloys (Rene' 41,

Inconel X-750, and Inconel 718) one transformation-hardening carbon steel (AISI 4130); and one precipitation-hardening aluminum alloy (6061-T6). Preliminary work showed alloy 6061 to be prone to hot short cracking, and it was dropped from the program. Typical chemical compositions of the remaining alloys are shown in Table I.

Welding parameters were established from a practical standpoint, i.e., welds which could be repeated reliably under production conditions of joint fit, gap, alignment, etc. From these parameters minimum mechanical properties would also be evolved rather than misleading information from precise laboratory procedures which would be difficult to duplicate in production. Low-voltage equipment was employed with a capacity of 30 kilovolts at 500 milliamperes. Preconceived weld criteria were based on fusion-zone geometry as a function of material thickness. Trial welds showed that sound welds could be obtained in 1/32-inch-thick material at a weld depth to width ratio of 1:1 (Figure 1), 1/8-inch-thick at 3:1 (Figure 2), and 1/4-inch to 3/8-inch-thick at 5:1 (Figure 3). Tensile tests of a screening nature were conducted which showed only the 5:1 depth-to-width ratio welds indicated mechanical properties significantly above annealed properties of the alloy involved. Testing was therefore limited to 1/4-inch-thick weldments.

All weld plates were heat treated to optimum strength levels prior to welding in accordance with the schedules shown in Table II. Note that two treatments were applied to Inconel 718. The early treatment (1800 to 1150 F) was used for all plain tensile testing. The later treatment (1950 to 1400 to 1200 F) was evolved after the program was partially completed, and was used only for the critical reinforcement tests described later. The primary reason for the change was to improve yield tensile strength.

Welding parameters were the same for all 1/4-inch-thick alloys (30 kv beam voltage, 150 ma beam current, 45 in./min welding speed) for an energy input of

TABLE I

COMPOSITIONS OF TEST MATERIALS

Element	Test Material Composition, Percent			
	Inconel 718[a]	Inconel X-750[b]	Rene' 41[c]	AISI 4130[d]
Carbon	0.10 maximum	0.08 maximum	0.12 maximum	0.27 to 0.33
Manganese	0.40 maximum	1.0 maximum	0.10 maximum	0.40 to 0.60
Silicon	0.45 maximum	0.50 maximum	0.50 maximum	0.20 to 0.35
Chromium	17 to 21	14 to 17	18 to 20	0.80 to 1.10
Nickel or Nickel and Cobalt	50 to 55	70 minimum	remainder	0.25 maximum
Cobalt[e]	1.0 maximum	1.0 maximum	10 to 12	---
Columbium and Tantalum	4.75 to 5.50	0.70 to 1.20	---	---
Titanium	0.70 to 1.40	2.25 to 2.75	3 to 3.3	---
Aluminum	0.20 to 0.80	0.40 to 1	1.4 to 1.6	---
Iron	remainder	5 to 9	5 maximum	---
Copper	0.30 maximum	0.50 maximum	---	---
Molybdenum	2.80 to 3.30	---	9 to 10.5	0.15 to 0.25
Boron	0.006 maximum	---	0.003 to 0.01	---
Phosphorous	0.015 maximum	---	---	0.025 maximum
Sulphur	0.015 maximum	0.01 maximum	0.015 maximum	0.025 maximum

[a] Rocketdyne Specification

[b] AMS 5542

[c] AMS 5545

[d] MIL-S-18729

[e] If Determined

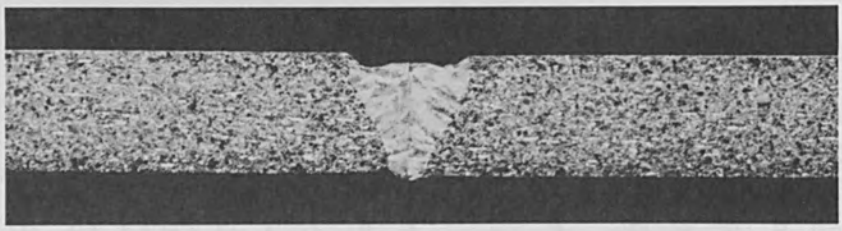

Figure 1. Typical Fusion Zone Geometry, 1/32-Inch-Thick Weld, Depth-to-Width Ratio = 1 to 1, Inconel 718 (Mag: 15X, Etchant: HCL and H_2O_2)

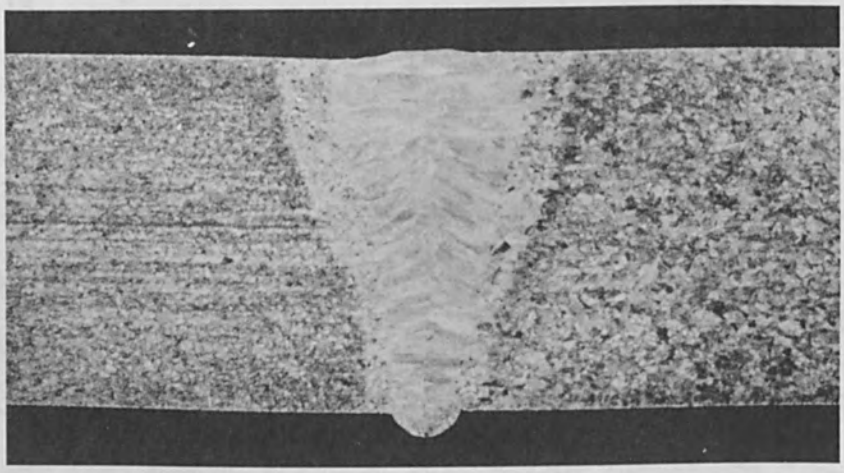

Figure 2. Typical Fusion Zone Geometry, 1/8-Inch-Thick Weld, Depth-to-Width Ratio = 3 to 1, Rene' 41 (Mag: 15X, Etchant: HCL and H_2O_2)

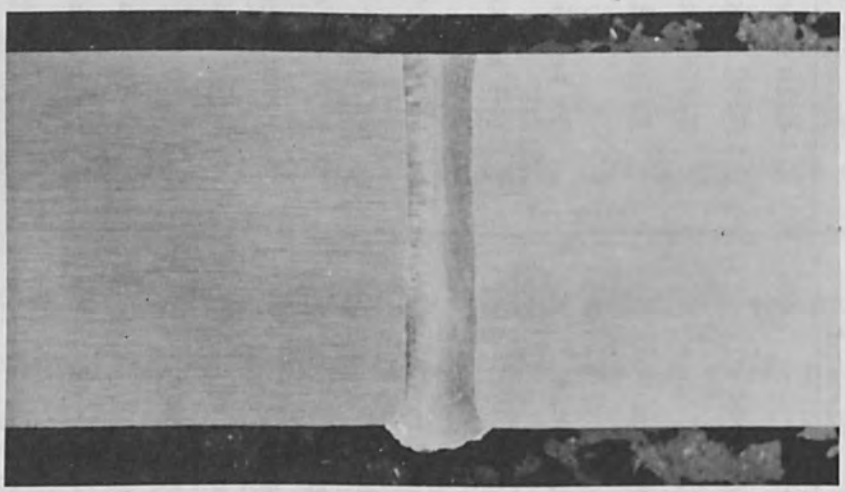

Figure 3. Typical Fusion Zone Geometry, 3/8-Inch Aluminum Alloy 6061-T6 Weld, Depth-to-Width Ratio = 6 to 1, Crown Machined Flush (Mag: 5X, Etchant: Keller's)

TABLE II

PREWELD AND POSTWELD THERMAL TREATMENTS

Test Material	Annealing Cycle	Aging Cycle
Inconel 718 (1)	1800 F, 1 hour, air cool	1325 F, 8 hours, furnace cool to 1150 F, hold for total aging time (1325 - 1150 F) 18 hours, air cool
(2)	1950 F, 1 hour, air cool	1400 F, 10 hours, furnace cool to 1200 F, hold for total aging time (1400 - 1200 F) 20 hours, air cool
Inconel X-750	1925 F, 1 hour, water quench	1300 F, 10 hours, air cool
Rene' 41	1975 F, 1 hour, water quench	1400 F, 16 hours, air cool
AISI 4130 (3)	1600 F, 1 hour, oil quench	900 F, 1 hour, air cool

(1) Treatment applied to plain tensile specimens

(2) Treatment applied to reinforced tensile specimens

(3) Hardening and tempering sequence

6000 Joules per inch. Spot diameter was minimum. A "scab" strip was employed on all welds to compensate for crown irregularities as shown in Figure 4. After welding, both sides of the weldments were machined to give a thickness of 0.2 inch.

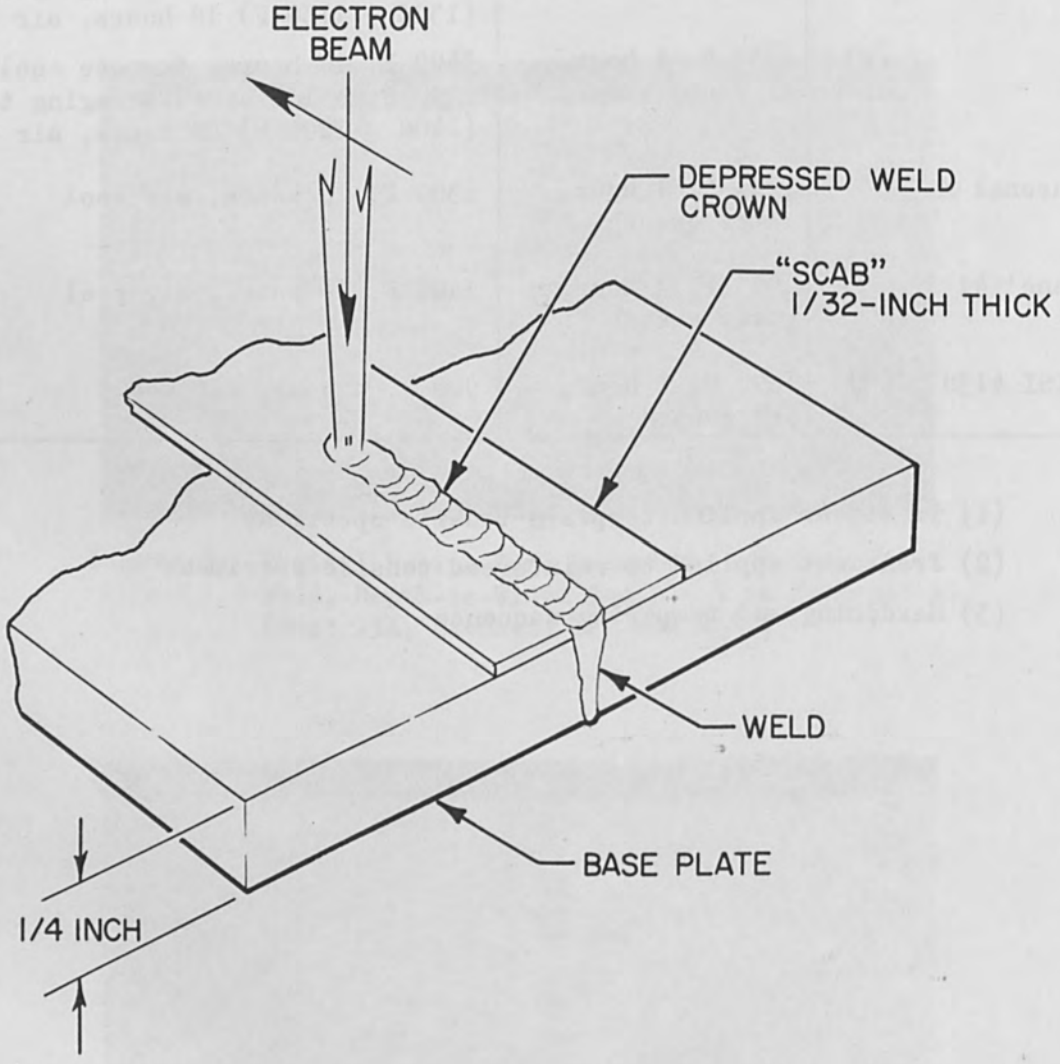

Figure 4. "Scab" Strip used to Compensate for Crown Depression and/or Undercut

Each weldment was radiographically and ultrasonically examined, and no defects were evident. Half the number of weldments of each alloy were reheat treated in accordance with the previously used schedules. The plates were then machined to tensile bars. Testing was conducted at room temperature, 1000, 1250, and 1500 F for the nickel alloys, and room temperature only for the carbon steel.

All 4130 specimens failed in parent metal at values given in Table III. A hardness check showed the weld zone to be Rockwell C 35. Apparently because of mass quenching from welding temperature, the fusion zone was largely martensitic.

The Rene' 41 welds exhibited as-welded properties circa 80 percent of reheat-treated properties as seen in Table IV. Figure 5 shows that the as-welded properties increased significantly at 1250 F. This was attributable to direct aging of the essentially annealed fusion zone at the temperatures involved during the test.

The Inconel X-750 and Inconel 718 results were similar. Table V gives efficiencies in excess of 80 percent for Inconel X-750, while Figure 6 shows a modest aging effect. As-welded Inconel 718 properties (Table VI), again showed efficiencies circa 80 percent of reheat-treated properties, and Figure 7 reflects the now typical aging effect at elevated temperatures. It is interesting to note that as test temperatures approached 1500 F, there was no significant difference in mechanical properties. From these data it could be assumed that an as-welded component operating in the range 1200 to 1500 F would shortly become directly aged, and would perform equivalently to a reheat-treated weldment. This would occur only if the weld could sustain the operating loads prior to the age strengthening.

The elongation data (Figure 8) showed as-welded ductility for Inconel X-750 and Inconel 718 to be approximately one-half that of the reheated ductility. This is not necessarily a true indication, since the elongation measurements were taken at one-inch and 1/2-inch gage length, whereas the major strain occurred in the

TABLE III

MECHANICAL PROPERTIES, ELECTRON-BEAM WELDS, AISI 4130
CARBON STEEL, 1/4-INCH THICK

Material Condition[a]	Test Temperature, F	Tensile Strength kpsi		Efficiency Percent		Elongation Percent	
		Yield[b]	Ultimate	YTS	UTS	In 1 inch	In 1/2 inch
Reheat Treated	Room	161	172	-	-	8	11
As Welded	Room	164	176	100	100	10	--

[a] All specimens were heat treated prior to welding

[b] 0.2 percent offset

NOTES: 1. All specimens failed in parent metal
2. Five tests minimum per condition
3. Weld crown and root machined smooth

TABLE IV

MECHANICAL PROPERTIES, ELECTRON-BEAM WELDS, RENE' 41 NICKEL ALLOY, 1/4-INCH THICK

Material Condition[a]	Test Temperature, F	Tensile Strength kpsi		Efficiency Percent		Elongation Percent	
		Yield[b]	Ultimate	YTS	UTS	In 1 inch	In 1/2 inch
Reheat Treated	Room	134	175	-	-	8.5	9
	1000	123	149	-	-	7	10
	1250	118	153	-	-	7.5	9.5
	1500	106	116	-	-	5.5	6.5
As Welded	Room	112	144	84	82	7	9
	1000	95	116	77	78	5	8.5
	1250	108	134	92	88	8	10
	1500	106	120	100	100	6.5	8.5

[a] All specimens were heat treated prior to welding

[b] 0.2 percent offset

NOTES: 1. All specimens failed in weld

2. Five tests minimum per condition

3. Weld root and crown machined smooth

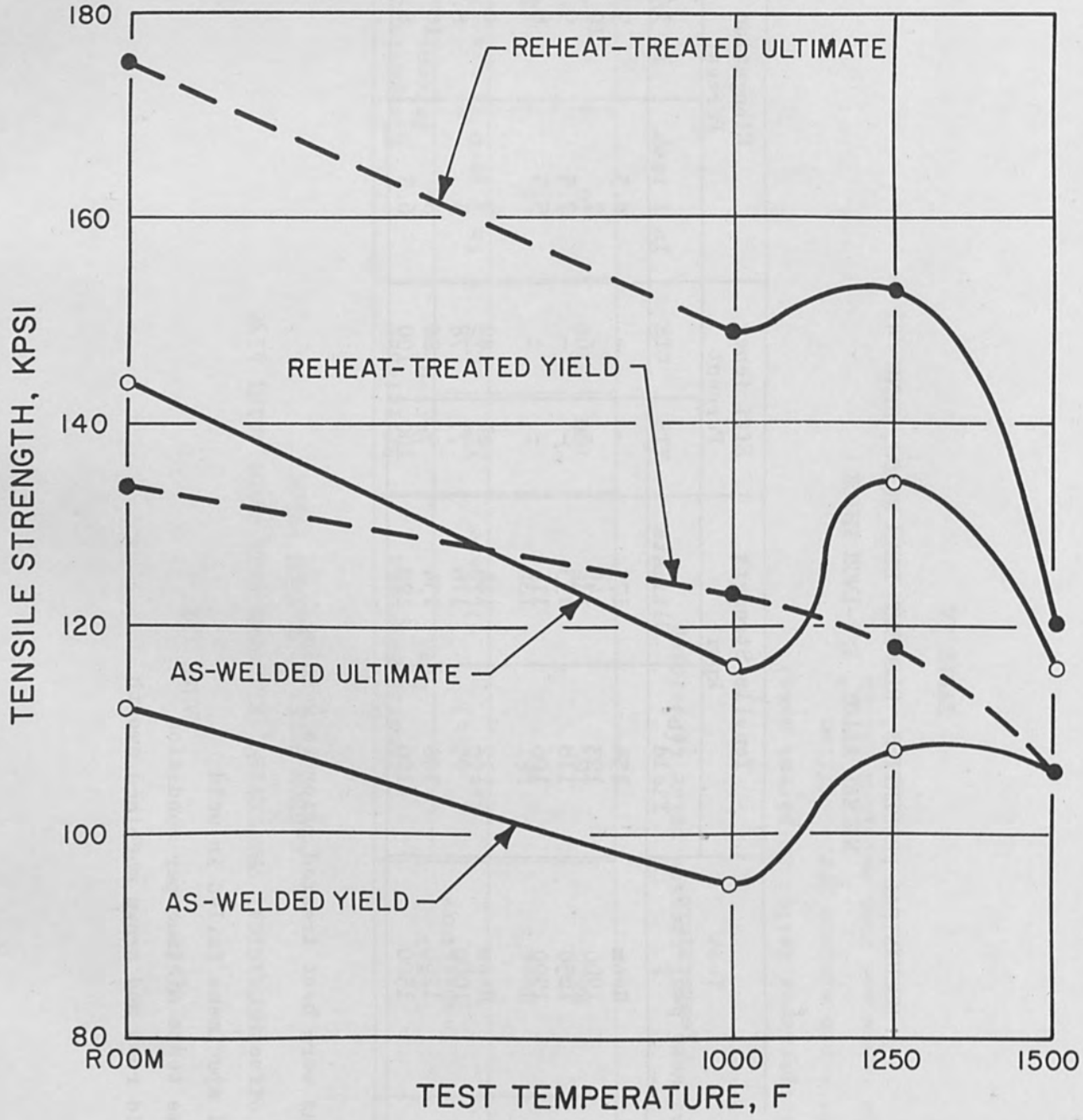

Figure 5. Tensile Strength, Rene' 41 Electron-Beam Welds, as Welded vs Heat Treated

TABLE V

MECHANICAL PROPERTIES, ELECTRON-BEAM WELDS, INCONEL X-750 NICKEL ALLOY, 1/4-INCH THICK

Material Condition[a]	Test Temperature, F	Tensile Strength kpsi		Efficiency Percent		Elongation Percent	
		Yield[b]	Ultimate	YTS	UTS	In 1 inch	In 1/2 inch
Reheat Treated	Room	113	165	-	-	18	24
	1000	101	140	-	-	17.5	25
	1250	99	126	-	-	10	11.5
	1500	70	76	-	-	6	12.5
As Welded	Room	101	131	89	79	9	14
	1000	86	113	85	81	8	16
	1250	89	96	90	76	5	9
	1500	64	70	92	92	8	12

[a] All specimens were heat treated prior to welding

[b] 0.2 percent offset

NOTES: 1. All specimens failed in weld

2. Five tests minimum per condition

3. Weld root and crown machined smooth

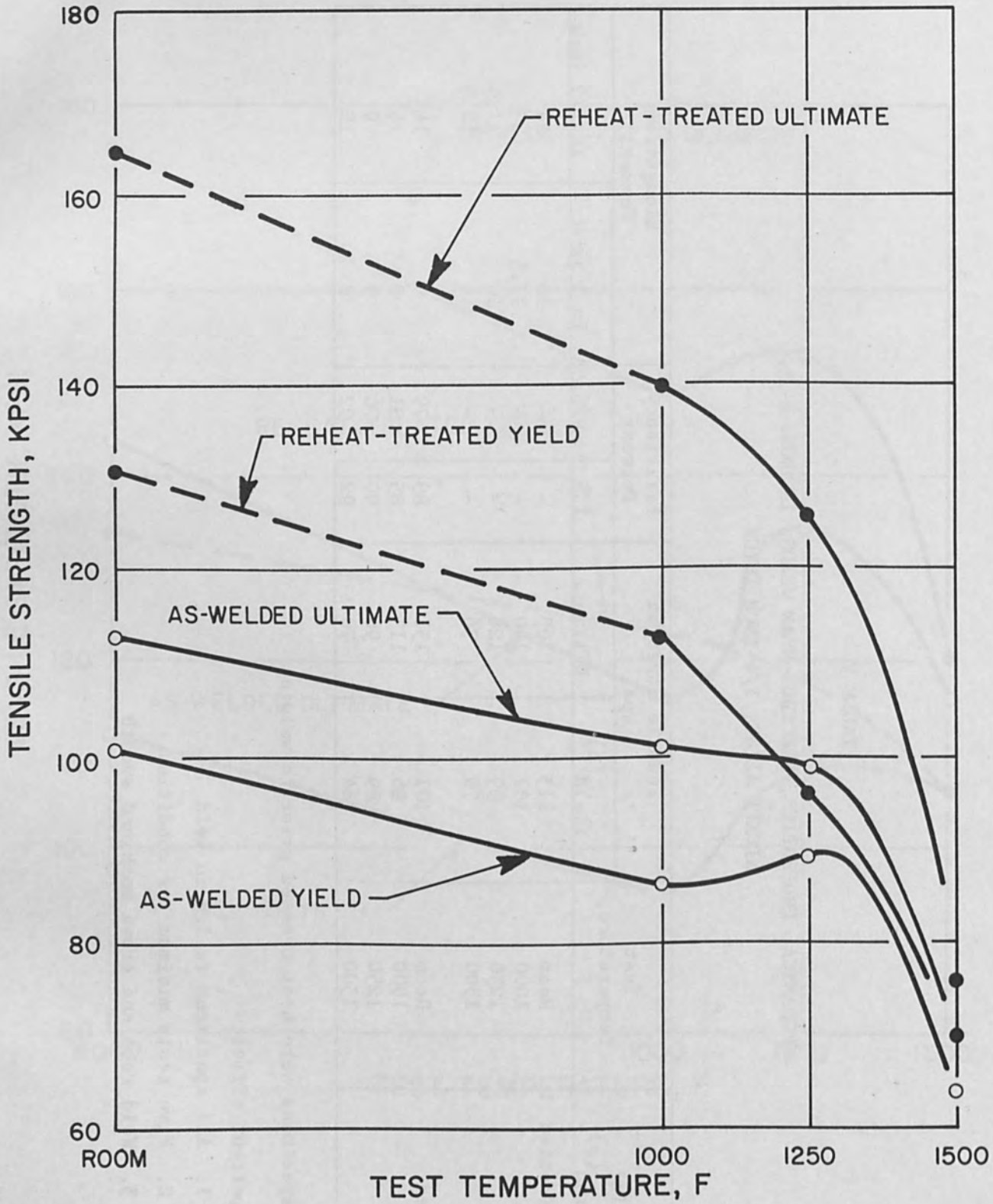

Figure 6. Tensile Strength, Inconel X-750 Electron-Beam Welds, as Welded vs Heat Treated

TABLE VI

MECHANICAL PROPERTIES, ELECTRON-BEAM WELDS, INCONEL 718 NICKEL ALLOY, 1/4-INCH THICK

Material Condition[a]	Test Temperature, F	Tensile Strength kpsi		Efficiency Percent		Elongation Percent	
		Yield[b]	Ultimate	YTS	UTS	In 1 inch	In 1/2 inch
Reheat Treated	Room	136	174	-	-	10	16
	1000	115	143	-	-	6.5	10.5
	1250	113	137	-	-	7	10.5
	1500	70	72	-	-	8	14
As Welded	Room	115	137	85	79	5	8
	1000	90	110	78	77	5	9.5
	1250	96	113	85	83	5	11.5
	1500	69	73	99	100	9	15.5

[a] All specimens were heat treated prior to welding

[b] 0.2 percent offset

NOTES: 1. All specimens failed in weld

2. Five tests minimum per condition

3. Weld root and crown machined smooth

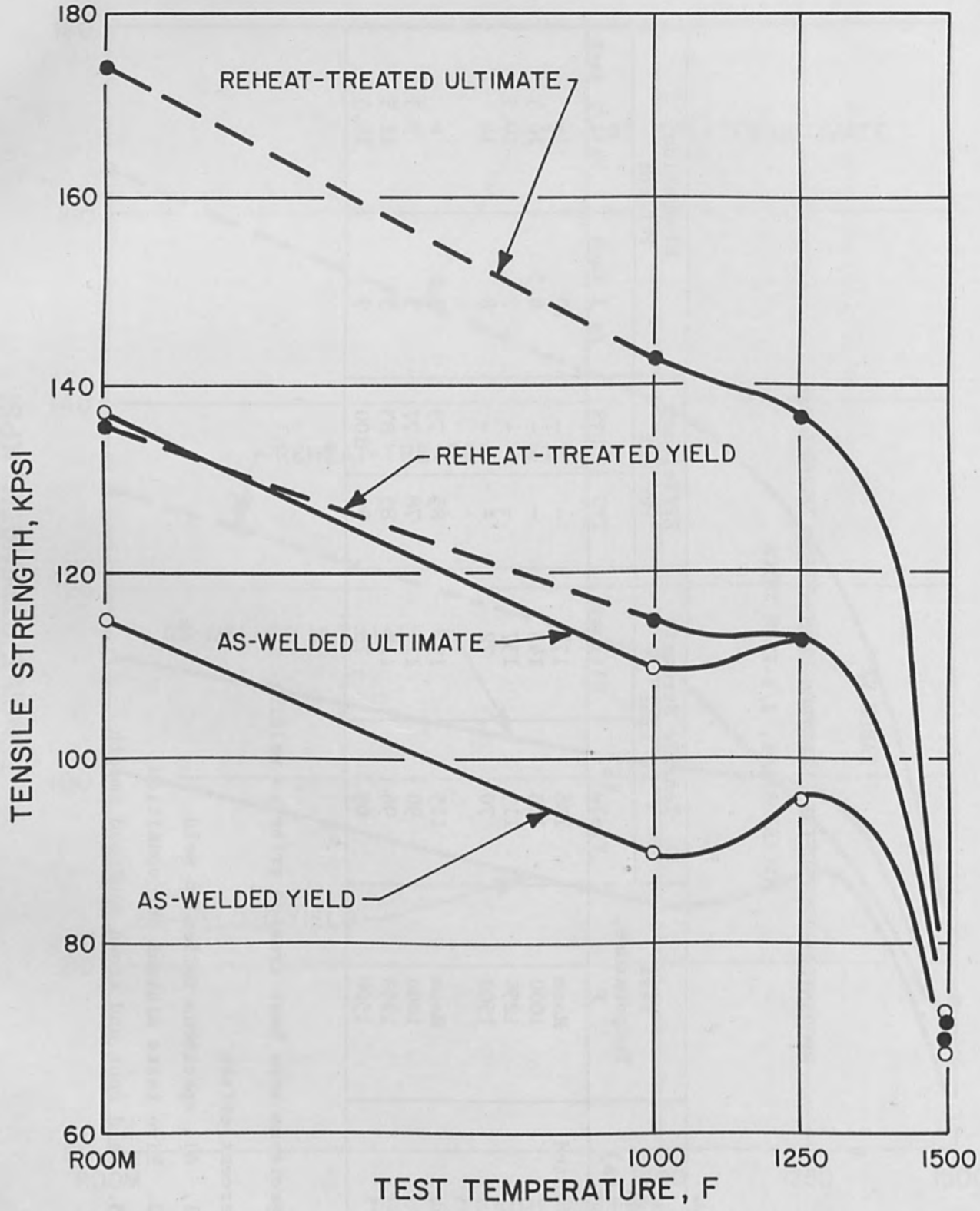

Figure 7. Tensile Strength, Inconel 718 Electron-Beam Welds, as Welded vs Heat Treated

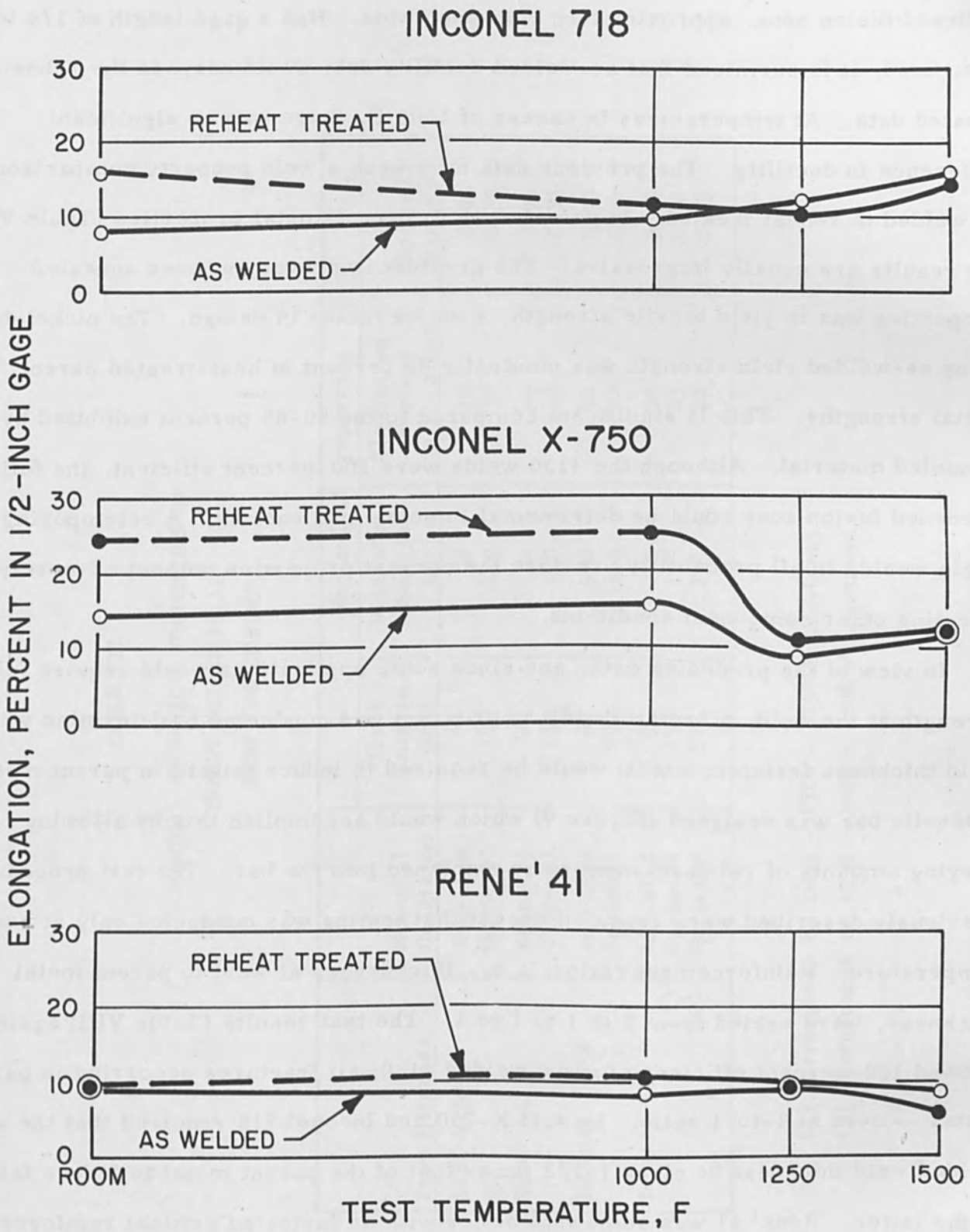

Figure 8. Comparison of as Welded vs Heat-Treated Elongation of Electron-Beam Welds

softened fusion zone, approximately 1/16-inch wide. Had a gage length of 1/4 inch been used, it is surmised that as-welded ductility data would surpass the reheat-treated data. At temperatures in excess of 1000 F, there was no significant difference in ductility. The previous data have been a weld property comparison, as welded to reheat treated. In comparison to parent-metal properties (Table VII), the results are equally impressive. The greatest improvement over annealed properties was in yield tensile strength, a major factor in design. The nickel-base alloy as-welded yield strength was nominally 80 percent of heat-treated parent metal strengths. This is significant compared to the 50-65 percent exhibited by annealed material. Although the 4130 welds were 100-percent efficient, the fully hardened fusion zone could be detrimental in some applications. A retempering cycle would, in all probability, restore the correct properties without adversely affecting other component conditions.

In view of the preceding data, and since some applications would require full strength at the weld, a brief subsidiary program was conducted to determine what weld thickness (reinforcement) would be required to induce failure in parent metal. A tensile bar was designed (Figure 9) which would accomplish this by allowing varying amounts of reinforcement to be machined into the bar. The test procedures previously described were repeated except that testing was conducted only at room temperature. Reinforcement ratios, i.e., thicknesses at weld to parent metal thickness, were varied from 2 to 1 to 1 to 1. The test results (Table VIII) again showed 100-percent efficiency for as-welded 4130; all fractures occurring in parent metal -- even at 1-to-1 ratio. Inconel X-750 and Inconel 718 required that the as-welded weld thickness be circa 1-1/2 times that of the parent metal to induce failure in the latter. Rene' 41 was somewhat better with an indicated critical reinforcement ratio of about 1-1/4 to 1. The mechanical properties of 1-to-1 ratio weldments (as welded to reheat treated) confirmed the results of the normal tensile tests, the efficiencies being equivalent (Table IX).

TABLE VII

NOMINAL MECHANICAL PROPERTIES OF
PARENT MATERIALS AT
ROOM TEMPERATURE

Test Material	Material Condition	Mechanical Properties			
		Yield Tensile kpsi	Ultimate Tensile kpsi	Elongation Percent in 2 inches	Rockwell Hardness
AISI 4130	Annealed	70	90	18	B 93
	Hardened	160	180	5	C 35
Rene' 41	Annealed	--	--	--	B 90
	Hardened	130	170	10	C 35
Inconel X-750	Annealed	65	130	40	B 90
	Hardened	100	155	20	C 30
Inconel 718	Annealed	75	140	30	B 90
(1)	Hardened	135	175	15	C 40
(2)	Hardened	145	175	12	C 43

(1) Corresponds to 1800 - 1325 - 1150 F treatment

(2) Corresponds to 1950 - 1400 - 1200 F treatment

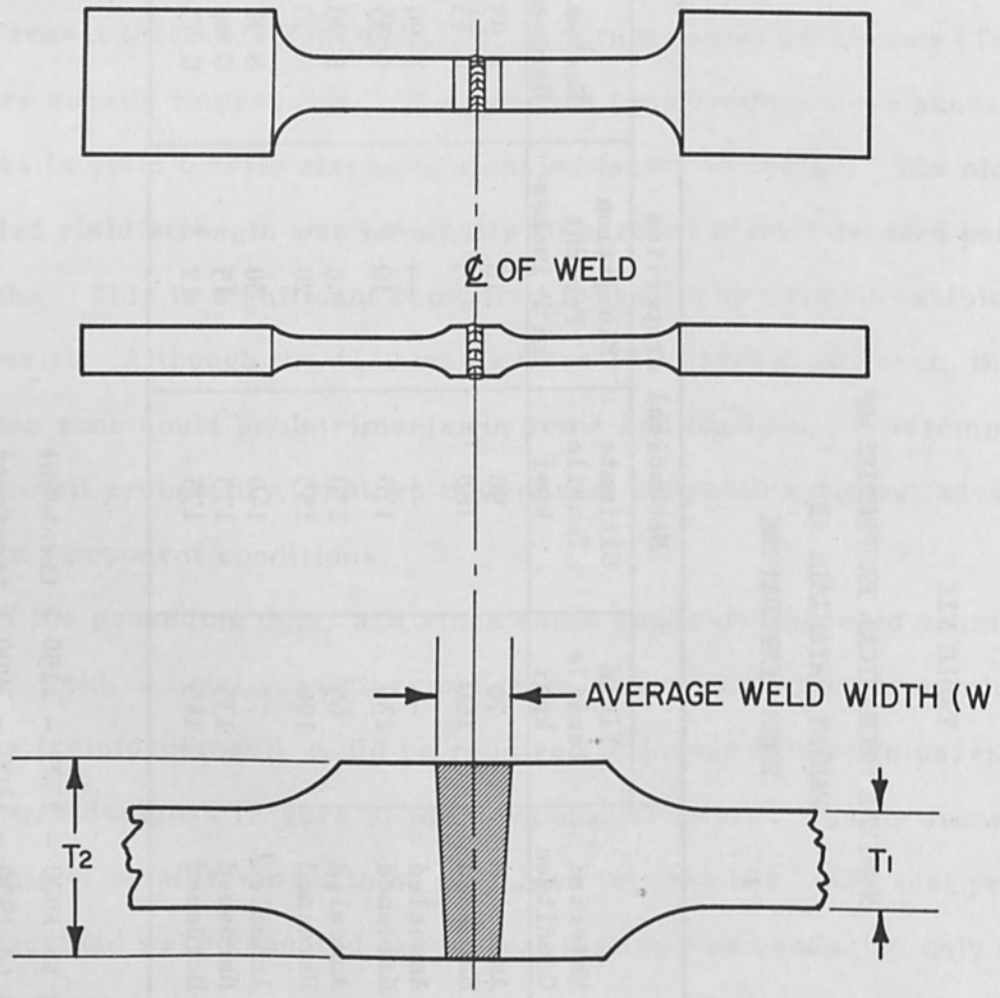

Figure 9. Critical Reinforcement Ratio of Tensile Test Bar
(Critical Reinforcement Ratio = T_2 / T_1
$T_2 / W \cong 5$ to 1)

TABLE VIII

CRITICAL-REINFORCEMENT TEST RESULTS

Test Material	Material Condition[a]	Reinforcement Ratio	Fracture Location
AISI 4130	As Welded or Reheat Treated	1 to 1 and Greater	Parent Metal
Inconel X-750	As Welded	1.48 to 1[b]	Parent Metal
		1.47 and Less	Weld
	Reheat Treated	1 to 1	Parent Metal
Rene' 41	As Welded	1.22 to 1 and Greater	Parent Metal
	As Welded or Reheat Treated	1 to 1	Weld
Inconel 718	As Welded	1.59 to 1 and Greater	Parent Metal
		1.49 and Less	Weld
	Reheat Treated	1 to 1	Weld

[a] All specimens were heat treated prior to welding

[b] One test only

NOTES: 1. Three tests minimum per condition except for[b]

2. Room-temperature tests

TABLE IX

AVERAGE MECHANICAL PROPERTIES OF 1-TO-1-RATIO REINFORCEMENT WELDS

Test Material	Material Condition[a]	Tensile Strength kpsi		Fracture Location
		Yield[b]	Ultimate	
AISI 4130	Reheat Treated	154	164	Parent Metal
	As Welded	163	174	
Inconel X-750[c]	Reheat Treated	107	162	Weld
	As Welded	94	123	
Rene' 41	Reheat Treated	126	178	Weld
	As Welded	123	153	
Inconel 718	Reheat Treated	143	199	Weld
	As Welded	128	148	

[a] All specimens were heat treated prior to welding

[b] 0.2 percent offset

[c] Two tests per condition only

NOTES: 1. Three tests minimum per condition except for[c]

2. Elongation not measured

3. Room-temperature tests

In conclusion, this program has shown that electron-beam welds in heat-treated materials do reduce mechanical properties, but not so drastically as those reductions which could be expected with arc-fusion practices.

Silicon Junction Diodes by Electron Beam Alloying

by

F. W. Leonhard and C. T. Naber
McDonnell Aircraft Corporation
St. Louis, Missouri

Introduction

The research described in this paper was undertaken to investigate the feasibility and technological merit of the fabrication of junction diodes in silicon wafers by electron beam techniques for microelectronic integrated circuit applications. Diode formation represents a preliminary task of establishing the potential usefulness of electron beam techniques in microelectronic device fabrication.

Electron beam techniques have been suggested and developed to some extent in the past decade as an effective tool in the processing of materials and devices for microelectronic circuits.[1, 2, 3, 4] The features that make electron beam techniques attractive in materials or device processing are:

- o The capability of applying thermal energy to a solid material in a controlled fashion by bombarding the material with an electron beam.
- o The capability of confining the energy influx to small well-defined areas by electron optical control of the beam.
- o The inherent cleanliness of electron beam processing.
- o The compatibility of electron beam techniques with automation.

The procedure for diode formation is to deposit a thin film of solid dopant of a particular conductivity type on the surface of a semiconductor wafer of the opposite conductivity type and then to bombard the wafer with an electron beam of a small cross section so as to locally heat the wafer and alloy the dopant to the semiconductor in the bombarded region. The semiconductor becomes doped with the deposited impurity in the alloyed region, and if the doping concentration is

sufficient, a p-n junction will be formed between the alloyed region and the remaining part of the semiconductor.

In this research project, approximately 100 n-type silicon wafers were processed. Usually nine diodes were formed on each wafer. Aluminum was the principal p-type impurity layer; however, a few junctions were formed using a boron impurity layer. The thickness of the dopant layer and the parameters of the electron beam, i.e., beam voltage, beam current, and the time of beam application were varied in order to find the optimum combination of values for diode formation. This investigation encompasses an evaluation of the electrical characteristics of the diodes and a brief analysis of the effect of the formation parameters on the diode characteristics.

Experimental Procedure

Electron Beam Processor

An electron beam processor was constructed as shown in Figure 1 for the performance of this research. The electron optical column was mounted on top of the vacuum dome. The target is located in the working chamber on a target positioner. Three dimensional motion of the target positioner is provided from outside the vacuum system by means of feed-through rods. A lead shield is mounted on the electron beam processor to provide x-ray protection for the operator. A mirror is mounted at an angle of 45^{o} above the target for convenient viewing. Two optical systems are available for viewing the target. One is a telescope system, the other is an opaque projection system which projects an enlarged image of the target onto a screen. When utilizing the opaque projection system, the target is illuminated through the viewing port and the image is reflected around the lead shield by three mirrors.

A cross section of the electron optical column is shown in Figure 2. The electron gun is of the telefocus design which consists of a hairpin filament, a

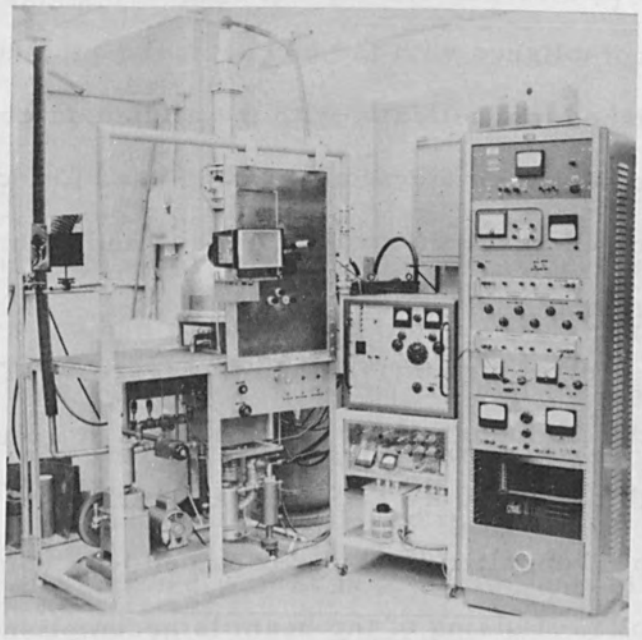

FIGURE 1 ELECTRON BEAM PROCESSOR

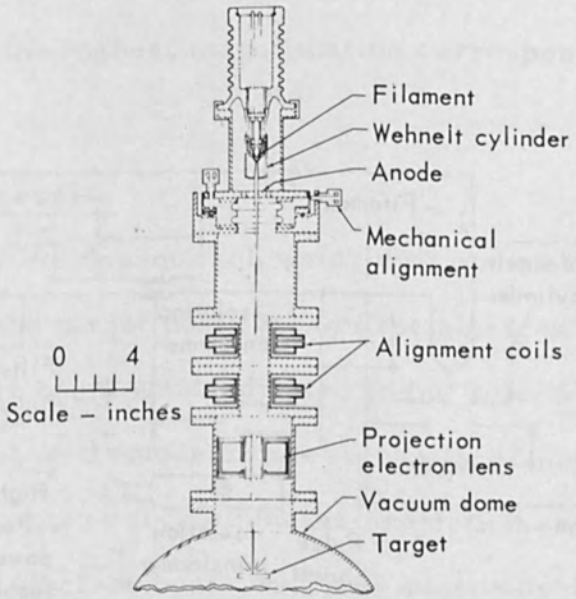

FIGURE 2 ELECTRON OPTICAL COLUMN

negatively biased cylindrical electrode (Wehnelt cylinder), and an anode. Coarse beam alignment is accomplished with the mechanical alignment screws and fine alignment is accomplished magnetically with the alignment coils. Since small spot size was not a requirement, one electron lens was used to focus the beam. A condenser lens is mounted above the projection lens and both lenses are used when small spot size is desirable.

The electron gun control circuit is shown in Figure 3. The negative high voltage is applied to the filament and the anode is held at ground potential. The beam voltage is variable up to 50 kV and the beam current is variable up to 4 mA. The bias voltage on the Wehnelt cylinder is provided by a voltage divider across a battery pack of 540 volts. Pulsing of the beam is accomplished by connecting the pulse circuit in series with the bias voltage. The beam is biased off by applying a sufficiently large negative voltage to the Wehnelt cylinder. A positive controlled square pulse is then supplied by the pulse circuit and the beam is switched on for the duration of the pulse. The pulse circuit is capable of supplying square pulses of 8 different durations from .01 sec to 2 sec. Since the electron gun circuit is

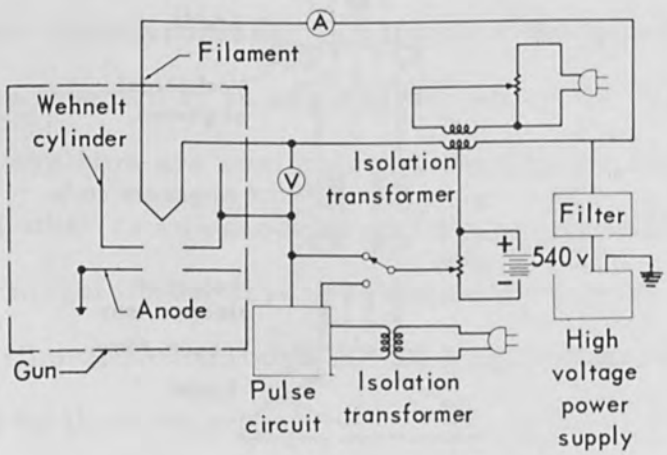

FIGURE 3 ELECTRON GUN AND CIRCUIT

operated at high voltage, it is sealed in a plastic box with nylon extensions to the controls. Isolation transformers are used to isolate the circuit from the 115 volt line.

Wafer Preparation

The n-type silicon wafers were sawed from single crystal boules of approximately 1 inch diameter and had resistivities ranging from 0.2 to 63.5 ohm-cm. Approximately 100 wafers were used. The majority of the wafers were 20 mils thick; the rest were 7 mils thick. These wafers were cleaned by etching in a solution of four parts HNO_3 and one part HF and then rinsing in distilled water. Aluminum was evaporated onto the wafers in a vacuum deposition system from a tungsten boat. Boron, with melting point of 2300°C, was deposited in an electron beam evaporation system. Both evaporation systems were equipped with shutter mechanisms so the dopant was always pre-evaporated onto the shutter to ensure cleanliness. A glass pilot slide was placed close to the wafers in the vacuum deposition systems, and the thickness of the aluminum or boron film on the pilot slide was measured with a stylus type surface profile recording instrument, for which the noise level at the highest magnification corresponds to approximately 25 Å.

Electron Beam Processing

After evaporation of the dopant each wafer was placed in a tapered hole of a stainless steel plate on the target positioner of the electron beam processor. The voltage and current of the beam were adjusted to the selected values, and the beam was focused to a fine spot on a fluorescent screen placed next to the wafer. The point of impact of the beam was located on the projection screen of the optical projection system. The electron beam was then successively applied to various points on the wafer. The beam voltage and current were held constant, and the pulse duration was changed with each application. Usually the beam was applied

nine times to each wafer. The diameter of the alloyed spots was about 0.4 mm.

The total heating effect of the electron beam depends on the total beam energy, i.e. product of beam voltage, beam current, and duration of beam application, and on the heat dissipating properties of the substrate. Two cases must be considered when the electron beam is used to locally alloy a metal to a semiconductor:[5]

1. In one case, the total beam energy is such that the temperature of the bombarded region is raised above the metal-semiconductor eutectic but below the melting point of the semiconductor. This process is similar to the conventional alloy junction and the alloying depth is determined mainly by the dissolution process.
2. In the other case, the total beam energy is such that the semiconductor is locally melted to a depth which depends on the beam energy. This is the case of interest in this research and most of the junctions fabricated were of this type.

Limiting Beam Power Values

It was found for the 20 mil thick wafers that a beam power of about 10 watts applied for 0.01 sec in the 0.4 mm spot was sufficient to locally melt the wafer, while when the beam power was increased above 30 watts applied for 0.01 sec in the 0.4 mm spot, the wafer was melted completely through in the bombarded region. For the 7 mil thick wafers, a beam power of about 5 watts applied for 0.01 sec in the 0.4 mm spot was sufficient to locally melt the wafer, while when the beam power was increased above 10 watts applied for 0.01 sec in the 0.4 mm spot the wafer was melted completely through in the bombarded region. It was found that for a given value of beam power, i.e., product of beam voltage and beam current, the beam was more stable for larger values of beam voltage and smaller values of beam current. For example, a 20 kV, 1 mA beam was found to be more stable than a 10 kV, 2 mA beam.

Preheating of Substrate

In the early stages of this research it was observed that a number of the wafers readily ruptured when bombarded with the electron beam. To prevent this, a nichrome heater was placed on the target positioner under the wafers, and the wafers were heated before being bombarded by the beam. It was found that by preheating the wafers to about 400°C the number of ruptures was considerably reduced.

Electrical Contacts

In order to measure the electrical properties of the p-n junctions, it was necessary to establish stable ohmic (nonrectifying) contacts to the alloyed regions and to the back side of the wafer. Since the alloyed regions are small, this presented a formidable problem. In the early stages of this research the unalloyed aluminum was etched away in HCl and a pressure probe was applied directly to the alloyed regions. This method was unsatisfactory in that difficulty was experienced in attaining stability and reproducibility of the electrical properties. A number of other techniques were attempted to establish stable ohmic contacts. The following proved to be the most successful. A thin film of silver was evaporated onto the side of the wafer where the alloyed regions were located, and gold doped with antimony was evaporated on the back side of the wafer. The thickness of the silver film was such that the alloyed regions were discernible through the silver film. The silver-coated alloyed regions were then masked by a technique similar to that suggested by S. Denda.[6] The wafers were placed on a tin oxide strip heater and a fine thread of apiezon W-40, black wax for sealing vacuum systems, was placed in touch with the silver-coated alloyed regions by using a specially designed masking facility under a stereomicroscope. The tip of the apiezon thread was melted by passing a current through the strip heater, leaving a masking dot over the alloyed regions. The entire back side of the wafer was masked with apiezon wax and the wafer was then etched in a solution of four parts HNO_3 and one part

HF. The etching was continued until the silver and the unalloyed aluminum were removed from the unprotected area. The apiezon wax was removed by benzene, and the wafer was then put through a cleaning cycle of acetone followed by methanol, followed by distilled water. By using this procedure, the wafer had the small alloyed regions coated with a thin film of silver and the entire reverse side coated with gold doped with antimony. The gold doped antimony assured an ohmic contact to the n region and the silver provided an ohmic contact to the alloyed regions. Electrical contacts were made to silver-coated alloyed regions with a pressure probe.

Cross-Sectional Profiles

In order to obtain cross-sectional profiles of the p-n junctions, a few junctions were cross sectioned and stained. These cross sections were obtained by cutting each junction from the wafer, mounting each chip in Koldmount (a self-curing resin), sawing the mounted chip a small distance from the junction, lapping away the material to the center of the junction, and then polishing the cross section. The junctions were stained by placing in a dilute solution of $CuNO_3$ and adding a few drops of HF while illuminating the junction with white light.[7] This staining technique causes the copper to plate on the n region more readily than on the p region, thus distinguishing the p region from the n region.

Results

Current-Voltage Characteristics

The current-voltage characteristics of the junctions were recorded on an oscilloscope type curve tracer. Typical characteristics with aluminum as the impurity layer are shown in Figure 4 for parameters of Table I. Similar characteristics were obtained when boron was used. Of particular interest are the low reverse leakage current and the sharpness of the breakdown voltage. This indicates the junctions are uniform and free of contamination.

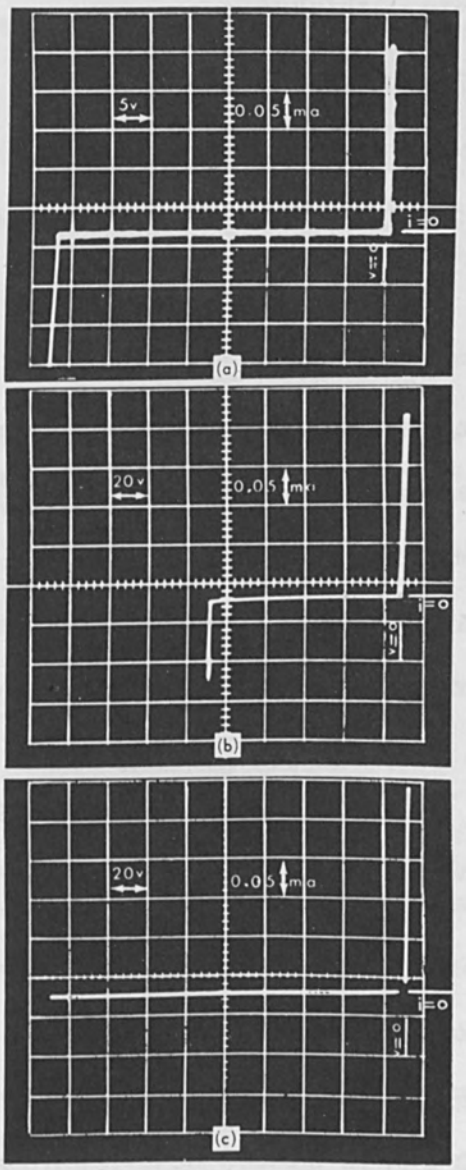

FIGURE 4 TYPICAL CURRENT-VOLTAGE CHARACTERISTICS OF ALUMINUM DOPED DIODES

TABLE I Formation Parameters for Junctions Shown in Figure 4

Base material - silicon wafer 20 mil thick
Dopant - aluminum

Fig.	Base Resistivity ohm- cm	Dopant layer thickness Å	Beam parameters kV	mA	Duration-sec
4a	0.5 ± 0.14	208	10	1.0	1.0
4b	2.0 ± 0.56	409	20	0.5	1.0
4c	55.0 ± 8.6	606	20	0.5	0.5

Breakdown Voltage

The breakdown voltage of the diodes was found to increase with increasing resistivity of the base wafers as shown in Table II. These results, showing tolerable agreement with other reported data[8] on silicon alloy diodes with n-type base material, indicate that alloy junctions formed by electron beam processing have breakdown voltages comparable to those formed by other techniques.

TABLE II Breakdown Voltage

Nominal Resistivity of base wafer	Observed Breakdown voltage
ohm-cm	volts
0.2 ± 0.036	24 ± 4
0.5 ± 0.14	41 ± 5
2.0 ± 0.56	87 ± 20
20.0 ± 5.4*	over 200
55.0 ± 8.6*	over 200

* Data on aluminum doped junctions only.

Frequency Response Characteristics

Frequency response characteristics were made on a number of diodes. The circuit shown schematically in Figure 5 was used to make these measurements. The input was a sine wave and the output was taken across the resistor and displayed on an oscilloscope. Typical frequency response characteristics are shown in Figure 6. Ideally, the output wave would be completely half wave rectified. As can be seen from Figure 6, no distortion occurs at 50 kc/sec, a small amount of distortion occurs at 500 kc/sec and more at 1 Mc/sec.

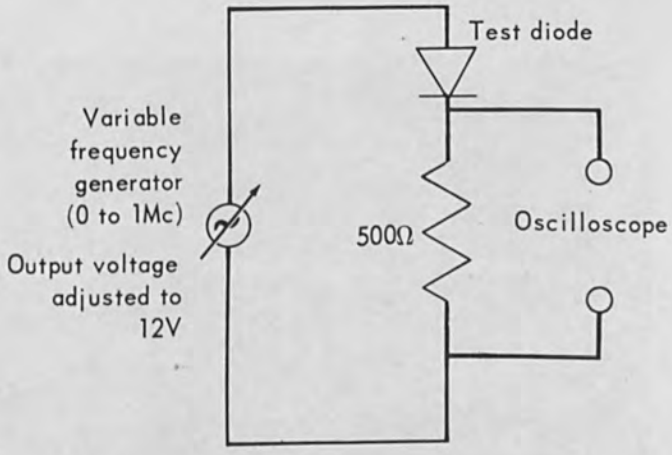

FIGURE 5 CIRCUIT USED FOR FREQUENCY RESPONSE MEASUREMENTS

Alloying Depth

Photomicrographs of the stained cross sections of two of the junctions are shown in Figure 7. The dark hemispherical region (A) is the alloyed p region, while the lighter region (B) is the n-type wafer. (C) is Koldmount. (D) is empty space where the Koldmount has buckled away from the wafer. Both junctions were taken from the same wafer. The thickness of the aluminum film was 490 Å. The junction of Figure 7a was processed with a 20 kV, 0.5 mA beam for 0.01 sec and has an alloying depth of 80 microns. The junction of Figure 7b was processed with a 20 kV, 0.5 mA beam for 2.0 sec and has an alloying depth of 200 microns. These

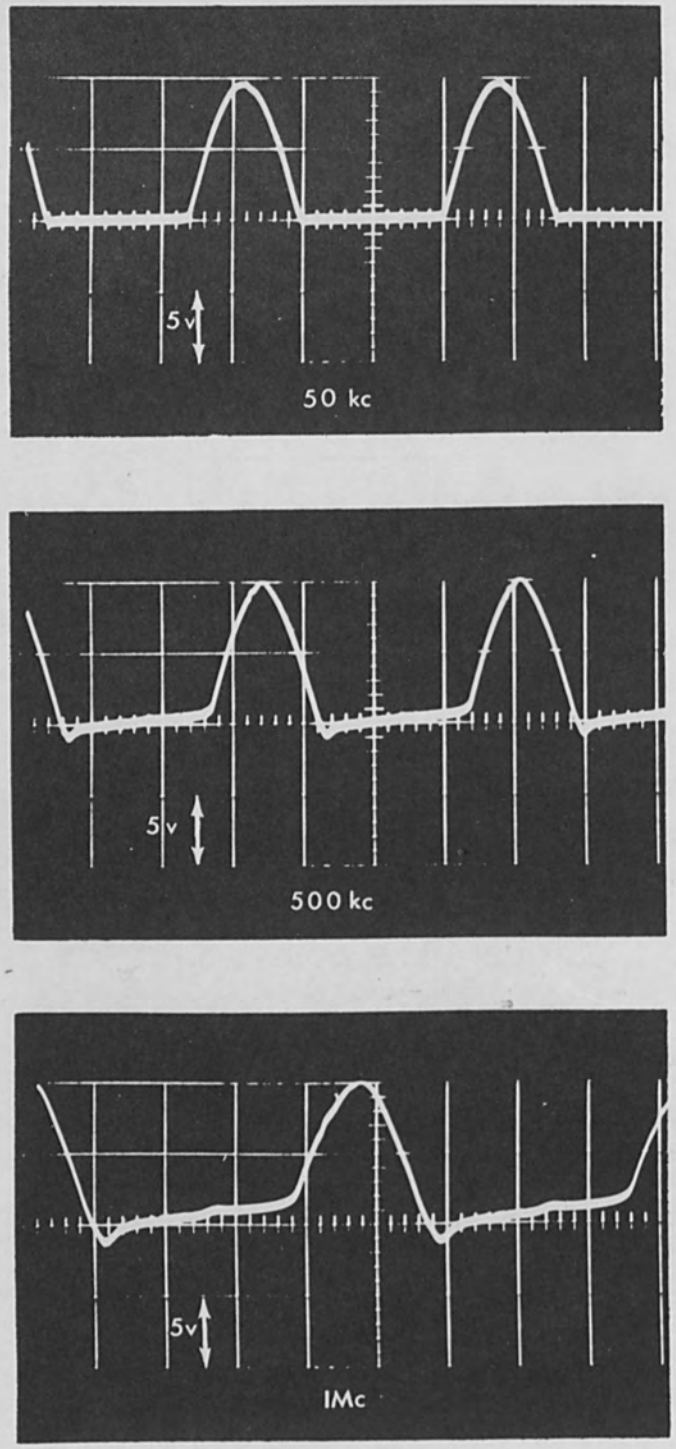

FIGURE 6 TYPICAL FREQUENCY RESPONSE CHARACTERISTICS

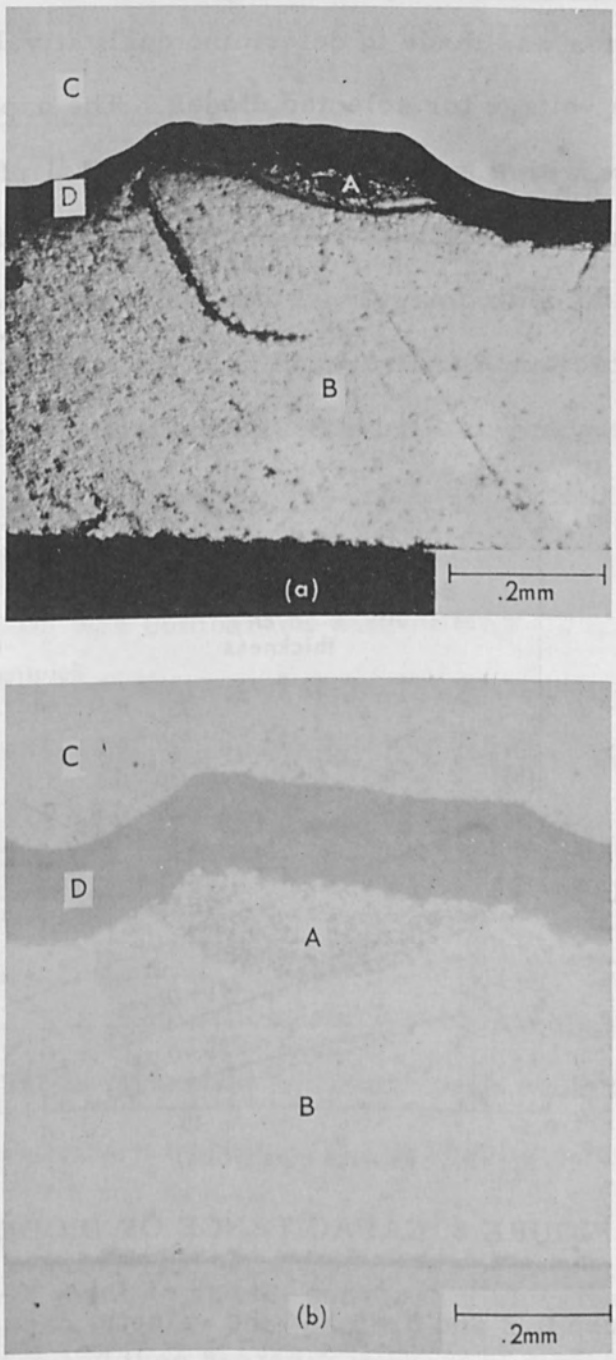

FIGURE 7 TYPICAL PHOTOMICROGRAPHS OF STAINED CROSS SECTION

cross sections demonstrate that the alloying depth can be controlled by controlling the duration of beam application.

Capacitance Measurements

A brief investigation was made to determine qualitatively the relationship of capacitance to reverse voltage for selected diodes. The capacitance was measured by an impedance bridge with a minimum sensitivity of 1.1 pF. When the capacitance was plotted against the reverse voltage on a logarithmic scale, an approximate straight line with a negative slope resulted at voltages below 10 volts, suggesting that the capacitance and reverse voltage are related by $C = \text{Const.}\ V^{-n}$. Three such curves are shown in Figure 8. Of the total group of diodes tested, the

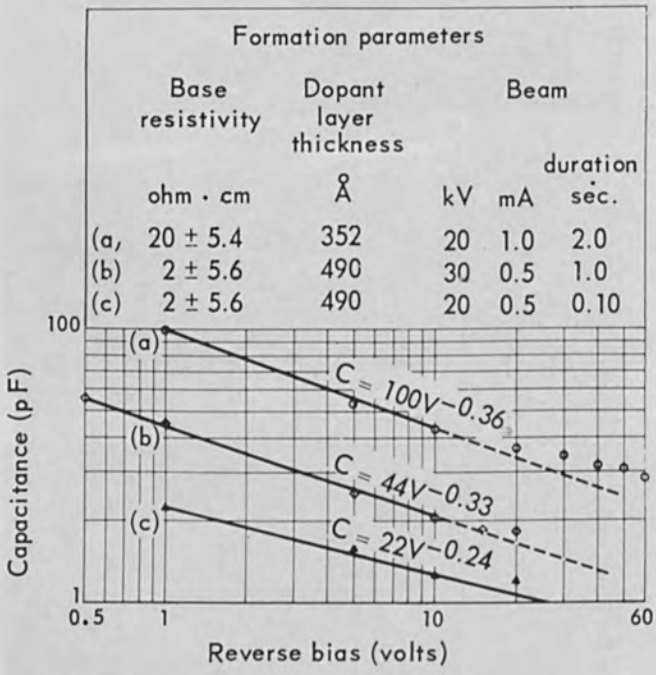

FIGURE 8 CAPACITANCE OF DIODES

value of n varied between 0.2 and 0.45 and the value of capacitance at 1 V reverse bias varied between 22 pF and 100 pF. It has been shown theoretically[9] that for step p-n junctions the capacitance and reverse voltage are related by $C = \text{Const.}\ V^{-0.5}$ and for linearly graded junctions the capacitance and reverse

voltage are related by $C = \text{Const.}\ V^{-0.33}$. Further investigation is required to determine the nature of the impurity gradient at the junctions formed by electron beams as well as other parameters which influence capacitance. However, these curves seem to indicate that the junctions are not abrupt.

Dislocations in Bombarded Region

In order to see what effect the bombardment of the electron beam has on the crystal structure of the silicon wafers, a few bare wafers were bombarded with an electron beam and then etched in a mixture of chromic acid and hydrofluoric acid. This etchant attacks the strained area surrounding the crystal dislocations producing etch pits which are discernible under a microscope. Typical photomicrographs of the etch pits in the region bombarded by the electron beam are shown in Figure 9. The region (a) was bombarded with a 10 kV, 1 mA beam for 1.0 sec and the region (b) was bombarded with a 10 kV, 1 mA beam for 0.10 sec. As can be seen from these photomicrographs, the dislocation density is high in the bombarded regions. By comparing the etch pit density of Figure 9a with that of Figure 9b, it can be seen that the total dislocation count decreases as the time of beam application decreases. These photomicrographs indicate that the dislocations are localized in the vicinity of the bombarded region and the remaining parts of the crystal are unaffected. The dislocations were also investigated by x-ray topographic techniques and by measurements of half-peak widths of diffractometry. The results of this investigation agreed with the results of the etch pit investigation.

Annealing Attempts

A few attempts were made to anneal out these dislocations. A wafer was bombarded with the beam and then heated in a vacuum oven held at 1000°C for two hours. This wafer was then etched and the etch pit densities were compared with those of a wafer which was bombarded with a similar beam but not annealed. There was no discernible difference in the etch pit densities of the annealed and the

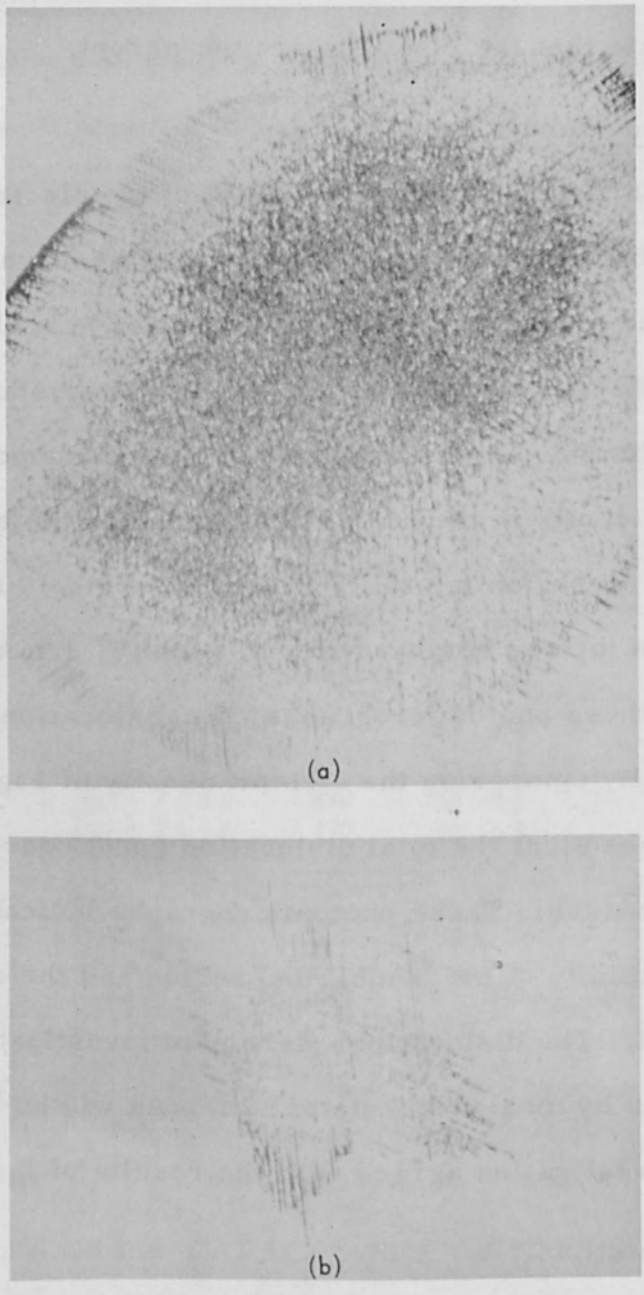

FIGURE 9 TYPICAL PHOTOMICROGRAPHS OF ETCH PITS IN BOMBARDED REGION

unannealed wafers. This indicates that the majority of the dislocations are not annealed out by heating to 1000°C.

Surface Effects

It should be pointed out that a considerable number of the junctions, especially the ones fabricated from high resistivity wafers, exhibited a relatively high reverse leakage current and an unstable breakdown at a value of reverse voltage considerably less than the values reported by McKay.[8] Since the electrical properties of a number of these junctions were improved by masking, etching, and cleaning again, it is believed that these undesirable effects are caused by surface contamination. As pointed out by numerous authors,[7, 10] these surface effects can be reduced by passivating the surface with a dielectric film. No surface passivation attempts were undertaken.

Yield

In order to determine the yield of these techniques, 76 diodes were fabricated using an aluminum film approximately 200 Å thick deposited on four silicon wafers which had nominal resistivities of 0.5 ± 0.14 ohm-cm. The 76 diodes were formed by applying a 20 kV, 0.5 mA beam for 0.5 sec. Of the 76 diodes, 52 had satisfactory current voltage characteristics similar to Figure 4a. This corresponds to a yield of approximately 69% for this operation.

Conclusions

The following conclusions can be drawn from the results of this research:

1. Functional diodes can be fabricated by applying electron beam techniques.
2. The alloying depth can be controlled by controlling the electron beam parameters.
3. The principal drawback, and perhaps the limiting feature, of

electron beam techniques in fabricating p-n junctions is the adverse effect of the beam on the crystal structure.

The electron beam appears to have a promising future in the fabrication and processing of microelectronic devices and circuits. Resolutions as high as 0.10 microns have been reported with some electron beam systems. Diodes of the order of 5 microns in cross section are believed possible.[4] As microelectronic devices and circuits become smaller and more sophisticated, fabrication techniques which have resolutions of this order of magnitude must be utilized.

Acknowledgements

Appreciation is extended to Mr. R. Wyatt for his technical assistance, to Miss Elaine Louis for performing numerous thickness measurements, to Mr. J. Froechtenigt for doing the boron evaporations, to Mr. W. R. Huelskoetter for designing the pulse circuit, and to Dr. G. Carron for the x-ray analysis of the crystal defects.

References

1. Shockley, W., U.S. Patent 2,816,847 (1957).
2. Wells, O. C., Proceedings Third Symposium on Electron Beam Technology (Alloyd Electronic Corp., Boston, Mass., March 1961), p. 291.
3. Steigerwald, K. H., Proceedings Third Symposium on Electron Beam Technology (Alloyd Electronic Corp., Boston, Mass., March 1961), p. 269.
4. Bakish, R., Electronics, July 28, 1961.
5. Pergalo, G. C. Della and S. A. Zeitman, Metallurgy of Semiconductor Materials (Interscience Publishers, New York and London, 1962), Vol. 15, p. 191.
6. Denda, S., Solid State Electronics 2, 69 (1962).
7. Holmes, P. J., The Electrochemistry of Semiconductors (Academic Press, London and New York, 1962), p. 371.

8. McKay, K. C., Phys. Rev. 94, 877 (1954).

9. Phillips, A. B., Transistor Engineering (McGraw-Hill Book Company, New York, 1962), p. 111.

10. Garrett, C. G. B., and W. H. Brattain, J. Appl. Physics 27, 299 (1956).

Optimum Parameters for Electron Beam Machining

by

O. C. Wells
CBS Laboratories
Stamford, Connecticut

Abstract

During electron beam machining, the peak attainable temperature is limited by electron penetration, by thermal conduction, by the lens aberrations, and by the electron-optical brightness condition. In an earlier paper, a calculation was made of the optimum parameters to give the smallest possible heat-affected zone for a given temperature rise. This calculation is extended to give the optimum parameters for the case in which the heat-affected zone is shallow instead of narrow.

Introduction

The size and the shape of the heat-affected zone that results when an electron beam strikes or scans across a solid workpiece has been calculated by several authors.[1-5] While such calculations are, of course, at best only approximate, it is nevertheless believed that they are valuable in that they indicate the fundamental limits.

The assumptions that are generally made are that the thermal properties of the material are independent of temperature, that no phase changes occur, that work done by the stresses that are set up in the material can be ignored, and that radiation from the surface can be neglected.

The four factors that are important are (1) the diameter of the incident electron beam, (2) the current contained in the beam as limited by electron-optical

conditions, (3) the electron penetration, and (4) thermal conduction.

In the electron-optical arrangement as shown in Figure 1, the independent parameters are the electron energy E volts, the Gaussian electron beam diameter at the workpiece D_g cm, the beam semi-angle at the workpiece θ radians, and the pulse duration t seconds. (In the case of a scanning beam then the final independent parameter will, of course, be the scanning velocity of the beam.) The remaining design parameters that restrain the performance of the system are the electron source temperature T degrees Kelvin, the electron source current density ρ_c amps/cm^2, the spherical aberration coefficient C_s of the focusing lens, and the physical parameters of the workpiece.

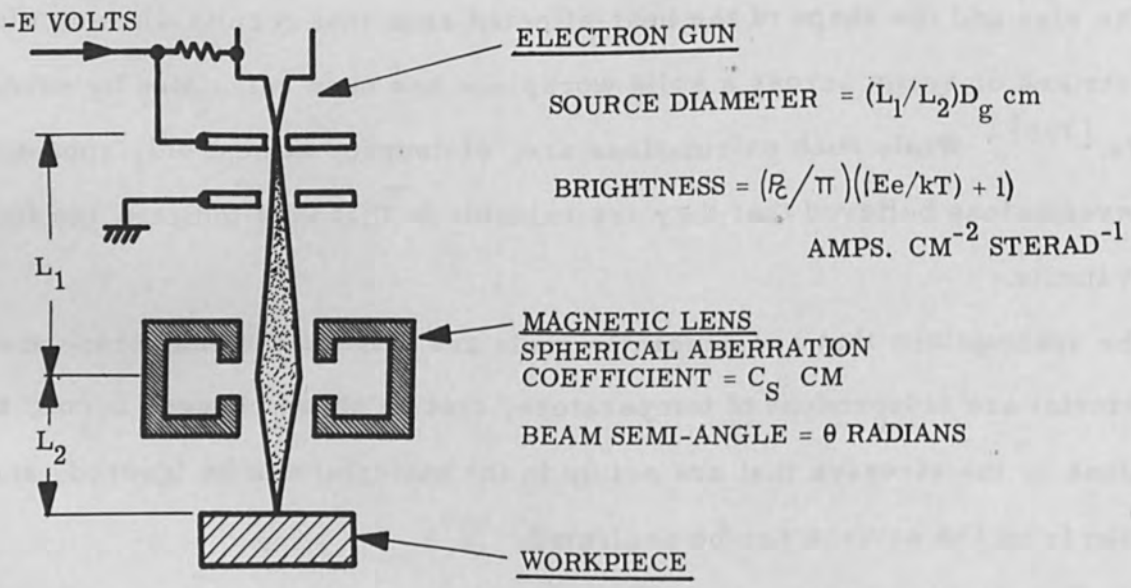

FIGURE 1 SCHEMATIC DIAGRAM

In the above paragraph, the Gaussian beam diameter at the surface of the workpiece is written as D_g. Throughout the present paper the symbol D (with a subscript) is used to denote a dimension measured parallel to the surface of the material, while the symbol Z (with a subscript) is used to denote a dimension measured in a direction perpendicular to the surface.

The difference between the D and the Z directions is, of course, that in the D direction the temperature distribution is defined jointly by the three factors, beam diameter, electron penetration (sideways scatter) and thermal conduction; while in the Z direction it is only the electron penetration and the thermal conduction that apply. Thus, if the electron energy is very high and the beam diameter is very small, then it is to be expected that the Z dimension of the heat-affected zone will be greater than the D dimension, but if low-voltage beam of large diameter is used, then the reverse condition will apply.

It turns out that if an attempt is made to calculate the thermal profile precisely, then it becomes extremely difficult to allow in a meaningful way for the effects of electron penetration, for the lens aberration, and for the electron-optical brightness condition. This is shown in Table I. Pittaway,[1] and Taniguchi and Maezawa,[2] both calculate the precise temperature profiles that exist in the material during and after the electron pulse, but in neither paper are the effects of the electron penetration or electron-optical limitations considered. Their approach consisted of a straightforward application of the heat-flow equations. The problem has been considered in one dimension taking penetration into account by Vibrans.[3] Vine and Einstein,[4] calculate the temperature-rise that occurs when an electron beam is stationary for an indefinite length of time on a semi-infinite solid, taking the electron penetration, the electron backscatter, and the brightness limitation into account. Their method was to calculate the temperature rise that would occur in the absence of both electron backscatter and electron penetration (the "disc

TABLE I

Scope of Published Papers

Author	calculated the precise temperature profile	allowed for electron penetration	allowed for electron-optical limitations	Situations Analysed
Pittaway[1]	✓	no	no	Pulsed and sweeping beams. Solid and foil targets.
Taniguchi and Maezawa[2]	✓	no	no	Pulsed case only. Solid Targets.
Vibrans[3]	✓	✓	no	One-dimension only. Solid targets.
Vine and Einstein[4]	no	✓	✓	Stationary beam only. Solid target.
Wells[5]	no	✓	✓	Pulsed condition only. Solid target only. "Narrow" case only.
This Paper	no	✓	✓	Pulsed condition only. Solid target only. "Shallow" case and Narrow case.

heating model"), and then to modify the formula to allow for the backscatter and the penetration (the "source dispersal effect"). It is quite possible that a similar analysis might also be successful for the pulsed condition.

In the present paper the method will be followed that was used in an earlier paper,[5] in which some rather severe assumptions are made concerning the resultant heat-affected zone.

Thus, even though it is appreciated that the energy distributions introduced by electron penetration and by thermal conduction are non-gaussian in form, it is found that if the resultant heat-affected zone is nevertheless assumed to be gaussian then a considerably simplified analysis can be made. In reference 5 this method is used to calculate the values that must be given to the independent parameters E, D_g, θ and t if the maximum possible temperature rise is to be achieved within a region of specified horizontal extent D_v (i.e., for the narrowest possible heat-affected zone). In the present paper the same method is applied to calculating the optimum values that must be given to E, D_g, θ and t if the dimension Z_v is to be minimized; i.e., if the heat-affected zone is to be shallow instead of narrow. The interest in shallow heat-affected zones arises, for example, in cases when it is desired to remove a thin film from certain areas on a substrate while minimizing the heat input to the substrate.[6]

The workpiece parameters that are specified in this paper are m = thermal diffusivity in cm^2/sec; ρ = density in gm/cm^3; s = specific heat in cals/gm deg and $K = m\rho s$ is the thermal conductivity in cals/cm sec deg.

Basic Equations

(a) RMS Diameter

Fundamental to any discussion must be the definition of the word "diameter" as applied to the heat-affected zone. In reference 5 the "RMS" diameters D_v and Z_v of a temperature distribution v(x, y, z) are defined as

$$D_v^2 = (5.51/V) \int_{-\infty}^{\infty} \int_{-\infty}^{\infty} \int_{-\infty}^{\infty} x^2 \cdot v(x, y, z)\, dx\, dy\, dz \qquad (1)$$

and

$$Z_v^2 = (5.51/V) \int_{-\infty}^{\infty} \int_{-\infty}^{\infty} \int_{-\infty}^{\infty} z^2\, v(x, y, z)\, dx\, dy\, dz \qquad (2)$$

where

$$V = \int_{-\infty}^{\infty} \int_{-\infty}^{\infty} \int_{-\infty}^{\infty} v(x, y, z)\, dx\, dy\, dz \quad . \qquad (3)$$

The coordinates are chosen with the origin at the point of impact of the electron beam and with the z axis extending downwards into the material. In evaluating these integrals, the temperature v is assumed to be defined also for points above the surface, such that $v(x, y, -z) = v(x, y, z)$.

The purpose of these definitions is that it then becomes possible to write down the following equations, which are exact:

$$D_v^2 = D_p^2 + D_t^2 + D_g^2 + D_s^2 \qquad (4)$$

and

$$Z_v^2 = Z_p^2 + Z_t^2 \qquad (5)$$

where D_v and Z_v are the RMS diameters in the x and z direction of the resultant heat-affected zone; where

$$D_p = Z_p = (6.6/\rho) \cdot 10^{-11} \cdot E^{1.65} \qquad (6)$$

are the RMS diameters of the electron penetration figure in the x and z directions (assumed to be equal); where

$$D_t = Z_t = 2.35 \sqrt{mt} \qquad (7)$$

are the RMS diameters of the thermal conduction figure; where D_g is an independent parameter; and where

$$D_s = (1/2)\, C_s\, \theta^3 \qquad (8)$$

is the beam enlargement introduced by spherical aberration. In equations 6 and 7 the numerical coefficients have been adjusted in accordance with equations 1-3 as discussed in reference 5.

It will be noted that in the above discussion, the presence of the surface has been allowed for by assuming that the heat-affected zone is the lower half of a zone that is symmetrical about the plane $z = 0$, and by assuming that there is an identical generation of heat at the points $(x, y, \pm z)$. This carries with it the assumption that the heat lost by radiation from the surface is zero. The quantity Z_v is the diameter in the z direction of the overall symmetrical zone. The depth of the heat-affected zone below the surface is therefore $(1/2)Z_v$.

(b) The resultant heat-affected zone

If a relation is to be established between the peak temperature and the dimensions of the resultant heat-affected zone, then a knowledge of the resultant temperature distribution is required. The incident electron beam consists of a 2-dimensional gaussian distribution; while the electron penetration figure and the zone-enlargement introduced by thermal conduction are both 3-dimensional and non-gaussian. The form of the resultant heat-affected zone is therefore difficult to calculate exactly.

In reference 5 the assumption is made that the resultant temperature distribution is gaussian in form, so that

$$v = v_{max} \exp\left[- \frac{x^2 + y^2}{0.36 D_v^2} - \frac{z^2}{0.36 Z_v^2} \right] . \qquad (9)$$

From this it follows that the quantity of heat Q calories that must be injected into the workpiece to give a peak temperature rise v_{max} at the center of the distribution must be

$$Q = 0.60 \rho s v_{max} D_v^2 Z_v \quad \text{cals.} \qquad (10)$$

The total heat that is transferred to the workpiece during a current pulse I amps for t seconds is given by

$$Q = 0.24\, p\, E\, I\, t \quad \text{cals.} \tag{11}$$

where p is the power-retention factor as derived by Vine and Einstein[4] to make allowance for the energy lost from the specimen in the back-scattered electrons.

(c) The brightness condition

The current contained in the beam is given by

$$I = (\pi/4)\, D_g^2\, \rho_c\, [\,(Ee/kT) + 1\,] \sin^2 \theta$$

$$\doteq (\pi/4)\, D_g^2\, \rho_c\, (Ee/kT)\, \theta^2 \tag{12}$$

where $e = 1.6 \times 10^{-19}$ coulombs is the elementary charge, and where $k = 1.38 \times 10^{-23}$ joules/deg K is Boltzmann's constant.

Optimization of the Equations

In reference 5 the above equations are optimized to determine the values that must be given to the independent variables E, D_g, θ and t if the maximum possible temperature rise is to be achieved within a region of specified horizontal extent D_v. It turns out that the depth of the heat-affected zone, $(1/2)Z_v$, must be equal to $0.37\, D_v$ if D_v is to be minimized for a given v_{max} (equation 43 in reference 5).

In the present paper, with Z_v fixed and small, it is desired to determine the minimum value that can be achieved for D_v for a given value of v_{max}. This optimization is achieved by writing

$$\begin{aligned} \mu_t &= D_t / Z_v \\ \mu_p &= D_p / Z_v \\ \mu_g &= D_g / Z_v \\ \mu_s &= D_s / Z_v \end{aligned} \tag{13}$$

so that

$$t = 0.18\,\mu_t^2\,Z_v^2/m \qquad \text{from equations 7 and 13}$$

$$E = (1.5 \times 10^{10}\,\rho\,\mu_p Z_v)^{0.606} \qquad \text{from equations 6 and 13}$$

$$D_g = \mu_g Z_v \qquad \text{from equation 13}$$

$$\theta = (2\mu_s Z_v/C_s)^{1/3} \qquad \text{from equations 8 and 13.}$$

(14)

We then have

$$Q = A\mu_t^2\,\mu_p^{1.212}\,\mu_g^2\,\mu_s^{2/3}\,Z_v^{5.88} \tag{15}$$

where

$$A = (1.36 \times 10^{15})\,(\rho^{1.212}\,p\cdot\rho_c)\,/\,(Tm\,C_s^{2/3}) \tag{16}$$

and where from equations 4 and 5

$$\mu_t^2 + \mu_p^2 + \mu_g^2 + \mu_s^2 = (D_v/Z_v)^2 \tag{17}$$

and

$$\mu_p^2 + \mu_t^2 = 1 \quad . \tag{18}$$

By differentiating equations 15, 17 and 18, it may then be deduced that the maximum attainable value of Q is

$$Q_{max} = 0.162\,A\,((D_v/Z_v)^2 - 1)^{4/3} Z_v^{5.88} \tag{19}$$

and that this maximum occurs for the following values of the parameters:

$$\begin{aligned} \mu_t &= 0.788 \\ \mu_p &= 0.613 \\ \mu_g &= 0.866\,((D_v/Z_v)^2 - 1)^{1/2} \\ \mu_s &= (1/2)\,((D_v/Z_v)^2 - 1)^{1/2} \quad . \end{aligned} \tag{20}$$

It therefore follows from equations 10 and 19 that the highest temperature v_{max} that can be achieved in a zone of width D_v and depth (1/2) Z_v is

$$v_{max} = A' \left((D_v/Z_v)^2 - 1 \right)^{4/3} \left(Z_v^{4.88}/D_v^2 \right) \tag{21}$$

where

$$A' = 3.67 \times 10^{14} \left(p \, \rho^{1.212} \, \rho_c \right) / \left(TK \, C_s^{2/3} \right) \tag{22}$$

The optimum values of t, E, D_g and θ are given by equations 12 and 18 to be:

$$t = 0.11 \, Z_v^2/m \tag{23}$$

$$E = 1.1 \times 10^6 \, (\rho Z_v)^{0.606} \tag{24}$$

$$D_g = 0.866 \left((D_v/Z_v)^2 - 1 \right)^{1/2} Z_v \tag{25}$$

$$\theta = \left((D_v/Z_v)^2 - 1 \right)^{1/6} \left(Z_v/C_s \right)^{1/3} \tag{26}$$

$$I = 7.53 \times 10^9 \left(\rho_c / TC_s^{2/3} \right) \rho^{0.606} \left((D_v/Z_v)^2 - 1 \right)^{4/3} Z_v^{3.27} \, . \tag{27}$$

For $D_v/Z_v \gg 1$ these equations simplify to give

$$v_{max} = A' \, D_v^{0.67} \, Z_v^{2.21} \tag{28}$$

$$D_g = 0.866 \, D_v \tag{29}$$

$$\theta = D_v^{1/3} \, C_s^{-1/3} \tag{30}$$

$$I = 7.53 \times 10^9 \left(\rho_c / TC_s^{2/3} \right) \rho^{0.606} \, D_v^{8/3} \, Z_v^{0.60} \, . \tag{31}$$

Discussion

In the present analysis, where D_v and Z_v are both specified, the adjustment of the parameters t, E, D_g and θ to give maximum power Q transferred into the workpiece is the same as the adjustment to give the maximum possible v_{max}. This was not the case in reference 5. In the analysis that was given there, D_v,

was held fixed and Z_v was varied until the power Q was a maximum, and this gave a slightly higher value for the ratio (Z_v/D_v) than would have been the case if v_{max} had been optimized instead of Q. This can be seen from Figure 2, where v_{max} as given by equation 21 is plotted against Z_v for D_v fixed. For each point on this curve the parameters t, E, D_g and θ are optimized according to equations 23 through 26 above.

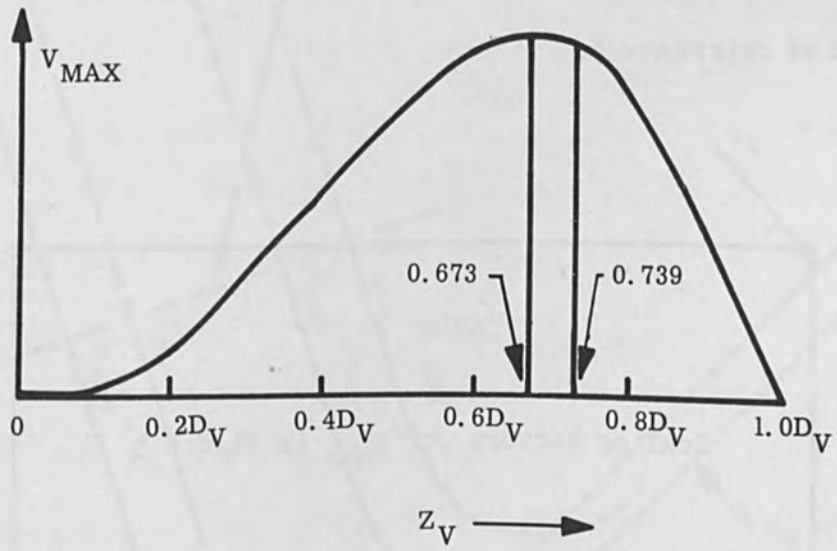

FIGURE 2 V_{max} AS A FUNCTION OF Z_v FOR D_v FIXED.

For small values of Z_v in Figure 2, both the voltage and the pulse duration must be small, and v_{max} is therefore small. At the value $Z_v = 0.739\ D_v$ the power Q transferred into the workpiece is maximum for fixed D_v, (as was shown in reference 5), and it will be found that if this value for Z_v is substituted into equations 21 through 27 above, then the precise equations for these quantities will be obtained as are given in reference 5. But if equation 21 is differentiated, then it is found that the maximum value for v_{max} occurs for $Z_v = 0.673\ D_v$. As can be

seen from Figure 2, the practical significance of this is probably negligible. It will be noted that these ratios are independent of the properties of the material.

The dependence of v_{max} on D_v and Z_v for copper is shown in Figure 3. The parameters that were assumed were $\rho_c = 2.7$ amps/cm^2 at $T = 2.700^{\circ}$K and $C_s = 30$ cm. At the points where the curves intersect the line $Z_v = 0.739\ D_v$ values of D_v are obtained corresponding to Figure 2 in reference 5. The points for which the present analysis is of interest lie above that line. For other materials, the values of v_{max} as given in Figure 3 must be multiplied by the scaling factors given in Table II. The physical properties of materials that were assumed are as shown in Table I of reference 5.

TABLE II

Scaling Factors for v_{max} in Figure 3

Cu, Ag	1.0	Fe	5.2
Al	0.62	W	5.9
Si	1.3	Ni	7.3
Au	3.0	Pb	12.4
Ge	3.8		

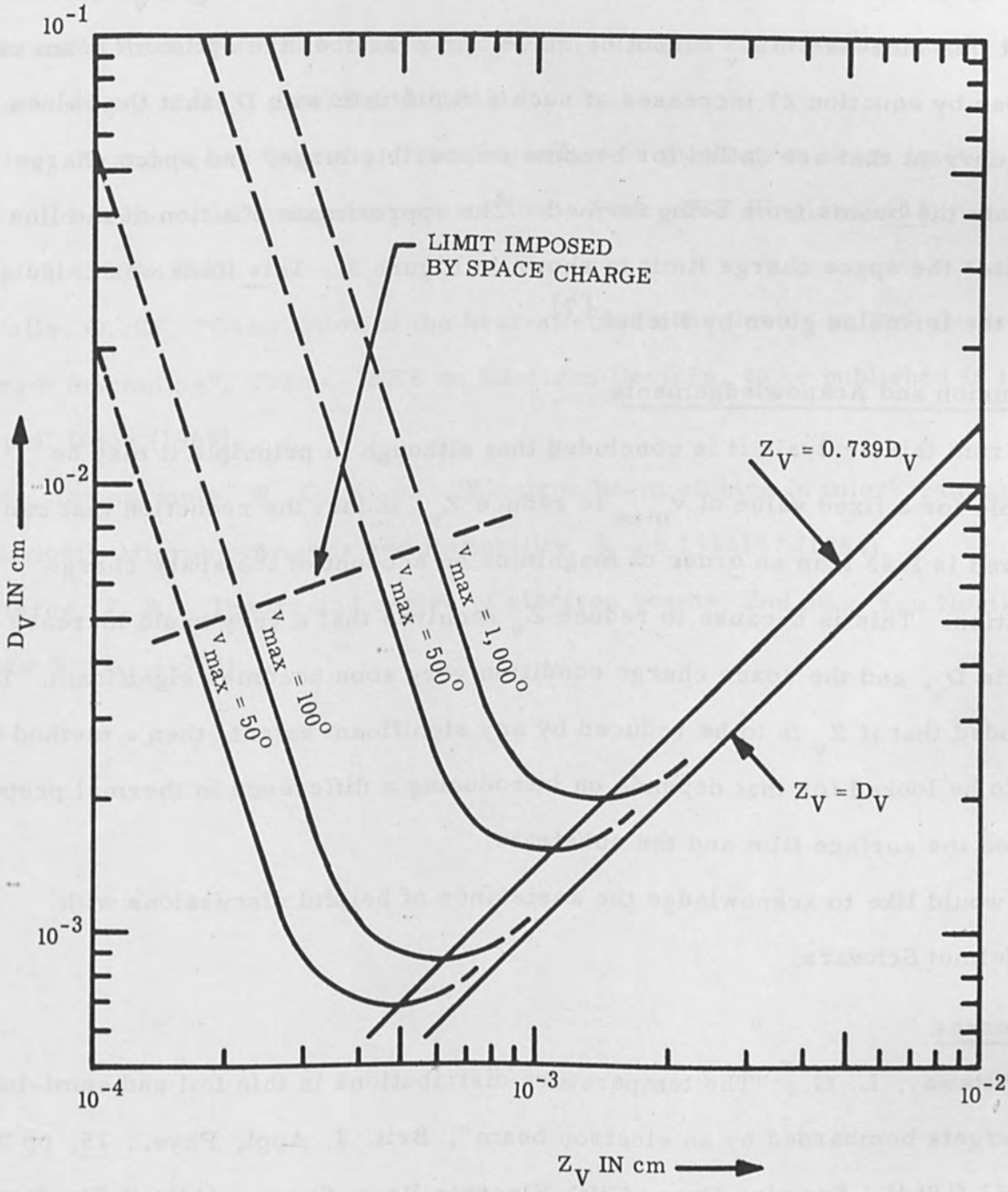

FIGURE 3 V_{max} AS A FUNCTION OF D_v AND Z_v FOR COPPER

One of the features of Figure 3 is the high slope of the curves, so that D_v must be increased by several orders of magnitude if Z_v is to be reduced significantly below the value that can be obtained for the condition when $Z_v = 0.739\ D_v$. In fact this increase in D_v cannot be made. In practice, the optimum beam current as given by equation 27 increases at such a rapid rate with D_v that the values of beam current that are called for become impossibly large, and space charge prevents the beams from being formed. The approximate position of the line that indicates the space charge limit is shown in Figure 3. This limit was calculated using the formulae given by Pierce.[7]

Conclusion and Acknowledgements

From this analysis it is concluded that although in principle it may be possible for a fixed value of v_{max} to reduce Z_v, in fact the reduction that can be achieved is less than an order of magnitude on account of the space charge limitation. This is because to reduce Z_v requires that a very rapid increase is made in D_v, and the space charge condition very soon becomes significant. It is concluded that if Z_v is to be reduced by any significant extent, then a method will have to be looked for that depends on introducing a difference in thermal properties between the surface film and the substrate.

I would like to acknowledge the assistance of helpful discussions with Dr. Helmut Schwarz.

References

1. Pittaway, L. G., "The temperature distributions in thin foil and semi-infinite targets bombarded by an electron beam", Brit. J. Appl. Phys., 15, pp 967-982 (1964). See also Proc. Fifth Electron Beam Symp., (Alloyd Electronics Corp., Cambridge, Mass.) pp 88-123 (1963).
2. Taniguchi, N. and S. Maezawa, "Temperature analysis of electron beam machining to get the optimum operating condition for pulsative method",

Proc. Fifth Electron Beam Symp., (Alloyd Electronics Corp., Cambridge, Mass.) pp 135-148 (1963).

3. Vibrans, G. E., "Theoretical temperature rise in materials due to electron beams", Proc. Fifth Electron Beam Symp., (Alloyd Electronics Corp., Cambridge, Mass.) pp 124-134 (1963).
4. Vine, J. and P. A. Einstein, "Heating effect of an electron beam impinging on a solid surface, allowing for penetration", Proc. IEE (England) 111, pp 921-929 (1964).
5. Wells, O. C., "Calculation of the heat-affected zone during pulsed electron beam machining", Trans. IEEE on Electron Devices, to be published in the April Issue (1965).
6. See, for example, W. C. Nixon, "Electron beam etching in micro-miniaturization", Microelectronics and Reliability, 3, pp 153-157 (1964).
7. Pierce, J. R., Theory and design of electron beams, 2nd ed., Van Nostrand, New York. (1954)

The Arc Spot as a Dense Plasma Maintained by Micro Analogs of Macro Beams

by

J. Rothstein
Laboratory for Electronics, Inc.
Boston, Massachusetts

Abstract

Focused electron, ion, and light beams can generate high density plasma conditions in the region of concentrated energy input. Phenomena in the high energy density region tend to become independent of the precise energy input or concentrating mechanisms, being dominated by the tendency of the hot microplasma to expand. In order to have a steady state, one must maintain a balance between energy concentrating and energy dissipating mechanisms. In the case of particle beams, plasma generation is generally incompatible with maintenance of beam concentrating field configurations, and can culminate in destructive arcs. Steady state arc spots (e.g. on mercury) are known, in which energy concentration mechanisms maintain a local dense plasma condition despite its explosive nature. A mechanism is proposed for arc spot maintenance which can be viewed as a microscopic limit of both the ion and electron beams. The energy input mechanism is viewed as a combination of focused beams of ions and electrons, the former impinging on the cathode surface from outside, the latter being essentially a "stream-line" flow of electrons from the bulk cathode into the sink provided by the cathode spot. An important role of space charge is then the maintenance of "beam focusing optics" for both electrons and ions on a microscopic scale. It is shown that plasma containment results in the spot region which is rather efficient. Analyses are given of this hot plasma theory of arc spot emission, and comparison made with other theories. An explanation of important arc spot properties including its retrograde motion, is given in terms of the dense plasma model. Brief

mention is made of the transition between conventional beams and destructive arcs, and the possibility of designing beam apparatus in which arcing can be useful rather than destructive.

Introduction

The interesting and puzzling phenomena at the cathode spot of an arc discharge are far from clearly understood even though the field is one of the oldest in electronics and intimately involved in many devices and phenomena of considerable practical importance. The chief problem is to explain how high arc spot current densities, variously estimated from a few thousand to 10^5, 10^6, 10^7, or even 10^8 amp/cm^2 can flow between a cold metal and a gas. Metallic work functions generally require temperatures of many thousands of degrees far in excess of the boiling points, to permit thermionic emission even within orders of magnitude of such values.[1] Means for concentrating ionic, rather than electron currents so that sufficiently high positive ion currents flow into the spot from the gas plasma to carry these current densities are hard to imagine.[2] Field emission[3] requires a high positive ion space charge near the cathode spot to pull the electrons through the cathode surface barrier. This leads to the same difficulty as having all the current carried by positive ions, namely the absence of a reasonable mechanism for concentrating a sufficiently high ion current density on the spot to maintain the required high positive space charge. Schottky lowering of the thermionic work function, by the field engendered by the incident positive ions, plus spot excitation by bombardment by the same ions, has been suggested as the basis of a combined field and thermionic emission mechanism (T-F emission).[4] Although the combined effects make both field and temperature requirements more moderate than for either emission mechanism alone, they do not provide a better solution to the mercury arc spot puzzle. For example, at a field of about 5×10^7 V/cm even a cathode temperature of 3000°K has little effect on total emission; at 10^7 V/cm a

temperature of 2000°K has a decisively large effect on emission, and at lower fields the emission is essentially thermionic. As mercury boils at 360°C T-F, emission faces either the same difficulties as thermionic emission or those of field emission, essentially. The idea that excited (metastable) atoms impinge on the cathode spot and thereby liberate electrons[5] encounters the difficulty that neutral metastables cannot be focused like charged particles. To achieve the required current density of metastables into the spot requires a continuous implosion of dense excited matter into the spot, which seems even harder to justify physically than a purely ionic current.

The arc spot mechanism adopted in the present paper is essentially the hot dense plasma model,[6] in which essentially metallic conduction into the spot is followed by a kind of quasi-thermal ionization of, or quasi-thermionic emission from, the hot exploding plasma. Electric fields play a vital role not only in maintaining the steady state spot excitation against the energy drain represented by the exploding plasma jet, but also in providing the "beam focusing optics" required. Magnetic fields associated with current flow through the spot are probably important for providing a "magnetic bottle" to contain the plasma spot against its tendency to expand in directions transverse to the current flow. On this model, much of the earlier disputation about mechanism becomes academic in the sense that the physical conditions needed to make any of them work (thermionic, ionic, field or excited atom) guarantee that a dense plasma spot will be formed. Its properties then dominate the situation, and one can associate its characteristics, to some extent, with any or all of those mechanisms. It is advisable to do this both for historical reasons and to illustrate the changes in classical concepts when they are extrapolated beyond the body of experience they were originally designed to coordinate.

The properties of the dense plasma are, to an appreciable extent, independent

of the precise energy input mechanism. In the original formulation[6] this was taken to be ionic bombardment. In an analysis of the physics of micromachining by focused laser beams[7] it was shown that a similar plasma spot would develop and some of its properties were explored. As energy dissipation in the spot could be by light or particle beams or by an entirely different mechanism, such as joulean heating, it seemed natural to consider the arc spot as an "exploding wire" tip.[8] The present paper can be considered as a more quantitative amplification of these concepts. Particular attention will be devoted to the beam-focusing aspects (perhaps stream-focusing would be a better description) of electron and ion flow needed to form the spot. It is believed that joulean heating in the spot and its immediate vicinity is often far more important in the energy economy of the spot than one would suspect from the arc spot literature.

Electron Stream Focusing and Power Dissipation Within the Cathode

Within the cathode one has ordinary ohmic current flow with the stream lines converging into the cathode spot. If the spot were a geometrical point the equipotentials would be spheres and the flow lines radii. If the spot is a disc, the equipotentials are oblate spheroids. For symmetry of revolution about an axis perpendicular to the plane of the surface and passing through the center of the spot, the equivalent radii in the point spot case form cones which become hyperboloids of one sheet orthogonal to the oblate spheroids in the disc case. The beam or flow aspects of the problem are thus fairly trivial; of greater interest is the power dissipation. The calculations involved are familiar from considerations of spreading resistance and crystal burnout.[9]

The thermal-continuity equation is

$$\nabla \cdot k \nabla \theta + Q = C \frac{\partial \theta}{\partial t} \qquad (1)$$

where θ is the temperature rise above ambient, k and C are respectively the

thermal conductivity and heat capacity per unit volume, and Q the power dissipated per unit volume. For an ohmic resistance, such as a bulk mercury cathode,

$$Q = \sigma \left| \nabla V \right|^2 \tag{2}$$

where σ is the conductivity and V the potential. In the steady state these equations yield

$$\nabla \cdot k \nabla \theta + \sigma \left| \nabla V \right|^2 = 0 \quad . \tag{3}$$

It is useful to regard the temperature as a sum $\theta_1 + \theta_2$, where θ_1 is the contribution produced in the spot by non-joulean processes like impacts, and θ_2 is produced by joulean dissipation in the spreading resistance. From (3), in the spreading region we have

$$\nabla \cdot k \nabla \theta_1 = 0 \quad . \tag{4}$$

If j is the corresponding thermal current density,

$$j = - k \nabla \theta_1 \tag{5}$$

then (4) becomes

$$\nabla \cdot j = 0 \quad . \tag{6}$$

There is complete analogy with electric current density i, for

$$i = - \sigma \nabla V \tag{7}$$

and

$$\nabla \cdot i = 0 \quad . \tag{8}$$

Just as electrical resistance can be found from

$$R_{elec} = \frac{\Delta V}{I} \tag{9}$$

where I is the total current flowing between two equipotential surfaces of potential difference ΔV, so can one compute a thermal resistance between two isothermal

surfaces with temperature difference $\Delta\theta$ in terms of the total heat flux J, namely

$$R'_{therm} = \frac{\Delta\theta}{J} \quad . \tag{10}$$

It is reasonable to regard the boundary between the bulk cathode and the cathode spot as an equipotential surface, for the former has true metallic conductivity, while the latter is to be regarded as a dense plasma whose conductivity is perhaps up to two or three orders of magnitude less than the metal, and almost certainly at least one order of magnitude less. It is also reasonable to take the boundary as an isothermal surface. One one side of it there is bulk cathode, and on the other side dense plasma. Boiling temperature is a well defined function of pressure, critical temperatures are well defined, and it seems sound to regard the transition between metal and plasma as well defined over the boundary; the temperature concept is certainly applicable to the bulk cathode.

With these two assumptions the electrical and thermal problems are formally identical and

$$\sigma R_{elec} = k R'_{therm} \quad . \tag{11}$$

Denote the contribution θ_1 at the boundary by θ_{1_o}. By conservation of energy, flux J is simply the power P_1 dissipated in the spot. We thus have

$$\theta_{1_o} = R'_{therm} P_1 \quad . \tag{12}$$

But the energy flux from the spot consists of two flows in parallel formally representable by the parallel combination of two thermal resistances. These are the thermal spreading resistance of the cathode, R'_s, and a formal representation of the resistance to flux of energy into the increasingly dilute plasma medium outside the spot, R'_m. We have

$$\frac{1}{R'_{therm}} = \frac{1}{R'_s} + \frac{1}{R'_m} \tag{13}$$

The quantity R'_m is to be understood here as a measure of the difficulty in carrying off energy in the form of kinetic energy of atoms emitted from the spot, excitation, thermal energy of the plasma jet, and so on.

We now return to the contribution θ_2 made by dissipation in the spreading resistance, which is θ_{2o} at the boundary. By (3),

$$\nabla \cdot k_s \nabla \theta_2 + \sigma_s |\nabla V|^2 = 0 . \tag{14}$$

Make the simplifying assumption, which is probably a good approximation, that θ_2 depends on the coordinates only through an explicit dependence on the potential V, ie.

$$\theta_2 = \theta_2 (V) . \tag{15}$$

The physical motivation stems from the analogous flow patterns for heat and electricity; V determines ΔV and thus the dissipation and the local temperature rise θ_2. Surfaces of constant V should thus be almost surfaces of constant θ_2, which says the same thing as (15). Even if σ_s and k_s are functions of θ_2, (15) may not become a worse assumption. By (7), (8), (14), and (15) we then find

$$\frac{d}{dV} \left(\frac{k}{\sigma} \frac{d\theta_2}{dV} \right) + 1 = 0 \tag{16}$$

which integrates to

$$\theta_2 = AV + B - \int \frac{\sigma}{k} V \, dV \tag{17}$$

where A and B are constants of integration. If they can be chosen to fit the θ_2 boundary conditions, (15) is exact. This can be done if the effective thermal conductivity, k_m, of the medium between the boundary (between spot and spreading region) and the dilute plasma away from the spot approaches zero or infinity; for intermediate cases it is an approximation. The boundary conditions are

$$\theta_2 = V = 0 \qquad \text{far from the boundary} \tag{18a}$$

$$V = V_o, \; k_s \left.\frac{\partial \theta}{\partial n}\right]_s = k_m \left.\frac{\partial \theta}{\partial n}\right]_m \quad \text{at the boundary} \qquad (18b)$$

Here n is a unit vector normal to the boundary, with the equation in which it appears stating heat flow continuity across the boundary.

Several clarifying remarks should be made at this point. First, as the subscript m was earlier used to refer to transport from the dense plasma to the dilute plasma, whereas here it refers to transport from the boundary between bulk and spot through the spot to the dilute plasma, the apparant discrepancy must be cleared up. Second, the spot is so violently non-equilibrium that one can question whether it makes sense to talk of a temperature θ within it.

The first discrepancy disappears if the effective thermal conductivity through the spot is very high, either because of its being extremely thin, because of other special conditions making energy transport through it very rapid, or because the objection is irrelevant to θ_2 (as distinguished from θ_1). Each of the three, it turns out, can remove the discrepancy. The spot is so thin that it can be neglected as a barrier to heat transport. Interatomic distances in liquids and solids are a few Angstrom units. Increasing the distance by one order of magnitude makes the density that of ordinary gases at moderate pressures and temperatures (three orders of magnitude below solid and liquid densities). The transition from condensed matter to gas (or plasma) as spot matter expands thus must be essentially complete some tens to a hundred or so Angstrom units away from the surface. The spot thickness itself should thus probably be taken as of the order of 10-20 Angstrom units.[10] Spot conditions are such that one would expect rapid energy sharing among the particles in it of atomic mass and rapid transport through it of thermal energy carried by electrons. For the latter are "sucked through" by the electric field due to the ions, if emitted quasi-thermionically they remove their "heat of

evaporation", if field-emitted their initial kinetic energy ($\sim kT$) goes with them. The former exchange energy by collision; at the high excitation level in the spot velocities of the order of 10^5 cm/sec are not unreasonable, the mean free path is of the order of 10^{-7} to 10^{-8} cm, so each atom collides every 10^{-12} to 10^{-13} seconds, so that energy sharing through the thickness of the spot should take perhaps 10^{-11} to 10^{-12} seconds. Lastly, θ_2 can clearly be calculated ignoring how the energy is transported from the boundary; one can introduce any transport matching the chosen boundary conditions.

The force of the non-equilibrium objection to use of the temperature concept in the spot comes from the fact that measures of temperature which coincide at equilibrium diverge (often strongly) from each other far from equilibrium. In terms of suitable average energies one could define atomic, electronic, and radiation temperatures for the arc spot and they would generally be very different. In discussing "evaporation" (or explosion) of the plasma jet produced by a focused laser beam[11] it was shown that no very serious error would result in an evaporation discussion if average atomic velocities calculated on an energy basis were used to calculate atomic temperatures assuming an equilibrium (Maxwellian) distribution. This is the general situation for any set of degrees of freedom within which there is sufficiently rapid equipartition of energy. If joulean dissipation is meaningful in the present discussion (and we think it is) then electron-atom collisions, or electron-phonon interactions couple electronic and atomic degrees of freedom sufficiently closely to make a common temperature a reasonable concept.

Integrating (17) from V = 0 to V = V_o and taking σ/k independent of temperature, and thus of potential also (if heat conductivity is mainly electronic this is justified) and using (18) we get B = 0 and

$$\theta_{2o} = AV_o - \frac{\sigma}{2k} V_o^2 \quad . \tag{19}$$

It can be shown that (18b) is not strictly compatible with (15), but expressed as an integral over the boundary S, it is. This gives

$$\int_S k_s \left.\frac{\partial \theta_2}{\partial n}\right]_s dS = \int_S k_m \left.\frac{\partial \theta_2}{\partial n}\right]_m dS \tag{20}$$

$$\frac{\partial \theta_2}{\partial n} = \frac{d\theta_2}{dV} \frac{\partial V}{\partial n} \tag{21}$$

and the right side of (20) is just J_m, which can also be written

$$J_m = \frac{\theta_{2_o}}{R'_m} . \tag{22}$$

Substituting (21) and (22) in (20) and setting

$$I = \frac{V_o}{R_s} = \int_S \sigma_s \left.\frac{\partial V}{\partial n}\right]_s dS \tag{23}$$

where R_s is the electrical spreading resistance of the bulk cathode, we find

$$\frac{k_s}{\sigma_s}\left(\frac{d\theta_2}{dV}\right)_{\text{boundary}} \cdot \frac{V_o}{R_s} = \frac{\theta_{2_o}}{R'_m} . \tag{24}$$

It then follows from (19) that

$$\left(\frac{d\theta_2}{dV}\right)_{\text{boundary}} = A - \frac{\sigma_s}{k_s} V_o \tag{25}$$

whence A is obtained from (24) and (25)

$$A = \frac{\sigma_s}{k_s} V_o - \frac{R_s}{R'_m} \frac{\theta_o}{V_o} . \tag{26}$$

From (19) we then get

$$\theta_{2_o} = \frac{1}{2} \frac{V_o^2}{R_s} \frac{1}{\frac{k_s}{\sigma_s R_s} + \frac{1}{R'_m}} . \tag{27}$$

Notice that reducing R'_m "refrigerates" the boundary. This refrigeration process can be done very efficiently by a plasma jet.[7] In the arc case electron emission (if quasi-thermionic) can also transport energy away efficiently. By (11) and (13), since V_o^2/R_s is the power P_s dissipated in the spreading resistance, we get

$$\theta_{2_o} = \frac{1}{2} P_s R'_{therm} \quad . \tag{28}$$

Combining (12) and (28) we get

$$\theta_o = R'_{therm} \left(\frac{1}{2} P_s + P_1 \right) \quad . \tag{29}$$

We note that if the major part of the total power P (equal to $P_s + P_1$) keeping the arc spot alive is fed in by dissipation in the spreading resistance, then

$$\theta_o = \frac{1}{2} R'_{therm} P \tag{30}$$

whereas if the major part is fed in by dissipation of ionic energy acquired in the cathode drop or brought by neutral excited atoms, the factor 1/2 is suppressed. It is possible that a θ_o for arc spots characteristic of particular cathode materials exists. If this is so, then the relative importance of P_s and P_1 may be determinable empirically. The externally applied power consists of P_s, P_1, and the dissipation in the plasma away from the spot. A disposable parameter might be R_s; cathode resistivity might be varied by control of cathode temperature or alloying; if the arc spot be regarded as a circular contact of radius a, R_s is simply $1/4\,\sigma a$. By (11) we then obtain

$$R'_s = \frac{1}{4 k_s a} \quad . \tag{31}$$

Clearly as $\underline{a}$ approaches zero R'_s goes to infinity. For a very small spot, therefore, energy removal necessarily utilizes the process symbolized by R'_m, such as jet and plasma formation and electron "evaporation". The analogous focused laser beam situation, where optical focusing replaces the stream "focusing"

inherent in current flow into a small spot has been analyzed,[7] and plasma jet formation shown to be inevitable for sufficiently high specific loadings. It will be shown below, equation (42), that the heat generated per unit volume, and the temperature, also diverge close to a small spot.

It is thus entirely reasonable to regard the arc spot as a dense microplasma, particularly as theory[7] and experiment[12] agree that the latter possesses the required emitting properties. The foregoing, which is a theoretical amplification of part of an earlier qualitative discussion,[8] shows that dissipation in the spreading resistance alone is capable of maintaining the spot. If spreading dissipation plays an important role in the arc mechanism there is no need to correlate the "cathode drop" with the ionization potential of the cathode vapor, and as is well known, the cathode drop for the mercury arc is too low to permit ionization by emitted electrons except perhaps by a step-wise process.[13] Even more interesting in this connection are the observations of Reece,[14] who found a "universal" curve relating the product of the boiling point and thermal conductivity to the arcing voltage for a number of metals. This is readily understandable for a spreading-plus-plasma mechanism, less so for mechanisms depending on processes outside the cathode. He also found deviations from the rule for ferro-magnetic metals. This is understandable for a plasma model, in which the self-generated magnetic field of the spot would form a short "magnetic bottle" helping to contain the plasma against lateral spread, and thus playing an important role in determining the energy needed to maintain it. Without the plasma model (e.g., for field, TF, thermionic, ionization or metastable mechanisms) one would expect unimportant deviations or none at all. As will be seen later, the plasma in a magnetic bottle explains the retrograde motion of the arc spot in a magnetic field, for which no satisfactory explanation has been put fourth on any other theory.

While spreading dissipation can maintain the arc in principle, and the above and

other data indicate that it may often, if not generally, do so in practice (particularly in the early stages of an arc, e.g., one ignited by a spark or by separating two contacts), the plasma model will work equally well with any kind of focused energy input. Historically, attention has most often been given to positive ions supplying energy to the spot by falling through the cathode drop. Their energy would provide spot excitation for a quasi-thermionic mechanism, their charges are thought to provide the high field needed for field emission by proponents of that theory, with both effects invoked for TF, and neither for the excited atom mechanism. It is very natural to adopt the view that positive ions provide at least some, if not the bulk of the energy input to the spot because in the glow discharge the ions generate most, if not practically all of the cathode electrons (photons are of importance for hydrogen and metastables can contribute in some cases); with increase in the applied voltage the current increases, ion bombardment becomes more intense (for refractory cathodes this can go over continuously to the thermionic arc with cathode temperature maintained by ion bombardment) and the current carrying area discontinuously contracts to a tiny area, the cathode spot. The discontinuity strongly suggests a change in mechanism, and this may not only be a change in spot emission mechanism but in energy supply mechanism as well. The almost universal assumption of energy supply from the gas may thus be incorrect in part (or completely).

The energy supply from, and delivery of energy to, the medium near the spot are represented by the parameters P_1 and R'_m, respectively. Conventionally they are taken as practically balancing each other, other losses like ordinary evaporation and heat conduction being negligible in comparison. Calculations of R'_m seem to be of dubious value, for the plasma jet energy removal mechanism is non-saturable;[7] it is more reasonable to view it as inoperable until some high θ_o is reached, which represents the energy concentration threshold for spot ignition.

Thereafter the jet simply removes all additional energy above that needed to maintain the cathode spot against cathodic energy drain. It thus becomes of interest to demonstrate that the spreading mechanism culminates in an "exploding wire tip".

Spot Development with "Focused" Current Flow

We now assume focused current flow in the sense previously used and calculate the time dependence of θ and the space dependence of Q. Spot ignition occurs in very short times, so no appreciable heat diffuses away from its site of generation during this transient build-up. This leads to

$$\theta = \frac{1}{C} \int_o^t Q \, dt \tag{32}$$

which is readily derived from (1) by suppressing the conduction term $\nabla \cdot k \nabla \theta$, where C is the heat capacity per unit volume. The spot is viewed as a current source on the cathode surface taken to be a disc of radius a. In the glow-arc transition the emitting area contracts to a small spot by magnetic pinch effect, and when an arc is drawn by separating two contacts, we clearly have the situation here assumed just before the contact is broken.

The edge of the disc, because of the crowding of lines of current flow, leads to a singularity in Q, and near a singularity conduction cannot be neglected. We must thus first find the Q distribution, which depends on solving the associated potential distribution problem (charged disc).[15] Take the origin of the (x, y, z) coordinates at the center of the disc, which lies in the plane x = 0, positive x direction into the cathode, x-axis thus an axis of symmetry, and introduce spheroidal coordinates ξ, ζ, Ω, with Ω the longitudinal angle, $\rho^2 = y^2 + z^2$, and ζ, ξ defined by

$$\frac{x^2}{a^2 \zeta^2} + \frac{\rho^2}{a^2 (1 + \zeta^2)} = 1 \tag{33}$$

$$-\frac{x^2}{a^2\,\xi^2} + \frac{\rho^2}{a^2\,(1-\xi^2)} = 1 \quad . \tag{34}$$

Equation (33) is a family of oblate spheroids for including the disc ($\zeta = 0$), while (44) is an orthogonal family of one-sheet hyperboloids of revolution. Take the disc as an equipotential, V as a function of ζ only, getting Laplace's equation as

$$\frac{d}{d\zeta}\,(1+\zeta^2)\,\frac{dV}{d\zeta} = 0 \quad . \tag{35}$$

This integrates to

$$V = A \tan^{-1}\zeta + B \tag{36}$$

with A and B constants. Taking $V(0) = 0$ and $V(\infty) = V_o$ we find

$$V = V_o \frac{2}{\pi} \tan^{-1}\zeta \quad . \tag{37}$$

Q is calculated from ∇V by (2),

$$\nabla V = \frac{1}{a}\left(\frac{1+\zeta^2}{\xi^2+\zeta^2}\right)^{1/2}\frac{dV}{d\zeta}$$

$$= \frac{2V_o}{\pi\,a}\,\frac{1}{[\,(1+\zeta^2)(\,\xi^2+\zeta^2)]^{1/2}} \tag{38}$$

whence

$$Q = \frac{4V_o^2\,\sigma}{\pi^2\,a^2}\;\;\frac{1}{(1+\zeta^2)(\xi^2+\zeta^2)}$$

$$= \frac{P}{\pi^2\,a^3\,(1+\zeta^2)(\xi^2+\zeta^2)} \tag{39}$$

where the total power P dissipated in the spreading resistance $R_s = 1/4\,\sigma a$ is simply V_o^2/R_s. It is thus clear that Q can be made arbitrarily large by taking a sufficiently small. Development of sufficiently high energies per particle to form

a spot microplasma is thus inevitable on the spreading resistance (exploding "tip") mechanism.

The singularity at the disc edge earlier referred to may dominate, particularly if a characteristic θ_o is needed to initiate the arc spot. We must thus investigate Q and θ in its neighborhood. Introduce the coordinate r given by

$$r^2 = x^2 + (\rho - a)^2 \tag{40}$$

and investigate the situation at points (x, ρ) near the edge, i.e., for small ζ and ξ. From (33), (34) and (40) we find

$$r \approx \frac{a}{2} (\zeta^2 + \xi^2) \quad . \tag{41}$$

From (39) and (41) we then obtain

$$Q \approx \frac{P}{2\pi^2 a^2 r} \tag{42}$$

so that Q approaches infinity as r goes to zero for any a. This expression is to be used in solving the thermal continuity equation

$$k \nabla^2 \theta + Q = C \frac{\partial \theta}{\partial t} \tag{43}$$

We are interested in the region $r \ll a$ so that the curvature of the edge can be neglected. For simplicity treat heat removal to the plasma as described by conduction with the same parameters k and C as the cathode, taken as constants. The edge is taken as a straight line taken at the origin of polar coordinates (r, φ). Plasma cooling is reduced to that of the cat's whisker in the crystal burn-out problem.[15] The whisker or jet is represented by a conducting cone making an angle φ_o with the extension of the disc in its plane (which can be taken as 2π as we are concerned with orders of magnitude only). The conditions on Q in (43) now become

$$\left.\begin{aligned} Q &= 0 \quad \text{outside the cathode} \quad (\pi < \varphi < \varphi_o) \\ Q &= \frac{P}{2\pi^2 a^2 r} \quad \text{in the cathode} \quad (0 < \varphi < \pi) \end{aligned}\right\} \tag{44}$$

and

$$\nabla^2 = \frac{\partial^2}{\partial r^2} + \frac{1}{r}\frac{\partial}{\partial r} + \frac{1}{r^2}\frac{\partial^2}{\partial \varphi^2} \quad .$$

The boundary conditions on θ for solving (43) are now

$$\left.\begin{aligned} \frac{\partial \theta}{\partial \varphi} &= 0 \quad \text{at} \quad \varphi = 0 \quad \text{or} \quad 2\pi \\ \theta &= 0 \quad \text{at} \quad r = \infty \\ \theta &= 0 \quad \text{at} \quad t = 0 \end{aligned}\right\} \tag{45}$$

and the solution in the plane $x = 0$ $(\varphi = \pi)$ is

$$\theta = \frac{P\sqrt{\pi K t}}{4\pi^2 a^2 k}\left[f\left(\frac{r^2}{8Kt}\right) - \sqrt{\frac{r^2}{8Kt}} \right] \tag{46}$$

where $K = k/C$ is the thermal diffusivity, and

$$f(x) = e^{-x}\left[(1 + 2x)I_o(x) + 2xI_1(x)\right] \quad . \tag{47}$$

Here $I_n(x)$ is the modified Bessel function of order n, i.e., $I_n(x) = j^{-n}J_n(jx)$. We have

$$\theta \approx \frac{P\sqrt{\pi Kt}}{4\pi^2 a^2 k} \quad , \quad (r^2/8Kt \ll 1) \tag{48}$$

$$\theta \approx \frac{1}{C}\frac{Pt}{4\pi a^2 r} \quad (r^2/8Kt \gg 1) \quad . \tag{49}$$

This last result is half that given by (32) because θ is evaluated at the surface

([1/2]Q rather than Q is the effective rate of heat generation at the surface).

The general time dependence of θ is now easily described. Near the edge θ is proportional to $W = Pt$ for very short times. For intermediate times θ rises more slowly, like $Pt^{1/2}$, and finally, when curvature is no longer negligible, θ becomes proportional to Pt^{0}, i.e. P, as in equation (30). In summary

$$\theta \propto Pt = W , \quad t \ll r^2/K \tag{50}$$

$$\theta \propto Pt^{1/2} = Wt^{-1/2} , \quad r^2/K \ll t \ll a^2/K \tag{51}$$

$$\theta \propto P = Wt^{-1}, \quad a^2/K \ll t \quad . \tag{52}$$

Is the "ring singularity" a mathematical artifact or does it correspond to some real physical properties of the spot? While it is hard to say anything reliable on this subject, the dense plasma model suggests that a "hot ring" may be part of the overall mechanism. The magnetic pinch is balanced, in the steady state, by the pressure of the hot plasma. If there is a characteristic θ_o for the arc spot, one would expect, roughly, a characteristic current density and plasma temperature. For any total arc current there would then tend to be a division into a number of spots of such size and current to satisfy the magnetic containment requirement as well as the current density and temperature requirements. As is well known[16] the spot divides when the current increases, and there is evidence of a "cellular structure" in the spot also. Now if the current density were maximum at the center, then the pinch would be stronger there and the core would contract further relative to outer regions. As a steady state has been assumed it follows that such further contraction is impossible, lending credence to the view that there may be a high current density ring, after the spot is formed, whose core can emit more, within limits, as more current is demanded by the external circuit. When the core emits enough to imperil stability, the spot divides. Also, if the current is

increased, so that more spots or cells are established, and then suddenly decreased to its original value, the current in each cell may be below its critical maintenance value. The arc can then extinguish even though the total current is above critical; the arc does not extinguish with gradual current reduction, in which the work of a "dying" cell is redistributed among the "live" ones.

Coalescence of Earlier Theories into the Plasma Model. Beam Aspects

In this section we consider the relation between the various arc spot theories put forth in the past and the plasma spot theory. In general the relationship is that if the old theory were true, then the conditions necessarily obtaining in order to permit it to be true would generate a plasma spot. Under those conditions one might force a description of plasma properties in terms of the old theory, but one would merely be preserving appearances.

We begin with Slepian's thermal ionization theory, because it probably has the fewest adherents. Kesaev's analysis leads to his table III, loc. cit. ref. 1, p. 64, showing that current densities now known to flow through the cathode spot (10^6 - 10^7 amp/cm^2, perhaps higher) require unreasonably high ion concentrations and thus pressures. As they are proportional to each other we need only cite that 10^7 amp/cm^2 requires a positive ion concentration of 3.1×10^{21}/cc and a pressure " > 115" atmospheres. He then points out that the degree of ionization of mercury vapor is not greater than 0.01 at 6300°K so that particle density and pressure would rise by a few orders of magnitude (the gas would then be denser than the cathode, apparently!). Actually the situation is not that bad, for when densities become comparable to the liquid (i.e., as criticality is approached), the overlap of atomic wave-functions begins to "collectivize" the outer electrons. One can view a metal as a giant molecule, from this point of view, with the work function for its first, second, ... ionization potential. When one follows this idea out one sees that the conditions required are simply those obtaining in the dense plasma spot. But now

the positive ions have such a small mean free path that they can hardly be viewed as carrying the current - the dark space they formerly carried charge across has shrunk to a few Angstrom units, and the theory coalesces with a thermionic or plasma theory.

It is clearly not necessary to discuss how thermionic theories turn into the plasma spot theory when critically examined, in view of earlier discussion, and likewise T-F theories.

The same thing happens to von Engel and Robson's theory as happens with Slepian's. As a metastable can free, at the very most, one or two electrons (actually appreciably less), one needs an inward flow density of metastables into the spot equal to that of the ions on Slepian's theory. On similar kinetic theoretical grounds one then needs the same high particle densities and pressures, and a means for feeding in the required excitation. The only way we could think of doing this boils down to the spreading resistance mechanism (excitation by collisions with electrons), or equivalently, maintenance of a plasma spot by ion bombardment.

Although it has apparently never been seriously proposed (with good reason), it is possible to envision photons freeing the spot electrons. The high photo densities required, because there is neither laser nor focusing optics at the spot, could only come from densely packed emitters in the immediate vicinity of the spot. The density becomes comparable to the solid so that a continuum, rather than spectral lines are emitted.

We now turn to the field emission theory, which has long been regarded as the most reasonable one. Kesaev's presentation of the thermal ionization theory is followed immediately by a similar analysis of the field emission case, culminating in his table IV (loc. cit. p. 65). He uses Mackeown's equation[3]

$$E_c^2 = 7.57 \times 10^5 \; U_c^{1/2} \; j_e \left[\left(\frac{m_p}{m_e} \right)^{1/2} \frac{j_p}{j_e} - 1 \right] \qquad (53)$$

and the Fowler-Nordheim equation[3]

$$j_e = 6.2 \times 10^{-6} (E_c^2/\varphi_o)\, e^{-6.8\times10^7 \varphi_o^{3/2}/E_c} \tag{54}$$

to obtain

$$j_e = 6.11 \times 10^9 \varphi_o^3 \left\{ U_c^{1/2} \left[\left(\frac{m_p}{m_e} \right)^{1/2} \frac{j_p}{j_e} - 1 \right] \ell n^2 \left\{ 4.69 \frac{U_c^{1/2}}{\varphi_o} \left[\left(\frac{m_p}{m_e} \right)^{1/2} \frac{j_p}{j_e} - 1 \right] \right\} \right\}^{-1} \tag{55}$$

from which j_e, the electronic current density, can be calculated if U_c (the cathode drop), φ_o (work function) and j_p/j_e (ratio of ion to electron current densities are known (m_p and m_e are ion and electron masses). E_c, of course, is the field at the cathode.

The following table contains the information in his table IV plus our calculations of j_p, d (thickness of the sheath, $E_c = V_c/d$, $U_c = 10$ V), and surface loading $j_p U_c$.

j_p/j_e	j_e, amp/cm^2	j_p, amp/cm^2	$j_p U_c$, watts/cm^2	E_c, V/cm	d, cm
1	5.22×10^6	5.22×10^6	$.522 \times 10^8$	8.64×10^7	11.6×10^{-8}
0.3	2.45×10^7	7.35×10^6	$.735 \times 10^8$	1.02×10^8	9.8×10^{-8}
0.1	1.09×10^8	1.09×10^7	1.09×10^8	1.24×10^8	8.06×10^{-8}
0.03	6.5×10^8	1.95×10^7	1.95×10^8	1.63×10^8	6.13×10^{-8}
0.01	4.57×10^9	4.57×10^7	4.57×10^8	2.34×10^8	4.27×10^{-8}

Notice first that the values for d are only a few times as great as the average interatomic distance in liquid mercury (one finds $(M/\rho N_o)^{1/3}$, the cube root of the atomic volume per atom, to be almost 3×10^{-8} cm). At such close distances the sheath concept itself is extremely dubious. Second, $j_p U_c$ represents the dissipation in watts/cm^2 at the spot due to the kinetic energy brought in by the ions. For the tabulated cases this reaches the astronomical range of the order of 10^8 watts/cm^2. This enormous power density cannot be carried off by electrons on a field emission theory, so a plasma jet would have to form. Lastly, one should consider what would be involved in actually focusing down an ionic beam in the required current range to such a small target area. How could one possibly overcome space charge limitations without the space charge neutralization possible only in an exceedingly dense plasma or condensed matter? It seems clear physically that the field emission mechanism, examined critically from the point of view of what occurs in the arc spot under the conditions needed to make it operable, would be a dense hot plasma spot mechanism instead.

Turning from emission mechanisms to spot excitation and maintenance problems, we find a similar coalescence of the older theories into the dense plasma theory. Exciting and maintaining a plasma, except in the case of high temperature equilibrium, requires energy input. This can be optical, as with a laser, chemical (combustion, explosion), radio frequency or microwave (as with RF breakdown of a gas), nuclear (mushroom-cloud physics), mechanical (shock waves), or via the energy picked up by charged particles in a D. C. field. This last, of course, is relevant to the arc spot problem. From the plasma viewpoint, as there are only two kinds of charged particles, electrons and positive ions, energy can only be fed in by having electrons or ions acquire energy from the applied field and dissipate it by collisions to generate and maintain the plasma state. Applied to a very dense plasma, the mean free path becomes so small that collision mechanisms go over

smoothly into an ohmic dissipation mechanism. Ordinary electronic impact excitation in the low pressure plasma thus joins the spreading resistance mechanism discussed earlier for the arc spot. The cathode drop U_d is then in part, or perhaps primarily, the IR_s drop in the spreading resistance. The traditional interpretation of the cathode drop leads to $j_p U_c$ as the power dissipation density at the cathode, and for the true thermionic arc this is essentially the entire input (spreading contributions are negligible for these large spots), used to heat the spot to thermionically emitting temperatures. It is customary to view ion drift in conventional plasmas as ohmically dissipative. When the ions converge on the spot they encounter increasingly dense matter; the ohmic picture then goes over to a spreading resistance picture with ions playing a role like that discussed previously for electrons. There is thus some justification for treating R_m and R'_m in the same way as done for R_s and R'_s.

It is pleasing to find this kind of symmetry between the two flows converging into the spot (the electron flow diverges again outside the cathode), each flow providing the space charge neutralization for the other necessary for both to flow, and by their collisions, maintaining the plasma state. But more is needed, for without some form of "container" for the hot plasma one can calculate that blast-off from the surface would be so rapid that it is hard to see how the discharge could be maintained. As mentioned earlier, the magnetic pinch contains the plasma against sidewise spreading. The ions now pump against longitudinal flow. Figuratively speaking, the plasma is compressed by an electrostatic piston in a magnetic cylinder, and the piston is permeable to electrons. The field is needed, therefore, to perform a number of vital functions. First, it is part, and may be a very important part, of the energy input needed to establish and maintain the spot. Second, the old field theory reappears in a new form in that without fields there could be no electron sink at the spot into which cathode electrons could stream. This can also be

regarded as space charge neutralization or as an electrostatic converging electron lens focusing the electron flow on the spot. Lastly, it plays a very important role in containing the dense hot plasma, both in providing an ion piston on the gas side and in providing an electron piston, in effect, on the cathode side. Thermal conductivity in metals is mainly electronic; without it the metal would be a good thermal insulator. The electron sink at the spot may well prevent much spot cooling by removing electrons to the plasma at such a high rate that thermal conduction by electrons to the bulk is substantially reduced.

Frequent mention has been made of the spot mechanism as a micro analog of a macro beam. It is thus of interest to see explicitly how an ion beam would tend to generate a cathode spot (an electron beam would generate an anode spot - these have been observed and have many properties analogous to those of cathode spots; anode pitting of contacts also has many resemblances to cathode erosion). It is clear that a focused ion beam, particularly with high energy, provides particularly favorable conditions for generating a cathode spot. Electron beams can free vapor from the anode and produce ions capable of establishing a spot back at the cathode. The cascade mechanism is sufficiently obvious at this point to make further discussion superfluous. It may be of interest, however, to make some remarks on how the arcing tendency might be either controlled or utilized.

The arc spot is a delicate balance between the forces maintaining and those tending to extinguish it. Ballast resistors, chosen to keep currents below the critical value for maintaining the spot are old reliable expedients for limiting arcing damage. Ion traps in cathode ray tubes, by preventing positive ions from bombarding the electron gun directly, have a similar protective function. Temporary interruption of the arc current lets the spot "cool" and, if it happens fast enough, will serve a protective function. The protection art is old, and has an elaborate technology. We turn from it to a consideration of whether it might be

possible to design beam apparatus in which transition to the arc might be useful.

Particle and laser beams are being used for welding and machining (arc welding and spark machining are used intensively), particularly on a macroscopic scale. It is attractive to consider the use of a precise beam to control arc initiation in a rapidly quenched circuit. One might thereby attain improved precision over conventional arc welding, and the ability to handle work on a much larger scale than can be done at present by beam methods.

Retrograde Motion of the Arc Spot

A classic puzzle for arc spot theorists is that the spot moves, when a magnetic field is applied parallel to the cathode surface, precisely in the wrong direction one would expect on the basis of charge motion. We now show how the dense plasma model predicts this simply on general grounds, in sharp contrast to the tortured and often far-fetched attempts at explanation given in the past.

The magnetic "bottle", when a parallel field is added vectorially to it, becomes weaker on one side and stronger on the other. A normal conductor carrying current would move toward the weaker field side as the configuration is then one of lower energy. For the arc spot, however, unlike the conductor, the magnetic field configuration is essential to the current carrying mechanism. Where the bottle weakens, the plasma expands and thus is cooled. This represents a drain on the energy; the emission mechanism becomes less efficient therefore, in that region, and the current flows through the more efficient region on the high field side. It is a well known theorem that the current density in a conductor distributes itself in such a way that the generation of heat is a minimum. [17] Less heat is generated in the high field region where containment is better. The spot therefore always moves toward the high field region of a magnetic field and thus in the "wrong" direction. At high ambient pressure one could have a reduction in this effect, for the plasma would have to do work against it. At sufficiently high pressure the magnetic field

would then contribute a low enough fraction of the total bottling effect for the normal tendency to overcome it. This is, in fact observed.

The above not only explains retrograde motion and its reversal, but also the stabilizing effect of a magnetic field and Kesaev's "maximum principle".[18]

The theorem of least dissipation appealed to above is a special case of a more general theorem of non-equilibrium thermodynamics based on Onsager's reciprocal relationships. Under rather general conditions the steady state is characterized by a minimum rate of generation of entropy.[19] We thus have considerable confidence in the above explanation of retrograde motion.

Conclusion

The foregoing has barely scratched the vast arc literature, but coordinates much of it that has not even been mentioned. The dense plasma model seems to have the attractive features of simplicity, intuitiveness, and ability to describe the facts. It has the strengths of all the earlier theories and avoids their weaknesses. It is hoped, therefore, that it will inspire new experiments to confirm or refute it, and to lead to new insights into the nature of matter.

Notes and References

1. For a recent excellent and exhaustive survey of arc spot phenomena see I. G. Kesaev, Cathode Processes in the Mercury Arc, Consultants Bureau (New York, 1964). The bibliography of 188 papers includes much Russian work, particularly that of the author, much of which is developed in the text. Pages 7-12 give a history of estimated current densities in the spot.
2. Following K. T. Compton's application of thermal ionization to the positive column of the arc, Phys. Rev. 21, 266 (1923), J. Slepian applied the concept to the gas in the neighborhood of the cathode spot, Phys. Rev. 27, 407 (1926), Jour. Frank. Inst. 201, 79 (1926), trying to explain the high current density as being carried by positive ions. Weizel, Rompe and Schoen, Zf, f. Phys. 115,

179 (1940), attempted to revive the theory.

3. The original suggestion that field emission could explain arc current densities stems from I. Langmuir, G. E. Rev. 26, 731 (1923). The theory was further developed by S. S. Mackeown, Phys. Rev. 34, 611 (1929). The Fowler-Nordheim equation, R. H. Fowler and L. H. Nordheim, Proc. Roy. Soc. A, 119, 173 (1928) predicted the necessity of much larger gradients than calculated by Mackeown, which caused many to reject the theory. The later, much higher current densities make the difficulties of reconciliation approach the vanishing point in this respect. See Kesaev, loc. cit. pp. 62-70. He concludes that field emission is probably the correct arc mechanism, an opinion shared by many. We wonder how many ion beam experimenters would share the view that an ion beam current density, say of 10^6 amp/cm^2, could be focused on a target area of a square micron or less by applying only 10 volts.

4. See A. Bauer, Zs. f. Phys. 138, 35 (1954), Ann. Phys. 18, 387 (1956); E. L. Murphy and R. H. Good, Phys. Rev. 102, 1464 (1956); T. H. Lee, J. Appl. Phys. 28, 920 (1957).

5. A. von Engel and A. E. Robson, Proc. Roy. Soc. A 243, 217 (1957).

6. J. Rothstein, Phys. Rev. 73, 1214 (1948) (L), erratum 74, 228 (1948); J. Appl. Phys. 19, 1181 (1948) (L); Phys. Rev. 75, 1323, 1335, 1336 (1949), 78, 331 (1950) abstracts.

7. J. Rothstein, National Electronics Conference Proceedings, Vol. 19, pp. 554-563 (Chicago, 1963).

8. J. Rothstein, Exploding Wires, Vol. III, pp. 115-123 Plenum Press (New York, 1964).

9. Vol. 15, Radiation Laboratory Series, Crystal Rectifiers, Chap. 8, McGraw-Hill (New York, 1948). The crystal burn-out problem is so similar in theory to the arc spot considered as an exploding wire tip that the mathematics is

applicable with negligible modification. Details of the physical discussion vary so much however, that it was felt necessary to repeat the mathematics in the new physical context. Merely giving the reference would make the exposition impossibly awkward and confusing.

10. This thickness is one to two orders of magnitude less than that cited in ref. [6], Phys. Rev. 73 above. It corresponds to the "supercritically" dense vapor region of the early paper. The entire region considered in 1948 encompassed not only this region but also the expanding plasma jet down to where it had normal plasma density and had cooled to where it could no longer be considered a quasithermionic emitter but simply part of the general plasma.
11. Ref. [7], sect. VI, equations (12) - (19).
12. D. Lichtman and J. F. Ready, Phys. Rev. Letters, 10, 342 (1963). Their data are briefly discussed in ref. [7] above, p. 557. Since then other workers have investigated several aspects of dense high temperature plasmas produced with lasers. A. F. Haught and R. G. Meyerand Jr., Bull. A. P. S. II, 10, 227 (1965) have exploded 100 μ particles in vacuo with a laser beam to produce high density, high temperature, plasma. A. W. Ehler and W. I. Linlor have reported ion directed kinetic energies up to 100 V and other data in various letters and abstracts: Ehler, Bull. A. P. S. II, 9, 563 (1963), 10, 227 (1965); Linlor, Bull. A. P. S. II, 7, 440 (1962), 10, 227 (1965); Appl. Phys. Lett. 3, 210 (1963); Phys. Rev. Letters 12, 383 (1964). It is of interest to note that high energies were reported for particles from arc spots many years ago. R. Tanberg, Phys. Rev. 35, 1080 (1930) found jet velocities from a copper arc of the order of 10^6 cm/sec, or a temperature of about 5×10^5 °K if the velocity were of thermal origin. E. Kobel, Phys. Rev. 36, 1636 (1930) found vapor stream velocities for mercury between 1.6×10^6 and 4.3×10^6 cm/sec. As 1eV of thermal energy corresponds to 10^4 °K, these jet energies are of the

order of 100 eV. V. Hermoch, Czech. J. Phys. 9, 221 (1959) found similar results for 17 metals, for anode streams as well as cathode streams. Kesaev, loc. cit. ref. 1, pp. 21-25 believes the jets to be of thermal origin. We view the data as powerful support for the exploding plasma theory of the arc spot.

13. Ref. 1, p. 13, and K. T. Compton, Phys. Rev. 37, 1077 (1931).
14. M. P. Reece, Nature 181, 475 (1958).
15. Ref. 9, pp. 249-251 and W. R. Smythe, Static and Dynamic Electricity, first ed., sec. 5.27 (McGraw-Hill, 1939).
16. Kesaev, loc. cit. ref. 1, particularly Ch. 3 and Ch. 4B and C.
17. See the proof in Smythe, loc. cit. ref. 15, pp. 228-9.
18. See Kesaev, Ch. 4, A and B. The maximum field principle is discussed on pp. 213-221.
19. See, for example, S. R. de Groot and P. Mazur, Non-Equilibrium Thermodynamics, Ch. V (North Holland and Interscience, Amsterdam and New York, 1962).

Ion Implantation Doping of Semiconductors*

by

D. B. Medved
Electro-Optical Systems
Pasadena, California

Abstract

Type conversion and junction formation in semiconductor targets bombarded by ion beams of potassium and cesium are being studied. Parameters affecting the results so far obtained are discussed.

Introduction

The use of ion beams of dope semiconductors with impurity atoms dates back almost to the beginning of the modern semiconductor art.[1-5] Although some interesting rectifying characteristics in silicon-metal point contact devices bombarded by a variety of gases were reported, there was no evidence that ions penetrated beyond the surface layers of the bombarded crystal. A short note by Rourke, Sheffield, and White[6] probably represents the first publication in the open literature of a successful junction formation by implantation. These investigators claimed to have doped silicon by samarium ions (in a range from 6 to 12 keV) to a depth of 1000 Å. Heavy doping concentrations on the order of 10^{18} atoms per/cm^3 were cited. More recently, McCaldin and his colleagues have reported on an extensive series of investigations employing cesium and sodium ions from 1 to 10 keV to achieve type conversion in bombarded silicon targets.[7-10]

We have shown that 5 keV cesium ions will dope silicon to depths in excess of 0.5 microns and that large area photovoltaic cells can readily be made in this relatively low energy regime.[11-12] In this paper we present the results of recent experiments on the use of Cs^+ and K^+ in the range 1 to 20 keV to dope silicon.

---

*Supported under contract with the Air Force Avionics Laboratory, AF33(615)-1989.

Emphasis is given to the variation of junction depth and implanted profile with crystal orientation, temperature, and target resistivity.

Experimental Apparatus and Techniques

Two distinct ion sources and bombardment chambers are utilized in this investigation. A small-beam system (designated as the A system) for generating potassium and cesium ions is shown in Figures 1 and 2.[13] Figure 1 is a photograph of the contact ionization source employed, and Figure 2 is a photograph of the target assembly showing rotatable mount, collimating apertures, and secondary electron collector. The small area system is capable of being operated from 1 to

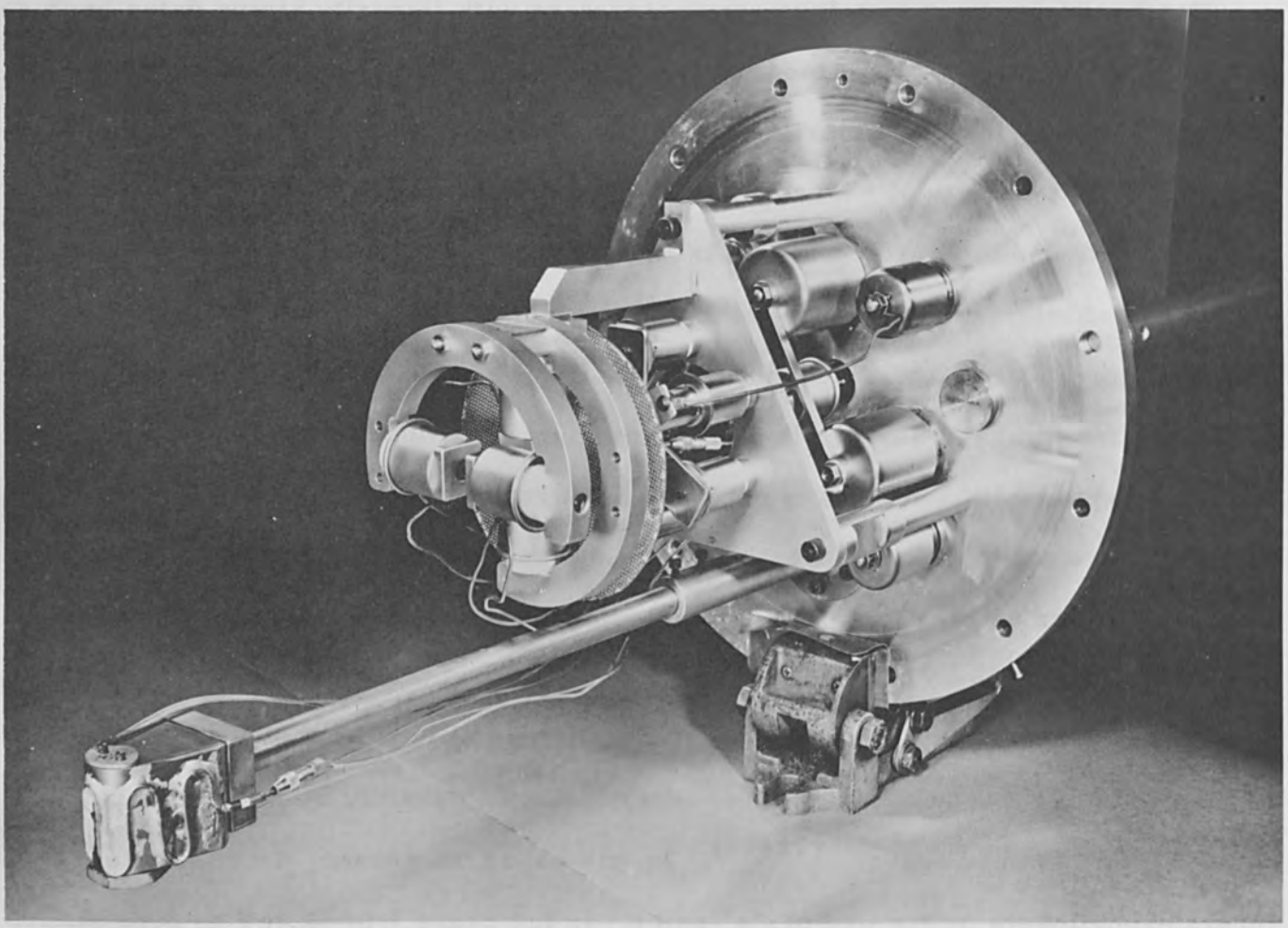

Figure 1 Contact Ionization Source (System A)

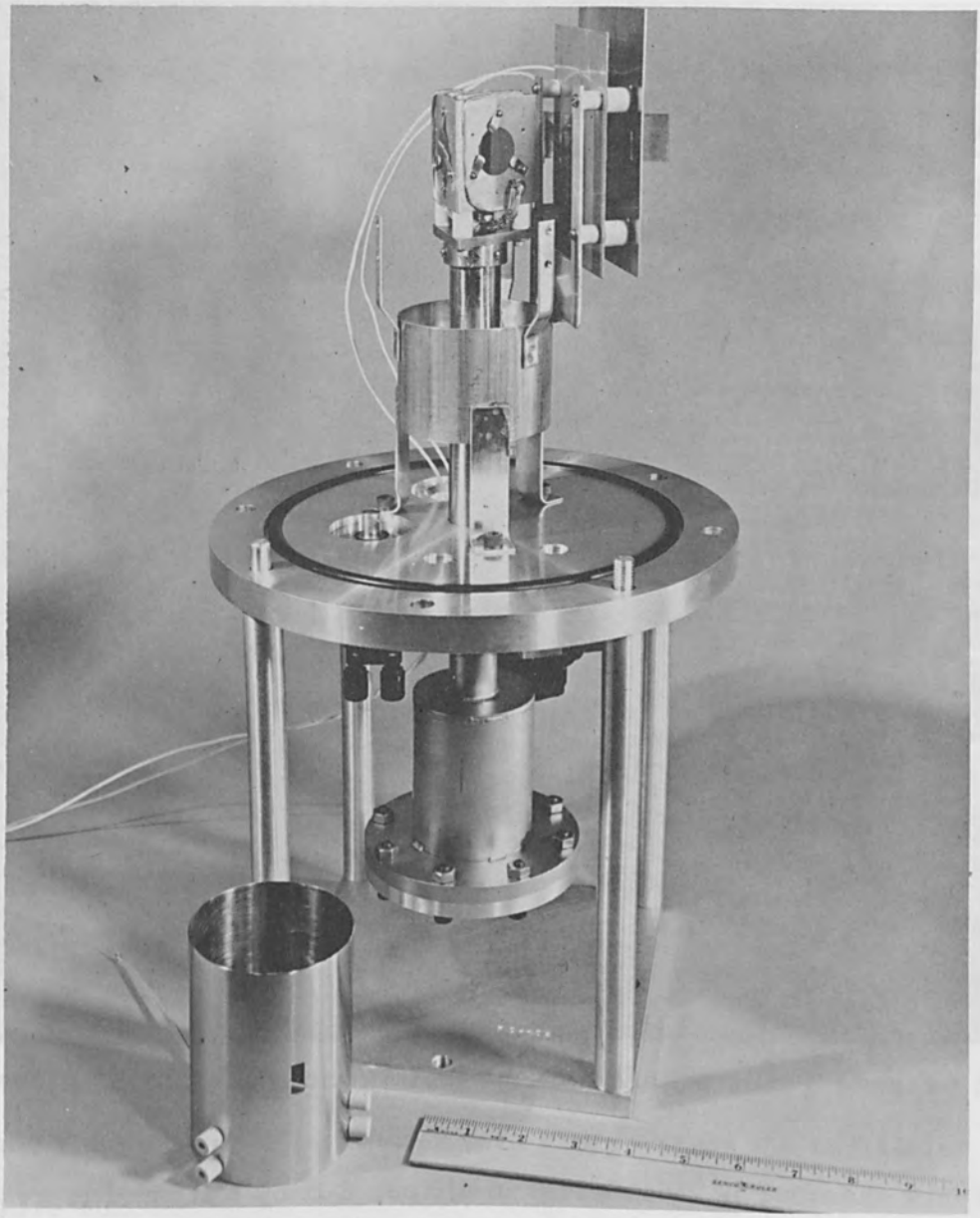

Figure 2 Target Assembly (System A), Showing Rotatable Mount and Target

30 keV and handles 3 samples of variable incidence angles. Figure 3 is a photograph of an electron bombardment source used in large-area implantations (system B) where many samples are exposed to identical bombardment conditions simultaneously. This source is capable of delivering beam current densities on the order of a milliamp/cm^2 over an area in excess of 100 cm^2 with reasonable uniformity and can operate from 1 to 5 keV. [14]

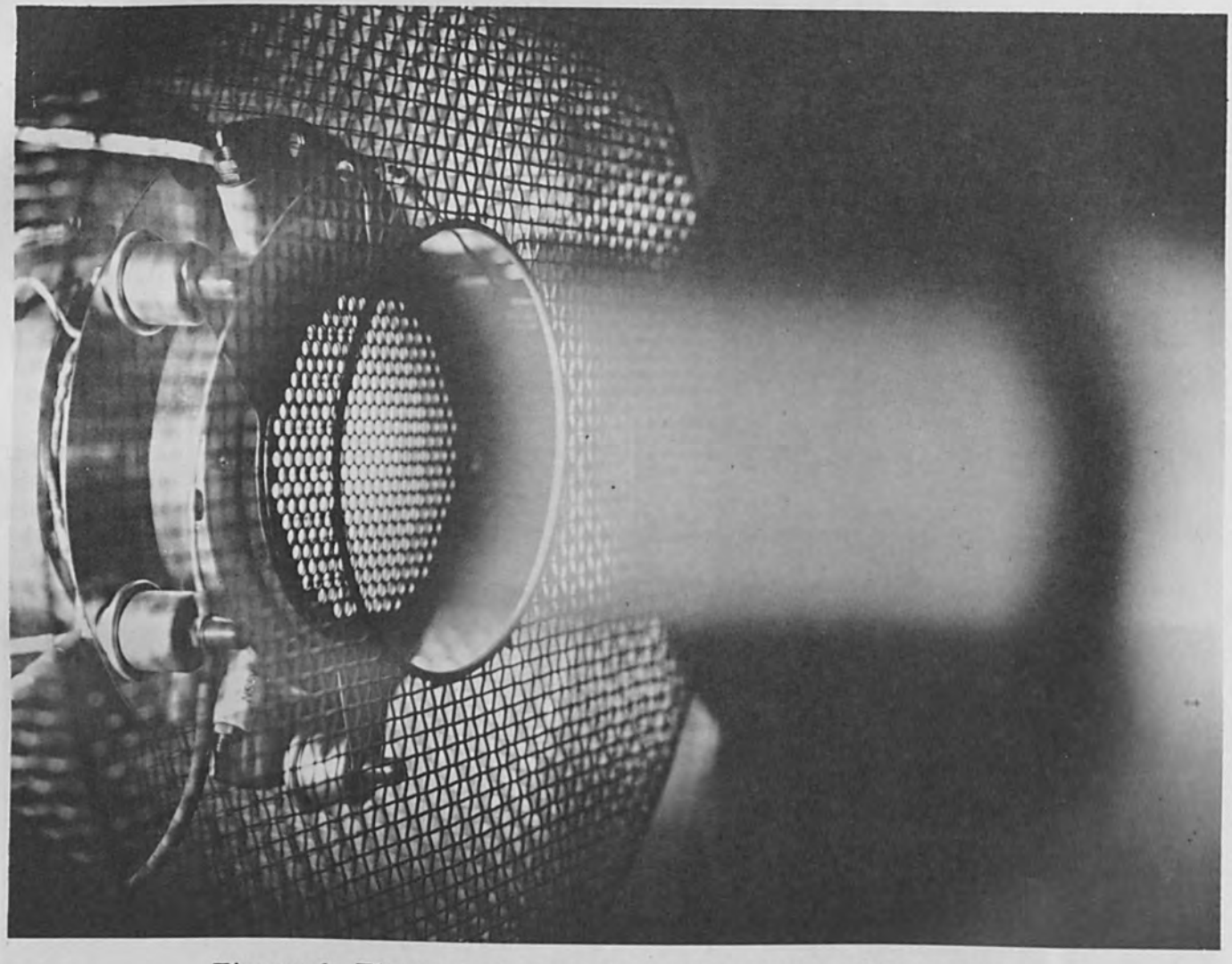

Figure 3 Electron Bombardment Ion Source (System B)

The vacuum chamber is cylindrical in shape, 2 ft by 6 ft, and is evacuated by two 10-inch diffusion pumps. The operating pressures are on the order of 5×10^{-6} torr.

Silicon samples that were to be mounted in the vacuum chamber were cut with a diamond saw to proper orientation, as determined by X-ray diffraction. Slices were then lapped to remove major work damage caused by the sawing procedure, and the side of the slice to be exposed to the ion beam was chem-etched to remove residual work damage caused by the lapping operation.

Following exposure to the ion beam, sample chips from implanted slices were

mechanically polished at angle of approximately 1^{o} to the implanted surface. This sectioning technique exposes a shallow cross-section of the implanted region, amplifying its depth. The angle section is stained, using a 48 percent solution of hydrofluoric acid under a bright light. This darkens the p-type base material, leaving the n-type region unstained. The depth of the implanted region can then be determined by standard interference microscopy, using a mercury arc lamp as a monochromatic light source. Sheet resistance measurements on each sample are determined by a 4-point probe apparatus. The p-n junction formed by implantation serves as an isolating boundary on the current injected by the apparatus.

The profile of the electrically active implanted species is determined by removal of thin layers, using a boiling water oxidation-acid etch procedure,[15] followed by successive 4-point probe measurements.

Experimental Results

Table I summarizes the conditions of ion bombardment for the various implantations and will be used with Table II in the discussion of the next section. Table II summarizes pertinent data of the target before and after ion bombardment. Column 1 gives the run number with A representing the small-beam system and B the large-area system. The number following the letter represents the particular sample in a multiexposure run.

The second column $< hkl >$ gives the crystalline orientation of the target to the beam direction and the fifth column tabulates the value of ρ, the target resistivity of the p-type silicon samples before bombardment. The sheet resistance R_s of the converted region is given in column 3 and the junction depths as determined by angle section listed in column 4.

The profile of electrically active implanted species for Run 6B9 is shown in Figure 4. The concentration is computed from the conductivity σ, which in turn is calculated by:

TABLE I

IMPLANTATION CONDITIONS

Run No.	Species	Energy (kev)	Temperature (°C)	Current Density (microamps/cm²)	Time (min.)	Integrated Particle Flux per cm²	Remarks
1A	Cs^+	10	360	20	66	4.95×10^{17}	
2B	Cs^+	5.1	370	200	6.65	5×10^{17}	
3B	Cs^+	5.1	360	200	1	7.5×10^{16}	
4A	Cs^+						Source and Vacuum Failure
5B	Cs^+	5.1	469	225	30	2.54×10^{18}	
6B	Cs^+	5.1	450	200	120	9×10^{18}	
7A	Cs^+	18.5	350	~14	120	6.25×10^{17}	
8A	K^+	18.5	350	~20	120	9×10^{17}	
9A	K^+	5.4	350	~17	120	8×10^{17}	
10B	Cs^+	5.0	400	210	30		Calibration Run
11A	K^+	Variable 2 - 18.5	360	1 - 70	20 min. at each energy		Steps of 18.5, 15, 10, 5, 2.5, and 2

TABLE II

IMPLANTATION RESULTS

Run No.	<hkl>	R_S ohms/cm^2	X_J (microns)	Base (ohm-cm) Resistivity	Remarks
1A3	<111>	-	-		Sputtering yield of SiO_2 layer ≈ 0.89
2B1	<111>	39,000	0.14	20	
3B1	<111>	1.4 megs	less than 0.1	20	
5B2	<111>	51,000	0.22	2,000	
5B6	<111>	-	-	170	Completely converted
5B7	<100>	26,800	0.51	19	
5B8	<110>	12,000	0.55	19	
5B9	<111>	21,800	0.57	19	
6B5	<100>	12,000	0.13	1	
6B6	<110>	24,000	0.13	1	
6B7	<111>	45,000	0.13	1	
6B8	<100>	29,000	0.34	19	
6B9	<110>	10,500	0.80	19	
6B10	<111>	15,000	0.68	19	
7A1	<100>	46,000	0.34	19	
7A2	<110>	37,000	0.38	19	
7A3	<111>	38,000	0.20	19	
8A1	<100>	5,800	0.10	19	
8A2	<110>	3,200	0.41	19	
8A3	<111>	6,500	0.30	19	
9A1	<100>	4,500	0.2	19	
9A2	<110>	2,700	0.35	19	
9A3	<111>	4,200	0.26	19	

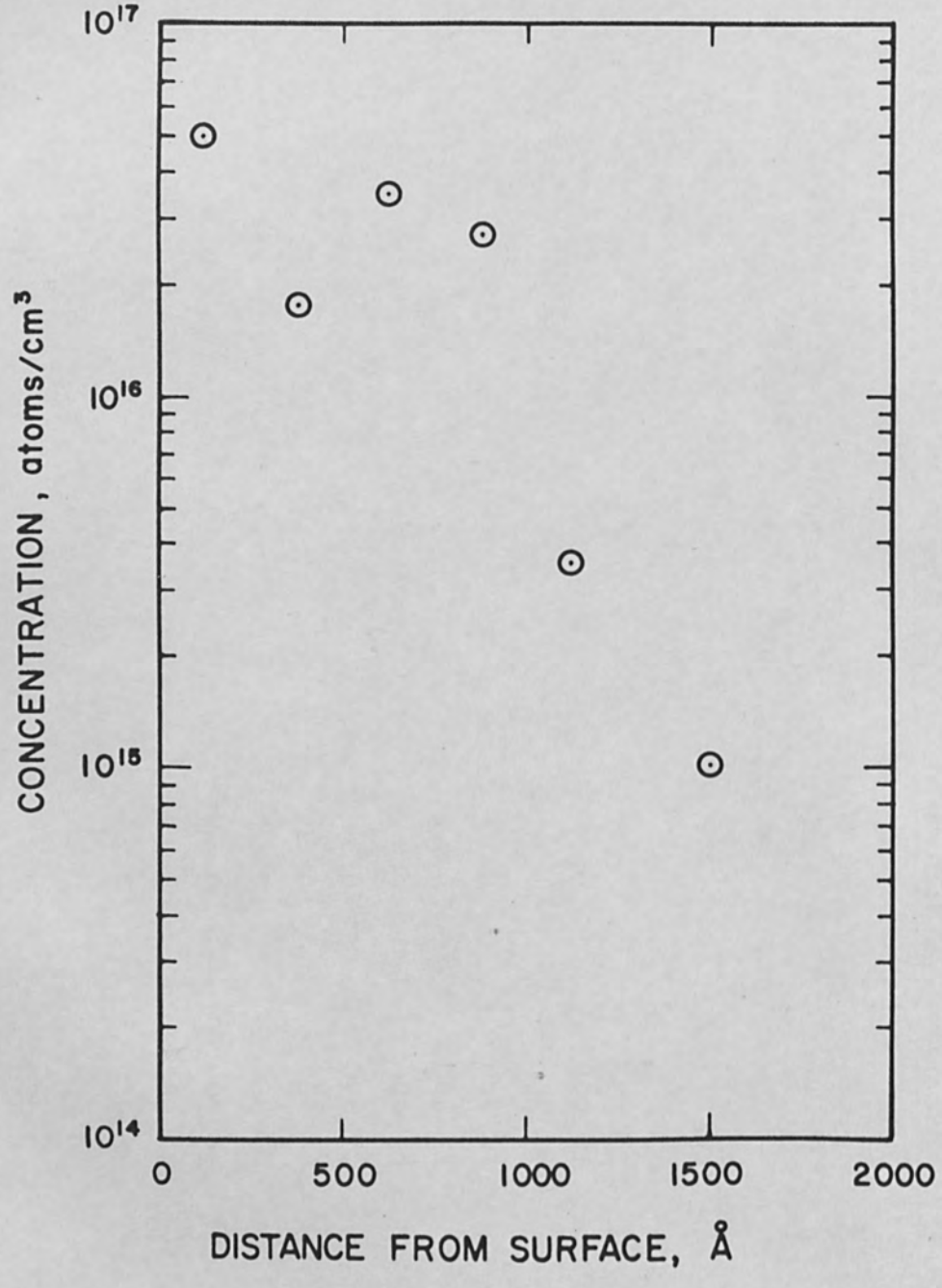

Figure 4 Concentration Profile of Electrically Active Dopants in Silicon, Produced by Ion Implantation as Determined from Peeling and Sheet Resistance Measurements (Sample 6 B9)

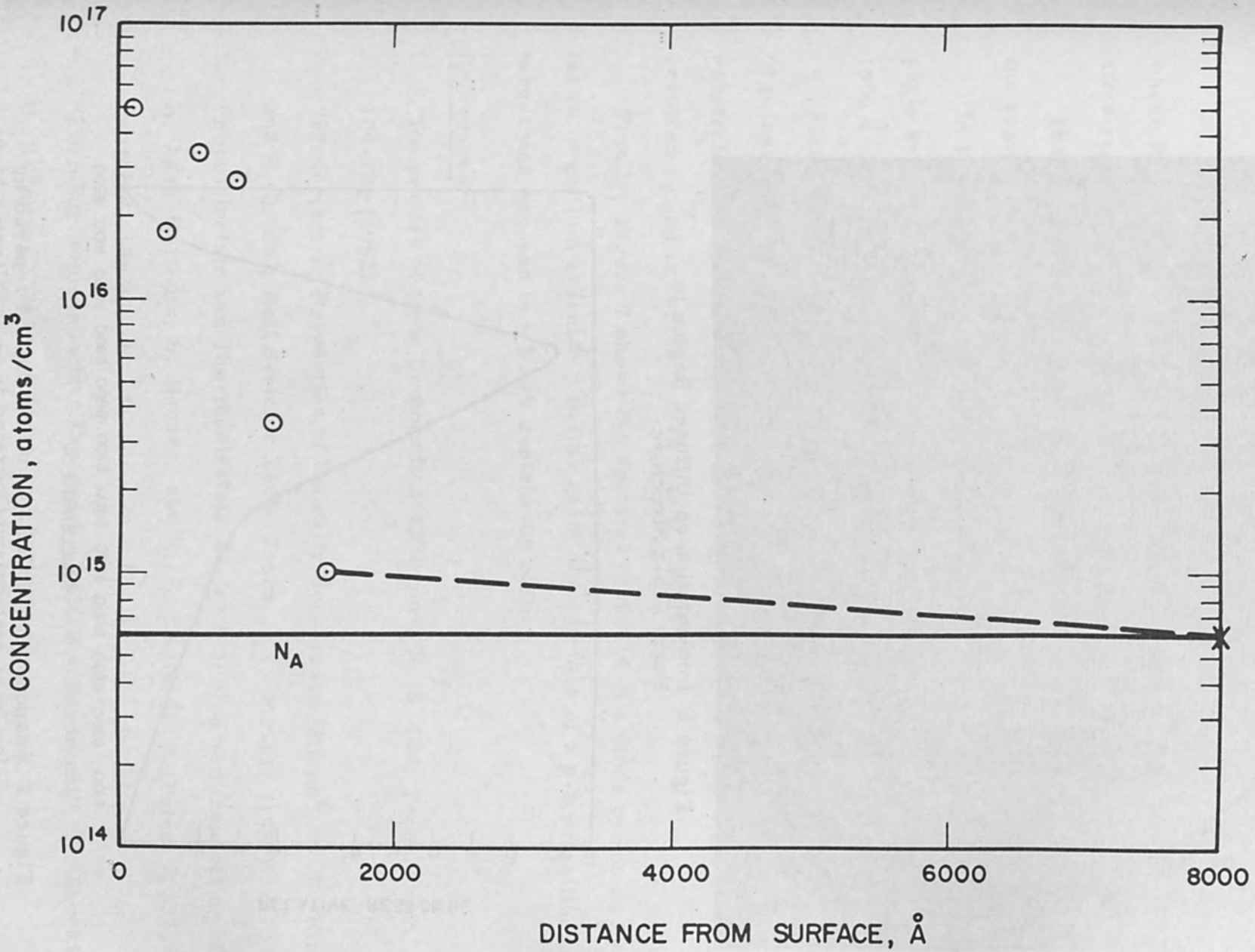

Figure 5 Concentration Profile of Electrically Active Dopants in Silicon, Produced by Ion Implantation as Determined from Peeling and Sheet Resistance Measurements (Sample 6 B9)

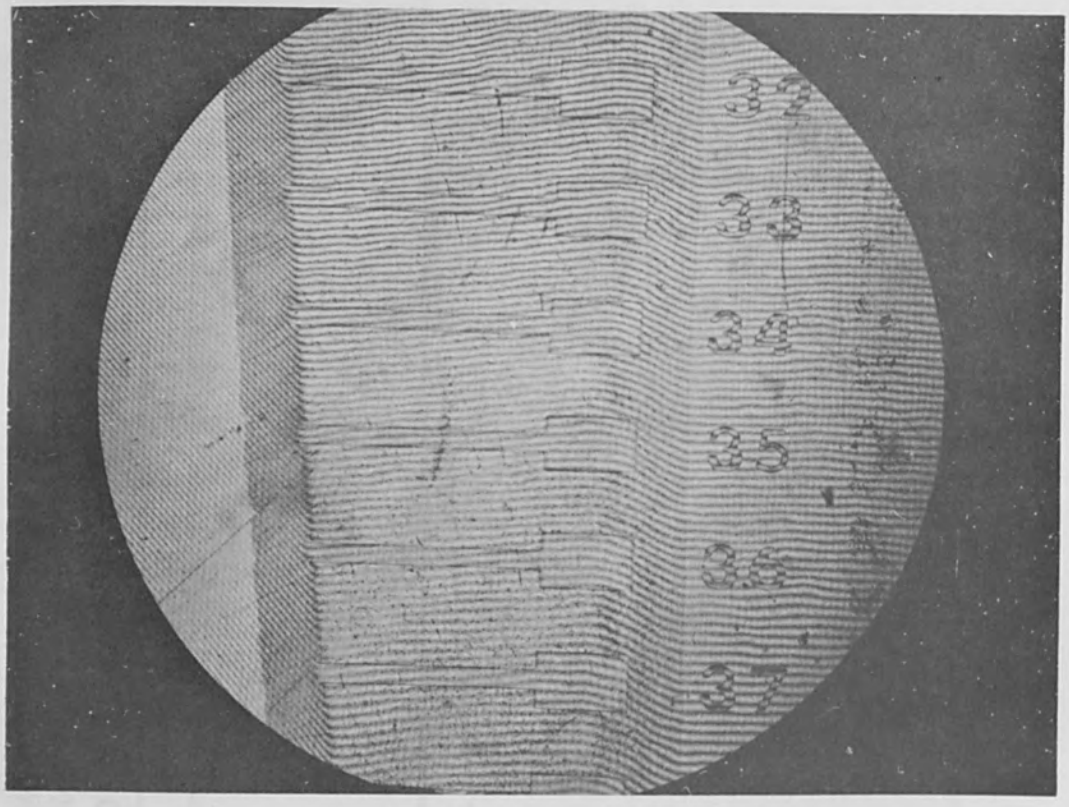

Figure 6 Implantation on Diffused Region to Form n-p-n Structure

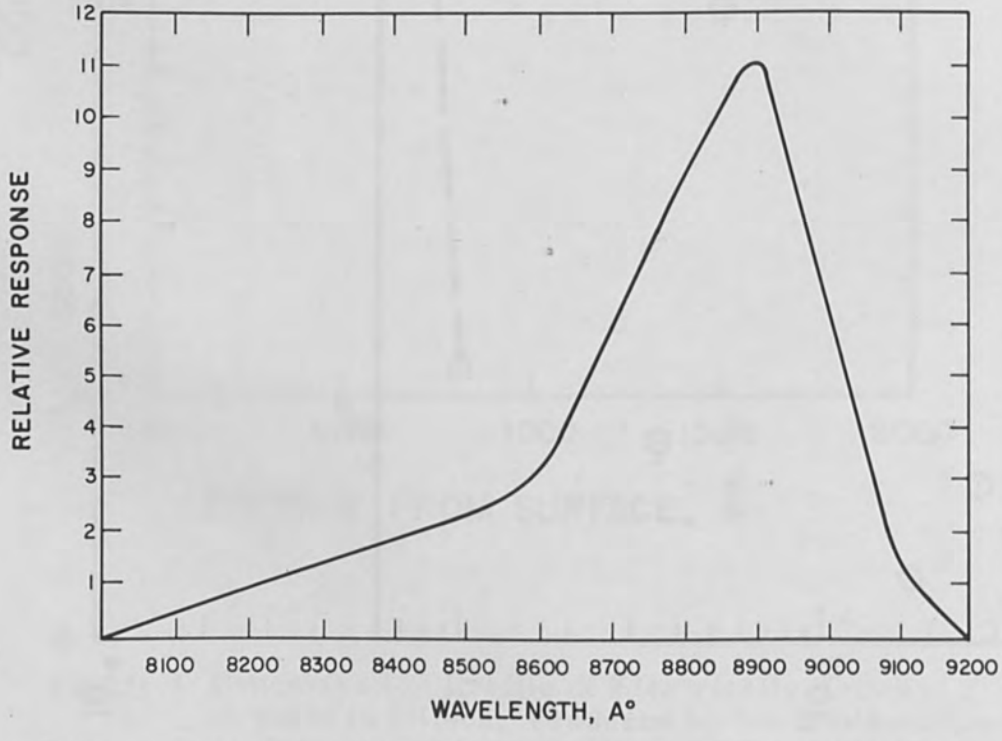

Figure 7 Responsivity of GaAs Junction Diode Prepared by Ion Implantation and Operated in Self-Filtering Mode

$$\sigma = \frac{1}{R_i} - \frac{1}{R_f} \frac{1}{\Delta X}$$

where R_i and R_f, respectively, represent the values of sheet resistance before and after removal of a layer of thickness, ΔX .

The assumption is made that the mobility does not vary through the depth of the sample.

In Figure 5, the data of Figure 4 is shown together with a point determined by angle section. The junction profile appears to have a region of high doping within 1500 Å and then a shallow straggling tail which extends out to the junction position.

Figure 6 is an angle section of a transistor structure formed by implantation of potassium ions into a previously diffused, highly doped p-type region on an n-type substrate. The junction depth of the over-compensated surface layer could not be resolved by and is certainly less than 0.1 micron.

Finally, Figure 7 shows the spectral response of a diode produced by implantation in gallium arsenide. In this case, the 110 face of a p-type gallium arsenide target was exposed to a 5 keV cesium ion beam.

References

1. "Properties of Ionic Bombardment Silicon", R. S. Ohl; Tech. Journ., 31, 104-121 (1952).
2. "Photoelectric Properties of Ionically Bombarded Silicon", E. F. Kingsbury and R. S. Ohl; Bell Systems Tech. Journ., 31, 902-815 (1952).
3. "Photoelectric and Thermoelectric Device Utilizing Semiconducting Material", K. Lark-Horovitz, S. Benzer, and R. E. Davis; U. S. Patent 2,588,254 (March 4, 1952).
4. "Forming Semiconductive Devices by Ionic Bombardment", W. Shockley; U. S. Patent 2,787,564 (April 2, 1957).
5. "Effects Produced by Ionic Bombardment of Germanium", W. D. Cussins;

Phys. Soc. of London Proc., B68, 213 (1955).

6. "Crystal Doping by Ion Bombardment", F. M. Rourke, J. C. Sheffield, and F. A. White; Rev. Sci. Inst., 32, 455 (1961).
7. "Silicon Heavily Doped by Energetic Cesium Ions", J. O. McCaldin and A. E. Widmer; J. Phys. Chem. Solids, 24, 1073-1080 (1963).
8. "Alkali Ion Doping of Silicon", J. O. McCaldin and A. E. Widmer; Proc. IEEE, 52, (1964).
9. "Comments on Differing Results Obtained in Doping of Semiconductors by Energetic Ions", J. O. McCaldin and A. E. Widmer; Journ. Appl. Phys. 35, 1985 (1964).
10. "Characteristics of Silicon p-n Junctions formed by Sodium and Cesium Ion Bombardment", M. Waldner and P. E. McQuaid; Solid State Electronics 7, 925 (1964).
11. "Properties of Silicon p-n Junctions Formed by Cs^+ Implantation at Low Energies", C. B. Medved, G. P. Rolik, R. C. Speiser, and H. L. Daley; Phys. Ltr., 3, 213 (1963).
12. "Implantation of Cesium Ions Oriented Silicon Single Crystals", D. B. Medved, G. P. Rolik, and R. C. Speiser; Bull. Am. Phys. Soc., 8, 593 (1963).
13. "Measurement of Cesium and Rubidium Charge Transfer Cross Sections", J. Perel, R. H. Vernon, H. L. Daley; submitted for publication to the Physical Review.
14. R. C. Speiser and L. K. Branson, ARS Paper No. 2664-62 (1962).
15. "Hot-Electron Emission from Shallow p-n Junctions in Silicon", D. J. Bartelink, J. L. Moll, and N. J. Meyer; Phys. Rev. 130, 972 (1963).

Megavolt Pulsed Electron Beam Techniques*

by

S. Graybill, H. Lackner and S. V. Nablo
Ion Physics Corporation
Burlington, Massachusetts

Abstract

Three experimental facilities have been developed for the production of very high intensity electron beams for the study of material behavior and pulsed/flash X-ray production. The first of these utilizes a conventional impregnated nickel matrix cathode with a grid-controlled injector in a 2 MeV Van de Graaff accelerator. Well-focused beams of 1 ampere in 20 μsec pulses are realized while post acceleration focusing of the beam provides beam diameters of 0.2 cm. Several of the diagnostic techniques used with the facility will be discussed. The same gun is capable of delivering 2 microsecond 40 ampere pulses when used with a novel, reliable bridgewire cathode. The production of peak power densities above 10^9 W/cm^2 through the use of single and multipoint field emission diodes has recently been achieved. Performance data for one of these tubes operating on an existing system at potentials above 1 MeV and delivering currents of 20,000 amperes for 20 nanosecond bursts will be presented.

Introduction

It is the primary purpose of this paper to present the facilities at Ion Physics Corporation currently used for the production of high energy pulsed electron beams. Electron energies are in the range 1 to 2 MeV, with beam currents of 0.5 ampere, 10 amperes and 20,000 amperes, available from a nickel matrix cathode, bridgewire plasma and field emission source respectively. The high voltage supply used

---

*This work was partially supported under Air Force Contract AF08(635)-3666.

is, in each case, a modified Van de Graaff generator. Total energy per pulse in the lower current devices is approximately 20 joules, and in the latter case, approximately 500 joules. Presently under investigation are the pulsed heating of metals, charge injection and breakdown in dielectrics, and the production of high intensity X-ray pulses from heavy targets.

Nickel Matrix Cathode Electron Gun

A schematic diagram of the electron gun appears in Figure 1. The cathode holder is in the shape of an inverted hat, the top of which is the cathode proper. This consists of an 8 mm diameter pellet of pressed and sintered material composed of 69% Ni, 2% ZrH and 29% (Ba, Ca, Sr)CO_3. Normal operating temperature is approximately 1100°C. In pulsed operation these cathodes can deliver between one and ten amperes/cm^2. This maximum current density varies with time for a given cathode, and is known to be a function of its operating history which sensitively controls the emissive surface condition.[1]

Emission is controlled by a high transmission grid covering the aperture in the focus cup. This structure consists of high work function surfaces and is normally biased beyond cutoff. Anode and focus electrode potentials may be varied from 0 to 20 and 30 kilovolts respectively. The current pulse is initiated by a neon bulb in the base of the accelerator. A multiplier phototube in the terminal detects the light signal and triggers a 3C45 thyratron, thus discharging a 40 μsecond delay line through its characteristic impedance. The resulting 1500 volt pulse is applied to the focus cup and grid, which is about 0.030 inch from the cathode face. Current pulses are typically 0.5 ampere for 40 μseconds with a roughly square pulse shape, as determined by the delay line characteristics.

Accelerator Facility

Figure 2 depicts the pulsed radiation facility presently being used. The electron gun is mounted on the accelerator tube of the 2 MV vertical Van de Graaff

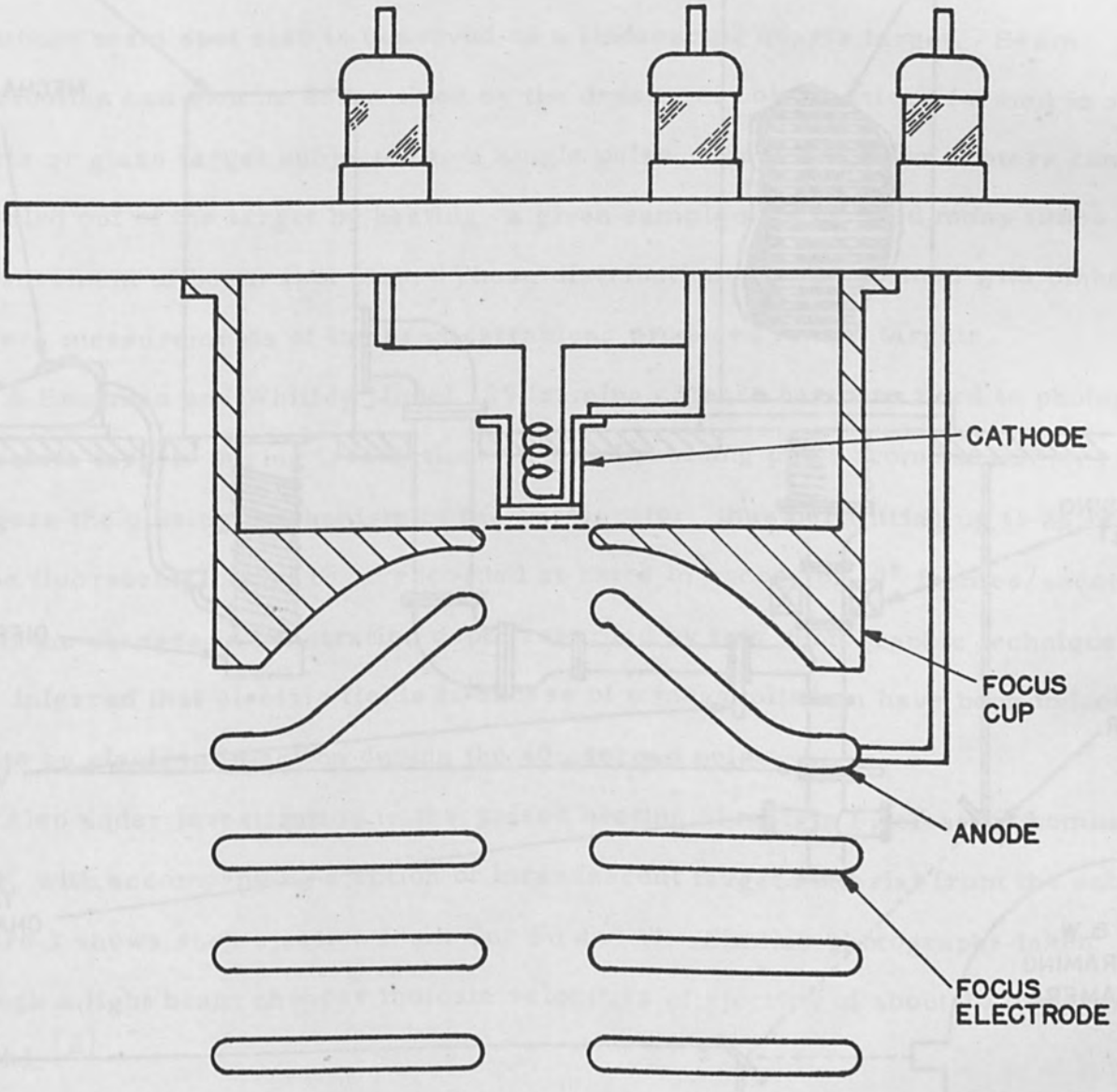

FIG. 1 Ni MATRIX CATHODE ELECTRON GUN

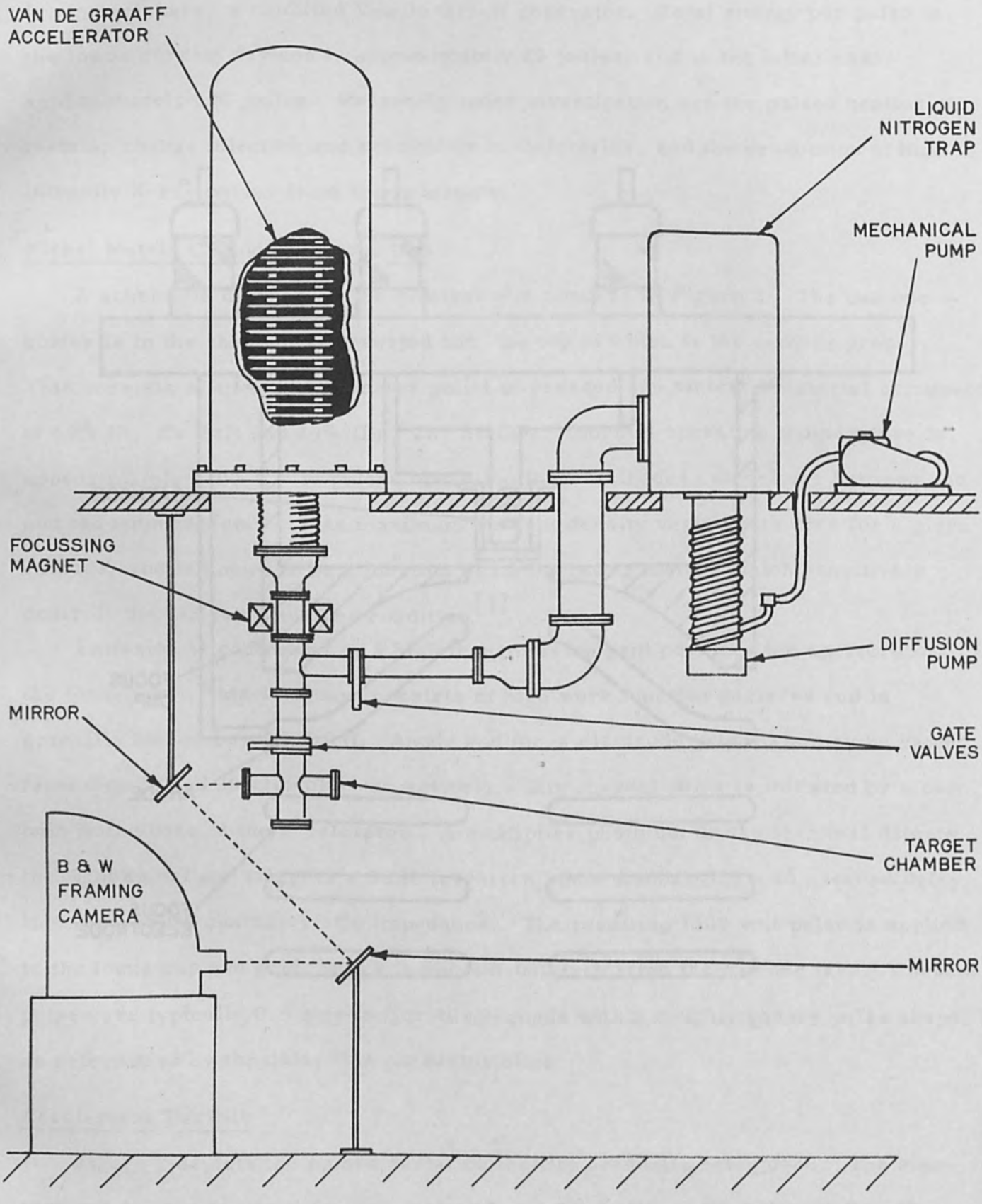

FIG. 2 ELECTRON IRRADIATION FACILITY

generator shown. A solenoid magnet below the base plate of the accelerator focuses the beam to about 4 mm in diameter on the target, which may be viewed by the operator through a telescope and mirror system. Optimum settings of the anode and focus controls are determined by manipulation of those controls until minimum beam spot size is observed on a fluorescing quartz target. Beam distribution can then be determined by the density of color centers formed in a quartz or glass target subjected to a single pulse. Since the color centers can be annealed out of the target by heating, a given sample may be used many times for measurement of beam spot size. These distributions are confirmed with pinhole camera measurements of the bremsstrahlung produced in thin targets.

A Beckman and Whitley Model 189 framing camera has been used to photograph dielectric targets during irradiation. A synchronizing pulse from the camera triggers the pulsing mechanism in the accelerator, thus permitting up to 25 frames of the fluorescing target to be recorded at rates in excess of 10^6 frames/second. From the changes in penetration depth recorded by this photographic technique we have inferred that electric fields in excess of 6 megavolts/cm have been induced in Lucite by electron injection during the 40 μsecond pulse.

Also under investigation is the pulsed heating of metals by electron bombardment, with accompanying ejection of incandescent target material from the substrate. Figure 3 shows such ejection from Cu, Sn and W. Similar photographs taken through a light beam chopper indicate velocities of ejection of about 20 meters/second. [2]

Bridgewire Cathode Electron Gun

During the course of some related experiments at this laboratory several attempts were made to explode small wires in high vacuum ($\sim 5 \times 10^{-5}$ mm). It was observed that a bright plasma appeared in the vicinity of this wire during discharge of the capacitor bank, but the wire fractured, after which no discharge

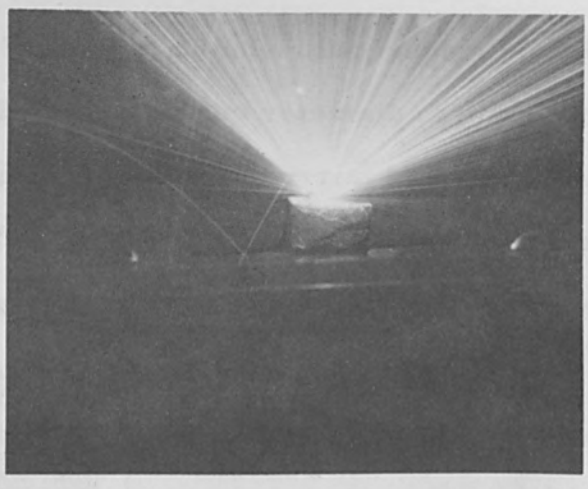

(a) Tin

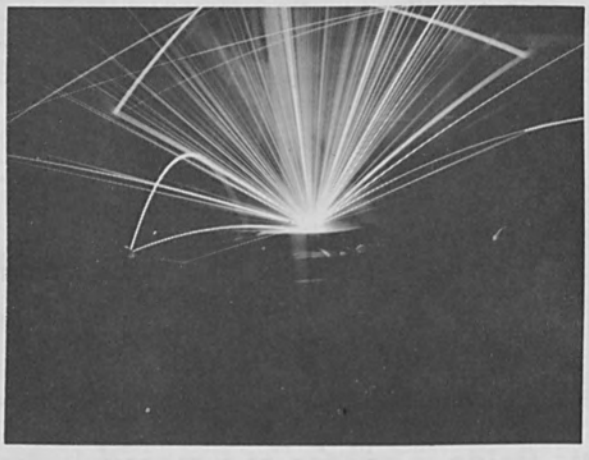

(b) Tungsten

(c) Copper

FIG. 3 EJECTION OF TARGET MATERIAL AFTER PULSED ELECTRON IRRADIATION

occurred. A similar phenomenon has been reported by Korneff[3] who observed the formation of a plasma around an exploding wire in vacuum. Once the plasma is formed, it shunts all of the current around the wire, thus preventing further deposition of energy in the wire. Since this plasma was presumably a rich source of electrons, it was proposed that it might replace the cathode in the electron gun described earlier.

After some experimentation it was empirically determined that a 0.005 inch diameter Ni wire of length 2 mm would consistently produce a satisfactory discharge with a 1 μf 2200 V capacity bank. Further, one such wire has survived over 300 discharges without fracture. Such a wire was installed in the electron gun and the system tried in the test rig shown schematically in Figure 4.

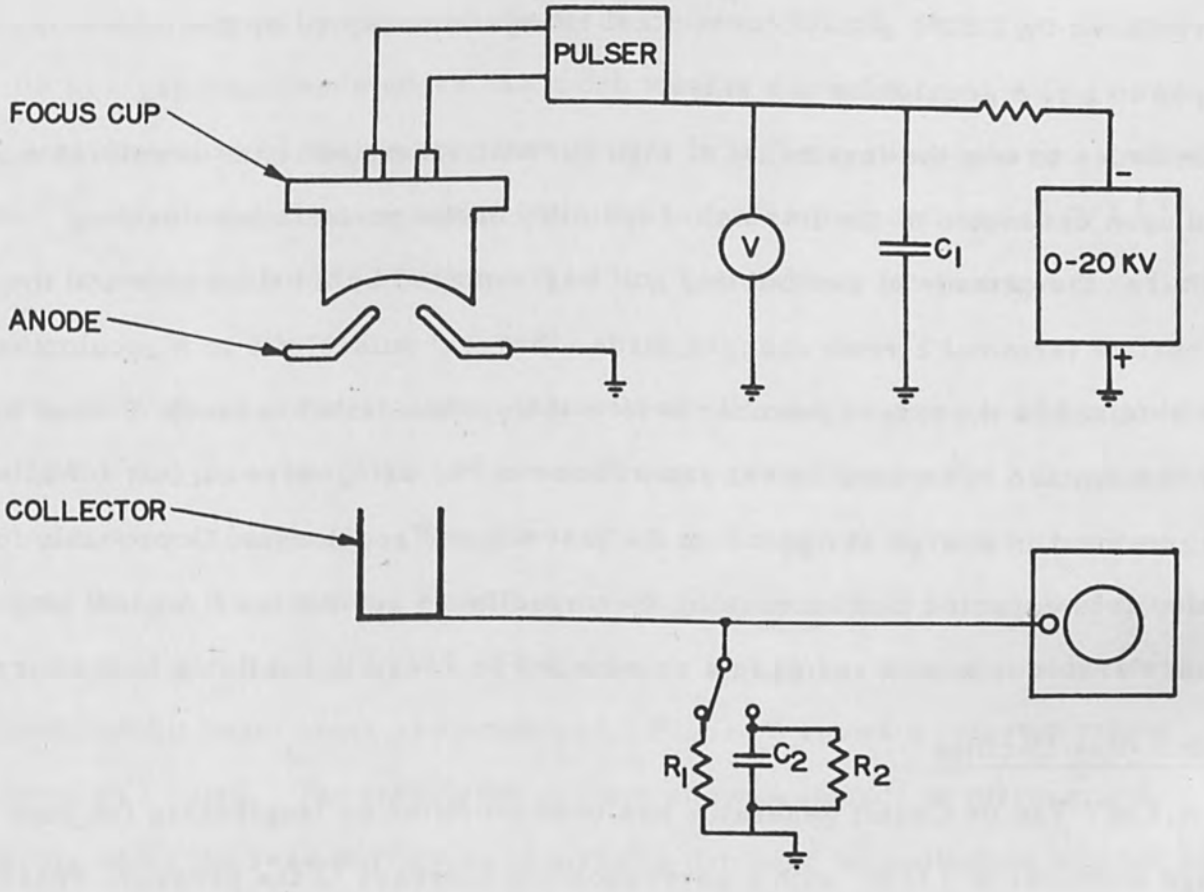

FIG. 4 BRIDGEWIRE ELECTRON GUN TEST RIG

The collector was a 1-inch diameter cup of length approximately 3 inches, at a distance of about 2 inches from the anode. The CRO could display either the current through R_1 or the total charge collected in C_2 during the pulse. Maximum current was observed at about 7 kV accelerating voltage at which point the current peak was 40 amperes with a half width of about 2 μseconds. This agreed with the charge measurements of 70 μcoulombs on C_2 with a decay characteristic of the R_2C_2 circuit (0.2 second).

The large current emitted during the pulse was sufficient to almost completely discharge the 0.1 μf capacitor C_1, indicating that most of the current emitted by the plasma was intercepted on the anode. Since the corresponding capacitor in the accelerator terminal was only 2000 pf, severe loading of the first stage of acceleration was expected to seriously reduce the beam current. Indeed, when C_1 was replaced by a 2000 pf capacitor, total charge intercepted by the collector dropped to 6 to 8 μcoulombs per pulse.

In order to test the feasibility of high current operation of the accelerator, based upon estimates of the intrinsic capability of the periodic accelerating structure, the cathode of the existing gun was replaced by a bridgewire and the appropriate terminal circuit changes made. Several pulses of 6 to 8 μcoulombs were obtained in the target chamber before the system failed because of what was later determined to be insufficient capacitance in the bridgewire circuit. While the agreement in charge per pulse on the test rig and accelerator is probably fortuitous, it is expected that increasing the capacitance across the first few stages of the accelerator tube will result in a substantial increase in available beam current.

Flash X-Ray Facility

A 3 MV Van de Graaff generator has been modified by lengthening the high voltage terminal to 9 feet, with a corresponding increase in the pressure vessel. The terminal and coaxial pressure vessel thus form a high voltage transmission

line with a nominal impedance of 45 Ω and total capacitance 280 pf, storing 1260 joules at 3 MV. A schematic of the facility is shown in Figure 5. Located near the hemispherical cap of the terminal is the flash X-ray tube shown in Figure 6. A triggered spark transfers the stored charge from the terminal to the diode cathode, raising its potential until field emission occurs. The cathode emitting surface consists of one or more points, or a sharp circular edge spaced several centimeters from the grounded anode. Normally the target is a high Z material for bremsstrahlung production, but other materials have been used. The cathode is insulated from ground by the capacitively graded dielectric structure[5] shown in Figure 6. This structure, which extends into the pressure vessel also forms the walls of the diode vacuum chamber.

When operating in the megavolt region it is relatively simple to make the cathode-anode geometry such that the field emission is space-charge-limited. This results in a gap impedance which has much weaker dependence on voltage and radius of curvature of the emitter than occurs in the non-space-charge-limited mode.[6] Since radiation intensity from the target is proportional to IV^3,[7] the gap impedance should be 3 times the "line" impedance for maximum radiation intensity.

Figure 7 shows some radiation intensity oscillographs provided by a plastic scintillator and photo diode placed about 2 meters from the anode. The time base is 20 nanoseconds/division. The pulses from A through D show the result of lowering the gap impedance. Since a considerable amount of energy is deposited in the anode during the pulse (~500 joules) anode damage becomes a problem when relatively small beam spots are employed. Figure 8 shows a tungsten target subjected to 1 pulse. The irradiated surface shows evidence of melting and cratering while the rear surface is apparently damaged by spallation induced by thermal or mechanical shock.

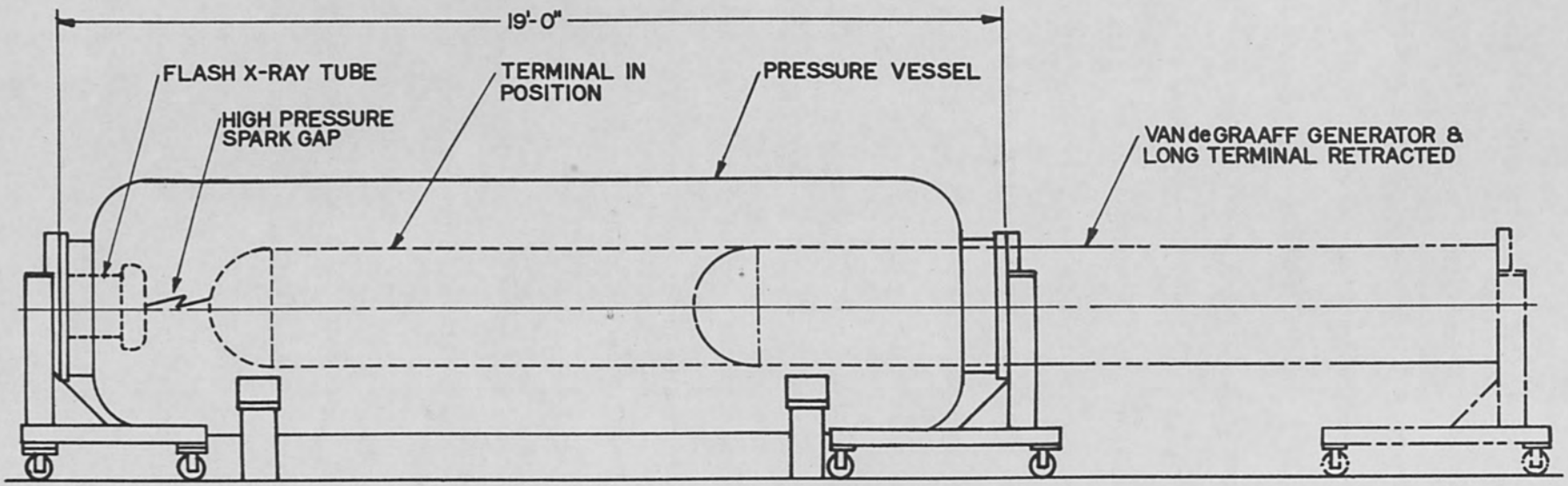

FIG. 5 SCHEMATIC OF FLASH X-RAY FACILITY

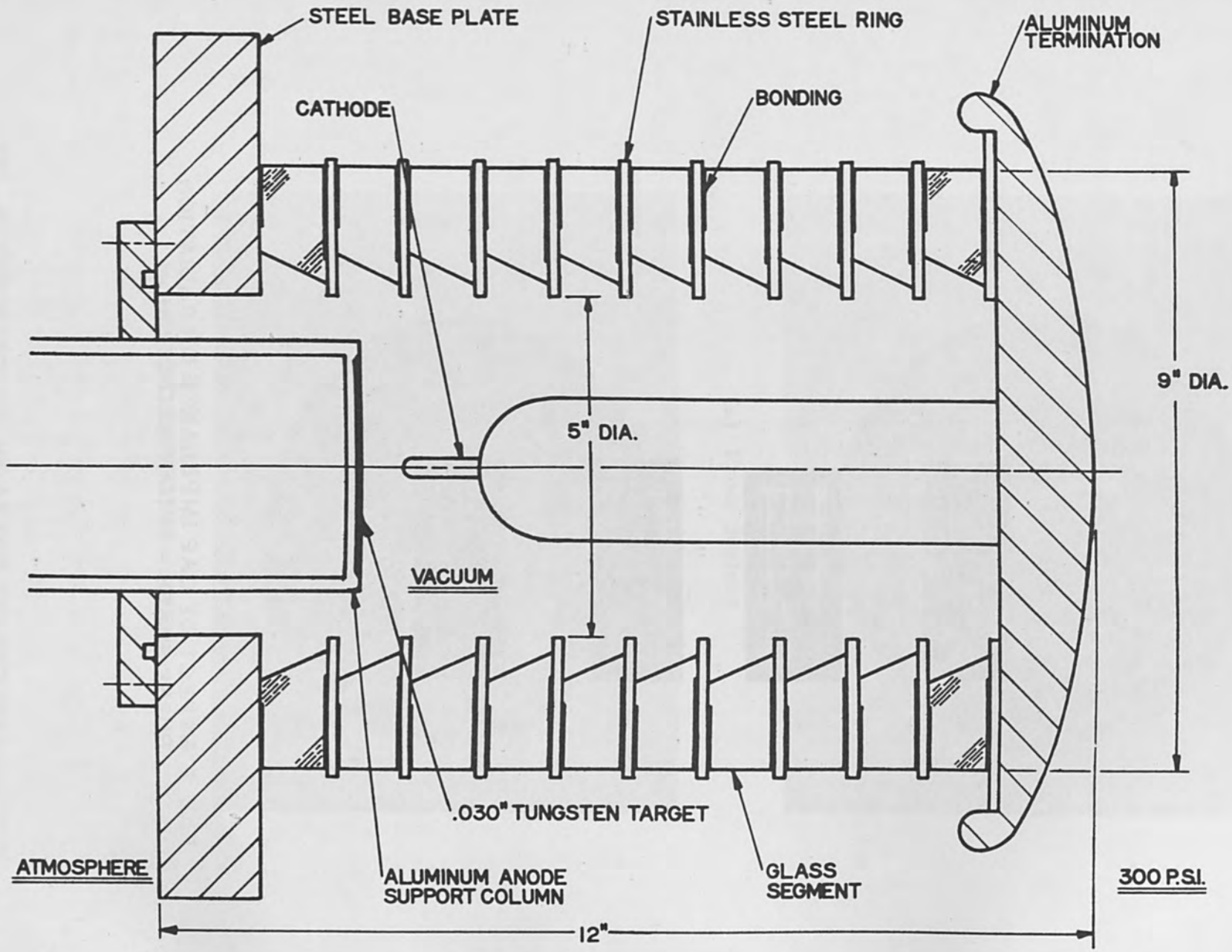

FIG. 6 HIGH VOLTAGE FIELD EMISSION DIODE

a.

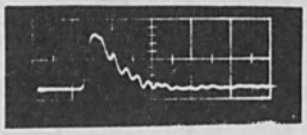

b.

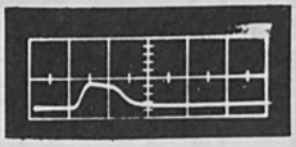

c.

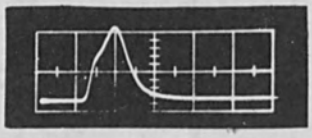

d.

FIG. 7 EFFECT OF GAP IMPEDANCE ON RADIATION PULSE SHAPE - 20 NANOSEC/DIVISION

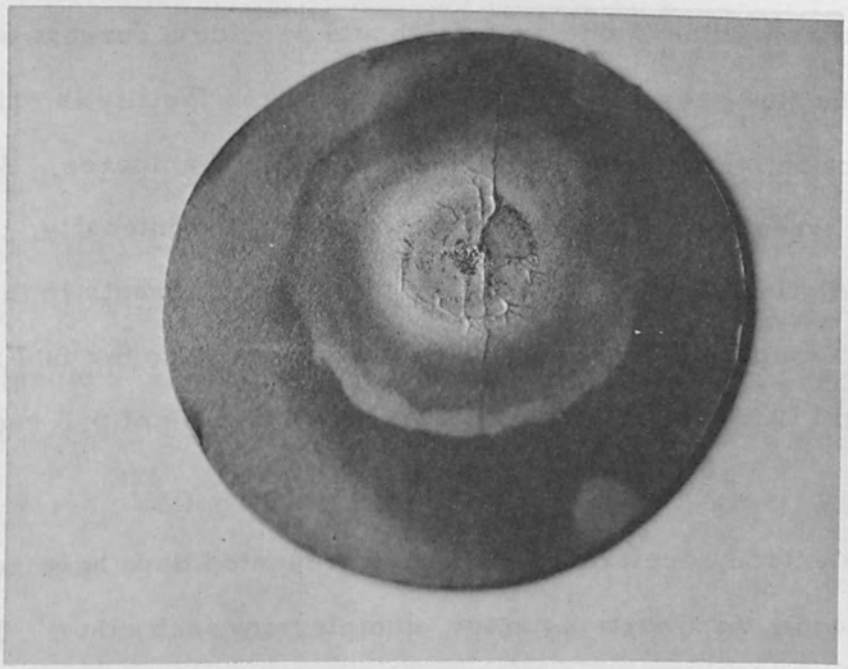

(a) Front Surface

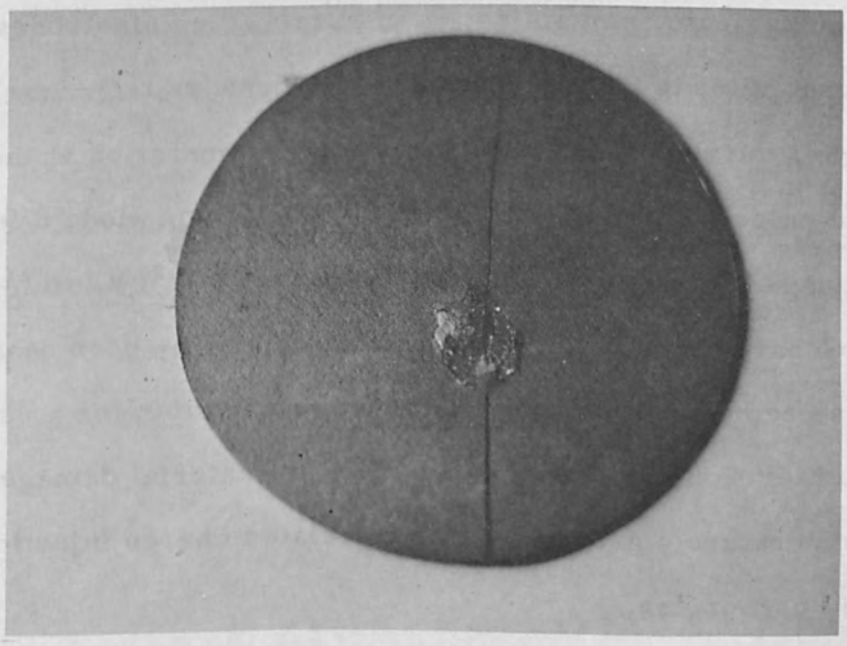

(b) Spalled Rear Surface

FIG. 8 TUNGSTEN ANODE AFTER PULSED IRRADIATION

This transmission line-diode system should provide a current of 3×10^4 amperes when the line sees a matched load. Since the facility is primarily for radiation production, the optimum current is 1.7×10^4 amperes. As yet there has been no direct current measurement, but from radiation intensity, terminal potential and radiation spectral quality, we infer peak currents in the range 1.5 to 2.0×10^4 amperes. The peak intensity observed so far is 7×10^7 R/sec at 1 meter with total flux density or dose delivered per pulse of 0.8 roentgen.

Conclusion

The three electron acceleration schemes presented here have advantages and disadvantages which, to a certain extent, complement each other. The Ni matrix cathode, while providing a well-defined emitting surface and permitting good beam control suffers from the difficulties of high temperature control, conditioning and heater power requirements, contamination of surrounding electrodes with emitting material, and susceptibility to poisoning. The bridgewire technique promises considerably higher current density and simplicity of operation at the expense of beam control and pulse shape. Finally, the field emission diode offers extremely high currents at unusually high peak power densities ($>10^{10}$ W/cm^2), limited largely by space-charge effects but suffers from relatively poor beam control. These techniques are now being used to produce information for a very wide range of the relevant irradiation parameters in studies of material damage, X-ray production, high temperature plasma studies and related charge injection/pulsed radiation-induced phenomena.

Acknowledgements

The authors would like to acknowledge the sustained interest and assistance of Lt. V. Hirschy, Detachment 4, RTD, Eglin AFB, Florida and of Mr. A. John Gale and Dr. A Stuart Denholm of Ion Physics Corporation in these studies. The authors are indebted to B. S. Quintal and his group for bringing the 3 megavolt system into

successful operation.

References

1. Beck, A. H. W., "High Current Density Thermionic Emitters: A Survey", Proc. IEEE, 106, 372, 1959.
2. Heil, O. and S. Vogel, "Pulse Heat ing of Materials by Highly Concentrated Electron Beams", AFCRL-62-167, Bedford, Mass., January, 1962.
3. Kornell, T. et al, "Exploding Wire Phenomena at Reduced Pressures", p. 104, Exploding Wires, Edited by W. G. Chace and H. K, Moore, Plenum Press, Inc. New York, 1959.
4. Vibrans, G. E., "Computation of the Spreading of an Electron Beam Under Acceleration and Space-Charge Repulsion", Report No. 38, Lincoln Lab., MIT, April, 1963.
5. Smith, I. D., "Pulse Breakdown of Insulator Surfaces in a Poor Vacuum", Proc. Symposium on the Insulation of High Voltages in Vacuum, 261, October, 1964.
6. Dyke, W. P. and W. W. Dolan, "Field Emission", Advances in Electronics and Electron Physics, 8, 89, Academic Press, New York, 1956.
7. Koch, H. and J. Motz, Rev. Mod. Phys. 31, 920, 1959.

Some New Developments in E. B. Welding

by

J. L. Solomon
Sciaky Bros., Inc.
Chicago, Illinois

P. R. Thome
Commissariat a l'Energie Atomique
Saclay, France

Abstract

Recent developments applicable to electron beam welding are discussed. Some of these are: the construction of a moving vacuum joint where vacuum is limited to the immediate welded line vicinity only; an electron beam gun with special pumping allowing welding operation under primary vacuum pumping; and also various control and programmation devices of the welding parameters.

Introduction

Electron beam welding is a fusion welding process conducted in a vacuum environment, and employing a finely focused beam of accelerated electrons whose high kinetic energy is transformed into heat, upon impact with the workpieces, causing rapid localized melting and fusion of the parts.

The geometry of the resultant weld is unique to the electron beam welding process, the fusion zone width being substantially smaller than the depth, generally by a factor of ten or more. Compared to conventional fusion welding methods, the electron beam process is attractive because no involved machining of profiles and chamfers is necessary to prepare the joint for welding -- a simple square-butt joint is all that is required -- and because the reduced energy input to the work and the unique weld geometry result in an important reduction in weldment distortion and shrinkage.

The work, the electron beam gun, and the manipulating devices are usually

housed in a rigidly constructed vacuum chamber whose dimensions are determined by the size of the workpiece. A typical EBW system is shown in Figure 1. It is apparent that the work is essentially inaccessible during the welding operation, and that the welding must be controlled from a remote position. This situation, together with the high degree of metallurgical and mechanical integrity that are required in the applications to which this process is often put, has necessitated the development of means for automation and remote control.

It certainly is true that the utilization of the EB welding process has benefited (and sometimes, only was possible) by the advances which have been made in the construction of large vacuum chambers. But likewise it is apparent that there could be substantial reduction effected in the equipment floor space and chamber size required if one were to localize the vacuum in the immediate vicinity of the weld joint using "local (vacuum) chambers" which could move or not with respect to the workpiece.

The role of vacuum in EB welding is well known, as are the means generally employed to develop and maintain the vacuum. However, it is suggested that the use of the process would be facilitated if, instead of using a high vacuum (on the order of 10^{-4} Torr), it were possible to work at a low vacuum or at least at a pressure of a few Torr. Then the problems involved in sealing and evacuation of the system should be substantially minimized. And, finally, it is an obvious advantage to completely eliminate the vacuum chamber, if one can arrive at a practical and economical solution.

In this paper we shall illustrate some of the points mentioned above.

Control and Programming

Since the work is enclosed in a vacuum chamber, Electron Beam Welding is essentially a remote, automatic process which requires appropriate control elements for the various functions of the machine. In addition, the Electron Beam

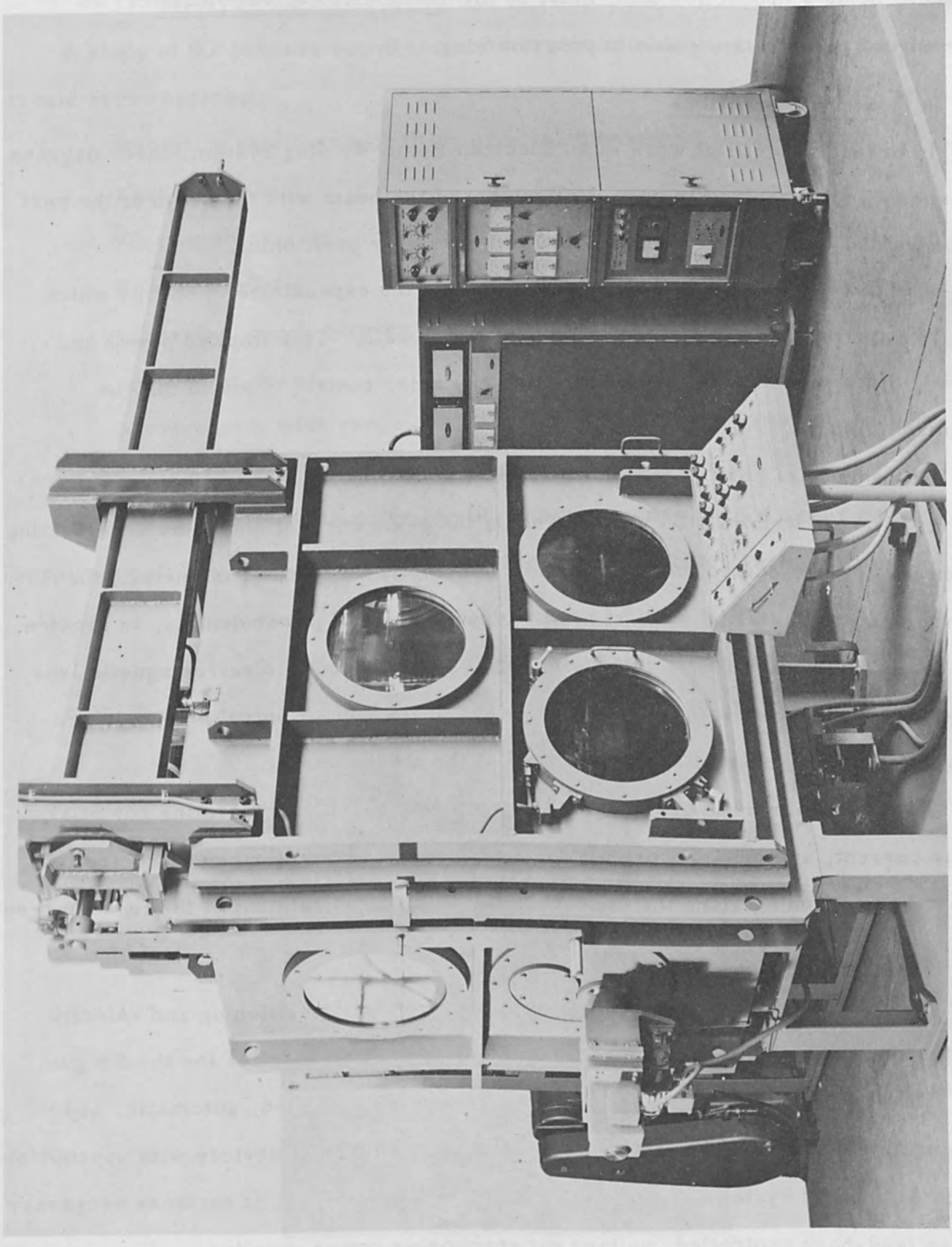

Figure 1 Typical EBW system, VX 68 x 46 x 68

Welder, being a production tool, must be furnished with control elements, so chosen that they are amenable to programming.

A. Machine Functions

In order to do useful work in an Electron Beam Welding System, three degrees of freedom are required to permit alignment of the beam with the seam of the part to be welded. This requires X, Y and Z motions for positioning.

The fusion of metal during welding requires the expenditure of energy which can be expressed in kilojoules per linear inch of weld. This implies power and speed. Since welding can take place along any axis, control of speed may be required along X, Y and Z.

The source of power for welding is the Electron Beam Gun, which is of the Pierce type, in which $I = KV^{3/2}$, where I is the beam current and V the accelerating potential. Thus, control of power can be accomplished by one parameter: the accelerating potential ($P = KV^{5/2}$). An added control of power density, to provide for desired surface effects, is accomplished by means of an electromagnetic lens which is mounted below the electrostatic lens of the gun. Control of the electromagnetic lens is accomplished by control of the focus current.

Thus, the four main parameters are: welding speed, accelerating potential, focus current, and gun-to-work distance. This last parameter can be controlled either by positioning along the appropriate axis or by adjustment of the focus current.

B. Controls

Two types of controls are required by the process: positioning and velocity controls for the mechanical devices and regulated power supplies for the EB gun.

The requirements that the process be remotely controlled, automatic, and programmable, necessitate the use of precision mechanical devices with appropriate electronic servo systems. In the case of the power supplies, it becomes necessary to use feed-back controlled, voltage programmable power supplies.

1. Sciakydyne Servo System

A study of the process requirements sets the following criteria for the electronic servo systems:

- Operation as either a position or a velocity servo.
- Fast response.
- Electronic reversal of the drive, with regenerative braking.
- Reproducibility.
- Linearity, which permits the use of direct reading dials to set position or speed.
- A reasonably wide range of speeds to avoid the use of gear changes.

These criteria are satisfied by the Sciakydyne Servo-System.

The SSS is a solid-state drive for DC motors consisting of a motor power supply, amplifiers, and a logic section. Figure 2 illustrates such a system.

Figure 2 5 HP SSS Control Cabinet

A block diagram of the system is shown in Figure 3. In this case the tachometer voltage is compared to the reference voltage and the system operates as a velocity servo.

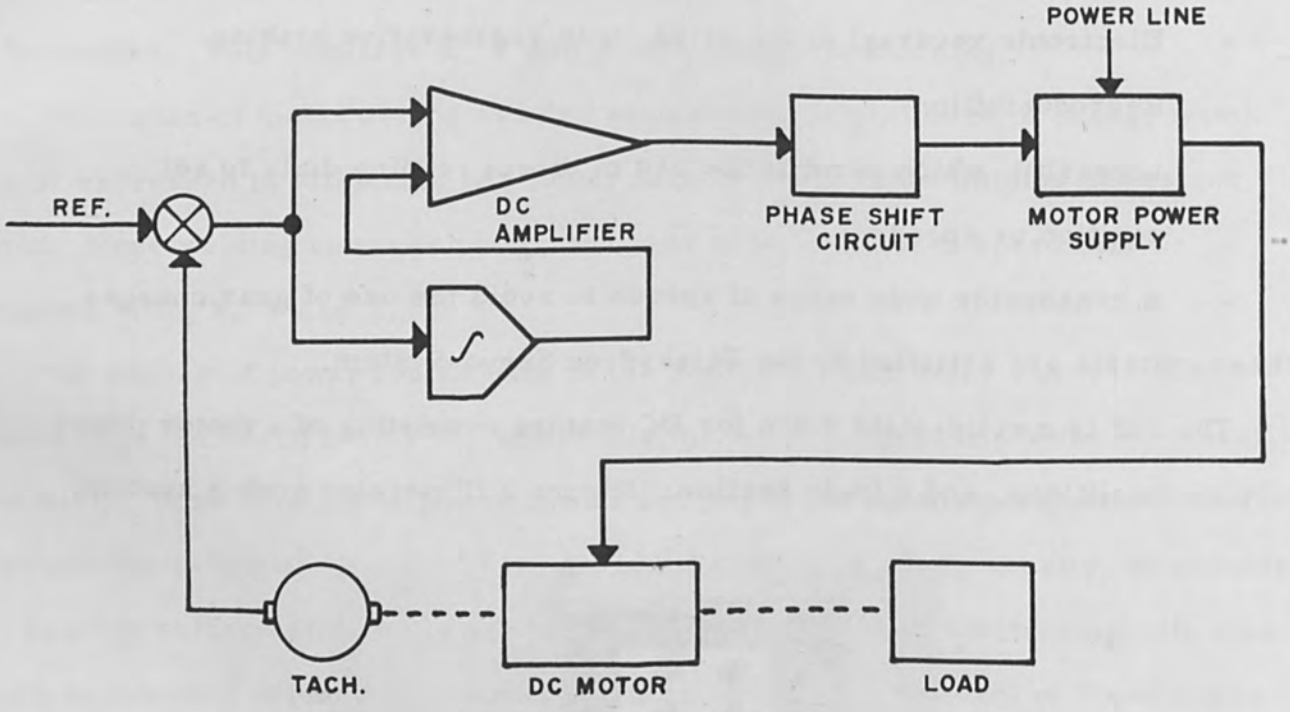

Figure 3 Block Diagram for Velocity Servo

A simple modification of the system, which is accomplished in the logic section, converts the system to a position servo as in Figure 4. In this case, a resolver, which can be a synchro or a multiturn potentiometer, provides a position indication which is compared to the reference voltage. Tachometer voltage is used to provide damping.

Two distinctive features of the SSS are the motor power supply, which supplies full wave reversible power to the motor, and the integrating amplifier which provides "zero-error" operation. A schematic representation of the motor power

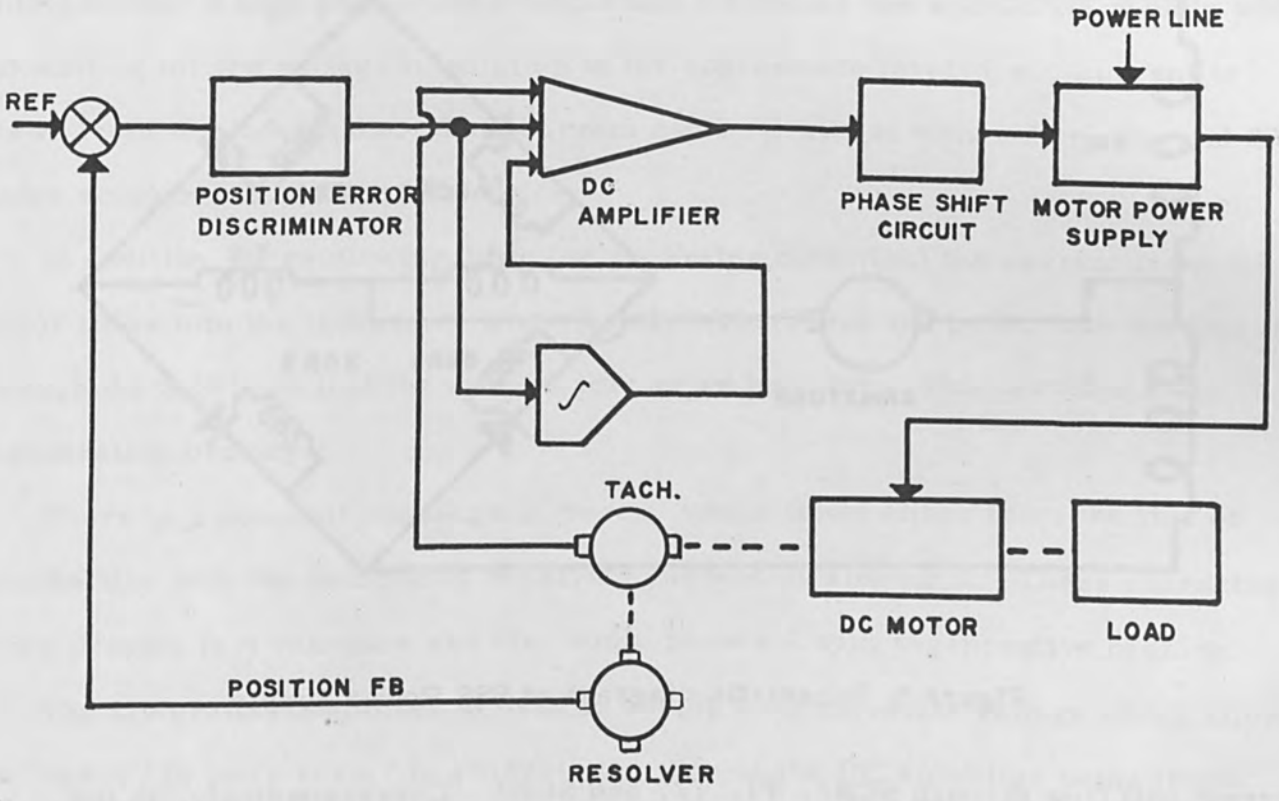

Figure 4 Block Diagram for Position Servo

supply is in Figure 5.

In this arrangement, TR1 is the power transformer, T1 and T2 are "storage" inductances, the four SCR fire in pairs of two (SCR1-4 and SCR2-3), the pulse transformers providing appropriate gate voltages.

At "zero" speed, the SCR's fire at 90° and in the positive cycle,. current flows through SCR2, T1, T2 and SCR3. In the negative cycle, current flows through SCR1, T1, T2 and SCR4. The current through the inductances is always in the same direction. There is no voltage developed between the center tap of TR1 and the center tap of T1-T2 and, therefore, no current flows through the motor.

If now the firing of SCR2 is advanced and of SCR3 retarded (by an equal amount), current will flow through SCR2, T1 and the motor, until SCR3 fires, when

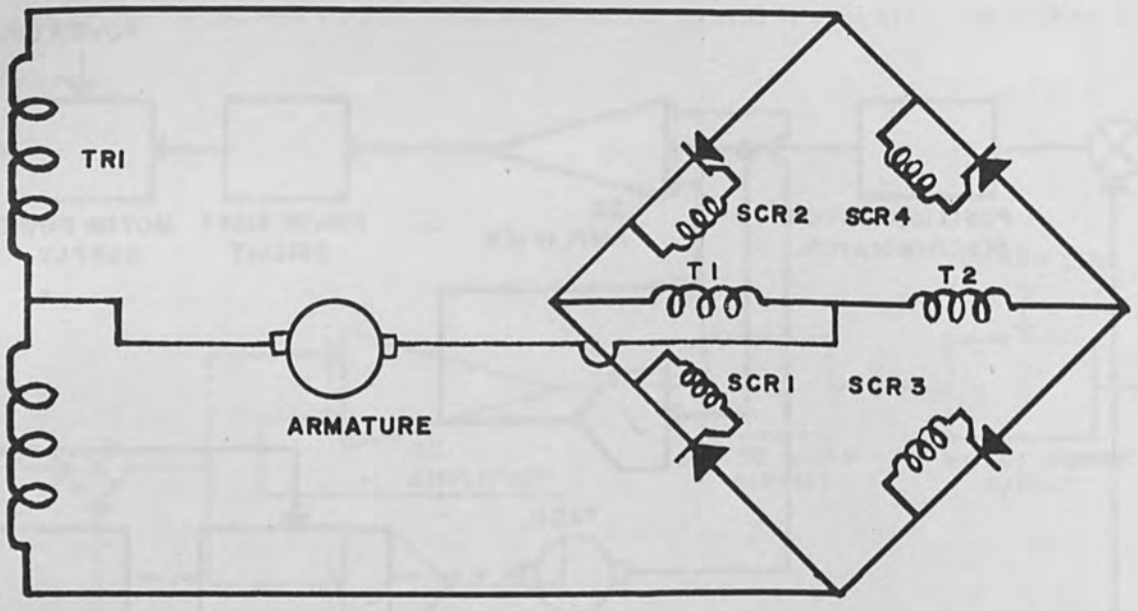

Figure 5 Schematic diagram of SSS Power Supply

current will flow through SCR2, T1, T2, and SCR3. Correspondingly, in the negative cycle, current flows through SCR1, T1, and the motor, until SCR4 fires, when current will flow through SCR1, T1, T2, and SCR4. Thus, current flows unidirectionally through the motor. This is the "forward" direction.

Conversely, if the firing of SCR2 is retarded and of SCR3 advanced, current will flow through SCR3, T2 and the motor until SCR2 fires. In the negative cycle, current flows through SCR4, T2 and the motor. The current flows unidirectionally through the motor (but reversed from the previous case). Thus, the motor "reverses".

Thus, the timing of the pulses permits control of the motor from maximum forward speed to zero speed to maximum reverse speed.

Inductances T1 and T2 serve several functions, intrinsic to the operation of SSS. At zero speed, the voltage across the inductance continues beyond the time when the supply goes to zero and thus maintains the firing of the SCR's until such

time as the other pair of SCR's fires. Thus, the SCR's fire for very nearly 180°. This provides a high gain at zero torque and the motor can accelerate rapidly without waiting for the voltage to build up to the appropriate level; i. e., current is drawn from the inductance. This current can be drawn in either direction and the motor accelerates in either direction.

In addition, when slowing down (or reversing direction) the current from the motor flows into the inductance immediately which feeds the power into the line through the SCR's so that the system acts as an inverter. This provides for regenerative braking.

There is a constant exchange of power, which flows either from the line or into the line with the inductance supplying current or storing it. These characteristics provide fast response and electronic reversal with regenerative braking.

The integrating amplifier is used to supply a steady-state voltage which allows the "error" to go to zero. In general, the gain of the DC amplifier being finite, say 1000, a fixed error is required to supply the drive for the motor. However, the integrating amplifier, has essentially an infinite gain and can provide the "error" to supply the drive, and the difference between the reference signal and the feedback signal goes to zero. Thus, the term "zero-error" servo.

In addition, the integrating amplifier provides a balancing operation, so that day-to-day variations of components do not affect the operation of the system. This provides for good reproducibility of the machine functions.

In the Electron Beam Welder, the SSS is used to control the motion of the Electron Beam gun (two degrees of freedom) and the motion of the work carriage (one degree of freedom) in both the position and the velocity mode.

In welding complex configurations, it is often necessary to trace a complex pattern, such as an air foil. Typically, one must traverse the periphery at constant speed and have the gun and carriage move simultaneously so as to trace the

pattern.

By using the SSS in the position mode and providing position information from a controller, the pattern can be traced. In addition, the controller contains position rate-of-change information so that the pattern is traced at constant speed. One way this can be done is to use a N/C system with digital-to-analog conversion.

Another and somewhat less expensive system uses a cam follower, consisting of a cam, driven by a velocity servo. Two cams are used, one for X and one for Y, which provide X and Y analog signals, driving two SSS in the position mode.

The cams are formed by the following analysis: The periphery L, of the pattern to be traced, is divided into n segments, such that $s_i = \frac{L}{a_i}$, $(i = 1, 2 \ldots n)$, with the a_i chosen to give suitable increments on the periphery. Starting with the first segment, points P_i are obtained. P_i has coordinates X_i and Y_i. If now a circle (radius = R) is divided into sectors $O_i = \frac{360}{a_i}$, so that each O_i corresponds to an s_i, there are radii R_i corresponding to each O_i. The radii are made so that $R_i = X_i$. A smooth curve drawn through the end of the R_i provides the locus of all X_i. Similarly, a second locus is obtained for the Y_i. (Suitable modifications must be made to take into account the diameter of the cam mounting hole and the radius of the cam roller).

As the cams rotate at constant speed, the time to traverse a O_i equals the time to traverse an s_i. Thus the welding speed is $S_w = NL$ where N is the rotating speed of the cams and L the periphery of the pattern to be welded. Figure 6 shows such a system.

2. Control of Accelerating Potential

As mentioned previously, the power into the weld is $P = KV^{5/2}$, and a 1% variation of the accelerating potential results in a 2.5% variation in the power. Thus, it is important to control the accelerating potential with precision and

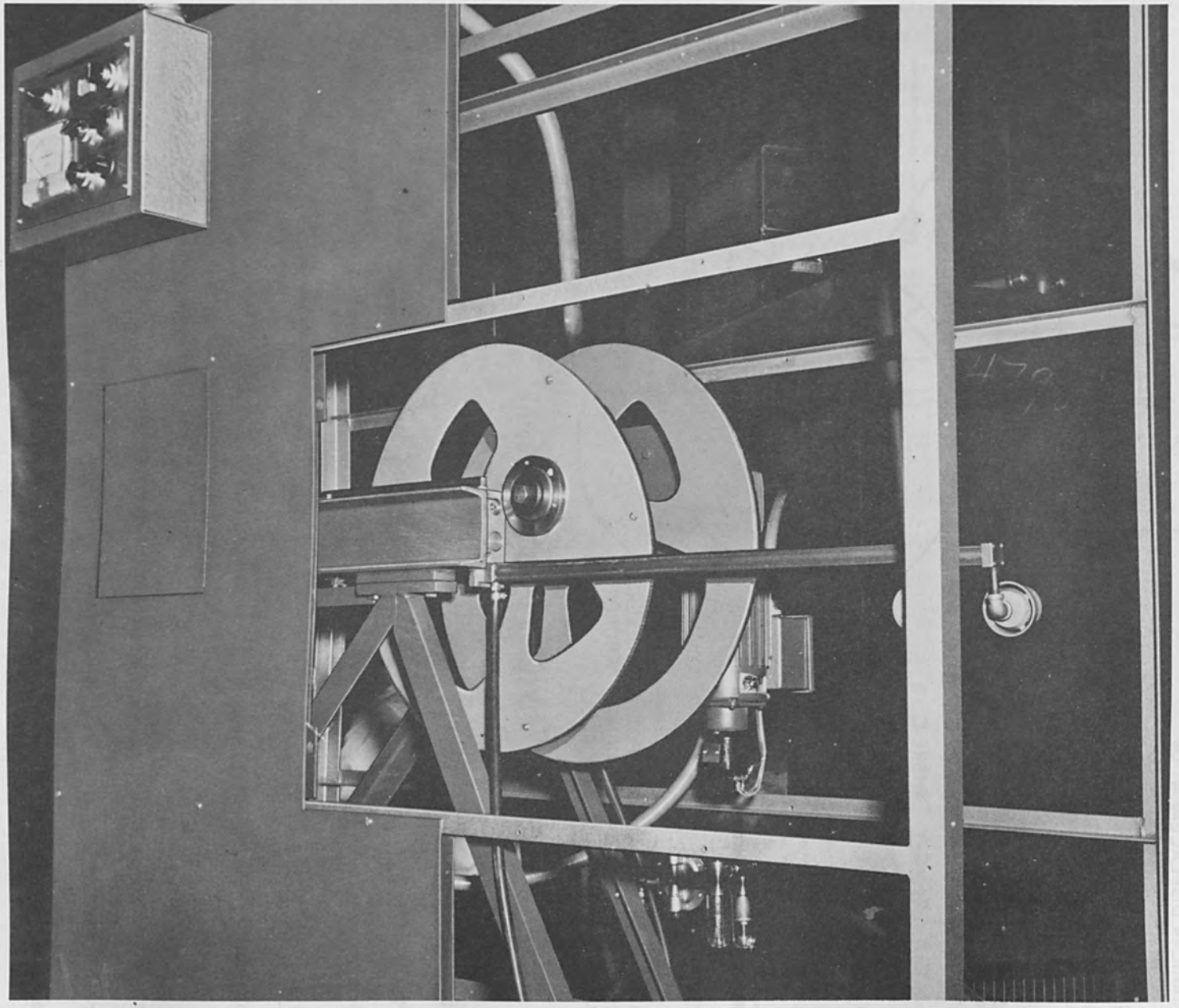

Figure 6 Two-axis program control by cams: a) the means

CAM DESIGN TO CONTROL X AND Y AXES TO WELD A RIGHT TRIANGULAR CONFIGURATION.

LET:

PERIMETER OF TRIANGLE: S = 24".
ANGULAR DISPLACEMENT OF CAM = θ.

THEN:

AS θ PROCEEDS FROM 0° TO 360°, S PROCEEDS FROM 0" TO 24".

THEREFORE:

AB = 10"; θ = 10/24 (360) = 150°
BC = 6"; θ = 16/24 (360) = 240°
CA = 8"; θ = 24/24 (360) = 360°

Rx = C+X Ry = C+Y WHERE C = 3

θ	S	X	Y	Rx	Ry
0°	0	3	5	6	8
150°	10	11	11	14	14
240°	16	11	5	14	8
360°	24	3	5	6	8

CAM FOLLOWERS ACTUATE POTENTIOMETERS GENERATING "COMMAND" SIGNALS PROPORTIONAL TO THEIR RISE AND FALL.

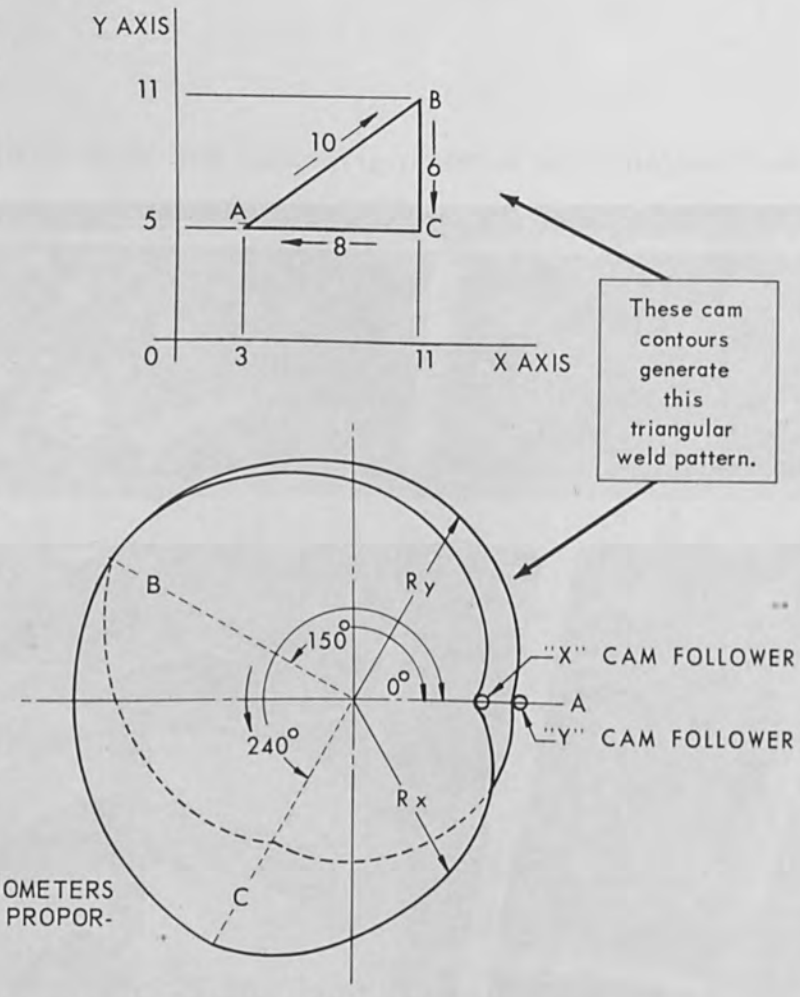

Figure 6 b) the scheme

repeatability.

The accelerating potential is provided by a full-wave three-phase rectified power supply. Several sizes of supplies are used: typically, 30KV at 500 ma, 60KV at 500 ma or 30KV at 1000 ma. Control of the power supply is through a motor-driven, three-phase, variable auto-transformer.

A high voltage rectifier power supply has a load regulation of the order of 15% and hence is not analog programmable through the full range of power, which may be required when welding sheets of variable thickness (tapered sheets). In addition, line variations must also be compensated for, to prevent varying amounts of penetration.

The use of the SSS (position mode) provides the means to modify the H. V. power

supply so that one can obtain 1% regulation for ±10% line variation and 1% regulation for 0 to full load variation. In addition, the H. V. power supply is programmable, as discussed above in the case of the X and Y axes.

A schematic representation is shown in Figure 7.

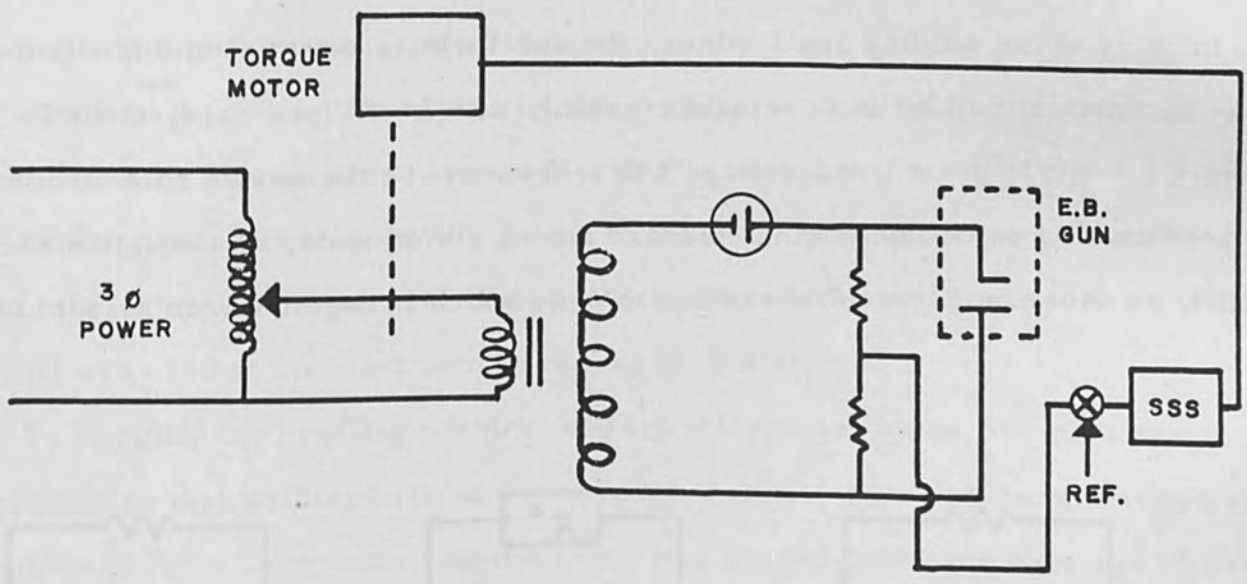

Figure 7 Schematic diagram of A. V. R.

A standard three-phase variable auto-transformer is modified and coupled directly to a torque motor (50 rpm rated speed) with tachometer. The reference voltage (which corresponds to the desired accelerating potential) is compared to the accelerating potential (through a 1,000 to 1 divider network) the error driving the torque motor to the desired "position" to provide the pre-set accelerating potential.

3. Control of Focus Current

The focal length of an electromagnetic lens is given by

$$f = \frac{KV}{(NI)^2}$$

where V is the accelerating potential and NI the ampere-turns of the electromagnet. It is thus seen that if the focal length is to remain constant and reproducible, for a

given accelerating potential, then the ampere-turns must remain constant.

The use of a constant current power supply is particularly indicated. Such a supply will maintain constant current under all conditions of load, including short circuit. A simple modification of a standard supply allows the use of a voltage reference (e), to program the supply, so that I = Ke.

In many of the welding applications, the accelerating potential is a function of some parameter, p. If f is to remain constant, then $I = KV(p)^{1/2}$ and, since I = Ke, we have $e = KV(1)^{1/2}$ i.e., the voltage reference must be the square root function of the accelerating potential. Using standard analog components, this equation can be solved, as shown in Figure 8 where $e_i = KV(p)$, which is negative with respect to

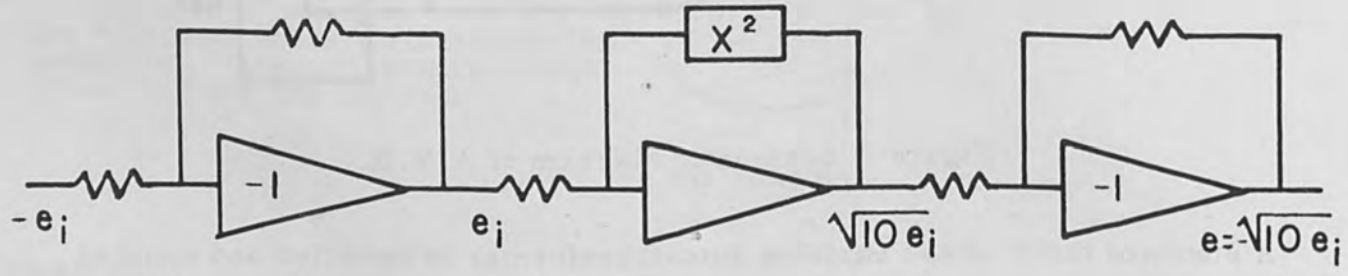

Figure 8 Square Root Extraction

ground. The voltage reference for the CC supply is also negative with respect to ground, hence the two inverters.

The X^2 function can be of the diode type or of the pulse width, pulse height modulation type.

C. Programming

A system incorporating the various components discussed above, which included an analog point-to-point programmer, was built to weld large structural members. These parts were segments (one-third or one-fourth) of a 33-foot diameter

aluminum ring having a non-uniform 2-foot high cross section, in the form of a Y. The thickness at the stem and legs of the Y varied from 1/2-inch to 2-3/8-inches.

In this system, only the joint and a small length on either side were enclosed in the vacuum chamber, with the remainder protruding through the chamber, with a local seal around it to permit evacuation of the chamber. The system was fully automatic with programming of all functions.

Preliminary tests showed that to obtain welds of equal width for varying thicknesses, it was necessary to set $P = Kt$ (t = thickness); since $P = KV^{5/2}$, then $V = Kt^{2/5}$. Also, since $I = KV^{1/2}$, $I = Kt^{1/5}$. Thus, knowing the thickness at any point, the values of the parameters were determined; the maximum power available (30KW) was used at the maximum thickness (2-3/8-inches).

To simplify the handling problem of such a large weldment, the part was positioned so that welding took place along the Z axis. Thus, all parameters were functions of Z. A forty-turn potentiometer was geared to the gun carriage (Z axis) to provide position indication.

The various functions of interest were:

$$V = V(Z) = Kt^{2/5}$$

$$I = KV(Z)^{1/2} = Kt^{1/5}$$

$v_Z = v_Z(Z)$ (the Z-velocity, held constant in this particular case)

$s_Y = s_Y(Z)$ (the Y-position, varied appropriately to maintain constant gun-to-work distance)

A plot of thickness was made, which became a plot of P when scaled appropriately. Plots of V and I were then made by solving the respective equations.

The plot for V was transferred to a Vernistat function generator which contains 30 points (auto-transformers) adjustable from 0 to 100%, with linear interpolation provided by a Vernistat interpolator. Similarly, the values for v_Z and s_Y were transferred to Vernistat functions generators. In the case of the focus current, in

lieu of a Vernistat function generator, a square-root extractor was used. The reasons being both lower cost and better accuracy.

Three Vernistat interpolators and a 40-turn potentiometer were driven by a two-phase servo motor by means of a ring gear. The difference, between the servo-driven 40-turn potentiometer and the 40-turn potentiometer mounted on the Z-axis, provided the error signal driving the servo amplifier. Thus, each position on the 30-point function generator corresponds to a definite Z.

The output of the function generators was converted to DC and served as the reference signal for the SSS. In the case of V and s_Y these were position signals with the SSS operating in the position mode; while in the case of v_Z, these were velocity signals with the SSS operating in the velocity mode. The output of the square root extractor served as the reference to the CC supply for the electromagnetic lenses.

Figures 9, 10, 11, 12 and 13 illustrate this system and the results obtained.

Guns with Special Pumping System

Two annular pumping units for an electron gun (Systeme de Pompage Annulaire pour Canons a Electrons) called "Space 1" and "Space 2" are presently being tested. The first uses an oil diffusion pump. The second uses pumping by sorption and sublimation of titanium. We shall limit ourselves to a brief description of the apparatus "Space 1" and to indicate some of the preliminary results.

A. Description

This system (Figure 14) contains three principal parts:

- The assembly of the heaters, the jets, and the anode.
- The outer housing with foreline connection.
- The upper part with the high voltage feedthroughs.

For the first apparatus of this type, the pump was largely dimensioned without

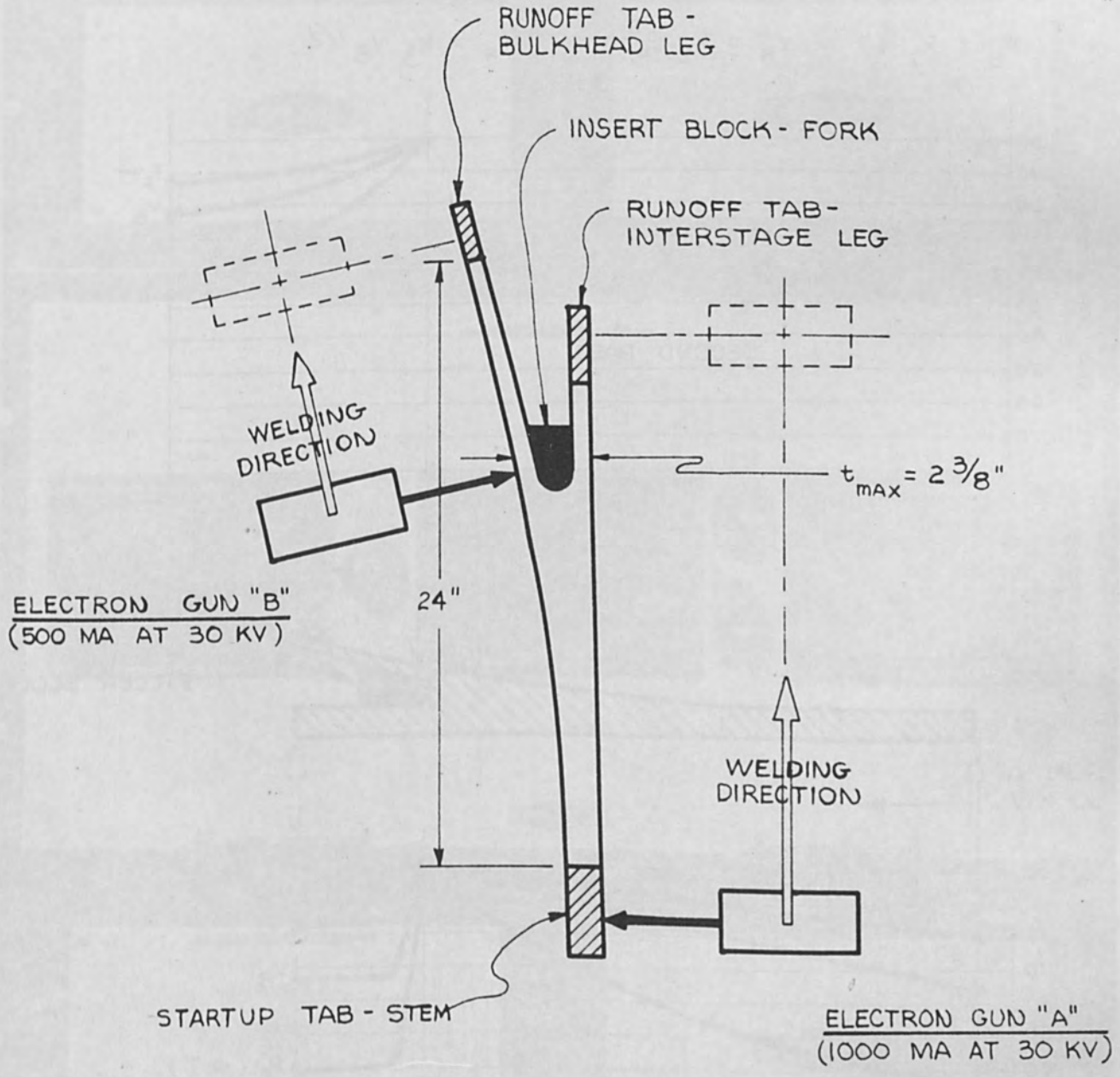

Figure 9 Welding Scheme for Y-Ring

I_F = FOCUS COIL CURRENT
V_B = ELECTRON BEAM VOLTAGE
P_B = ELECTRON BEAM POWER
T = MATERIAL THICKNESS

$P_B = k_1 T$ $\quad V_B = k_2 P_B^{2/5}$ $\quad I_F = k_3 V_B^{1/2}$

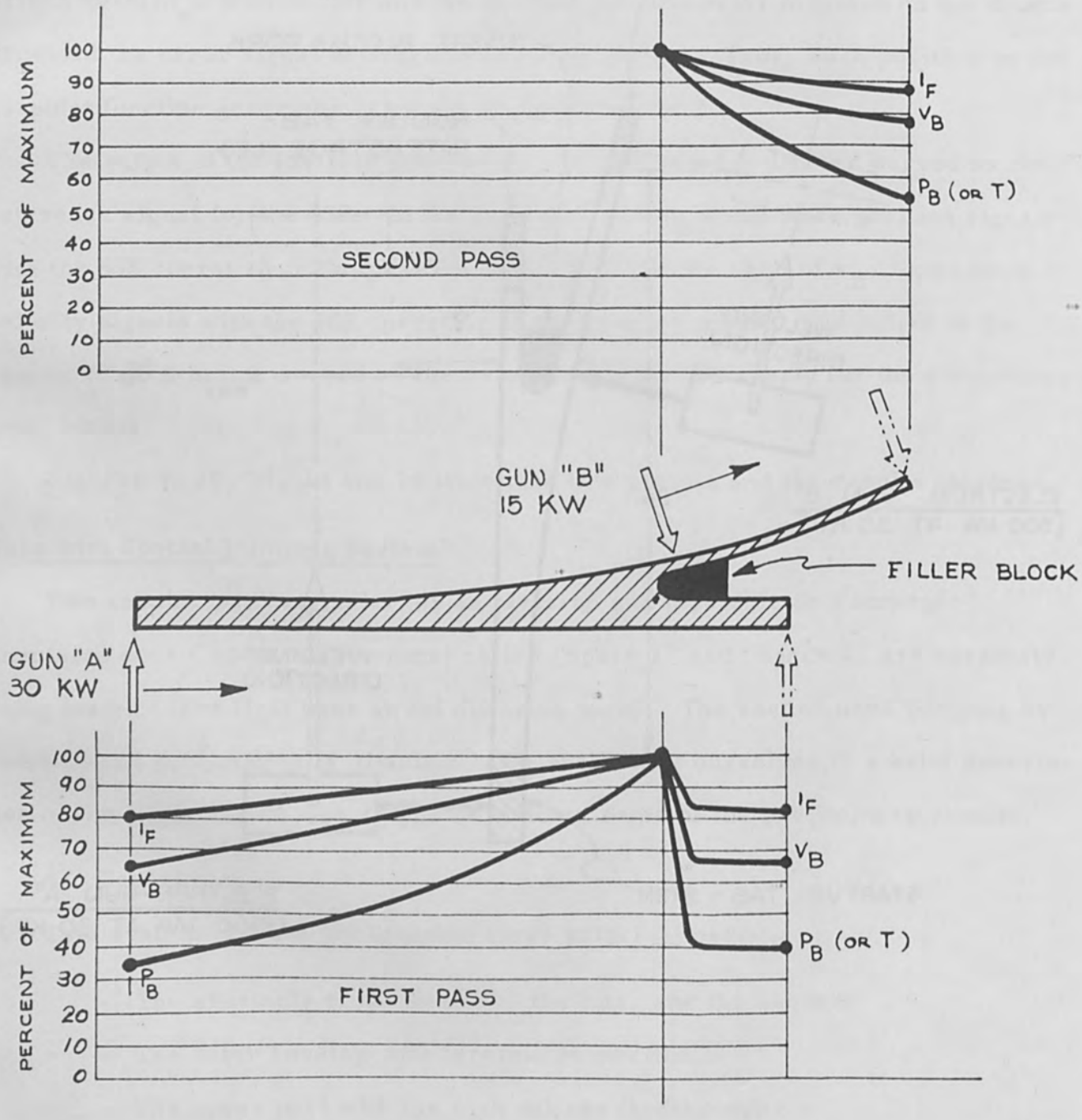

Figure 10 Programming of Y-Ring Welding Parameters

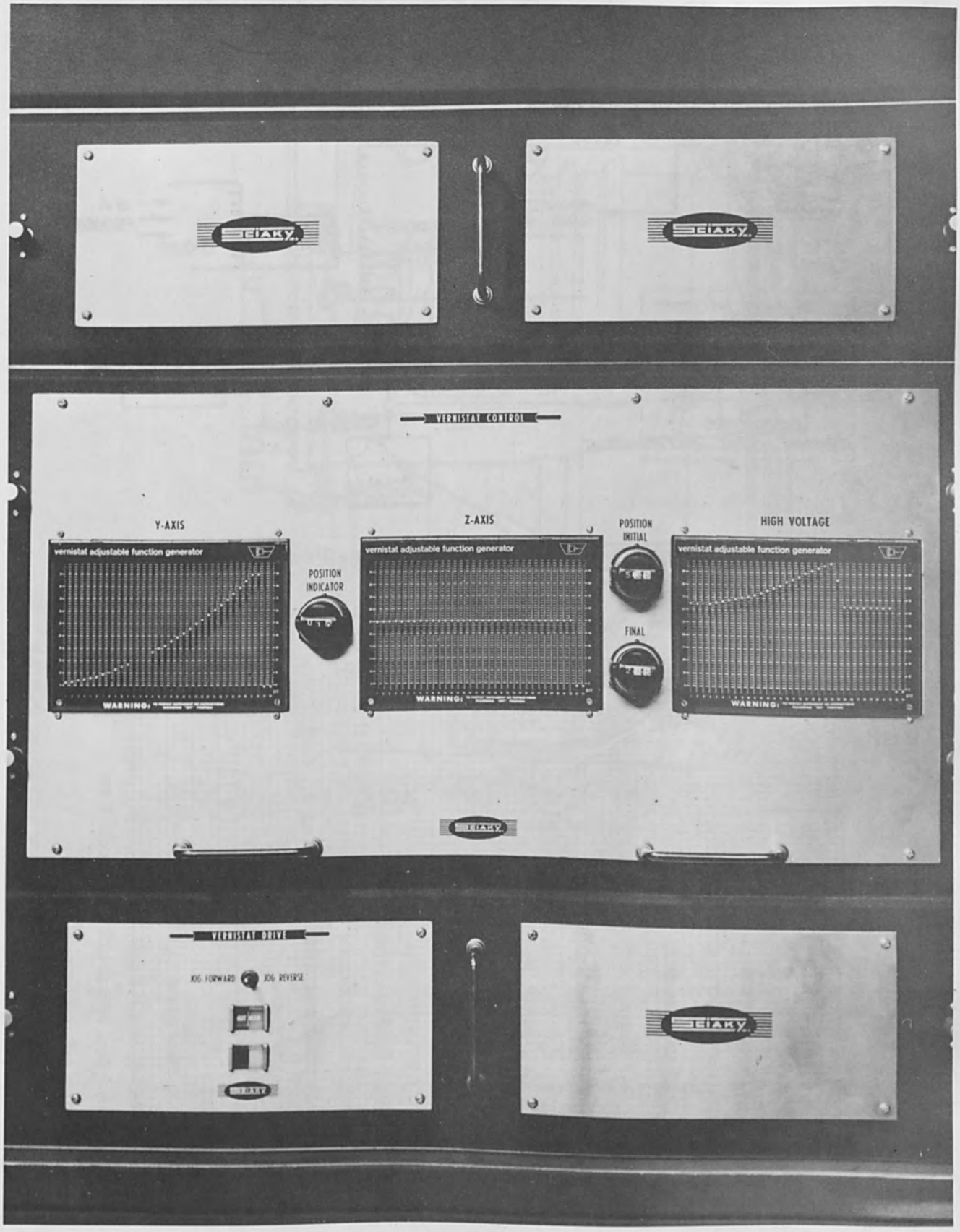

Figure 11 Analog Programmer for Y-Ring EBW

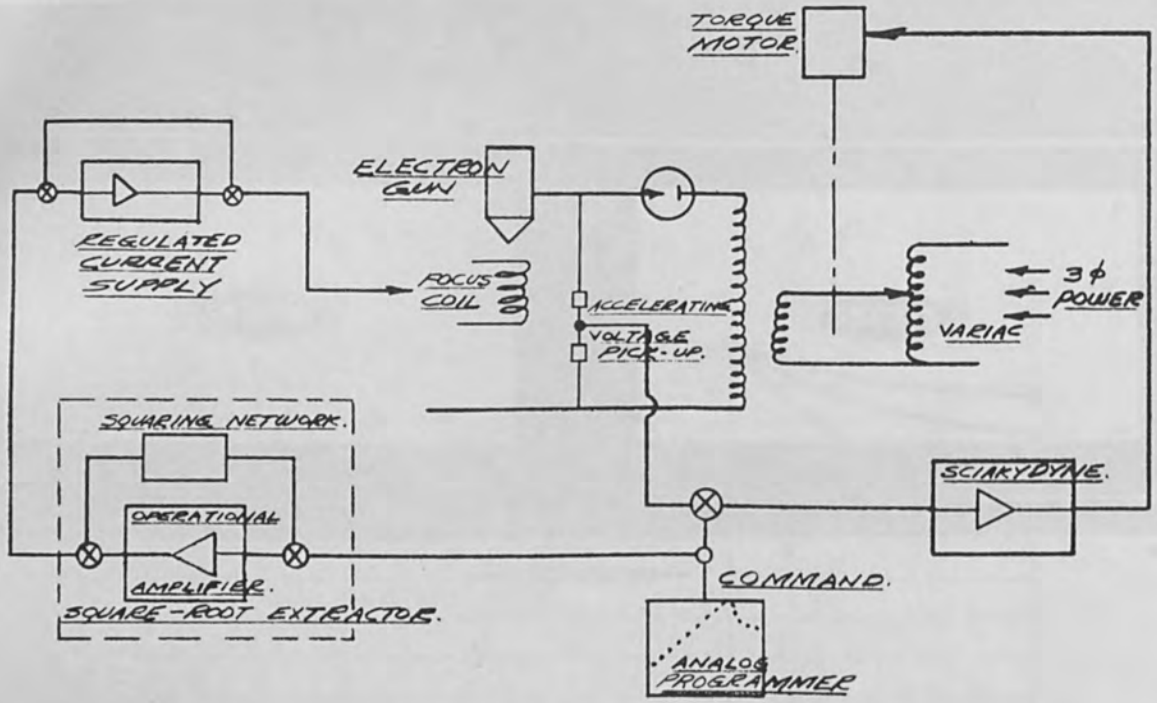

Figure 12 Method used to program Beam Power and Focus

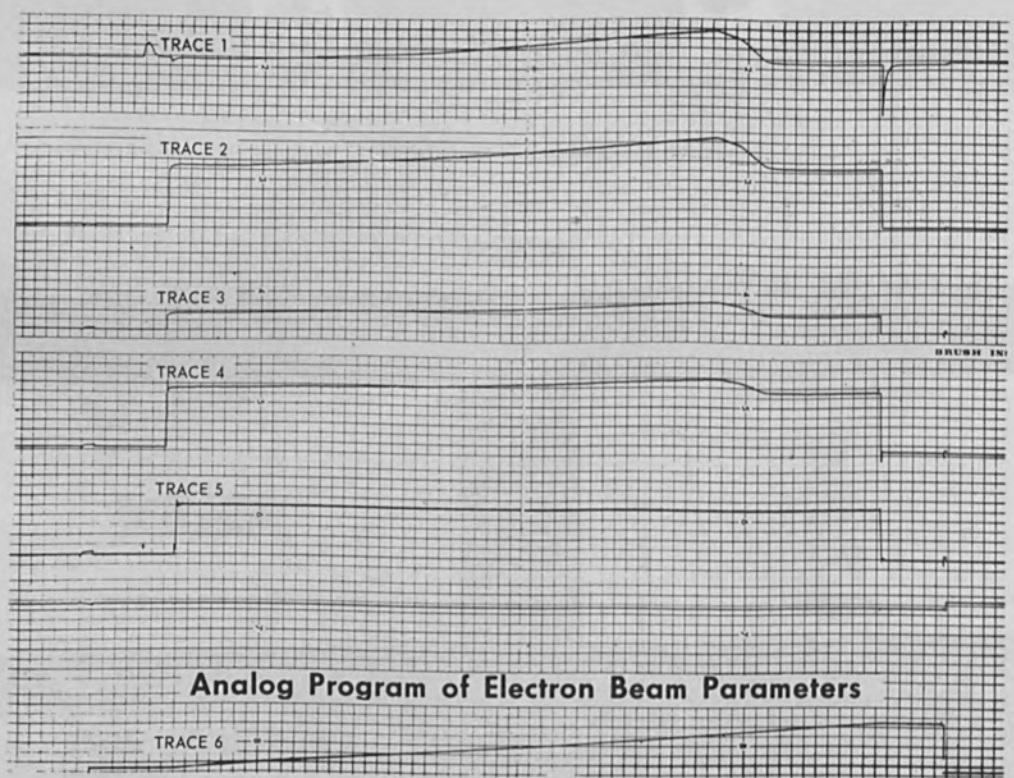

Figure 13 Analog Program of Y-Ring EBW Parameters

1. High voltage feedthrough and filament heater
2. Vacuum tight seal
3. Opening for pumping electron gun
4. Diffusers
5. Water container
6. Heater
7. Water circulator
8. Supporting plate
9. Pact of high voltage supply of the electron gun
10. Pumping connection
11. Water container
12. Anode
13. Focusing coil

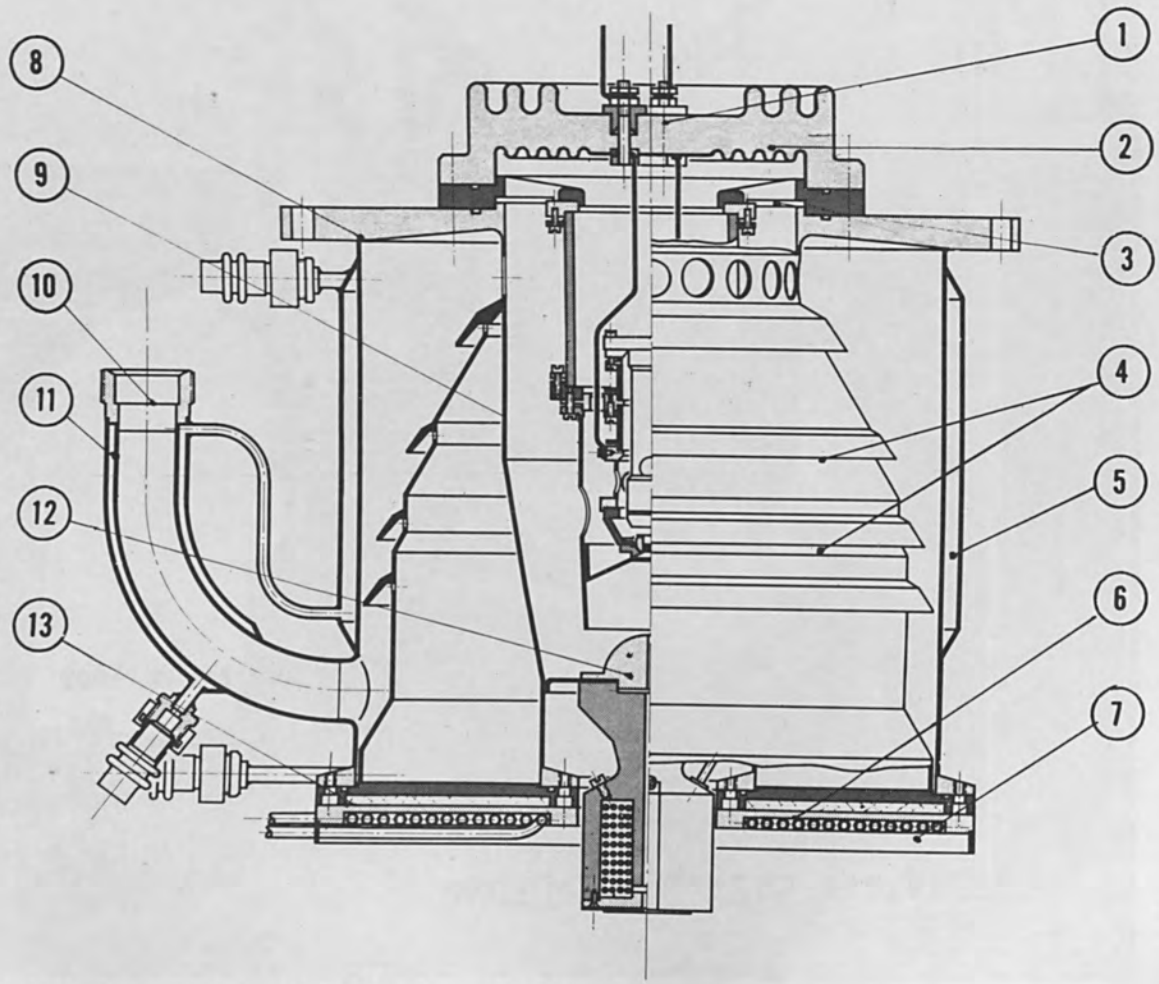

Figure 14 Annular Pumping System for EB Gun

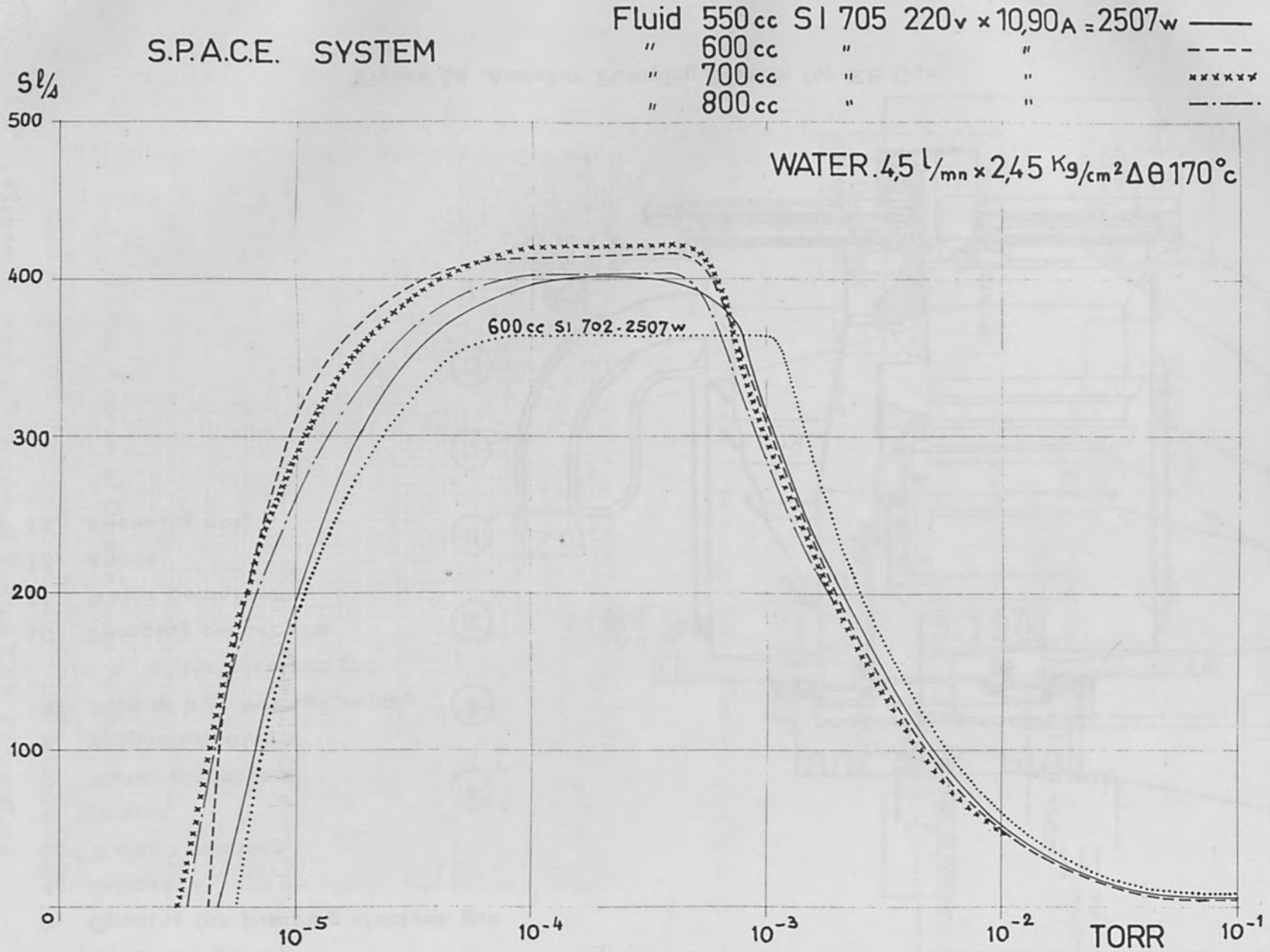

Figure 15 "Space 1" performance characteristics

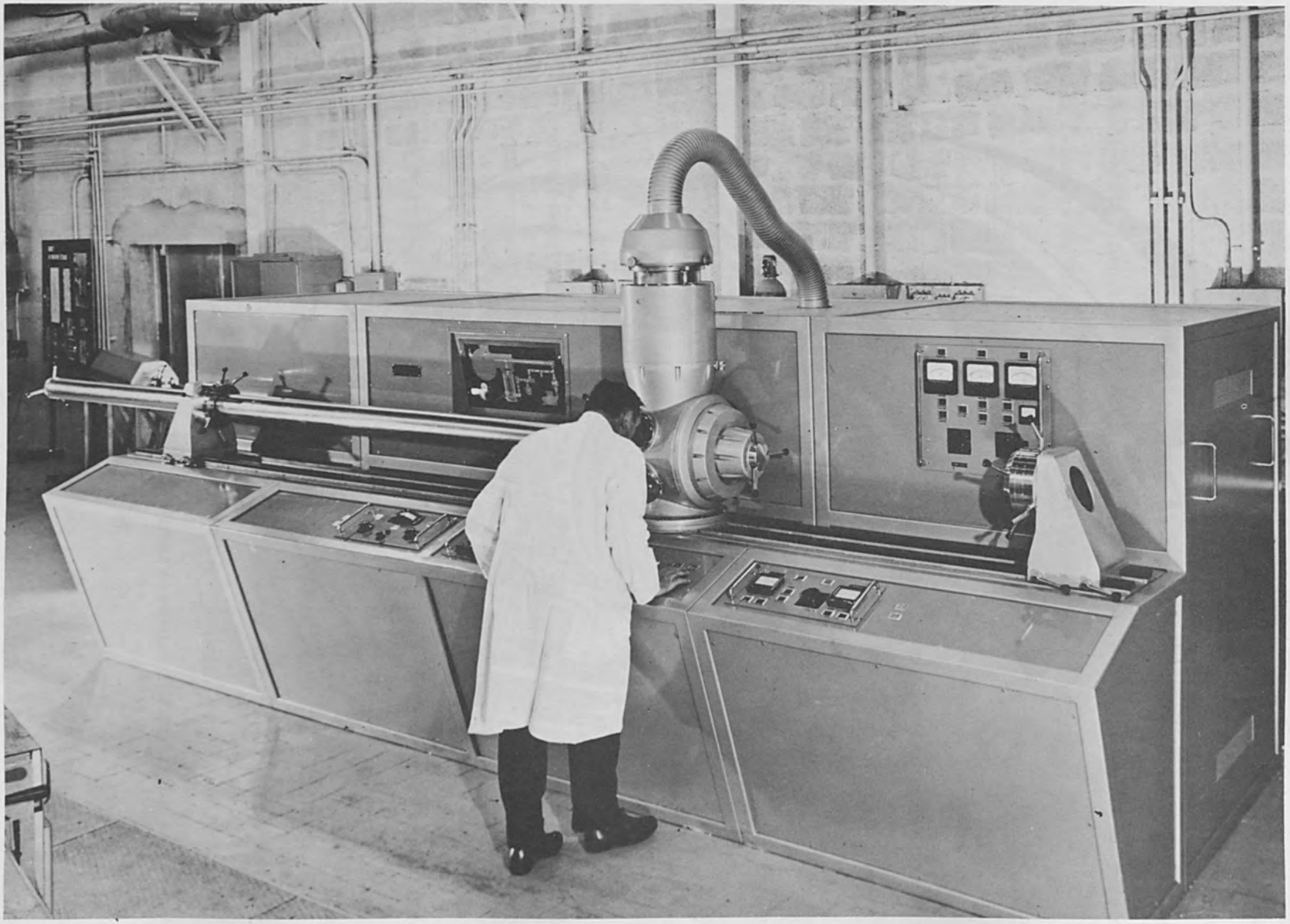

Figure 16. A "local chamber" EBW system for butt welding tubing

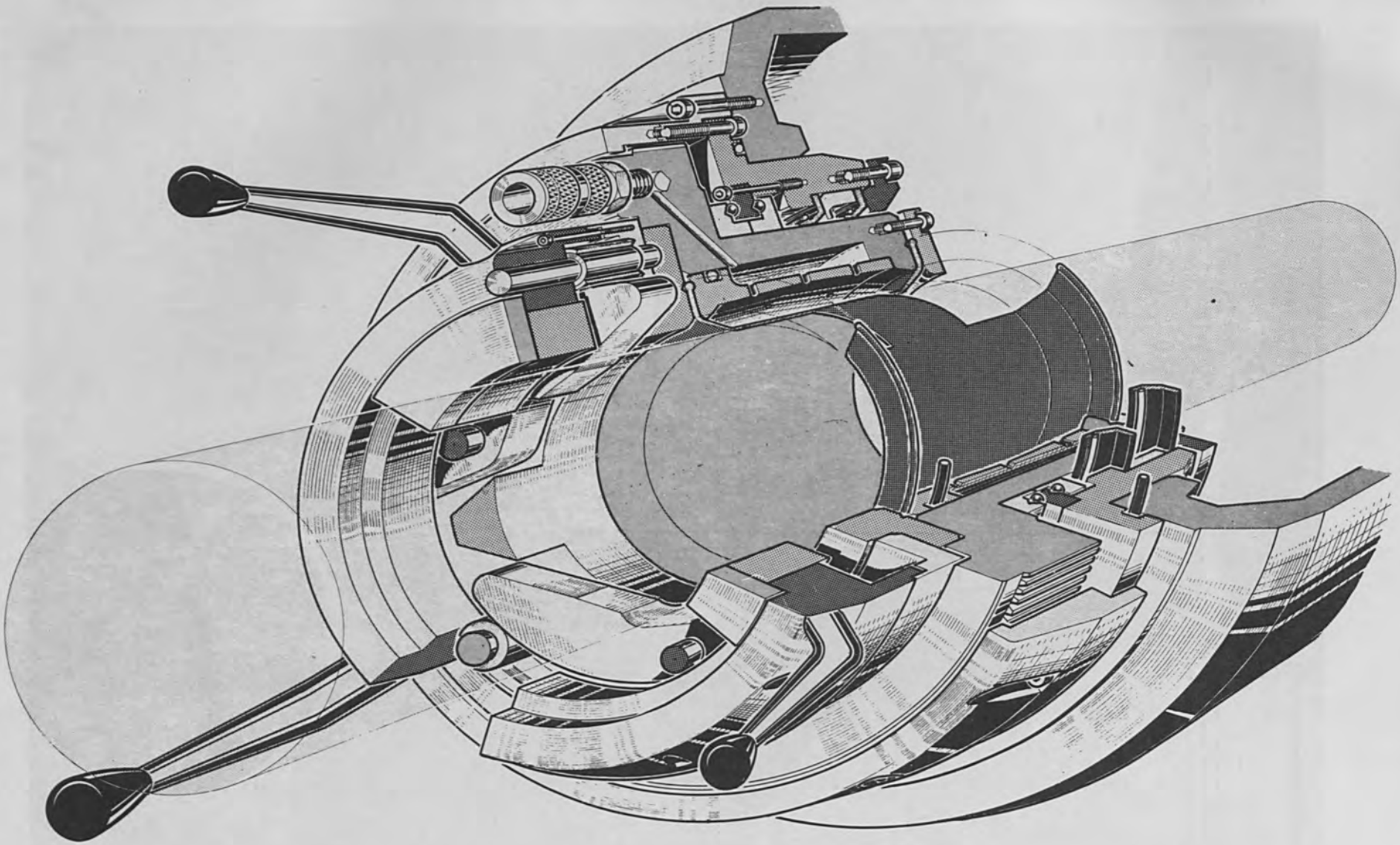

Figure 17. Inflatable rotary vacuum seal for tubing

regard to its size or its mobility. The results obtained during the tests of pumping and of welding will permit a dimensional reduction for the future units. The electron beam gun which employed this pumping system, is a 10KV 180 ma gun, with indirectly heated cathode. The four-stage pump that was devised is very compact, being 12.7-inches in diameter and 13-inches in height.

1. Assembly of heaters, jets, and anode

The pump has four stages. In this prototype, there was no provision for a first ejector stage which would have carried a significant flow of oil vapor to the roughing line towards the vacuum chamber. The disassembly is easily made from the bottom.

2. Outer housing with foreline connection

The outer housing and the foreline connection are water cooled. All the tubulation and connections are flexible in order to permit gun travel.

3. Upper part and high voltage feedthroughs

The vacuum seal is obtained on top by the flange which holds the assembly and by a high voltage insulator, and between them there is a centering flange which centers the gun with the anode hole. The high voltage leads are shielded (not shown on the drawing) so that the external housing of "Space 1" can be grounded.

B. Preliminary Results

The heater has very little thermal inertia which permits the introduction of air into the pump five minutes after the current has been turned off. The first tests were made to optimize the heater power, the oil quantity, and the size of the orifices on the gun. (See Figure 15.) The measurement of pumping speeds is made at constant pressure following Dayton's method.

There was no trace of oil backstreaming in the gun whose temperature is always above 100°C, because of the pump heaters.

At present, studies continue on the effect of welding on the speed of the pump, the life of the cathode, and the reproducibility of the welding parameters as a function of the pressure in the vacuum chamber.

Vacuum Chamber with Moving Vacuum Seals

This is a special device adapted to the particular problem of butt welding zircaloy tubes used in the construction of the French reactor EL4.

Electron beam welding was chosen to minimize possible distortion, as well as the extent of the heat-affected zone. This process produces perfectly sound welds and eliminates the need for post-weld surface treatment to give corrosion protection of the specimen.

This welding equipment differs from that previously described since only part of the tube to be welded is placed under vacuum; the vacuum chamber is therefore very much reduced in size. Considerable attention has been paid to the adjustment of the vacuum sealing around the tubes; these tubes have normal manufacturing tolerances and must revolve accurately beneath the electron gun. The tubes have heavier walls at the edges.

A. General Description

The equipment consists of a console and a bench with removable tooling (Figure 16). The console contains the pumping system, high voltage power supply, and system controls. The bench tooling consists of the vacuum chamber and its electron gun, the means for rotating the tubes, and a plate with rails along with adjustable supports. The pumping equipment and safety controls are similar to those described in previous papers. The floor space required is 16.5 ft. x 7.25 ft.

B. Vacuum Equipment Including Inflatable Seals

The vacuum equipment includes a static and a dynamic seal, shown in Figure 17.

The static seal fits directly on to the specimen to be welded and is made to rotate within the dynamic seal. The static seal consists of:

- A flexible membrane which is made to bear on an appreciable length of the specimen passing through the seal unit, by means of gas pressure applied to the unit.
- To allow the loading and unloading of the tubes a cavity is made between the flexible membrane and its seat, so that the membrane seats itself and at the same time leaves a space for the removal of the tube.

This static seal is satisfactory for the tolerances and surface conditions of the zircaloy tubes.

The tube and static seal together comprise a unit which is rotated on the vacuum chamber by means of a classical rotary vacuum seal.

C. Electron Gun Displacement Under Vacuum

The mounting plate for the electron gun is connected to a hollow mandrel passing right through the vacuum chamber, so that the chamber volume does not alter. Very slight effort is sufficient for such displacement. This device has been found to be particularly useful.

Conclusion

The new developments that have been reported in this paper illustrate some of the many advances that are being made in the application and implementation of the electron beam welding process. They are indicative of the growing use and acceptance of this welding process particularly for the fabrication of assemblies which require the highest degree of weld strength and reproducibility.

The adaptation of the process equipment to various shapes of structures has demonstrated the possibility, in certain instances, to substantially reduce the size

of the vacuum chamber by enclosing in the chamber only the locality of the weld joint.

The innovation of the various programming devices discussed has made possible an extent and refinement of control of the welding parameters and their values which is far beyond the simple manual means of control that were used in the early days of electron beam welding. These techniques, lending themselves to automation and reproducibility as they do, have made possible significant advances in the use of the electron beam for welding, and continuing efforts in this direction can be expected for future developments.

A Versatile Electron-Beam Evaporator System

by

G. C. Riddle
ITT Semiconductor, Shockley Laboratory
Palo Alto, California

Abstract

A small compact electron-beam evaporation source was combined with several deposition monitors, automatic deposition control, and a servo-controlled evaporation power supply. The 2 KW evaporator has proven to be sufficient for vaporizing any vacuum-compatible material, using interchangeable cooled and uncooled crucibles. Evaporation rate is stabilized and controlled by a constant-current mode operation of the electron gun. Three process monitors, each using different detection principles, permits the controlled deposition of multiple layers of resistive and dielectric films during one vacuum cycle. The monitors can also control the evaporation rate. The complete system is designed for patch-panel-type operation, thereby providing maximum flexibility of use. The monitor and control system is all solid-state circuitry using commercially available operational amplifiers extensively. The application to a materials property study is discussed.

Introduction

The use of high-energy electron beams in both laboratory and production processes for thin-film vacuum deposition is increasing at a rapid rate. As more versatile and less expensive auxiliary equipment is made available, the evaporation process is becoming more a controlled science and less a "cookbook" art.

A plain resistance-heated tungsten filament is not considered sufficient equipment for thin-film deposition where the properties of the film are important. Contamination introduced to the evaporant from the filament or boat can no longer be tolerated in many applications such as the investigation of the electrical

characteristics of ultra-pure films.

Automatic process monitors and controls are becoming more necessary to insure reproducibility of deposition conditions. Such process controls include evaporation-rate monitoring, deposition-rate monitoring, film resistance monitoring, substrate temperature monitoring, evaporation-rate controlled by the rate monitor, deposition controlled by the deposition and resistance monitors, and substrate temperature maintained by the temperature monitor.

An evaporator system was designed and built to incorporate the desirable features mentioned above. A survey was made of the commercially available equipment presently on the market, and the best features of these were combined to provide a flexible system meeting our requirements.

Electron-Beam Evaporator

The commercially available electron beam equipment was found to be unsatisfactory for our application, most units requiring more space and more power than desired. It was decided to use a scaled-down version of an evaporator designed earlier for a similar application.[1] The use of a water-cooled copper hearth was mandatory since the application involved the evaporation of highly reactive material such as pure silicon. The oxide contamination which silicon scavenges from ceramic crucibles was not acceptable. A work-accelerated-type electron gun was employed to help reduce the physical size, although a negative-bias focusing grid was included to concentrate the electron beam to a small area. The structure of the gun was shaped to minimize the exposure of the filament to the evaporant and to the substrate. A cross-section of the evaporator is shown in Figure 1, a corresponding profile is pictured in Figure 2, and a general view is given in Figure 3.

The evaporator is used in a program that requires protection of the film prior to exposure to the atmosphere. Three evaporators are used, two of them being the resistance boat type. Figure 4 shows the electron-beam evaporator during

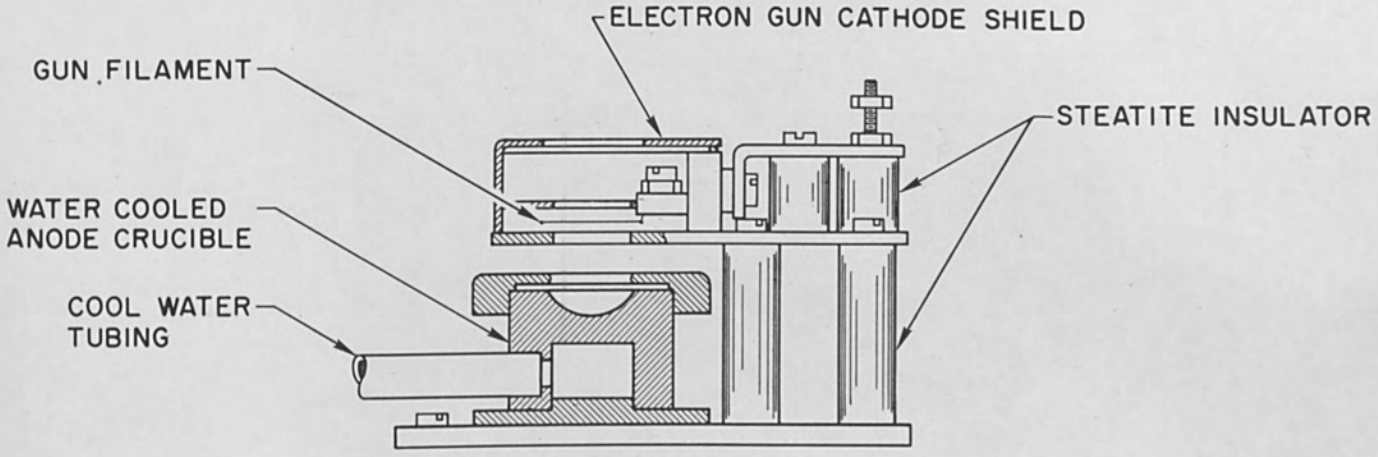

Figure 1 Evaporator Assembly Diagram

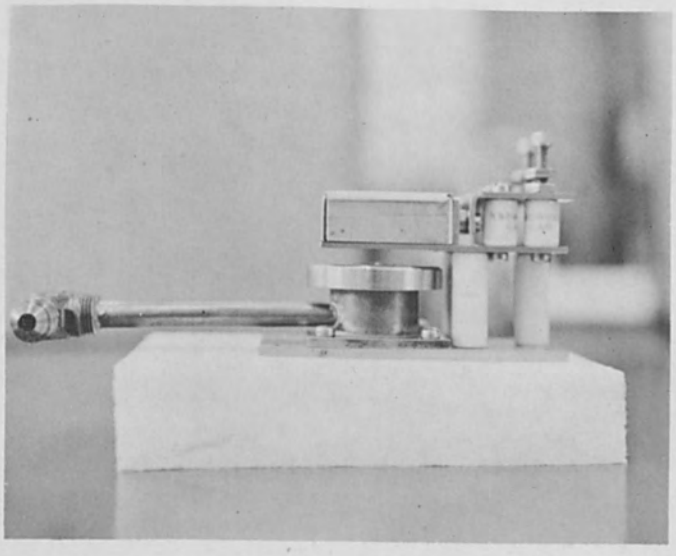

Figure 2 Profile of Assembled Evaporator

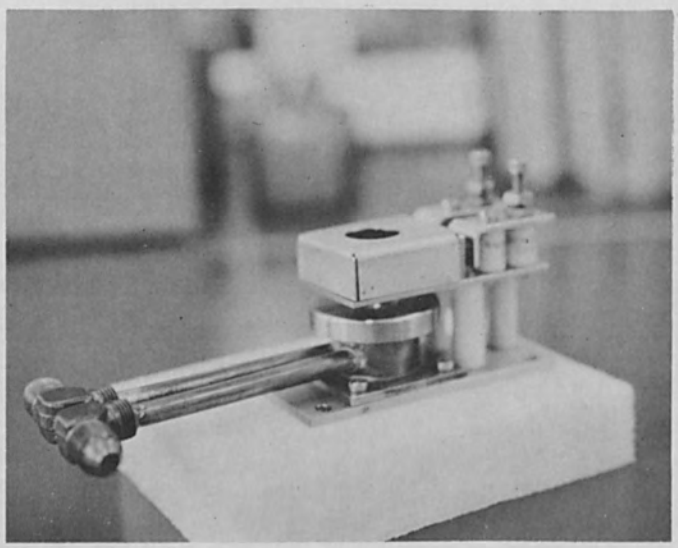

Figure 3 Electron Bombardment Evaporator

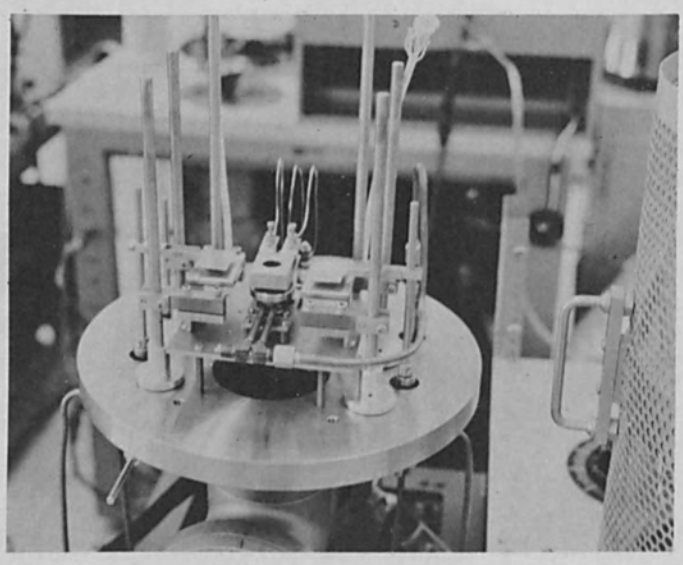

Figure 4 Evaporator Being Installed Between Two Resistances

installation in the vacuum system, and Figure 5 shows the completed installation with the rate-meter detector, deposition control shutters, and substrate-mask support framework in place. The teflon-insulated leads from the feed-through are not yet connected in this picture and are fanned out prior to fastening to a connection block.

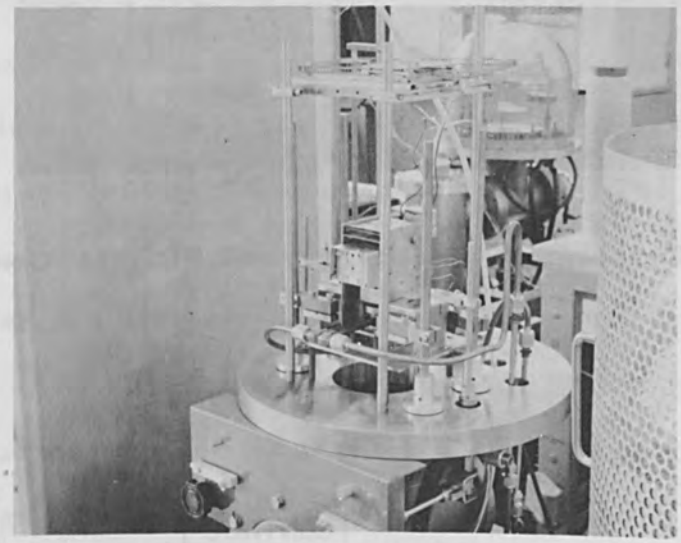

Figure 5 Completed Evaporator Installation

Power Supply and Filament Control Circuit

Several special features were desired in the evaporator control unit. The electron gun is designed to have a negative bias between the cathode shield and filament, and this bias voltage needed to be provided. It was also required that a feedback signal from the monitor equipment be able to control the evaporator to maintain a constant evaporation rate. The power supply was a compromise between high-voltage/low-current and low-voltage/high-current operation. The 6 KV-300 ma supply proved sufficient for our application which included tantalum evaporation.

Figure 6 shows the rack-mounted power supply and control panel and Figure 7 gives the block diagram of the evaporator system. The schematic of the filament

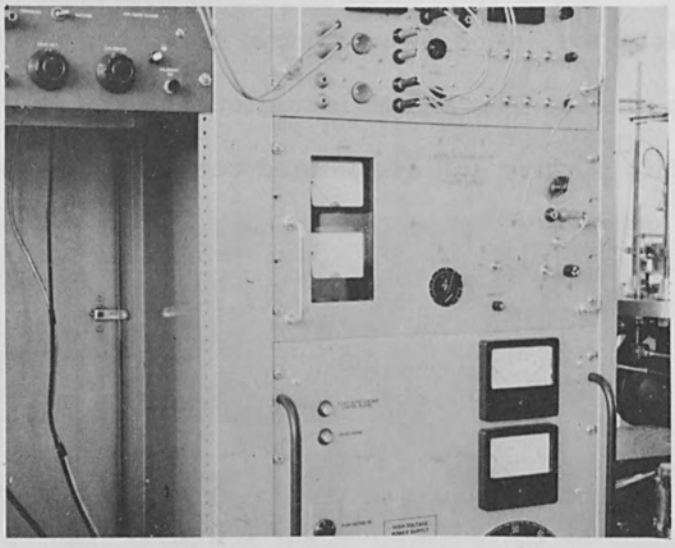

Figure 6 Evaporator Power Supply and Filament Control Panel

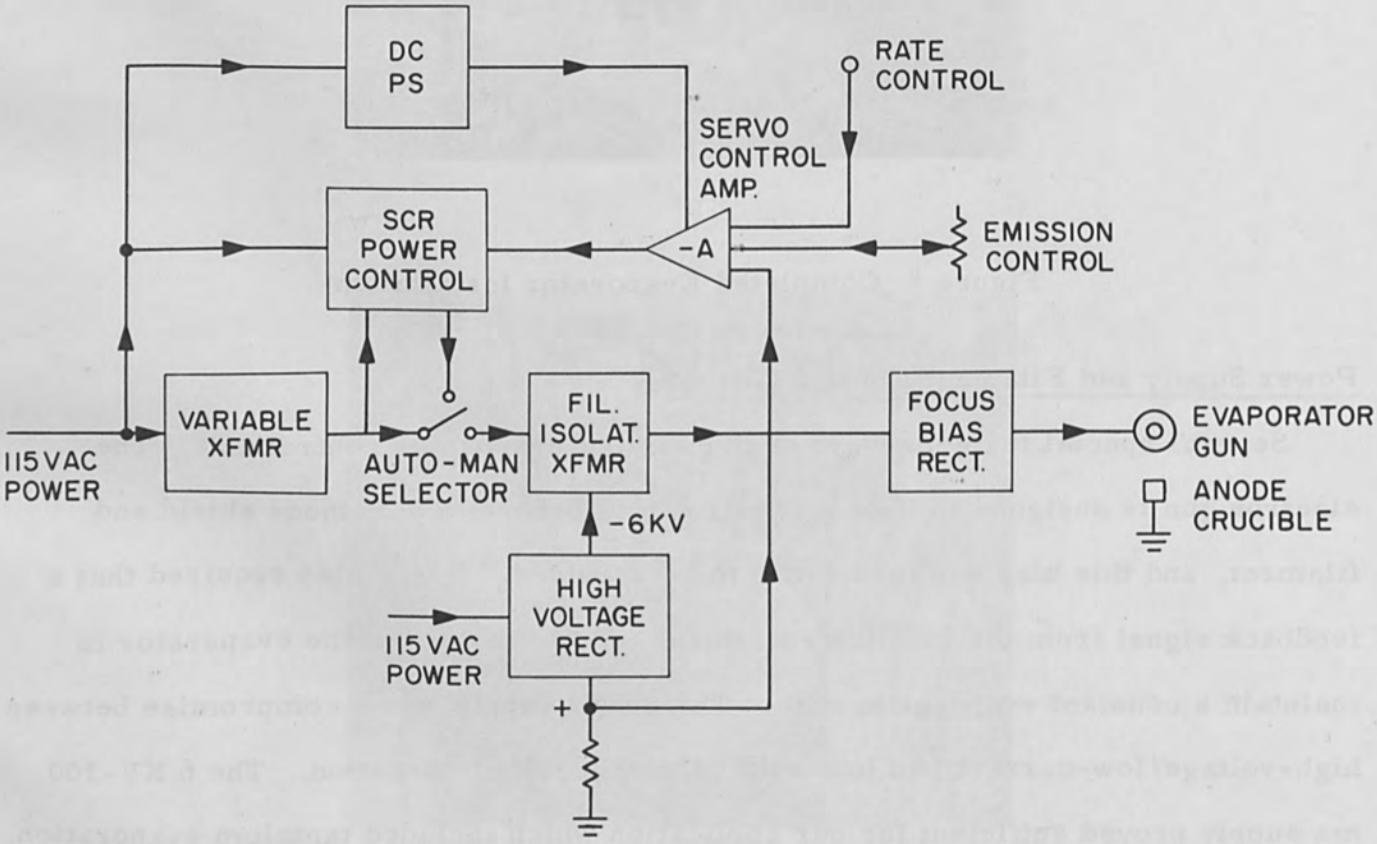

Figure 7 Electron Bombardment Evaporator Diagram

control circuit is presented in Figure 8. The use of a GE TRIAC instead of a pair of SCR's permitted a simplified pulser circuit, and eliminated the need for a surge suppressing device across the transformer. The differential amplifier is a commercial packaged plug-in unit[2] and by being connected as an operational amplifier allows the combination of positive and negative control signals. The current, "I", feedback signal from the rectifier provides constant-current operation.

The bombardment power is controlled by variation of the filament emission current, and this current in turn is controlled by the temperature of the filament. The TRIAC circuit delivers clipped half-cycles of the supply line power, the clipping being proportional to the setting of the emission control. The accelerating voltage is maintained constant throughout the range of bombardment current.

The bias rectifier is a bridge-type voltage tripler connected across the gun filament secondary. This bias voltage, used to focus the beam to a smaller area, also prevents diode action between the filament and shield during alternate cycles of the filament voltage. Since no current is drawn through the bias rectifier during normal operation, this circuit can use low-current diodes. The filament is a loop of 10 mil tungsten, and requires only 6 amperes at 8 volts to deliver full emission of 300 ma.

If a tungsten sheet is placed across the crucible top, the image of the filament loop is seen. This image, from a 5/8-inch loop, is only 1/4-inch and illustrates the concentration of the electron-beam onto the evaporant.

Deposition Control System

A view of the instrumentation assembled for controlling the deposition process is given in Figure 9 and the various sections are identified in Figure 10. All units are independent except for a common power supply. The units are interconnected by front panel patchcords and the arrangement can be changed quickly to permit different monitor units to have control. The individual units will be described in

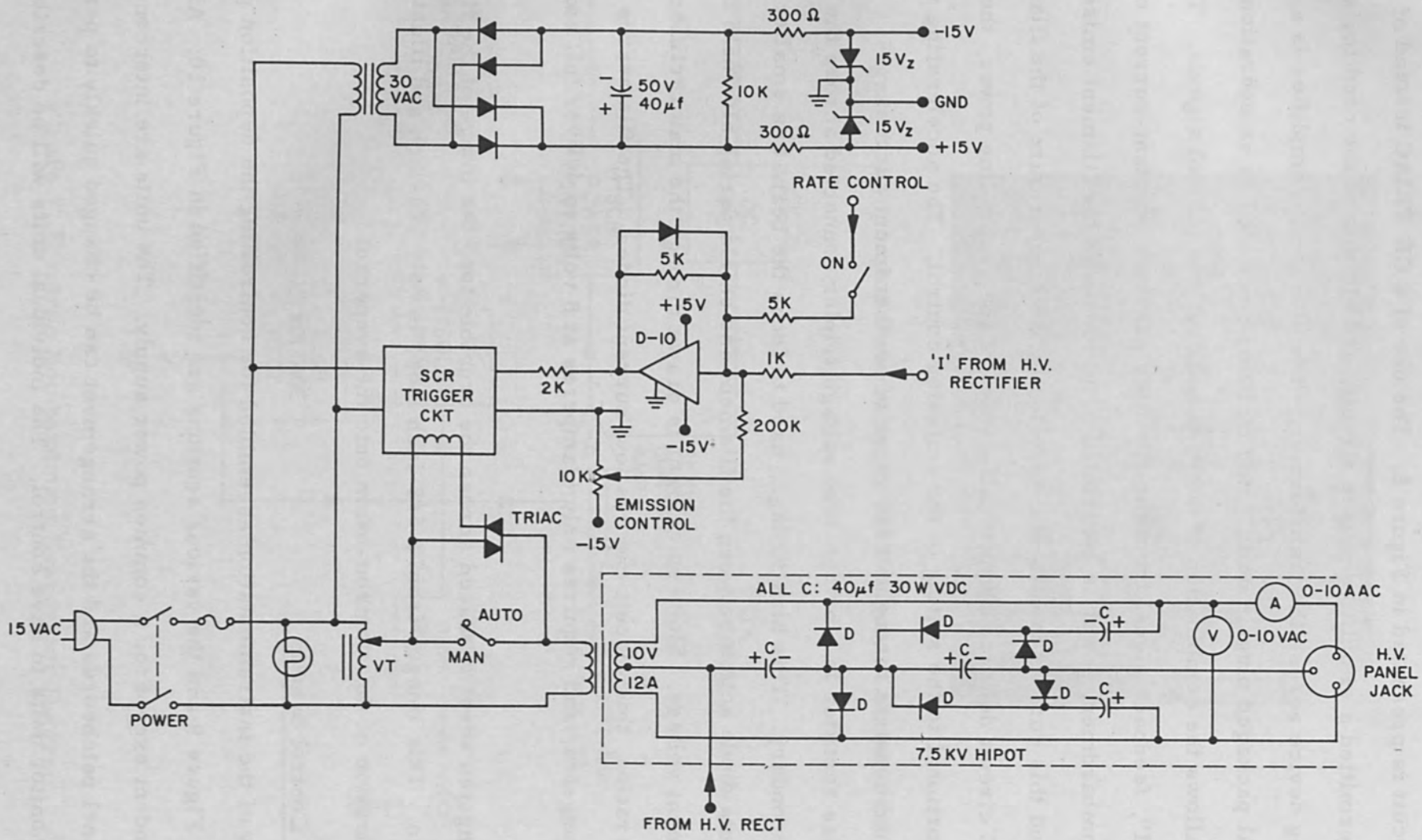

Figure 8 Filament Control Panel Schematic Diagram

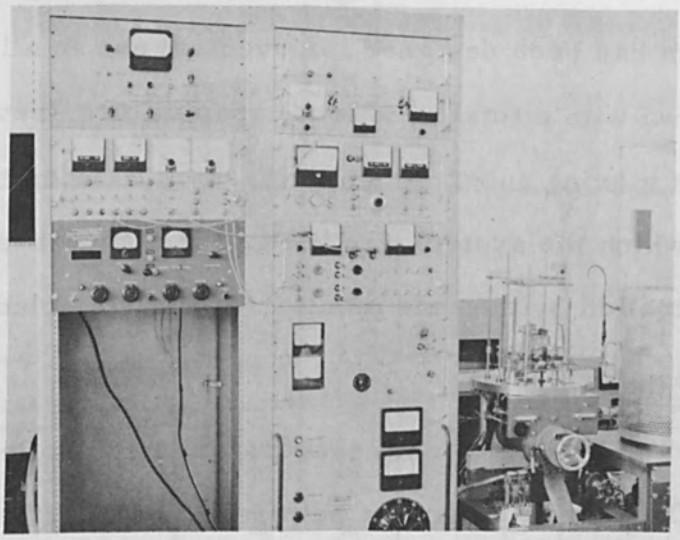

Figure 9 Thin-Film Deposition Control Rack and Vacuum System

	P. S.
	SUBSTRATE TEMP. CONT.
RESISTANCE MONITOR	DEPOSITION MONITOR
EVAPORATION MONITOR	DEPOSITION CONTROL
	FILAMENT CONTROL
	6KV RECT. P. S.

Figure 10 Deposition Control Rack Arrangement

separate sections to follow.

The basic system has been designed for eventual use in a larger vacuum system than that shown with a total of four (4) evaporators, several substrate stages, and means of moving substrates and masks. Besides the electron-beam evaporator, around which the system was built, resistance-heated evaporators capable of being controlled by the rate monitors are also included.

Deposition Control Panel

Deposition from the electron-beam evaporator is controlled by a solenoid-operated shutter. The shutter in turn is powered from the control panel shown in Figure 11. The control panel circuit, shown in Figure 12, consists of two (2) holding relays, associated push-button switches, shutter selector switches (the unit is for use with four (4) shutters although only one (1) is presently connected), and patch-plug jacks for insertion of automatic control from the other units. Each relay includes a SPDT switch which is brought out to the front panel and can be used to transfer control signals relative to the deposition sequence.

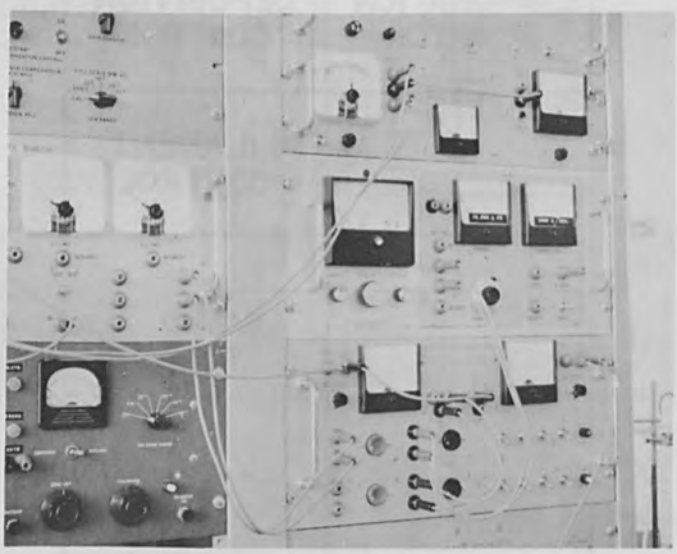

Figure 11 Close-Up of Control Panel, Deposition Monitor, and Substrate Temperature Control

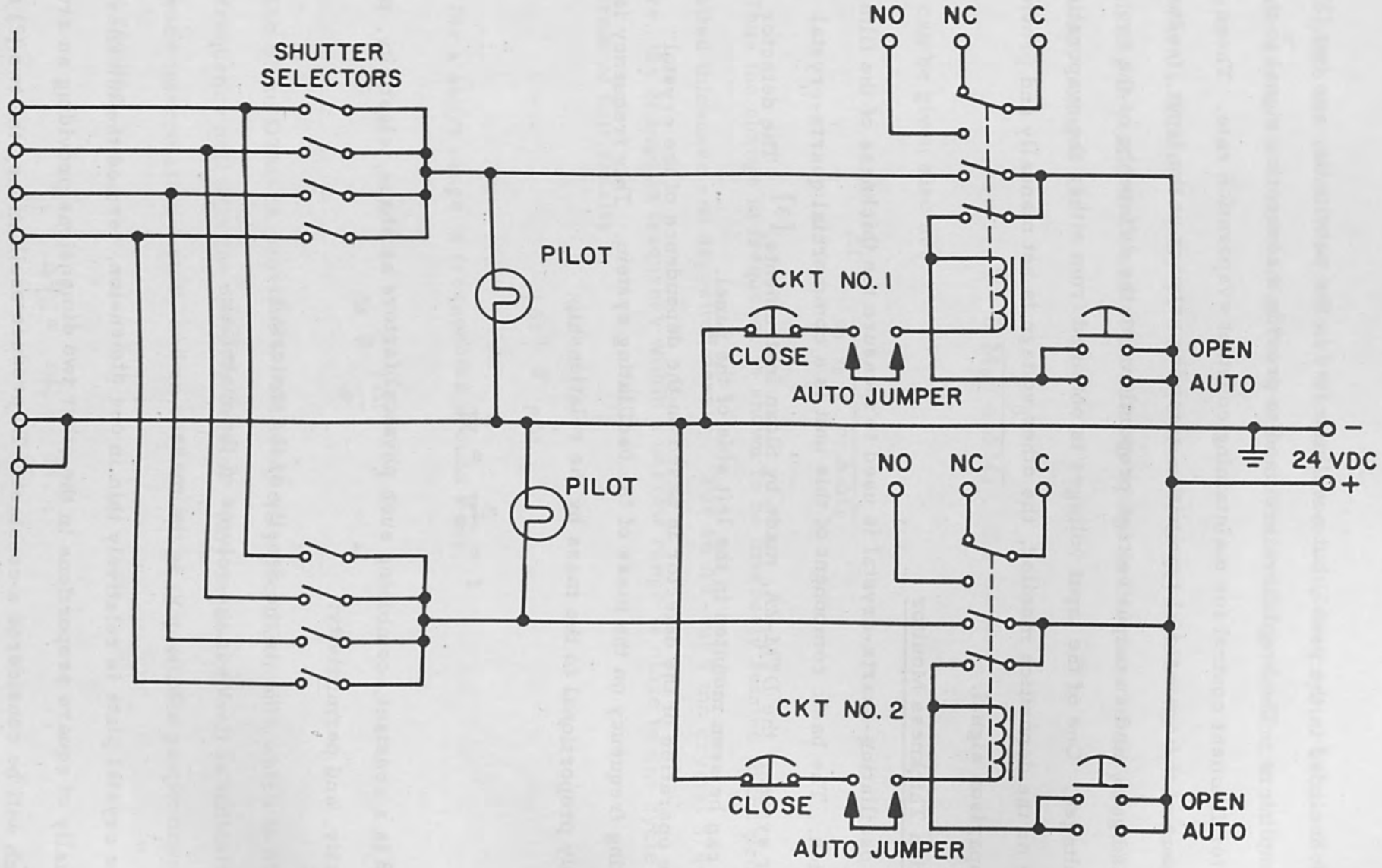

Figure 12 Deposition Control Panel Schematic

Also included in the panel, but not illustrated in the schematic, are two (2) rate-error amplifiers. The amplifiers are used to provide a correction signal to the evaporator filament control for maintaining constant evaporation rate. These amplifiers are of the operational type with a summing network at the input, feedback controlled gain, and an output voltage proportional to the difference of the two (2) input voltages. One of the input voltages is obtained from either the evaporation monitor or the deposition monitor, the other voltage is set manually and provides the comparison signal.

Deposition Thickness Monitor

An oscillating-quartz-crystal is used to measure the thickness of the film during deposition. The basic component of this unit is a commercial quartz-crystal detector system, the DTM-2A, made by Sloan Instruments.[3] The detector control can be seen mounted in the left side of the panel.

The operation of the detector is based on the dependence of the crystal oscillating frequency on the mass of the oscillating system. This frequency is inversely proportional to the mass by the relationship:

$$f = \frac{\beta}{\rho V} = \frac{\beta}{M}$$

where β is a constant, combining such physical factors as shape, elasticity, piezo-electricity, and permittivity;

ρ is the density of the material;

V is the volume of the material;

$M = \rho V$ is the mass.

The crystal plate is relatively thin in one dimension, termed the thickness t, and usually of square proportions in the other two dimensions providing an area, A, which will be considered a constant. To produce oscillations, the two (2) sides

of the plate are metallized to form a capacitance with the crystal as the dielectric, and the crystal is connected as the frequency determining element in an oscillatory circuit.

When a film of density ρ_1 and thickness t_1 is deposited onto the surface of an oscillating crystal, the mass of the film is added to the mass of the crystal and the frequency changes as:

$$\Delta f = \frac{\beta}{M_0 + \Delta M_1} \quad .$$

This can be given also as:

$$\Delta f = \frac{\beta}{\rho_0 V_0 + \rho_1 A \Delta t_1} \quad .$$

Thus the change in frequency is shown to be inversely related to the product of deposited thickness and deposited density. For an AT-cut 5 mc crystal 3/4-inch square, the change in frequency within a narrow range is close to one cycle per angstrom of unit density

$$|\Delta f| \cong \rho \Delta t \quad .$$

Thus for a short range of frequencies around 5 mc:

$$\Delta t \cong \left| \frac{\Delta f}{\rho} \right| \quad .$$

The Sloan DTM-2A provides a beat frequency oscillator with which to obtain a zero frequency null with the detector crystal. Any degree off null is indicated on a frequency interpolation meter, and an output voltage is available proportional to the meter reading.

$$\Delta V \propto \Delta f \propto \Delta t \quad .$$

By using a potentiometer calibrated in bulk density (specific gravity) to effect the $1/\rho$ factor, the output voltage of the detector can be calibrated directly to represent thickness. This is performed by a differential amplifier circuit shown in Figure 13. The detector is set to the 0-10 Kc scale of frequency and the thickness meter is calibrated in 0-10,000 angtroms. The circuit is arranged so that a linear 10-turn pot with a dial reading 1 to 11 performs the proper calibration directly.

A differentiating circuit provides an indication of deposition rate in angstroms per second. The maximum indicating rate is 1000 or 10,000 as set by the range switch. The deposition rate also provides a voltage which can be used to control the evaporator.

It is necessary to make an initial calibration of the system to determine the accurate bulk densities of the evaporated films of each material to be used. This is especially true of compounds and mixtures. Elemental bulk densities as reported in physics handbooks can be used.

The DTM-2A has a built-in SPDT limit relay which can be set to any point of the meter scale and can be used to actuate the deposition control shutters.

Substrate Temperature Control

One of the principal factors affecting the adhesion of evaporated films to the substrate is the preparation of the substrate surface. Besides the necessity of a thorough cleaning procedure, the substrate must be raised in temperature after being placed in the vacuum to effect the evaporation of residual surface contamination, including adsorbed gases. Standard evaporations are done on substrates held between 200 °C and 400 °C, and some work is being done at 600 °C. The higher temperatures are involved where special film properties are desired, such as macrocrystallinity. Temperatures near 1200 °C are required for single-crystal films. [See Figure 14]

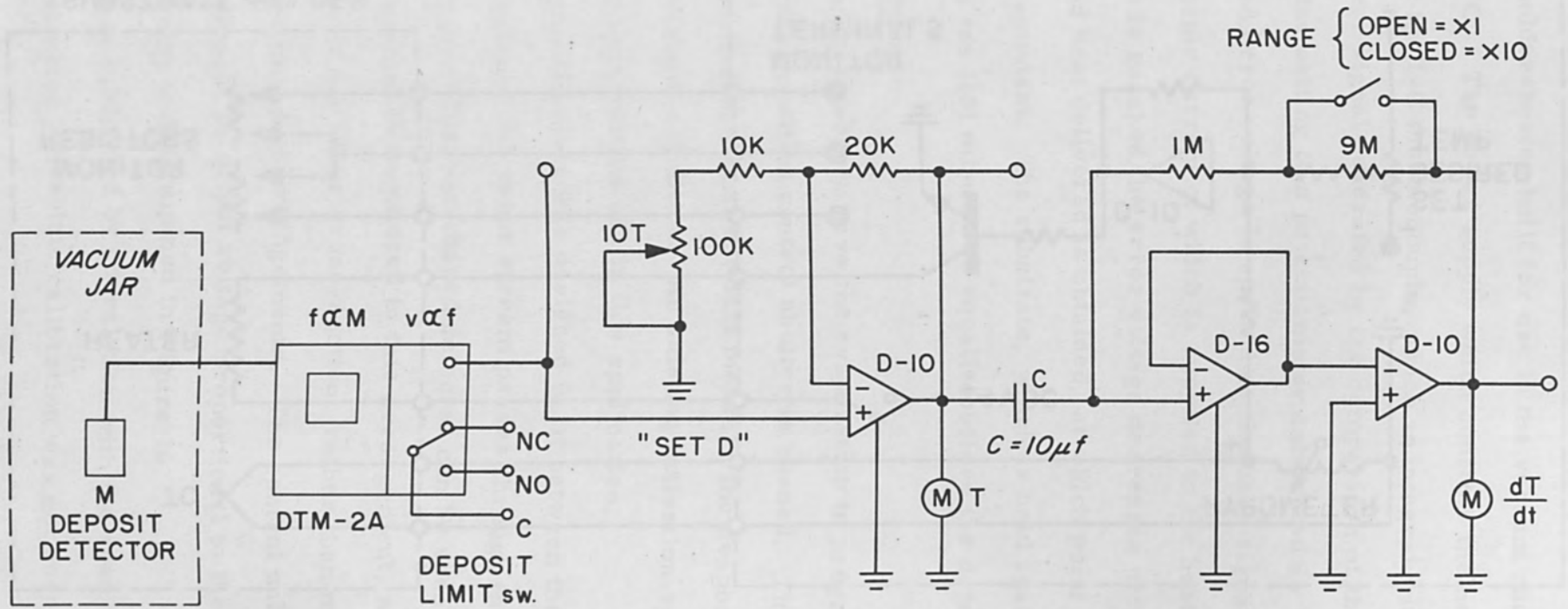

Figure 13 Deposit Thickness Monitor Panel Diagram

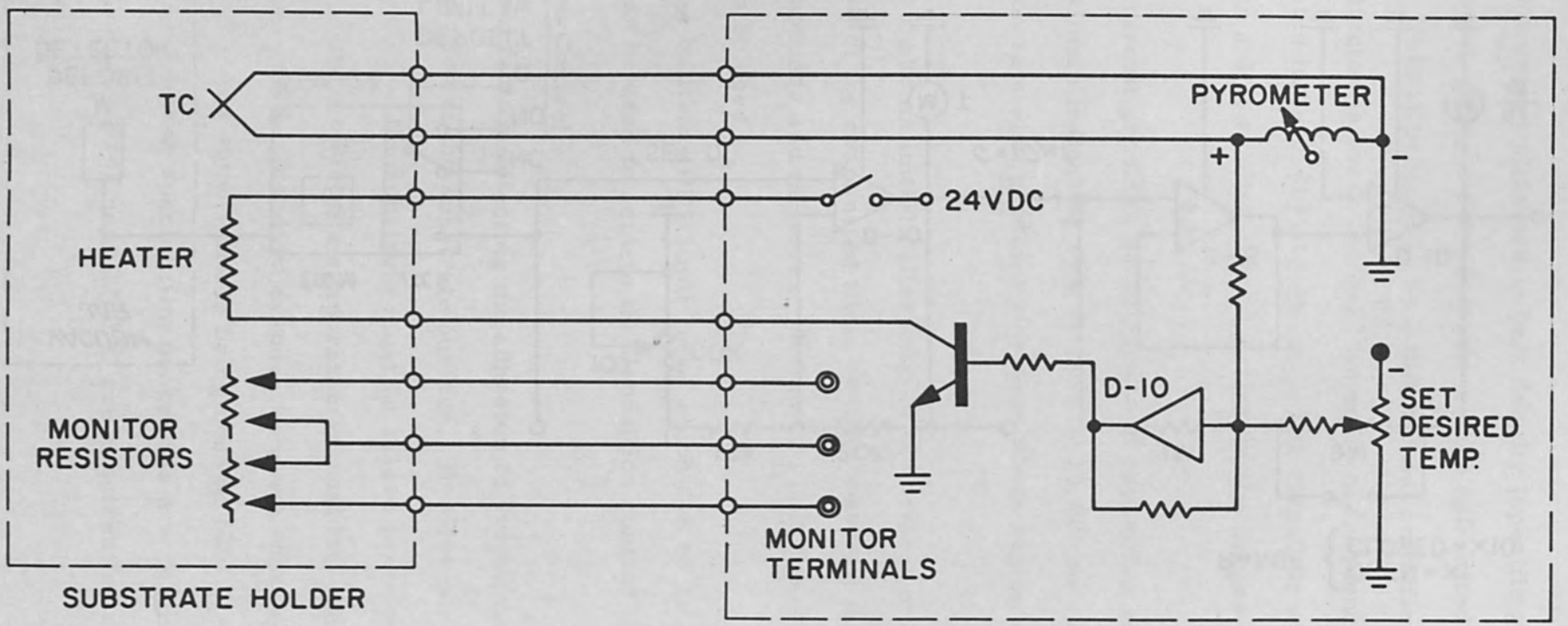

Figure 14 Substrate Temperature Monitor and Control Diagram

The substrate holder-heater built for use in the vacuum chamber is capable of temperature of 500°C. The power supply which controls the heater obtains a signal directly from the I-C thermocouple, which is integral with the heater block, and amplifies an error signal generated by the comparison of the TC voltage to a voltage obtained by the setting of a potentiometer calibrated as "desired temperature". The amplified error voltage is applied as the base signal of a power transistor, the collector current of which is supplied to the heater filament. As the desired temperature is reached the error voltage decreases until the equilibrium between heat loss and heat delivered is obtained, at which point the substrate heater temperature is held constant. The substrate, which is held against the heater block by springs, requires ten (10) minutes to equalize before the deposition is started.

Evaporation Rate Monitor

It was considered desirable to have the evaporation in progress at the proper rate at the moment the deposition control shutter is opened. Thus an evaporation-rate monitor was installed such that it would measure the evaporation rate independent of the control shutter position. An existing ionization-type vacuum gauge control was modified to permit its use in this application.

An ionization-gauge chamber was designed to fit between the evaporator and the shutter. In this position the vapor stream passes through the detector toward the shutter and substrate. The box-shaped detector can be seen in position in Figure 5. The total stream is monitored in this arrangement, and the reading represents an average of the vapor cross-section, rather than merely some fringe portion as done by several other arrangements. The control unit, shown in Figure 15, was modified to provide an output voltage proportional to the meter deflection. The detector construction is diagrammed in Figure 16.

The rate monitor is calibrated by correlation with the readings obtained on the deposition thickness monitor. Absolute calibration was not possible due to

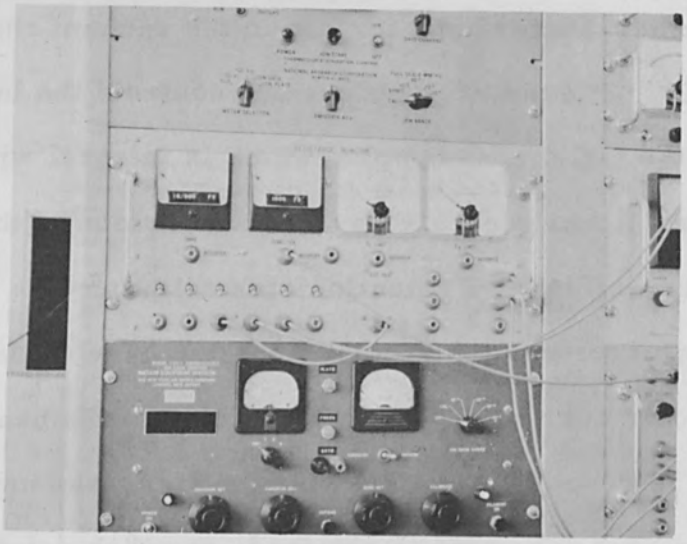

Figure 15 Close-Up of Rate Monitor and Resistance Monitor

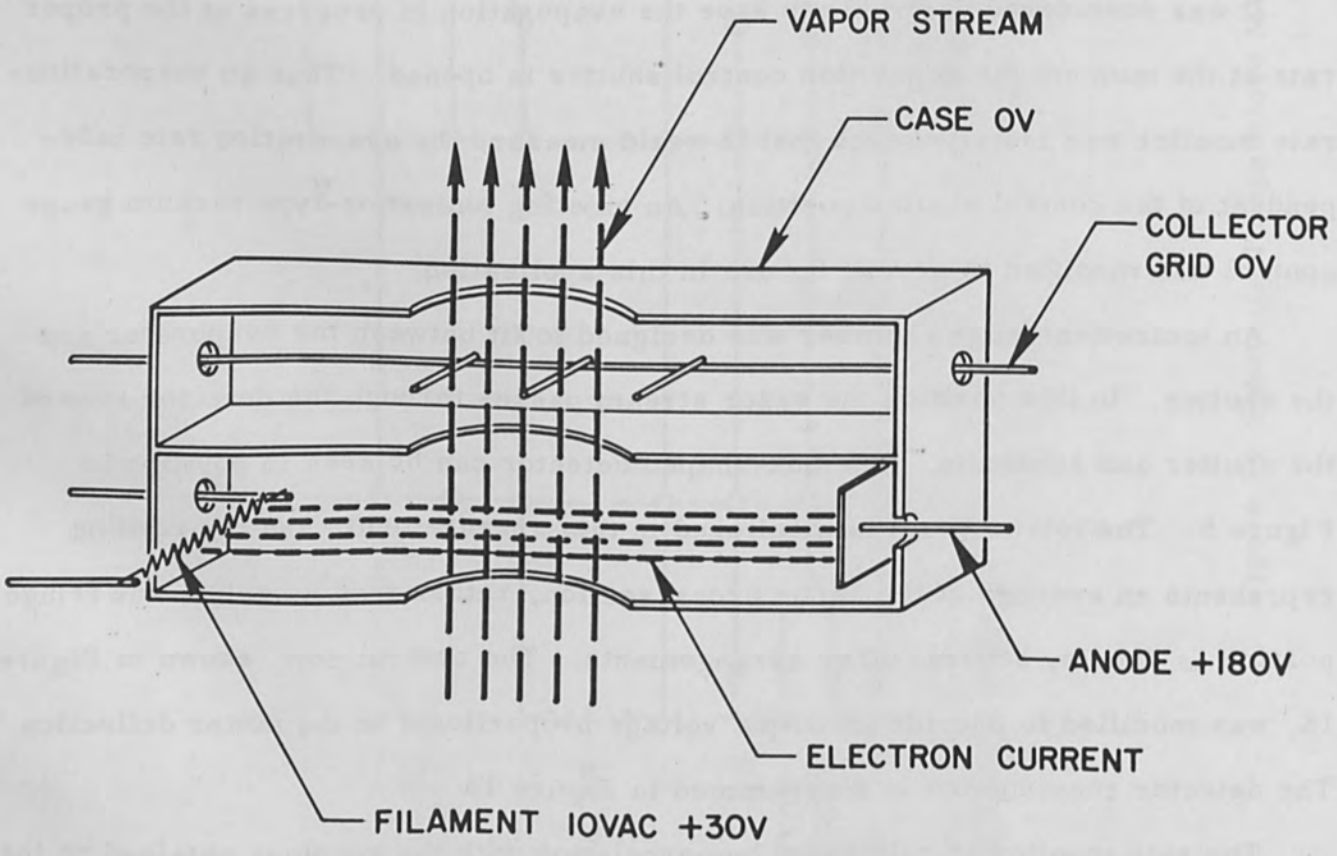

Figure 16 Diagram of Rate Detector Chamber

variations in vapor material characteristics, but a relative calibration curve was made for each material. Some ionization of the vapor was found to exist due to the bombardment heating, but this was found to be a proportionality and was absorbed in the monitor calibration curves.

Resistance Monitor

Since the program of this development was concerned with the electrical properties of thin-films, it was quite necessary that a provision be made to dynamically measure the film resistance during deposition. A linear ohmmeter was employed for this purpose.

A total of six (6) sample resistors can be accommodated with the monitor circuit represented by the partial schematic of Figure 17. The six (6) constant-current sources each deliver one milliampere at a maximum coercive force of 15 volts. The sample resistors are patched into each current source separately, and these systems can be switched into the meter circuit individually, or collectively to obtain an average of the resistance spread of the several samples.

The meter is calibrated to 10 kilohms, and a differentiation circuit measures the rate of change of resistance up to 1000 ohms per second. Since, for a constant deposition rate, the rate of change of resistance is a logarithmically decreasing function it cannot be used as a control signal, but it nevertheless is an important factor in the later evaluation of the deposition process.

Coupled with the ohmmeter are two (2) SPDT limit switches activated by two (2) meter relays. These relays can be set independently to close when the resistance (decreasing with time) reaches certain desired values. The limit switches can serve to trigger various activities of the deposition process, and, together with the limit switch provided with the deposition thickness monitor, can automatically control the deposition of thin-film resistors from start to finish.

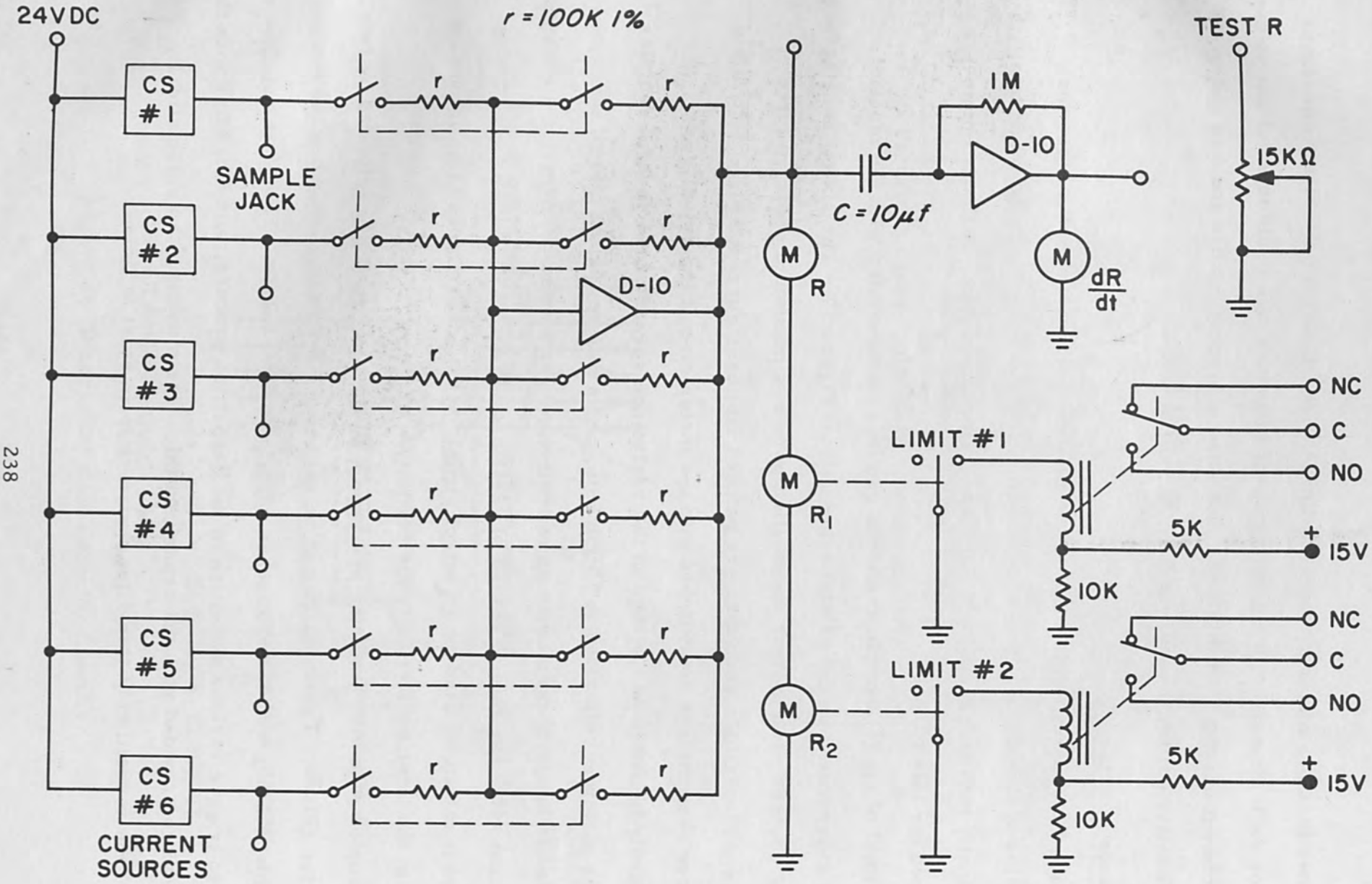

Figure 17 Resistance Monitor Diagram

System Operation

The several units of the deposition system are arranged in the vacuum system as illustrated in Figure 18. These units can be used independently and manually or they can be interconnected by patch cords to permit a high degree of automatic process control.

The evaporator can be controlled by the rate-error signal from either the deposition thickness monitor or the evaporation-rate monitor. In standard operation the evaporation monitor has control until the shutter is opened, at which time the deposition monitor is switched into control.

The shutters can be controlled by the limit relay of the deposition monitor, the limit relays of the resistance monitor, or, when two or more shutters are installed, by the relay of the opposite shutter. With the latter arrangement, the resistance limit can open shutter No. 2, the relay of shutter No. 2 can close shutter No. 1, and then the deposition limit can finally close shutter No. 2. By this sequence, the resistive element can be deposited through shutter No. 1, and the overcoat deposited through shutter No. 2, the process automatically terminating at set points. This removes the manual operator variable and permits greater reproducibility between runs.

The output voltages available from the many units, besides serving as process control signals, can be recorded for future evaluation of process variables. These recordings also permit a check on the reproducibility of the measured parameters from run to run, and to indicate the success of the process controls.

Once the desired control function has been patched into the equipment, the limit points of the several sensing relays can be easily and quickly changed for testing the effect of these deposition variables. The fact that these limit points can be accurately set means that it is possible to return to any specific conditions once a series of tests have been made to determine the optimum settings.

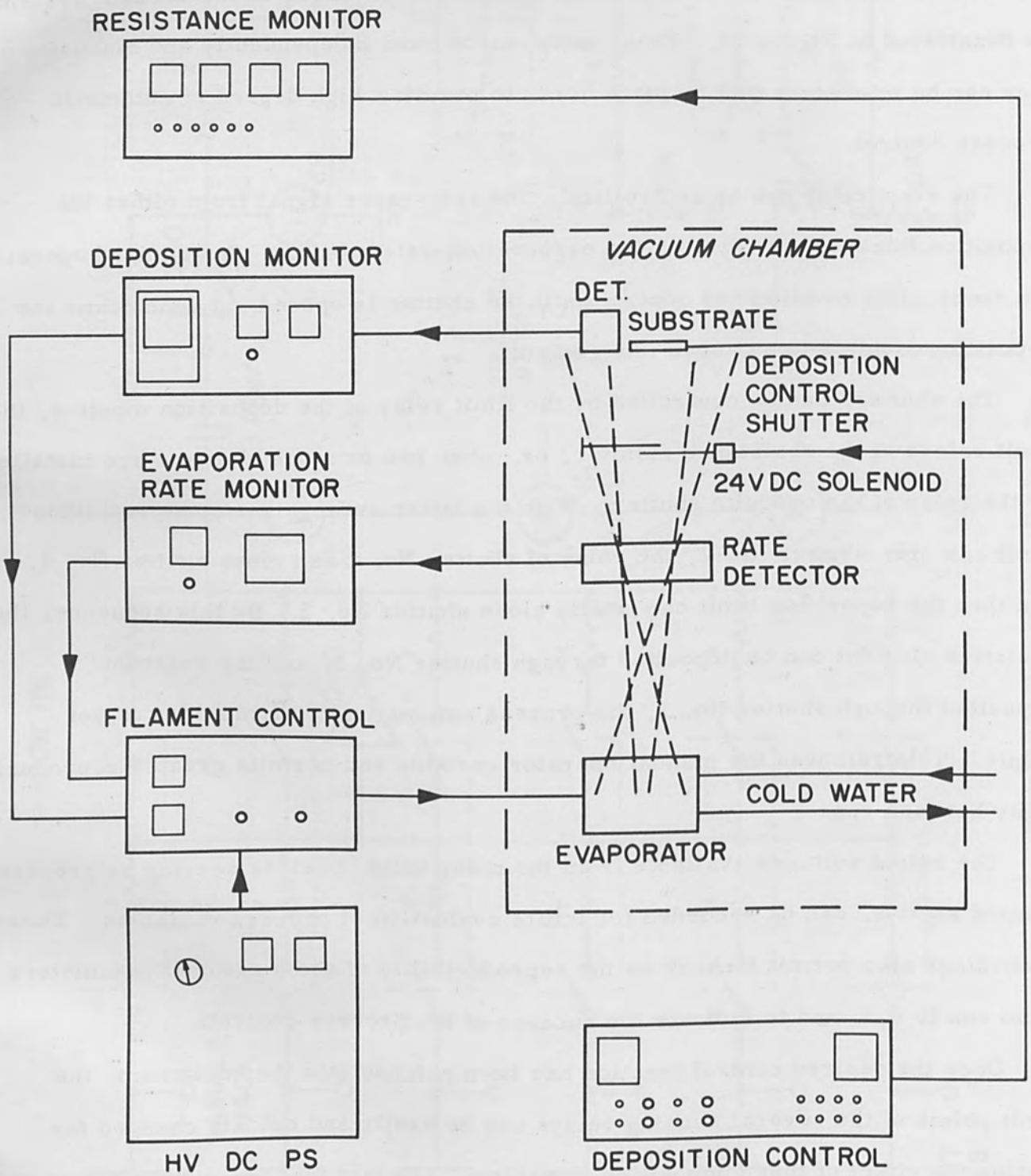

Figure 18 Vacuum Deposition System

Application

The development of the above-described system had a two-fold purpose. The use as a basic research tool for the investigation of thin-film material properties, and to produce pilot quantities of thin-film components for some unique integrated circuit applications. Such generalized application as a basic tool required the system to be readily adaptable to unusual situations, while the requirement for a pilot production capability called for close control and high reproducibility. These characteristics were met in the flexibility of this system.

In the basic investigation, several dielectric compounds have been deposited for the evaluation of their dielectric properties in the UHF region. These dielectrics are being studied for possible use with a new transistor structure under development.[4] The compounds extended from the standard silicon monoxide to the more exotic cerium sulfide.

For the integrated circuit application, miniature resistors of both high and low resistivity elements and compounds were deposited. This was done to determine the applicability for use as stabilizing resistor components in a developmental circuit device. String-type resistors of titanium, nichrome, tantalum, and molybdenum were evaluated as well as were sandwich-type resistors of silicon and several other semiconducting compounds.[5] The effect of resistivity on the temperature coefficient of resistance in both thin and thick films was studied.

Conclusion

Instrumentation by means of which the thin-film vacuum deposition process can be monitored and controlled is becoming more sophisticated as the application of the process expands. And, as the process becomes better instrumented and controlled it can be employed more frequently in preference to cruder existing fabrication methods. The capability of setting prescribed values of process variables into the system and having the system perform reproducibly is a big

step toward acceptance of the vacuum-deposition process as an economically competitive production method.

References

1. Riddle, G. C., A Thin-Film Deposition Production Facility, Proceedings Fourth Symposium on Electron Beam Technology, 1962, pp. 340-371.
2. Data Device Corporation, 240 Old Country Road, Hicksville, New York.
3. Sloan Instruments Corporation, 331 North Milpas Street, Santa Barbara, California.
4. Hooper, W. W. and W. Shockley, The Surface Controlled Avalanche Transistor, Presented at Wescon 1964, August 25-28.
5. Riddle, G. C., Sandwich-type Resistors Offer Space Savings, to be presented at the Fourth Annual Microelectronics Symposium, IEEE, May 1965.

Electron Beam Focusing Effects in Beam-Generated Plasmas*

by

D. A. Dunn and A. S. Halsted
Institute for Plasma Research
Stanford University
Stanford, California

Abstract

A kilovolt electron beam of a few mm diameter passing through a gas at pressures of 10^{-2} Torr or lower will not be significantly scattered by collisions with neutrals in distances of many beam diameters. The beam will ionize the gas and generate a plasma that has a potential distribution that will cause the beam to be pinched toward its axis. This electrostatic pinch effect is compared with the magnetic pinch and the electrostatic pinch is found to be the dominant effect at low voltages and currents. Recent experiments have confirmed the results of early German experiments at a few hundred volts and have also demonstrated that the electrostatic pinch exists at higher voltages and can be more important than the magnetic pinch at voltages up to the order of 100 kv. Computer studies of beam trajectories in a simulated beam-generated plasma have been made that provide an explanation for the detailed structure of the beam profiles that have been observed. It is believed that these effects play an important role in beam welding and beam penetration of thick slabs of metal.

Introduction

A kilovolt electron beam of a few mm diameter passing through a gas at pressures of 10^{-2} Torr or lower will not be significantly scattered by collisions with neutrals in distances of many beam diameters. The beam will ionize the gas and a plasma can form in the vicinity of the beam that has a density that may vary

---

*This work was supported by the U. S. Army Electronics Laboratories under Contract DA36-039-AMC-00094(E).

from a value comparable to the beam density at low pressures such as 10^{-6} Torr to a value hundreds of times the beam density at pressures of the order of 10^{-2} Torr. The electrostatic potential within the plasma has a shape such that an inward force acts on the beam electrons that generated the plasma. This force will cause an initially parallel beam to shrink in diameter. An extensive literature exists on this subject[1-18] which was studied experimentally in the 1930s primarily in Germany and was usually called "gas focusing" or "ion focusing". As will be seen, there are very close parallels between this effect and the usual magnetic pinch effect[19-23] and we prefer to call it the "electrostatic pinch effect". Another group of papers exists[24-28] on the related subject of ion trapping, but these papers do not deal with the effect of interest here.

We have recently used a computer to obtain accurate theoretical values of potential and density in a beam-generated plasma, both in planar[29] and cylindrical geometry,[30] following the work of Langmuir and Tonks.[31] These results may be used to make accurate predictions of beam profiles in such a system, also using a computer, and some of these results are presented here and compared with experimental data. Early theories of beam profiles in such systems necessarily (in the absence of computers) allowed only crude estimates to be made of the potential distribution and the resulting beam profiles.

Figure 1 is a cross-section of the configuration being studied. An electron beam partly fills a cylindrical glass or metal tube. In the absence of a gas the potential distribution would have the shape indicated by curve I. When a gas is present the beam ionizes the gas molecules. The electrons produced by the ionizations are swept out and the ions collect in the negative potential well, forcing the potential to rise at least to the wall potential, as in curve II, where it would stay if both ions and electrons were created with zero initial velocity and never acquired any velocity other than zero. In practice the potential at the center could go either

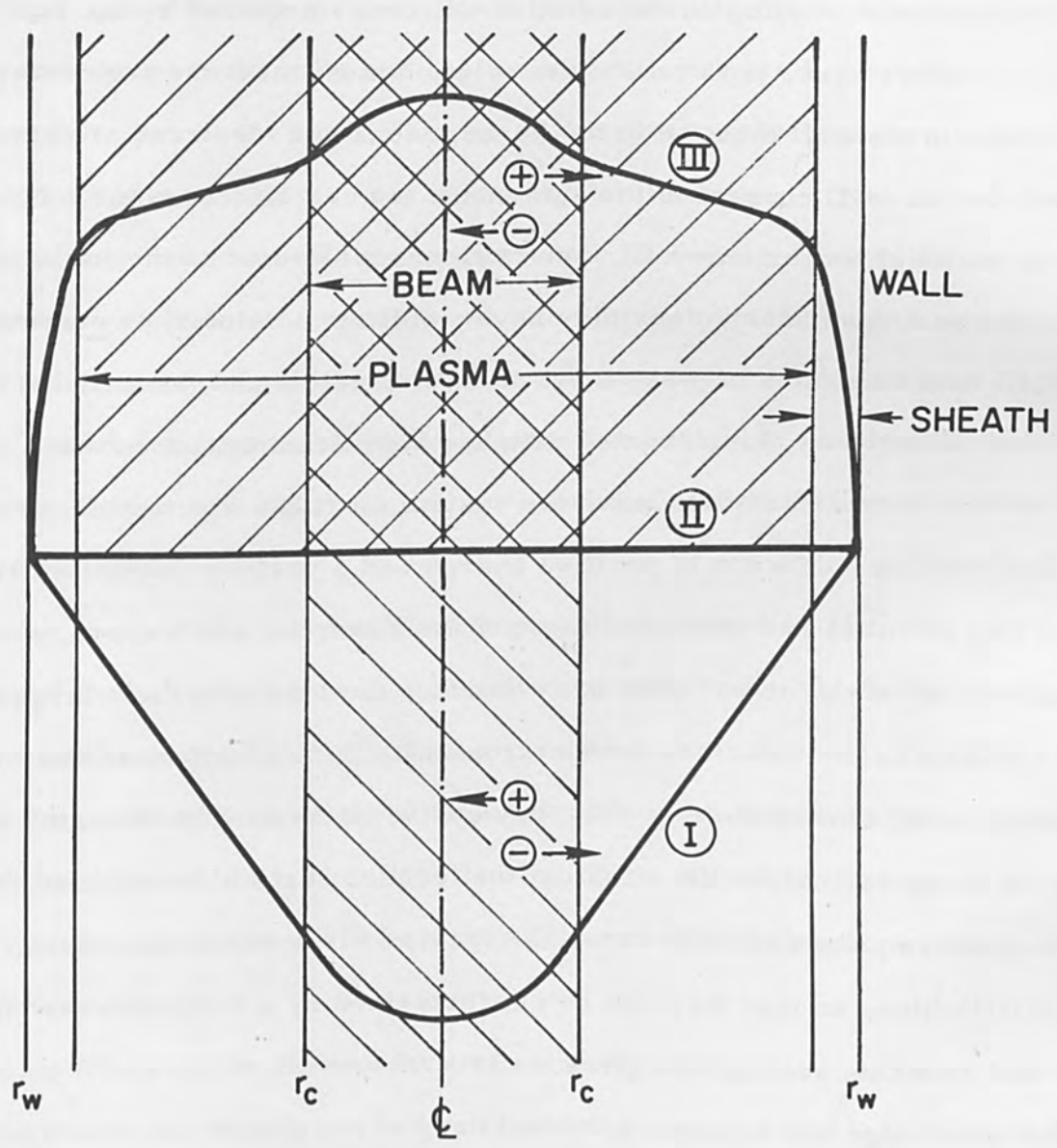

Figure 1 Potential vs. radius for three conditions. Curve I corresponds to the potential depression caused by the negative space charge of an electron beam flowing along the axis of a cylindrical tube in the absence of a gas. If a gas is present so that ions and electrons are generated by the beam, the potential will rise to Curve III. Curve II, representing a field free space, is not a possible equilibrium solution for a physical plasma.

positive or negative depending on the relative velocities acquired by the ions and the electrons. In either case, the equilibrium solution must meet the requirement that the net current to the wall must be zero, because ions and electrons are created at equal rates and the wall current is the sum of the ion and electron currents. If the potential is positive, as for curve III, ions will be accelerated to the walls and electrons will be turned back unless they have a sufficient velocity to overcome the potential hill they encounter between their point of creation and the wall. If the electrons are pictured as being created with any significant initial velocity, as is the case in fact, they will rapidly leave the system, if it has a potential curve of type II, thus causing an excess of positive charge and a positive potential curve of Type III. The potential will rise until most of the electrons are trapped, at which point equal ion and electron currents are obtained, the ions with their large mass being accelerated to the walls and the electrons with their small mass and high initial energy being slowed down so that they arrive at the wall at the same rate as the ions. In order to analyze the situation that occurs next, it is assumed that collective or other processes will cause the trapped electrons to acquire a random velocity distribution, so that they can be characterized by a temperature. An analysis that uses this assumption gives a curve of type III with a small potential drop at the beam edge and a larger potential drop at the sheath near the wall. The height of each drop in potential is set by the plasma electron temperature.

The magnitude of the inward force in the electrostatic pinch is therefore determined by the plasma electron temperature. Experimentally, a typical beam-generated plasma has a temperature of a few electron volts. This relatively high temperature is primarily determined by two factors. First, the ionization products of an ionizing collision of a kilovolt beam are normally: a) a beam electron that is slowed by about 30 volts, b) a plasma electron with about 10 to 15 volts energy and c) an ion with a few tenths of a volt energy (for monatomic gases).[32-33]

For diatomic gases the ion may acquire a volt or two energy. In any case, most of the difference between 30 volts and the ionization energy is imparted to the plasma electron rather than to the ion. This energetic plasma electron then becomes part of the plasma and eventually a nearly Maxwellian velocity distribution of plasma electrons is obtained at some temperature such as 3 volts. In addition to the large initial energy with which the average plasma electron starts its existence, it can acquire further energy from the beam through beam-plasma rf interaction processes, and these processes further raise the plasma temperature. In low-pressure plasmas, collisions with neutrals are rare and the randomization processes usually involve rf mechanisms.

We may now picture a typical beam-generated plasma at 10^{-4} Torr as consisting of three components in a positive potential well: (1) the beam electrons with a directed energy of kilovolts and a very small random energy; (2) the plasma electrons with a density about three times the beam density and a temperature of a few volts; and (3) the ions with a density slightly in excess of the sum of the plasma electron density and the beam density and with a negligible random energy, falling freely to the walls.

This sort of beam is often described as neutralized, but it is important to understand that it is not neutral, but positive at the center and that there is a net self-pinching field acting on the outer beam electrons that is approximately equal to the electron temperature of the plasma in volts divided by the beam radius. As the beam voltage is increased, the self-magnetic field of the beam becomes important and the inward force due to the usual magnetic pinch effect can become greater than the inward force due to the electrostatic pinch. The voltage at which the two effects are equal in magnitude is a function of the beam current and the plasma electron temperature. For a typical case the plasma temperature might be 3 volts and the beam current 300 milliamps. The beam voltage in this case for

which the magnetic and electrostatic pinch effects produce equal inward forces would be 25 kilovolts. A detailed comparison of these effects is given in a later section.

Experimental verification of the theory has been obtained for the electrostatic pinch at a few hundred volts and has been extensively reported in the literature.[1-18] We have recently observed the effect at voltages up to 8 kilovolts using a Pierce gun as the beam source. Some of these results are reported in a later section. Since, as will be shown, the magnetic pinch effect in a beam-generated plasma produces exactly the same measurable results as the electrostatic pinch, the two effects can only be distinguished experimentally by comparing the dependence of the beam profile on current and voltage. As the plasma temperature will vary with beam current and voltage in an unknown way, it is only possible to estimate the dependence of the beam profile on the voltage. However, as will be shown, almost any reasonable estimate leads to a predicted dependence that should be easy to observe.

The Magnetic Pinch Effect

The pinch effect due to the self-magnetic field of the beam is well known,[19-22] and it has been observed in many plasma configurations, such as high current arcs.[23] It does not seem to have been observed in electron beams, probably because a high-voltage properly neutralized beam with carefully controlled entrance conditions is required in order to observe the effect and this is not a readily available configuration. Here we derive the basic equations and compute the shape of the beam profile for an initially parallel beam, such as could be produced from a well-designed electron gun.

We assume that, for this calculation, the beam is perfectly neutralized, so there are no space charge forces acting. The self-magnetic field at radius r inside a beam of radius r_b is calculated from the Biot-Savart law

$$H_\theta \, 2\pi r = J_b \pi r^2 = I_b \frac{r^2}{r_b^2} \tag{1}$$

where

J_b is the beam current density

I_b is the beam current equal to $J_b \pi r_b^2$

r is the radius

r_b is the outer radius of the beam

H_θ is the θ-directed magnetic intensity,

so that,

$$H_\theta = \frac{I_b}{2\pi} \frac{r}{r_b^2} \quad . \tag{2}$$

The force on an electron at radius $r_e < r_b$ is, from the Lorentz force law, using Equation (2),

$$F_{rm} = - e v_b B_\theta$$

$$= - e \, v_b \, \mu_o \, H_\theta \quad .$$

$$= - e \, v_b \, \mu_o \frac{I_b}{2\pi} \frac{r_e}{r_b^2}$$

$$= -\left[\frac{e\mu_o}{2\pi r_b^2} \left(\frac{2e}{m} \right)^{1/2} \right] \left(\frac{I_b}{V_b^{3/2}} \right) V_b^2 \, r_e \tag{3}$$

where

F_{rm} is the r-directed force due to the magnetic field

B_θ is the θ-directed magnetic flux density

μ_o is the permeability of free space

v_b is the beam velocity

r_e is the radius of an electron within the beam

e is the charge of an electron

m is the mass of an electron

V_b is the beam voltage, where $v_b = (2 \frac{e}{m} V_b)^{1/2}$

$\frac{I_b}{V_b^{3/2}}$ is the beam perveance, a quantity fixed by the design of the electron gun, with a typical value of less than 10^{-6}.

It is seen from Equation (3) that the force is negative and is thus directed inward. The value is proportional to the radius and is also proportional to the product of the beam current and the square root of the beam voltage, here expressed in terms of perveance and voltage which are often somewhat more convenient parameters than current and voltage.

We now derive the equation of motion of an electron, pictured as moving through a beam of fixed diameter, so that r_b is constant and r_e varies as a function of time. The force equation is, for non-relativistic beam velocities

$$m \frac{d^2 r_e}{dt^2} = F_m$$

$$\frac{d^2 r_e}{dt^2} = - \omega_m^2 r_e \qquad (4)$$

where, from Equation (3)

$$\omega_m^2 = \frac{\mu_o}{4 \pi r_b^2} \left(\frac{2e}{m} \right)^{3/2} \left(\frac{I_b}{V_b^{3/2}} \right) V_b^2 \qquad (5)$$

The solution of Equation (4) is, for an electron initially parallel to the axis so that $\dot{r}_e(0) = 0$,

$$r_e(t) = r_{eo} \cos \omega_m t \tag{6}$$

where $r_{eo} = r_e(0)$. Evidently, since ω_m is not a function of r_e, the equation of motion for electrons starting at all values of $r_e(0)$ is the same. The frequency is the same, so all electrons arrive at the axis that is at $r_e = 0$ at the same time, independent of their initial radius $r_e(0)$. An initially ordered set of electrons thus keeps its ordering, so the radial density distribution of the pinched beam remains uniform, if it started uniform. The r-z trajectories of an initially parallel set of electrons are given by

$$r_e(z) = r_{eo} \cos \beta_m z \tag{7}$$

where

z is the axial distance

$$\beta_m = \frac{\omega_m}{v_b} = \frac{2\pi}{\lambda_m} \tag{8}$$

$$z = v_b t \quad .$$

A set of trajectories according to Equation (7) is given in Figure 2.

We now examine a model that is somewhat closer to the problem of a beam that starts out initially parallel and that is pinched as a whole. This problem has been treated by Lawson.[21] In the preceding calculation we had the problem of the motion of a particle acted on by a force that varied linearly with the radius, because the beam radius was assumed fixed. Here we allow the beam radius to vary with time and we wish to solve for $r_b(t)$. All of the current is contained within r_b and we will start with the assumption that the beam retains its initial ordering, so that whatever is the outer electron at $t = 0$ remains the outer electron. We later check this assumption and find it is indeed consistent with the equations of motion that we obtain.

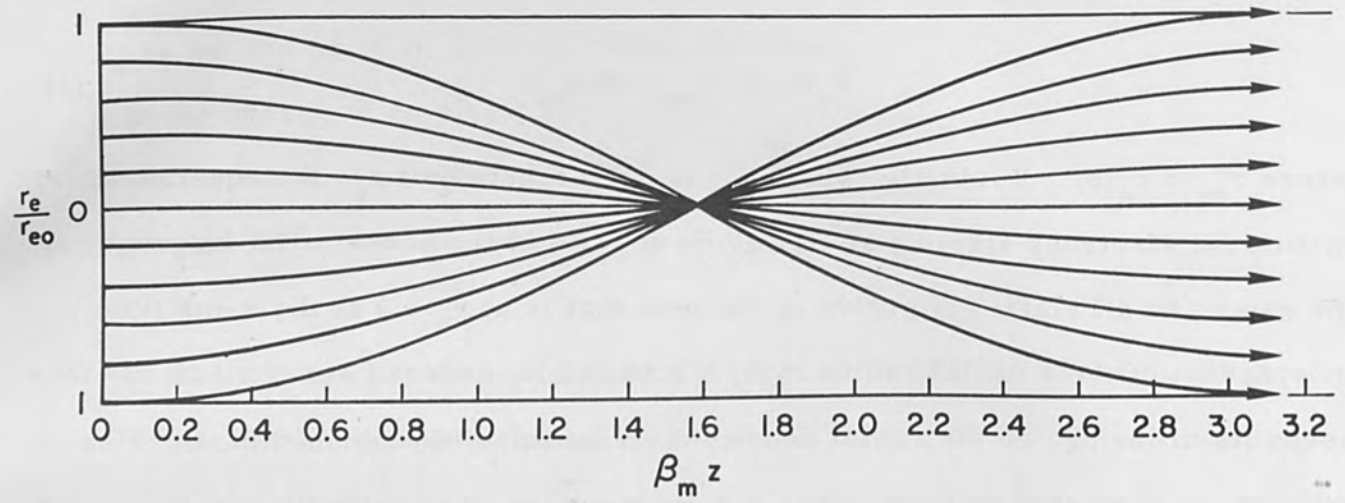

Figure 2 Electron radius as a function of axial distance for electrons in a beam of uniform radius that start initially parallel and are subject to an inward force which increases linearly with the radius. The electrons will oscillate sinusoidally at the same frequency independent of their initial radius, and the radial density distribution of the pinched beam will remain uniform.

The force equation in this case is, for non-relativistic velocities, as before

$$m \frac{d^2 r_e}{dt^2} = F_m \tag{9}$$

but now we take $r_e = r_b$ so that using F_{rm} from Equation (3), Equation (9) can be written in the form

$$\frac{d^2 r_e}{dz^2} = - \frac{\Omega_m^2}{r_e} \tag{10}$$

where we have replaced the time derivative by a space derivative using $(d^2/dt^2) = v_b^2 (d^2/dz^2)$ and where Ω_m is a dimensionless parameter given by

$$\Omega_m^2 = \frac{\mu_o}{4\pi} \left(\frac{2e}{m}\right)^{1/2} \left(\frac{I_b}{V_b^{3/2}} \right) V_b$$

$$= 0.0593 \left(\frac{I_b}{V_b^{3/2}} \right) V_b \qquad (11)$$

$$= \beta_m^2 \, r_b^2 \quad .$$

Lawson[21] has shown that the solution to Equation (10) is an error function that may be written in the following form

$$\beta_m z = \frac{\Omega_m z}{r_{eo}} = (2^{1/2}) \int_o^{\ell n(r_{eo}/r_e)^{1/2}} \exp(-u^2) du \qquad (12)$$

For low velocities and completely neutralized beams our Ω_m^2 is the same as Lawson's (-K). A plot of Equation (12) is given in Figure 3 where this curve is

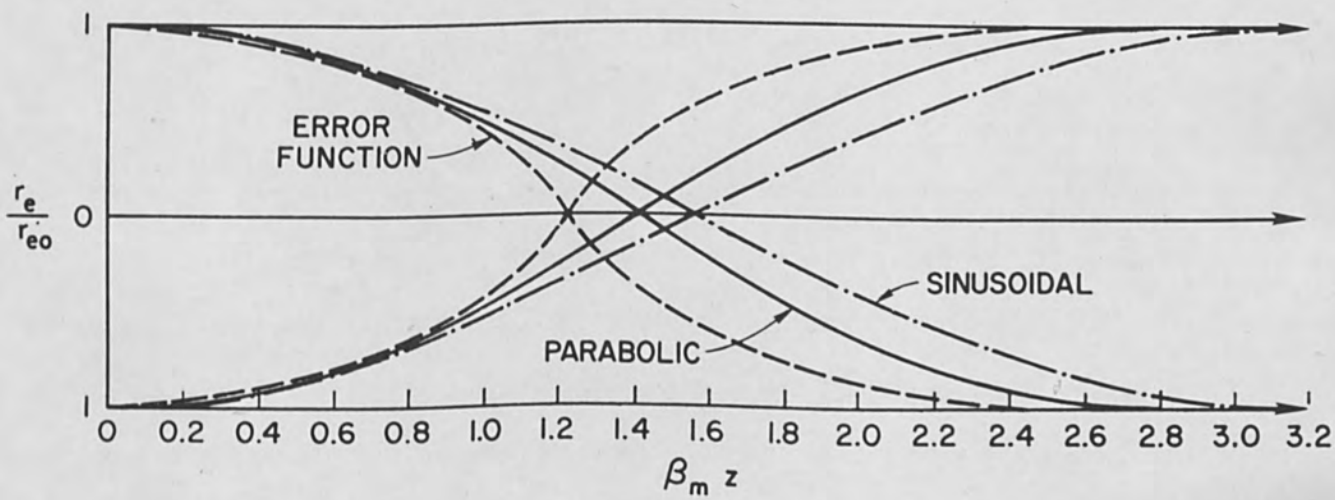

Figure 3 Electron radius as a function of axial distance resulting from different radial force laws: the sinusoidal curve from a force increasing linearly with the radius, the parabolic curve from a constant force independent of the radius, and the error function curve from a force varying inversely with the radius.

compared with a sinusoidal and a parabolic curve. It is of considerable importance that all of these curves are so similar, indicating that the distance to the focus is quite insensitive to the form of the force law. As we have seen, for the magnetic pinch, the force law depends on whether we assume a constant diameter beam or a beam that is pinched as a whole. We have examined the case in which the force increases linearly with the radius which led to the cosine curve for the constant diameter beam and the case in which the force decreases inversely with the radius which led to an error function for the beam pinched as a whole. The parabolic curve of Figure 3 would be the result of a constant force, independent of the radius.

It is also of some interest that Equation (12) predicts a curve of (r_e/r_{eo}) as a function of $\beta_m z$ that is only a function of Ω_m which is a parameter, independent of r_{eo}. Thus, as before, an ordered set of beam radii will stay ordered and all of the beam electron trajectories will have the same shape and cross the axis at the same point. The beam current density distribution will stay uniform if it starts uniform and the outer beam electron is always the initially outer electron.

The Electrostatic Pinch Effect

While the magnetic focusing forces on the beam may be obtained from the beam parameters alone if the beam space charge is assumed to be neutralized, the electrostatic forces are much more difficult to calculate since the radial fields are determined by the distribution of the plasma charge in the space. It can be shown [29-30] that to a good approximation the beam serves only to generate the plasma within the beam cross-section, and that the focusing field is directly proportional to the plasma electron temperature. Here we give only enough of the analysis to allow an understanding of the method used and to allow a discussion of the results.

In order to solve for the electrostatic forces acting on the beam in the presence of the plasma, we define the following model in cylindrical geometry:

1. A static potential V(r) exists which is zero at r = 0 and decreases monotonically with r.

2. The plasma electrons are assumed to be in thermal equilibrium corresponding to the temperature T_e.

3. Ions of mass m_i are generated at a rate G per unit volume per second with zero initial velocity, and drift radially to the wall without collision.

Based on these assumptions, the value of the space charge density at a radius r may be calculated and substituted into Poisson's Equation which is written in cylindrical geometry as

$$\frac{d^2V}{dr^2} + \frac{1}{r}\frac{dV}{dr} = -\frac{e}{\epsilon_o}(n_i - n_e) \tag{13}$$

where e is the electronic charge, ϵ_o the permittivity of free space, and n_e and n_i are the number density of electrons and ions respectively.

The total electron density is given by the sum of the plasma electron density and beam electron density n_b,

$$n_e = n_{eo} \exp\left(\frac{eV}{kT_e}\right) + n_b \tag{14}$$

where n_{eo} is the axial electron number density, V is the potential measured with respect to zero potential at r = 0, k is Boltzmann's constant, and T_e is the electron temperature.

The ion density n_i at r is obtained by summing the ion charge contributions originating from all ξ less than r,

$$n_i = \frac{1}{r}\int_o^r \xi\, dn_i(\xi) = \frac{1}{r}\int_o^r \frac{\xi dJ_i(\xi)}{ev_i(\xi)}$$

where $dJ_i(\xi)$ is the contribution of ion current from ξ which may be related to the generation rate $G(\xi)$ at ξ by

$$dJ_i(\xi) = eG(\xi)d\xi$$

and $v_i(\xi)$ is the velocity at r of ions created at rest at ξ where the potential is V_ξ, and is given by

$$v_i(\xi) = \left(\frac{2e}{m_i}\right)^{1/2} (V_\xi - V)^{1/2} .$$

The above three equations combine to yield for the ion density

$$n_i = \frac{1}{r} \int_o^r \frac{G(\xi)\,\xi\,d\xi}{\left(\frac{2e}{m_i}\right)^{1/2} (V_\xi - V)^{1/2}} . \qquad (15)$$

Substituting Equations (14) and (15) into Poisson's Equation, we obtain

$$\frac{d^2V}{dr^2} + \frac{1}{r}\frac{dV}{dr} = -\frac{e}{\epsilon_o}\left\{\frac{1}{r}\int_o^r \frac{G(\xi)\,\xi\,d\xi}{\left(\frac{2e}{m_i}\right)^{1/2} (V_\xi - V)^{1/2}} - \exp\left(\frac{eV}{kT_e}\right) - n_b\right\} \qquad (16)$$

which may be solved to obtain the potential throughout the space.

Assuming that all of the ionization is caused by beam-neutral collisions, the ion generation rate G(r) may be expressed as

$$G(r) = \frac{J_b(r)Np}{e}$$

where J_b is the beam density, p the gas pressure in mm Hg, e the electron charge, and N the number of ion-electron pairs produced per beam electron per unit length per mm Hg, often called the probability of collision. N is a function of the type of gas and of the beam voltage and may be obtained from the literature.[34-35]

For a beam with uniform density n_b and radius r_c, $G(\xi)$ is a constant for $r \leq r_c$, and zero for $r > r_c$ so that for $r_c < r < r_w$ in Equation (16) the upper limit of integration must be replaced by r_c and the beam density n_b set to zero.

Equation (16) may be simplified by introducing normalized variables, and then

solved as an initial value problem to obtain solutions for the potential in the space. (For a discussion of the normalization and numerical solution, see References 29-30.)

The wall position r_w at potential V_w is determined by the requirement that in equilibrium the rate of ion-electron pair generation must be equal to the ion and electron currents to the wall, so that the net current to either an insulating or conducting wall must be zero. The equilibrium ion current density at the wall may be obtained from the rate of ion generation

$$J_{i_{wall}} = \frac{e}{r_w} \int_o^r G(\xi)\xi d\xi = \frac{J_b N p r_c^2}{2 r_w} \quad . \tag{17}$$

while the outwardly directed random electron current density, is given by

$$J_{e_{wall}} = n_{eo} e \left(\frac{kT_e}{2\pi m_e} \right)^{1/2} \exp \left(\frac{eV_w}{kT_e} \right) \quad . \tag{18}$$

Solving Equation (16) and equating Equations (17) and (18) after introducing normalized variables leads to a family of curves for the possible potential profiles in the space, each profile being characterized by a dimensionless parameter α. As an illustration of the type of solution obtained when the beam partially fills the space so that plasma generation is restricted to a small central portion of the tube, the radial variation in potential for different values of α for the case of an electron beam in argon with $r_w/r_c = 8$ is shown in Figure 4. The smaller values of α (e.g. $10^{-3/2}$) represent a plasma many times denser than the beam so that the effect of the beam density term in Equation (16) may be neglected. For larger values of α (e.g. $10^{-1/2}$), the beam and plasma density may be comparable and the effect of including finite beam space charge in Equation (16) is shown in the figure.

In these solutions, a low-potential sheath is seen to form at the edge of the beam which is separated by a region of slowly varying potential from a second,

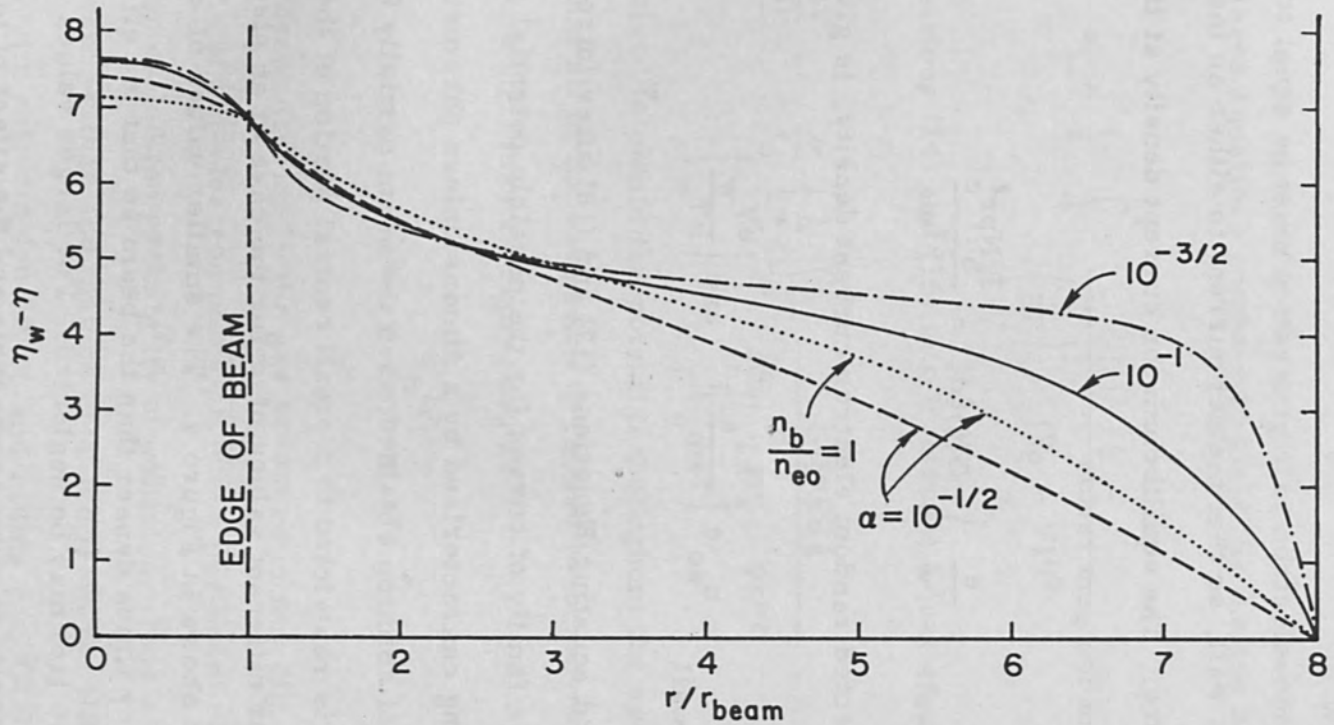

Figure 4 Representative radial potential profiles satisfying Poisson's Equation and zero total current to the walls, calculated for an electron beam with a radius one-eighth of the tube radius, in argon. Here $\eta_w - \eta = e(V - V_w)/kT$, is the normalized potential with respect to the wall. The parameter α is related to the plasma electron density on the axis.

higher-potential sheath at the wall. For a different gas, the profiles would be the same except for a change in the height of the sheath at the wall, while for a different ratio of r_w/r_c the height of the beam and wall sheaths remains constant and only the length of the region of slowly-varying potential outside the beam changes. The potential in the region of the beam is seen to vary only slightly with α and to have a total drop of slightly less than (kT_e/e) volts from the axis to the edge of the beam.

The parameter α for a given experiment may be calculated either from

$$\alpha = \left\{ \frac{J_b Np}{e^2} \quad (\epsilon_o m_i)^{1/2} \right\} \frac{1}{n_{eo}^{3/2}} \tag{19}$$

which relates α to the axial plasma density in terms of measurable experimental parameters, or by

$$\alpha^2 = \left[\frac{8\pi^2 e \epsilon_o^2}{m_i} \right]^{1/2} \frac{s_c^3}{Npr_c I_b} \left(\frac{kT_e}{e} \right)^{3/2} \tag{20}$$

which relates α to the plasma electron temperature. The quantity s_c appearing in Equation (20) is a number obtained from solving Equation (16), and is dependent on α and on the ratio r_w/r_c. It has a value between 0.6 and 0.8 for typical conditions.

Equation (20) has been plotted in Figure 5 in such a way as to allow an approximate value of α to be determined if the plasma electron temperature and the experimental parameters N, p, r_c, m_i and beam current I_b are known. As an example, consider a 5000 volt, 100 ma beam $\left(\frac{I_b}{V_b^{3/2}} \cong 3 \times 10^{-6} \right)$ of 3 mm diameter drifting in a 1" diameter tube in argon at 2×10^{-3} Torr. At 5 kv, Reference [34] gives N = 0.79, so for the above conditions

$$Npr_c m_i^{1/2} I_b \times 10^6 = (0.79)(2 \times 10^{-3})(0.15)(40)^{1/2}(10^{-1}) \times 10^6 = 150$$

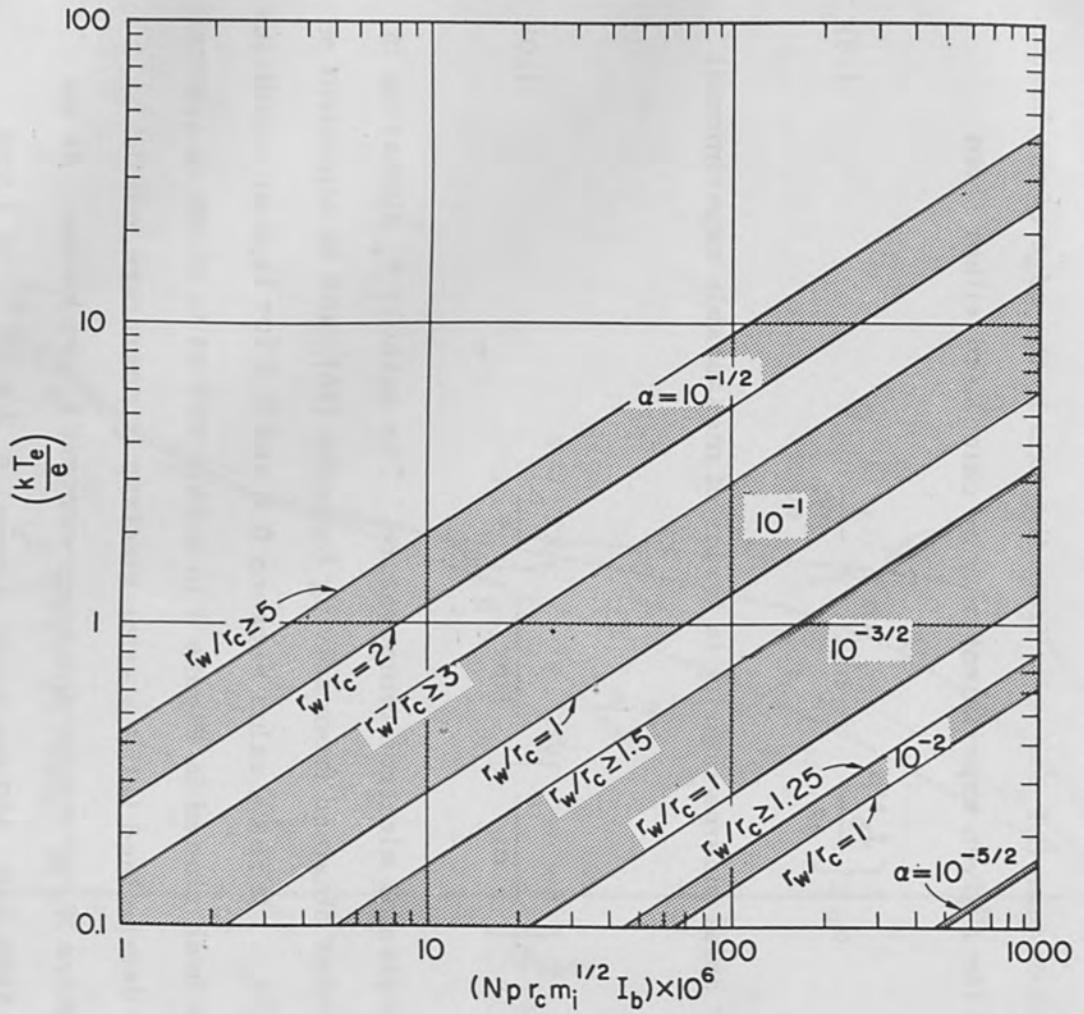

Figure 5 Plasma electron temperature in volts vs. the product $(Npr_c m_i^{1/2} I_b) \times 10^6$ of the experimental parameters $N(Torr^{-1}\text{-}cm^{-1})$, p(pressure, Torr), r_c(beam radius, cm), m_i (ion mass, a.m.u.), and I_b (beam current, amps), for various values of α and various ratios of wall radius to beam radius (r_w/r_c); from Equation (20).

and we see from Figure 5 that a plasma electron temperature in the range of 1 to 12 volts will correspond to values of α of $10^{-3/2}$ to $10^{-1/2}$. Since $r_w/r_c = 8$ for this case, the potential in the space will appear as shown in Figure 4.

Of primary importance in considering electrostatic pinch effects is the electric field acting on the beam as a result of the formation of the plasma in the space. This field may be obtained from the potential calculations discussed above and is shown in Figure 6 for the interesting range of α. As has been mentioned, the potential variation within the beam for a given value of α is independent of the particular type of gas and of the ratio of beam radius to wall radius. This allows us to consider the behavior of the beam when acted upon by the electric fields without having to consider further the plasma and fields existing outside the beam.

The electric fields in Figure 6 have been obtained by assuming a uniform beam of fixed diameter to generate the plasma. In the following discussion we shall consider the case of a pinched beam of continually varying radius. We do so in an approximate manner, assuming that the field given in Figure 6 is correct for a pinched beam as well as a constant diameter beam, i.e. we assume that the field acting on the outer electron is independent of the radius, and that the field varies with the radius as in Figure 6.

Beam trajectories have been calculated on a computer using a forward integration technique for a beam subject to the focusing fields of Figure 6. For beam electrons moving in an exactly parabolic potential, this calculation would result in a parabolic beam profile as shown in Figure 3 and all electrons would be focused to the same point, as in Figure 2, and the focus would repeat. The results of calculations based on the actual electrostatic focusing fields are shown in Figure 7 for three different focusing fields. In each case the maximum beam diameter is unchanged despite periodic necking down of the beam to form focus points. The smaller α (denser plasma) fields focus the beam rapidly due to the non-linear

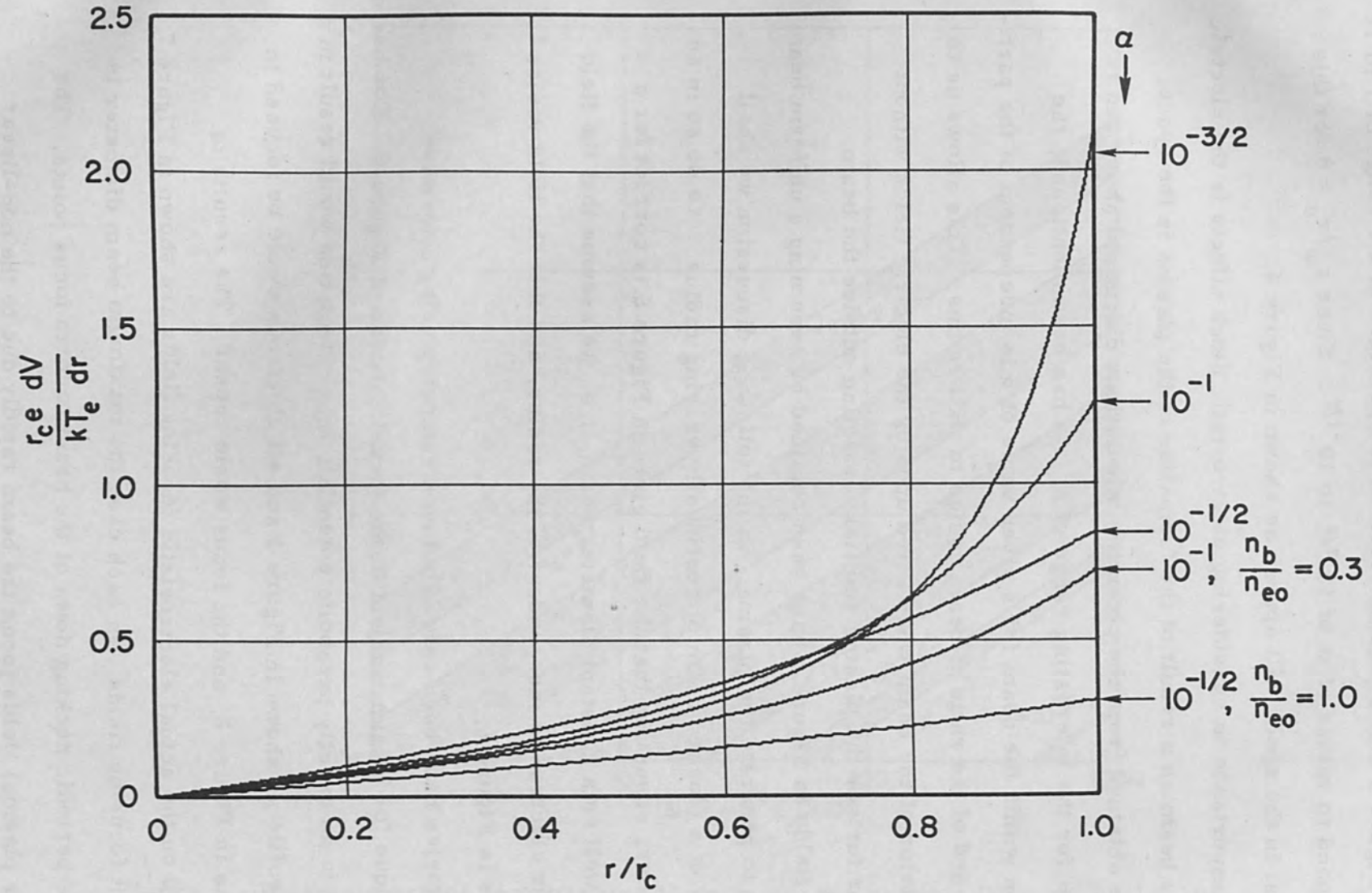

Figure 6 The radial electric field acting on the beam is shown as a function of the radius, for several values of α. For a dense plasma (small α) the electric field increases sharply near the beam edge, while for a lower density plasma (larger α) the field varies almost linearly with the radius.

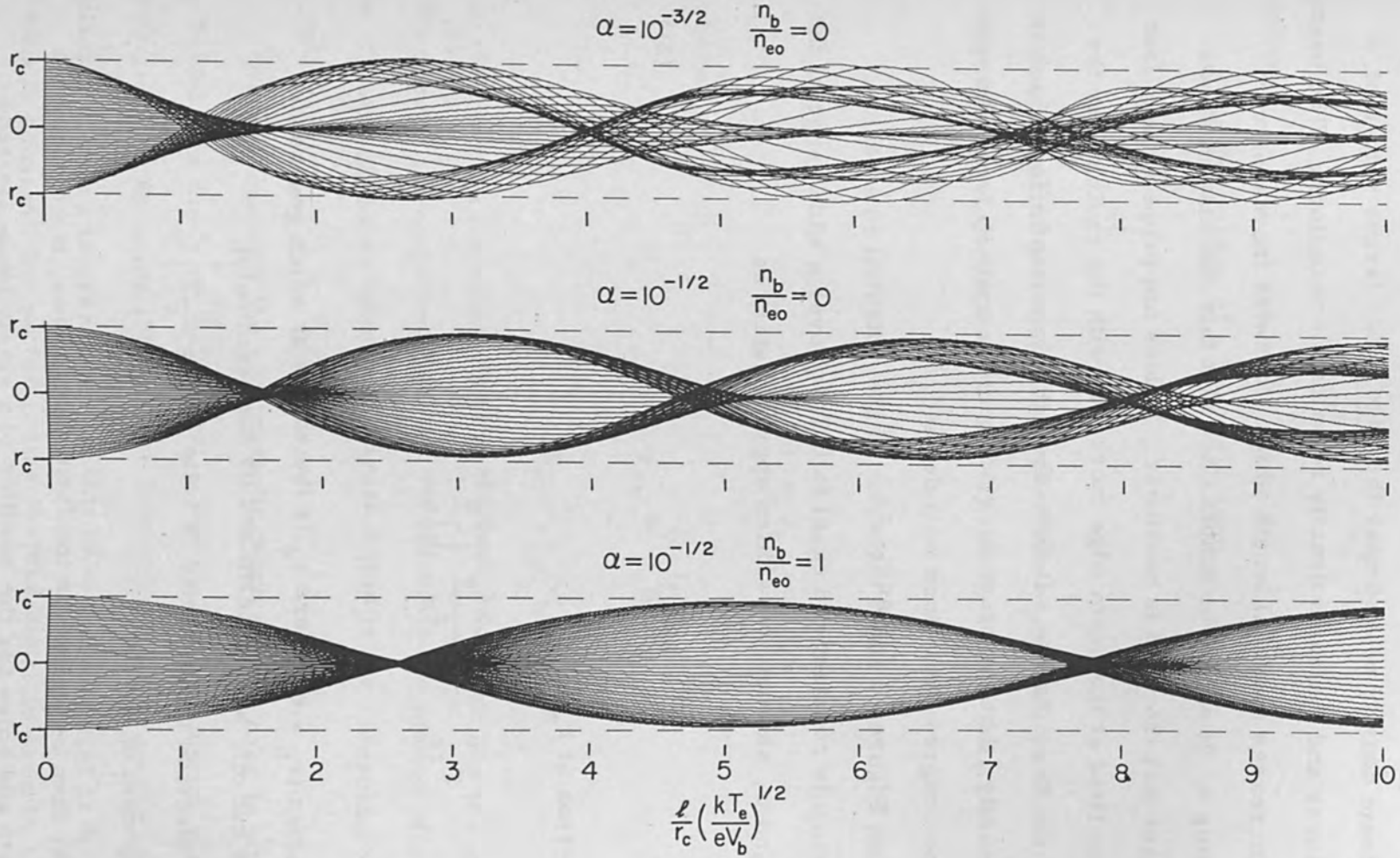

Figure 7 Electron radius as a function of axial distance for several values of α, assuming that the fields shown in Figure 6 act on the outermost beam electron independent of its radius. Due to the field nonlinearity, the beam density does not remain uniform and the beam does not come to a sharp focus.

increase in the electric field near the beam edge (see Figure 6), and produce a semi-hollow beam with the beam density peaked near the edge. For larger values of α the fields are nearly linear and the beam density remains more uniform. The beam space charge greatly increases the focal length which otherwise increases very gradually with increasing α. It should be emphasized that this calculation shows only the effect of the fact that the field is nonlinear. It does not properly take into account the fact that the field at the beam edge increases with the radius, nor the fact that α varies with the beam radius. It does show the important effect which is due to the field nonlinearity, that the beam does not come to a sharp focus and that successive foci become progressively less well defined.

As we can see from Figures 4 and 6 the value of the potential in a beam-generated plasma is roughly constant and equal to (kT_e/e) over a wide range of the parameters (n_b/n_{eo}) and α, and may be written approximately as

$$V = \left(\frac{r}{r_b}\right)^2 V_e \quad . \tag{21}$$

So the force on an electron at r_e is

$$F_{re} = - \frac{2eV_e}{r_b} \left(\frac{r_e}{r_b}\right) \tag{22}$$

where

r_b is the beam radius ($r_b = r_c$ where r_c is the radius at which generation of plasma is cut off, here determined by the beam only),

V_e is the plasma electron temperature in volts $\left(V_e = \frac{kT_e}{e}\right)$,

F_{re} is the r-component of the force.

The force equation may then be written in the form that follows, if we assume a constant diameter beam and solve for the position of a single beam electron

$$\frac{d^2 r_e}{dt^2} = -\omega_e^2 \, r_e \quad , \tag{23}$$

where

r_e is the radius of a beam electron

$$\omega_e^2 = \frac{2e}{m} \frac{V_e}{r_b^2} \quad .$$

The equations of motion for this case can be written in the same forms as for the magnetic case, Equations (6) and (7), using $\dot{r}_e(0) = 0$ as before

$$\begin{aligned} r_e(t) &= r_{eo} \cos \omega_e t \\ r_e(z) &= r_{eo} \cos \beta_e z \quad , \end{aligned} \tag{24}$$

where

$$\begin{aligned} r_{eo} &= r_e(0) \\ \beta_e &= \omega_e / v_b \quad . \end{aligned} \tag{25}$$

So the electron trajectory for the electrostatic pinch has the same exact equation as the one for the magnetic pinch, if we calculate the motion of a single particle within a constant diameter beam. In Figure 3 this is the sinusoidal trajectory with β_m replaced by β_e.

We now examine the electrostatic pinch for the case in which the beam is pinched as a whole so that $r_e = r_b$, making the assumption that the field and potential are given by Equation (21) and are determined solely by the beam radius and the plasma electron temperature. In this case the potential at the outer surface of the beam is constant, but as the radius shrinks the field seen by an electron at r_b increases linearly, just as in the magnetic case. The force equation can then be

written in the same form as Equation (10)

$$\frac{d^2 r_e}{dz^2} = -\frac{\Omega_e^2}{r_e} \tag{26}$$

where

$$\Omega_e^2 = \frac{2eV_e}{m v_b^2} = \frac{V_e}{V_b} = \beta_e^2 r_b^2 \tag{27}$$

and where the solution to the equation of motion is an error function given, by analogy to Equation (12), as

$$\frac{\Omega_e z}{r_{eo}} = \beta_e z = (2^{1/2}) \int_o^{\ell n (r_{eo}/r_e)^{1/2}} \exp(-u^2)\, du \tag{28}$$

And again Figure 3 can be considered a plot of the electrostatic pinch if the scale is changed from $\beta_m z$ to $\beta_e z$ and the curve marked error function is used.

A Comparison of the Electrostatic and Magnetic Pinch Effects

As we have seen, the electrostatic and magnetic pinch effects result from inward forces on the beam electrons that can be described approximately by motion in a parabolic potential well that shrinks in radius with the beam, so that the outer electron of the beam sees a force that increases linearly as the radius decreases. The beam, according to these approximate theories, reaches a focus at a distance ℓ from an injection plane at which the beam is parallel, after traversing a curve of r vs. z that can be described by an error function. Here we examine the variation of the force on an outer beam electron and the distance to the first focus as a function of the beam parameters for both types of pinch effect. We find that the variation of both force and distance to first focus with beam voltage is quite different

for the two effects and should be observable experimentally, even though the shape of the beam profile may not be very different for the two effects.

From Equations (3), (11) and (22) we have the values of the magnetic and electric forces on the outer beam electron in terms of the beam parameters and the plasma electron temperature, which may be expressed as

$$-\left(\frac{r_b}{2e}\right) F_{rm} = 0.0593 \left(\frac{I_b}{V_b^{3/2}}\right) V_b^2$$

$$-\left(\frac{r_b}{2e}\right) F_{re} = V_e = \frac{kT_e}{e} \qquad (29)$$

Figure 8 is a plot of normalized force vs. beam voltage for several values of plasma electron temperature and beam perveance. The way the force has been normalized in Equation (29) it is expressed as a potential in volts. The electrostatic pinch force is independent of the beam voltage and much larger than the magnetic force at low voltages. The magnetic pinch force is proportional to the square of the beam voltage and is much larger than the electrostatic force at high beam voltages. For a typical case of a beam with a perveance of 10^{-7} and a plasma with a 1 volt temperature we might expect to follow the dashed line in Figure 8 between the two appropriate asymptotes defined by Equation (29).

The distance ℓ_f to the first focus for the magnetic case (ℓ_{fm}) and for the electrostatic case (ℓ_{fe}) may be obtained as follows:

From Figure 3 we read

$$\beta_m \ell_{fm} = \beta_e \ell_{fe} = 1.24$$

Substituting this in Equations (12) and (28), we obtain

$$\frac{\Omega_m \ell_{fm}}{r_b} = 1.24 \quad \text{and} \quad \frac{\Omega_e \ell_{fe}}{r_b} = 1.24$$

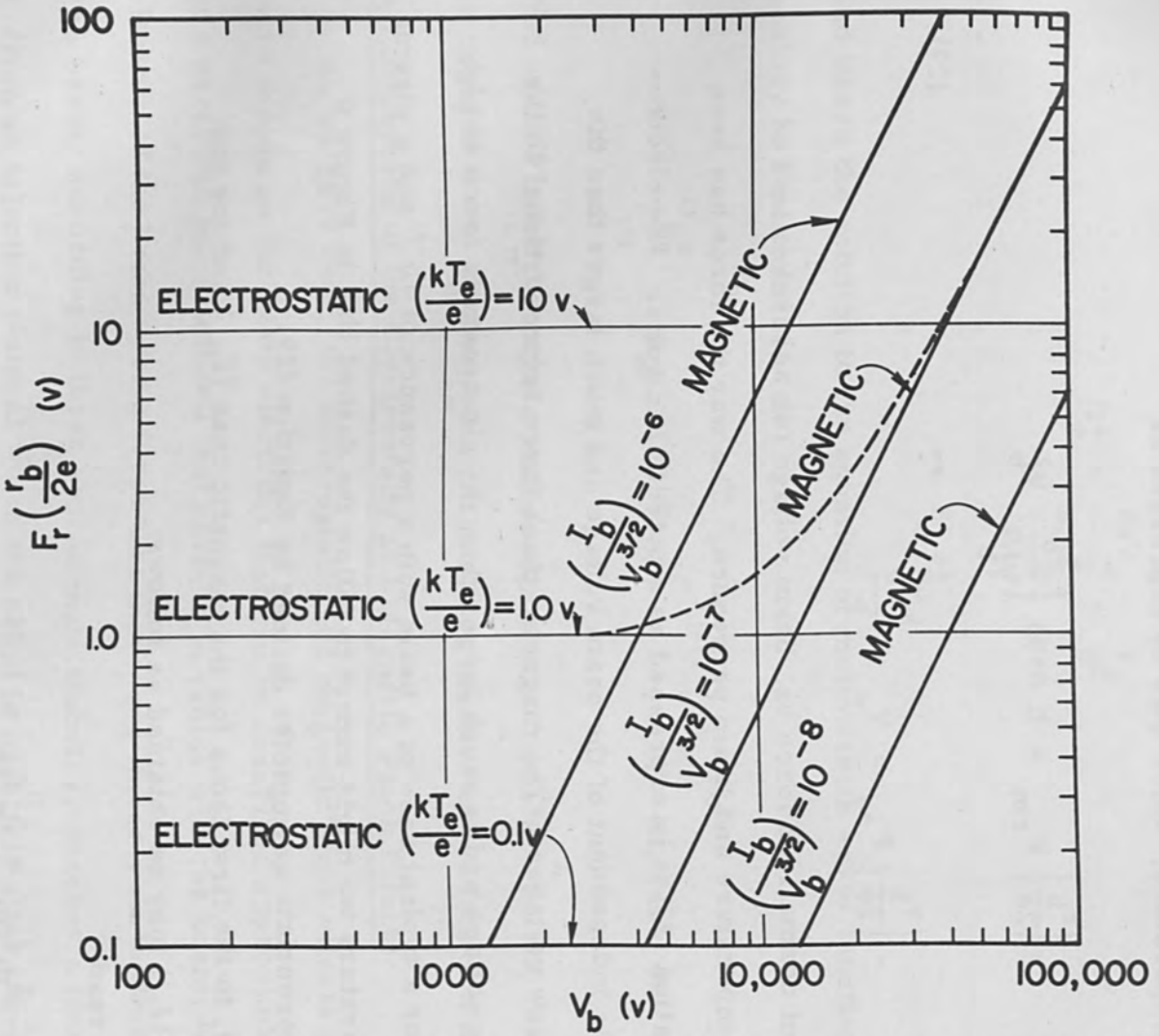

Figure 8 Normalized electrostatic and magnetic pinch forces as a function of beam voltage V_b for several values of plasma electron temperature and beam perveance. The electrostatic pinch force is independent of V_b and is much larger than the magnetic force at low beam voltages. The magnetic pinch force is proportional to V_b^2 and is much larger than the electrostatic force at high beam voltages.

But, from Equation (11) and Equation (27) we have

$$\Omega_m = \sqrt{0.0593}\left(\frac{I_b}{V_b^{3/2}}\right)^{1/2} V_b^{1/2} \quad \text{and} \quad \Omega_e = \left(\frac{V_e}{V_b}\right)^{1/2}$$

Therefore

$$\frac{\ell_{fm}}{r_b} = \frac{5.1}{\left(\frac{I_b}{V_b^{3/2}}\right)^{1/2} V_b^{1/2}} \quad \text{and} \quad \frac{\ell_{fe}}{r_b} = 1.24\left(\frac{V_b}{V_e}\right)^{1/2} . \tag{30}$$

Figure 9 is a plot of (ℓ_f/r_b) vs. beam voltage V_b for several values of electron temperature and beam perveance, according to Equation (30). It is seen that the value of ℓ_f for the electrostatic pinch increases with the beam voltage while for the magnetic pinch the value of ℓ_f decreases as the beam voltage is increased. As before, a typical case of a 1 volt temperature and a perveance 10^{-7} beam has been followed and the dashed line is an estimate of the value of (ℓ_f/r_b) between the two asymptotes defined by Equation (30).

Evidently an experiment should show up a value of (ℓ_f/r_b) that increases with voltage at low voltages and such an experiment is described in the next section. At high voltages (ℓ_f/r_b) should start to decrease, and an observation of this condition should be a conclusive proof that the magnetic pinch is the dominant effect in that region.

Experimental Studies of the Electrostatic Pinch

Experimental work on electrostatic pinch effects has been carried out in our laboratory both to provide experimental verification of the theory discussed above and to investigate some of the practical problems in establishing and controlling pinched beams. The results presented below are chosen to illustrate the type of focusing effects which are observed and to indicate the success with which the theory has been applied to explain these effects.

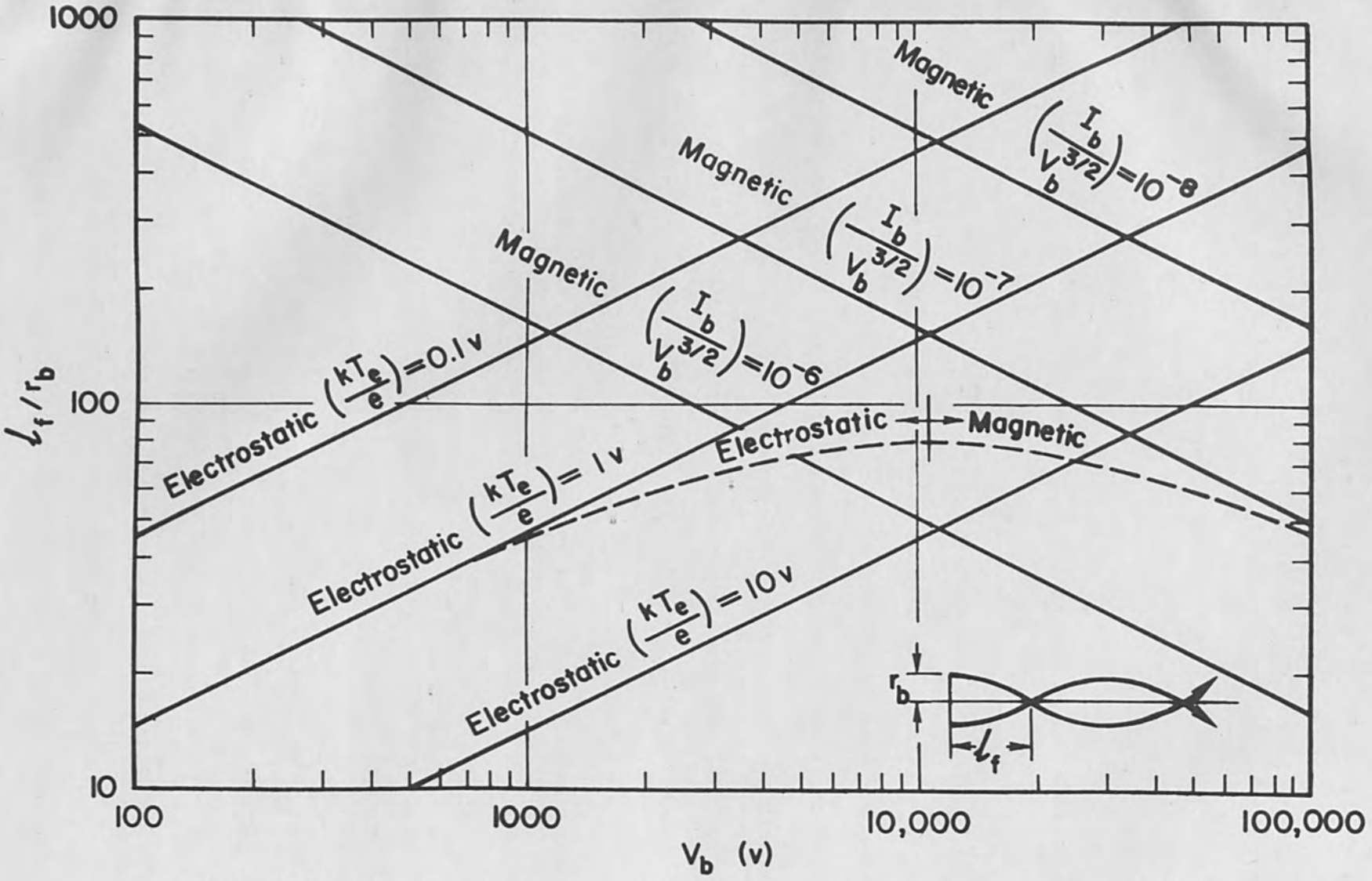

Figure 9 Plot of the distance to the first focus, ℓ_f, in beam radii r_b as a function of beam voltage V_b for several values of electron temperature and beam perveance. The value of ℓ_f for the electrostatic pinch increases with the beam voltage while for the magnetic pinch the value of ℓ_f decreases as V_b is increased.

The experimental apparatus is shown in Figure 10. The target gas, collector, and probing arms are enclosed in an 18-inch diameter pyrex bell jar 22 inches in height and capped top and bottom with 1 inch thick stainless steel plates.

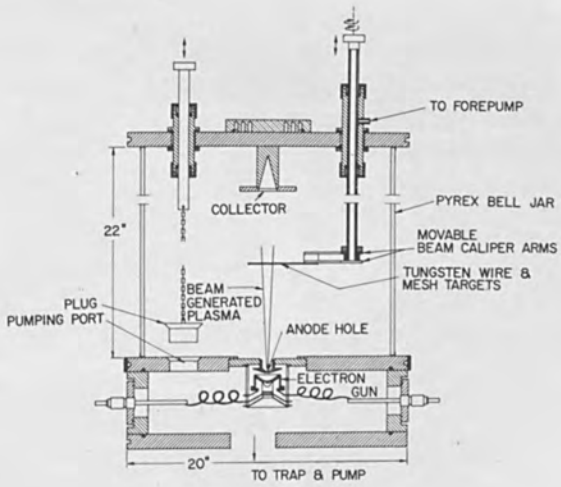

Figure 10 The experimental apparatus used to investigate electron beam pinch effects in a beam-generated plasma.

A Pierce gun located below the base plate introduces an electron beam with a perveance of 0.3×10^{-6} into the target gas chamber. The convergence of the electron gun may be varied from 0° to 3° by changing the anode to cathode spacing, and the beam voltage may be varied from 0 to 8 kv. The electron emitter is a tantalum button 0.3 inches in diameter, heated by electron bombardment from a tungsten filament. The gun construction is of a standard, stacked ceramic, conically supported design.

Thermocouple and ionization gauges to measure the pressure are mounted on the top plate along with an adjustable leak valve for varying the target gas pressure. The rate of pumping from the space is controlled by raising or lowering a plug in the lower plate. The target gas pressure may be varied from 2×10^{-7} to 10^{-2} Torr.

Two caliper arms may be moved within the space so as to intercept the beam,

and fine tungsten wires fastened to the arms indicate the beam contour and current density by their incandescence.

To maximize the radial pinching force acting on the beam, the flow of ions from the beam should be purely radial since the same fields which accelerate the ions toward the wall also pinch the beam toward the axis. To enhance the radial flow of the ions, open-ended glass, mesh, or metal tubes of up to 2-1/2 inch diameter can be mounted coaxially surrounding the beam by means of a metal and ceramic stand as shown in Figure 11.

In experiments using argon as a target gas, electrostatic pinch effects have been observed at pressures of 10^{-4} to 4×10^{-3} Torr. At these pressures the electron beam is clearly defined by a blue-violet colored region arising from atomic excitation of neutrals by the high-energy beam electrons. The radius of the beam observed in this way agrees with measurements based on the incandescence of the tungsten mesh on the caliper arms. The beam profile is conveniently photographed using a dark blue filter to eliminate the bluish-white plasma glow from atomic excitation by the low energy plasma electrons and the background light emitted by the white-hot cathode.

Photographs of pinched beams obtained in this manner are contained in Figures 12 and 13. In the upper two photographs of Figure 12, the electron beam which is normally 2 to 3 mm in diameter has been purposely defocused near the anode to increase the beam diameter so that the periodic focus points may be observed. The focus points on a normal, small diameter gas-focused beam may be observed visually but are difficult to photograph, as shown in Figure 12c.

The variation of the focus length with beam voltage, current, and gas pressure is as predicted by the theory. The focus point may be adjusted over a range of several inches by small changes in the beam parameters or in the gas pressure. As an example, the effect on the focus point of varying the gas pressure is shown

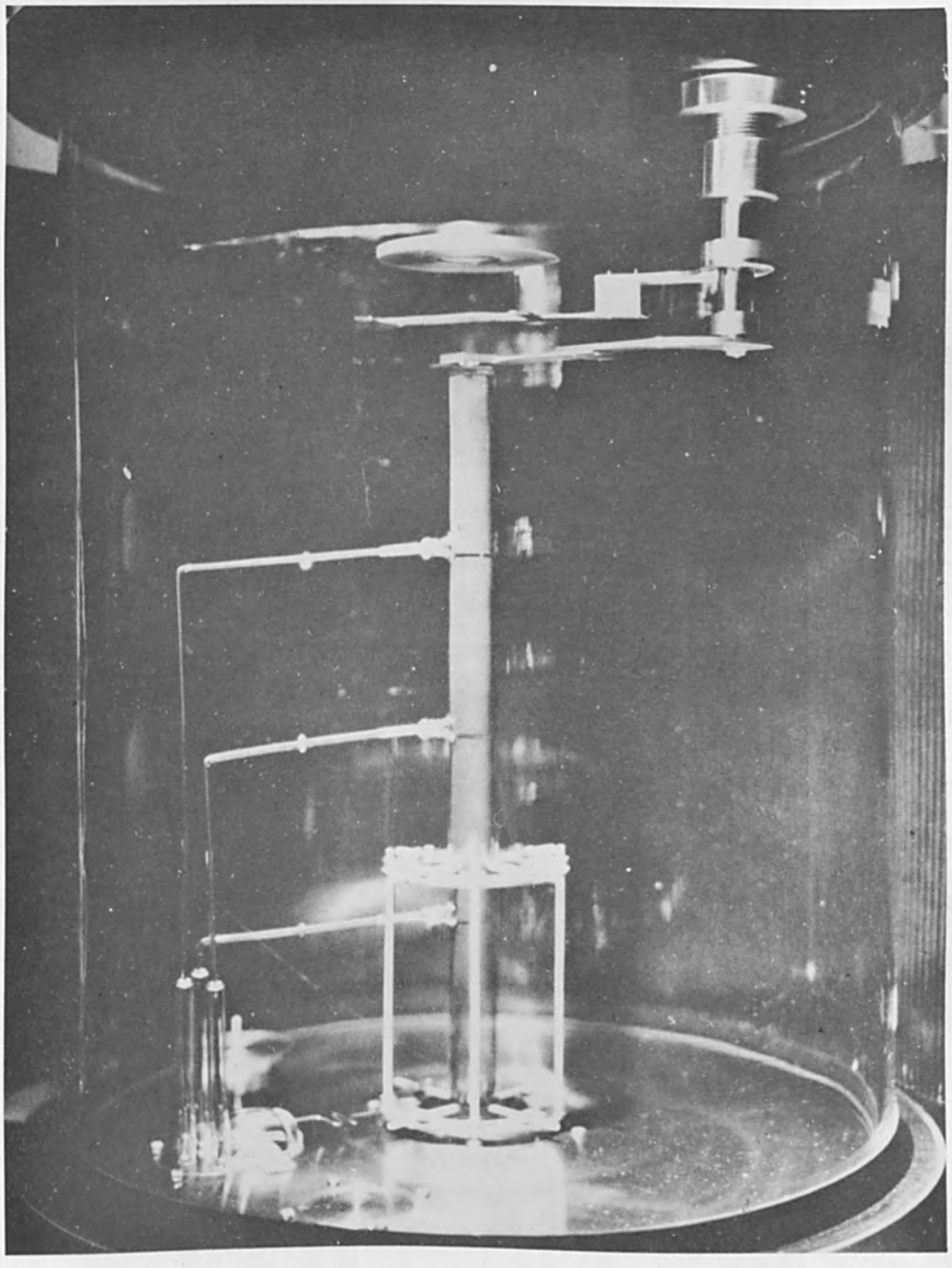

Figure 11 Metal or dielectric tubes of various diameters may be mounted coaxially with the beam within the bell jar. In this case a 16 inch long, 1 inch diameter glass tube in which are mounted four sections of metal mesh is shown. Such an arrangement allows separate voltages and currents to be monitored along the axis of the tube.

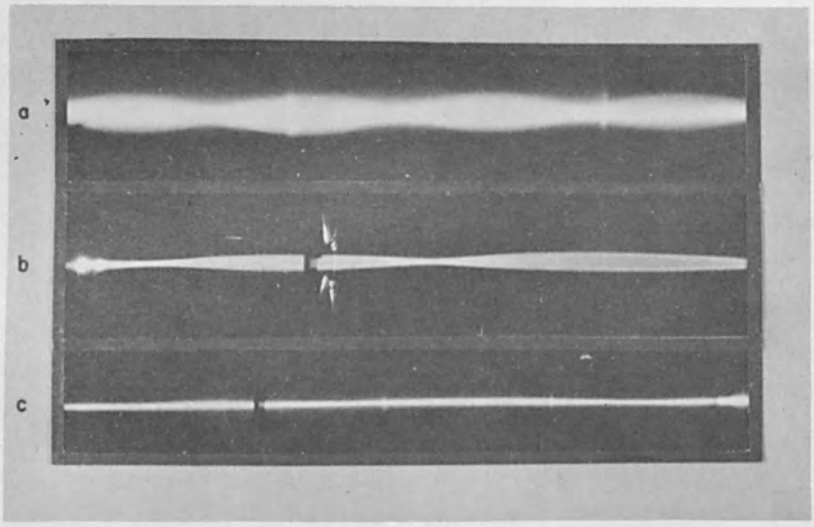

Figure 12 The profiles of gas focused electron beams may be conveniently observed by the light emitted by atoms excited by collisions with the high energy beam electrons, as shown by these photographs of pinched beams in argon at pressures of about 10^{-3} Torr. (a) A 700v pinched beam drifting in the mesh-lined tube of Figure 11. (b) A 320v beam without any surrounding tube. The pinching force is less than for (a) because of axial drainage of ions from the beam. (c) A focused 4000v beam which is launched parallel to the axis.

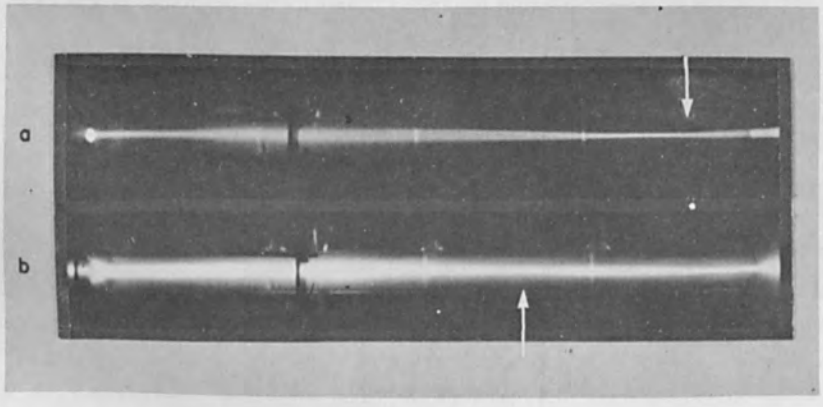

Figure 13 The length to the focus point of a pinched beam may be varied by changing the beam parameters or the gas pressure. Here the focus point of a 5000v beam, as indicated by the arrow, is shortened by increasing the gas pressure from 10^{-3} Torr in (a) to 2×10^{-3} Torr in (b).

in Figure 13.

When the tungsten mesh is used to observe the beam density at a point midway between focus points under small α conditions, a donut-shaped incandescent pattern is obtained, indicating a hollow beam. For large α the beam density appears uniform. This behavior is in agreement with the calculated beam trajectories of Figure 7.

Measurements of the potential surrounding a low-voltage gas focused beam reported by Rollwagen in 1934[14] are shown in Figure 14. In his experiment $r_w/r_c = 35$ so that the region between the beam and the wall sheath is longer than for the computed curves of Figure 4.

An important quantity which may be measured and compared with the theory is the value of the pressure required for different gases to give an equal radial focusing force on the beam. An experiment may be conducted to measure this quantity by holding the beam voltage and current constant and adjusting the pressure for each different gas until the same beam profile is obtained. If we assume that in these equilibrium states the plasma electron temperatures are equal for the different gases, then in each case we are adjusting the pressure to obtain the same value of α. Under these conditions, Equation (20) may be written as

$$f(\alpha) = \frac{\alpha^2}{s_c^3} = \frac{(\text{const.})}{N p m_i^{1/2}}$$

so that we would expect from the theory that the product $(Npm_i^{1/2})$ should be a constant for each gas.

Such an experiment as described above was carried out by Richter in 1933[12] in which the focusing of a 350 v. beam was observed in five gases. The observed range of pressure to observe similar focusing effects in the different gases is shown in Table I.

The calculated value of the product $(Npm_i^{1/2})$ is shown to be relatively constant

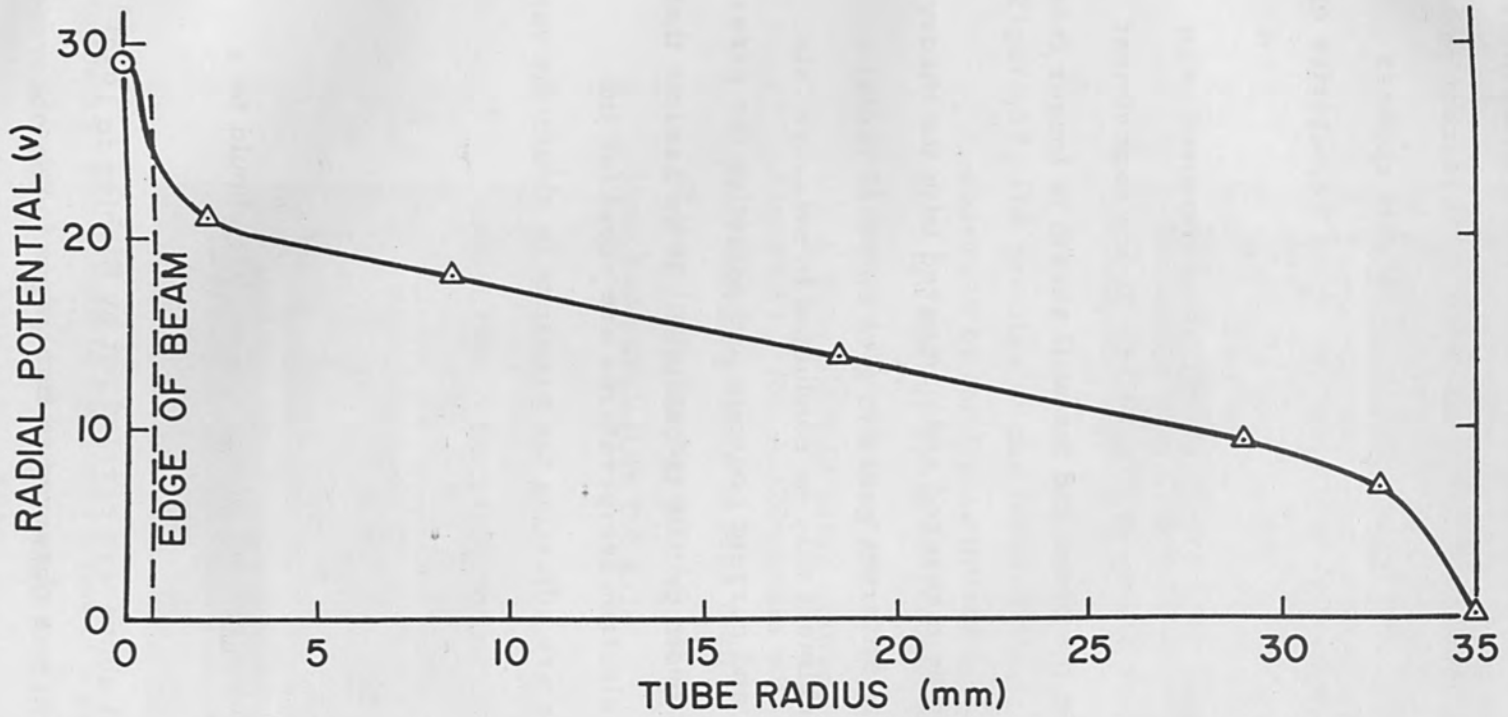

Data from W. Rollwagen
ZS f. Phys., 89, 395 (1934)

Figure 14 Measured values of the potential distribution surrounding a low-voltage (212v) gas focused beam in argon at $p \approx 10^{-3}$ Torr. The data points marked by triangles were obtained using an incandescent probe to measure the space potential, while the data point indicating the value of the potential on the axis was obtained by measuring the maximum radial ion velocity at the wall using a Faraday cage. This curve should be compared with the theoretical potential profiles of Figure 4.

TABLE I

TYPE OF GAS	N $(Torr-cm)^{-1}$	m_i (a.m.u.)	p^* $(Torr \times 10^{-3})$	$Np\sqrt{m_i}$
H_2	1.8	2	8–10	21–26
H_e	0.9	4	19–20	34–36
N_e	2.3	20	4.6–5.4	47–56
N_2	7.0	28	0.8–1.6	29–58
A	6.8	40	0.9–1.1	38–43
AMOUNT OF VARIATION	8/1	20/1	1/20	2/1

*Data from E. F. Richter, Physik. Zeitschr. 34, 457 (1933)

as compared to the amount of variation of the individual quantities, indicating that indeed the plasma electron temperature is nearly constant from gas to gas as assumed.

Conclusion

Kilovolt electron beams that can be started with their initial velocities nearly parallel to the axis in a gas at pressures up to the order of 10^{-2} Torr will be pinched either by the electrostatic or magnetic pinch effect described and compared in detail in this paper. Experimental data demonstrating the electrostatic pinch at voltages up to 5 kv has been presented and the effect has been observed up to the limit of the power supplies used (8 kv). A criterion for determining which effect is the dominant pinching force has been shown to be the variation of the distance to the first focus with the beam voltage. If the focal length increases with increasing beam voltage, the electrostatic pinch effect is dominant; if the focal length decreases with increasing beam voltage, the magnetic pinch is dominant.

The results are of interest in explaining some of the effects observed in beam melting and welding systems in which a gas pressure of the order of 10^{-3} Torr is used in the heating chamber.[36] These results can also be used to explain some of the behavior of electron beams in beam welding and beam penetration of thick slabs of metal in which a beam generated plasma is established within the vaporized metal.

Acknowledgement

The authors wish to acknowledge the contributions of R. P. Lagerstrom to the design of the experiment described.

References

1. Johnson, J. B., "A Low Voltage Cathode Ray Oscillograph", J. Optical Society of America, 6, 701 (1922)

2. Buchta, J. W., "A Low-Voltage Electron-Beam Oscillograph", J. Optical Society of America, 10, 581 (1925).

3. Arnot, F. L., "The Passage of an Electron Beam Through a Field-Free Enclosure", Proc. Roy. Soc. London, 129, 361 (1930).

4. Brüche, E., and W. Ende, "Filamentary, Visable Electron Beams", ZS f. Phys., 64, 186 (1930).

5. Ende, W., "Gas Focusing of Electron Beams", Phys. ZS, 32, 942 (1931).

6. Rogowski and Graupner, "Gas Concentration of Electron Beams", Arch. f. Elektrot, 26, 807 (1932).

7. Engel, K., "Comments on the Space Charge Field of a Gas-Focused Electron Beam", ZS f. Phys., 79, 231 (1932).

8. Brüche, E., "The Geometry of Acceleration Fields and Their Importance in Gas-Focused Electron Beams", ZS f. Phys., 78, 26 (1932).

9. Brüche, E., "Bending Electron Beams", ZS f. Phys., 78, 177 (1932).

10. Siebertz, K., "On e/m Measurements Using a Filamentary Beam", Phys. ZS, 33, 895 (1932).

11. Scherzer, O., "Theory of Gas-Focusing of Electron Streams", ZS f. Phys., 82, 697 (1933).

12. Richter, E. F., "The Dependence of Electron Beam Focusing on the Type of Gas", Phys. ZS, 34, 457 (1933).

13. Brüche, E., "Electron Beams and Gas Discharges", Ann. d. Phys., 16, 377 (1933).

14. Rollwagen, W., "Potential Measurements of a Filamentary Beam", ZS f. Phys., 89, 395 (1934).

15. Zinke, E., "Space Charge Phenomena in Gas-Focused Electron Beams", Ph. D. Dissertation, Friedrich-Wilhelms University, Berlin, 19 Dec. 1935.

16. Bakhrakh, Denisov, and Kiryashkin, "Some Characteristics of Ion Focusing of

Electron Beams", Radio Eng. and Electr. Physics (USSR), 7, 1096 (1962).

17. Bakhrakh, I. E. and P. A. Turlov, "Ion Focusing of a Hollow Cylindrical Electron Beam", Radio Eng. and Electr. Physics (USSR), 7, 1310 (1962).
18. Berezin, Stupak, Bolotin, and Berezina, "Transmission of Intense Pulsed Electron Beams Through Dielectric Tubes", Part I and II, Soviet Physics-Technical Physics, 7, 431 (1962).
19. Bennett, W. H., "Magnetically Self-Focusing Streams", Phys. Rev., 45, 890 (1934).
20. Bennett, W. H., "Self-Focusing Streams", Phys. Rev., 98, 1584 (1955).
21. Lawson, J. D., "Perveance and the Bennett Pinch Relation in Partially Neutralized Electron Beams", J. Electronics and Control, 5, 146 (1958).
22. Lawson, J. D., "On the Adiabatic Self-Constriction of an Accelerated Electron Beam Neutralized by Positive Ions", J. Electronics and Control, 3, 587 (1957).
23. Rose, D. J., and M. Clark, Jr, "Plasmas and Controlled Fusion", Wiley, 1961.
24. Field, L. M., R. Helm, K. Spangenberg, "Control of Electron-Beam Dispersion at High Vacuum by Ions", Elec. Commun., 24, 108 (1947).
25. Linder, E. G., and K. G. Hernqvist, "Space-Charge Effects in Electron Beams and Their Reduction by Positive Ion Trapping", J. Applied Physics, 21, 1088 (1950).
26. Ginzton, E. L., and B. H. Wadia, "Positive Ion Trapping in Electron Beams", Proc. IRE, 42, 1548 (1954).
27. Hines, M. E., G. W. Hoffman, and J. A. Saloom, "Positive Ion Drainage in Magnetically Focused Electron Beams", J. Applied Physics, 26, 1157 (1955).
28. Barford, N. C., "Space Charge Neutralization by Ions in Linear Flow Electron Beams", J. Electronics and Control, 3, 63 (1957).
29. Dunn, D. A., and S. A. Self, "Static Theory of Density and Potential

Distribution in a Beam-Generated Plasma", J. Applied Physics, 35, 113 (1964).

30. Halsted, A. S., "Static Theory of Density and Potential Distribution of a Cylindrical Plasma Column", to be published.
31. Tonks, L. and I. Langmuir, "A General Theory of the Plasma of an Arc", Phys. Rev., 34, 876 (1929).
32. Valentine, J. M., and S. C. Curran, "Average Energy Expenditure Per Ion Pair in Gases and Gas Mixtures", Repts. on Prog. in Phys., 1, 1 (1958).
33. Sommermeyer, K., and H. Dresel, ZS f. Phys., 141, 307 (1955).
34. Smith, P. T., "The Ionization of Helium, Neon, and Argon by Electron Impact", Phys. Rev., 36, 1293 (1930).
35. McClure, G. W., "Specific Primary Ionization of H_2, He, Ne, and A by High Energy Electrons", Phys. Rev., 90, 796 (1953).
36. Lemmond, C. Q., and L. H. Stauffer, "Energy Beams as Working Tools", IEEE Spectrum, 1, 66 (July 1964).

Measurement of Resistances Using an Electron Beam

by

C. Munakata and H. Watanabe
Central Research Lab., Hitachi Ltd.
Kokubunji, Tokyo, Japan

Abstract

The use of an electron beam for the measurement of electrical resistances is described and the errors of the measurement are analyzed. Two measuring methods, one using a potentiometer and the other a bridge are used. To avoid the error due to the thermoelectromotive force the beam is pulsed. The errors due to the spreading of the beam are negligible when the length of the sample is fifty times larger than the radius of the electron beam. Secondary and reflected electrons cause errors when a small resistance very near the end of a sample has to be measured.

Introduction

A fine focused electron beam is the essential requirement of numerous electron devices. It is used, for example, (a) for X-ray generation in an electron probe microanalyser,[1] (b) for the generation of heat in an electron beam machine,[2] (c) for the production of reflected and secondary emitted electrons in a scanning electron microscope[3] and (d) as a current carrier.[4]

One example not listed above is the use of a fine focused electron beam for impedance measurement. This is the subject matter of this paper.

There is a constant trend towards the further reduction in the size of elements of circuits in several branches of electronics. This reduction has now reached the stage where it is difficult to examine the minute circuits with the usual solid wire probe whose diameter is relatively larger than the point to be examined. In addition, the contact between the tip of the needle and the sample is often irregular which

makes it difficult to position the probe exactly at the point to be inspected.

An electron beam can be focused to a very fine spot and can be accurately positioned by electrostatic and/or magnetic deflection. Also, the contact between the beam and the point to be examined is independent of the surface conditions as long as the material is a conductor.

It appears at first glance that the use of a fine focused electron beam will eliminate the difficulties of a wire probe discussed above. However, as was indicated in the first paragraph, this same beam can produce x-rays, generate heat, liberate secondary electrons, etc. While these effects are very desirable in many cases, they are detrimental to our present objective and methods of eliminating them will be described.

Choice of Measuring Procedure

Two simple measuring methods, the potentiometer and the bridge, were selected and will be described. More sophisticated methods making use of numerous electron or ion beams will be developed in the future.

a) Potentiometer Method

Figure 1 shows the basic well-known circuit. The current I_s is adjusted to have zero current through the galvanometer. We then have

$$r = \frac{I_s}{I_B} R_s \qquad (1)$$

In this method, the error is decreased as the beam current and the galvanometer sensitivity are increased.

b) Bridge Method

The circuit is shown in Figure 2.

When the electron beam hits the Q point, we have, if the bridge is balanced,

$$[R_B + (x - r)] R_A = rR_c \qquad (2)$$

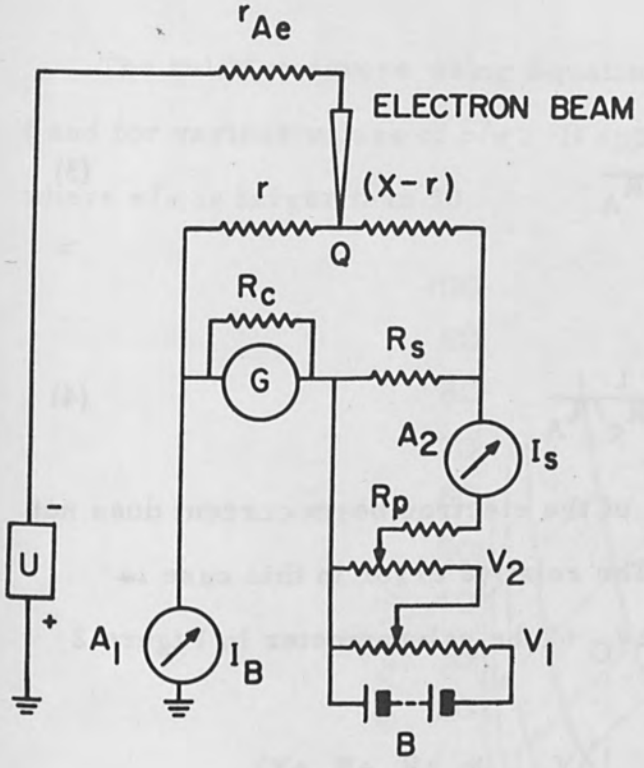

U : ACCELERATING VOLTAGE

B : BATTERY

G : GALVANOMETER

A_1, A_2 : μA AMMETER

r_{Ae} : EQUIVALENT ANODE RESISTANCE

R_c : DAMPING RESISTOR 1 kΩ

R_s : STANDARD RESISTOR (0.5 %)

R_p : PROTECTING RESISTOR 100 kΩ

V_1 : VARIABLE RESISTOR 2 MΩ

V_2 : HELIOSTAT 100 kΩ

Figure 1

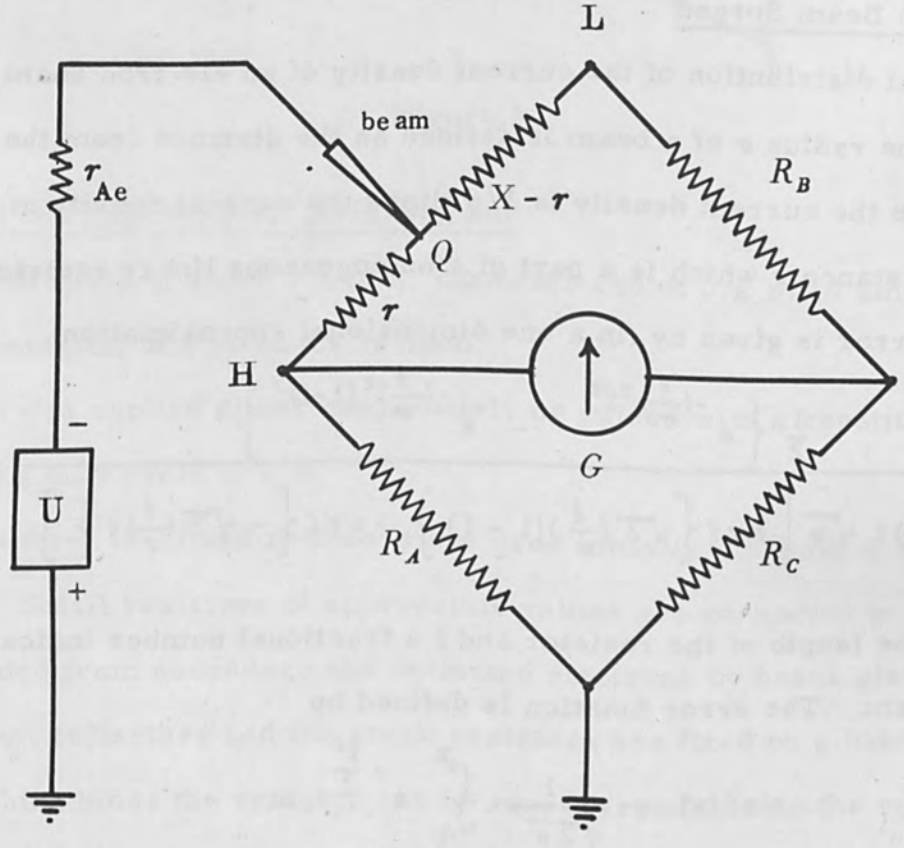

Figure 2

and

$$r = \frac{R_B + X}{1 + R_c/R_A} \tag{3}$$

If R_B is zero, we then have

$$r/X = Z = \frac{1}{1 + R_c/R_A} \tag{4}$$

It is clear that in this method the magnitude of the electron beam current does not affect the sensitivity of the measurement. The relative error in this case is determined by the least detectable voltage ΔV_G of the galvanometer in Figure 2 and is given by

$$\left|\frac{\Delta r}{r}\right| \leq \frac{|\Delta V_G|}{I_B} \frac{(R_A+R_B+R_C+X)}{r(R_A + R_C)} \cong \frac{|\Delta V_G|}{I_B} \frac{(R_A+R_B+R_C+X)}{R_A(R_B + X)} . \tag{5}$$

Errors Due to Beam Spread

The radial distribution of the current density of an electron beam is generally Gaussian. The radius σ of a beam is defined as the distance from the axis of the beam to where the current density is 1/e times the current density at the axis. When the resistance r which is a part of a homogeneous linear resistor is measured, the relative error is given by (in a one dimensional approximation)

$$\frac{\Delta r}{r} = \frac{\frac{1}{2}\left\{ e^{-(\frac{\ell}{\sigma})^2 f^2} - e^{-(\frac{\ell}{\sigma})^2 (1-f)^2} \right\}}{(\frac{\ell}{\sigma}) f \sqrt{\pi} \left[erf\left\{\sqrt{2}(\frac{\ell}{\sigma})(1 - f)\right\} - erf\left\{ -\sqrt{2}(\frac{\ell}{\sigma}) f \right\} \right]} \tag{6}$$

where ℓ is the length of the resistor and f a fractional number indicating the position of the beam. The error function is defined by

$$erf(x) = \frac{1}{\sqrt{2\pi}} \int_o^x e^{-\frac{t^2}{2}} dt \tag{7}$$

The relative errors using Equation (6) are plotted in Figure 3 as a function of f and for various values of e/σ. It appears that the errors are negligible except where e/σ is larger than 50.

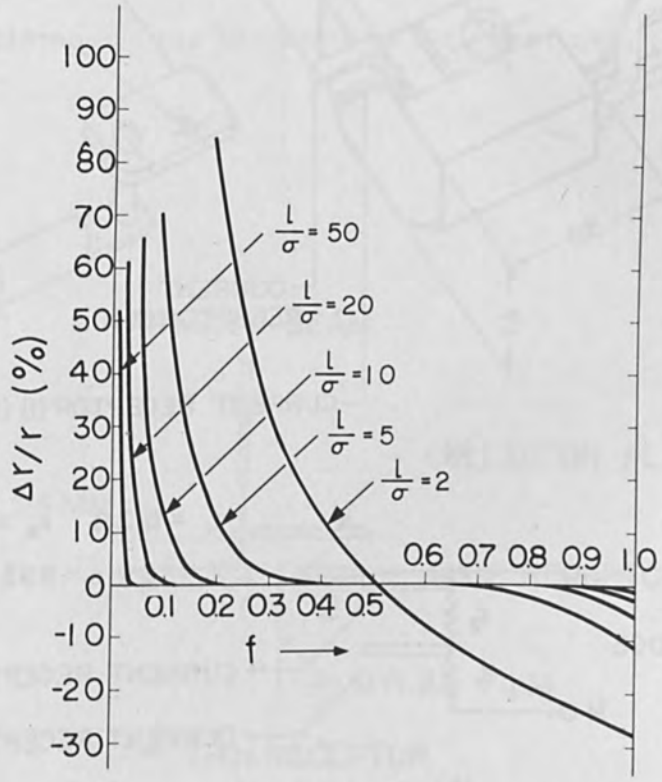

Figure 3

Description of the Experimental Arrangement

An electron beam of about 0.5 mm. diameter and of 0.2 to 10 amps with an accelerating potential of 5 to 20 KV is used.

The beam was applied either continuously or pulsed with a repetition rate of 1 Kc/sec. and a duty cycle of 0.5.

For simplicity, idealized resistors are used initially. Figure 4 shows the arrangement. Small resistors of appropriate values are connected in series and they are shielded from secondary and reflected electrons by brass plates.

The current collectors and the small resistors are fixed on a bakelite plate. A teflon bar which holds the resistor can be moved from outside the vacuum chamber. Figure 4 also shows the arrangement to collect the secondary emitted

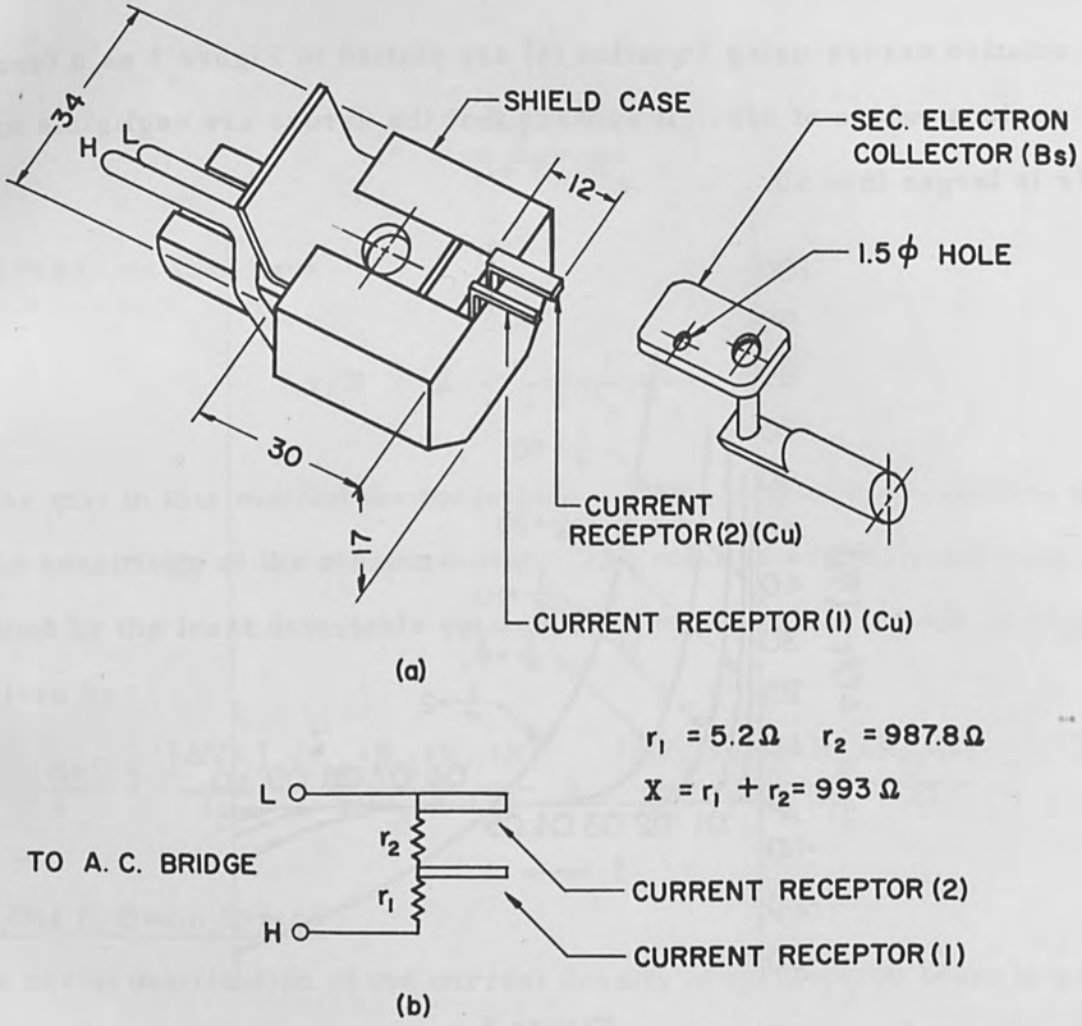

Figure 4

electrons.

The standard values are determined by a Wheatstone bridge or an a. c. bridge using a solid probe.

Results

The temperature of the point irradiated by the beam becomes slightly higher than the remaining part of the circuit. A thermoelectromotive force is thus generated which shifts the zero point of the galvanometer and consequently introduces an error. This can be avoided by pulsing the above with an appropriate duty cycle.

To avoid the error due to secondary emitted or reflected electrons, a

positively biased collector is used. It was found that 20 volts on the collector eliminates the error. If V_c is positively biased by more than 20 volts, the error becomes negative due to the collection of positive ion current by the receptor.[2] See Figure 4. Figure 5 shows the variation of the error as a function of V_c for a mylar film.

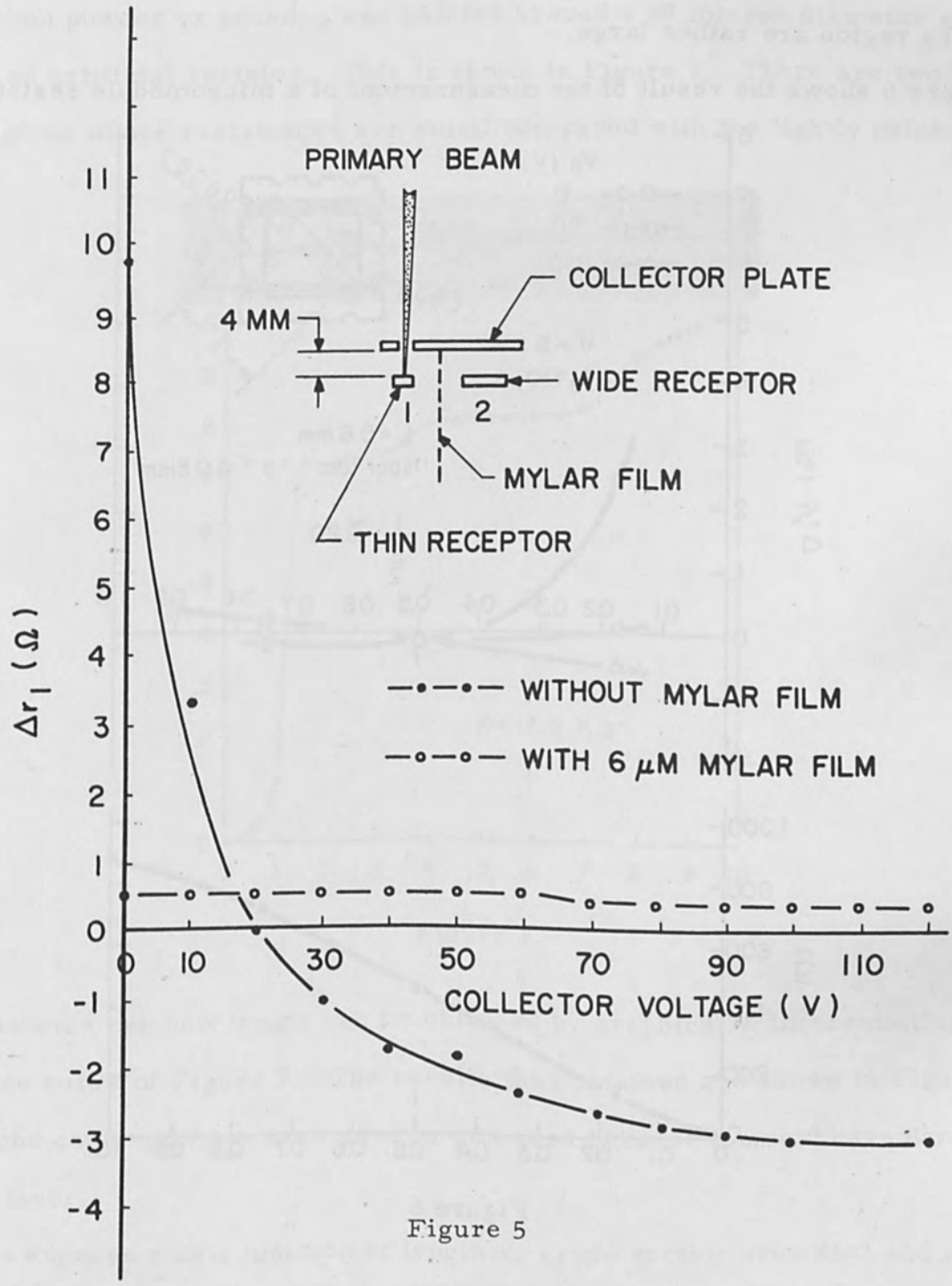

Figure 5

The error Δr_1 is given by

$$\Delta r_1 = r_2 \frac{\beta}{1+\beta} \approx r_2 \beta \text{ for } (\beta << 1) \qquad (8)$$

where β is the ratio of the currents in collectors (2) and (1). Even if β is small, Δr_1 is rather large since r_2 is large. This is why the relative errors in a low resistance region are rather large.

Figure 6 shows the result of the measurement of a micromodule resistor.

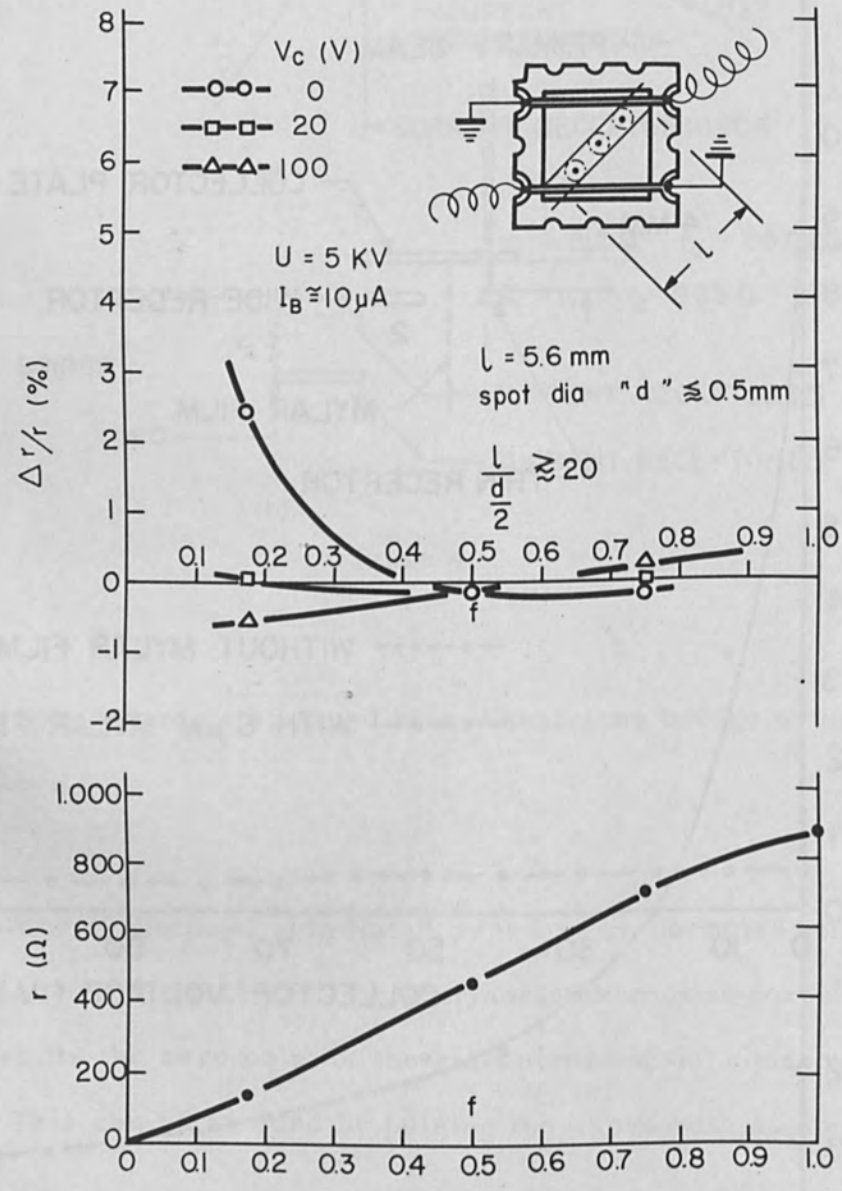

Figure 6

When V_c is zero, the relative error agrees qualitatively with those of Figure 3. When V_c is large the errors become negative for low resistances. This can be easily shown mathematically. Resistances of 130 ohms and 710 ohms of a micromodule of total resistance 880 ohms were measured with relative errors of less than 2.5% and 0.2% respectively.

Carbon powder or aquadag was painted around a 50 micron diameter glass fiber to form an artificial resistor. This is shown in Figure 7. There are two very thick regions whose resistances are small compared with the lightly painted region.

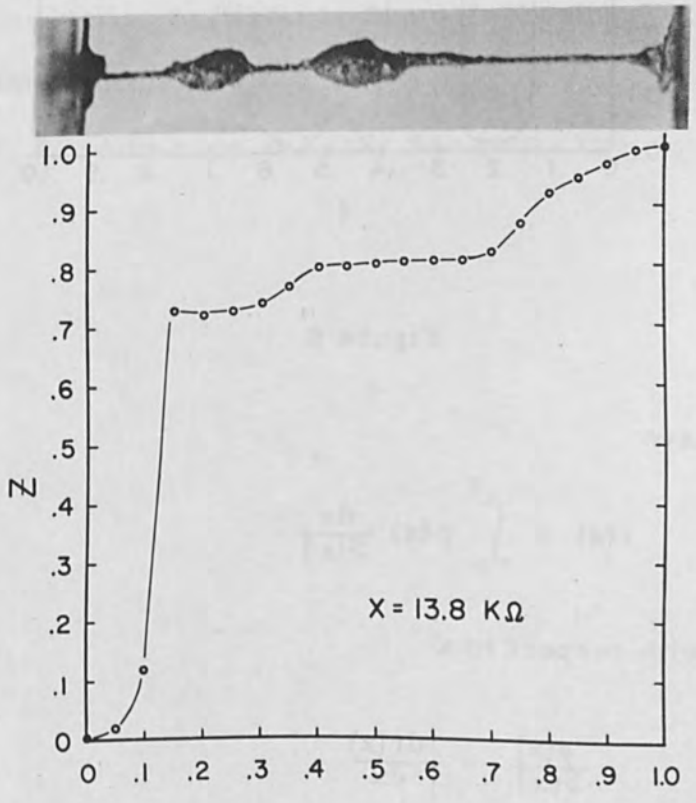

Figure 7

The resistance per unit length can be obtained by graphically differentiating the resistance curve of Figure 7. The results thus obtained are shown in Figure 8. A solid probe could not have been used in this case because it would have damaged the aquadag layer.

If we express r as a function of length x, cross section area S(x) and specific

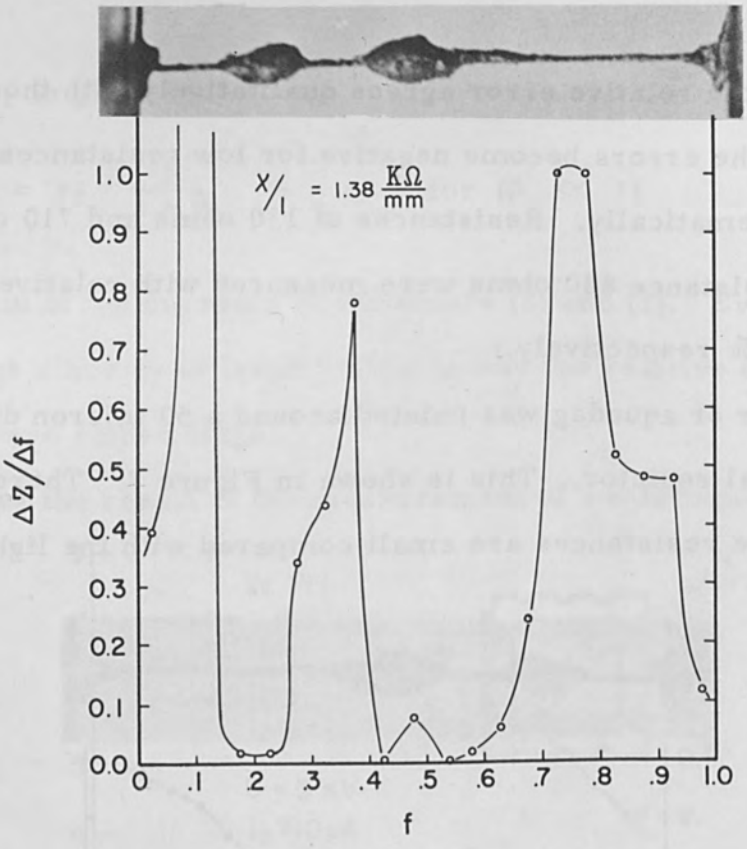

Figure 8

resistance $\rho(x)$, we have

$$r(x) = \int_0^x \rho(x) \frac{dx}{S(x)} \tag{9}$$

or by differentiating with respect to x

$$\frac{\rho(x)}{S(x)} = \frac{dr(x)}{dx} . \tag{10}$$

It is now possible to determine the change in the cross section or the temperature variation.

There are, therefore, other possible benefits in this method of measurement. The application in the case of semiconductors will be reported at a later date.

Acknowledgements

The authors wish to express their thanks to T. Suzuki, N. Aoki, H. Okano,

S. Kishino, T. Komoda, M. Sebine, S. Kobayashi, and H. Todakoro for their assistance in this project. They are grateful for the encouragement given by Dr. H. Kimura and Dr. Z. Abe throughout this study.

References

1. Duncumb, P., and V. E. Cosslett, X-ray Microscopy and Microradiography, p. 374, 1957.
2. El-Kareh, A. B., An Electron Beam Machine, RCA Review, March 1963, Vol. XXIV, No. 1.
3. Wells, O., Introduction to Electron Beam Technology, p. 354, John Wiley, 1962, R. Bakish, Editor.
4. Heinrich, K. F. J., Advances in X-ray Analysis, Vol. 6, p. 291, 1963.

An Investigation of the Effect of the Non-Rotational Geometry of the Tungsten Hairpin Emitter

by

K. Amboss
Hughes Research Laboratories
Malibu, California

Abstract

In a large number of electron guns a heated tungsten "hairpin" filament is used as the electron source. The shape of the filament and the magnetic field produced by the heating current produce field asymmetries which give rise to source aberrations. The paper describes an experimental study of these aberrations. The method of investigation consists in observing the aberration figure in the focussed image which results when an annular aperture is used. Separation of the source aberrations from those of the imaging lens and of the optical bench is achieved by rotation of the filament assembly.

I. Introduction

A large and steadily growing number of devices utilize extremely small, high energy density electron spots under relatively poor vacuum conditions. The heater tungsten hairpin filament is an ideal electron source in such devices since it is capable of high emission densities over extended periods, not susceptible to poisoning, and moreover extremely cheap to manufacture.

The focussed spot from such a source is usually not perfectly circular even after the most stringent alignment since most electron optical systems suffer from axial aberrations[1] caused by small departures from rotational symmetry.

The hairpin filament possesses two-fold symmetry and it would therefore seem that such an arrangement should produce appreciable aberrations, in particular, since the heating current itself produces a non-rotationally symmetric magnetic field. The observed aberration in the image plane is the vector sum of the

contributions of the lens, the degaussing frame and of the source, and in order to study the aberrations of one component, it is necessary to separate the various contributions. In Section II we describe briefly the method of separation and measurement of the aberrations[2] and in Section III the experimental study of a typical tungsten hairpin source.

II. The Method of Measuring Aberrations and Description of Apparatus

When a point source of electrons is imaged by an imperfect electron optical system the image consists of a highly complicated intensity pattern. This pattern is greatly simplified if the beam defining aperture is replaced by an annular stop. In this case the effect of spherical aberration is eliminated and the resultant pattern is a Lissajous figure which depends on the ratio of the various aberrations present and on the location of the plane of observation with respect to the Gaussian image plane. Typical aberration figures are shown in Figure 1. They are taken with a circular aperture and an annular stop for a mixture of astigmatism and "anti-coma" (the dominant axial aberration produced by a threefold asymmetry) in the vicinity of the Gaussian image plane. Similar aberration figures produced by deflection coils have been shown by Glaser[3] and Wendt[4] and for systems of double symmetry by Burfoot.[5]

Wendt analyzed his aberration figures to obtain the magnitudes and phases of the constituent aberrations by comparing the figures with charted patterns. This method is time consuming and not particularly accurate. The method adopted by the author consists of introducing additional field asymmetries by means of lenses of two-fold, three-fold and where needed, of four-fold symmetry. These lens elements are used to cancel out the various aberrations of the system. The correctors are calibrated empirically in a particular arrangement of lenses by energizing them individually to such an extent that a large amount of only one aberration is produced. Accurate measurements are then made on this remaining aberration figure. The

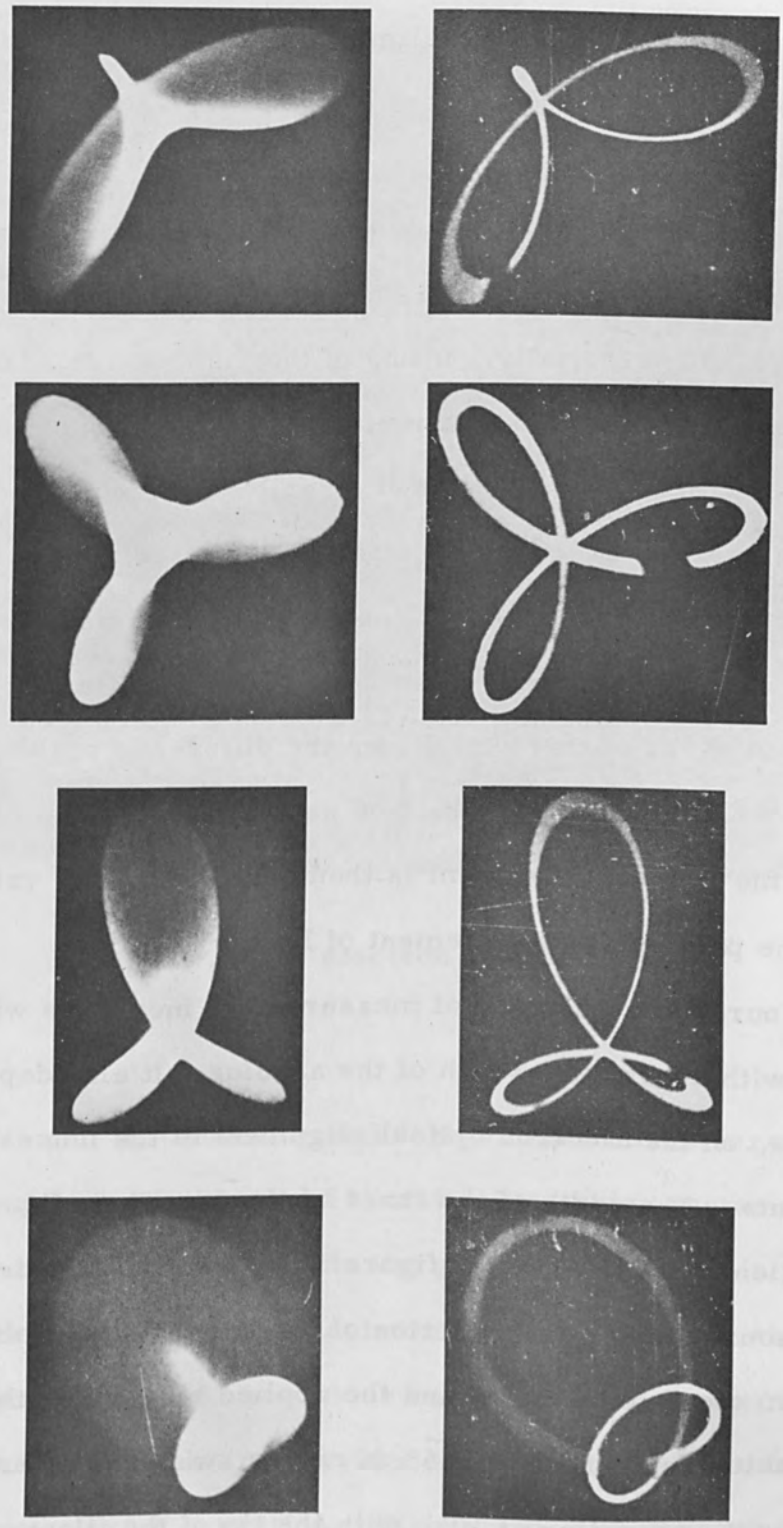

Figure 1 Aberration figures of anticoma and astigmatism in the vicinity of the Gaussian image plane taken with a circular aperture (a) and with an annular stop (b).

auxiliary field coils cannot be used to eliminate coma. Under suitable conditions this aberration may be eliminated by a transverse displacement of the annular aperture.

In order to separate the contributions of the various components of the electron optical system from the aberration figure of the image, we utilize the fact that the various aberrations add vectorially. If one of the components of the system is rotated about its axis of approximate symmetry the aberration figure changes shape and any specific aberration passes through a series of maxima and minima, the number depending on the degree of symmetry of the associated perturbing field. The method of measurement consists of compensating out the aberrations at each azimuthal setting of the component. This requires a specific excitation current and azimuthal setting of every corrector. From the difference of the maximum and minimum values of the excitation current of each corrector and from its calibration the aberration of the rotated component is then obtained. This value applies, of course, only to the particular arrangement of lenses.

For a point source the accuracy of measurement increases with the radius of the aperture and with decreasing width of the annulus. It also depends, as detailed analysis[2] shows, on the electron optical alignment of the lenses and of the correcting elements. The width of the trace of the Lissajous figure ultimately limits the resolution of the aberration figure. This width depends on the size of the image of the source which is a function of the accelerating voltage, the distance of the hairpin from the grid aperture and the applied bias. For the arrangement described below using an annulus of 1.5 cm radius, which is about half of the internal radius of the lens, operating at 10kv with the tip of the filament withdrawn one grid hole diameter, it was possible to resolve a difference ΔF in focal length F of the lens due to a deliberately introduced astigmatism amounting to $\frac{\Delta F}{F} \approx 5.0 \times 10^{-3}$.

Figure 2 is a photograph of the electron optical bench showing the arrangement

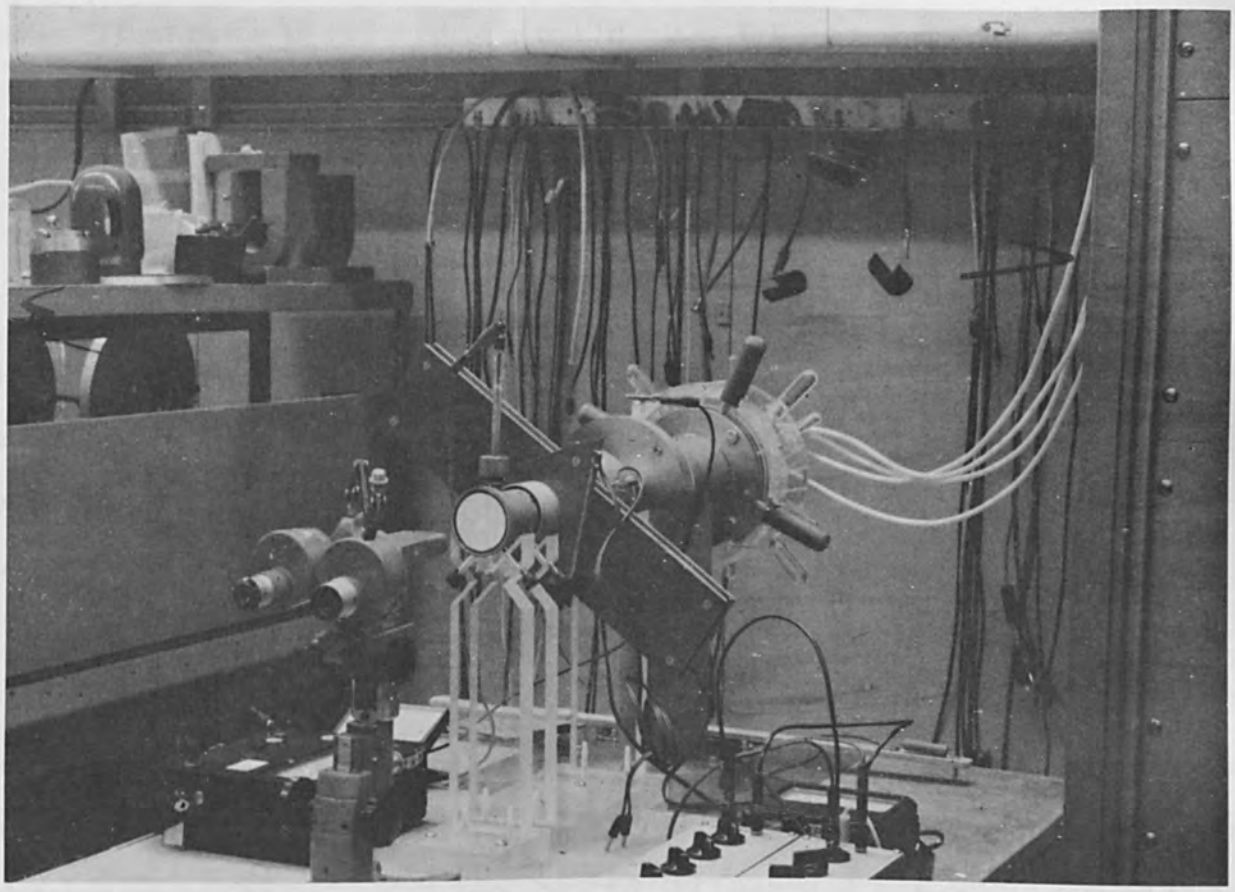

Figure 2 The electron optical bench.

of the focussing lens and the mounting and design of the correctors for two-fold and three-fold asymmetries. The gun head contains means for centering the filament and for adjusting its axial position within the grid electrode. It is insulated from the anode by a piece of Lucite. The insulator contains a groove which mates with a protrusion on the pumping "Tee" and which centers the head assembly and permits it to rotate. Insulating handles are provided so that all adjustments may be carried at full voltage during operation. Figure 3 is a photograph of the head assembly removed from the pumping tee. Figure 4 is a schematic of the apparatus giving its dimensions and showing the location of the aperture and of the various components. All experiments were conducted at unit magnification since it can be

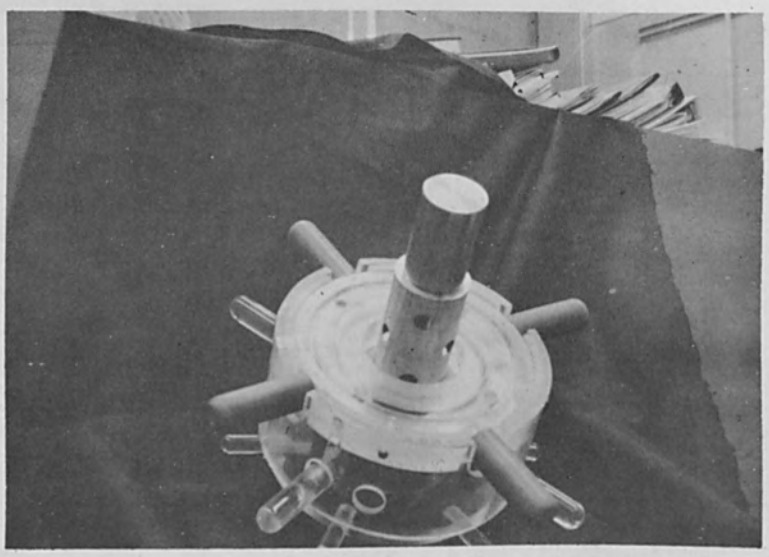

Figure 3 The head assembly mounted on the Lucite insulator.

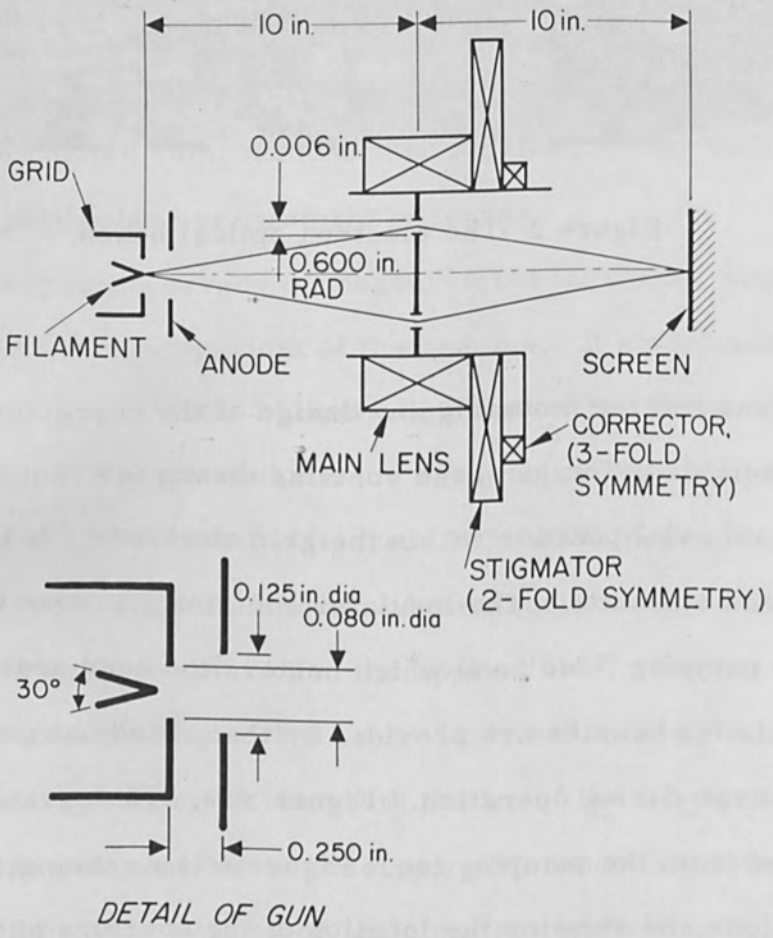

Figure 4 Schematic of the electron optical bench.

shown[2] that coma is reduced to a minimum under these conditions.

III. Description and Results of the Experimental Study

Since aberrations are introduced by transverse misalignment the first step of the study consisted in an accurate alignment of the system.

First the mechanical centering of the grid filament assembly was tested. With the anode removed the arm of the "Tee" opposite the heat assembly was blanked off by means of a glass plate. The head assembly was then rotated and the grid hole viewed through the glass by means of a traveling microscope. The grid hole alignment was found to be .003" T. I. R.

Next the filament was aligned mechanically in the following manner. After centering by eye in air, a small plate of conducting material was placed over the grid hole and the filament then pushed forward until its tip made contact with the plate. The system was then evacuated and the filament heated. After connecting a resistance meter between filament and grid the filament was gently moved to one side until it made contact with the grid. The position of the appropriate transverse alignment screws was noted and the filament was then moved in the opposite direction until contact was established there. From the new and the previous positions of the alignment screws the centered setting was found. The procedure was then repeated with other alignment screws.

With a circular aperture in position the lens was then aligned electron optically by the usual procedure of current reversal. All experiments were for convenience conducted at 10kV. The correcting elements, as Figure 2 shows, are mounted on the lens alignment tube and therefore not capable of independent adjustment. Variation of grid bias, with the beam well underfocussed showed that the "illumination" on the screen was not cut off uniformly; a small transverse adjustment of the filament was necessary to produce the desired condition. Several photographs of the illumination were taken under these conditions with the tip of the hairpin withdrawn to various

depths below the surface of the grid. Figures 5a and b show the illumination with the tip withdrawn .050" i.e., about half a grid hole diameter for two values of grid bias. The two fold symmetry of the illumination is clearly visible. Rotation of the gun head produced a corresponding rotation of the elliptic figure. Figure 5c shows the effect of withdrawing the filament a further .050". The grid bias in this case was adjusted to produce the same emission of 8μA as in Figure 5b.

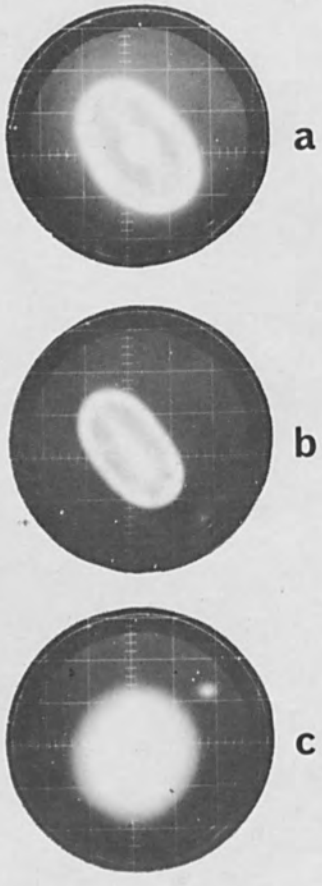

Figure 5 Intensity distribution of highly underfocussed image under various conditions. Operating voltage 10kV. a) filament withdrawn .050" grid bias - 60 volts b) as for (a) but with -100 volts bias. c) filament withdrawn .100" bias - 12 volts. Beam current in (b) and (c) is the same.

In the next experiment the circular aperture was replaced by the annular stop. The annulus was aligned by the removal of coma from the image and the system freed from the other aberrations by suitable setting and excitation of the correctors. With the beam very nearly focussed the width of the trace of the Lissajous figure was measured to be about .006" and the focussed spot within which it was impossible to resolve the aberration figure was found to be about .012". Next with the beam very slightly defocussed the gun head was rotated and the change in the aberration figure observed. With the filament setting as in Figure 5a and b a very small change in the figure was found which could at each azimuthal setting be removed by a small alteration in corrector current and by a rotation of the stigmator through approximately the same angle the head had been moved.

The average stigmator currents required for correction at each azimuthal setting was of the order of the value required to produce a resolvable variation and it was therefore not possible to make precise measurements.

With the filament withdrawn .100" it became impossible to resolve any variation due to rotation in the aberration figure. This result is in agreement with the observations of the illumination which show that the withdrawn filament produces a very nearly circular patch.

Conclusions

From the results obtained it would appear that the two-fold symmetry of the filament has an effect on the quality of the image if the filament is not withdrawn too deeply behind the grid. The magnitude of the axial astigmatism, measured in terms of the change in position of the two astigmatic line foci was estimated to be of the order of $\Delta F/F = 5 \times 10^{-3}$ when the tip of the filament was .6 grid hole diameters below the top of the grid. A much smaller value of the aberration, well below the resolving capability of the system was obtained when the filament was withdrawn to 1.2 grid hole diameters.

References

1. Sturrock, P. A., Proc. Roy. Soc. A, Vol. 243, p 387-429, 1951.

2. Amboss, K., Ph. D. Thesis Univ. of London "Electron Optics: Aberrations of Aircored Magnetic Lenses", 1959.

3. Glaser, W., "Grundlagen der Elektronenoptik" Springer Verlag, p 483, 1952.

4. Wendt, G., Annales de Radioélectricité, Vol. 4, No. 37, 1954.

5. Burfoot, J. C., Proc. Phys. Soc. B, Vol. 67, p 523, 1954.

Crystallization of Vacuum Evaporated Germanium Films by the Electron Beam Zone-Melting Process

by

Susumu Namba
The Institute of Physical and Chemical Research
Bunkyo-ku, Tokyo, Japan

Abstract

Micro-zone melting by electron beam scanning was used to recrystallize vacuum evaporated p-type germanium thin films in the n-type crystal. Vacuum evaporation and micro-zone melting techniques were used to construct a p-n thin film germanium diode having characteristics similar to those of ordinary p-n junctions.

Introduction

Vacuum evaporated semiconductor films have been generated by applying the epitaxial process on single crystal substrates. Recently, the electron beam zone-melting process, a new application of this technique, has been used to recrystallize vacuum evaporated films on non-crystalline substrates.[1-6]

This paper describes a method of growing single crystal germanium films on molybdenum or tungsten substrates by using the electron beam zone-melting process. Characteristics of a germanium thin film diode composed on an n-type recrystallized germanium film and a p-type vacuum evaporated germanium film are given. To construct a germanium thin film diode for application in micro-electronics the following requirements should be met:

(1) The vacuum evaporated germanium film should be crystallized in the required areas on substrates of various sizes.

(2) The surface of the crystallized film should be flat.

(3) The crystallized film should adhere firmly to the substrate with ohmic contact.

Experimental Procedure

The conditions for making germanium by evaporation in vacuum are given in Table 1. Tungsten or molybdenum, which are used as substrates, are cut into

Table 1. Conditions for preparing vacuum evaporated Ge films.

evaporant	n-type Ge single crystal (Sb-doped, 0.1 Ω cm)
degree of vacuum during evaporation	$1 - 2 \times 10^{-5}$ mmHg
source heater	Mo- or W-boat
source temperature	about 1300 °C
substrate temperature	about 150 °C
rate of deposition	about 20 Å/sec

appropriate sizes, for example 6 mm. by 100 mm., and then ultrasonically cleaned in a detergent solution for one hour. After this cleaning, a substrate is placed into vacuum and cleaned by passing an electric current through it. The current raises the temperature of the substrate to 1000 °C. During the evaporation process the substrate temperature is maintained at about 150 °C. The evaporation of germanium is performed by the resistance heating of a tungsten boat. High evaporation rates are desirable because contamination of the film is minimized. Suitable film thickness is about 3-8μ.

The electron beam apparatus, as shown in Figure 1, consists of an electron gun, two focusing lenses, deflection plates, and a sample holder.

The tungsten hairpin filament is 0.2 mm. in diameter. The electrons emitted by the filament are accelerated by 50 kv and focused to a spot size of 50-100μ in

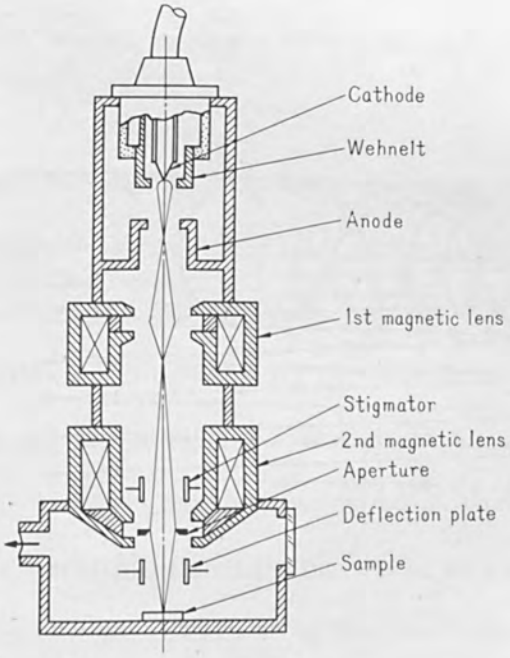

Figure 1 Schematic diagram of electron beam apparatus.

diameter at the film sample. The beam current of the spot at the film sample is 10 μA-2 mA. The film holder can be moved in two directions (X, Y) by an appropriate mechanism. The film holder can be heated to about 700 °C by an auxiliary heater.

As shown in Figure 2, the germanium film is bombarded by the electron beam which scans at a speed of 300 cps. A fine melting zone of 0.1 mm. width and 3 mm. sweep distance is created. The film is slowly moved perpendicular to the scanning beam until the molten zone has traversed the desired area. The molten zone velocity is about 1 mm./sec. when the electron beam of 50 kv acceleration has 100μA in a spot size of about 100μ in diameter at the film. In Figure 2 the X and Y directions are the directions of scan and molten zone movement respectively.

During the zone melting process, the germanium film is heated to approximately 600 °C by an auxiliary heater. This heating is essential to insure the growth of a

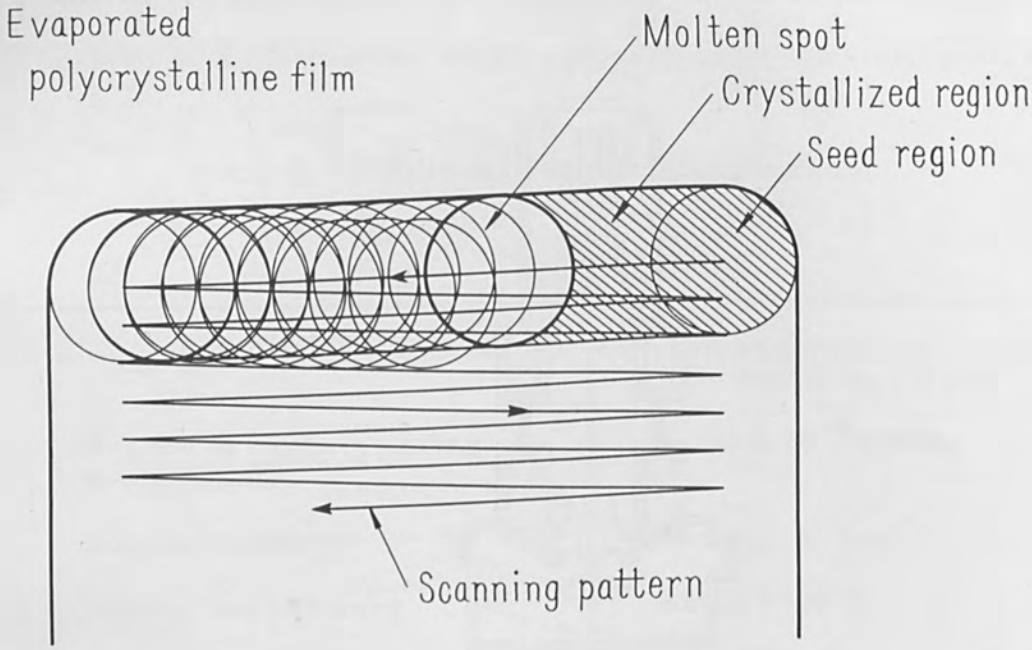

Figure 2 Schematic representation of movement of molten spot in germanium film by electron beam heating.

single crystal film, without it a flat crystal film would not be obtained. The conditions suitable for the zone melting process are given in Table 2. Under these

Table 2. Conditions of the zone-melting.

electron beam current	50 - 100 μA
accelerating voltage of beam	50 kv
sub-heated substrate temperature	about 600 °C
deflection frequency	300 cps
deflection length on film	3 mm
speed of zone movement	about 1 mm/sec
width of melting zone	about 100 μ

conditions, the red-colored melting line that appears in the film is observed to move slowly in the Y direction. Unless the beam is as fine as mentioned above, an appropriately fine melting line which is desirable cannot be obtained.

Crystal Growth

Microphotographs of the zone-melted surface indicate that the crystals in the germanium films are grown in the direction along which the melting zone moves. A typical example of the crystal growth is shown in Figure 3. Figure 3(a) shows the part of the film where crystallization caused by the electron beam was initially discernible. Figure 3(b) and (c) show well-crystallized areas before and after etching by CP-4, respectively. Lines in the sweep or X direction may be caused by unevenness of the Y direction movement. The crystals are grown in a dendritic manner in the Y direction and are independent of the metallic substrate which does not have a dendritic structure.

Figure 4(a) shows the boundary between the zone-melted and the untreated areas. The fine patterns in the untreated area are caused by the surface structure of the substrate during the deposition process. The width of the melted zone is approximately 100μ. Figure 4(b) shows a central part of the zone-melted area with dendritic growth of the crystal in the film.

Typical examples of the zone-melted films are shown in Figure 5. By electron diffraction analysis of the zone-melted films, the films are found to have their (110) plane strongly oriented parallel to the substrate plane.

The movement of the molten spot on the film as shown by the scanning pattern in Figure 2 may give rise to many crystal seeds in the initial area shown in Figure 3(a). Only one seed crystal is desirable for the growth of a single crystal thin film.

To produce a single seed crystal the following zone-melting methods are proposed:

(a)

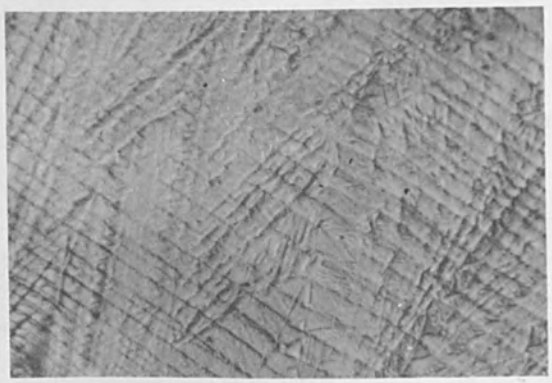

(b)

100 μ

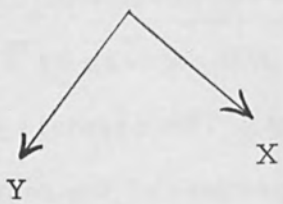

Conditions

beam current	50 μA
sub-heating temperature	600 °C
scanning	2 times

(c)

Figure 3 Microphotographs of zone-melted germanium surfaces.
(a) initial part of crystallization,
(b) well-crystallized part before chemical etching,
(c) well-crystallized part after chemical etching.

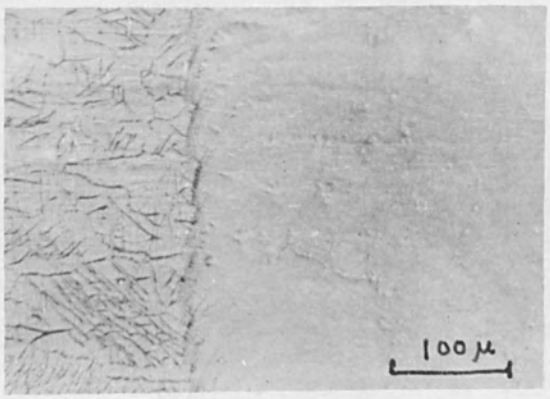

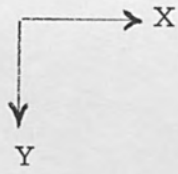

(a)

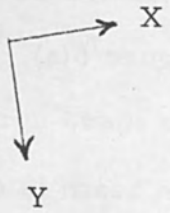

(b)

Conditions

beam current	100 μA
sub-heating temperature	610 °C
scanning	1 time

Figure 4 Microphotographs of zone-melted germanium surfaces.
(a) boundary between untreated and zone-melted areas,
(b) central part of zone-melted area.

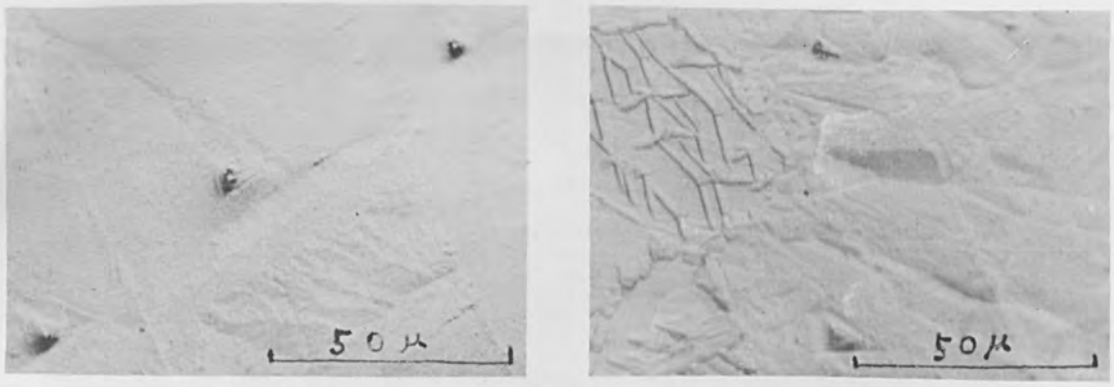

(a) (b)

Figure 5 Microphotographs of zone-melted germanium surfaces.
(a) example of etch pits,
(b) boundary area.

(1) The film on the substrate is specially shaped by mask deposition as shown in Figure 6(a). The electron beam is scanned as shown in Figure 2.

(2) The electron beam is controlled to scan a special pattern as shown in Figure 6(b). In this case, the intensity of the electron beam should be made proportional to the sweep length.

By these methods, one single seed crystal can be produced at the pointed vertex of the melted area.

Figure 7 shows a microphotograph of a germanium surface which has been zone-melted by the method of Figure 6(a). It can be clearly seen that crystallization started at the pointed vertex. These improved methods are effective in making one single seed crystal for crystallization in the film. This fact can be seen by comparing Figure 3(a) and Figure 7.

Diode Characteristics

It is known that vacuum evaporated germanium films always show p-type conduction even though they are made from n-type germanium. Among the many

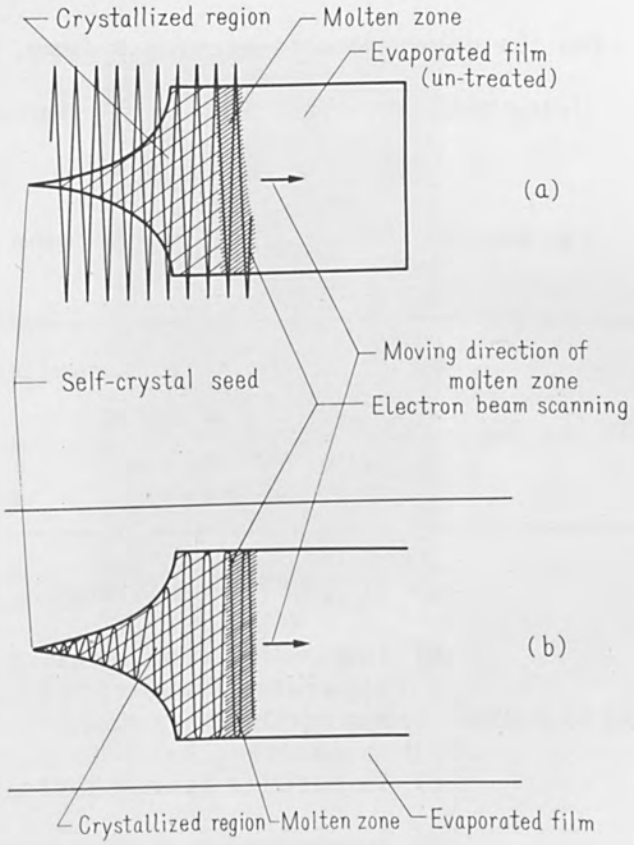

Figure 6 Schematic representation of electron beam zone-melting.

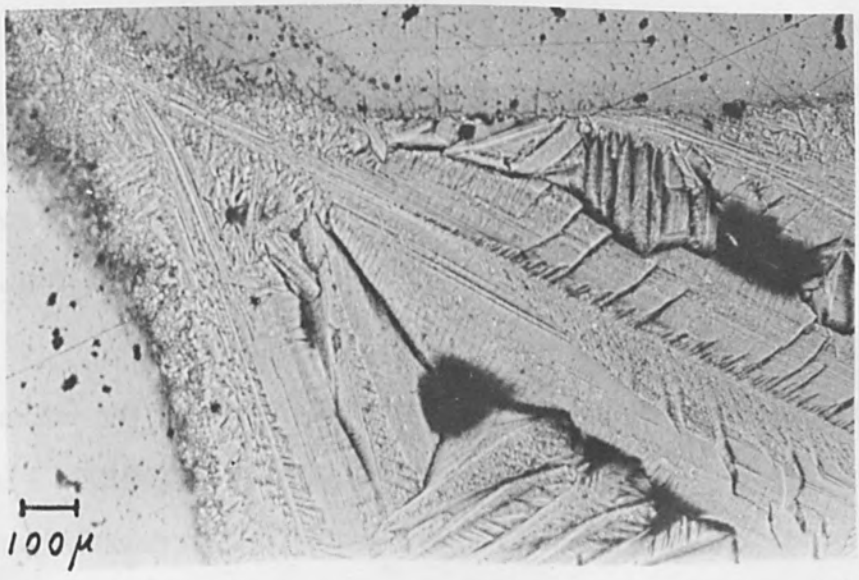

Figure 7 A microphotograph of zone-melted germanium surfaces.

causes listed in Table 3 for the conduction to become p-type, lattice defects may play an important role. Using the zone-melted process, the crystallized germanium

Table 3. Causes for the conduction to become p-type.

structure defects	a) lattice defects (vacancies, dislocations, stacking faults) b) grain boundaries
impurities	a) oxygen (or other residual gas molecules) b) impurities from various part of the apparatus (substrate holder, bell jar, source heater, etc.) c) impurities from substrate d) impurities in evaporant (doped impurities in the case of p-type evaporant)

film shows n-type conduction when the evaporant is n-type germanium. This change of conduction type could be caused by a decrease in the number of lattice defects, changes in vacancies, grain boundaries, etc.

The point contact of a gold whisker on a zone-melted germanium film shows a rectifying character as shown in Figure 8. This characteristic curve is in contrast to that obtained from an untreated film which gives no rectifying effect as can be seen in Figure 9.

Etching germanium films with CP-4 demonstrates that the untreated germanium film is quickly removed while the zone-melted portion of the film remains firmly on the substrate. By using this method, the zone-melted portions of the film are allowed to remain on the substrate as an array of islands, after CP-4 etching removes the untreated portion of the germanium film. After applying suitable

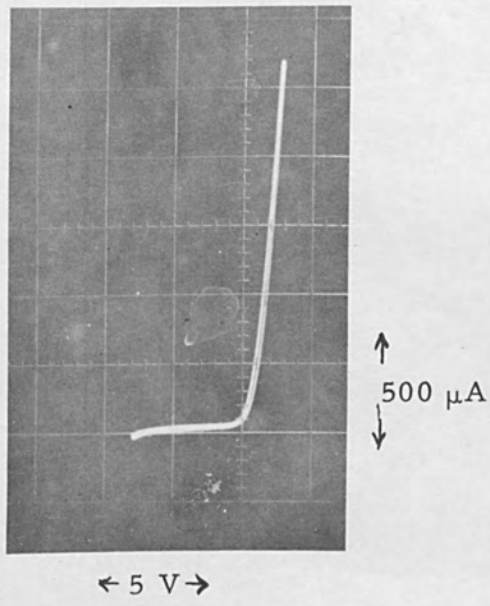

Figure 8 Diode characteristic by point contact of gold whisker on crystallized germanium film.

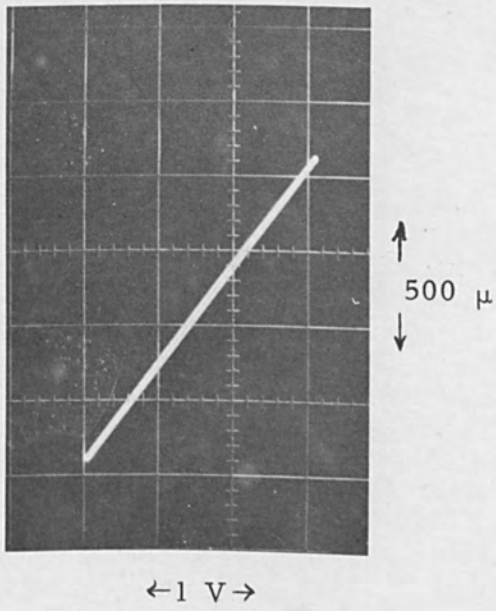

Figure 9 Diode characteristic by point contact of gold whisker on untreated germanium film.

masking, another germanium film, but with p-type conduction, is deposited on the film. An indium electrode is melt-bonded in vacuum to the p-type germanium layer of the film. The germanium thin film diode, as constructed by the above method, is shown in Figure 10.

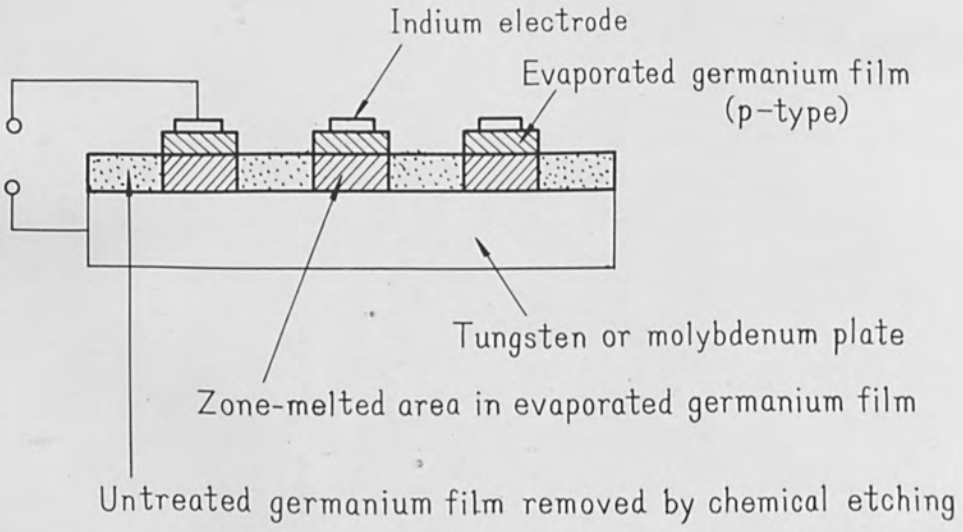

Figure 10 Schematic diagram showing construction of germanium thin film diode.

The germanium thin film diode has a rectifying characteristic similar to that of an ordinary p-n junction diode. The characteristic curve of a germanium thin film diode is shown in Figure 11. The breakdown voltage of the diode, which is about 20 volts, depends upon the electrical properties of the zone-melted film.

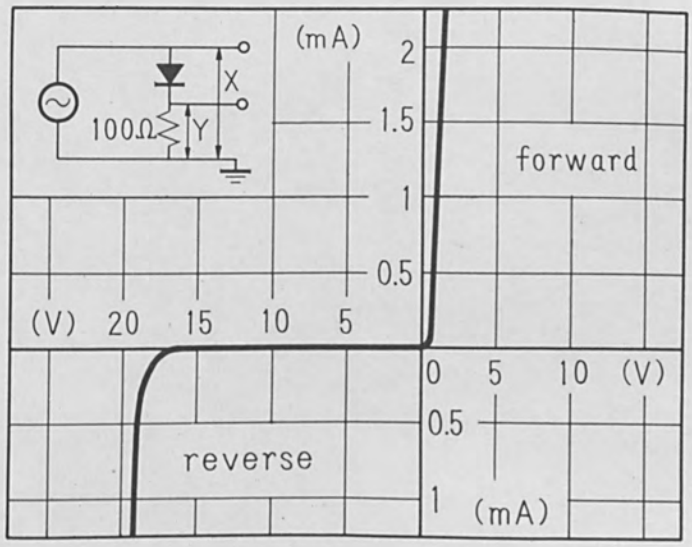

Figure 11 Diode characteristic of germanium thin film diode composed of
tungsten disc electrode,
crystallized n-type germanium film,
evaporated p-type germanium film,
melt-bonded indium electrode.

References

1. Gilbert, G. B., et al, J. App. Phys. 32, 1597 (1961).

2. Kurov, G. A., et al, Soviet Physics - Crystallography 7, 625 (1963).

3. Weinreich, O. A., et al, J. App. Phys. 34, 225 (1963).

4. Maserjian, J., Solid-State Electronics 6, 477 (1963).

5. Namba, S., et al, Oyo Buturi (in Japanese) 33, 450 (1963).

6. Poechler, T. O., et al, "Single Crystal Films", 129, Pergamon Press (1964).

Application of the Plasma Electron Beam to Welding

by

K. L. Boring and R. V. Pohl
General Electric Company
Schenectady, New York

Abstract

Recent developments in the design of non-thermionic hollow cathode electron guns are described and beam control problems are discussed. Data on focal spot diameter, welding speeds and heat affected zones are presented for aluminum and steel alloys. Special applications, including welding in inert gases are described together with the results of welding experiments.

Introduction

Increased understanding of gas discharge phenomena and accelerating activity in the electron beam field have stimulated interest in the hollow, non-thermionic cathode as an electron beam source.[1] The simplicity of such a cathode and its ability to function in a rough vacuum environment are desirable from the standpoint of electron beam welding. In this paper, an advanced design, hollow non-thermionic, gas discharge cathode is discussed together with its use as a gun for electron beam welding.

Stauffer and Boring[2] have described the operation of such hollow cathodes of both screen and shielded construction. The screen cathode consists of a cylinder or sphere of wire mesh or perforated metal mounted on an insulated bushing projecting into a chamber in which an inert gas can be maintained at a pressure in the range of 1 to 50 x 10^{-3} Torr. When a high negative voltage in the range of 10 to 20 kV is applied to the cylinder with respect to the walls of the chamber, an electron beam is seen to emerge from an aperture in the end of the cylinder. Figure 1 shows such a "Plasma Electron Beam", the path of which is luminous as

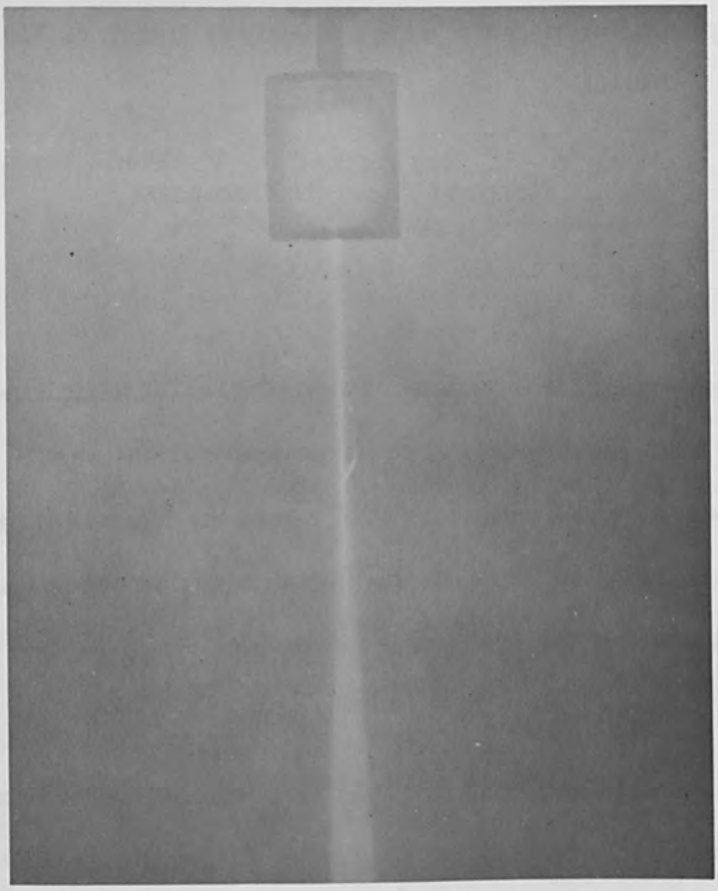

Figure 1 Plasma electron beam from screen cathode.

the result of excitation of gas atoms by the electrons. A plasma body within the cathode is visible as well as the path of diffuse electron emission through the perforated side walls of the cylinder. Such a beam from a screen cathode is somewhat inefficient in that only 30 to 50 percent of power input is available in the usable beam.

In the more recently developed shielded cathode, the perforated walls of the cylinder are replaced by solid metal and a metallic grounded shield surrounds the cathode. The spacing between the shield and cathode sidewall is such that, in accordance with Paschen's law, a gaseous discharge cannot occur. However, a discharge does occur between the shield and the region around the aperture. Figure 2 shows a shielded cathode emitting an electron beam which is focused by an

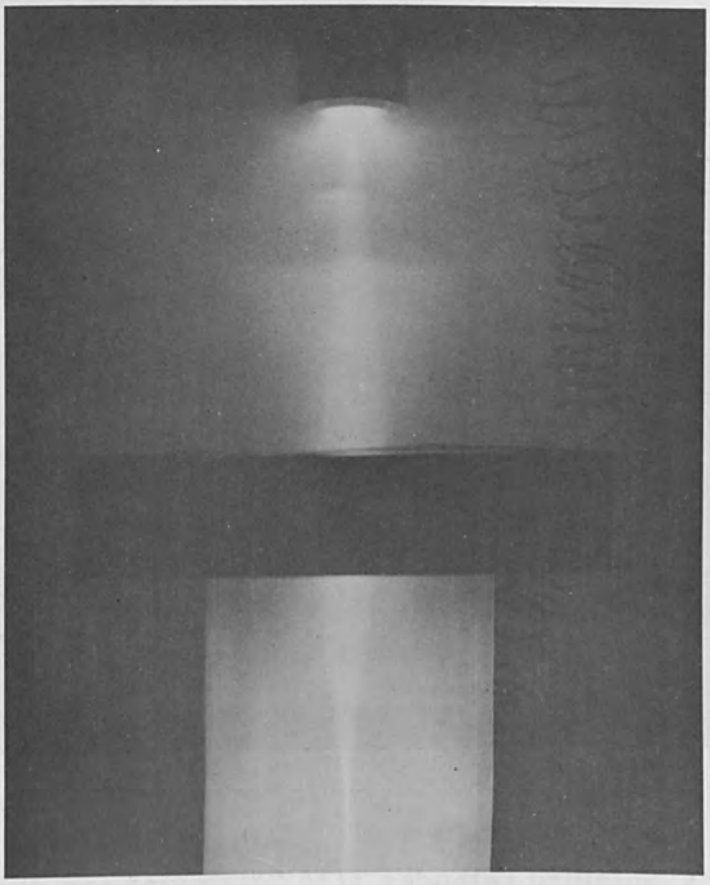

Figure 2 Focused plasma electron beam from a shielded cathode.

electromagnetic lens to a small spot. Shielded cathodes have been built in a range of sizes ranging from 3/16" to 3" in diameter as illustrated in Figure 3. They have been operated in hydrogen, helium, air, nitrogen and argon. The internal operation of the shielded cathode has been analyzed in a previous paper.[3]

With the current interest in electron beam welding, it was natural that the plasma electron beam would be considered for such applications. Since operating gas pressures are in the range of 1 to 50 x 10^{-3} torr, chamber sealing and degassing problems are less severe than with thermionic cathodes which require pressures of 10^{-4} torr or less. This allows the use of mechanical pumps such as Roots blowers rather than diffusion pumps. Chamber pump-down is rapid, which is an advantage with production work on large chambers. The cathode itself is simple and rugged,

Figure 3 Shielded cathodes 3/16" diameter and 3" diameter.

and is little affected by the evolved gases and metal vapor of welding.

PEB Guns used in Welding Investigations

For the light-duty work to be described, the shielded gun of Boring and Stauffer[2] is employed. Typical operating conditions for this 1-1/8" diameter gun, shown in Figure 4, are 24 kV and 150 ma.

Welding of somewhat-heavier sections to be described is performed with a 1-1/2" diameter model shown in Figure 5. This advanced design gun employs improved shielding, rounded corners and highly polished surfaces to enhance its high voltage performance. Typical operating parameters are 40 kV and 250 ma.

Although plasma electron beams have been operated in many gases, including hydrogen, helium, air, water vapor and mercury vapor, the gases found to be most suitable for welding are nitrogen and argon. Nitrogen pressures range from

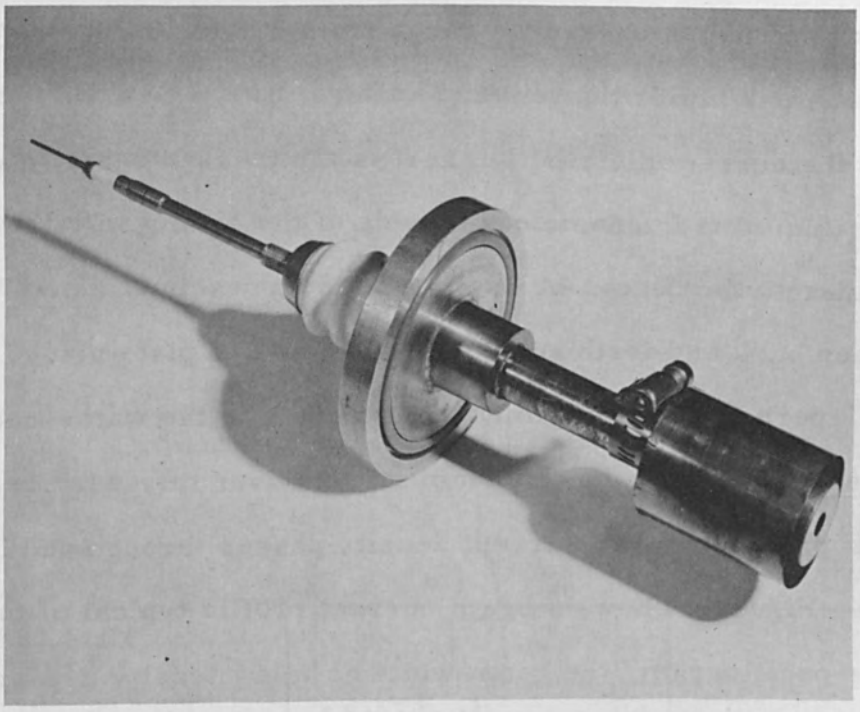

Figure 4 1-1/8" diameter shielded cathode.

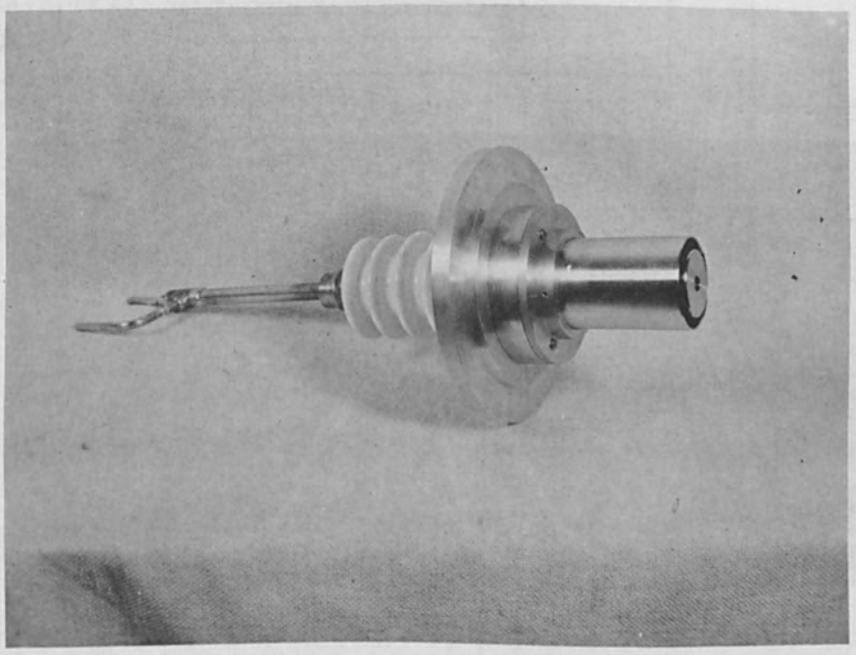

Figure 5 1-1/2" shielded cathode.

5 to 7 x 10^{-3} torr and argon pressures range from 2.5 to 10^{-3} torr, depending on the cathode and the particular current and voltage.

To observe the current distribution across the focused beam, a pair of Helmholtz coils is mounted, one on either side of the beam, with the axis of the coils perpendicular to the beam. A 60-cycle current excites the coils and causes the beam to sweep back and forth across a water-cooled plate placed in the focal plane. A small aperture (.010" diameter) is located in the water-cooled plate at the center of the swept area. As the beam sweeps over the aperture, a small electron current proportional to current density passes through and is displayed on an oscilloscope. Figure 6 shows a beam current profile typical of those used in welding. On the oscillogram, the beam width at half intensity appears to be .013", but is less than this because of the finite size of the scanning aperture. Efficiency studies showed that more than 70 percent of the total cathode current appeared as beam current, with only slight variation with operating conditions.

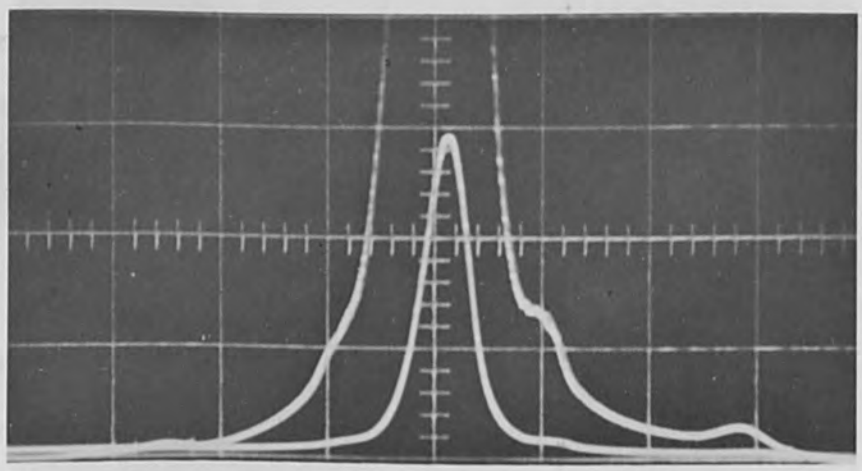

Figure 6 Current density distribution at focal spot.
(1-1/2" Cathode, 40 kV, .145 a., Argon 2.5x10^{-3} torr)

Welding Systems

A light-duty system was built for the special application of welding a niobium cup into a niobium ferrule. Since the end use of the device required that the weld be made in 20 torr of argon, it was a natural application for the plasma electron beam. Figure 7 is a line drawing of the system. Argon from a pressure cylinder

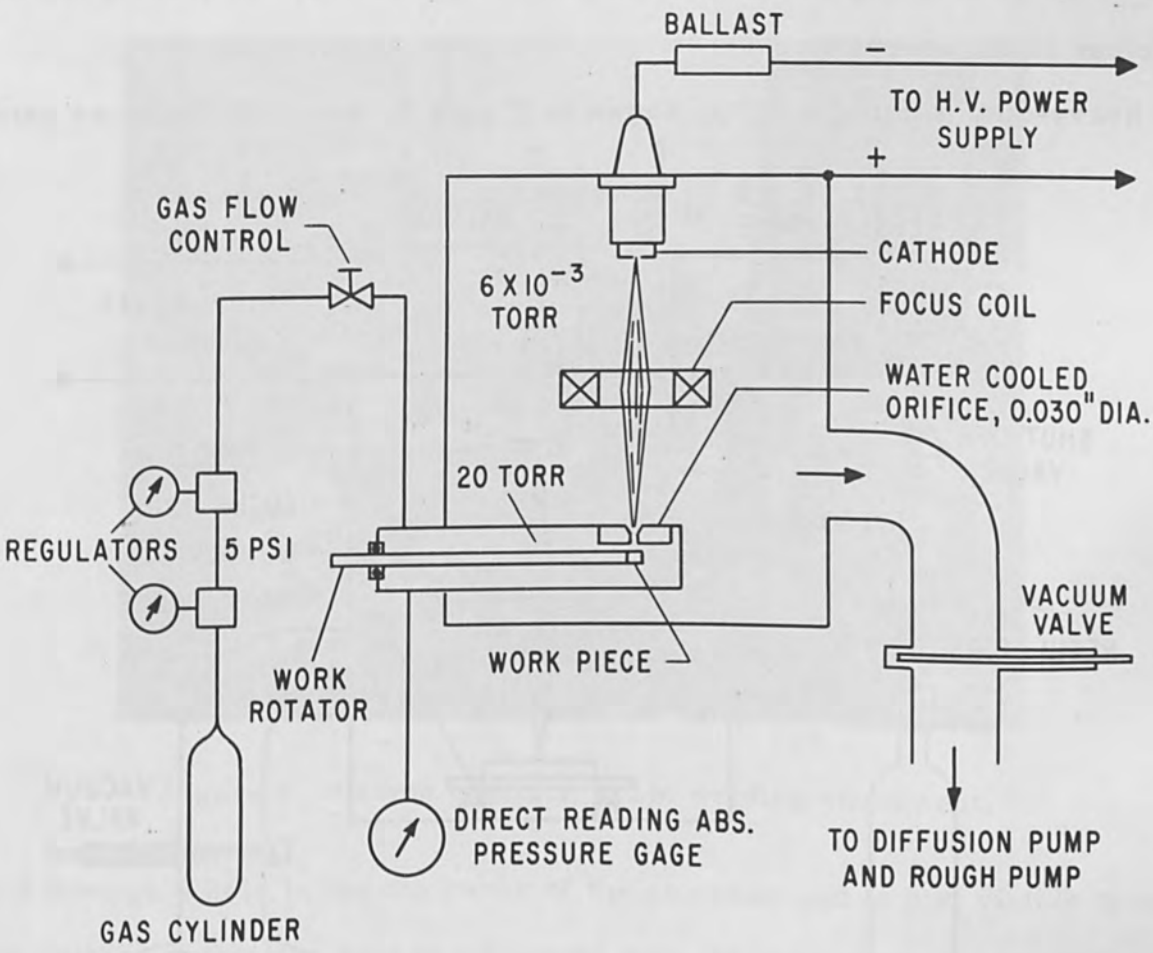

Figure 7 Light-duty welding system schematic diagram.

is fed through two states of pressure regulation to the chamber where the weld is to take place. An electromagnetic lens focuses the beam onto an aperture .030" in diameter which allows the beam to enter the chamber. Argon is fed into the welding

chamber through a needle valve as shown and is allowed to escape through the aperture into the main chamber. The needle valve is adjusted to maintain the required 20 torr in the welding chamber. A diffusion pump exhausts the main chamber to provide the pressure necessary for the operation of the plasma electron beam cathode. A single-stage of pumping makes it possible to generate the beam at 6×10^{-3} torr and weld at 20 torr. While considerable scattering of the beam occurs in the 20 torr region, good quality welds can be made by placing the work piece close to the aperture.

A heavy-duty welding facility, shown in Figure 8, was built for more general

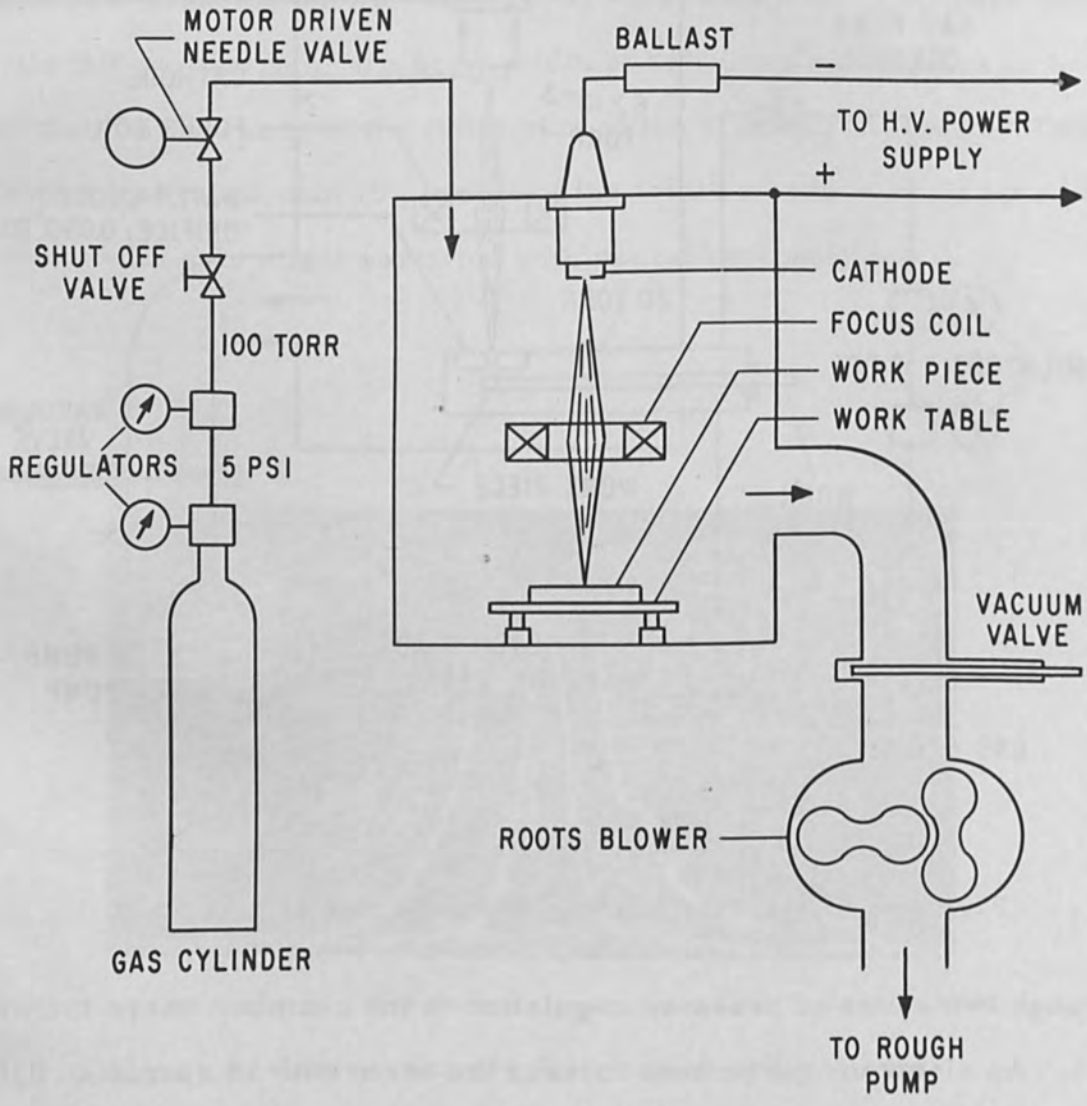

Figure 8 Heavy-duty welding system schematic diagram.

investigations. The gas pressure is dropped in two stages to approximately 100 torr. From this pressure a needle valve controls flow into the welding chamber. The chamber is continuously exhausted with a Kinney KMBV 520/KDH-65 mechanical booster pumping system. Gas in-flow is adjusted to provide gas pressure such that the desired beam current is realized.

Figure 9 is a front view of the chamber and the control panel. The gun is

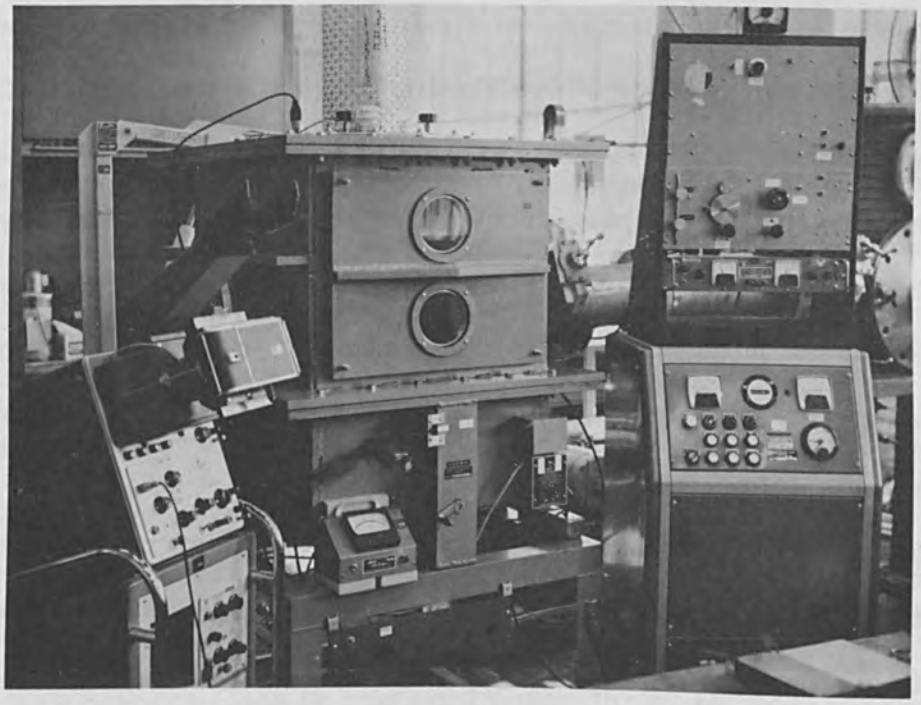

Figure 9 Plasma electron beam welding equipment.

mounted through a hole in the top cover of the chamber and is just visible through the high voltage protective screen. Situated with its centerline 12" below the cathode face is an electromagnetic focus coil. Located 8" below the center of the focus coil is the work table. The crank in the lower center of the picture provides manual side-to-side motion of the work table while a variable speed motor provides motion in the direction in which welds are made. A pair of beam sweep coils, as mentioned previously, is mounted between the focus coil and the work table. A

water-cooled aperture plate for analysis of the sweeping beam is mounted on the work table beside the work piece. An electrode mounted below the work table intercepts electrons which pass through the aperture. This current is displayed on an oscilloscope and used to assure that the system is in proper focus.

Technology of Welding with the Plasma Electron Beam

In the application of the plasma electron beam to welding, a major problem to be overcome was the control of pressure to maintain the desired beam current. The mass flow pumping characteristic of a diffusion pump slopes downward with increasing pressure at pressures above 1×10^{-3} torr. Therefore, if a diffusion pump is used without throttling, an increase in gas flow causes an increase in pressure and a decrease in pumping speed. This can lead to instability or, at best, to a system which is difficult to maintain in balance. If a throttling aperture is introduced between the pump and the welding chamber, the rising characteristic of the aperture can be substituted for the falling characteristic of the pump, but at a much lower pumping rate. Another solution is the use of a mechanical pump which has a rising characteristic in the range of 1 to 100×10^{-3} torr. This sytem is stable and fast and the pressure can be set at any value in this range merely by adjusting gas flow.

For welding, however, the settling of a pressure is not sufficient to maintain current, since there is some gas pressure change during welding and this can affect the beam current. Therefore, it was necessary to employ an electromechanical means of automatically controlling gas pressure.

Figure 10 is a block diagram of the automatic current control system. Total cathode current is measured by means of a shunt in the ground end of the power supply. The voltage across this shunt is compared with a reference voltage, the difference being the error which actuates the needle valve in the gas supply line. Position feedback is employed to cause the valve to open or close by an angular

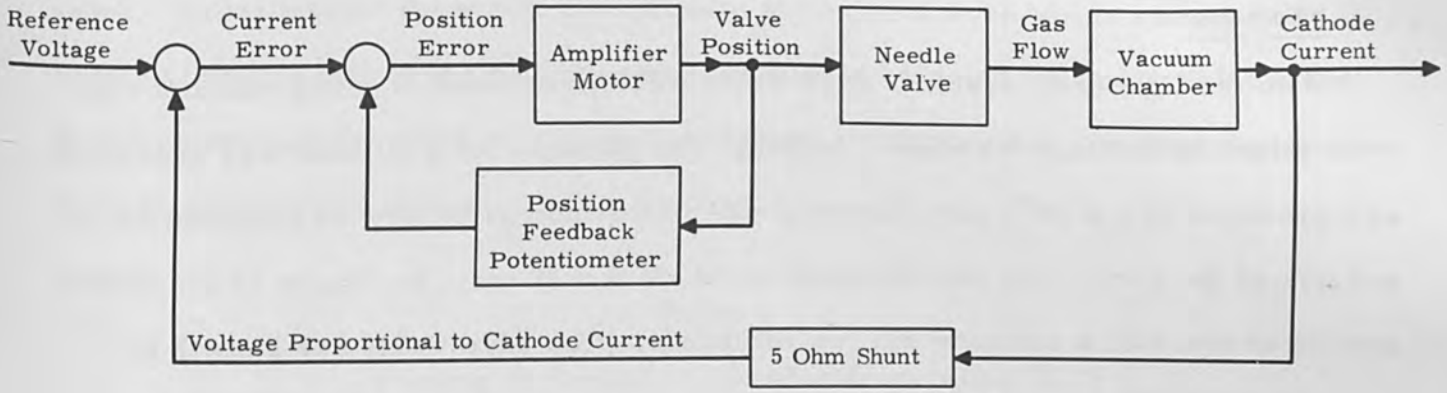

Figure 10 Block diagram - automatic current regulator system.

amount proportional to the error signal. This results in a stable system when the time constant of the chamber is long compared to the other time constants in the systems. This system of automatic current regulation is now in routine use on the heavy duty welding systems.

When initiating a beam, it is desirable to start at a known voltage in order that the focus system may be adjusted accordingly. To accomplish this, the chamber is pumped down to a pressure of approximately 1×10^{-3} torr before application of the high voltage. At this low gas pressure, no discharge occurs. The sweep coils are excited and the aperture plate is centered under the gun. Opening the gas shut-off valve (see Figure 8) allows the pressure to rise. As soon as a beam appears, the operator actuates the automatic current control and adjusts the reference voltage until the required current is obtained.

Focus of the beam can be checked by referring to the beam profile as indicated on an oscilloscope. If the work has been precisely aligned with the aperture plate, the weld can be completed by starting the work table drive and, at the appropriate time, cutting off the beam sweep. While the techniques of using the plasma electron beam are different from those for high vacuum beams, adequate control and stability have been obtained.

Results of Selected Welding Experiments

Niobium

With the light-duty system, edge welds were performed in which niobium cups were joined to niobium ferrules. Although the plasma electron beam was generated at a pressure of 6×10^{-3} torr the weld was performed at 20 torr as required by the end use of the part. The gun operated at 22 kV and 30 ma. In Figure 11 the welded part is shown with a common pin for reference. The edge welds are smooth in appearance and have proved to be vacuum tight and metallurgically sound.

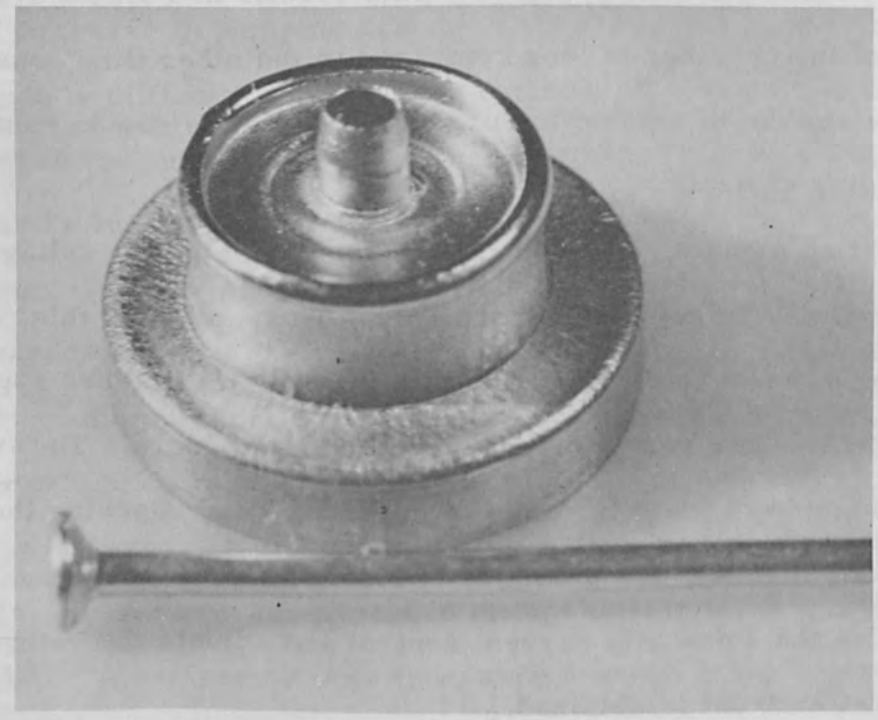

Figure 11 Edge weld made in argon at 20 torr.

Aluminum

As part of a continuing development program,* welds have been made in type 2219 aluminum alloy. Typical welding parameters for various thicknesses are

*Supported by Marshall Space Flight Center, Contract No. NAS8-11803.

listed in Table I. Figure 12 shows a cross section of a typical butt weld in 1/2" stock. Tensile tests show that the ultimate strength of such welds ranges from 70 to 80 percent of that of the parent metal. It should be noted that no special baffle or apertures are required to protect the plasma electron beam gun from the vapor and gas evolution of aluminum alloy welding.

Table I

Welding Parameters for Aluminum Alloy 2219

Thickness inches	kV	Cathode amps	Gas	Speed in/min.
.090	25	0.20	Ar	94
.090	25	0.15	Ar	94
.250	40	0.13	N_2	49
.359	40	0.18	N_2	49
.478	40	0.25	N_2	49

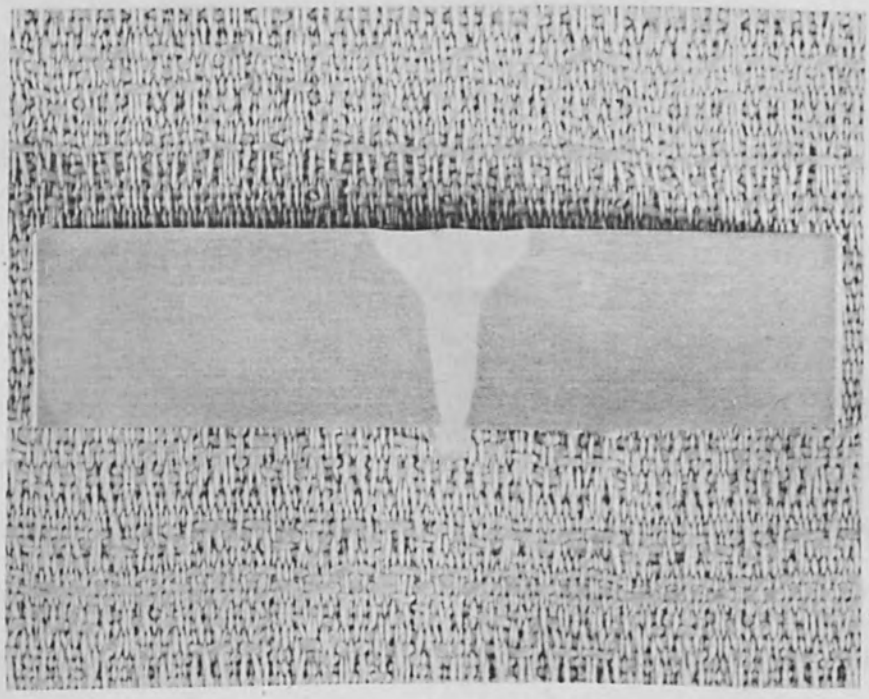

Figure 12 Butt weld in 1/2" aluminum alloy 2219.

Alloy Steel

Figure 13 shows the cross section of a 1" thick butt weld in 12-chrome alloy steel. A 1-1/2" cathode was employed in nitrogen at approximately 5×10^{-3} torr with 29 kV, 0.40 a. at 5"/minute. With a gun efficiency of 70 percent, the beam power was 7.1 kW. Again, no trouble from metal vapor was experienced.

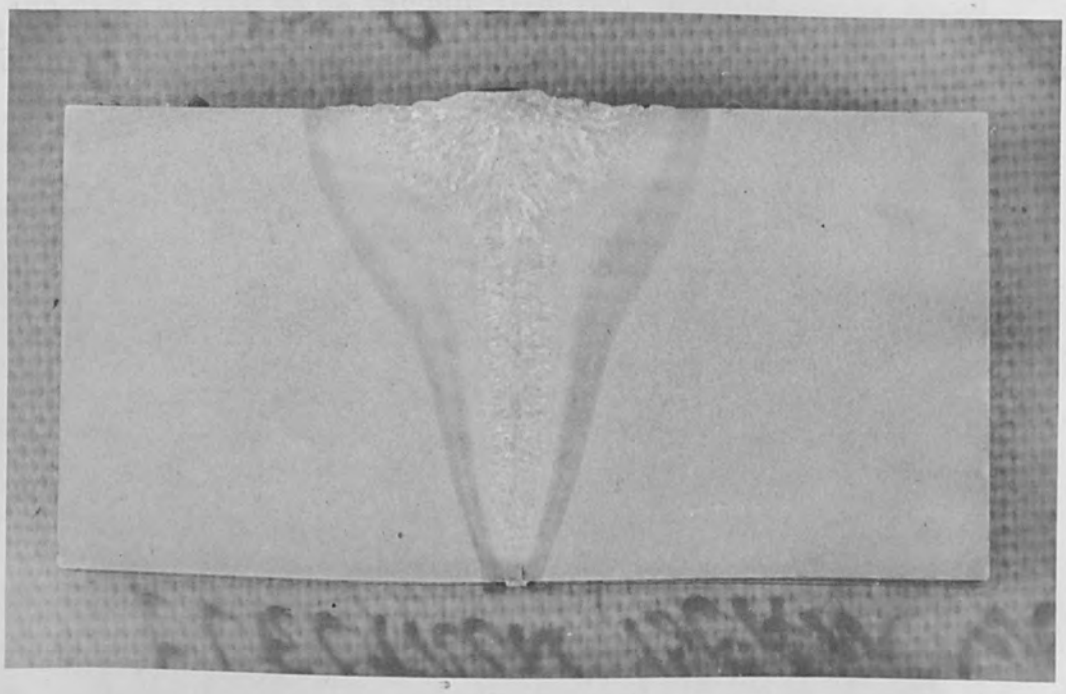

Figure 13 Butt weld in 1" thick 12-chrome alloy steel.
(29 kV, 0.4 a. Cathode Current, 5" per Minute)

Low Carbon Steel

Figure 14 illustrates the results obtained with 3/4" thick low carbon steel. These two bead-on-plate welds, shown in cross section, were made with a 1-1/2" cathode in argon at approximately 3×10^{-3} torr with 0.3 amperes cathode current at 35 kV. Assuming a gun efficiency of 70 percent the beam power was 7.35 kW. Traverse speeds were 10" per minute for the weld at the left and 15" per minute for

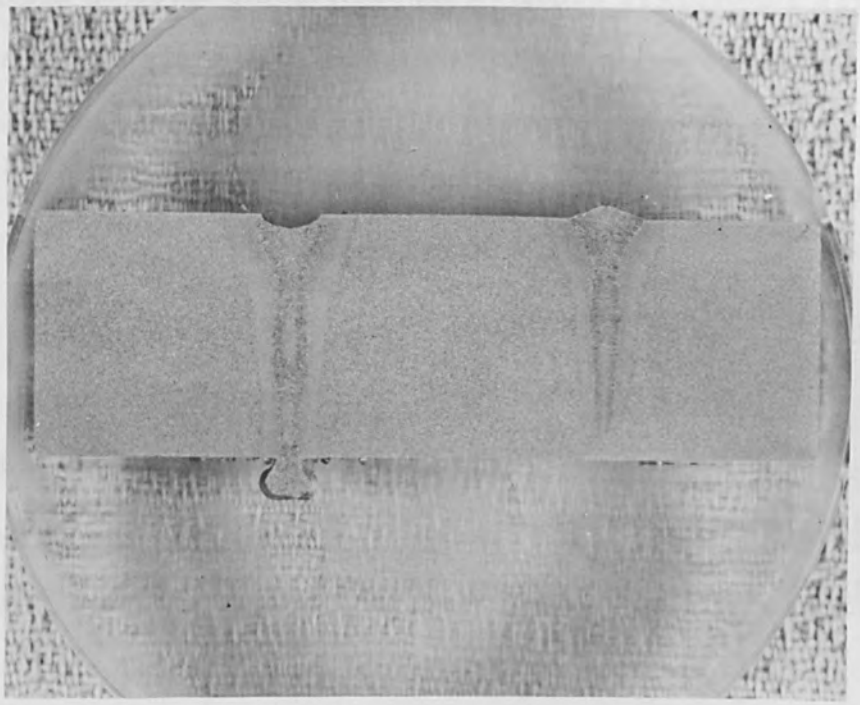

Figure 14 Bead-on-plate welds in 3/4" thick carbon steel.

the weld at the right. It should be noted that the weld at 10" per minute completely penetrated the 3/4" thickness, with a depth-to-width ratio of 7:1 for the fusion zone, if the wide portion at the top is neglected. On the same basis, the depth-to-width ratio of the shallower weld is 8:1. These weld dimensions approach those obtained with high vacuum beams of comparable voltage and power levels.

Conclusions

The plasma electron beam gun has been able to provide total power and power density with which welds greater than 1/2" deep in aluminum alloy and 1" deep in steel have been made. Rapid development of this technology is continuing.

Regulating systems and techniques have been developed which provide the precise control necessary for welding.

PEB cathodes have relatively long life and metal vapors and gases from the work do not interfere with their operation.

The inert gas atmosphere required for the plasma electron beam system enhances its value where welds are to be made at relatively high pressures. For ordinary welding, pump down times are shorter and chamber leakage requirements are less severe than with high vacuum equipment.

References

1. Stauffer, L. H., and K. L. Boring, "Hollow Cathode Enhances Plasma Electron Gun", Electronics 35, No. 49, p. 60 (December 7, 1962).
2. Boring, K. L., and L. H. Stauffer, "A New Non-Thermionic Electron Gun", Proc. National Elec. Conference 19, 535 (October, 1963).
3. Stauffer, L. H., and J. H. Terhune, March 1964 Electron Beam Symposium.

Laser Beam Micro-Processing

by

P. H. Kim and S. Namba
The Institute of Physical and Chemical Research
Komagome, Bunkyo, Tokyo

I. Ida and S. Nakayama
The Electrical Communication Laboratory, N. T. T.
Midoricho, Musashino, Tokyo

Abstract

Optimum power density for drilling and welding has been determined on the basis of the relationship between power density and surface temperature which was obtained by measurement of the velocity distribution of electrons emitted from the irradiated area of the surface. It is shown that the surface temperature is determined only by the evaporation rate in the case of intense laser irradiation (larger than 10^7 W/cm^2).

Introduction

A number of papers on laser induced thermionic emission have recently been published. The results of the measurements of the surface temperature of metals heated with a pulsed and focused laser beam seem to be widely different. Lichtman[1] estimated the temperature below the melting point and Honig [2] believes it is above the boiling point. The results of the measurement of the surface temperature of some metals heated by a ruby laser, and the relation between the surface temperature and the irradiating power density are given in this paper. The efficiency and optimum conditions for welding and machining are discussed.

Description of the Apparatus and Experimental Results

In a vacuum diode, even if the anode is negatively biased, only a fraction of the electrons emitted from the cathode reach the anode. The current collected by the anode is given by

$$i_A = i\, e^{-iV/kT} \tag{1}$$

where i_A is the anode current per unit area, i the cathode thermionic emission per unit area, k is Boltzmann's constant, V is the retarding voltage and T is the temperature of the cathode.

The surface temperature can be obtained from the slope of a semilog plot and is given by

$$m = -\frac{e}{kT} \log_{10} \varepsilon = -\frac{5040}{T} \tag{2}$$

Figure 1 shows a schematic of the experimental arrangement. A 0.3 joule laser beam is focused with a lens of focal length of 50 mm on the cathode of a vacuum diode. A negative voltage is applied on the anode and the emission current caused by each pulse of the laser is measured with an oscilloscope. An example of oscilloscope traces is shown in Figure 2. The irregularity of the thermionic current seen on the figure is due to the fluctuation of the surface temperature caused by the laser spikes.

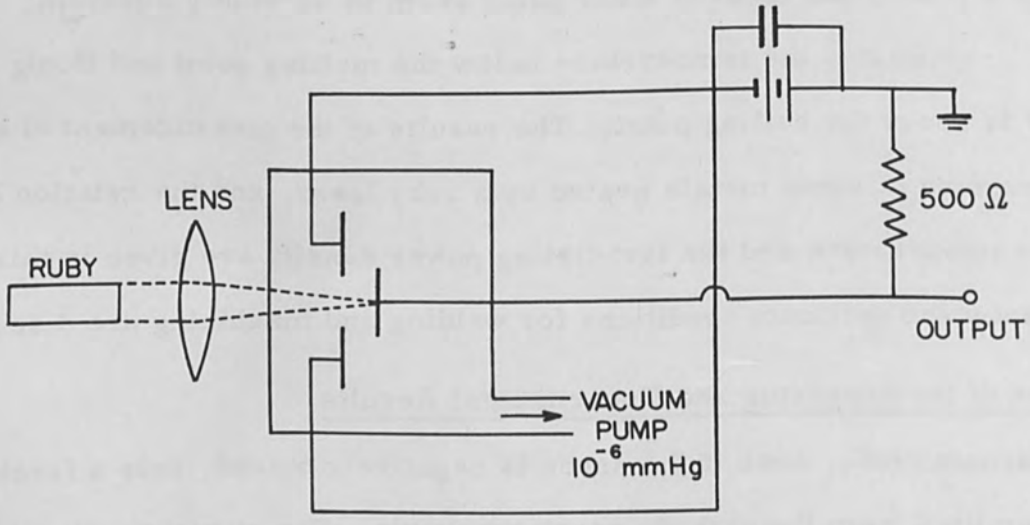

Figure 1 Experimental arrangement.

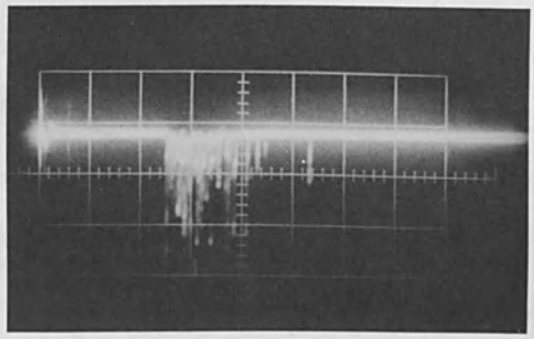

Figure 2 An example of thermionic current.
(0.2 msec/div)

The results are shown in Figure 3 and the measured temperatures are compared with the boiling points in Table 1. From these comparisons, it can be seen

Table 1

Measured temperatures and boiling points.

	Measured temperature	Boiling point
W	4300 °K	5900 °K
Mo	4000	5100
Ti	3400	3600
Ni	2700	3100

that the surface temperature of tungsten and molybdenum are about 1000 °K above their boiling points while those of nickel and titanium are nearly equal to their boiling points. It is not possible to explain this difference on the basis of heat conduction because tungsten and molybdenum have a higher thermal conductivity than nickel and titanium.

The curves in Figure 4 represent the relation between input power density and surface temperature. These are calculated using the heat transfer equation for

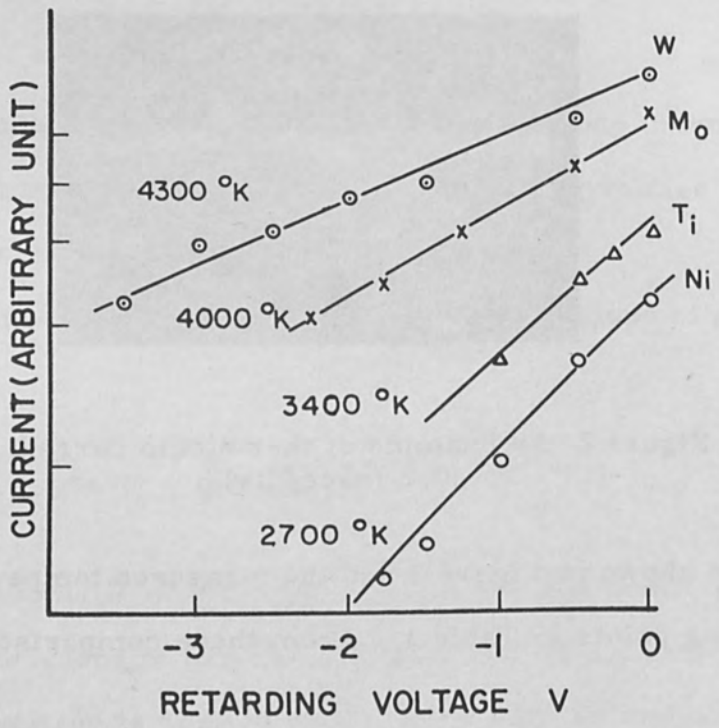

Figure 3 The experimental result.

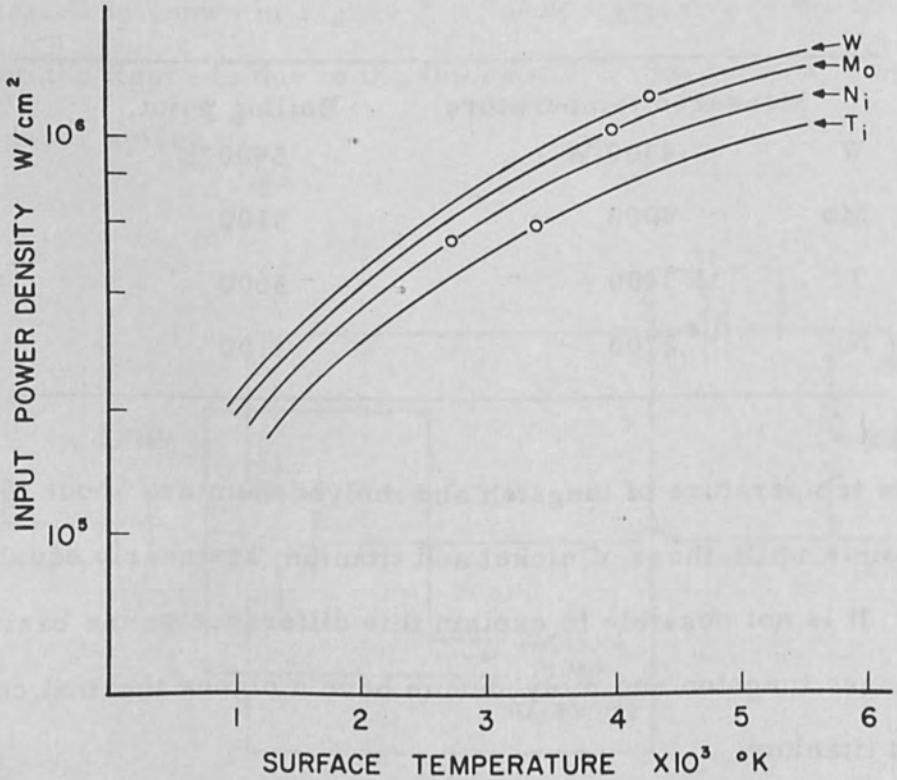

Figure 4 The relation between the surface temperature and the input power density.

uniform surface heating of a semi-infinite solid.[3] The circles on the curve represent the measured surface temperatures. The power density of the laser was estimated to be about 10^6 W/cm^2. The measured surface temperature of molybdenum and tungsten are nearly equal to those calculated; however, in the case of nickel and titanium the measured results correspond to calculated values for lower power density. This is due to the fact that the latter are more readily vaporized than the former.

The surface temperature was determined by the difference between the input power and the power losses which consist mainly of the energy loss due to vaporization and the heat conduction loss. The loss due to vaporization becomes very significant at high temperatures and cannot be neglected because the evaporation rate increases steeply with the temperature.

As shown in Figure 5, the vaporization loss for tungsten heated by irradiation of 10^6 W/cm^2 is negligible. On the other hand, the surface temperature of nickel will depend on both the evaporation and conduction losses. The total is represented by the dashed curve.

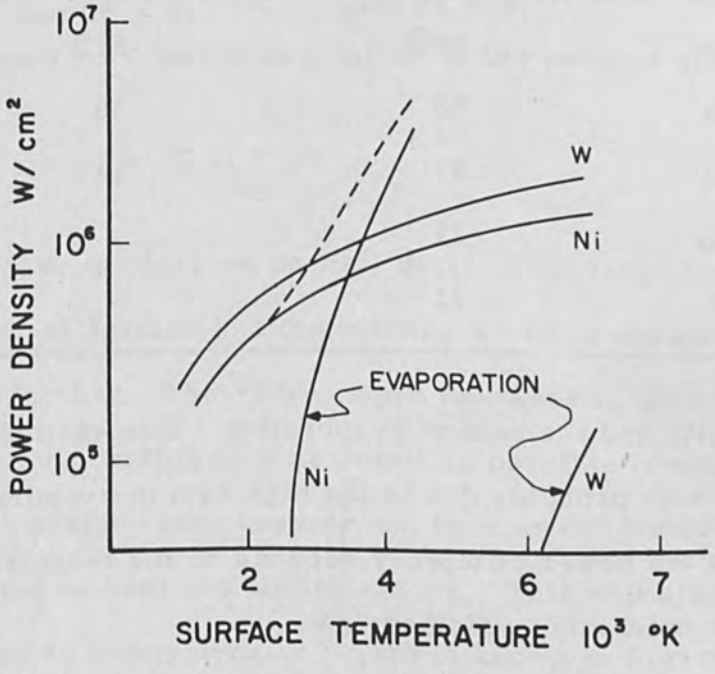

Figure 5 The effect of evaporation.

Efficiency of Laser Processing

When evaporation is assumed to be the only cause of removal of the material the power efficiency of the laser machining is defined as the ratio of the energy utilized in vaporizing the material to the input energy of laser beam and is given by

$$\eta = \frac{W}{W_L} \times 100\% \qquad (3)$$

where W_L is the total energy of the laser beam and W is the total energy of vaporization.

The power efficiency can be obtained by measuring the difference in weight before and after irradiation using a microbalance. This is shown in Table 2 for 15 mm and 50 mm focal lengths of the lens. The power efficiency is influenced by

Table 2

Power efficiency.

	focal length f = 15 mm	focal length f = 50 mm
Zn	68%	51%
Ti	58	38
Ni	51	11
Cu	21	-
W	21	-

the thermal diffusivity and the rate of evaporation. For example, with zinc the power efficiency is high probably due to the high rate of evaporation while with copper and titanium the power efficiency depends on the thermal diffusivity.

If we define the machining efficiency as

$$\eta = \frac{\text{vaporized volume}}{\text{input energy}}$$

we can see that this will depend on the boiling point, the thermal diffusivity and the latent heat per unit volume. Table 3 gives the machining efficiency for various

Table 3

Machining efficiency.

	focal length f = 15 mm	focal length f = 50 mm
Zn	54×10^{-6} cc/J	40×10^{-6} cc/J
Ti	17	11
Ni	9	2
Cu	4	-
W	2	-

materials and with focal lengths of the lens of 15 mm and 50 mm. An empirical plot of the machining efficiency versus the product of the thermal diffusivity, latent heat and boiling point is shown in Figure 6. It can be clearly seen from this figure that the efficiency decreases with increasing values of the product and also varies with the power density.

Welding Condition

Contrary to the case of electron beams, most of the laser beam energy is absorbed by the material surface and the melting which is essential for welding is produced by heat conduction. Therefore, when the laser is used for welding it is desirable to keep the evaporation loss as small as possible compared with the conduction loss. The surface temperature can then be estimated and the melting zone can be determined by heat conduction theory. This will also make it possible to compute the irradiated power density. This is shown in Figure 4 and Figure 5.

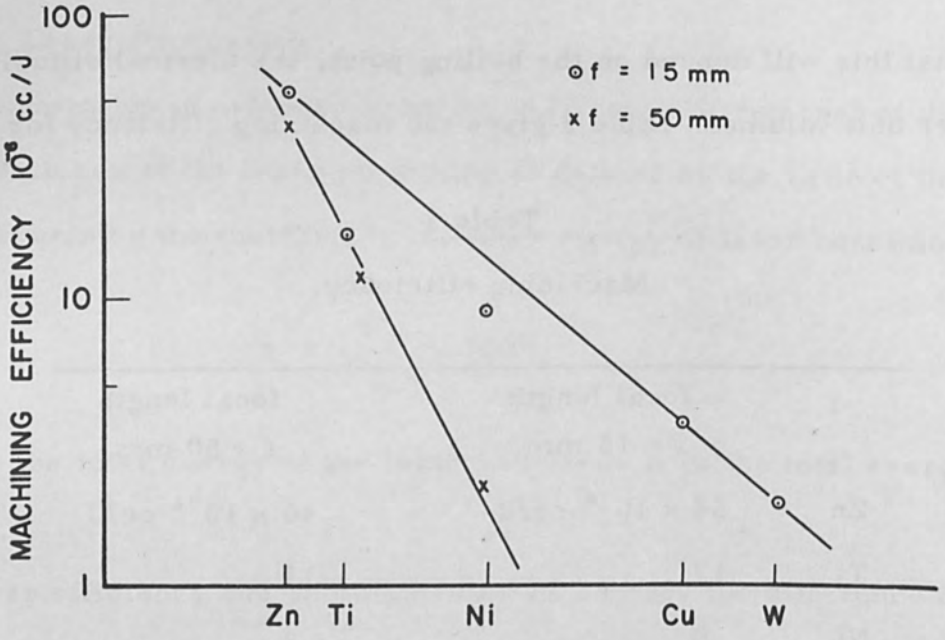

Figure 6 Machining efficiency vs. product of thermal diffusivity, latent heat and boiling point.

References

1. Lichtman, R., and J. Ready, Phys. Rev. Lett. 10, 342 (1963).

2. Honig, R., Appl. Phys. Lett. 3, 8 (1963).

3. Carslaw, H., and J. Jaeger, Conduction of Heat in Solids, Oxford (1959).

Laser Welding of Microcircuits

by

T. A. Osial and K. B. Steinbruegge
Westinghouse Research and Development Center
Pittsburgh, Pennsylvania

P. Scharf
Westinghouse Aerospace Division
Baltimore, Maryland

Abstract

This paper briefly reviews the various types of microcircuits which are currently employed in the electronics industry and discusses some of the basic criteria used to determine the relative merits of different electronic packaging techniques. Various welding processes and equipment developed in recent years to meet the requirements of this new packaging technique are presented. One of the most recent and most promising of these is the laser. A discussion of laser principles is presented together with characteristics which make the laser so attractive for welding applications as well as some of its limitations. A laser welding system is described. Results of laser welds made on various microcircuits is presented. Data is presented on the weld characteristics as a function of laser output energy and pulse duration.

Introduction

The miniaturization of electronic components, circuits, and systems has dominated the efforts of the electronics industry for the past decade. With the pace of development quickened by such catalysts as the Nation's advanced weapons and space programs, great strides have been made in reducing the size, power consumption and, in some instances, even the cost of electronic systems, while improving their overall reliability. Accompanying these developments has been the tremendous increase in the complexity of these advanced systems.

With increasing system complexity and improved component reliability, it has

become evident that new, more effective, and more widely applicable joining techniques must be developed. A modern radar or fire-control system contains thousands of components, and several times that many interconnections. A failure in any one of these joints may put the whole system out of service. Furthermore, with ever increasing component densities, techniques for welding to microminiature components in normally inaccessible locations must be improved. Several new techniques are currently being investigated. One of the most promising of these is the laser welder.

The laser has great potential for becoming an important microwelding tool, capable of meeting the stringent requirements of modern electronics. Because of some of its unique attributes, it offers the possibility of producing reliable welds in a large variety of materials and sizes, and by means of highly automated techniques.

Electronic Packaging Techniques

The basic criteria used to determine the relative merits of different electronic packaging techniques are: reliability, component density, production cost, repairability, and of course, the mechanical and electrical properties of the joints and circuitry. Every new packaging technique offers some major advantages over the others with regard to one or possible several criteria. But the improvement in one characteristic usually results in the degradation of another; no single packaging concept has universal applicability. It is the duty of the responsible engineer to choose the circuit concept which fulfills his specific requirements. Some of the more important electronic packaging techniques that are now in use or under active development include:

1. Printed circuit boards (Figure 1),
2. Wire-welded (cordwood) modules (Figure 2),
3. Pre-formed weldable circuits (Figure 3),
4. Planar-mounted integrated circuits (Figure 4),
5. Hybrid thin film circuits (Figure 5).

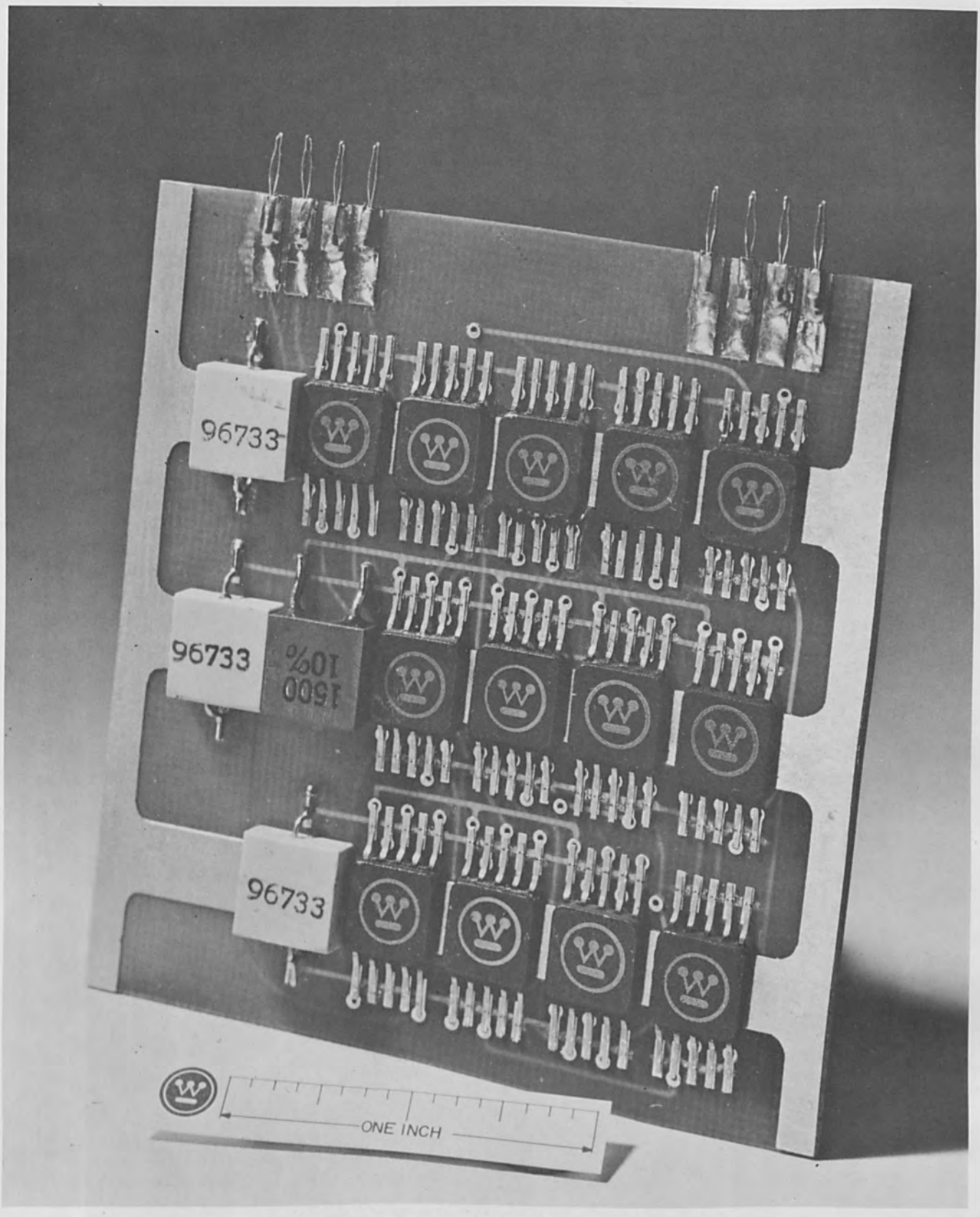

Figure 1 Printed circuit board with welded flat packs.

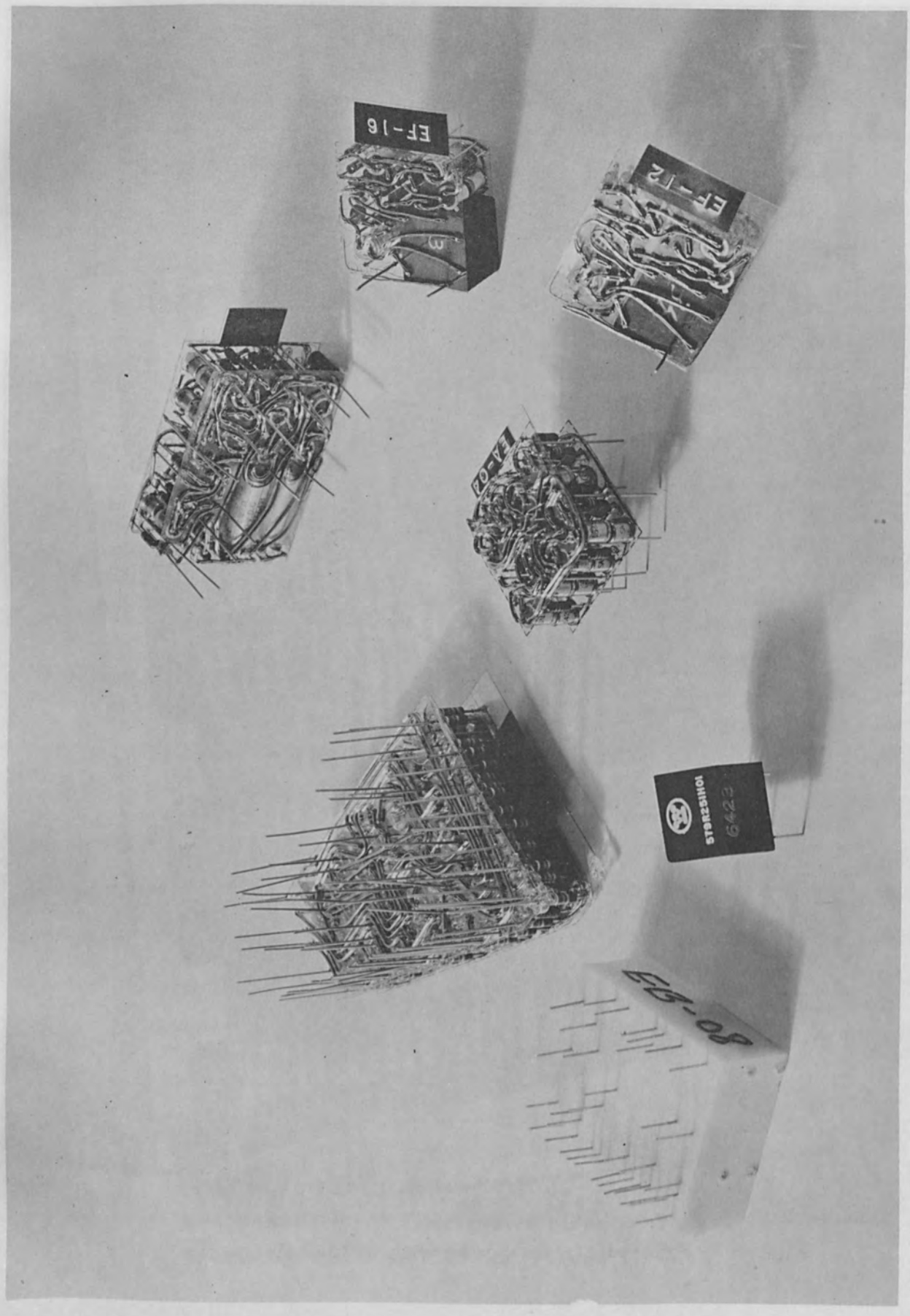

Figure 2 Wire welded modules.

Figure 3 Polyweld circuit board.

(Photograph courtesy of Litton Industries)

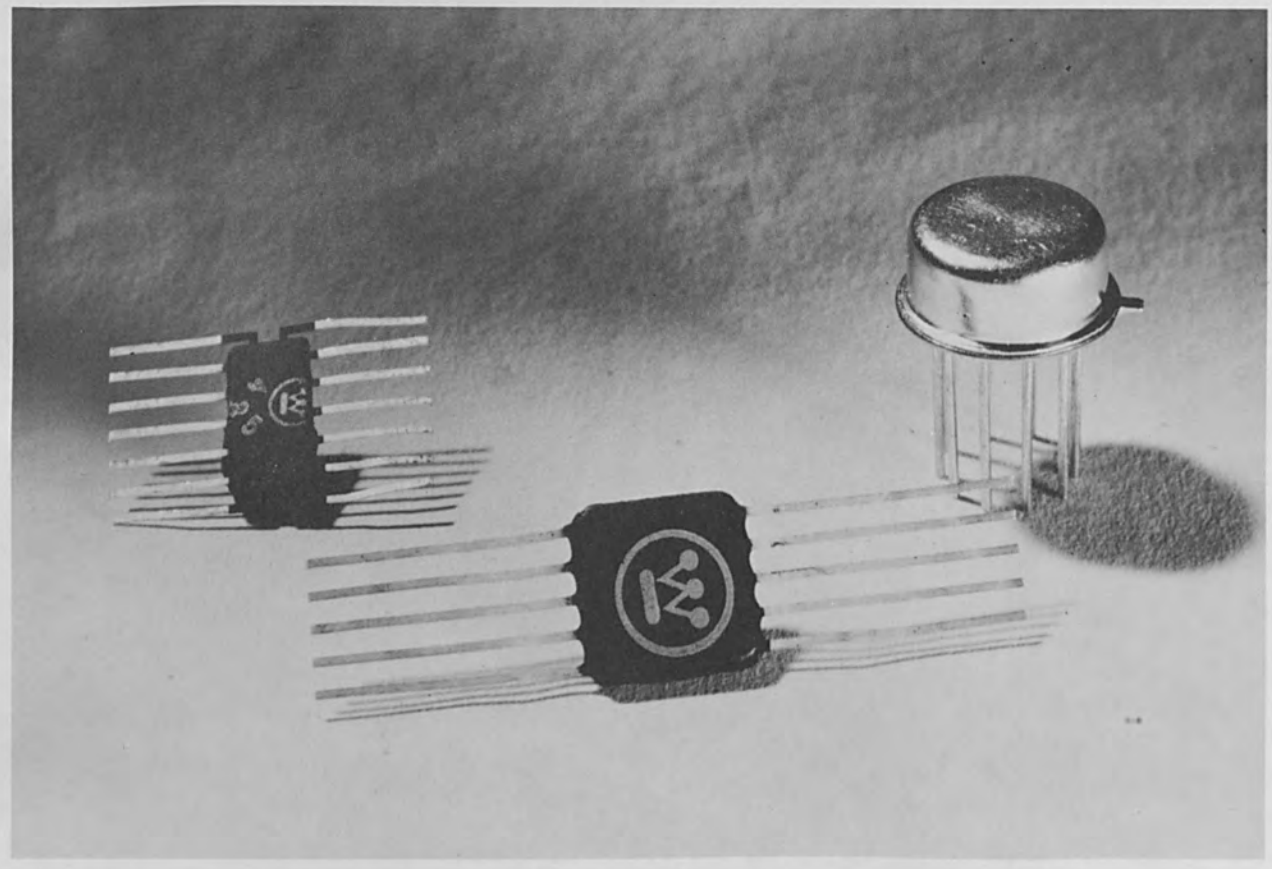

mechanical characteristics

G style FLAT-PAK • 0.1 grams

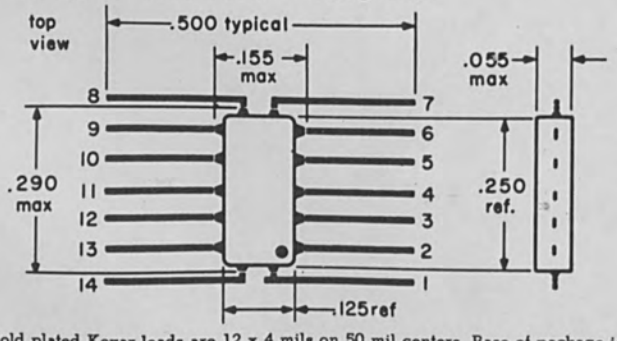

Gold plated Kovar leads are 12 x 4 mils on 50 mil centers. Base of package is ceramic. Lid is gold plated Kovar.

T package—12 pins • 1.1 grams

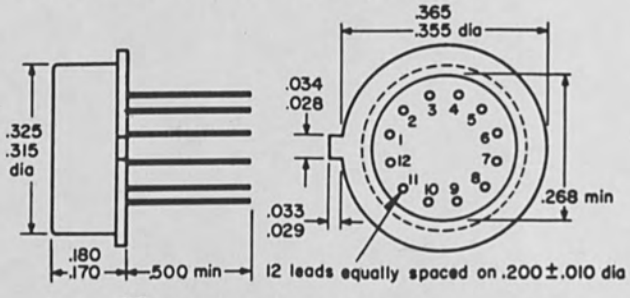

Q style FLAT-PAK • 0.25 grams

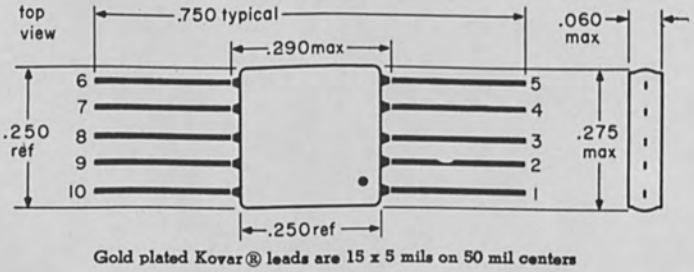

Gold plated Kovar® leads are 15 x 5 mils on 50 mil centers

Figure 4 Flat packs and T-package.

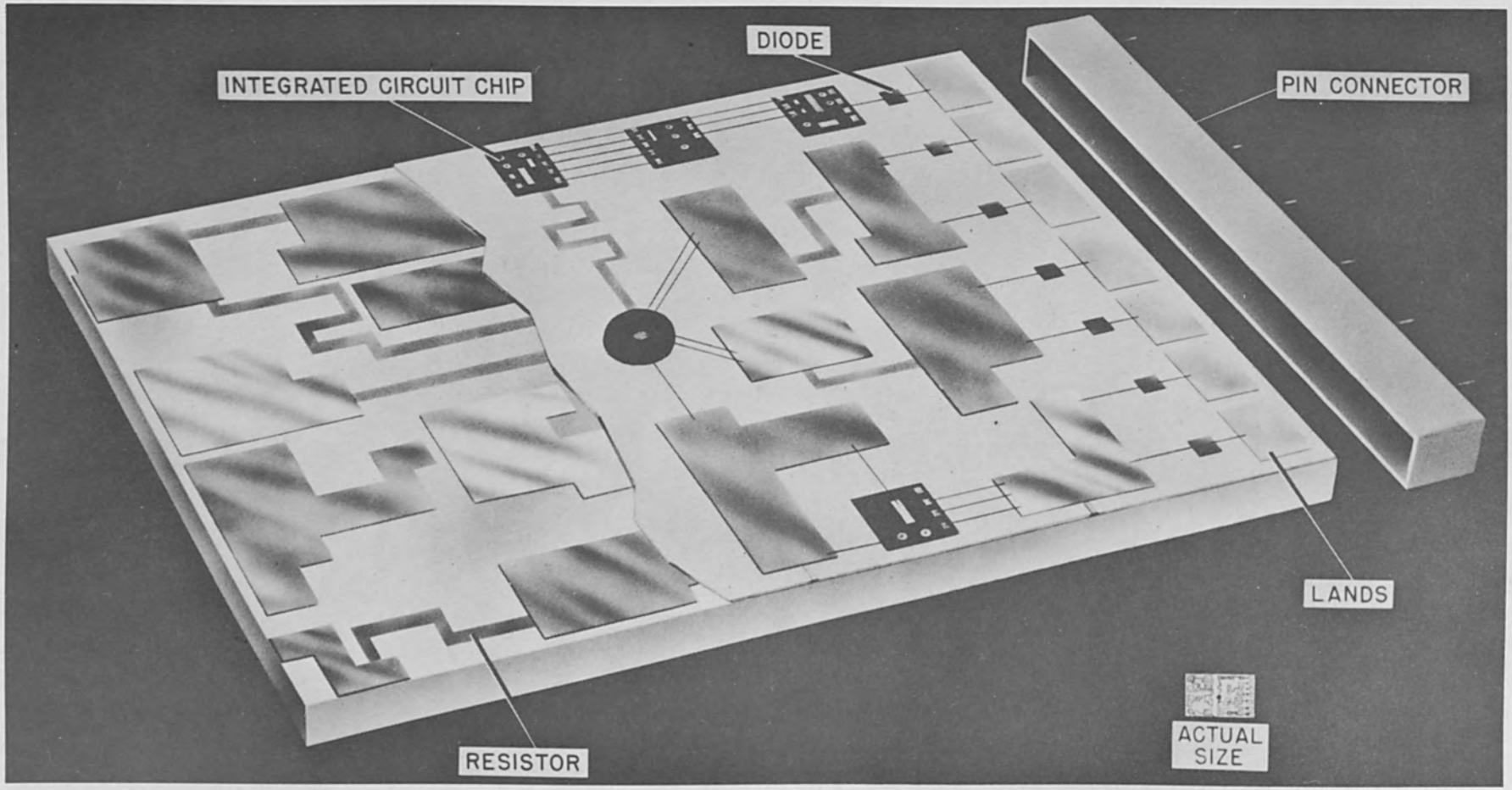

Figure 5 Multilayer thin-film circuit board.

As the various packaging techniques have evolved, they have been accompanied by a wide variety of welding processes and equipment to meet the requirements imposed by these packaging techniques. Most welding tools have been designed to fulfill the requirements of specific types of circuitry. However, some recently developed welding techniques -- such as laser welding -- have a high degree of flexibility and can be used advantageously with a wide variety of configurations and material combinations. Among the more prominent welding systems which are currently in use for microcircuit welding are:

1. Cross-wire resistance welding,
2. Parallel-gap welding,
3. Ultrasonic welding,
4. Thermocompression bonding,
5. Electron beam welding,
6. Laser welding.

Laser welding is one of the most recent and most promising techniques now available. Welding with a high energy beam of light offers a number of unique advantages and has many unique applications. Before discussing laser welding, however, it is appropriate to briefly review laser principles and characteristics. A more comprehensive treatment can be found in the References 1, 2.

The Laser

The word "Laser" is an acronym for Light Amplification by Stimulated Emission of Radiation. A laser was proposed by Schawlow and Townes[3] in 1958 and was demonstrated by T. H. Maiman in 1960.[4] The Maiman laser used a ruby crystal as the active laser material. Since then, many other types of solids as well as gases and liquids have also exhibited laser action and the list of materials is continually growing.[5]

Types of Lasers

The types of materials used to produce laser action and the method of excitation

define the four classes of lasers: optically pumped solid state lasers, gas lasers, injection or semi-conductor lasers and liquid lasers. In their present state of development, only the optically pumped solid state lasers have the necessary characteristics to make them suitable for welding applications. The gas laser's chief attribute lies in its monochromaticity, its small beam divergence, and its ability to be operated continuously. The power output, however, is too low to make it suitable for welding applications. The injection laser is a high efficiency device and can be operated continuously. The power output is too low for it to be a candidate for welding applications. It further suffers from a relatively high beam divergence. The liquid laser has the potential for becoming a high average power laser but it is not yet developed sufficiently for use as a practical welding tool. The liquid laser also suffers from a high beam divergence.

Of the numerous optically pumped solid state materials which have exhibited laser action, ruby and neodymium in glass appear the most attractive for welding applications because of their laser characteristics and their superior physical characteristics. Ruby is crystalline aluminum oxide (sapphire) to which has been added about 0.05% concentration of chromium ions. The neodymium in glass utilizes various kinds of glass as the host material with concentrations up to about 4% of neodymium. Because of the high pump powers required for operating ruby and Nd-glass, laser welders utilizing these materials must be operated on a relatively low duty cycle pulsed basis.

Laser Characteristics

The laser basically is a light source. But the laser possesses several characteristics which distinguishes it from conventional light sources. The laser characteristics which are most pertinent to welding applications are:

1. Directivity,
2. Total energy output,
3. Peak power output;

4. Pulse duration.

The light which is emitted by a ruby or Nd-glass laser is extremely directive with a beam divergence typically about 5×10^{-3} radians. The spot diameter (d) to which a light beam can be focused is determined by the angular beam divergence (θ) and the focal length (f) of the lens used. For small (θ), this relationship is given by:

$$d = f\theta$$

As an example, with a lens of 1 cm. focal length, the laser can be focused to a spot diameter of 5×10^{-3} cm. or an area of about 2×10^{-5} cm.^{2}. The theoretical limit of the spot diameter is imposed by diffraction effects and for a typical laser rod of 1 cm. in diameter, the spot diameter is a few microns (about 0.0001 inch).

Optically pumped solid state lasers in their present state of development are capable of delivering energies of from tenths or hundredths of a joule up to hundreds of joules in a pulse duration of tenths of a milli-second to tens of milli-seconds. Peak powers ranging from kilowatts to megawatts are available from such systems. In one mode of operation called "Q-spoiling" peak powers of up to 10^9 watts are available in times of about 10^{-8} seconds. A pulsed laser delivering 100 joules in 1 milli-second delivers a peak power of 10^5 watts. If the beam from such a laser is focused onto a surface with a 1 cm. focal length lens, and if the beam divergence is 5×10^{-3} radians, the peak power density at the focal spot becomes 5×10^9 watts/cm.^{2}. Such a power density is sufficient to vaporize most known materials. Power densities of this order have proved very useful for laser machining and drilling applications. For welding applications, however, such power densities are excessive.

The skin depth or depth of penetration of optical radiation in metals is extremely small, typically of the order of 10^{-6} cm. Laser welding, therefore, must be achieved by surface heating and thermal conduction through the metal. The power

density at the surface of the metal must be sufficient to raise the temperature of the surface up to the fusion point but below the vaporization point. The energy must be supplied in a time short enough to permit localized heating but in a time sufficiently long to permit penetration of the molten zone by thermal conduction. The achievement of these goals with a laser system requires a control of the total energy, the rate of delivery of energy (the pulse shape and pulse duration) and the power density at the surface (the focused spot diameter).

Since the pulsed laser is a well collimated, high power light source, it is well suited for welding of microcircuit components. Its major advantages for this application are:

1. Heat input to the work piece is relatively small and is delivered in a short period of time, thereby reducing the danger of thermal damage to the substrate.
2. The laser energy is delivered to the work piece without mechanical force which could induce strains and mechanical deformation.
3. Since electrodes are not required, welding is performed with freedom from electrode contamination and freedom from high currents which can cause damage to delicate electronic components.
4. The laser can be located at a convenient distance from the workpiece, permitting welding in areas which are not readily accessible.
5. The workpiece can be located in an enclosure which is evacuated or which contains a controlled atmosphere. Laser beam entry into the enclosure can be provided by a transparent window.
6. The laser beam can be focused onto a small area permitting the welding of high density microcircuit components.
7. A wide variety of materials can be welded.
8. The laser can be readily adapted to highly automated welding

techniques.

Laser Welder

As a result of preliminary experiments performed on various microcircuit components, a laser welder was constructed which provides the required parameters and versatility for welding of a wide range of microcircuit components. The laser welding unit consists of a laser head, a power supply, an energy storage and pulse forming network and an optical system for focusing the laser beam.

The head contains a 6 inch long ruby rod in a focusing cavity. The ruby rod is pumped by a xenon-filled flash lamp located close to the rod with the optical coupling provided by a high-efficiency reflector system. The entire laser head is constructed to permit either air cooling or water cooling of both the ruby rod and the flash lamp. Water cooling of the laser head permits operation at high pulse repetition rates and further serves to maintain constant temperatures which are necessary to insure reproducibility. Nominal overall efficiencies of the laser head exceed 1% and slope efficiencies greater than 2% have been achieved.

The laser output energy is controlled by the electrical input to the flash lamp which is determined by the voltage and the total capacity of the pulse forming network. The power supply is designed to provide the required voltages and currents to charge the pulse forming network between laser pulses.

The pulse forming network consists of a combination of inductors and capacitors arranged in a manner which provides an approximately rectangular flash lamp pulse and a similar rectangular laser output envelope. Control of the laser output pulse duration is obtained by switching of appropriate inductor and capacitor combinations.

The optical system for focusing the laser energy and for accurately registering the samples consists of a trinocular microscope with a sliding prism which permits either entry of the laser beam or viewing of the samples. The microscope is

equipped with three objective lenses on a rotatable turret for varying the viewing magnification or the spot diameter of the laser beam. Safety features are provided to protect the operator from exposure to the laser beam.

This laser welding system described above and shown in Figure 6 is capable of delivering up to 10 joules of output energy at a repetition rate of 12 pulses per minute with variable pulse durations of 1, 2, 3-1/2, and 5 milli-seconds. Output energies up to 20 joules with the same pulse durations are available at a reduced repetition rate.

Experimental Results

The laser welding experiments performed on various microcircuit configurations were guided by two major objectives: to investigate laser parameters that govern the quality of welds and to develop techniques for effective and advantageous utilization of laser welding in the production of sophisticated electronic equipment. Some of the types of circuitry which were utilized in the experiments and the results are described below.

Polyweld

Among the preformed weldable circuits, Polyweld is best suited and can be most easily adapted for laser welding. The tubelet configuration facilitates the effective control of lead positioning and spacing relative to the circuitry. Also, the large area of contact between the leads and tubelets results in a large, reliable weld.

Pull tests were performed on laser welds between .020 inch diameter Dumet, nickel, and Kovar wire and Polyweld with .023 inch inside diameter tubelets. For all three combinations, at least two joules at approximately 1 ms. pulse duration were required to produce welding. Some typical figures for energy applied and strength of Dumet to Polyweld welds are:

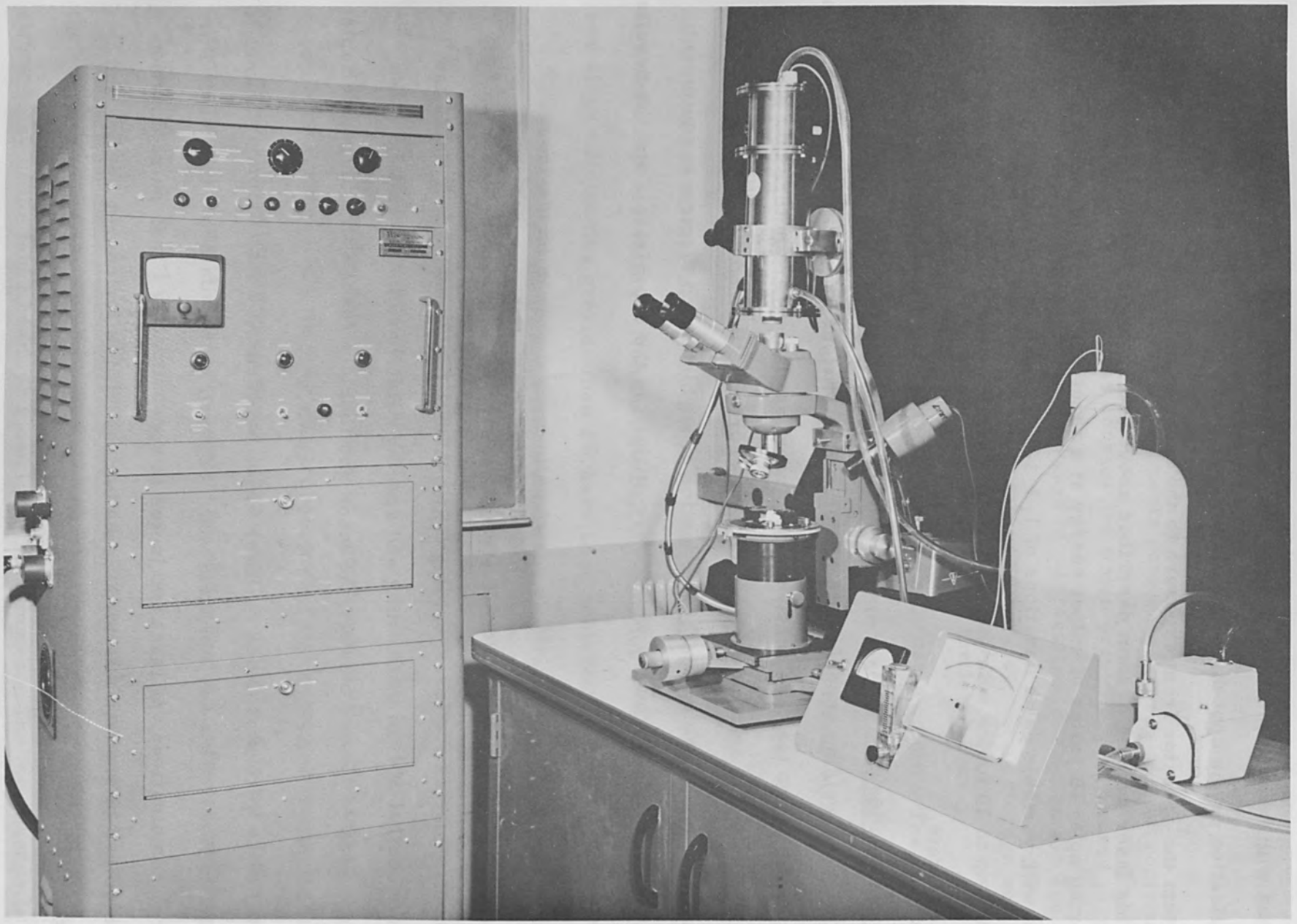

Figure 6 Laser welding system.

Energy Applied	Weld Strength
2 joules	2.5 lb.
3 "	6.8 "
4 "	10.4 "
6 "	11.8 "
8 "	12.7 "

Further work with Polyweld and nickel wire revealed the effect of spot size and pulse duration on weld quality. Figure 7 shows three columns of welds between nickel wire and Polyweld. For column 1, laser pulses of 8.8 joules and about 4.2 msec. duration were focused on top of the lead by means of a 50 mm. focal length lens. For column 2, the pulse duration was decreased to 1.7 msec. For column 3, the beam was focused through a 25 mm. lens while the energy and pulse length were the same as for column 1. External appearance, pull tests and photomicrographs all indicate that the welds produced using the longer pulse length and longer focal length lens were superior. Photomicrographs of the welds in column 1 (Figure 8) showed a large joint area and little porosity. The cross sections of welds from column 2 (Figure 9) showed that metal expulsion had occurred and that the welds were relatively porous. The welds in column 3 were similar to those of column 1, although not as uniform and consistent. Table 1 outlines the characteristics of these three sets of welds.

The results in Table 1 show that relatively long laser pulse lengths are required to produce consistently good laser welds. The Polyweld configuration lends itself to automated welding techniques. There are two major problems inherent in laser welding to Polyweld circuitry. They are: (A) any waviness in the supporting substrate will position the weld area at a point other than the focal point of the beam, and (B) leads that extend excessively above the tubelets frequently cause weak welds.

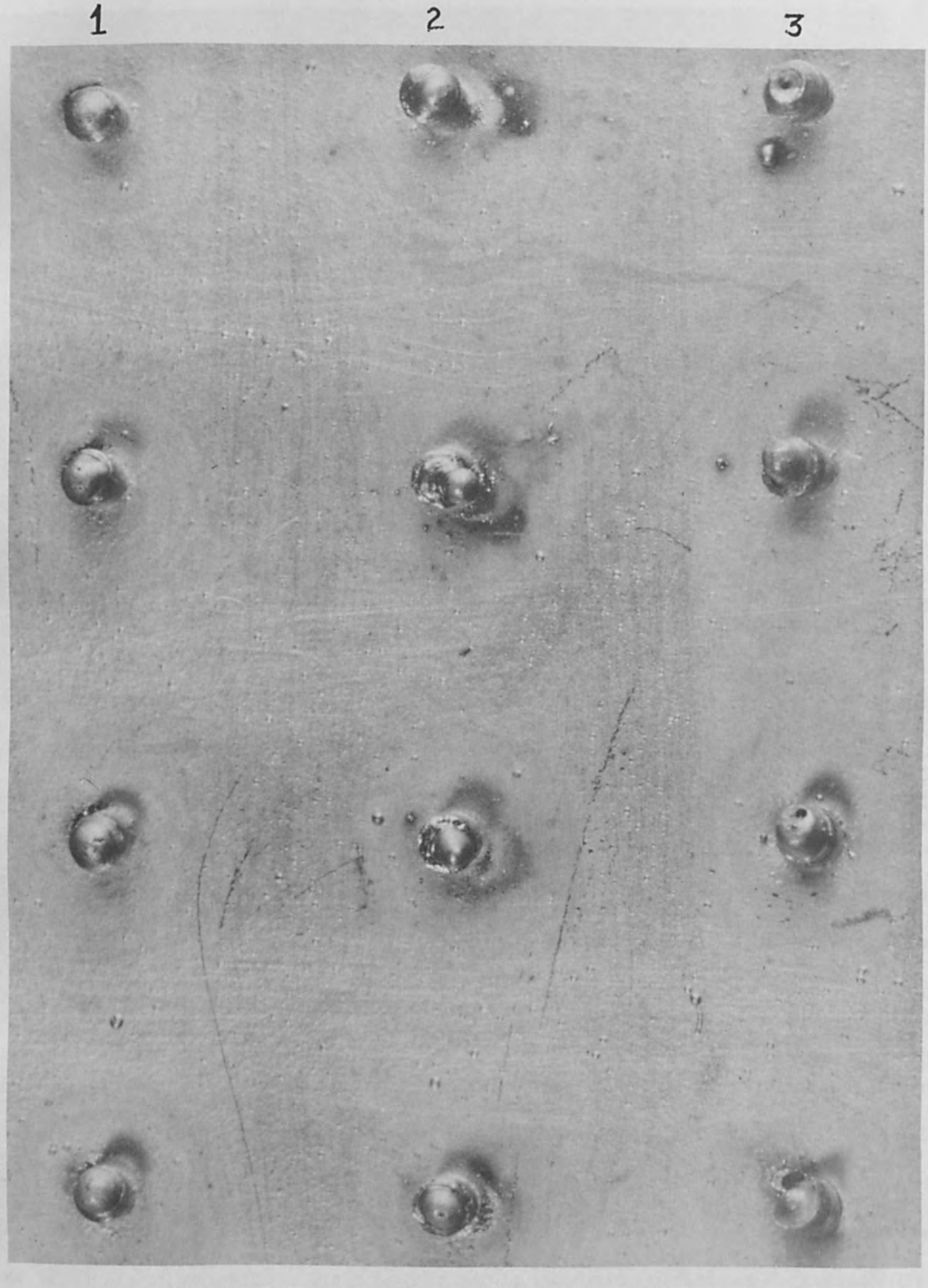

Figure 7 Laser welds of nickel wire to Polyweld.

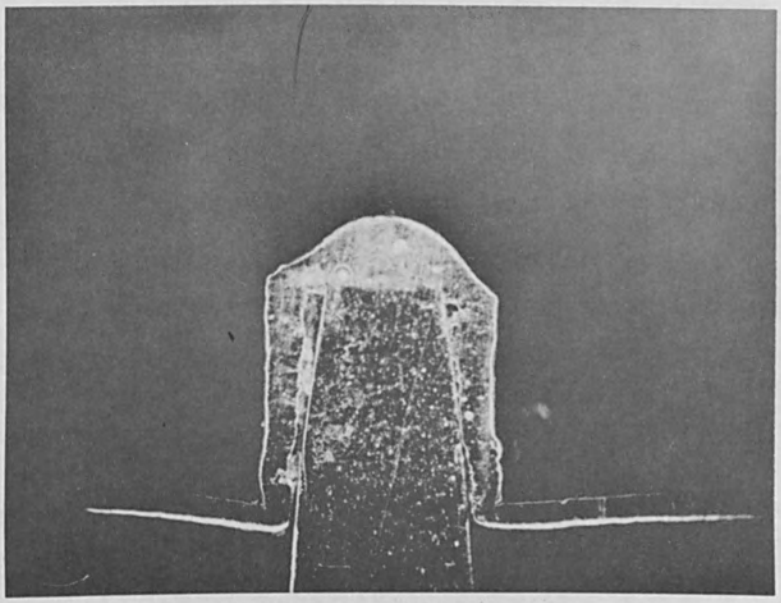

Figure 8 Laser weld of nickel wire to Polyweld. (8.8 joules, 4.2 ms., 50 mm. lens).

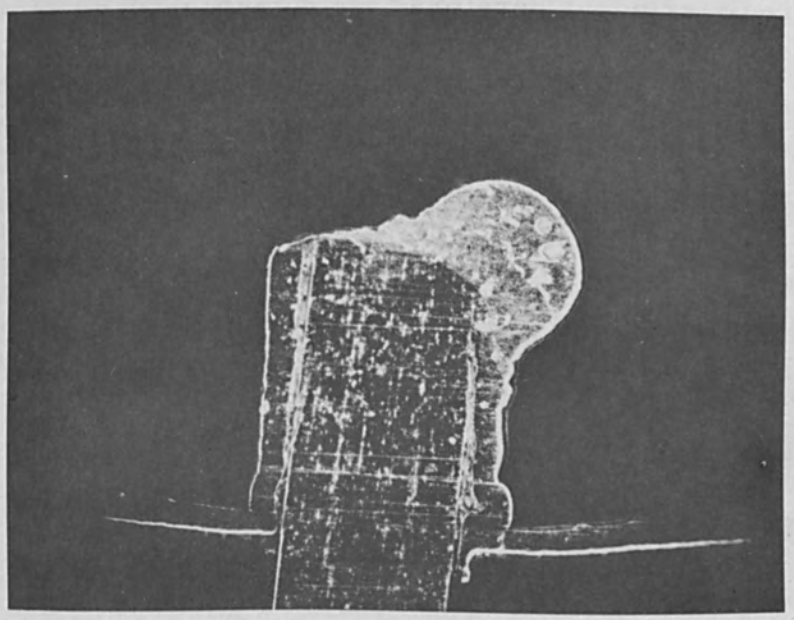

Figure 9 Laser weld of nickel wire to Polyweld. (8.8 joules, 1.7 ms., 50 mm. lens).

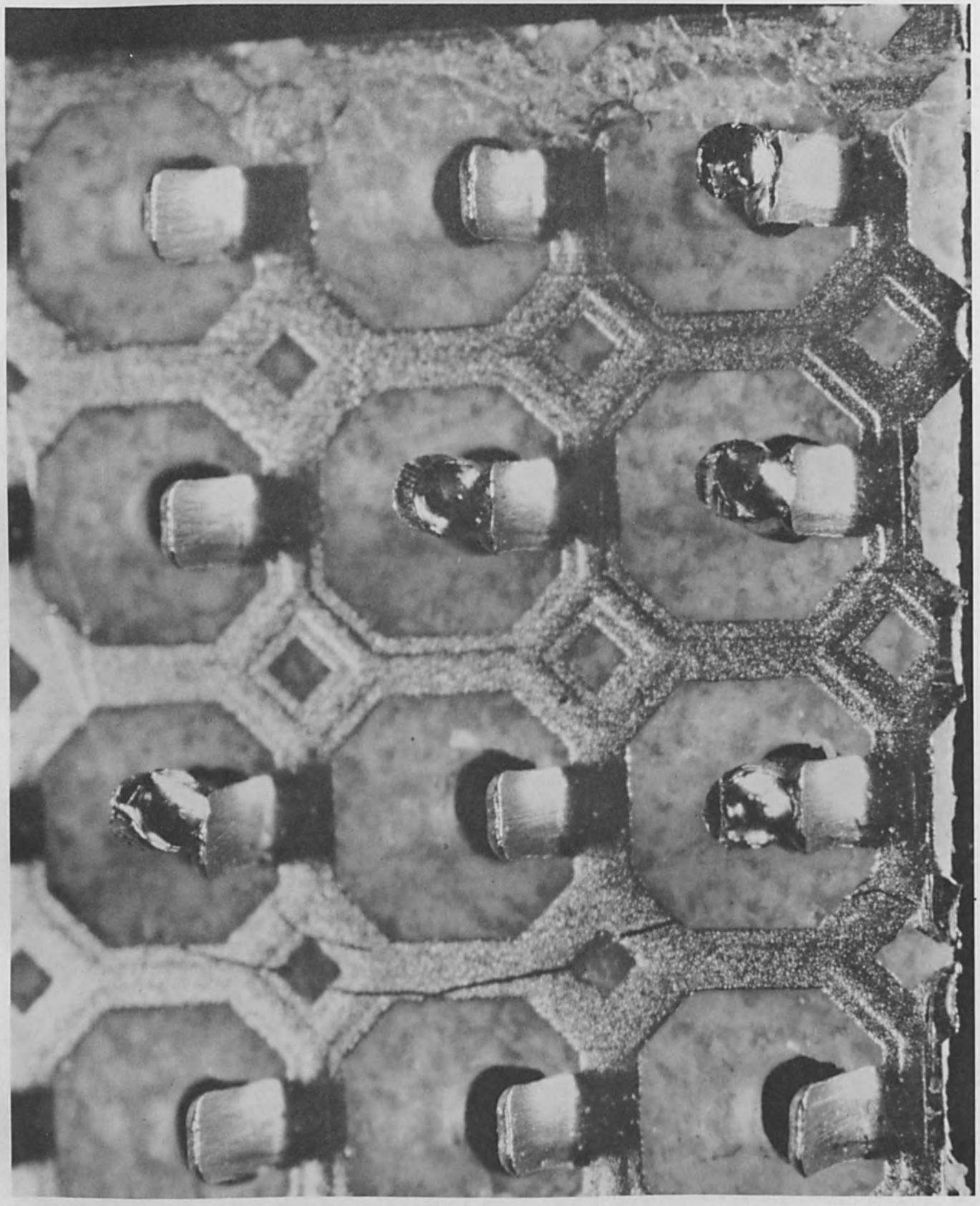

Figure 11 Nickel leads laser welded to intercon.

Flat Packs

The laser is one of the best tools for welding flat-packs to printed circuit boards. However, to insure consistent and reliable welding to ordinary printed circuits necessitates the utilization of some device for holding the lead in the proper location during welding. This fixturing device should also insure that the lead and circuitry are in contact during welding.

To eliminate the need for complex fixturing, and to enable laser welding of flat packs to be done automatically, "slotted printed circuits" have been developed (Figure 12). The flat-pack lead fits snugly into the slot or groove in the circuitry, thus providing for built-in fixturing. Contact between the lead and groove is not critical since welding occurs between the lead and the walls. The weld that results is basically a lap weld, and is relatively strong. During pull tests, the circuitry normally lifts from the substrate before the joint fails. Figure 13 shows a slotted printed circuit board with flat-packs that have been laser welded to it. Twenty joules at 3 ms. pulse length and a 30 mm. lens was used to make the welds.

Miniature Magnetic Devices

Welding is relatively little used in the production of magnetic devices -- inductors, transformers, etc. This is primarily due to the inherent difficulty of welding insulated copper wire by ordinary welding techniques. The laser, however, can be used to weld both insulated and bare copper wire, and can be used advantageously in the production of miniature components that utilize these materials.

Figure 14 shows a miniature transformer that has been welded to a Kovar "T-package". The welding was performed without prior removal of the insulation from the copper wire. The joints produced in this manner may not be as strong as those produced by welding bare copper wire. However, in many instances the strength and consistency of these bonds will be more than sufficient to meet requirements.

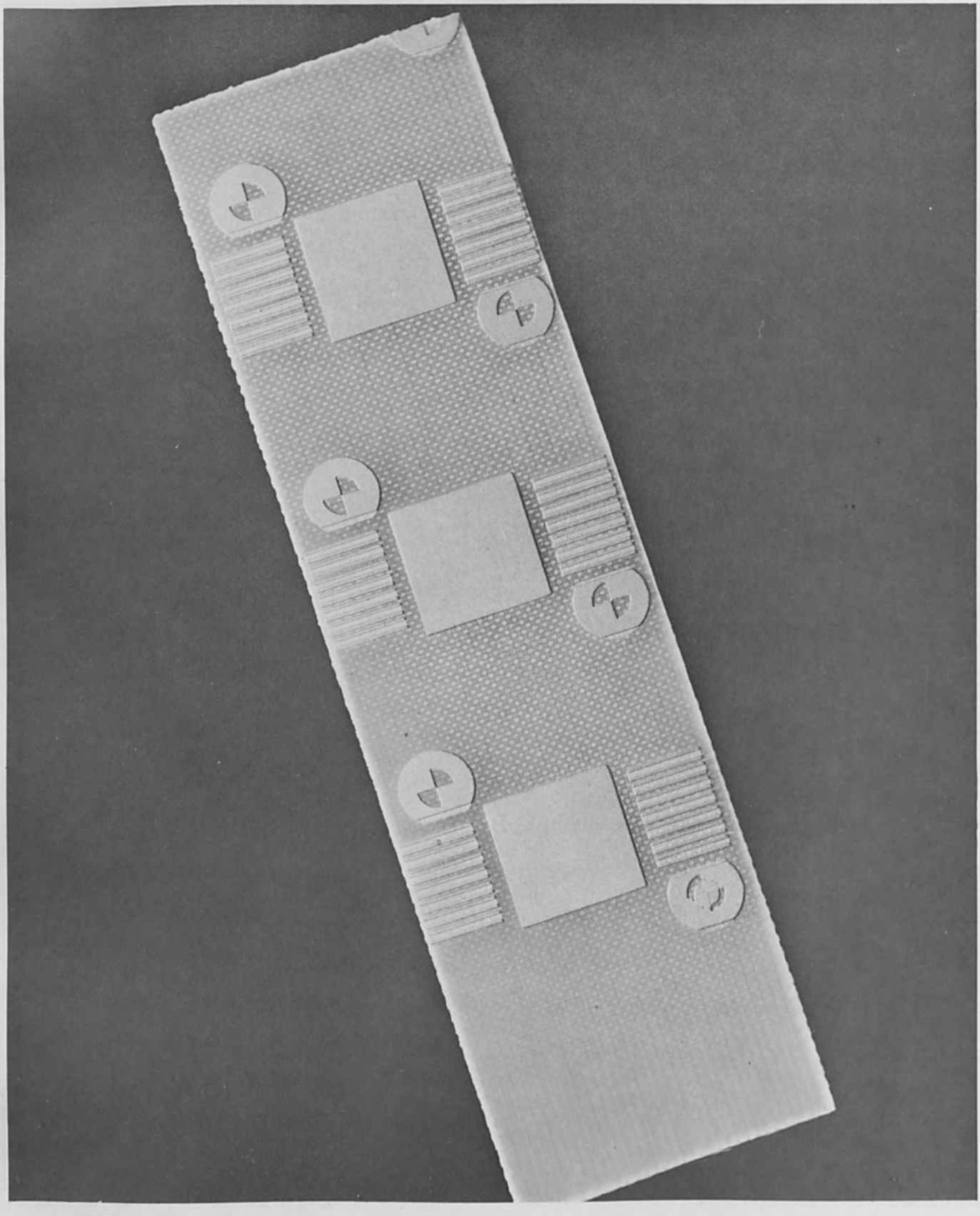

Figure 12 Slotted printed circuit board.

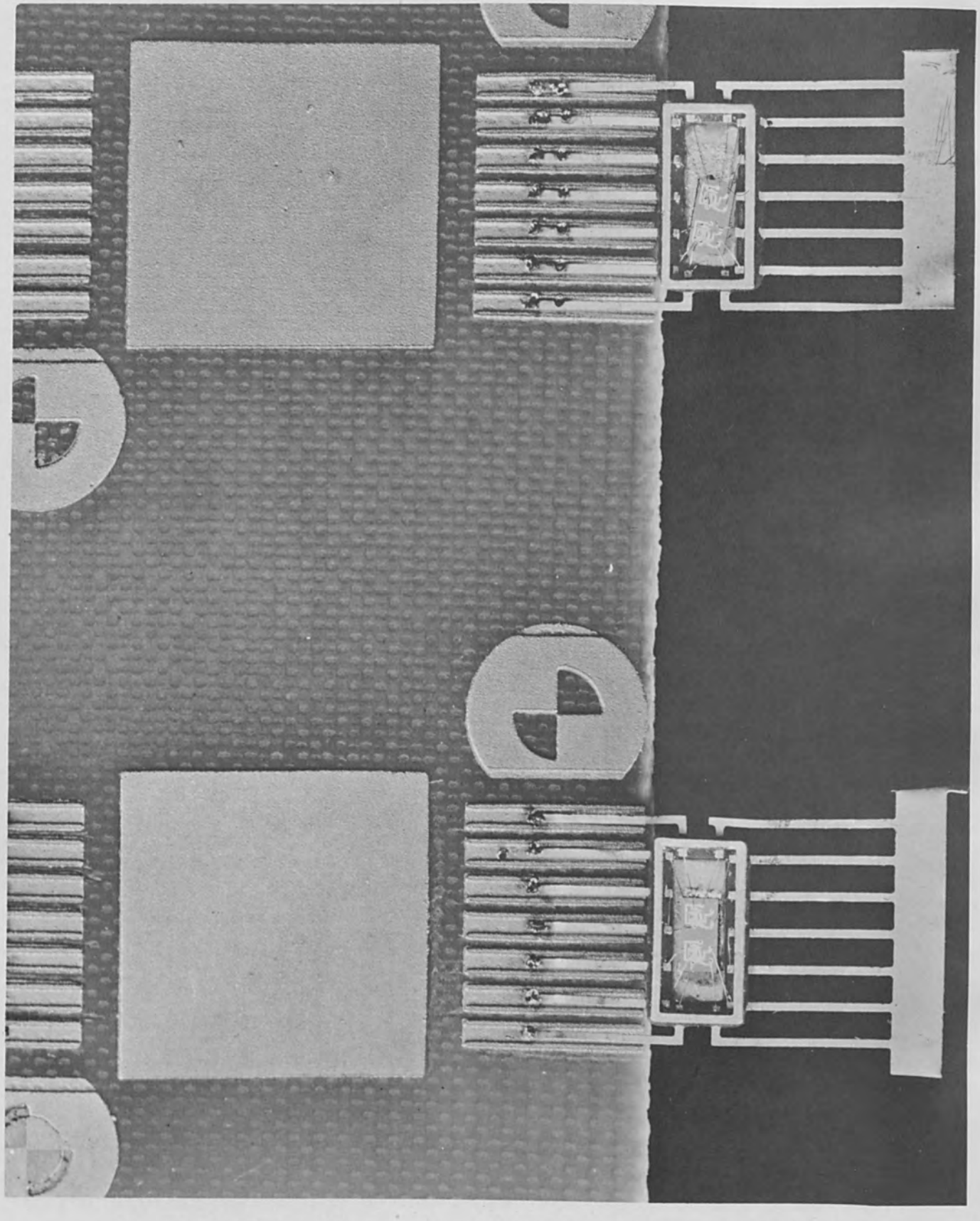

Figure 13 Flat packs laser welded to slotted printed circuit board.

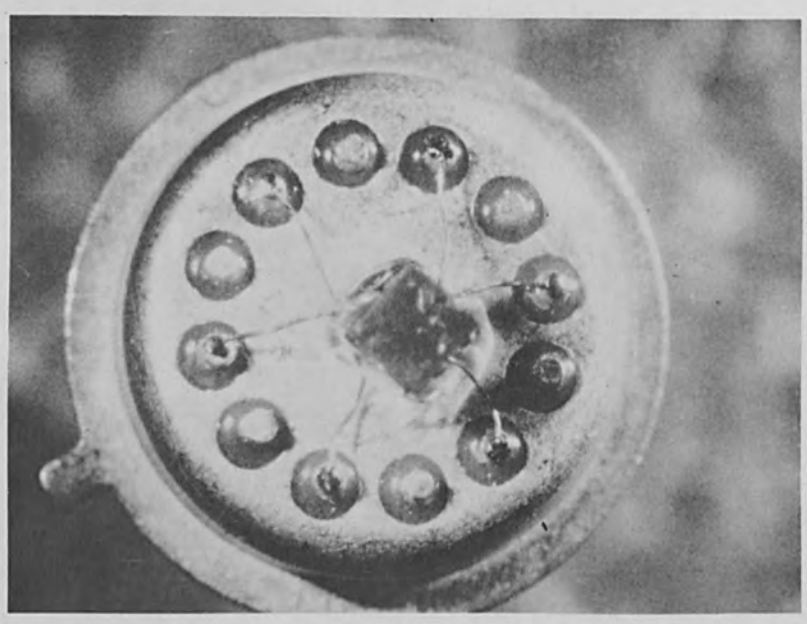

Figure 14 Miniature transformer laser welded to Kovar T-package.

The laser can be used to remove these insulating coatings. A one joule beam, focused through a 25 millimeter focal length lens, will cleanly remove the insulation from 2 to 4 mill "transformer wire". The small section of a bare copper wire can then be easily and effectively laser welded. As would be expected, welding insulated wire requires more energy. Depending on the lenses used, energies between 1.5 and 2.3 joule were found necessary to weld 2 mil insulated copper wire to kovar header pins, 17 mils in diameter.

Thin Films

Welding fine wires to thin film or integrated circuit chips is a very delicate process. To accomplish this effectively with the laser requires precise control over both the welder and the parts being joined. The total energy, pulse duration and power density of the laser beam must be held within very narrow tolerance limits. Also, great care must be exercised to insure that the wire and circuitry to be welded are in contact. A stereoscopic microscope should be used to insure that

contact does occur, thereby improving the reliability and consistency of the joints produced.

A 1.5 joule beam was used to weld 0.003" diameter gold wire to 200 Angstrom thick gold circuitry that was deposited on a silicon substrate (Figure 15). Using a 25 mm. focal length lens, it was necessary to focus the beam about .020" above the lead to achieve a relatively good joint. Micrographic inspection revealed that the gold wire had bonded to the silicon substrate as well as to the gold circuitry.

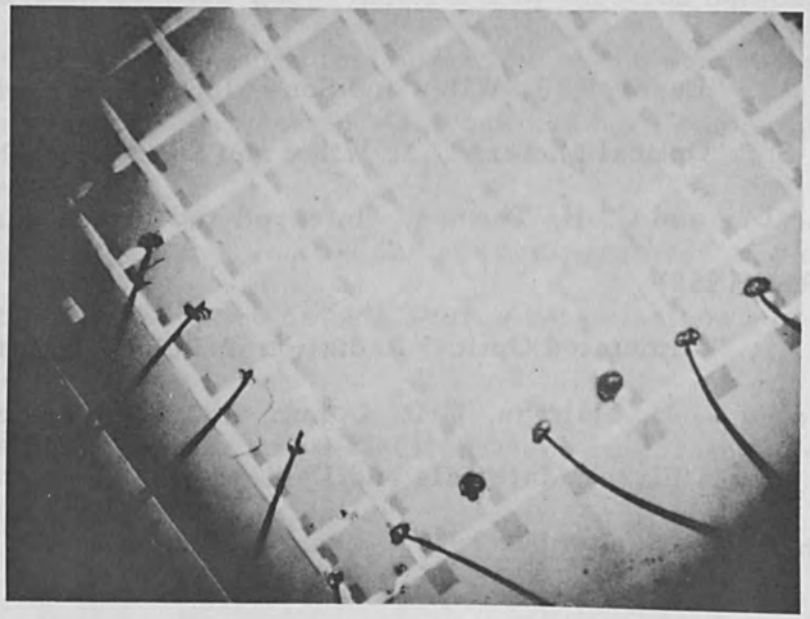

Figure 15 0.003" gold wire laser welded to 2000 Angstrom thick gold.

A laser that can produce a beam of precisely controlled energy and pulse duration would find several important applications in thin film and semiconductor production and packaging. It offers the advantages of not requiring the application of pressure, nor does it induce stray currents in the delicate components.

Conclusions

The results of the laser welding experiments of microcircuits reported here as

well as other experimental results show that laser welding of microcircuits has great potential. The laser provides a new tool for the manufacturing engineer in the assembly of a large variety of microcircuit packages under conditions which were previously unattainable. Although the laser is still in its infancy, the laser and its related equipment for welding purposes are undergoing rapid development and the range of applicability is continuously being broadened. We can look forward to continued rapid development not only in the area of microcircuit welding, but also in the welding of much larger and more exotic materials.

References

1. Lengyel, B. A., "Lasers", J. Wiley and Sons, Inc., New York (1962).
2. Heavens, O. S., "Optical Masers", J. Wiley and Sons, Inc., New York (1964).
3. Schawlow, A. L., and C. H. Townes, "Infrared and Optical Masers", Phys. Rev. 112, 1940 (1958).
4. Maiman, T. H., "Stimulated Optical Radiation in Ruby", Nature, 187, 493 (1960). See also T. H. Maiman, Brit. Comm. and Electronics 7, 764 (1960).
5. Haun, R. D., Jr., "Laser Materials and Devices -- A Research Report", Electro-Technology, September 1963.

New Electron Beam Evaporator and its Characteristics

by

H. Kimura and H. Tamura
Hitachi Central Research Lab.
Kokubunji, Tokyo, Japan

K. Mori
Hitachi-Koki Co. Ltd.
Katsuta, Ibaragi, Japan

Abstract

During the vacuum evaporation of materials by electron bombardment, the reflected electrons frequently cause fine scratches on the evaporated film. To avoid this problem, the behavior of reflected electrons has been studied using the resistance network method.

Electron beam trajectories and the surface temperatures of the target being bombarded have been investigated using a Pierce type electron gun and a high AC accelerating potential.

From the results obtained, a new electron beam evaporator has been designed which has many advantageous features.

Introduction

Several papers[1, 2, 3] have been published elaborating on the advantages of electron beam evaporation of refractory metals. While depositing thin films by electron beam evaporation, the authors have frequently observed fine scratches and blurs on the film. These defects were caused by the electric discharge due to the reflected electrons during the electron bombardment. Deflecting electric or magnetic fields have been quite effective in preventing these defects.

An electron beam evaporator is generally more expensive than the conventional vacuum evaporator. This is due to the fact that it is necessary to have an electron gun, a high voltage supply, an electron lens and a constant current supply to energize the lens. The properties of a Pierce type telefocus gun without the use of an

electron lens have been studied with AC accelerating potentials rather than DC to minimize the cost of the electron beam evaporator.

As a result of the above study, a new electron beam evaporator has been designed which permits the solution of difficult problems in the study of semiconductors as well as microcircuitry.

Effect of Reflected Electrons

A typical electron beam evaporator is shown schematically in Figure 1(a). Figure 1(b) shows an example of a defective molybdenum film on a glass substrate.

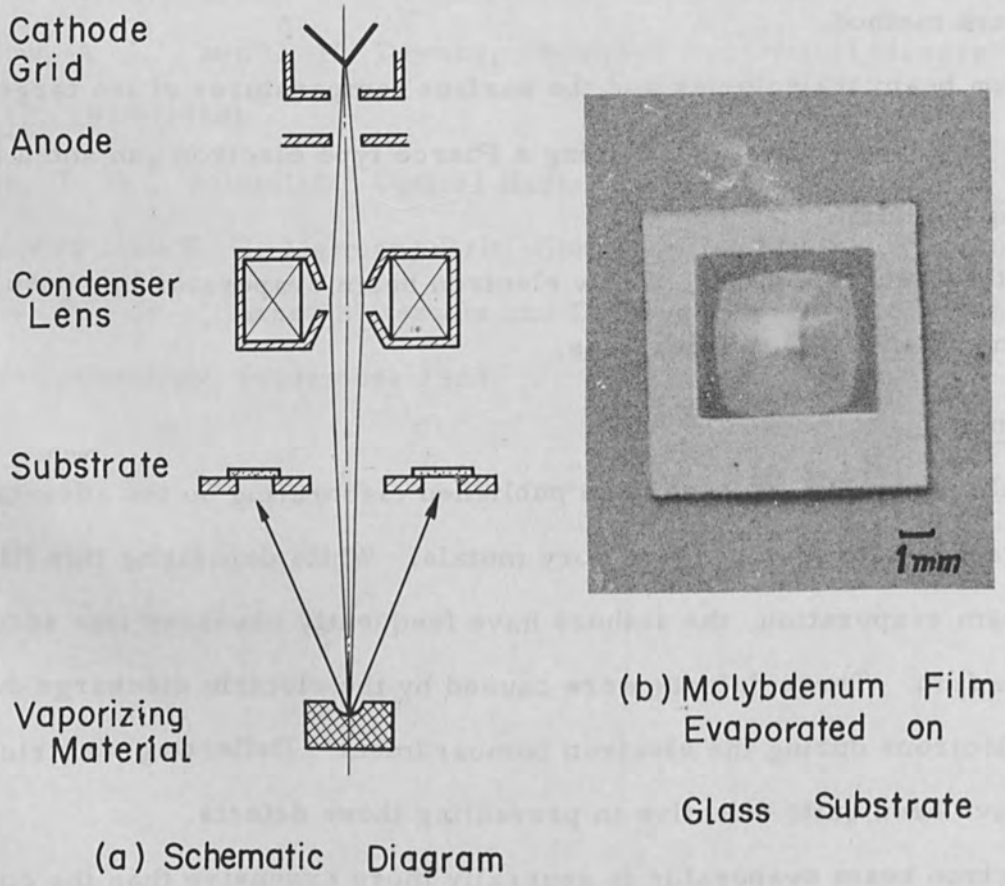

(a) Schematic Diagram

(b) Molybdenum Film Evaporated on Glass Substrate

Figure 1 (a) Schematic diagram of a conventional evaporator.
(b) An example of the effect of reflected electrons.

Figure 2(a) and (b) show light microscope images of silicon and boron on which many scratches appear. These films were made in a vacuum of 10^{-5} mm. Hg with 30 kV DC and 5 ma beam current. The evaporating speed was 100 Å/sec. In order

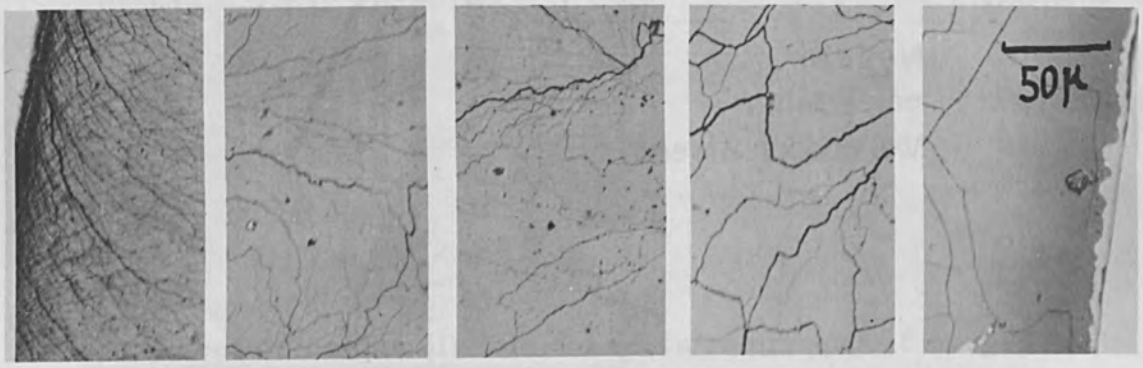

(a) Silicon Film

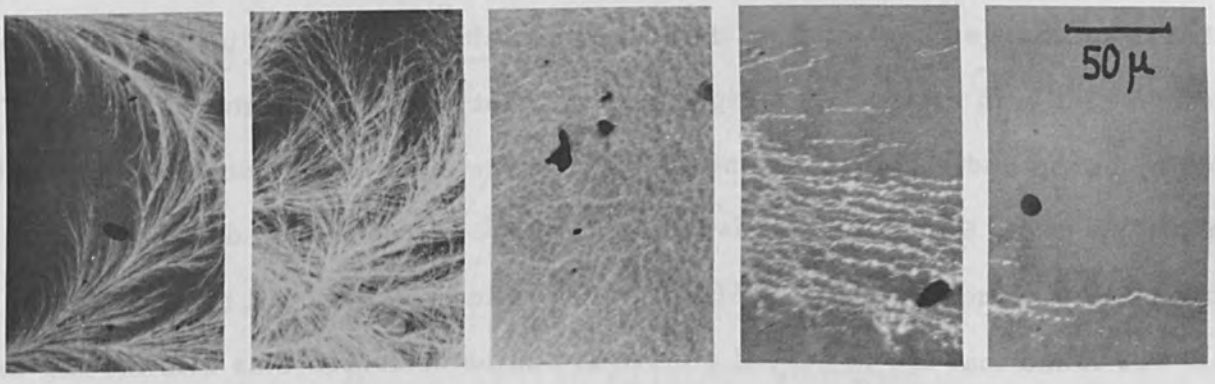

(b) Boron Film

Figure 2 Light microscope images of evaporated films on glass substrates by means of usual electron beam evaporation.

to explain this phenomenon in detail, another experiment was performed. As shown in Figure 3, a fine needle is positioned 1 mm under a glass substrate placed on insulating supports. During the electron beam evaporation, electric discharges between the tip of the needle and the glass substrate have been observed. The dependency of the discharge on the accelerating potential at three values of the latter, 15, 20 and 40 kV. was not very clear.

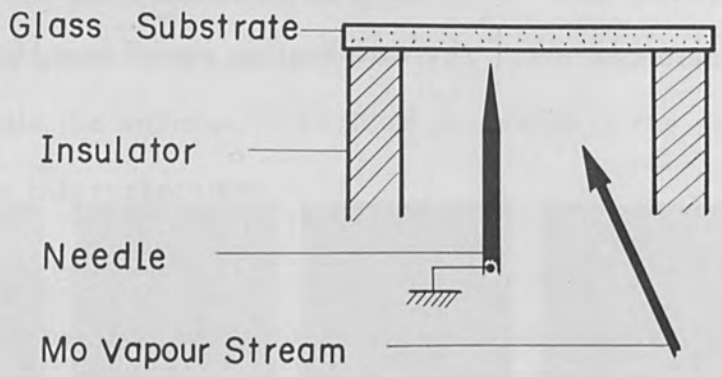

Figure 3 Experimental device of reflected electrons.

It was obvious that the fine scratches and blurs on the film were caused by the discharge of charged particles on the insulated substrate. The discharges were more frequent with materials of high melting point and large atomic number. For example, boron and antimony whose melting points and atomic numbers are 2500 °C and 630 °C and Z = 5 and Z = 51 respectively, have shown larger defects than aluminum whose melting point is 660 °C and atomic number Z = 13.

It was found that the reflected electrons can be deflected thus eliminating this problem. With this in mind, the cathode and the metal bell jar were placed at ground potential while the anode and the vaporizing material were raised to a high potential. The electrostatic field between the metal cylinder of the anode and the bell jar deflects the reflected electrons and prevents them from striking the substrate. This method has the additional advantage of eliminating the use of an insulation transformer for the filament heating supply.

Figure 4 shows a schematic diagram of the evaporator. The equipotential lines and the trajectories of the reflected electrons were traced using the resistance network method. The result is shown in Figure 5. The results obtained with this

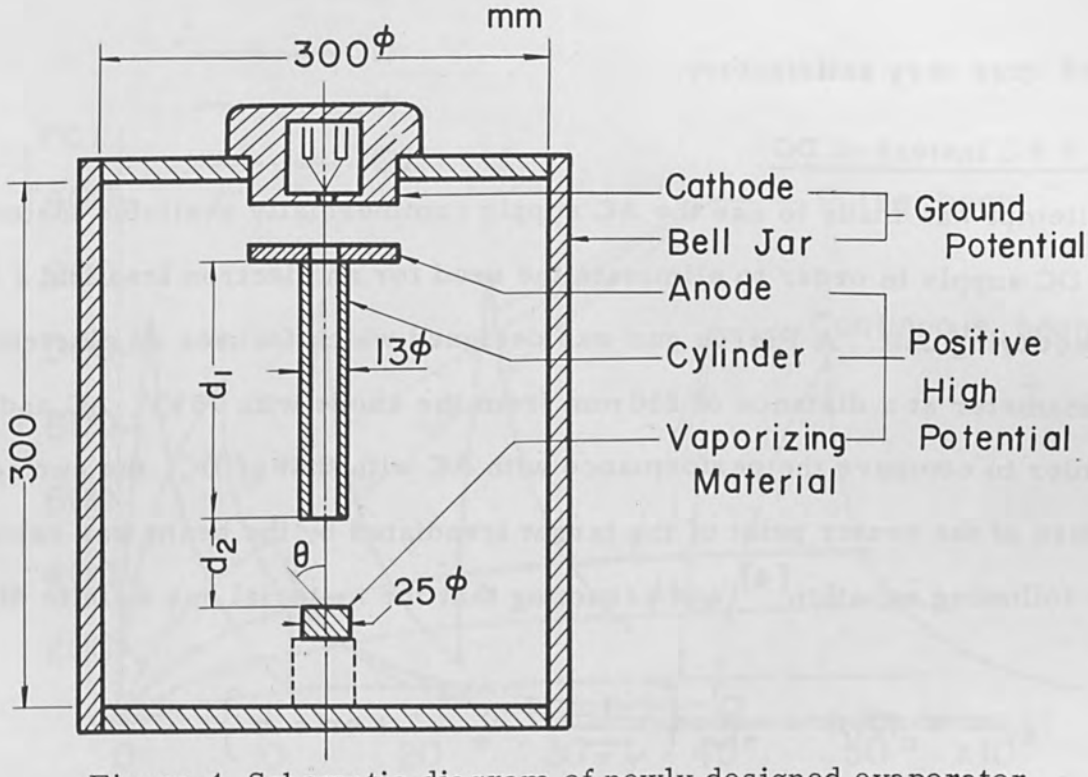

Figure 4 Schematic diagram of newly designed evaporator.

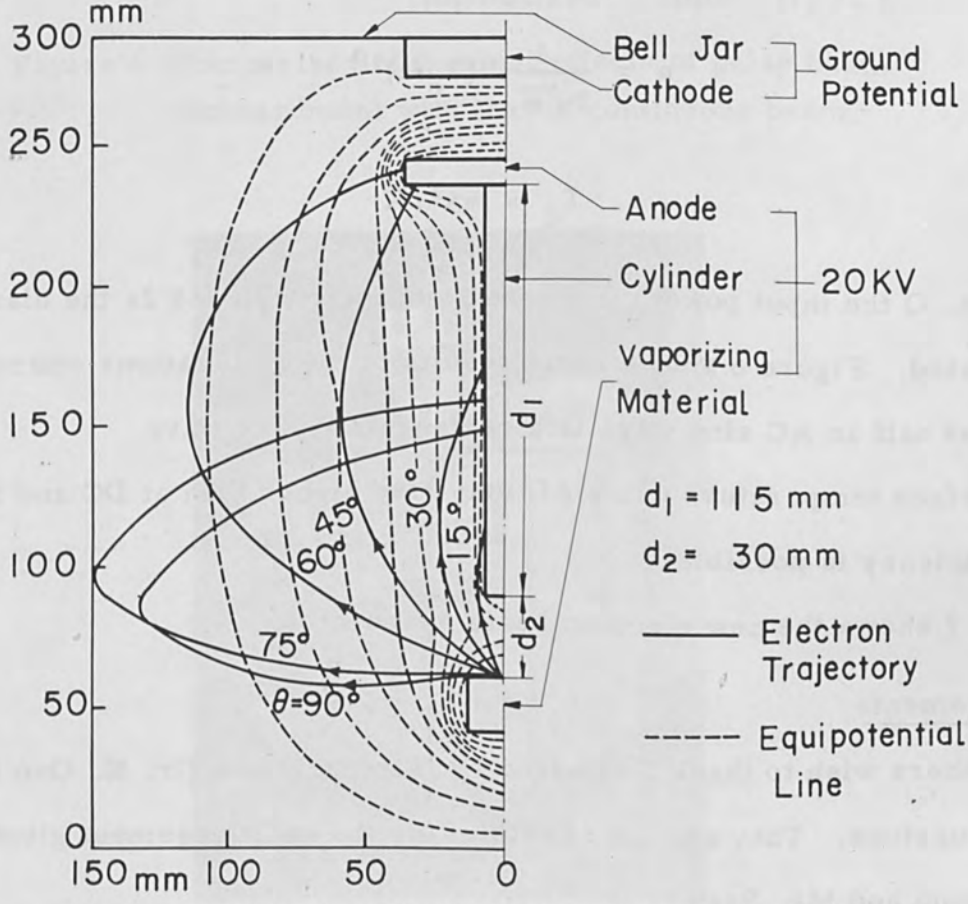

Figure 5 Electron trajectory and equipotential lines.

evaporator were very satisfactory.

The Use of AC Instead of DC

An attempt was made to use the AC supply commercially available instead of a rectified DC supply in order to eliminate the need for an electron lens and a high voltage rectifying unit. A Pierce gun was designed which focuses an electron beam to 2 mm diameter at a distance of 250 mm from the anode with 15 kV. AC and 44 mA.

In order to compare the performance with AC with that of DC, the surface temperature of the center point of the target irradiated by the beam was calculated using the following equation[4] and assuming that the material has infinite dimensions

$$V_n(O,t) = \frac{Q}{\pi K a}\left\{\frac{1}{\sqrt{\pi}}\ \frac{1-e^{-\alpha^2}}{\alpha} + \operatorname{erfc}\ \alpha\right\}$$

where

$$\alpha = \frac{1}{2\sqrt{\pi}}\ (T_c/t)^{1/2}$$

$$T_c = \pi a^2/K$$

t is the time, Q the input power, K the heat conductivity, and 2a the diameter of the area irradiated. Figure 6 shows some results of the calculations where we have assumed that half an AC sine wave is a rectangular pulse wave.

The surface temperature using AC may rise higher than at DC and hence better thermal efficiency is possible.

Figure 7 shows the new electron beam evaporator.

Acknowledgements

The authors wish to thank Professor N. Taniguchi and Dr. K. Ono for their helpful discussions. They are also grateful for the encouragement given by Dr. B. Tadano and Mr. Saga.

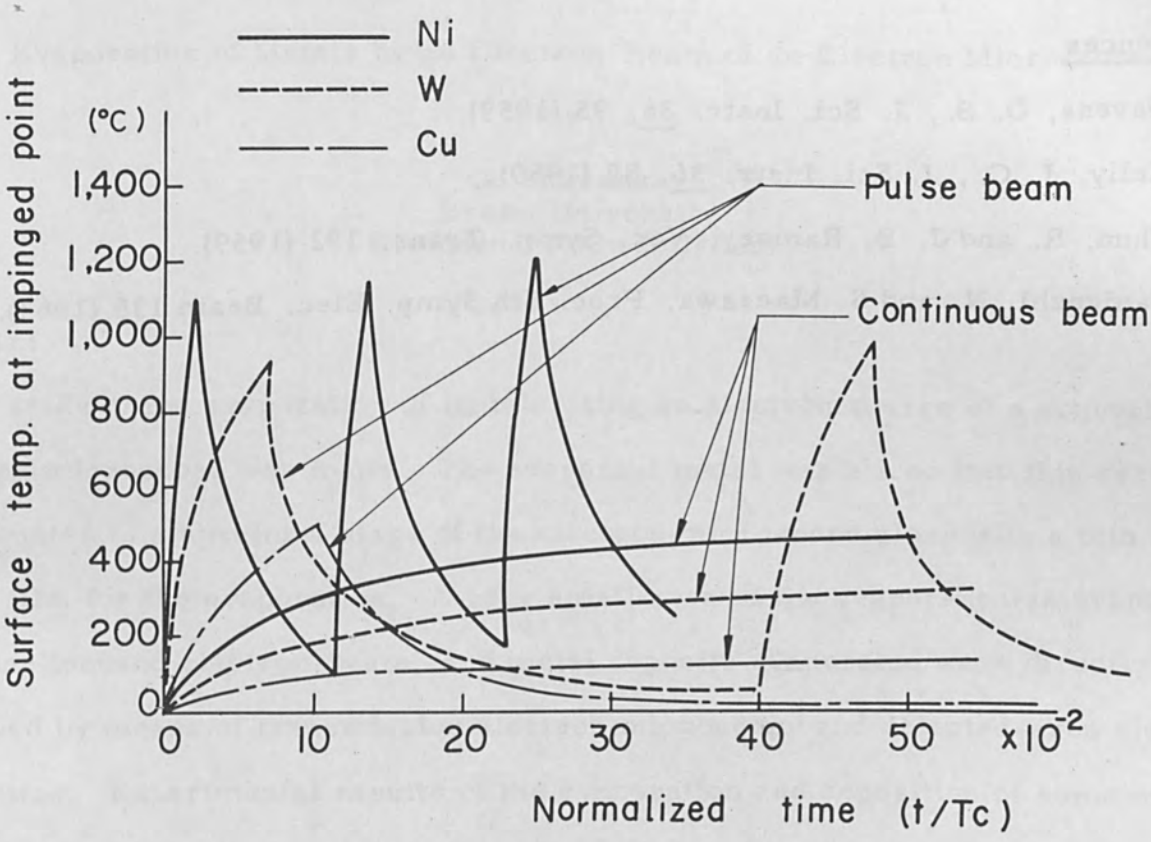

Figure 6 Comparison of thermal effects of pulse beam bombardment with that of continuous beam.

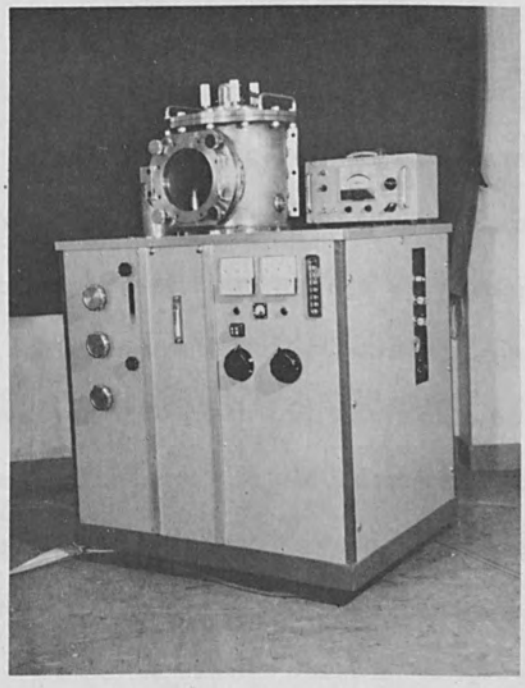

Figure 7 External view of new electron beam evaporator.

References

1. Havens, O. S., J. Sci. Instr. 36, 95 (1959).

2. Kelly, J. C., J. Sci. Instr. 36, 89 (1959).

3. Thun, R. and J. B. Ramsey, Vac. Symp. Trans. 192 (1959).

4. Taniguchi, N. and S. Maezawa, Proc. 5th Symp. Elec. Beam 135 (1963).

Evaporation of Metals by an Electron-Beam of an Electron Microscope*

by

G. Shimaoka
Brown University
Providence, Rhode Island

Abstract

A study of the evaporation of metals using an electron source of a conventional electron microscope was made. The evaporant metal was sliced into thin sections and mounted in a specimen stage of the electron microscope along with a thin substrate film for the evaporation. A very small area of the evaporant was evaporated by a fine focused electron-beam, and metal deposits evaporated were directly observed by means of transmission electron microscopy and selected-area electron diffraction. Experimental results of the evaporation and deposition of some metals, such as cadmium and zinc, on an amorphous carbon film are described. The results suggest that the technique is applicable to the study of the very early stages of thin film growths.

Introduction

In transmission electron microscopy of metals, it is generally known that when a specimen is thin enough to allow an electron beam to pass through, (in general, ~1000 Å thick or less for 50 ~ 100 kV electrons) the interaction between the specimen and the electrons is not so important, but when a specimen is too thick to transmit the electrons an inelastic collision of the electrons occurs, and the energy of the electrons absorbed is converted into heat and often causes the specimen to be heavily deformed. Thermal effects of the electron beam of a conventional electron microscope on various kinds of specimens have been studied by some investigators, [1-3] and it has been shown that under certain conditions the specimen may be

*This work was supported by the Advanced Research Project Agency.

heated to temperatures in the neighborhood of 1000 °C.[3] Conspicuous structural changes due to the thermal effect of the electron beam have been reported for many inorganic substances, such as WO_3,[3] MoO_3,[4-7] PbO,[3] CuS,[8] etc. These data strongly suggest that the electron source of an electron microscope can also be used for the evaporation of metals. If such an evaporation is made and a suitable thin film is used as a substrate in a specimen stage of the electron microscope, the vacuum deposition of metals on the substrate can be observed. The purpose of the present work is to develop evaporation techniques of this type and to directly observe the metal deposits using transmission electron microscopy and selected-area electron diffraction. Experimental results of the evaporation and deposition of cadmium and zinc on an amorphous carbon film are described.

Description of the Experiment

An example of the arrangement of evaporant and substrate materials for the evaporation inside a specimen stage of an electron microscope is shown schematically in Figure 1. Sliced thin sections of metallic cadmium or zinc (about 1 μ thick or

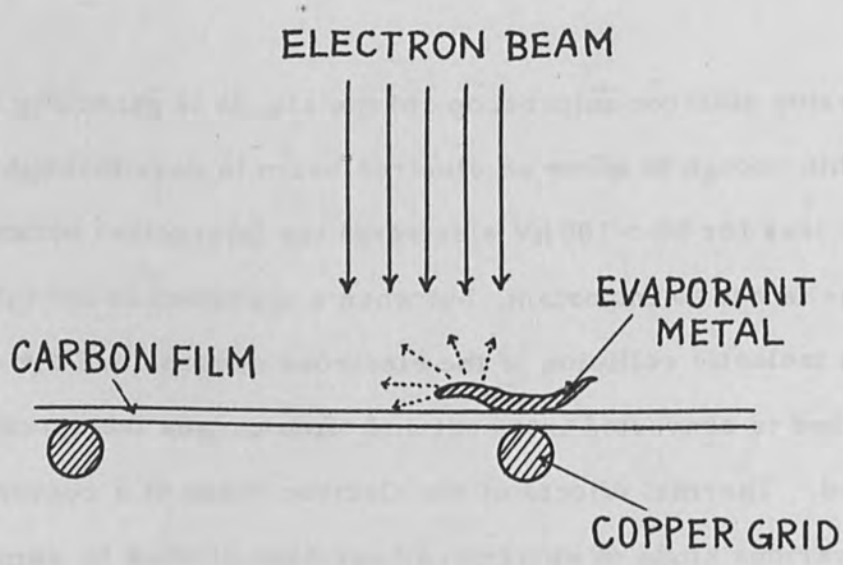

Figure 1 Schematic view of the arrangement of the evaporant and substrate materials for electron-beam evaporation inside a specimen stage of an electron microscope.

less at the edge) were placed on an amorphous carbon film supported by a 200 mesh copper grid. The assembly was mounted in the specimen holder of the electron microscope. Prior to the evaporation experiments, a suitable section of the evaporants on or near the carbon substrate film was selected by electron microscopy using a weak electron beam, then the edge or surface of the thin section was irradiated by a strong electron beam. When the edge of the thin section was properly chosen, melting or evaporation at the edge was directly observed by electron microscopy. Metal deposits produced on the carbon substrate by the evaporation were directly observed by transmission electron microscopy and selected-area electron diffraction. The electron microscope used in this experiment was Hitachi HU-10 with a double condenser lens and a three lens system. The irradiation of the evaporant metal was controlled by adjusting the condenser aperture or by changing the second condenser lens current. The pressure at the specimen position was measured using an ion gauge connected to the microscope. Most of the experiments were carried out with an accelerating voltage of 75 kV, and a beam current of 20 to 50 μA, and in a pressure of about 5×10^{-5} mmHg.

The evaporant materials were 99.95% Zn. The amorphous carbon film was prepared by vacuum evaporation onto a surface of a glass slide, and removed from the glass by floating it in distilled water and collecting it on a 200 mesh copper grid.

Results and Discussion

Cadmium

Figure 2 shows an electron micrograph and a corresponding selected-area electron diffraction pattern from a substrate carbon film used in this experiment. The micrograph indicates that the film is quite structureless and smooth. The diffraction pattern shows diffuse haloes due to the amorphous structure.

An example of an electron micrograph showing the evaporation of cadmium produced by irradiation of the strong electron beam is given in Figure 3. The dark

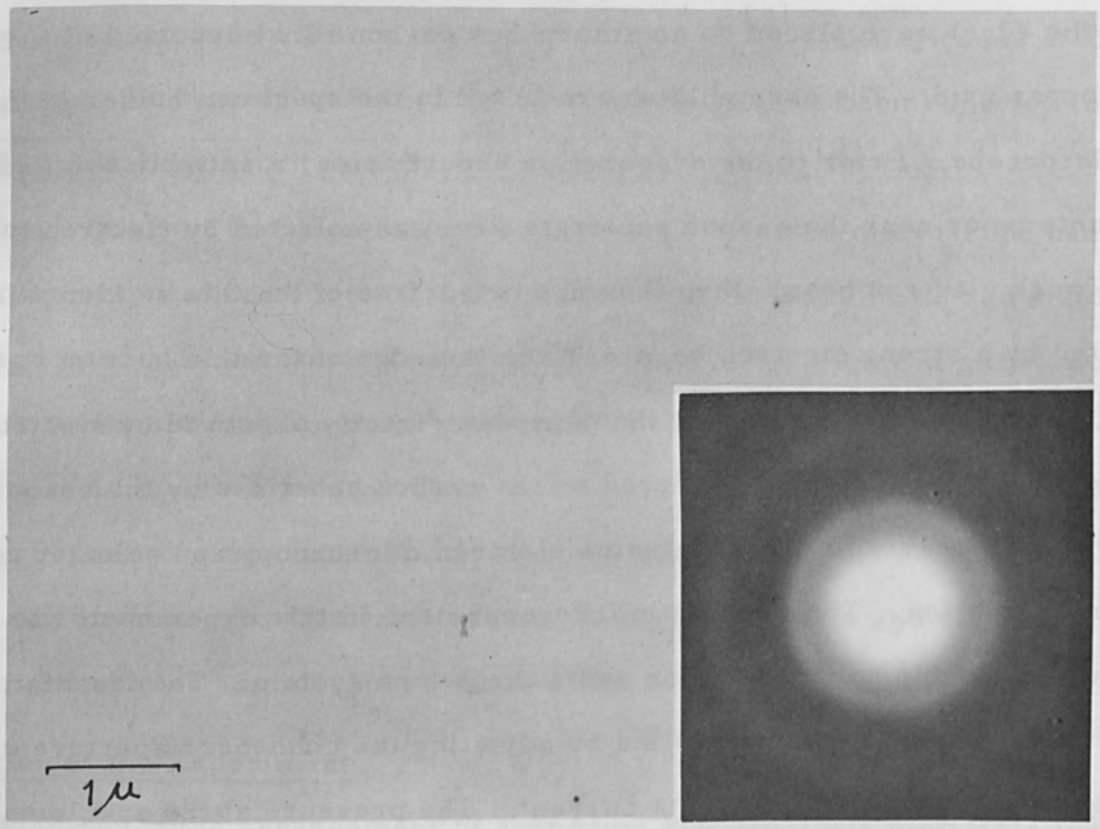

Figure 2 Electron micrograph and the corresponding diffraction pattern (lower right) of the substrate carbon film.

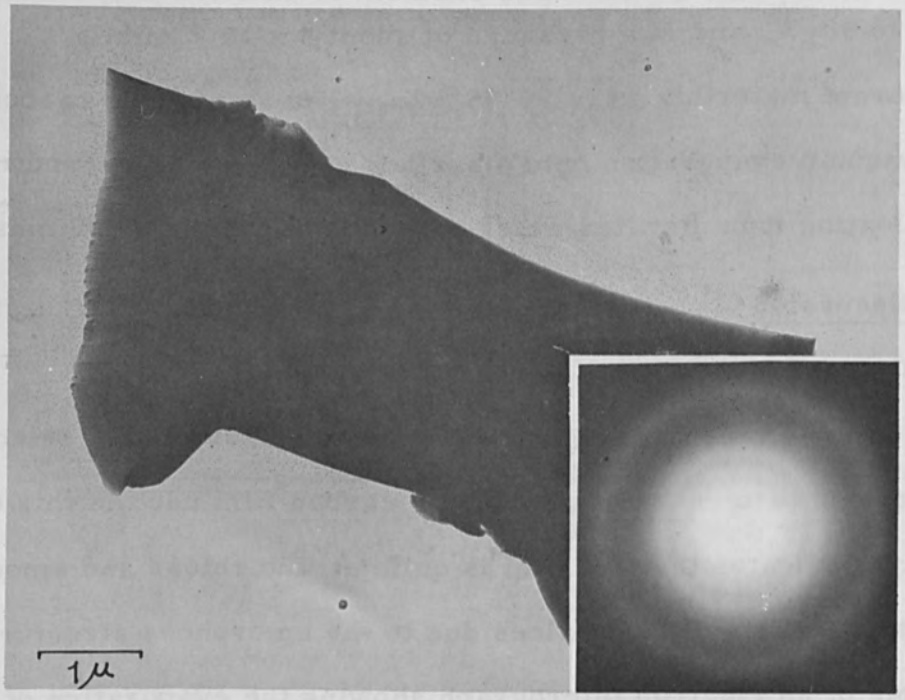

Figure 3 Electron micrograph showing the evaporation of cadmium from the edge of a cadmium section, and the electron diffraction pattern (lower right) of the evaporated cadmium.

part in the micrograph shows a thin section of the cadmium evaporant. In the vicinity of the edge of the section, many deposited particles (80 ~ 200 Å in size) can be seen on the carbon substrate, and numbers of fine particles (approximately 40 Å in size or less) can be observed at a short distance from the edge. The electron diffraction pattern corresponding to the deposited area showed a slightly diffused ring due to the (100) reflection of cadmium crystal (hexagonal close-packed structure). Deposition of such fine particles was sometimes effective for shadow casting. An example of the shadow casting produced by the evaporation of cadmium is shown in Figure 4. The roughness formed on a carbon film was well shadowed, and deposited particles could not be resolved in the micrograph. Dark parts in the micrograph indicate single crystals of cadmium produced by evaporation after the shadowing. Single crystals of this type were sometimes deposited by rapid evaporation of cadmium, as will be described later. When the evaporation was made in relatively poor vacuum, for instance in a pressure higher than $\sim 10^{-4}$ mmHg, oxidation of the deposited crystals was often observed. An example is shown in Figure 5. The dark part of the micrograph shows the edge of the cadmium evaporant. In the vicinity of the edge, dark patches (about 200 Å in size) show deposited cadmium particles and the bright cracks are due to the oxidized regions produced by the strong irradiation of the electron beam. From a selected-area electron diffraction pattern, shown in the figure, and using dark-field electron microscopy technique, these bright cracks were identified as CdO (NaCl type structure).

Examples of electron micrographs and corresponding selected-area diffraction patterns from cadmium deposited in a pressure of about 5×10^{-5} mmHg inside the electron microscope are shown in Figure 6. The micrographs show the variation of distribution, size and shape of the deposits. Figure 6(a) shows the distribution of microcrystals deposited by very slow evaporation which was controlled by the irradiation of the electron beam. The deposits consisted of small crystalline

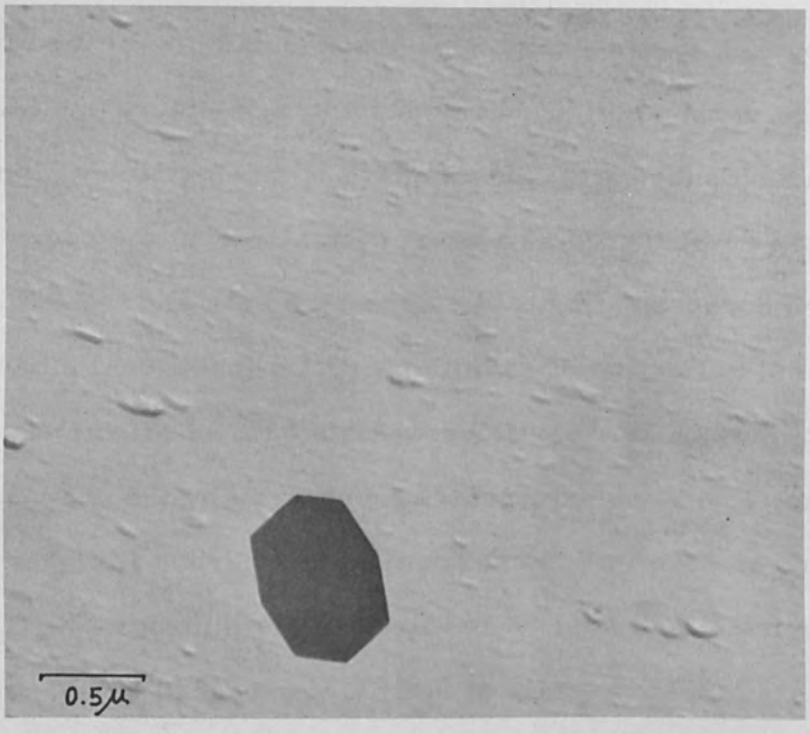

Figure 4 Electron micrograph of a carbon film shadowed by evaporated cadmium. The dark part shows a single crystal of cadmium produced by evaporation after the shadowing.

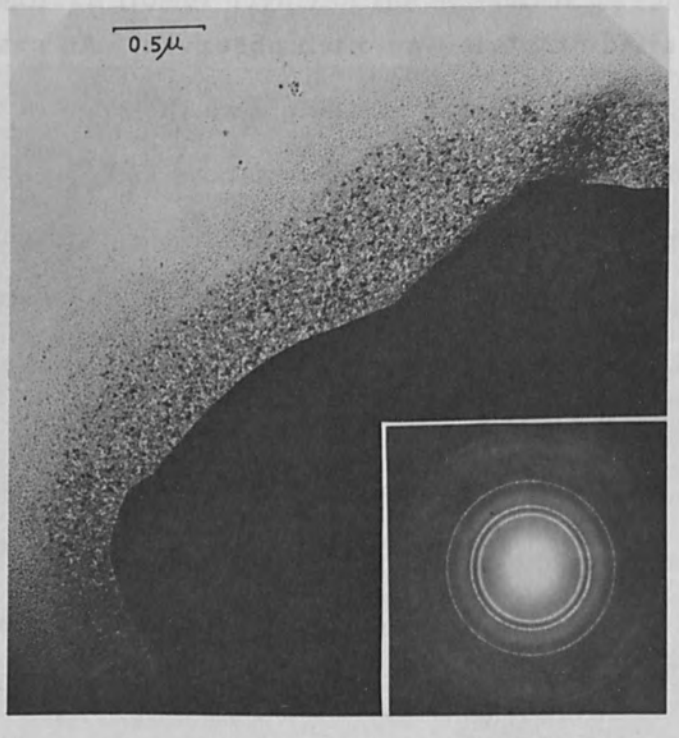

Figure 5 Electron micrograph showing cadmium deposits oxidized by the severe irradiation using an electron beam under poor vacuum. The electron diffraction pattern (lower right) of the oxidized region.

agglomerates scattered on the carbon substrate. The size of the deposits varied from 40 to 200 Å. These facts suggest that the surface mobility of cadmium on the carbon substrate is great.[9] Corresponding diffraction patterns showed sharp rings due to crystallized cadmium. Figure 6(b) shows the shape of individual cadmium crystals deposited by slow evaporation. Many interesting shapes, such as hexagonal, triangular, rectangular, and rhombic deposits can be seen in the micrograph. The size of these deposits varied from 100 to 500 Å. Large free areas between these deposits can be seen. These results are very similar to those obtained by other investigators with the usual evaporation of cadmium onto collodion or glass.[9] Corresponding diffraction patterns consisted of arc-patterns showing a fiber structure of cadmium crystals, as is shown in the figure. Such a diffraction pattern was analysed by checking the inclination of the substrate to the electron beam and the rotation angle between the micrograph and the selected-area diffraction pattern. It was found that the cadmium crystals were preferentially oriented with the (001) plane parallel to the substrate surface. Figure 6(c) shows interesting structures of cadmium deposits evaporated with medium speed. Many hexagonal platelets (approximately 800 A in diameter), double triangles and a few triangular platelets can be seen in the micrograph. Most of the hexagonal platelets were oriented with their hexagonal planes nearly parallel to the substrate surface. In the thick parts of the deposits, many hexagonal platelets were connected by their hexagonal planes. Corresponding diffraction patterns showed spotted rings due to coarse grains of cadmium, suggesting that the grains were preferentially oriented with the (001) plane parallel to the substrate surface. When the evaporation was made more rapidly relatively big cadmium crystals were deposited on the sub-strate. Figure 6(d) shows an example of this case. Many hexagonal shaped crystals (approximately 2000 Å in diameter) and double-triangular crystals can be seen in the micrograph. It is of interest to note that many big crystals are composed of

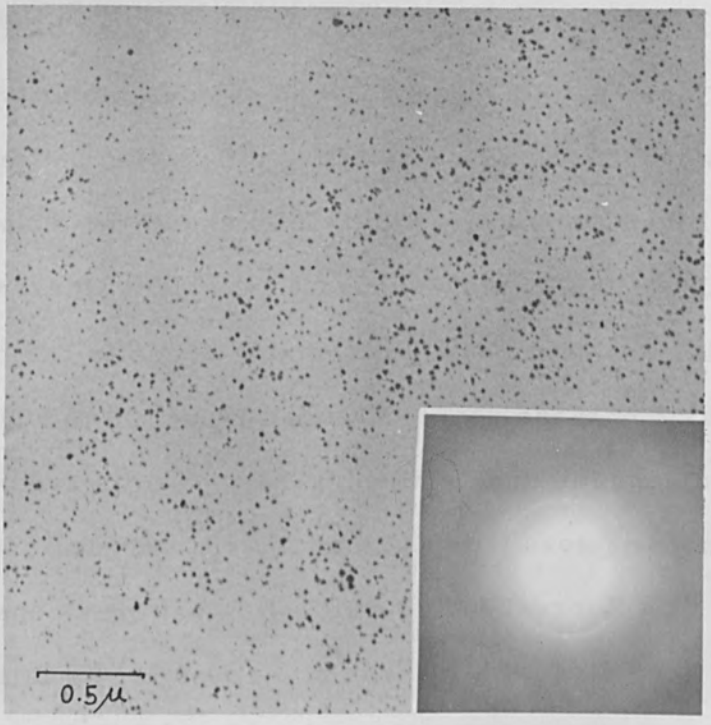

(a)

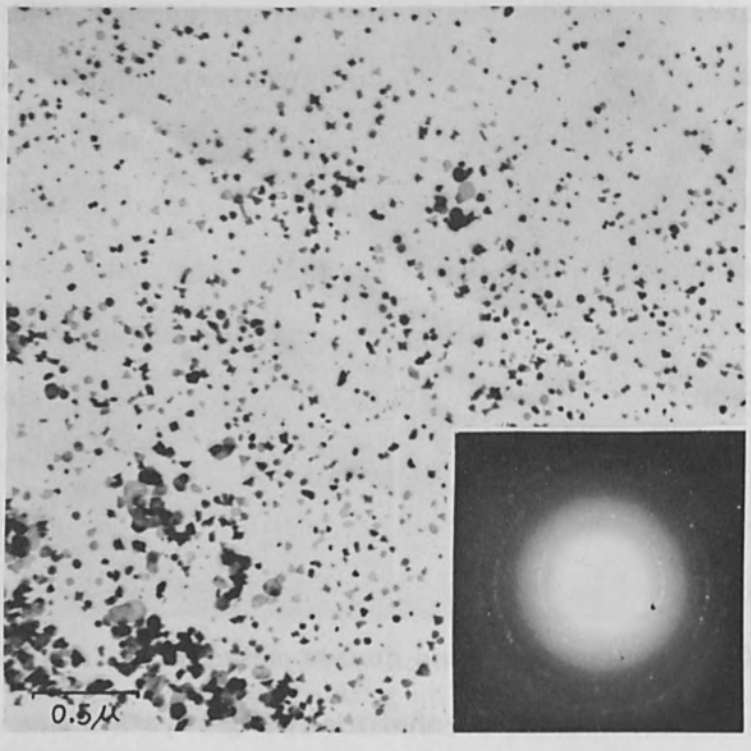

(b)

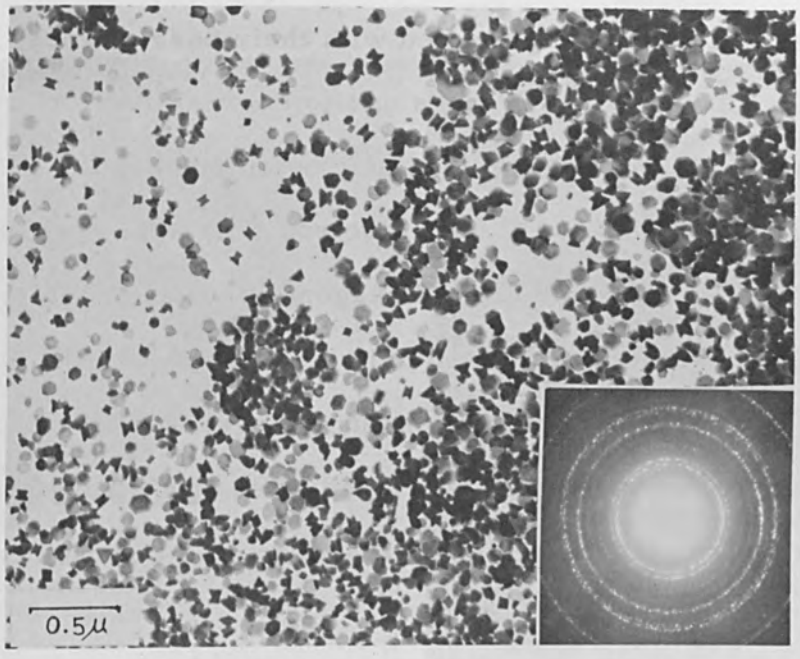

(c)

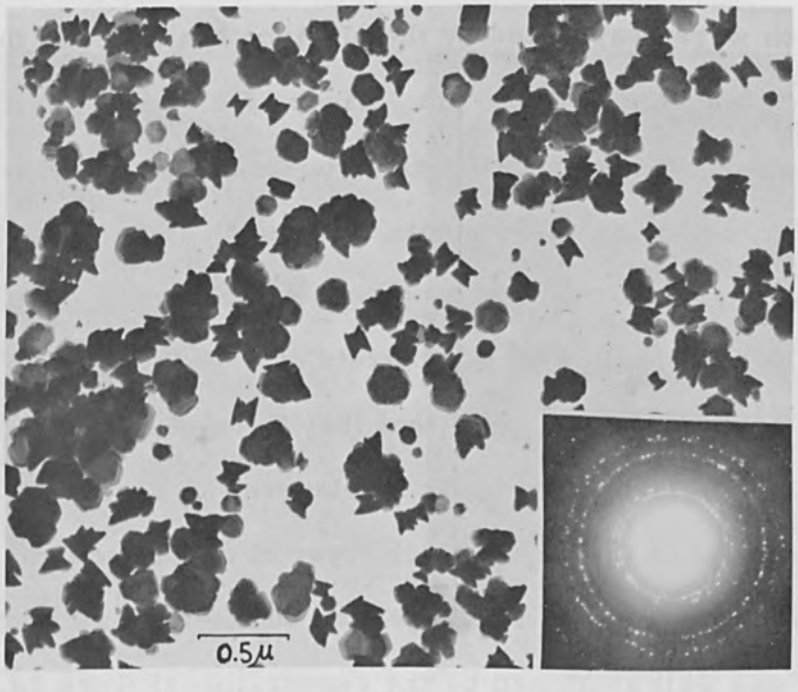

(d)

Figure 6 Electron micrographs and corresponding diffraction patterns (lower right) from evaporated cadmium, showing the variation of distribution, size and shape of the deposits. a, b, c, and d were obtained by very slow, slow, medium-speed, and rapid evaporation, respectively.

several thin hexagonal crystals connected with their basal planes. Corresponding diffraction patterns showed spotted rings due to coarse grains of cadmium, suggesting that the grains were preferentially oriented with the (001) plane parallel to the substrate surface. Selected-area electron diffraction results on individual hexagonal crystals also showed that the hexagonal crystals consist of a single crystal of cadmium, oriented with the (001) plane parallel to the hexagonal surface and with the [110] axis parallel to the hexagonal edge. In addition to these, when such cadmium deposits were oxidized by irradiation of a strong electron beam, the following orientation relation was observed between the cadmium and the cadmium oxide:

$$(001)_{Cd}//(111)_{CdO}//\text{substrate carbon film.}$$

Zinc

Zinc specimen were evaporated by the electron beam inside the electron microscope as with the case of cadmium. Figure 7 gives an example of electron micrographs showing a sequence of the electron-beam evaporation of zinc. When the edge of the thin section of zinc evaporant (Figure 7a) was irradiated by the strong electron beam, evaporation of zinc occurred from the edge and very small particles of zinc were deposited on a substrate carbon (Figure 7b, taken after 5 min.). These particles were so small that they were not resolved in the micrograph. Triple layers of evaporated zinc can be seen in Figure 7(c) (taken after 7 min.). In the vicinity of the edge a thick layer of deposited zinc was observed; however, the size of the deposits was less than 20 Å. A small protuberance on the carbon substrate was well shadowed by the evaporation (Figure 7d, taken after 10 min.).

Examples of electron micrographs and corresponding selected-area diffraction patterns from zinc deposited in a pressure of about 5×10^{-5} mmHg inside the electron microscope are shown in Figure 8. The micrographs show the variation

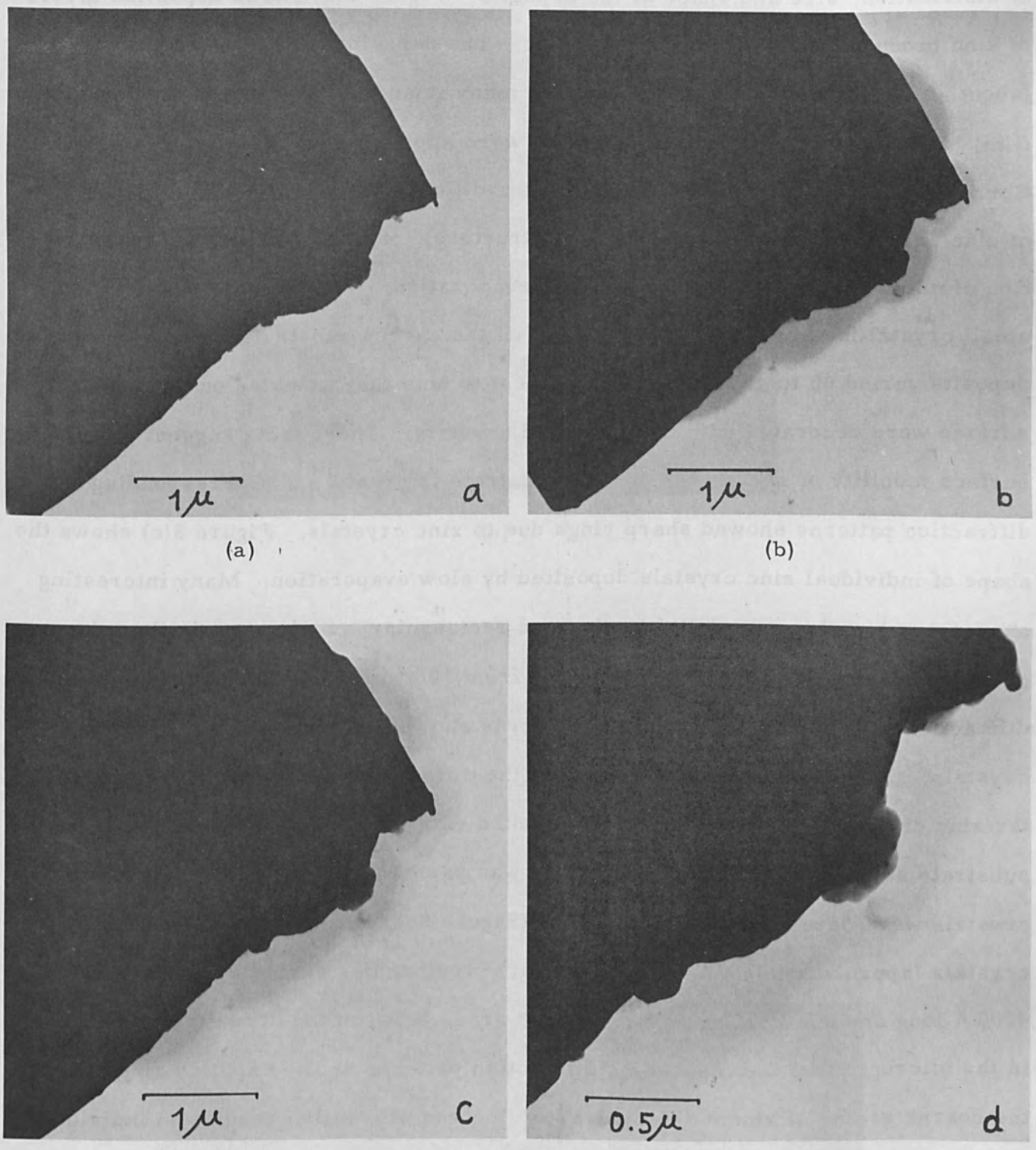

(a) (b)

(c) (d)

Figure 7 Electron micrographs showing sequence of evaporation of zinc. a, b, c, and d were taken at initial stage, after 5, 7, and 10 min. irradiation of electron beam, respectively.

of distribution, size and shape of the deposits. Figure 8(a) shows deposited layers of zinc produced by very slow evaporation. The deposited layers were very thin (about 40 Å thick or less) and consisted of many islands distributed on the substrate film. The size of the deposited particles were approximately 80 Å or less. Corresponding diffraction patterns showed a diffuse ring due to the (100) reflection of zinc crystal (hexagonal close-packed structure). Figure 8(b) shows the distribution of micro-crystals deposited by slow evaporation. The deposits consisted of small crystalline agglomerates scattered on the carbon substrate. The size of the deposits varied 60 to 160 Å. It is of interest to note that wrinkles on the substrate surface were decorated with the deposited crystals. These facts suggest that the surface mobility of zinc on the carbon substrate is great.[9] Corresponding diffraction patterns showed sharp rings due to zinc crystals. Figure 8(c) shows the shape of individual zinc crystals deposited by slow evaporation. Many interesting shapes, such as hexagonal, triangular and rectangular, can be seen in the micrograph. The size of these deposits varied from 100 to 200 Å. Corresponding diffraction patterns consisted of arc-patterns showing a fiber structure of zinc crystals, as is seen in the figure. From the diffraction pattern, it was found that the zinc crystals were preferentially oriented with the (001) plane parallel to the substrate surface. When the evaporation was rapidly made relatively big zinc crystals were deposited on the substrate (Figure 8d). Many hexagonal shape crystals (approximately 1400 Å in diameter), rectangular shaped crystals (e. g. 4000 Å long and 400 Å wide) and large free areas between the deposits can be seen in the micrograph. Corresponding diffraction patterns showed spotted rings due to the coarse grains of zinc. Selected-area electron diffraction results on individual hexagonal crystals showed that the hexagonal crystals consist of a single crystal of zinc, oriented with the (001) plane parallel to the hexagonal surface and with the [110] axis parallel to the hexagonal edge. In addition to these, when such zinc

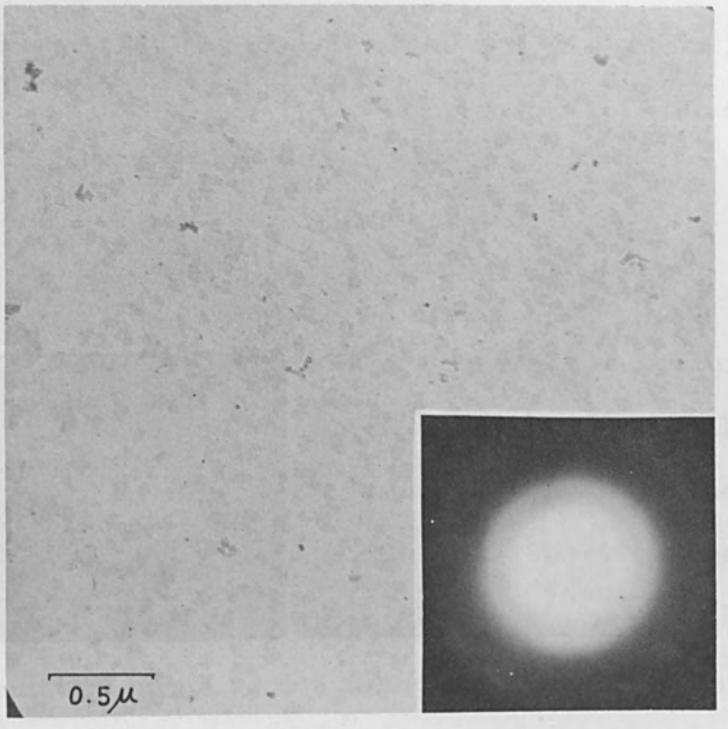

(a)

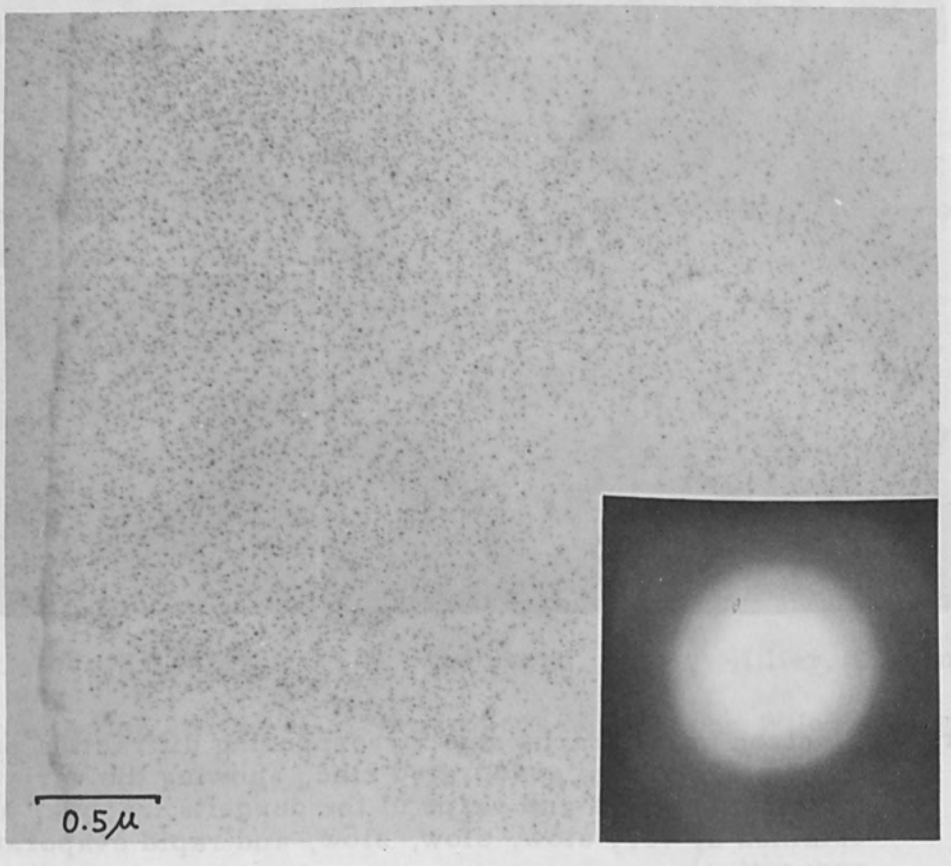

(b)

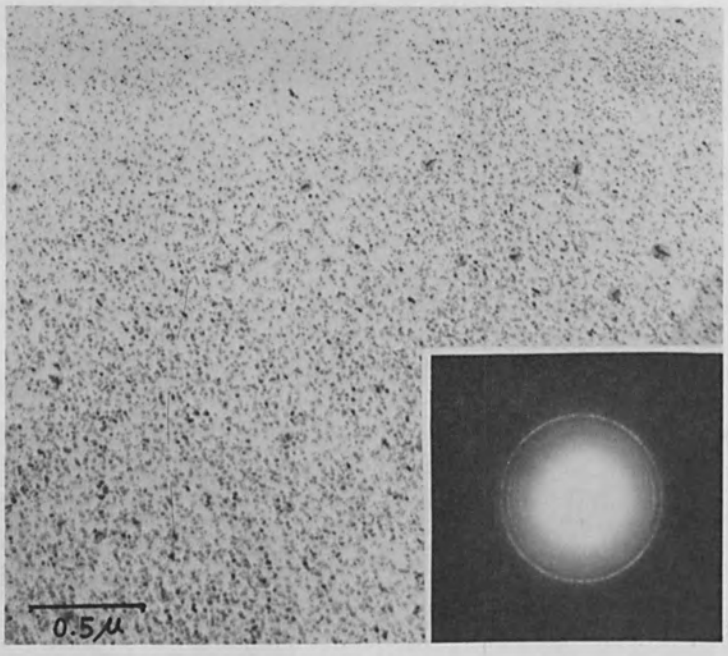

(c)

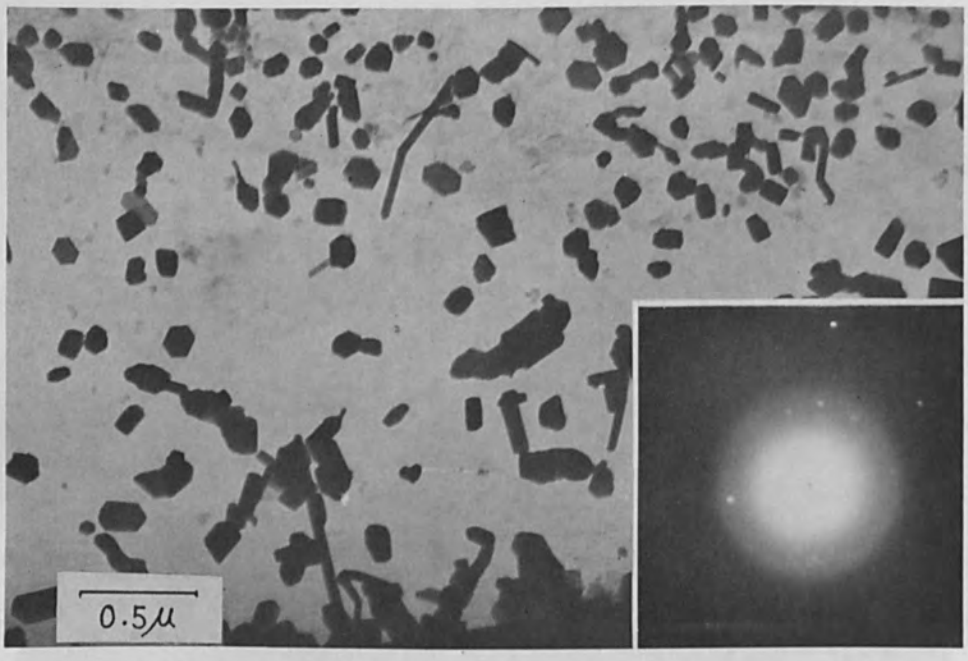

(d)

Figure 8 Electron micrographs and corresponding diffraction patterns (lower right) from evaporated zinc, showing the variation of distribution, size and shape of the deposits. a, b, c, and d were obtained by very slow, slow, slow, and rapid evaporation, respectively.

deposits were oxidized by the irradiation with a strong electron beam, the following orientation relation was observed between the zinc and the zinc oxide (hexagonal, wurtzite type structure):

$$(001)_{Zn}//(001)_{ZnO}//\text{substrate carbon film.}$$

These results suggest that the evaporation technique used in this study is particularly suitable for the study of very early stages of thin film growths. In the present work, cadmium and zinc were evaporated on an amorphous carbon film held at room temperature. Both metals have hexagonal close-packed structures, and showed preferential orientation with their basal planes parallel to the substrate surface. This orientation might be due to their high mobility on the substrate surface and their crystal habit. It is of interest to note that very small deposits of cadmium and zinc had single crystal structures.

References

1. von Ardenne, M. B., "Elektronen-Übermikroskopie" (1940).
2. von Borries, B., and W. Glaser, Koll. Z. 106, 123 (1944).
3. Kanaya, K., Nippon Kinzoku Gakkai-Si A-15, 405 (1951); J. Electron Microscopy 3, 1 (1955).
4. Konig, H., Z. Phys. 130, 483 (1951).
5. Takagi, R., Kikaishikenjo-iho 6, 131 (1952).
6. Rang, O., and F. Schleich, Z. Phys. 136, 547 (1954).
7. Hashimoto, H., J. Phys. Soc. Japan 9, 150 (1954).
8. Hashimoto, H., Denshikenbikyo 5, 15 (1956).
9. Zworykin, V. K., Morton, G. A., Ramberg, E. G., Hillier, J., and A. W. Vance, "Electron Optics and the Electron Microscope", John Wiley and Sons, Inc., New York (1945).

A Compact Non-Vacuum Electron Beam Welder

by

J. Lempert, J. Lowry, F. Seaman and C. Williams
Westinghouse Electric Corporation
Pittsburgh, Pennsylvania

Abstract

A compact electron beam welder of the non-vacuum portable type is discussed. A description is given of the electron optical system, the pumping system and power supply. The discussion includes design of an electron beam heated source of electrons for the device, the interaction of the beam with the atmosphere and some of the initial results obtained in welding tests.

Introduction

Vacuum electron beam (EB) welding has developed rapidly in the last decade. However, vacuum EB production welding has several serious drawbacks: first, unless special, rather expensive precautions are taken, the size of the workpiece is limited by the size of the vacuum chamber and its entrance ports; second, separate pumpdown is required for each workload, making the process prohibitively expensive for many production and some special applications; third, it is sometimes difficult or awkward to manipulate the work or the welding gun in the vacuum chamber.

The non-vacuum equipment which is described in more detail in the next section circumvents many of the difficulties described above by bringing the beam directly into the atmosphere where it can be used to perform the desired welding function. At the same time, as a result of special attention given to equipment variables, it has proved possible to produce an atmospheric welding gun in which the gun and associated equipment including diffusion pumps can be packaged in a compact, easy-to-handle mobile piece of equipment weighing less than 210 pounds.

Basic Principles of Non-Vacuum Welder

Electrons are released from the cathode of the gun and focused through differentially pumped orifices by a combination of electrostatic and electromagnetic electron optical systems. A positive pressure is applied at a special gas protection orifice which is located just below the exit orifice of the gun, producing a flow of gas to the work area which directs contamination emanating from the work away from the pumping orifices. This technique has been very effective in minimizing contamination of the vacuum system, both by material vaporizing from the work and by the dust which is usually present in manufacturing areas. The use of the protective gas nozzle also permits control of the atomic number of the gas which is pumped into the vacuum system.

The atomic number of the gas through which the electrons pass in traversing the system is an important factor in determining the energy losses and scattering of the beam. For example, the range of 150 kv electrons (i. e., the distance required to cause them to lose all of their energy) is 64 inches in helium gas but only 10 inches in nitrogen gas at NTP. Since helium produces significantly less electron beam scattering and loss of electron beam energy per unit weight of gas traversed than does nitrogen, the procedure has been followed of using helium when the welder is in operation; it is possible to conveniently switch to nitrogen whenever the electron beam is not energized. Gas emanating from the protective gas nozzle, in addition to minimizing contamination of the system, also helps control the atmosphere in the immediate vicinity of the welds.

Vacuum and Pumping Requirements

The pumping requirements on an atmospheric welder are largely defined by the two principal boundary conditions: atmospheric pressure is required at the exit orifice of the gun, and a vacuum is required in the chamber housing the cathode assembly. There are several important reasons why a vacuum of the order of

10^{-4} torr or better is required in the high vacuum stage of the device. First, it is important that the ambient gas at this stage of the device does not react with the hot cathode. Second, the electrical insulating properties of a vacuum deteriorate rapidly as the pressure rises above values of the order of 10^{-5} to 10^{-4} torr. Third, it is important to accelerate the electrons under conditions where the mean-free path is relatively long so that interaction in terms of energy loss and scattering by the ambient gas is small for electrons which have not reached full velocities. Once the beam has approached maximum velocity and interaction is at a minimum, it is desirable to subject the beam to the pressure gradient necessary for reaching atmospheric pressure in as short a distance as practicable in terms of the other requirements of the welder.

Careful attention to the design of the orifices and the pumping dynamics has resulted in a system in which no pump having a speed greater than 80 liters/second is required.

Electron Beam Scattering

The principal interactions[1] of the beam with the gaseous environment can either be in terms of an inelastic interaction in which some loss of beam energy occurs with very little change in direction, or an elastic interaction in which no loss of energy occurs and slight, though appreciable, changes of electron trajectories are experienced. Spencer[2] has developed a theory from which the energy losses incurred by high speed electrons as they traverse a plane perpendicular target of infinite thickness can be calculated as a function of their fractional range. Figure 1 gives a plot of the fractional energy absorption experienced by high speed electrons, A_E, as a function of their fractional residual range for different materials. These graphs were obtained by numerical integration of Spencer's data. The concept of fractional range is used to eliminate beam voltage as a parameter on the graphs. For voltages of present interest, say 50 to 200 kv, there is little change in the data

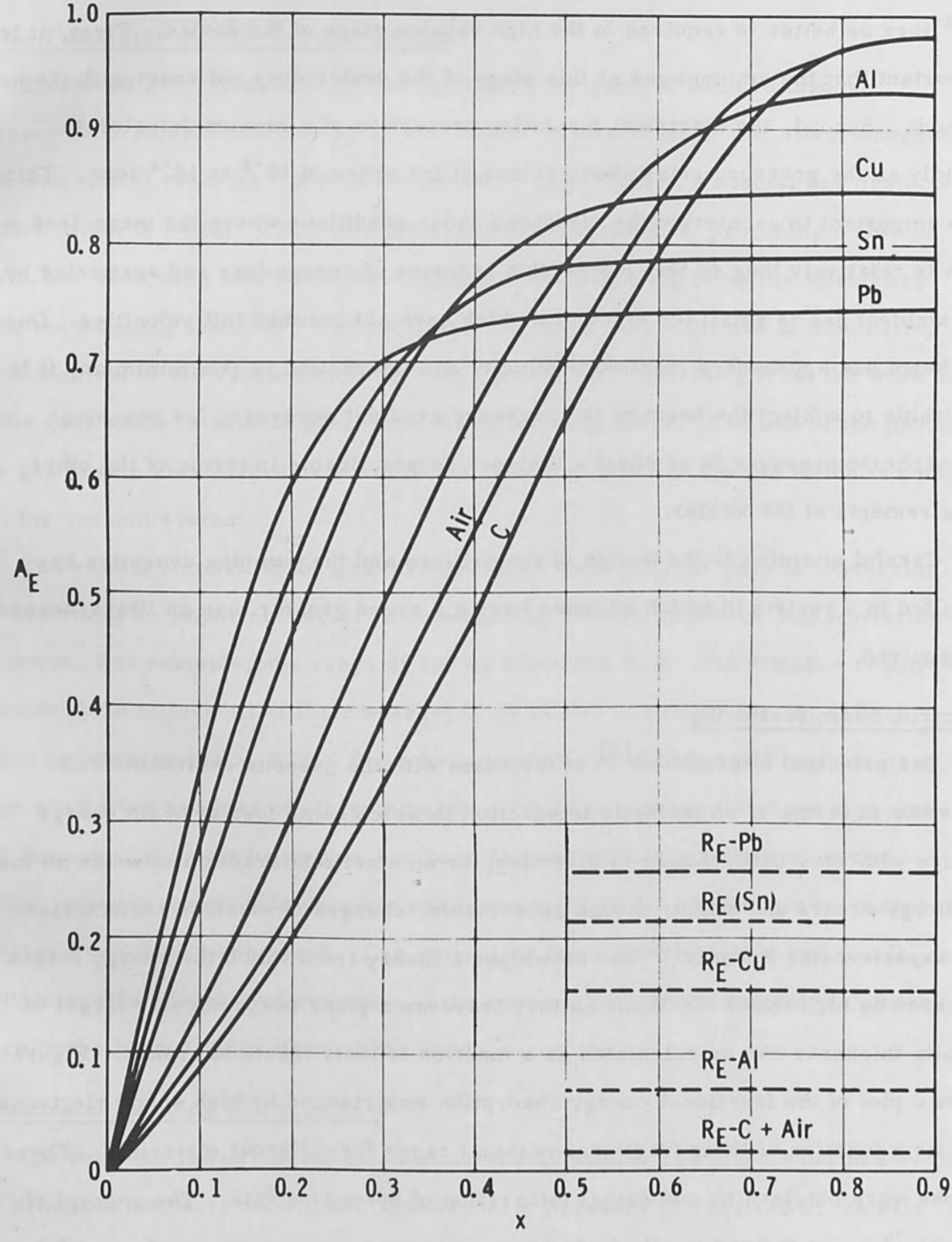

Fig. 1—A_E and R_E versus fractional range x for thick materials

represented in Figure 1 with change in beam energy. The decrease in the fraction of beam energy absorbed with increase in voltage is determined by the decrease in fractional range which occurs for a given thickness of material as the voltage is increased due to the increase in range with voltage. The dashed lines in Figure 1 represent the fraction of the total energy reflected at high values of fractional range.

In Figure 2 the fraction of beam energy absorbed, A_E, is plotted as a function of atomic number for different values of fractional range for a target of infinite thickness. The fractional reflected energies corresponding to high values of fractional range are shown at the top of the figure.

The data in Figures 1 and 2 can be used to estimate the energy losses incurred by the beam as it passes through the gun and the atmospheric pressure region between the exit orifice of the gun and the work. In order to assist in estimating beam energy losses, the range[3] in several materials is plotted in Figure 3 as a function of beam voltage. The data for gases are shown in units of the atmosphere-inches at NTP, for aluminum in inches of thickness.

The values of gas thickness expressed in atmosphere-inches at NTP which correspond to 10% of the fractional range are listed in Table 1 as a function of

Table 1

A_E, Fraction of electron beam energy lost in 0.1 fractional range expressed in atmosphere-inches

	A_E	50KV	100KV	150KV	200KV	250KV	300KV
H_e	.06	.97	3.25	6.4	10.2	14.6	19.2
N_2	0.1	.16	.52	1.0	1.6	2.27	3.0

voltage for helium and nitrogen. From Figure 2 an electron beam will lose 10% of its energy in traversing 10% of its range in helium. At 150 kv, the 0.1 fractional

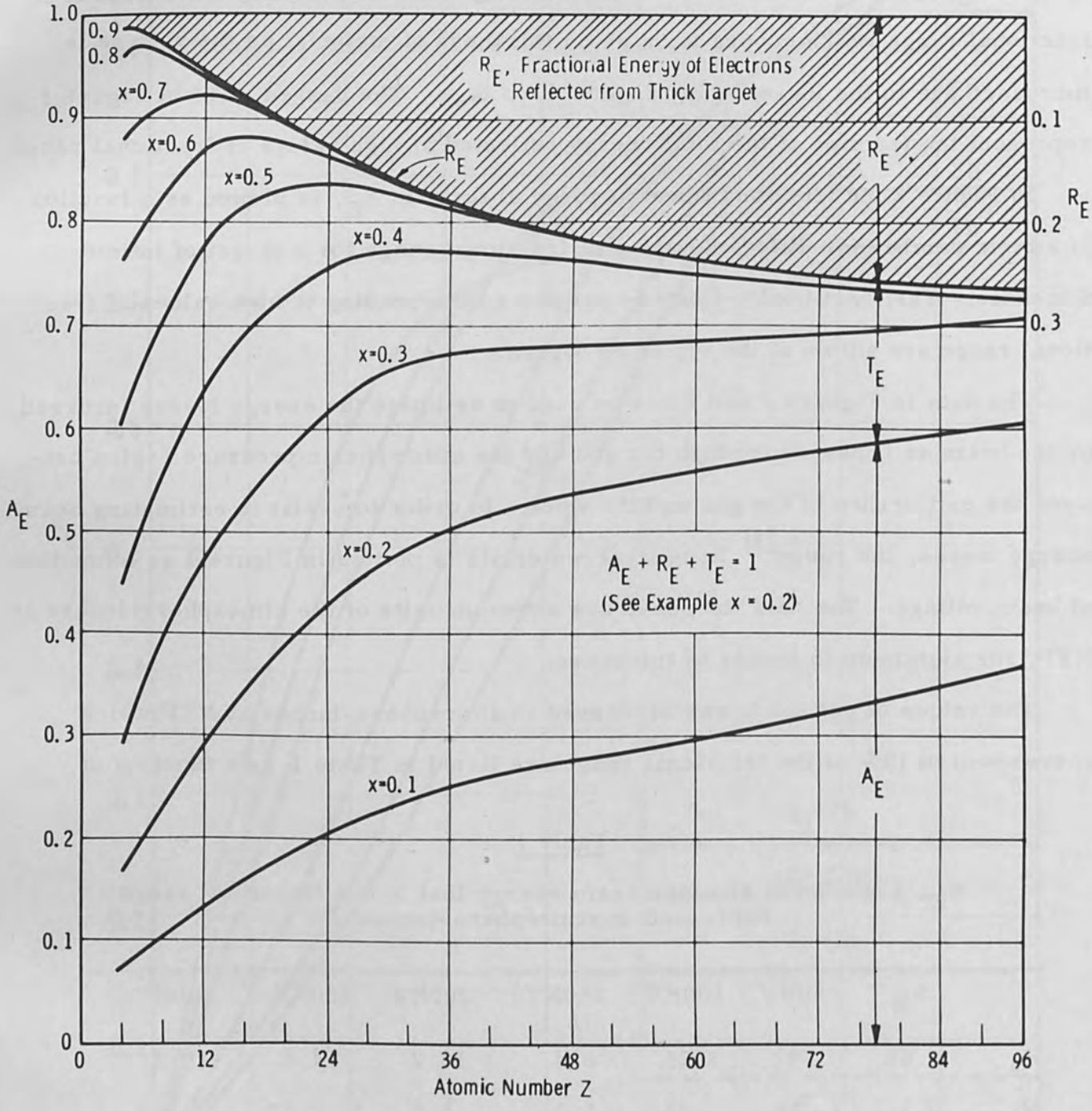

Fig. 2–A_E, fractional energy absorbed and T_E fractional energy transmitted as function of fractional range x

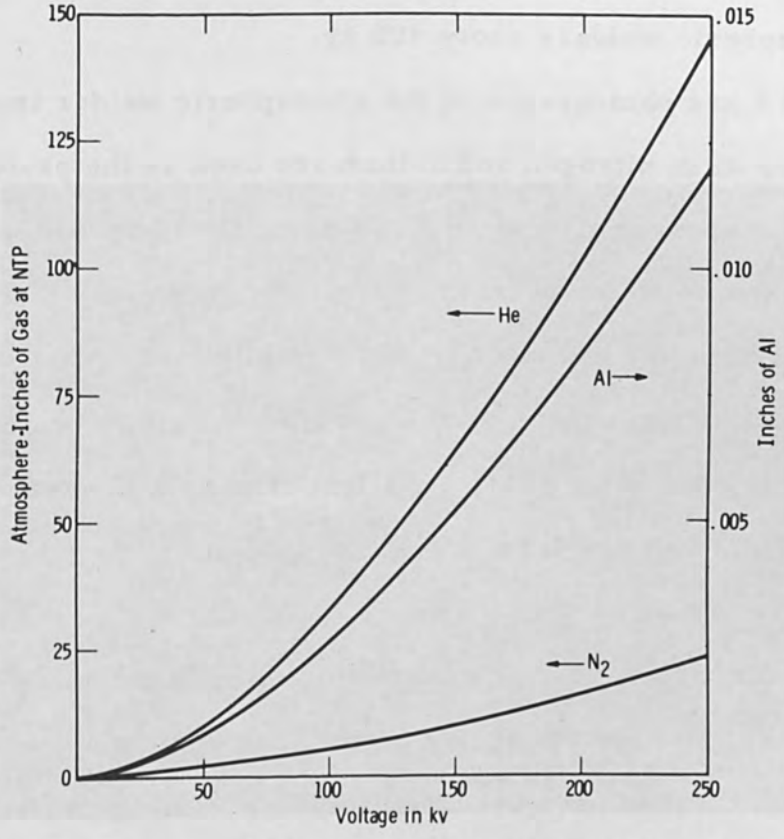

Fig. 3 — Range of He and N_2 gases and Al solid as function of kv

range for helium corresponds to 6.4 inches at NTP. The corresponding figure for nitrogen is only 1 inch. Since the beam traverses less than 0.1 equivalent atmospheric-inch of helium in traveling the entire length of the gun, it is evident that absorption of energy by the gas does not significantly affect the power transmitted by the gun.

Thus, even if the beam were to pass through as much as 1/2 inch of nitrogen in traversing the atmospheric pressure region between the exit orifice and the work, the energy loss by the beam would be only of the order of 5% of the total beam energy. From Table 1 it is evident that energy absorption in the atmosphere between the gun and the work begins to be a serious factor when voltages are dropped below 100 kv. For this reason, in addition to scattering considerations described below, there appears to be merit from the standpoint of loss of energy by the beam

in operating atmospheric welders above 100 kv.

Figures 4 and 5 are photographs of the atmospheric welder transmitting a beam into the atmosphere when nitrogen and helium are used as the protective gases, respectively. These photographs were taken using the light released by excitation of the gases to demonstrate the beam trajectories. It is clear that the beam associated with the helium flush gas has substantially less initial scattering and thus is much sharper and better defined than the beam emerging when nitrogen is employed. Secondly, from the relatively slight change in electron range as the gases are changed, as deduced from visual consideration, it is evident that the helium content in the area below the beam is not high. Scattering of the beam electrons by the ambient gas is thus a major factor in determining any changes in electron trajectories which occur once electrons have left the gun. Since direct energy loss by the beam has been demonstrated to be small, beam scatter remains as the major factor responsible for the higher powers required by a non-vacuum welder as compared to powers required for a vacuum welder to achieve the same depth of penetration within a given metal.

Schumacher and Aruja[1] have investigated the single-scattering of high speed electrons as a function of voltage, both in regard to theory and experiment. Their experimental data on beams passing through nitrogen at low pressures are in fair agreement with the theory of Wyrwych and Lenz.[4] According to these data, the gas pressure necessary to produce a given percentage of single-scatter events in which electrons are lost from the beam varies with a power of voltage which is significantly greater than unity for voltages in excess of 100 kv. Thus, both absorption and scattering data confirmed the desirability of increasing acceleration voltage above 100 kv for the non-vacuum welder in the interest of increasing beam density.

From the literature[5, 6] it is evident that the deep penetration in a metal

Figure 4 Photograph of electron beam entering atmosphere when N_2 protective gas is used.

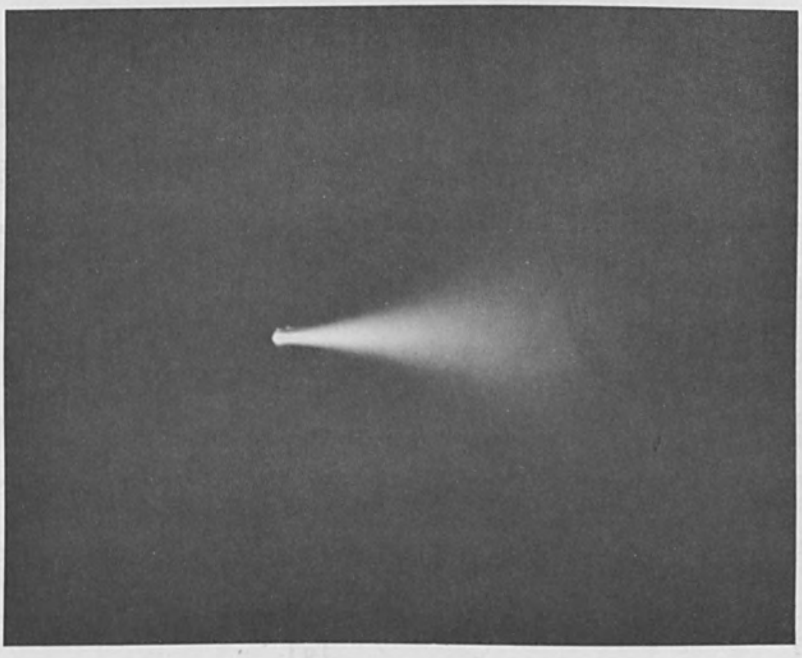

Figure 5 Photograph of electron beam entering atmosphere when He protective gas is used.

associated with EB welding is achieved by impressing beam power densities of the order of 10^5 to 10^8 watts per cm^2 into a given metal such that instantaneous volatilization of the metal occurs. The penetrations which are characteristic of EB welding are essentially the result of the lower absorption and scattering cross sections which the metal vapor presents as contrasted with the solid metal. The linear increase in penetration with increase in power which occurs at low beam power inputs at a given welding speed is probably associated with superheating of the vapor in the cavity, thus lowering the density of the vapor as power increases. As power is increased the exponent in the relationship between depth of penetration and power becomes less than unity when the effective range in the metal vapor is approached at higher powers. (It is possible that the theoretical power density limit which can be obtained in a beam at a given voltage is approached before full saturation of depth can be realized.)

It is clear that the decrease in electron beam absorption and scattering which is associated with increase in voltage should be responsible for a significant increase in penetration if power were increased by increase in voltage at a given current rather than by increase in current at a given voltage. The greater than linear relationship of range as a function of voltage observed in Figure 3 is a reasonable basis for this expectation. Essentially, increasing voltage should decrease the beam energy dissipated normal to the beam path at a particular power, making more energy available for achieving deeper penetration. The depth of penetration achieved represents a balance between the power input by the beam and the energy dissipated in vaporizing the material to a given depth, melting a local volume of metal in the immediate vicinity of the cavity, and heating by conduction a local volume immediately surrounding the molten zone. The benefit of increase in voltage in terms of increased penetration has been verified for type 302 stainless steel[7] in vacuum and type 304 stainless steel[8] for the non-vacuum welding

instance.

It is important to note that the benefits of increase in voltage should be more apparent in a non-vacuum welder since in addition to the deeper penetration within the work discussed previously, increase in voltage should reduce scatter in the gun and also in the gap between the exit orifice of the gun and the workpiece. As scattering is reduced, the higher power density characteristic of the electron optical system operating in a high vacuum is approached.

Electron Optical Characteristics

An electron bombardment heated tungsten rod[9] or "bolt" is employed as the source of electrons for the gun. Such a structure is more rugged than filamentary designs, and due to symmetry characteristics associated with it is inherently a more satisfactory source of electrons from the electron optical standpoint. The required electron emission density is produced at temperatures which result in little tungsten evaporation. Thus, the life of these "bolt" assemblies has been very satisfactory under operating conditions.

A number of techniques have been used to investigate the nature of the electron trajectories in the region of the first crossover. The use of computer programs to trace electron trajectories has proved to be a very powerful tool. The technique has involved the determination of an equipotential plot of the particular gun configuration employed using appropriate boundary conditions. Once the boundary conditions have been substituted in the program, the axial potentials are determined and used in the Gans[10] approximation to solve the paraxial ray equation. The initial radius of incidence and the slope of electron path for use in the Gans approximation are calculated on the assumption that the field at the cathode is determined by the potential at the location of the nearest grid in the computer field plot. Once the field at the cathode has been determined, it is a simple matter to compute the electron trajectory from the cathode to the first grid of the

equipotential diagram on the basis of the assumed initial velocity and direction of the electrons leaving the cathode. Since in the Gans approximation the axial potential distribution is represented by a series of straight lines, once a computer program has been set up it is desirable to use all of the available axial information to increase the accuracy of the interpolation.

Typical electron trajectories are shown in Figure 6. The initial velocities of the electrons leaving the cathode in Figure 6 are assumed to be 0, 0.1, 0.5, and 1.0 ev, respectively in the direction normal to the axis of the gun. The telefocus convergence of the lens is evident, focus occurring slightly over two inches from the cathode. The electrons of different initial velocities essentially represent parallel sets of rays which approach the lens in a direction which is not parallel to the axis. It is interesting to note that each of the sets of different velocity electrons focus at common off-axis points in the focal plane, as would be expected from the laws of optics. The electrons with no initial velocity focus on the axis in the same plane.

The distribution of energies in the crossover can be computed from a knowledge of the initial velocity distribution of electrons leaving the cathode. For example, less than 1% of electrons leaving the cathode have velocities in excess of 1 ev, and less than 15% of them have velocities in excess of 0.5 ev. As a result of the Maxwellian distribution leaving the cathode, a Gaussian distribution is expected in the crossover region.

As indicated previously, a magnetic lens is used to refocus the beam leaving the first crossover. The crossover image is focused with a magnification of nearly unity through the exit orifices of the gun onto the workpiece.

The development of suitable experimental techniques for determining beam trajectories has been a problem because of the high beam powers employed. A useful method of roughly approximating electron trajectories is by interposing a series

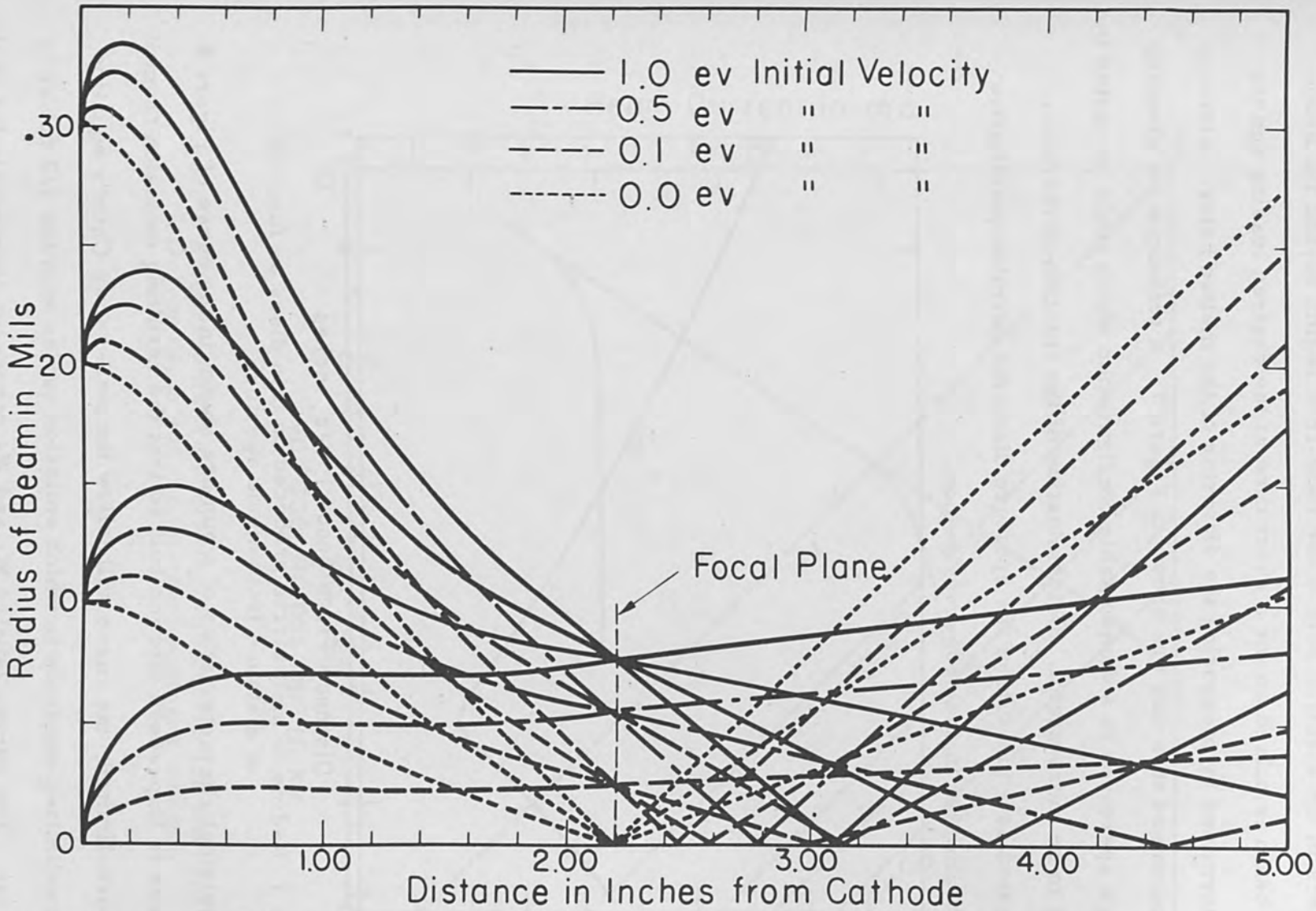

Fig. 6-Electron beam trajectories as function of distance from cathode for various values of initial electron beam energy assumed to be tangent to cathode and away from axis

of thin metal discs in the electron path in the field-free region beyond the anode aperture. The beam is pulsed on for a short time at the desired loading and the trajectories determined by measuring the diameter of the melted holes. Electron trajectories determined this way are shown in Figure 7. A technique for shooting the beam through apertures in a demountable configuration which could be varied in size has proved to be more useful. Determination of the fraction of the beam current transmitted as a function of the aperture diameter permits quantitative assessment of beam size in the crossover region.

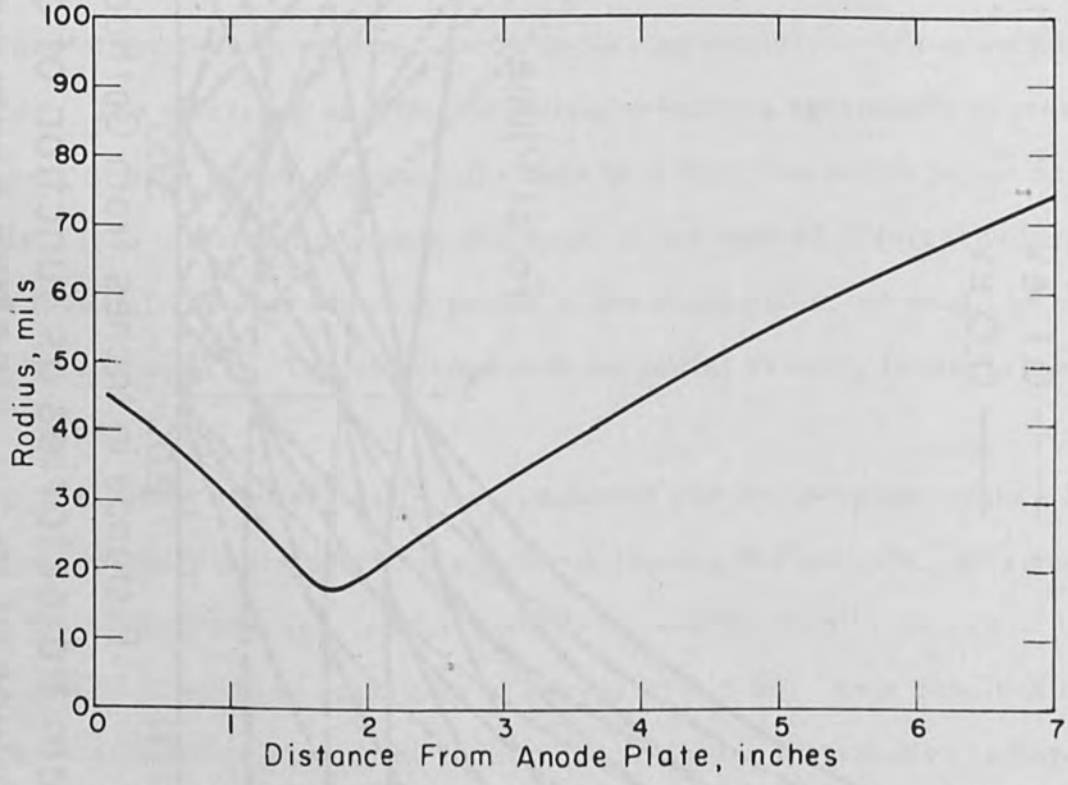

Figure 7 Radius of melt circle produced on thin discs as function of distance from anode aperture

Typical electrical characteristics of a gun are shown in the curve of Figure 8. If sufficient power is impressed into the bolt so that the resulting emission from it is not temperature-limited, the curve will follow the well-known Child's equation for space-charge-limited emission in which emission varies with the 3/2 power of the applied voltage. The curves labeled W_1 and W_2 represent characteristics of the gun when lower power is applied to the bolt and the electron emission leaving its

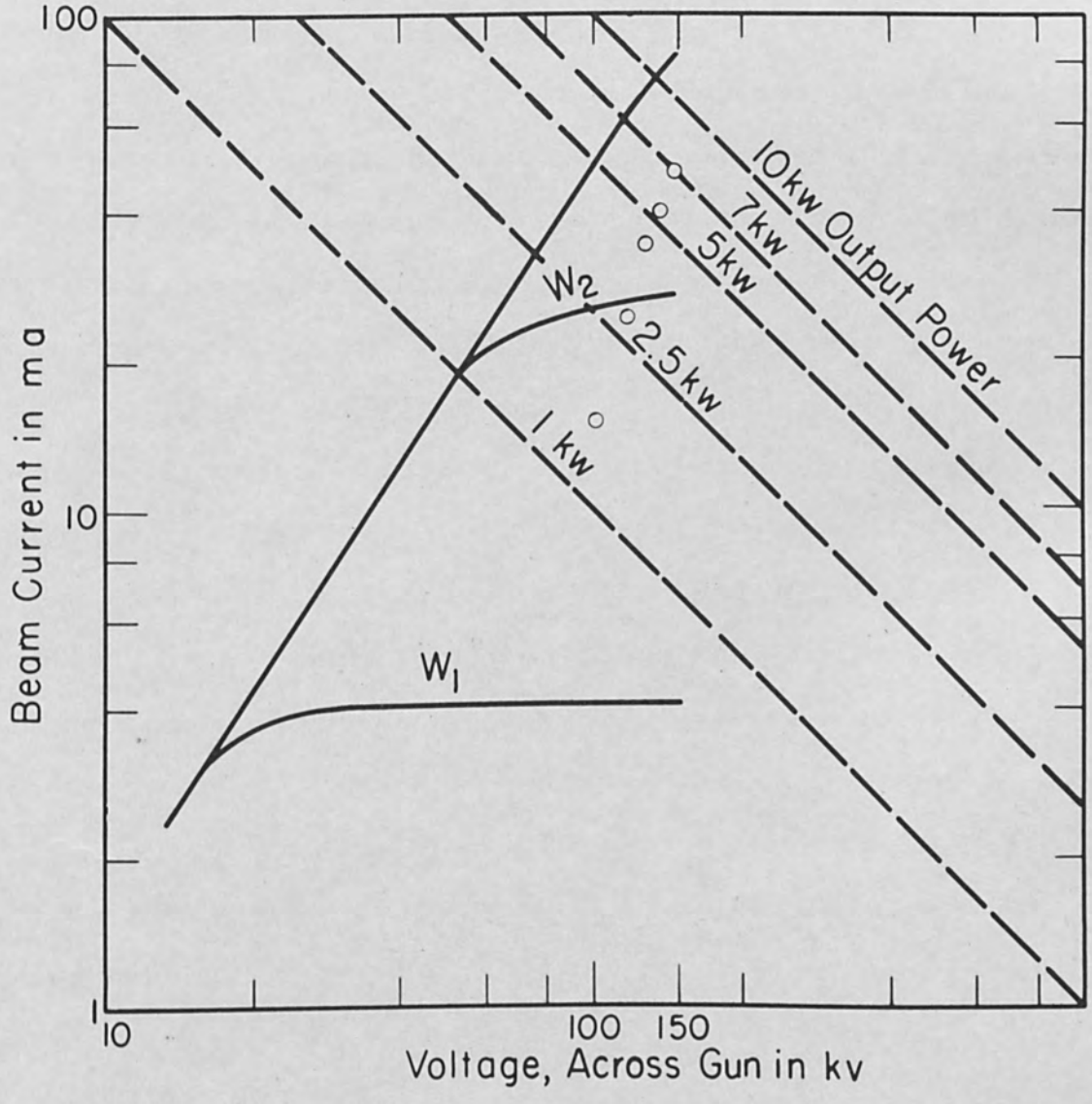

Figure 8 - Representative characteristic curves for atmospheric electron beam gun for different wattages into bolt

surface is limited by temperature considerations. Figure 8 illustrates a means of independently varying current and voltage to permit operation of the gun at the desired voltage and power. Such guns have been used experimentally to transmit as much as 15 kw of power through a set of orifices. The open circles on the graph represent some power points used in experimental welding.

Increasing negative grid bias decreases the effective perveance of the gun, shifting the curve of beam current versus beam voltage to the right of Figure 8 and increasing the slope of the curve. As grid voltage is increased the convergence of the beam is also increased, effectively shifting the crossover region closer to the cathode.

Bas[11] has reported an axial movement of beam crossover as emission current is varied. Measurements taken on this gun in the region of the first crossover confirm these data. At low currents the beam converges sharply and the crossover position is close to the emitting surface. With increasing beam current, the crossover position moves farther away from the bolt, presumably due to changes in the electric fields near the bolt resulting from the increased space charge densities associated with high currents. This shifting of the crossover region with changing beam current is of little practical concern since the geometry of the gun and the orifice system can be designed to optimize the transmission in the power region of direct concern.

Operational Data

A laboratory prototype unit on which many of the operational and welding tests were conducted is shown in Figure 9. The gun was mounted in a lead cabinet having a lead glass window in the access door to permit viewing of the welding. Referring to the photograph, the cylinder at the top of the gun houses an oil-insulated section designed to permit the use of high voltage cables as a means of feeding power to the gun. The section of the unit marked by the Westinghouse trade mark W is the

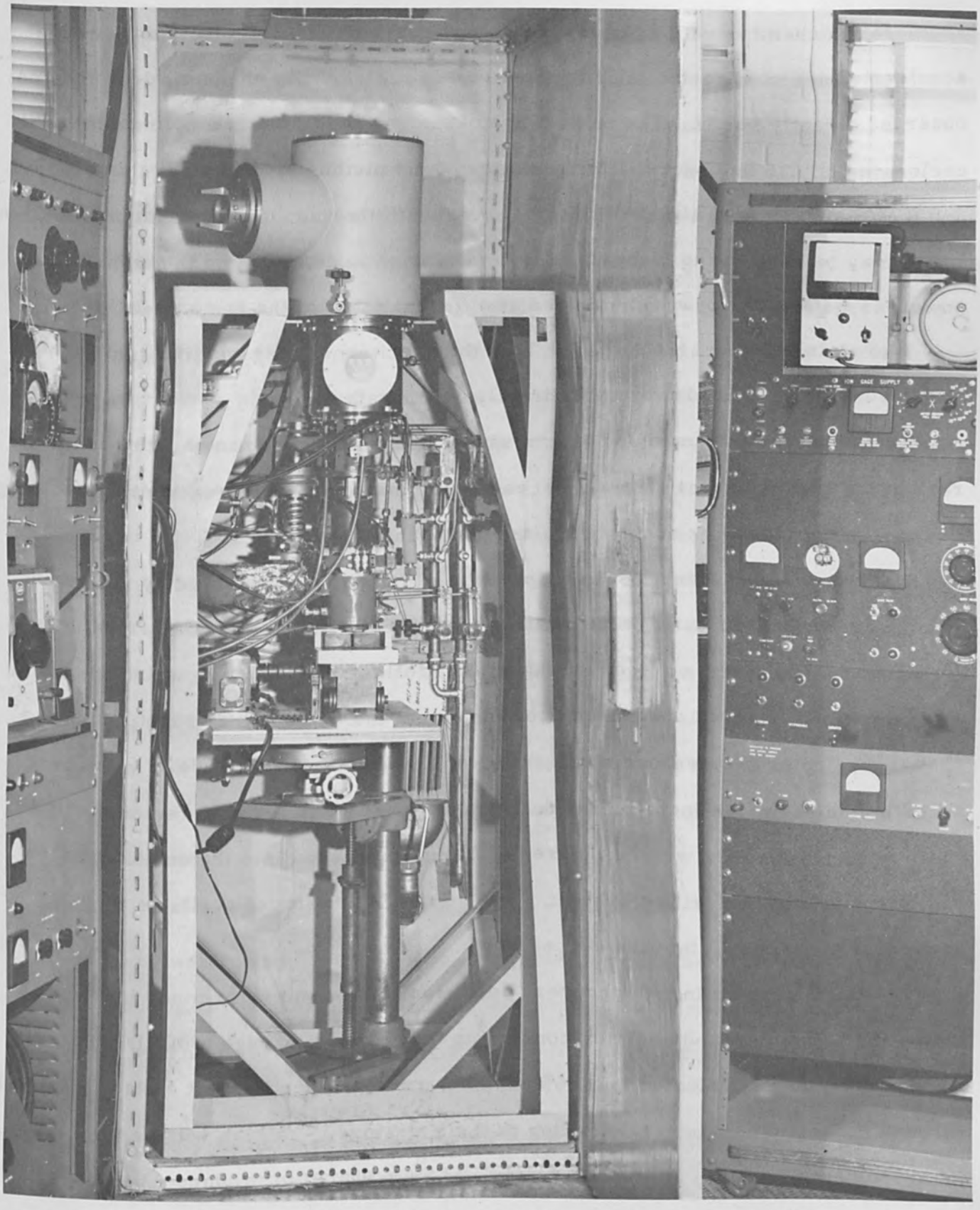

Figure 9 Photograph of laboratory atmospheric welder.

acceleration chamber which houses the cathode assembly. The electron beam is accelerated and electrostatically focused in this region. The magnetic lens may be observed directly below. The exit orifice of the gun is housed in a cylindrical lead enclosure and can be observed in the center of the picture immediately above a rack and pinion-driven cart situated directly underneath the gun. The plumbing connections which may be seen at the right of the gun were used in determining the transmitted power as well as the power dissipated at different parts of the gun system.

Two stainless steel blocks which hold the specimen during welding can be observed on the power-driven cart directly underneath the gun.

The controls for pumps and the pressure monitoring system are situated on the rack at the right, and the controls necessary for performing non-vacuum EB welding are mounted on the rack at the left of the photograph.

The beam power transmission capability of the gun was assessed by determining the power dissipated in the orifice system using thermal data derived from the water cooling of the orifices and a copper "collector" block onto which the beam was impressed, located about a quarter inch from the exit orifice of the gun.

According to the measurements, when 8040 watts of electric power were produced by the beam, as indicated by beam current and voltage measurements, 7070 watts of thermal power were measured as being impressed into the combination "collector" block and orifice system. 93% of the 7070 watts of available thermal power was transmitted into the copper block.

The beam current into the copper "collector" block was determined by insulating it from ground and then connecting it to ground through a milliammeter. The measurements indicated that 86% of the current leaving the bolt exited to ground through the milliammeter. According to the literature,[12] high voltage electron bombardment of a given copper surface would be expected to produce a back-scatter fraction of electrons having velocities in excess of 50 ev corresponding to 30% of

the input beam. Since a deep crater of irregular shape forms in the area bombarded by the beam, and the gap between the work and the gun is at atmospheric pressure, it is difficult to determine on the basis of available data just what fraction of electrons will reach the gun after having scattered from the work. Thus the measurement of beam current to the work can only be used as a rough indication of the electron transmission characteristic of the gun.

Of the order of 1,000 watts or 12% of the total beam power was unaccounted for in the thermal analysis just presented. The indications are that the missing power represents beam power which impinged upon the work and reflected from it. From Figure 2, according to Spencer's theory, 15% of the beam energy impressed on the thick copper target would be expected to reflect from it. Again, it is difficult to estimate the fraction of this thermal power which would be dissipated in heating the exit orifice of the gun in view of the fact that helium flow from the protective gas orifice produces a forced convection of gas away from the gun. The indications are that the missing power is at least roughly accounted for on the basis of Spencer's theory.

On the basis of Figure 2 it would appear that as much as 25% of the power impressed onto a workpiece of high atomic number does not perform a useful welding function.

Mobility

In many welding applications it is desirable to move the head rather than the work. Each of the components has been designed for minimum size and weight. The total weight of the power supply, gun and diffusion pumps is approximately 210 pounds.

These components have demonstrated excellent high voltage performance and have been used experimentally at 150 kv to transmit 12 kw beams for many hours continuously.

X-Ray Protection

A commonly accepted maximum radiation level recommended for personnel working with x-ray corresponds to a dosage of 0.1 roentgens per week. The exposure which will produce this irradiation level is shown in Figure 10 as a function of the millimeters of lead protection employed, the distance from the source of x-rays, and the voltage input to the electron beam generator operating at 80 ma on a 50% duty cycle for a 40-hour week. The graph is based on data by Braestrup.[13] The difference in x-ray output between materials of high atomic number and low atomic number are taken into account in the solid curves which are for tungsten and the dashed curves which are for aluminum.

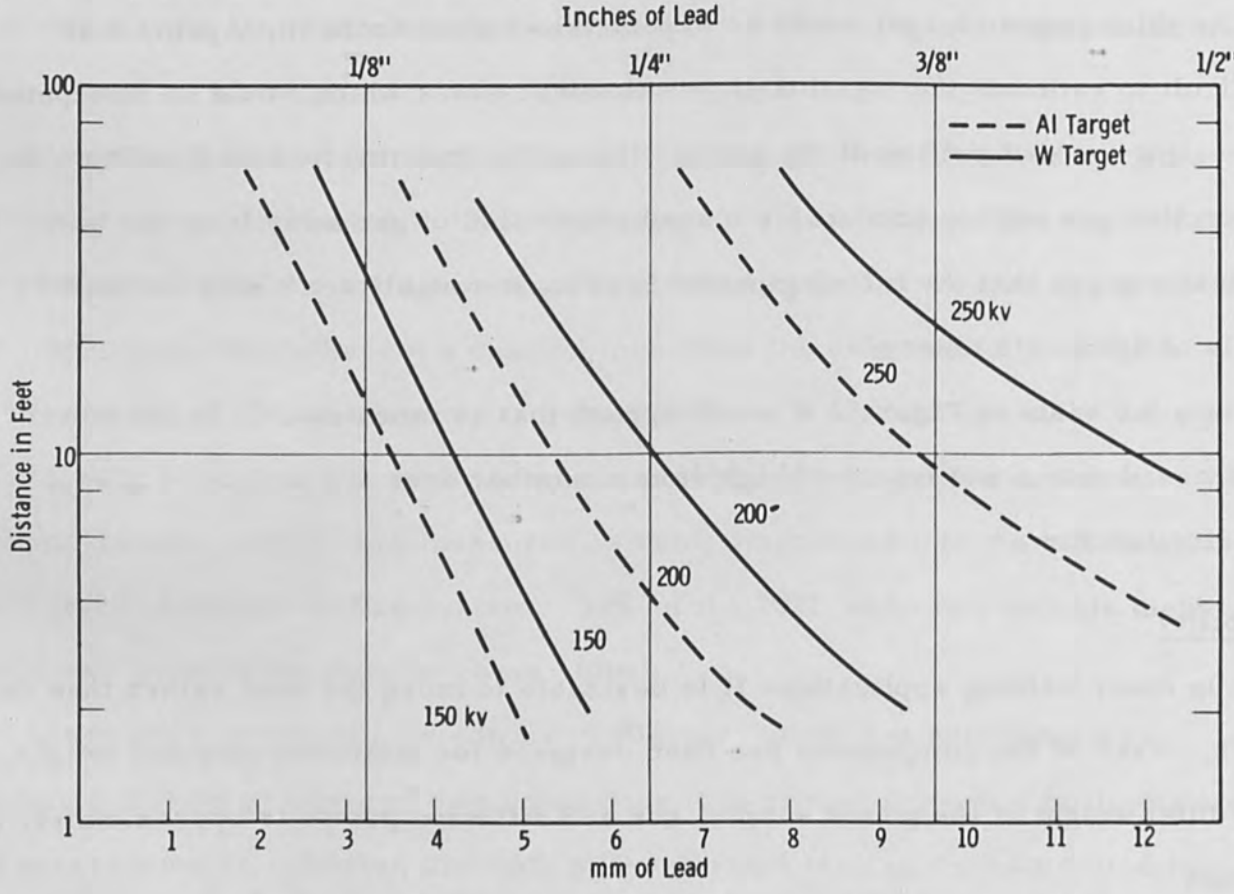

Fig. 10—0.1 R/Week x-ray protection parameters for 20 hours/week operation at 80 ma

X-ray protection can be provided most economically by placing it as close as possible to the source of x-rays. Thus it is desirable to encase parts of the gun which may serve as possible x-ray sources with appropriate thicknesses of lead.

The technique for providing the required x-ray protection from the remaining major source of x-rays, namely the work, depends to a considerable extent on the geometry. It is necessary to interpose x-ray protection directly between the source of x-rays and affected personnel. While scattered[14] x-rays are usually reduced in intensity by a factor of 1000, it is necessary nevertheless to insure that an adequate thickness of lead protects personnel from both direct and indirect sources of x-rays. Lead glass can be utilized to permit close viewing of the work. Fiber optics or electronic imaging are alternative techniques.

From the data in Figure 10 it is evident that a quarter inch of lead will provide ample protection for a 12 kw welder operating at full loading on a 50% duty cycle basis for a 40-hour week if personnel are to be located at distances of two feet or greater from the welder during operation.

Preliminary Welding Results

The purpose of the preliminary welding study was to compare non-vacuum welding with such competing processes as TIG, MIG, Plasma Arc, and the parent process, in-vacuum EB welding, in terms of the ability to weld at high rates of speed and the ability to penetrate significant thicknesses of metal with a single pass. A further objective was to determine the role that the various parameters play in the welding process, in order to establish some guidelines for procedure refinement.

Non-vacuum EB Welding

In order to arrive at sound comparisons, the process was optimized by systematically applying it to over 200 test specimens involving several thicknesses of 2219-T37 aluminum alloy and carefully examining the specimens metallographically, visually and, for selected conditions, by tensile tests. All welds were of the bead-through plate type with emphasis on full penetration, in order to permit direct observation of the interaction between speed, heat input, and porosity.

The basic approach involved the use of a linear series of experiments (see

Figure 11). In this series two of the three major variables (accelerating voltage and current) were fixed to produce a given power level while the third, process speed, was increased from a condition of over-welding to a condition of under-welding.

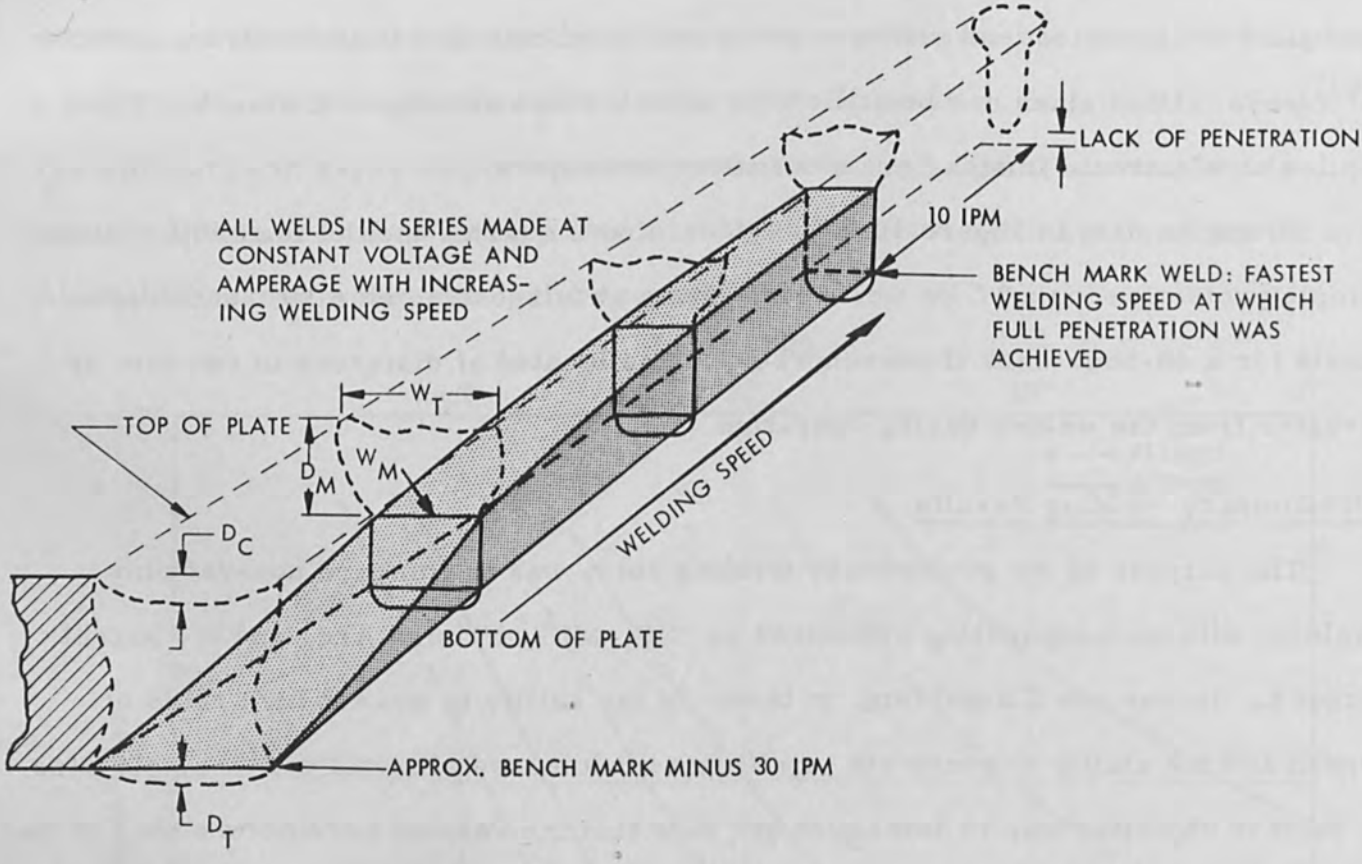

Figure 11 Development of weld cross section with increasing speed

The over-welding condition was defined as the speed at which diffusivity obscured the deep penetration action of the beam. This is shown by the TIG-like weld at the left-hand end of the series shown in Figure 11. Anchoring the opposite end of the experimental series is the "bench-mark weld", which represents the highest speed, lowest energy weld that exhibited full penetration. The bench-mark

weld serves as an excellent point of comparison. Further, it serves as a reference point for other procedures at slower speeds. (The term bench-mark minus 20 ipm refers to a weld produced with the given voltage and current but at a speed 20 ipm below the bench-mark speed.)

The outline of the fusion zone of a weld, which is the melting isotherm, permits certain deductions as to the amount and nature of the heat input as well as the heat flow away from the heat source. The contour of the weld surfaces, for the simple "bead-through-plate" weld, also reflects the temperature distribution in the work-piece during solidification. For example, sharp undercut or dropthrough (for a given welding speed and power) has been observed to be associated with sharp thermal gradients near the weld.

One of the most desirable features which a weld could have would be a fused-zone cross-section that indicated confinement of the melting and heating action to a very narrow zone between the faces of the pieces being joined. Rapid heating and cooling effects are implicit in such a joint and under tension such a weld would closely match the properties of the surrounding wrought material in much the same manner that a braze does. This very narrow joint would also be expected to produce only a minimum of shrinkage during solidification, thus reducing residual stresses and distortion.

In high diffusivity materials such as aluminum the out-of-vacuum electron beam weld retains some of the appearance of the in-vacuum weld (Figure 12) but the effect of electron scatter is evident in the broadened upper portion. Heat transferred from the scattered electrons controls the cross section of the upper one half to one third of the out-of-vacuum welds when they are made in aluminum plates 0.224-0.350 thick. Increased speed normally minimizes the tendency for unnecessary heating at right angles to the weld but does not always eliminate the scatter dominated portion of the weld in the out-of-vacuum welds in aluminum. However, at high speeds the

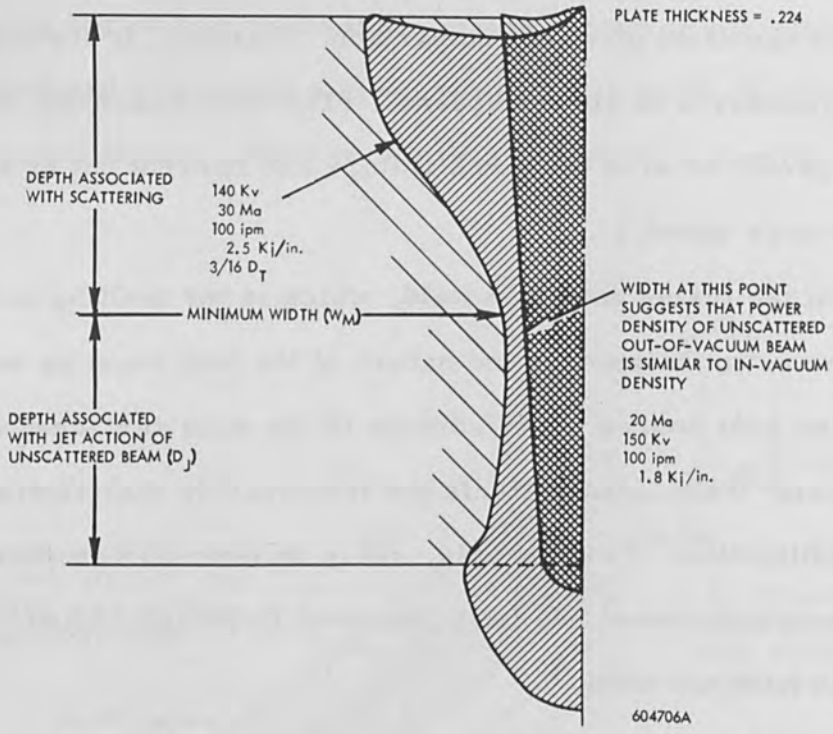

Figure 12 Comparison with in-vacuum E. B. Weld - 2219 Aluminum

"jet" action of the out-of-vacuum weld is prominent in the lower portion of the weld and appears comparable to that of an in-vacuum weld (Figure 12).

A number of the welds (including the weld in Figure 12) show a bulge at the intersection of the fusion zone with the undersurface of the weld. The suggestion is that a third heat source is active in the lower portion of the weld. The extremely hot lower surface of the vapor cavity suggested by Schwartz [6] would certainly be capable of acting as such a source. Learning to control the temperature and location of this source may provide the process with considerable control of the under-bead contour (an important feature where weld finishing costs are considered).

Figure 13 summarizes the relationship observed between weld power and speed. The thicknesses evaluated permitted penetration with available powers over a broad range of speeds, giving the process considerable latitude in terms of power and speed. For any given power, the jet-like characteristic of the electron beam melting phenomenon only becomes apparent as the process speed approaches

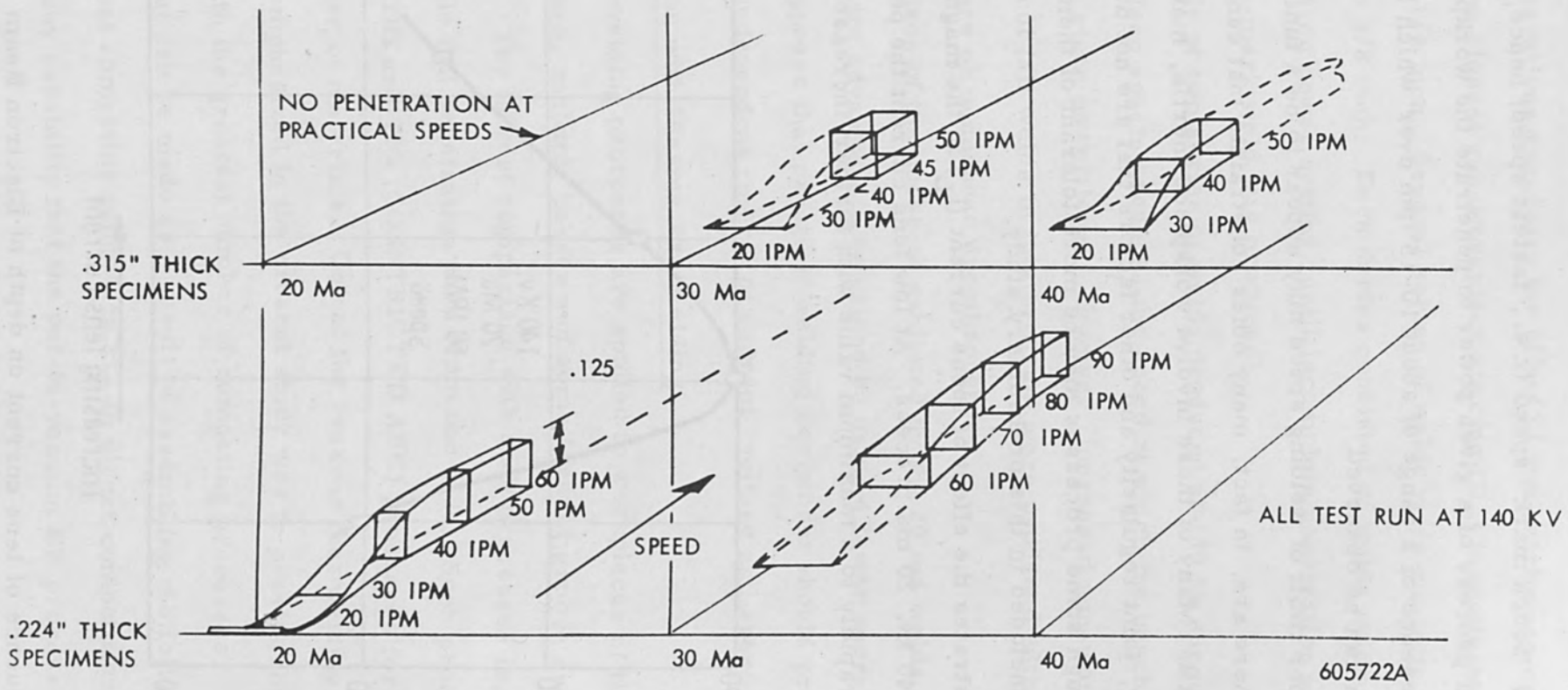

Figure 13 Relationship of Practical Welding Ranges
at Various Power Inputs and Thicknesses

within 20-30 ipm of "bench mark" speed (i. e., fastest speed; hence, lowest energy input that permits a process of a given power to penetrate the workpiece). Figure 13 indicates the presence of a range of about 10-15 ipm over which little significant change in jet action can be observed.

Though the upper limit of welding speed may appear to be a function only of available power, there are, in fact, many other constraints that can be placed on this procedure detail. Many of these involve workpiece inertia, manipulator or positioner stability, joint regularity and other factors that are not directly related to the process (though some processes may be more tolerant of them than others) and have not been included in this preliminary study.

Figure 14 illustrates the effect of focus current (I_L) in the magnetic lens on penetration for a 140 kv, 20 ma process. At low lens current the penetration is low but increases rapidly to a maximum value with further increase in current and then decreases.

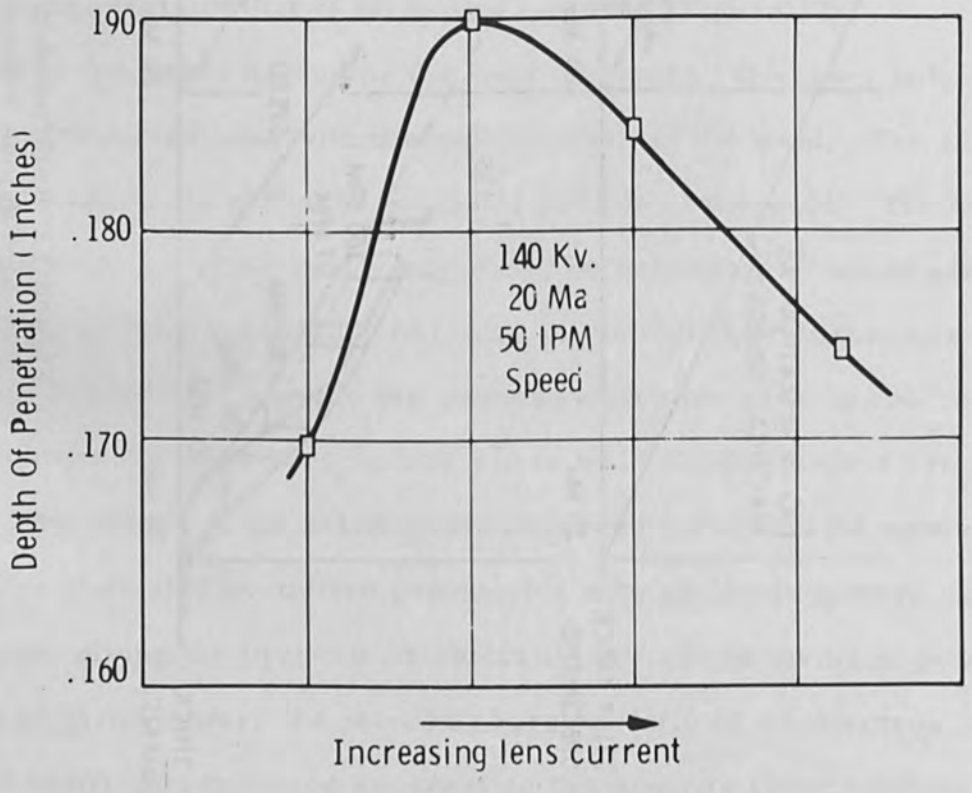

Figure 14 Influence of lens current on depth of Electron Beam penetration

Some observations regarding the effect of gun-workpiece spacing are shown in Figure 15. The closest gun-workpiece spacing (D_T) investigated was arbitrarily established at 1/8 inch. Several series of welds were run with the workpiece at distances up to 3/8 inch. Each series consisted of welds made at increasing speeds, at a given power setting, until incomplete penetration was observed (i. e., until the bench-mark weld was produced).

An analysis of two series of welds produced at 140 kv suggested that increasing the gun-workpiece spacing reduces the speed at which the bench-mark weld is observed for a given power level. However, increased gun-workpiece spacing reduces undercut (all welds in this program were produced without filler) and may have an influence on underbead dropthrough.

A comparison of the undercut exhibited by the 20 ma welds and the 30 ma welds reveals a distinct advantage to be gained by using a lower current setting when possible. It appears that practical welding equipment should provide the welding operator with independent control of current, voltage and speed.

Comparison with Plasma Arc Welding

When arc welding processes are applied to workpieces of thicknesses greater than 1/8-1/4 inch, multiple passes and some form of groove are required to complete the joint. The fairest comparison with such processes is, therefore, on the basis of a single full penetration pass from one side. Such procedures have been developed for TIG and TIG (CONSTRICTED ARC) processes for thicknesses of 1/4 inch in a number of materials. One of the reasons that welding in 0.224 inch thick material was emphasized in the present study was to provide the broadest basis for comparison with the greatest number of competing processes. In fact, the observation that can be made as a result of assembling the following comparative data is that most competing processes are in direct competition up to only about 3/8 inch, and any capability that the out-of-vacuum EB process may have to

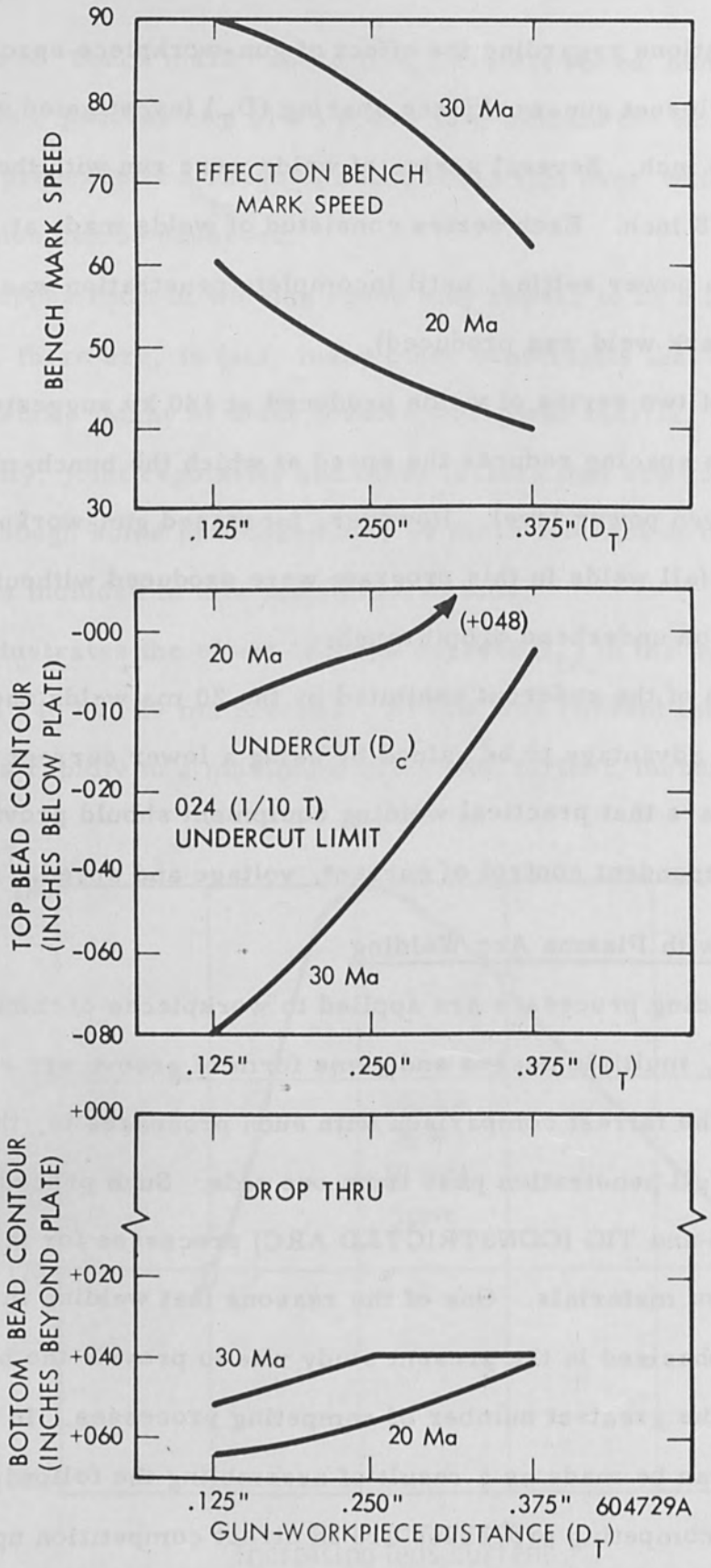

Figure 15 Effect of Gun Work Piece Distance

penetrate materials beyond this thickness without resorting to multiple passes, filler material and complex joint geometries is almost entirely unchallenged except by the less flexible in-vacuum process. The comparisons set forth in the following paragraphs, therefore, are limited to comparing out-of-vacuum electron beam welding with more conventional processes in the highly competitive 1/8-3/8 inch range of thicknesses.

The constricted and shaped arc TIG process involves a transferred arc (as does conventional TIG), but the cathode is in a chamber where high pressures exist and auxiliary gas jets are provided as the arc leaves the chamber to further "shape" the plasma. The manufacturer has observed that constricting and shaping the arc produces higher welding speeds and narrower welds.[15] This new process then would seem to be directly competitive with electron beam welding and particularly with the out-of-vacuum processes since major applications include parts too large for vacuum chambers (rocket casings) and high speed continuous production lines (such as tube and pipe welding).

Figure 16 compares the carefully optimized Plasma Arc weld in 0.224 inch wall, Type 304 stainless steel tubing. This process cannot yet be applied to aluminum so the comparison must be made in stainless steel. The reference notes that the 14 ipm welding speed for Plasma Arc represented an 8 ipm increase over conventional TIG. Figure 16 also shows the much narrower weld that can be produced by the out-of-vacuum electron beam welder even though the same speed was used for this illustration in order to permit direct comparison of the heat input characteristics of the two processes. Produced at 120 kv and 20 ma, the out-of-vacuum weld at this speed does not represent the full potential of the process, and it would appear reasonable to expect narrower welds and higher speeds as optimization studies proceed on this material.

Thus, the out-of-vacuum process appears capable of welding at higher speeds

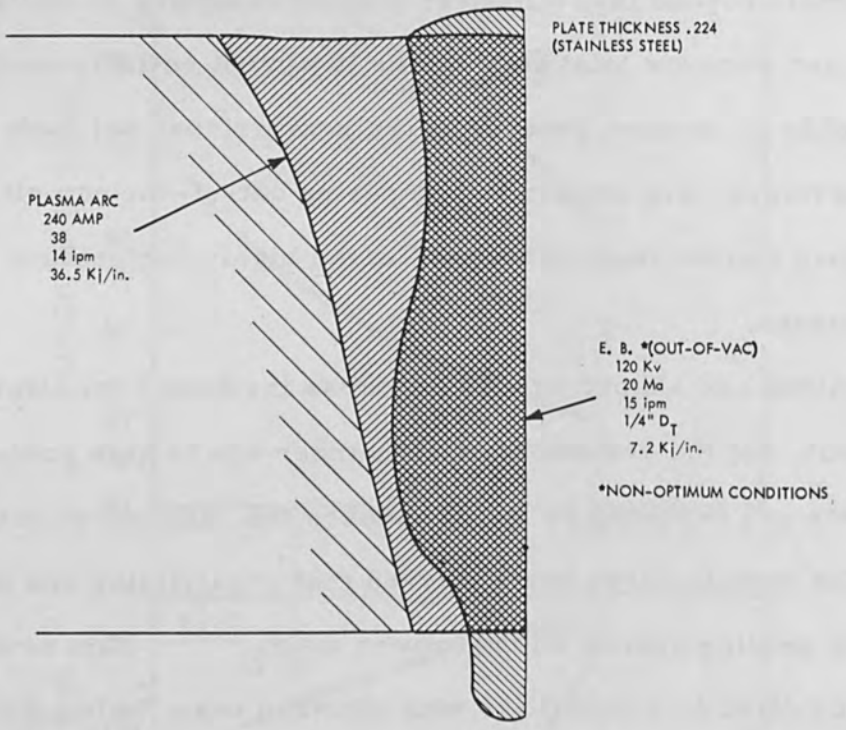

Figure 16 Comparison of Plasma Arc * in Type 304 Stainless

and penetrating greater thicknesses, since reportedly Plasma Arc is limited to 3/8 inch stainless steel while out-of-vacuum EB readily accomplishes 3/8 inch welds in highly conductive aluminum, producing narrower welds in the thicknesses compared.

Comparison with Conventional TIG

Unlike the Plasma Arc process, the conventional TIG process can be applied to aluminum so a direct comparison with out-of-vacuum electron beam welding on the basis of alloys and thicknesses is possible. Furthermore, TIG has been subjected to extensive development on the 2219 alloy in the 0.224 thickness. Therefore, a comparison of the effectiveness of the out-of-vacuum EB as a means for producing a weld with a minimum amount of metallurgical disturbance and with the least possible distortion can be made in 0.224 inch 2219 aluminum alloy.

Figure 17 compares a carefully optimized TIG weld with some out-of-vacuum EB welds. The TIG weld involves 360% more molten metal than does the out-of-

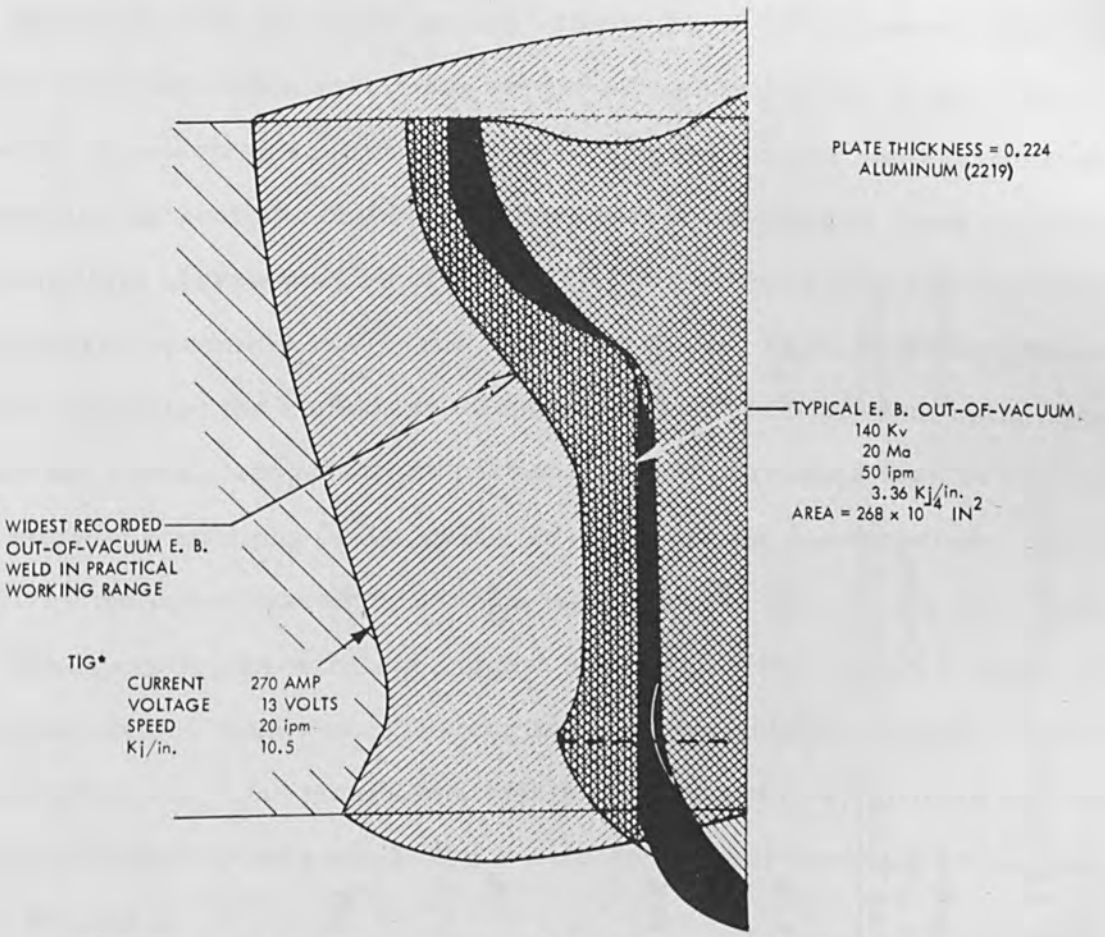

Figure 17 Comparison with Tig* in 2219 Aluminum

vacuum electron beam weld. The reduction in melted volume as a result of the application of the out-of-vacuum electron beam process would suggest a proportional reduction in gross weld stress and consequently in distortion.

Comparison of Tensile Results

A series of tensile tests was run on several welds produced at 140 kv, 30 ma and 70 ipm in 0.224 inch 2219-T37 alloy. An average ultimate tensile strength of 41 ksi was achieved (see Table 2). Had conventional MIG or TIG equipment been applied the results might have been expected to range between 38 ksi and 41 ksi. Thus, it appears on the basis of a systematically developed procedure that out-of-vacuum electron beam welding competes with the best one-pass, one-side TIG results.

Table 2

TENSILE TESTS OF 14.4 kj/inch/inch WELDS

Speciman	Tensile (psi)	Yield (psi)	Elongation % in 1/2" (across Welds)	Original Appearance	Initiation of fracture
202-14.4 A-1	41,550	26,440	12%	OK	Face
A-2	41,990	29,370	9%	OK	Root
A-3	41,940	28,200	10%	OK	Face
Avg	41,827				
202-14.4 B (Root Removed)	36,460	24,240	9%	OK	-
202-14.4 C (Face Removed)	43,770	28,820	6%	OK	Root

One specimen from the above series was machined to remove the lower half (narrow) of the weld. This specimen, representing the portion of the weld dominated by the electron scatter failed at 36,460 psi. When another specimen was tested with the scatter dominated portion machined away to leave only the characteristically narrow portion of the weld, the specimen failed at 43,770 psi. Failure occurred randomly at the face and at the root. Thus, the strengths of these welds represent the composite effect of the weak scatter-dominated upper portion and the much stronger lower portion; greater strengths may be realized by changing thermal conditions in the weld. In any event the narrow cross section that characterizes the out-of-vacuum electron beam process and the low heat input required to achieve full penetration suggest a reduced effect on the strength of the joint in the as-welded condition. The commercial desirability of such a feature is rapidly increasing as high strength materials are applied to structures that are too large for post-weld heat treatment (e.g., ship hulls, architectural structures, and aerospace vehicles).

Summary of Welding Observations

In terms of competitive features such as high welding speed and low distortion the out-of-vacuum process is clearly superior to comparable TIG or MIG processes. It is faster, involves less heat input to the workpiece, and will weld more materials than the highly competitive TIG (constricted plasma) process. The metallurgical properties exhibited in initial tests equal or exceed recorded values for TIG welded heat-treatable 2219 aluminum alloy.

As a practical welding process, out-of-vacuum electron beam techniques exhibit no unique problem areas that would limit their applications. In these tests there was no evidence of any characteristic (such as sensitivity to the thermal or physical characteristics of the workpiece or to the evolution of vaporized material) that would prevent the out-of-vacuum EB process from fusing weldable materials.

Neither did the process exhibit critical features that would require procedural development or control beyond what would be required by any mechanized inert gas arc welding process.

The out-of-vacuum technique proved amenable to manipulation of parameters (such as selection of proper voltages, currents, gun-workpiece spacing, speed, and shielding techniques) as a practical means of controlling such fundamental weld qualities as bead contour and weld soundness.

The most striking welding characteristics are the high welding speeds with low heat inputs. For 0.224 inch thick 2219 aluminum:

Speed:	80-90 ipm
Heat Input:	2.8-3.2 kilojoules/inch
Distortion:	Less than 0.005 inches

It would appear on the basis of these welding tests that practical welding equipment should permit some selection of voltage and current since control of speed alone does not always permit the achievement of an optimized procedure.

Acknowledgements

It is a pleasure to acknowledge the valuable assistance of Dr. Schumacher of the Ontario Research Foundation, and the engineers and scientists of many Westinghouse Divisions, including the Surface Division, the Electronic Tube Division and the R and D Center.

References

1. Schumacher, B. W., Aruja, E., and H. R. Falckenberg, Forthcoming Third International Vacuum Congress, Stuttgart, June, 1965.
2. Spencer, L. V., NBS Monograph 1, 1959.
3. Nelms, A. T., NBS Circular 577, 1956.
4. Wyrwych, H. and F. Lenz, Z Naturforsch. 13a, p. 515.

5. Wells, O. C. and T. E. Everhart, Proceedings Fourth Symposium on Electron Beam Technology, 1962, p. 105.

6. Schwartz, H., Journal of Applied Physics, July 1965, p. 2020.

7. Meier, J. W., Proceeding Third Symposium Electron Beam Technology, 1961, p. 145.

8. Meier, J. W., International Conference Electron and Ion Beam Science and Technology, Toronto, 1964.

9. Bas, E. B., Zeit. für Angew. Phys., 7, 337-344, 1955.

10. Gans, R., Zeit. für Tech. Phys., vol. 18, 1937, p. 41.

11. Bas, E. B., International Conference Electron and Ion Beam Science and Technology, Toronto, 1964.

12. Sternglass, E. J., Physical Review, vol. 95, 1954, p. 345.

13. Braestrup, C. B., Industrial Standardization, May 1946, p. 116.

14. Johns, E. J., The Physics of Radiology, Charles Thomas Publisher, 1961.

15. Filipski, Stanley, P., Welding Journal, Nov. 1964, p. 937.

The Energy Released by an Intensive Electron Beam as it Passes Through Matter

by

J. Lindner and H. Müller
University of Mainz
Germany

The goal of these considerations is a theory concerning the interaction between an intensive electron beam and certain materials (for example, steel) which are penetrated by it. The theory obtained should be physically feasible and in agreement with experimental results. The area of application which is of primary interest is electron beam welding. We do not intend to proceed from any heuristic, physical postulates. The point of departure which we have chosen is based on general, well-founded concepts regarding the interaction between electrons and atoms; and, by means of specialization, we will attempt to adapt these to actual test conditions. In specific terms, we are seeking relationships which will unite the following:

a. Beam data (current, voltage, cross-section),

b. Material data (atomic number, atomic weight, density, specific heat, melting temperature, heat of sublimation),

c. Work data (depth of weld channel, rate of feed).

We schematize the release of energy of the electron beam in the material as follows: a single electron penetrates the material at a point x (x is the normal coordinate, $x = 0$ for the surface of the metal, where the electron beam collides with the material). Suppose a single electron penetrates the solid material around a piece Δx, after the electron has traveled a distance x in the material which is already vaporized, it releases its kinetic energy $E(x)$ along Δx. The energy $E(x)$ available to the electron at the point x serves to vaporize a layer of the thickness Δx. The energy of the electron as a function of the coordinate is determined

primarily by the distance x which it has traveled in pre-vaporized material and by the density of the vapor. If the boundary layer between pre-vaporized and solid material is so far forward that the electrons give up all their initial energy in the vapor which they had upon entering the vapor channel, then the weld channel has reached its greatest depth.

If the channel depth and the rate of feed are actually to be defined as functions of beam and material parameters, i. e. as functions of current, voltage and cross-section on the one hand, and of atomic number, atomic weight, melting temperature, etc., on the other hand, this pattern of the release of energy in metal must obviously now be supplemented by precise formulations concerning:

a. The energy balance - 1) the total energy of the beam electrons and
   2) that energy which is required to heat and vaporize the material,
b. The type of interaction between electrons and metal,
c. The heat conduction processes.

If one takes into account only the energy balance, one gets a relationship between the rate of feed on the one hand and the beam data, the material data and the energy distribution on the other. If this energy distribution is known, the channel depth must obviously be defined by means of $E = 0$. Accordingly, rate of feed and depth of penetration can be calculated if the type of interaction which exists between electrons and metals is known.

Suitable postulates regarding the type of interaction lead to a relation which was stated by Bethe and Heitler. It has the form of an ordinary differential equation of first order for $E(x)$. Its integration leads therefore to the determination of the energy of a single electron dependent on the distance which the electron has traveled in the material, if the material data (atomic number, atomic weight, density, etc.) are known. This differential relation is relatively easy to derive by using semiclassical methods which do not take into account relativistic effects

and the spin-spin interaction. One point should be taken into consideration, however, the differential equation is unrelated to the aggregate state of the metal. The number of atoms per unit volume which are in the beam-penetrated body is far more essential. Thus, we can use the Bethe-Heitler relation for the solid and gaseous states if we use the corresponding densities for the solid and gaseous material. This integration yields a complicated expression for electron energy E(x) which is still available after passing through a vapor channel of length x. The energy distribution is diagrammed as follows:

From the condition E = 0 we get a relation for the penetration depth depending on the initial energy of the electrons and the material data. This expression for channel depth could lead to some doubts because it contains only material and beam constants and contrary to experience, appears to be unrelated to rate of feed. However, the channel depth is inversely proportional to the vapor density, which is not an actual material constant but is dependent on temperature which is a function of rate of feed. If the channel depth increases, the temperature decreases, then according to the Clausius-Clapeyron equation, the vapor density increases. The channel depth actually does decrease at an increasing rate of feed. The same relationship can be derived from the expression for the rate of feed, which was mentioned earlier, i.e. as the density is lowered by an increase in temperature, the depth of the channel will be greater. A more detailed discussion shows that as the rate of feed becomes lower the material is heated to a greater degree by the beam. The temperature in the metal is limited by heat transfer, hence there is a minimum vapor density and a maximum channel depth which cannot be exceeded even when the rate of feed approaches zero. This agrees with the experimental results.

By means of this method, penetration depths and rates of feed are obtained which are of the same magnitude as those derived from experimental results. In

general, however, they are too large. Improved results are obtained when heat conduction processes are taken into account. Proceeding from the differential equation for heat transfer (which is set up for an unlimited plate of fixed thickness, using the usual postulate for isotropic and homogeneous media) one calculates heat conduction and heat transfer on the boundary surfaces for a line source which is moved at a uniform speed. One examines what portion of the total beam energy contributes to the increase in temperature of the actual weld zone - i. e., what portion of this energy is not immediately rendered useless due to its dissipation. The completed calculation shows that only a part of the total energy is of use in the weld process. The penetration depths which result when heat conduction is taken into account agree with experimental results.

Compensation of Deflection Distortion in a High Power Electron Beam Melter

by

K. Kanaya and H. Kawakatsu
Electrotechnical Laboratory
Tokyo, Japan

I. Okazaki and T. Takizawa
Japan Electron Optics Laboratory Co., Ltd.
Tokyo, Japan

Abstract

It is often necessary to deflect the beam by relatively large angles to improve the efficiency and quality of production of an electron beam melter. Using a six pole magnetic compensater, deflection angles as high as 30 degrees are possible without appreciable distortion. An increase in efficiency as much as 50% can be expected with this system of distortion compensation.

Introduction

Although it was only about half a century ago, in 1907, that Pirani indicated the practical utilization of an electron beam melter, its application has already been fully recognized, particularly in connection with the production of high purity metals such as Ti, Zr, Hf, Nb, Ta, Mo, and W. Because of the increased demand for these metals, the construction of melters of large size has become necessary.[1] Several important design considerations for melters are listed below:[2, 3]

a) The electron beam melter should be as efficient as possible for economical reasons.

b) The system should be capable of fairly large electron beam deflections without appreciable distortion.

c) The electron bombardment system should be of the multiple-gun type for effective operation. However, the maximum number of guns should be less than five from practical considerations.

A large, high power electron beam melter has recently been designed and constructed in our laboratory. It has two bombardment systems and provides a maximum beam power of 120 KW. The system is shown in Figure 1. Ingots having diameters of 60, 80, and 100 mm. have been produced.

In the design of the electron bombardment system a theoretical and experimental study of the efficiency of the deflected beam bombarding the molten pool was conducted. When the beam was magnetically deflected, the beam image was distorted because of the aberrations of the deflector. Accordingly, a theoretical analysis was made of the aberrations incurred when the beam was deflected in the melter. The analysis has shown that this image distortion can theoretically be compensated for and the electron beam melter was designed accordingly.

Theoretical Analysis of Magnetic Deflection of the Electron Beam[4]

Magnetic fields are generally used for deflection in electron beam melters. The field distribution in a deflector can be represented by:

$$B(x, y, z) = \frac{B_o}{1 - \left(\frac{x}{a}\right)^2 + \left(\frac{y}{a}\right)^2 + \left(\frac{z}{b}\right)^2} \qquad (1)$$

where B_o is the maximum field strength

2a is the width along the x and y axes

2b is the width along the z axis.

The directions of the incident beam, magnetic flux and beam deflection are represented by the Z, X, and Y axes, respectively. The image formed by a deflecting field given by equation (1) can be expressed as follows:[5]

$$\begin{aligned} x &= M + (A_4 - z)X_o + A_9 Y_o + 2a_8 X_o Y_o \\ y &= N + (A_5 - z)Y_o + A_9 X_o + a_8 X_o^2 + a_{13} Y_o^2 \end{aligned} \qquad (2)$$

where, $X_o = x_o / \ell = \omega \cos \chi$

$Y_o = y_o / \ell = \omega \sin \chi$

$A_4 = - [a_4 + (a_{10} + 2a_8 / \ell) y_s]$

$A_5 = - [a_5 + (a_{12} + 2a_{13}/\ell) y_s]$

$A_9 = - (a_9 + 2a_8 / \ell) x_s$

$$M = (1 + a_2 + \frac{z + a_4}{\ell}) x_s + (a_7 + \frac{a_9 + a_{10}}{\ell} + \frac{2a_8}{\ell^2}) x_s y_s$$

$$N = \alpha \ell + a_1 + (1 + a_3 + \frac{z + a_5}{\ell}) y_s + (a_6 + \frac{a_9}{\ell} + \frac{a_8}{\ell^2}) x_s^2$$

$$+ (a_{11} + \frac{a_{12}}{\ell} + \frac{a_{13}}{\ell^2}) y_s^2$$

ℓ is the distance from the deflector's principal plane to the image plane

ω is the half angle of the beam aperture

α is tne deflection angle

z is the deflection defocusing

(x_o, y_o) are the coordinates of the beam in the principal plane

(x_s, y_s) are the coordinates of the beam in the image plane

$a_1, a_2 \ldots . a_{13}$ in Eq. 2 are aberration constants, and they are given by the following equations according to Glaser.[6]

$$a_1 = \int_{z_a}^{z_b} \left[\frac{1}{2} e'^3 + \frac{1}{2} \eta B_2 e^2 (z - z_b) \right] dz \qquad (3a)$$

$$a_2 = \int_{z_a}^{z_b} \left[\eta B' e' (z - z_b) - \eta B_2 e (z - z_b) \right] dz \qquad (3b)$$

$$a_3 = \int_{z_a}^{z_b} \eta B \; e(z - z_b)\, dz \tag{3c}$$

$$a_4 = \int_{z_a}^{z_b} \left[\frac{1}{2} e'^2 + \eta B' e' (z - z_b)^2 - \eta B_2 e (z - z_b)^2 \right] dz \tag{3d}$$

$$a_5 = \int_{z_a}^{z_b} \left[\frac{3}{2} e'^2 + \eta B^2 e (z - z_b)^2 \right] dz \tag{3e}$$

$$a_6 = \int_{z_a}^{z_b} \left[\frac{1}{2} \eta B' - \frac{1}{2} \eta B_2 (z - z_b) \right] dz \tag{3f}$$

$$a_7 = \int_{z_a}^{z_b} -\eta B_2 (z - z_b)\, dz \tag{3g}$$

$$a_8 = \int_{z_a}^{z_b} \left[\frac{1}{2} e' + \frac{1}{2} \eta B' (z - z_b)^2 - \frac{1}{2} \eta B_2 (z - z_b)^3 \right] dz \tag{3h}$$

$$a_9 = \int_{z_a}^{z_b} \left[\eta B' (z - z_b) - \eta B_2 (z - z_b)^2 \right] dz \tag{3i}$$

$$a_{10} = \int_{z_a}^{z_b} - \eta B_2 (z - z_b)^2 \; dz \tag{3j}$$

$$a_{11} = \int_{z_a}^{z_b} \frac{1}{2} \eta B_2 \; (z - z_b) \; dz \tag{3k}$$

$$a_{12} = \int_{z_a}^{z_b} \eta \; B_2 (z - z_b)^2 \; dz \tag{3l}$$

$$a_{13} = \int_{z_a}^{z_b} \left[\frac{3}{2} e' + \frac{1}{2} \eta B_2 (z - z_b)^3 \right] dz \tag{3m}$$

where, $|e| = \alpha z$ $\quad |e'| = \alpha$

note: this e is not the electronic charge.

$$B_2 = \frac{2B_o}{a^2\left[1 + \left(\frac{z}{b}\right)^2\right]^2}$$

$$B' = \frac{2B_o z}{b^2\left[1 + \left(\frac{z}{b}\right)^2\right]^2}$$

also

$$\eta = \sqrt{\frac{e^*}{2m\Phi}}$$

where, e^* is the electron charge

m is the electron mass

Φ is the accelerating voltage.

If the deflector is designed in such a way as to obtain a field which satisfies $a = b$, i.e.

$$B(x, y, z) = \frac{b^2 B_o}{b^2 - x^2 + y^2 + z^2} \tag{4}$$

the aberration constants in equation (3) can be expressed approximately as follows:

$$\left.\begin{aligned}
&a_1 = \frac{1}{4}\alpha^3\ell \qquad a_2 = 0 \qquad a_3 = -\alpha^2 \\
&a_4 = \frac{1}{2}\alpha^2\ell \qquad a_5 = \frac{5}{2}\alpha^2\ell \qquad a_6 = -a_{11} = \frac{\alpha\ell}{2b^2} \\
&a_7 = \frac{\alpha\ell}{b^2} \qquad a_8 = -a_{13} = \frac{\alpha\ell^3}{2b^2} \qquad a_9 = \frac{\alpha\ell^2}{b^2} \\
&a_{12} = -a_{10} = \frac{\alpha\ell^2}{b^2}
\end{aligned}\right\} \tag{5}$$

Therefore, the general deflection formula in equation (2) can be written as follows:

$$x = \left[r_s + \frac{z}{\ell} (r_s - r_o) + \frac{1}{2} \alpha^2 (r_s - r_o) \right] \cdot \cos\chi + \frac{\alpha \ell}{2b^2} r_o^2 \cdot \sin\chi \qquad (6a)$$

$$y = \alpha \ell + \frac{1}{4} \alpha^3 \ell + \left[r_s + \frac{z}{\ell} (r_s - r_o) - \alpha^2 \left(\frac{5}{2} r_o - \frac{3}{2} r_s\right) \right] \cdot \sin\chi$$

$$+ \frac{\alpha \ell}{2b^2} r_o^2 \cos 2\chi \qquad (6b)$$

where, r_o is the beam radius in the principal plane

r_s is the beam radius in the image plane

Figure 2 shows the beam image for various deflection angles at ℓ = 31 cm, photographed from an angle of 45°. This image was formed by the beam which passed through a magnetic deflector having a field distribution with a = b = 5.6 cm. Figure 3 shows the theoretical images in accordance with equation (6) under the same conditions as those for the beam images in Figure 2. As can be seen, these images are in good agreement with each other. It can also be noted that the beam image distortion due to the field coma aberration given by $\frac{\alpha \ell}{2b^2} r_o^2 \sin 2\chi$ and $\frac{\alpha \ell}{2b^2} r_o^2 \cos 2\chi$ in equation (6) grows in proportion to α.

Compensation of the Deflected Beam Image Distortions

It is often necessary to increase the beam deflection angle for many reasons. For example, this is required to insure effective drip melting of rod-shaped materials.

In practice, the thermal distribution in the molten pool is considered to be one of the most important factors in determining ingot quality. It is, therefore, evident that a large beam deflection would be very advantageous.

A theoretical analysis to compensate the third order astigmatic aberrations has been made.[7] The same analysis is also applicable in the case of a magnetic

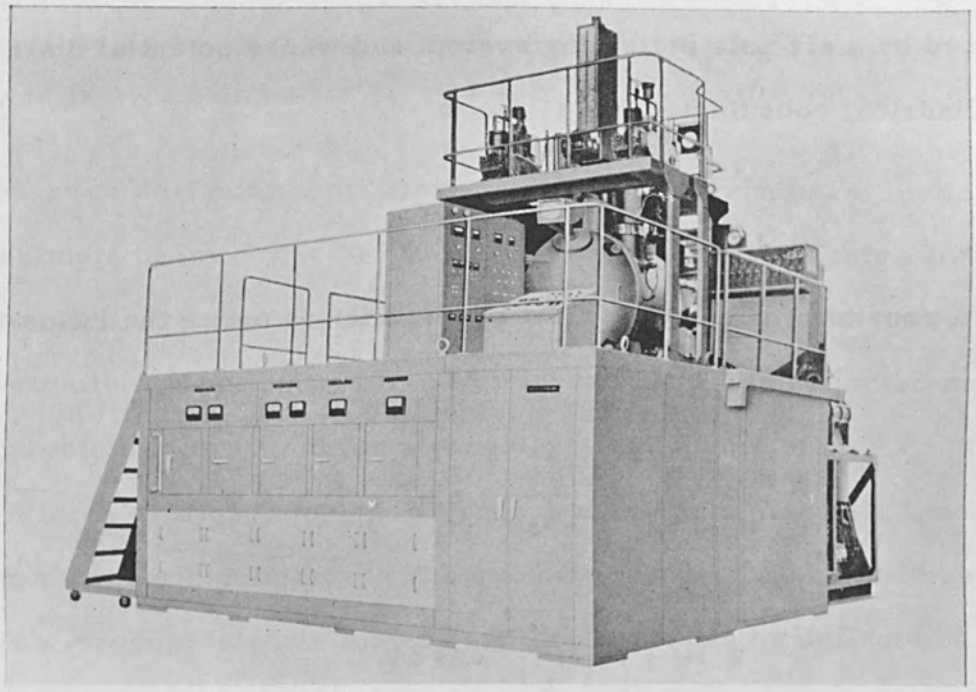

Figure 1 Production-purpose JEBM-12B type electron beam melter.

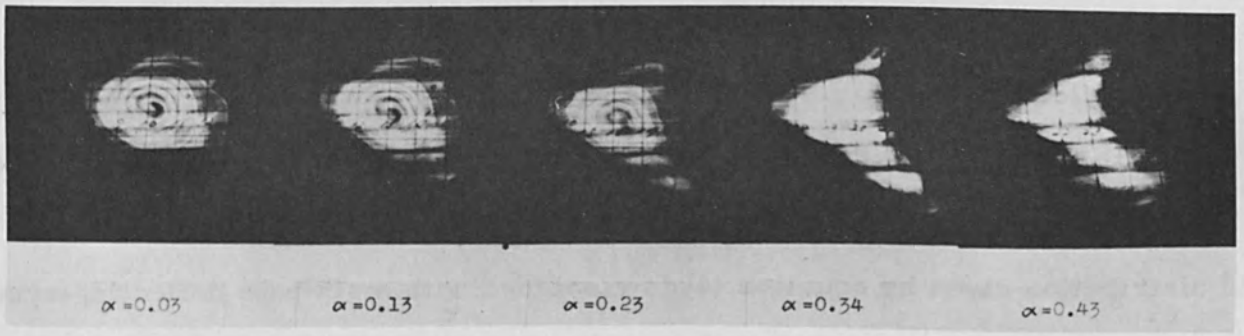

Figure 2 The experimental results that show the variations of the deflected beam images for different deflection angles.

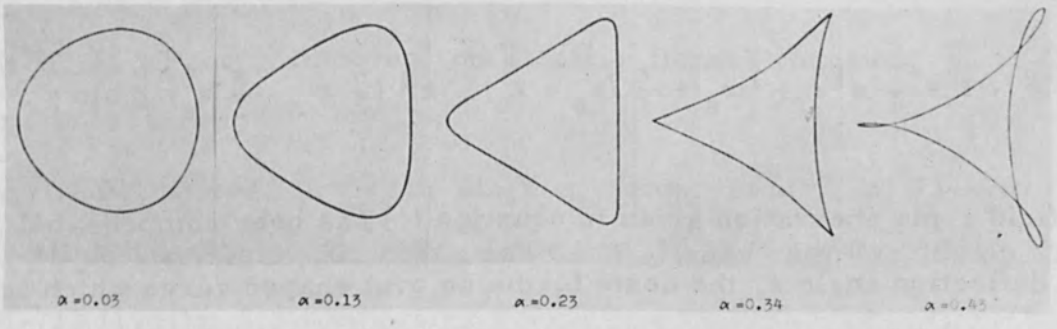

Figure 3 The theoretical beam images under the condition of Figure 2.

field produced by a six pole deflecting system and whose potential distribution is given in cylindrical coordinates by:

$$\psi(r, x) = C r^3 \cos 3\chi \tag{7}$$

where C is a constant. The cylindrical beam which is under the influence of that field is given by:

$$x = -A \left(\frac{r_s}{\ell_s}\right)^2 \sin 2\chi$$

$$y = -A \left(\frac{r_s}{\ell_s}\right)^2 \cos 2\chi \tag{8}$$

where r_s is the beam radius

ℓ_s is the distance from the six pole magnetic field to the image plane and A is a function of the field strength and the dimensions of the deflector.

It is, therefore, possible to find a value for A in equation (8) which corresponds to $a_8 = -a_{13}$ in equation (5). This can be done if a magnetic deflector with a field distribution given by equation (4) is combined with a six pole deflecting system. The superposition of equation (6) and equation (8) gives:

$$x = \left\{ r_s + \frac{z}{\ell} (r_s - r_o) + \frac{1}{2} \alpha^2 (r_s - r_o) \right\} \cos \chi$$

$$y = \alpha \ell + \frac{1}{4} \alpha^3 \ell + \left\{ r_s + \frac{z}{\ell} (r_s - r_o) - \alpha^2 \left(\frac{5}{2} r_o - \frac{3}{2} r_s\right) \right\} \sin \chi \tag{9}$$

The field coma aberration given in equation (6) has been compensated. Even with high deflection angle x, the beam forms an oval shaped curve which is due to the deflection astigmatism given by:

$\frac{1}{2}\alpha^2 (r_s - r_o)$ and $-\alpha^2 (\frac{5}{2} r_o - \frac{3}{2} r_s)$ in equation (9)

In the course of designing a production oriented electron beam melter which exhibits a maximum beam power of 120 KW, it was decided to design and test the 60 KW electron bombardment system shown in Figure 4 taking the previously mentioned aberration compensation into consideration. This column type electron bombardment system is designed for an accelerating voltage of 25 KV. The system consists of a Pierce type gun, magnetic lenses, a six-pole magnetic beam image corrector and a magnetic deflector. The distance between the cathode and the molten pool is approximately one meter, and the beam can be deflected by as much as 30 degrees.

Figure 5 shows the result of the bombardment of Tungsten by an electron beam when it was deflected as described earlier.

Figure 6(a) shows the theoretical image shape of the deflected beam using equation (9) while Figure 6(b) shows the image obtained using equation (6). As can be seen, the experimental result agrees with the theoretical conclusion.

Figure 7 shows a tantalum ingot 80 mm. in diameter produced at the rate of 10 kg/hour melting speed, with a mean beam power of 80 kw. The melting efficiency was approximately 125 g/kwh. The 35 to 50 per cent increase in the melting efficiency is attributable to the improved deflection system.

References

1. Smith, H. R., Proc. 2nd Symp. on Electron Beam Processes, p. 15-24 (1960).
2. Sibley, C. B., and M. L. Torti, 8th Vac. Symp. Trans., p. 714-721 (1961); Smith, H. R. Jr., Hunt, C. d'A., and C. W. Hanks, 8th Vac. Symp. Trans., p. 708-713 (1961); Gruber, H., Z. Metallkde, 52, p. 291-309 (1961), Vacuum 14, p. 362 (1961).

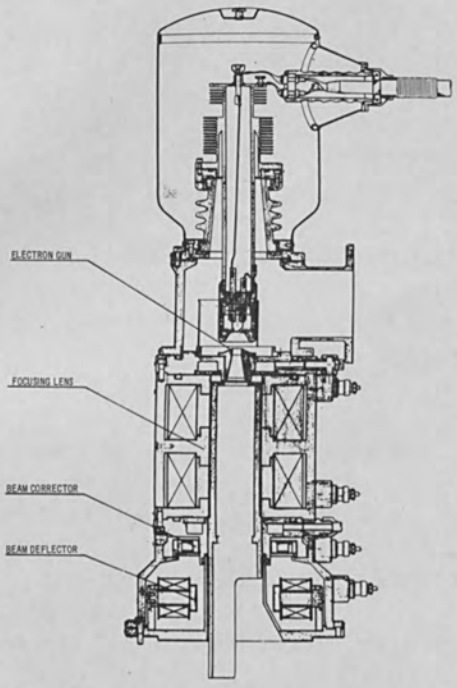

Figure 4 Column type electron bombardment system. Maximum beam power 60 KW.

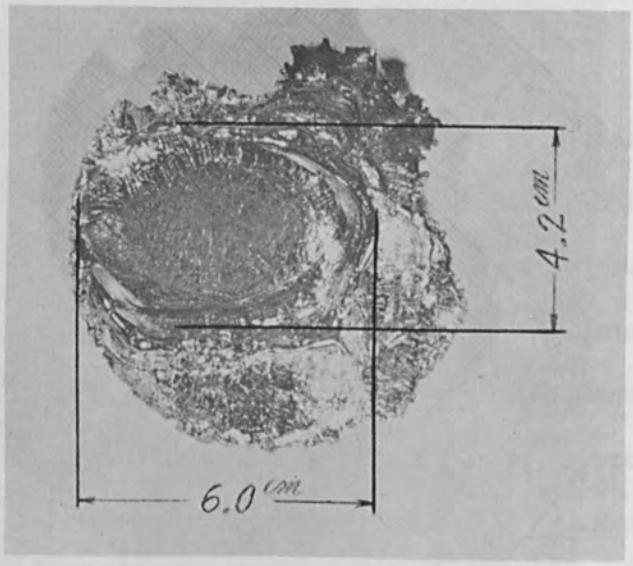

Figure 5 Mark produced by the image of the deflected beam on molten tungsten.

(a) (b)

Figure 6 Deflected beam image calculated theoretically for the same conditions as Figure 5, (a) by equation (9); (b) by equation (6).

Figure 7 80 mm diameter tantalum ingot made by large scale electron beam melter.

3. Gruber, H., Dietrich, W., Erben, E., Heimerl, S., and H. Stephan, Vacuum-Technik, 12, p. 65-77 (1963).

4. Kanaya, K., Kawakatsu, H., Okazaki, I., and T. Takizawa, Bulletin of Electrotechnical Lab., 27, p. 65-77, (1963).

5. Grumm, H., Optik, 18, p. 32-43 (1953).

6. Glaser, W., Grundlagen der Elektronenoptik, Springer-Verlag, Wien, p. 473-486 (1952).

7. Kanaya, K., Kawakatsu, H., Bulletin of Electrotechnical Lab., 25, p. 801-814 (1964).

Digital Computer Analysis of Electron Flows

by

J. E. Boers
The University of Michigan
Ann Arbor, Michigan

Abstract

A brief description of the digital computer programs for the analysis of axially symmetric and planar electron guns will be presented followed by some of the results obtained with them.

The programs are for electrostatic, electromagnetic and relativistic electron guns and employ simple relaxation techniques on a large matrix (up to 10,000 points) which is used to describe the electric fields within the gun. The programs completely determine the current and voltage distributions within the gun starting from a basic description of the geometry. A new program for relativistic electrons which includes induced and applied magnetic effects will be described.

Included in the results is a description of a magnetically confined but rippling beam in which shearing and counterrotating electrons are found. The effects and magnitudes of self-induced magnetic fields in relativistic and nonrelativistic beams will be described for several beams.

Also to be presented are the results obtained with a special grid analysis program. The focusing and scattering effects of the grid wires in a space-charge-limited triode will be shown. Special attention is given to the formation of separate beam sections for positive grids and the effect of changing the grid voltage on the focusing of these separate sections.

Introduction

Digital computer programs have been developed for the analysis of virtually any axially symmetric or planar geometry electron gun. The execution time required

ranges from 4 to 24 minutes on an IBM 7090 digital computer, the time depending primarily on the type of analysis desired, i.e., electrostatic, cross-field, electromagnetic or relativistic, and to a lesser extent on the accuracy desired. The programs are written in FORTRAN and require a 32,000 word core for execution.

All the programs employ relaxation techniques where electric fields and trajectories are alternately computed until two consecutive sets of trajectories essentially repeat themselves. The electric fields can be represented on a matrix containing up to 10,000 points, but for most purposes a matrix containing 7200 points in a 120 by 60 array has been adequate. Solved exactly these will produce values for the electric fields with a theoretical accuracy of better than 0.02 percent, the actual accuracy attained by the program is better than 0.1 percent.

A general flow chart for the programs is shown in Figure 1. Execution starts by reading in a description of the gun geometry electrode voltages and scaling information. Constants and tables to be used later in the program are then computed and initial, approximate voltage and space-charge distributions are laid out.

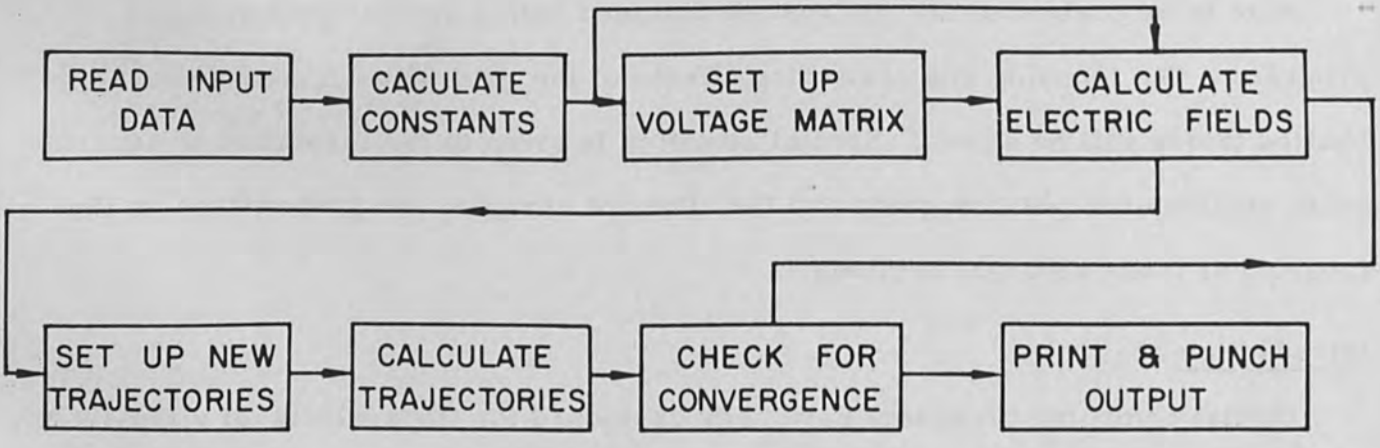

Figure 1 General flow chart for digital programs.

The initial relaxation of the electric fields is then carried out followed by the calculation of the trajectories through the gun. This is repeated until the program converges by repeating similar trajectory calculations.

The results are then printed out and may be saved in binary form for restarts later if desired.

The Computer Equations

The voltages within the gun region are solved by iteratively applying Poisson's equation at each point of the voltage matrix. For an axially symmetric geometry the difference equations are

$$V_{i,j} = \frac{V_{i+1,j} + V_{i-1,j} + V_{i,j+1} + V_{i,j-1}}{4} + \frac{\Delta r}{r_j}(V_{i,j+1} - V_{i,j-1}) + \frac{J(\Delta r)^2}{4\epsilon_o v} \quad (1)$$

and on the axis

$$V_{i,j} = \frac{4V_{i,j+1} + V_{i+1,j} + V_{i-1,j}}{6} + \frac{2}{3}\left[\frac{J(\Delta r)^2}{4\epsilon_o v}\right], \quad (2)$$

where i,j are shown in Figure 2, Δr is the length of one matrix square, r_j the radius to the jth matrix point, J the current density at the point i,j and v the electron velocity at i,j. These equations are accurate up to the fourth-order term.

Similarly for rectangular coordinates

$$V_{i,j} = \frac{V_{i+1,j} + V_{i-1,j} + V_{i,j+1} + V_{i,j-1}}{4} + \frac{J(\Delta x)^2}{4\epsilon_o v}, \quad (3)$$

where Δx is the length of one matrix square and the other terms as above.

The space-charge term $J(\Delta r)^2/4\epsilon_o v$ is obtained directly from the trajectory calculations and is stored in a separate matrix which is identical in size and shape to the voltage matrix.

The (nonrelativistic) trajectory equations can be derived from the Lorentz

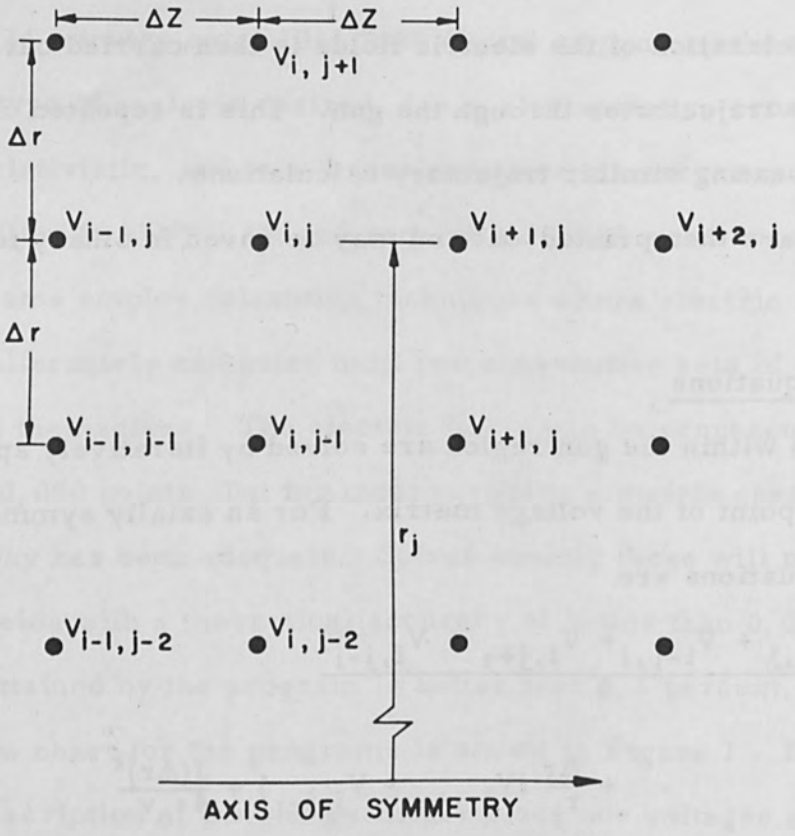

Figure 2 Matrix definitions.

force equation

$$\overline{F} = - e (\overline{E} + \overline{v} \times \overline{B}) \quad , \tag{4}$$

where, for the axially symmetric case, $\overline{B}$ can be described in terms of the magnetic vector potential by

$$\overline{B} = \text{curl } \overline{A} \quad . \tag{5}$$

The expressions for an axially symmetric system then become

$$r \dot{\theta} = \eta \left(A_\theta - \frac{r_o}{r} A_{\theta_o}\right) \quad , \tag{6}$$

$$\ddot{r} = \eta \left[- E_r + \eta \left(\frac{r_o}{r} A_{\theta_o} - A_\theta \right) \left(\frac{\partial A_\theta}{\partial r} + \frac{r_o}{r^2} A_{\theta_o} \right) \right] \tag{7}$$

and

$$\ddot{z} = \eta \left[-E_z + \eta \left(\frac{r_o}{r} A_{\theta_o} - A_\theta \right) \frac{\partial A_\theta}{\partial z} \right] , \qquad (8)$$

where A_θ is the θ component of the magnetic vector potential, r_o the initial radius of the trajectory, $A_{\theta_o} = A_\theta(r_o, z_o)$, E_r and E_z the electric fields and η the charge-to-mass ratio. These become in difference form

$$r_{k+1} = 2r_k - r_{k-1} - \eta (dt)^2 E_r + (\eta dt)^2 \left(\frac{r_o}{r} A_{\theta_o} - A_\theta \right) \left(\frac{\partial A_\theta}{\partial r} + \frac{r_o}{r_k^2} A_{\theta_o} \right) \qquad (9)$$

and

$$z_{k+1} = 2z_k - z_{k-1} - \eta (dt)^2 E_z + (\eta dt)^2 \left(\frac{r_o}{r_k} A_{\theta_o} - A_\theta \right) \frac{\partial A_\theta}{\partial z} , \qquad (10)$$

where dt is the time increment, E_z and E_r are determined from the voltage matrix and A_θ can be expressed in terms of the magnetic field. It usually is not necessary to solve for $\dot{\theta}$.

The crossed-field equations can also be derived from equation (4) and are in difference form

$$\left(1 + \frac{z^2}{4}\right) x_{k+1} = 2x_k - \left(1 - \frac{z^2}{4}\right) x_{k-1} + z(y_k - y_{k-1}) - \left(E_x + \frac{z}{2} E_y\right)(dt)^2 \qquad (11)$$

and

$$\left(1 + \frac{z^2}{4}\right) y_{k+1} = 2y_k - \left(1 - \frac{z^2}{4}\right) y_{k-1} - z(x_k - x_{k-1}) - \left(E_x - \frac{z}{2} E_x\right)(dt)^2 , \qquad (12)$$

where $z = \eta B\, dt$.

For a relativistic, axially symmetric beam one can start with the Lagrangian,

$$L = eV - e(\overline{A} \cdot \overline{v}) - m_o c^2 \sqrt{1 - (v/c)^2} , \qquad (13)$$

from which the following trajectory equations can be derived:

$$r\theta = \eta \sqrt{1 - \beta^2} \left(A_\theta - \frac{r_o}{r} A_{\theta_o}\right) \quad , \tag{14}$$

$$\frac{d}{dt}\left(\frac{\dot{r}}{\sqrt{1 - \beta^2}}\right) - \eta z \left(\frac{\partial A_r}{\partial z} - \frac{\partial A_z}{\partial r}\right)$$

$$- \eta^2 \sqrt{1 - \beta^2} \left(\frac{r_o}{r} A_{\theta_o} - A_\theta\right)\left(\frac{r_o}{r^2} A_{\theta_o} + \frac{\partial A_\theta}{\partial r}\right) = 0 \quad , \tag{15}$$

and

$$\frac{d}{dt}\left(\frac{\dot{z}}{\sqrt{1 - \beta^2}}\right) - \eta \frac{\partial V}{\partial z} - \eta \dot{r} \left(\frac{\partial A_z}{\partial r} - \frac{\partial A_r}{\partial z}\right)$$

$$-\eta^2 \sqrt{1 - \beta^2} \left(\frac{r_o}{r} A_{\theta_o} - A_\theta\right) \frac{\partial A_\theta}{\partial z} = 0 \quad , \tag{16}$$

where $\beta^2 = (v/c)^2$, and

$$v^2 = \frac{\dot{r}^2 + \dot{z}^2 + \eta^2 \left(\frac{r_o}{r} A_{\theta_o} - A_\theta\right)^2}{1 + \frac{\eta^2}{c^2} \left(\frac{r_o}{r} A_{\theta_o} - A_\theta\right)^2} \quad . \tag{17}$$

c is the velocity of light, A_r and A_z are respectively the radial and axial components of the magnetic vector potential and the other terms are as defined above. The method for solving these equations is quite complex and will not be discussed completely here, however, some of the major points can be discussed.

Some of the terms are readily apparent such as

$$B_\theta = \frac{\partial A_r}{\partial z} - \frac{\partial A_z}{\partial r} \tag{18}$$

which can be determined from

$$B_\theta = \frac{\mu_o}{r} \int_0^r r J_z \, dr \quad , \tag{19}$$

where J_z is the axial component of the current density. A_θ is now somewhat more complex if the induced axial field is to be included. From the definition of A_θ one obtains

$$A_\theta = \frac{1}{r} \int_0^r r \, B_z(r) \, dr = \frac{r B_z(0)}{2} + \frac{1}{r} \int_0^r r b_z(r) \, dr \quad , \tag{20}$$

where $b_z(r)$ is the induced field and $B_z(0)$ is the axis value of the applied magnetic field, the axis value being assumed to extend radially to infinity since this is usually the only information available or easily obtainable experimentally. It can be shown that $b_z(r)$ for a nonrippling beam (no radial motion) can be expressed as

$$b_z(r) = \mu_o \int_r^{r_b} J_\theta(r) \, dr \quad ,$$

where r_b is the beam radius, μ_o is the magnetic permeability and J_θ the azimuthal component of the current density. It has not been possible to develop a more accurate expression, but the effects of this induced field seem to be quite small and may be negligible under most circumstances.

The induced fields are recomputed only when the beam advances forward one matrix square, since they are quite complex. All other terms, including magnetic and electric fields are computed for each increment of time dt.

The model used for the space-charge and trajectory calculations is shown in Figure 3. First the current density at each matrix point along the cathode is computed using the second matrix point in front of the cathode and Child's law. Then

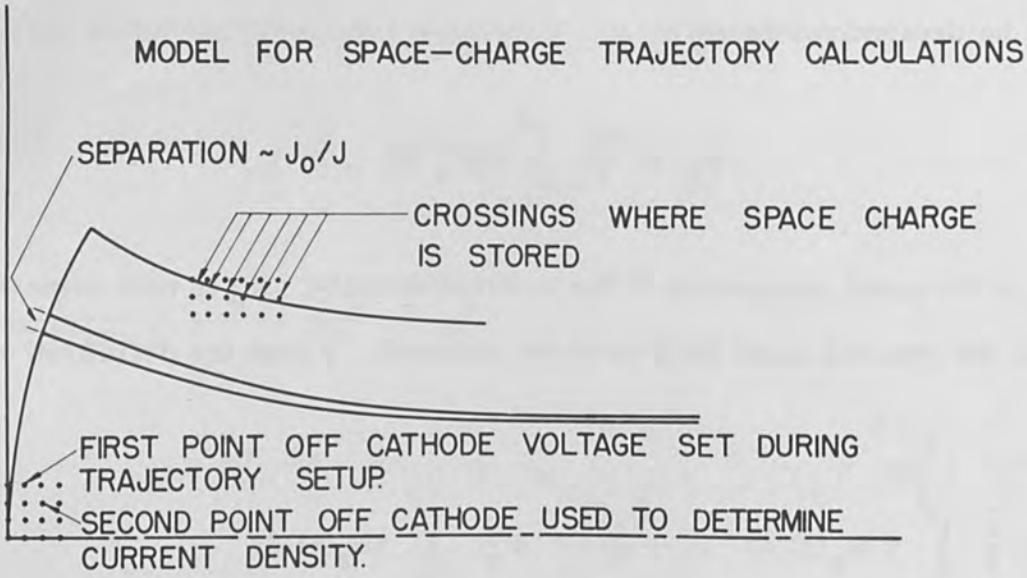

Figure 3 Model for space-charge and trajectory calculations.

the starting points of the trajectories are laid out along the cathode, their spacing being inversely proportional to the current densities at each point. Also, the voltages at the first matrix points in front of the cathode are set employing Child's law solved for the voltage and the current densities computed earlier. It would be difficult to compute these voltages during the field calculations since irregular distances to the cathode would be involved.

The trajectories are then calculated using the equations described above. For all the programs but the relativistic, the trajectories are computed serially, i.e., each trajectory is completed before the next is started. For the relativistic program the trajectories are computed in parallel since induced magnetic effects must be calculated as the beam progresses. It is the complexity of this parallel computation that makes the execution time for the relativistic program two to four times as long as the other programs.

Space charge is added to the space-charge matrix each time an electron crosses a horizontal or vertical line formed by the voltage matrix. Space charge is added to the adjacent matrix points between which the electron passes, the amount added to each point being inversely proportional to the distance of the trajectory from the

point.

Usually four or five voltage-trajectory cycles is sufficient to give a good idea of the gun performance, but two or three additional cycles are needed to obtain greater accuracy. An accuracy of five percent or better should be easily attained. Results obtained have been in generally good agreement with theory and experiment.

Results

Relativistic Program

The relativistic digital program, including induced and applied magnetic fields, is the most recently developed of the digital programs. Presented here will be a summary of relativistic effects on a high perveance electron gun.

Figure 4 shows representative trajectories through the gun at 65 kv. The microperveance (P_μ) for this voltage is 1.86 and the diameter at the beam minimum is 0.945 in scaled units. The cathode current density distribution is shown in the upper right of this figure. The trajectories shown are the outermost trajectory from the cathode, the outermost trajectory at the exit plane and two inner trajectories. The outer edge of the beam is also shown.

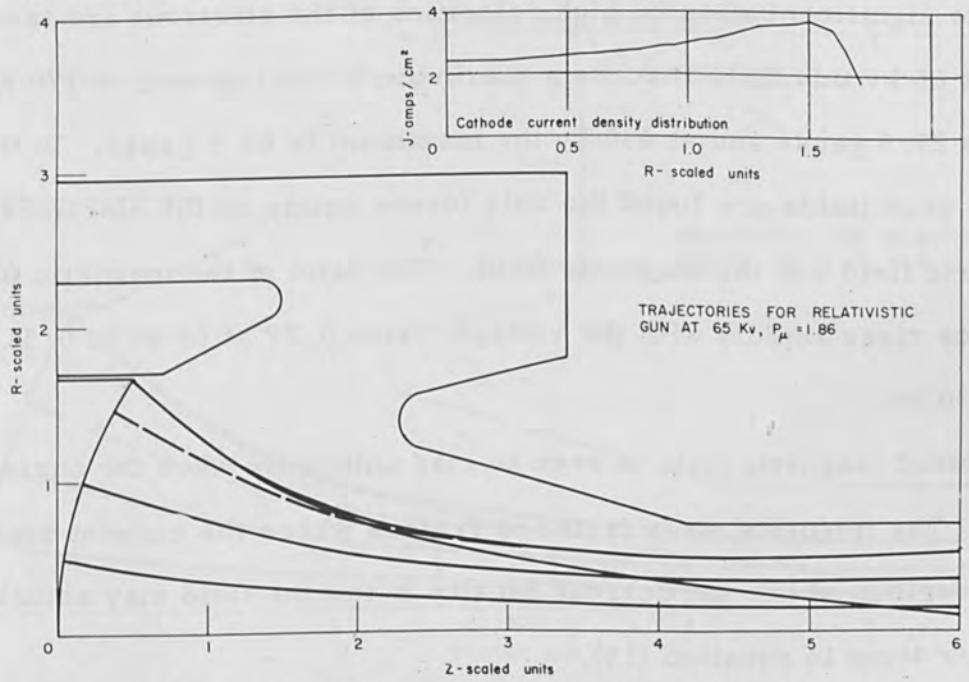

Figure 4 Microperveance 1.86 gun at 0.5 kv.

Figures 5 and 6 show the same trajectories for this gun at 170 and 430 kv. The scaling is changed to maintain approximately the same current density from the cathode. The microperveance is 1.83 at 170 kv and 1.80 at 430 kv. The beam diameter is 0.933 at 170 kv and 0.765 at 430 kv.

The perveance of the gun would be expected to decrease as the voltage is increased due to the relative slowing of the electrons caused by the relativity effect on the mass. The beam diameter on the other hand might be expected to grow from this same effect due to the relative increase in the space-charge density.

The reason for the reduced diameter is seen in Figures 7, 8 and 9 where the equipotentials, the induced B_θ field and the space-charge density distribution for the three conditions are shown. The equipotentials at 65 kv and 170 kv were very similar. The greater potential depression caused by the smaller beam at 430 kv is evident from comparison of these drawings.

The space-charge density distribution shows the beam to be basically uniform, although the density tends to be higher at the outer edge of the beams.

The induced magnetic fields while not large by ordinary focusing field standards become quite significant when the high velocities of the electrons are taken into account. At 65 kv this field reaches a maximum of 13.1 gauss, at 170 kv the maximum is 27.5 gauss and at 430 kv the maximum is 65.5 gauss. In the region where these peak fields are found the only forces acting on the electrons are the radial electric field and the magnetic field. The ratio of the magnetic force to the electric force rises rapidly with the voltage, from 0.29 at 65 kv to 0.31 at 170 kv to 0.71 at 430 kv.

The induced magnetic field is seen to rise uniformly when the current density is uniform. The intensity rises faster in regions where the current density is higher. In regions where the current density is low the field may actually decrease due to the 1/r term in equation (19).

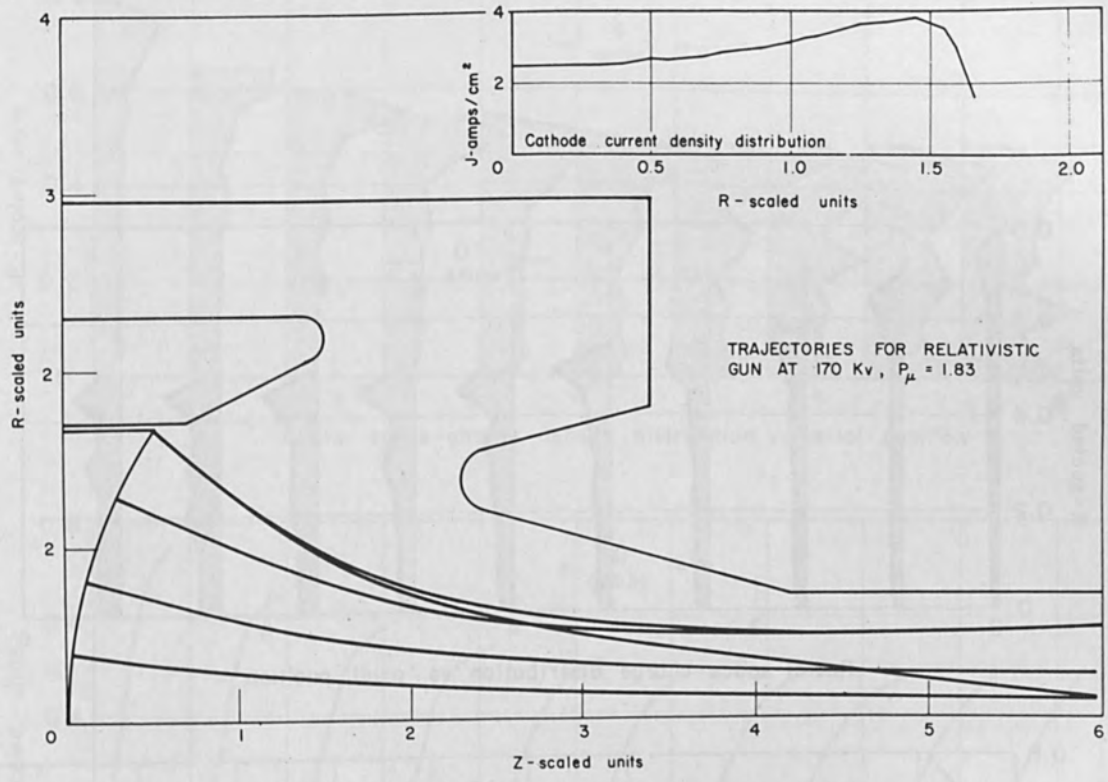

Figure 5 Microperveance 1.83 gun at 170 kv.

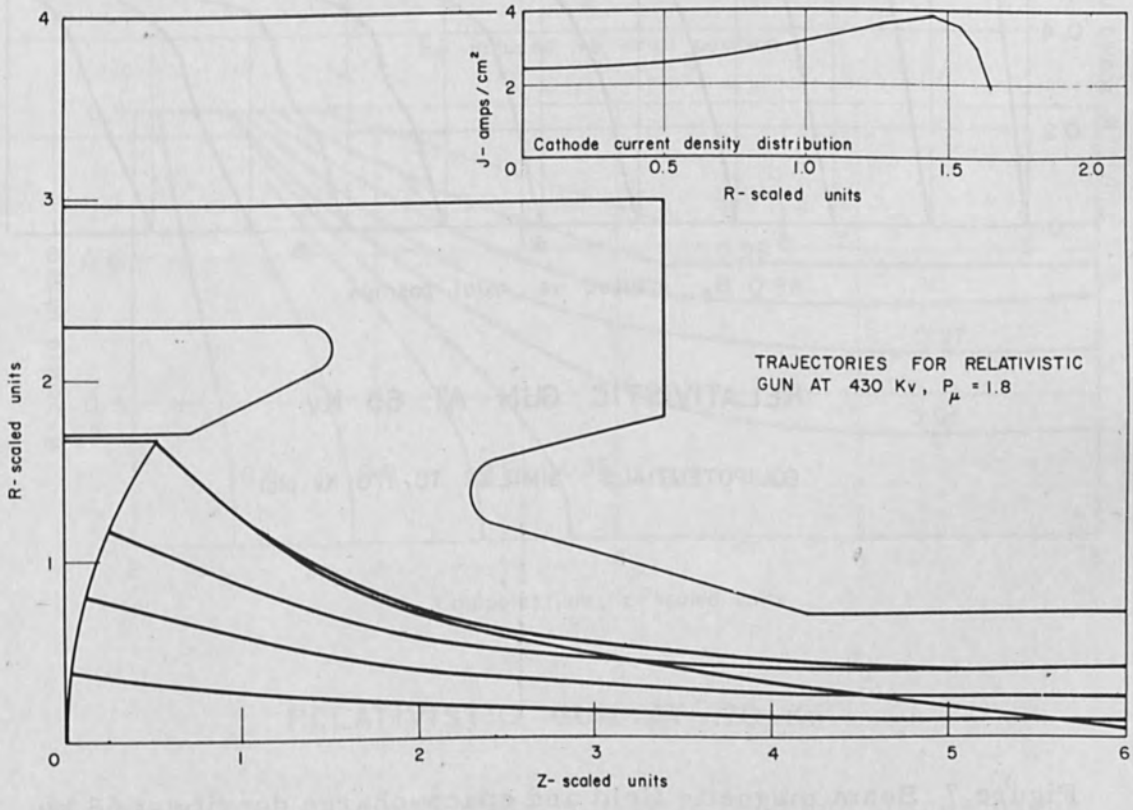

Figure 6 Microperveance 1.80 gun at 430 kv.

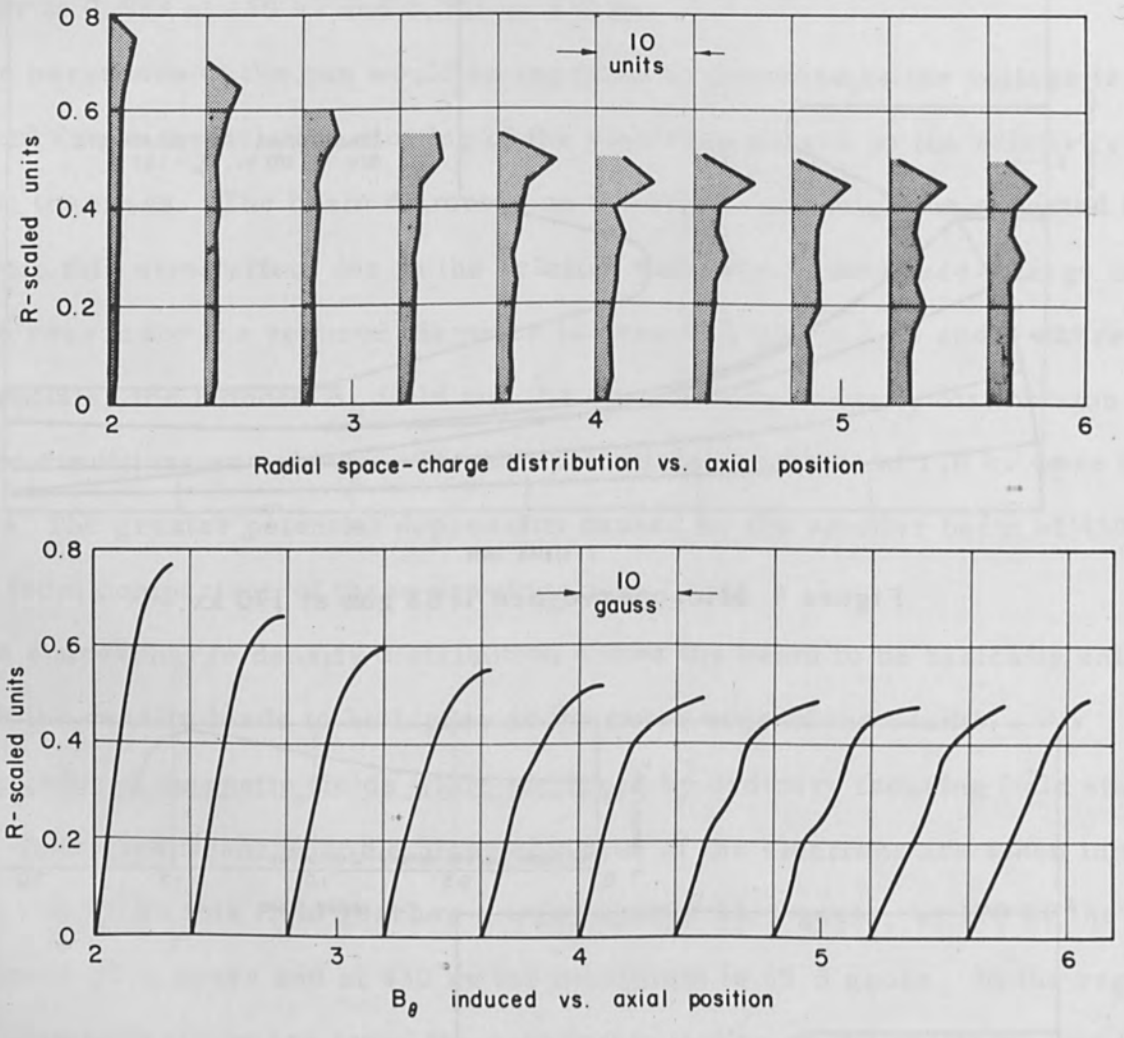

RELATIVISTIC GUN AT 65 Kv

EQUIPOTENTIALS SIMILAR TO 170 Kv plot.

Figure 7 Beam magnetic field and space-charge density at 65 kv.

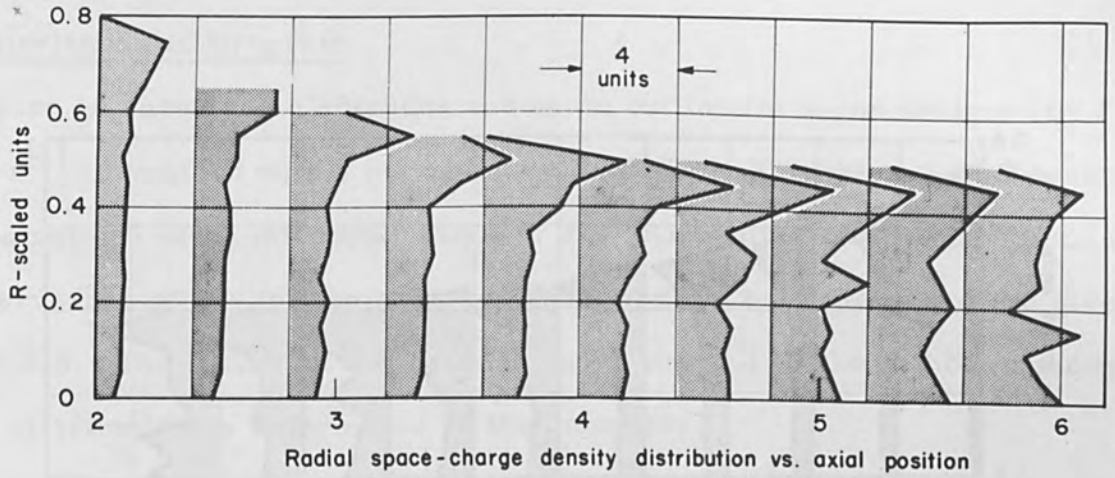

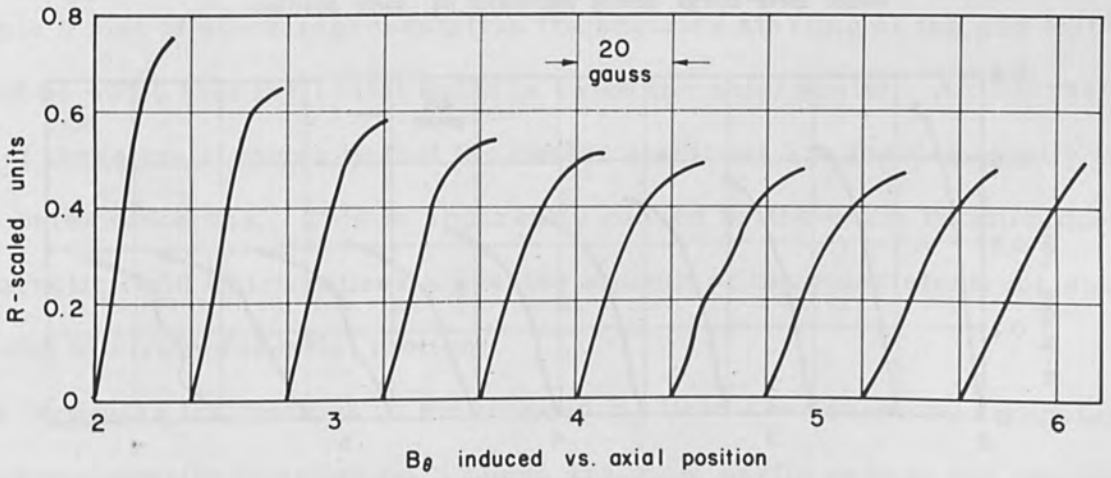

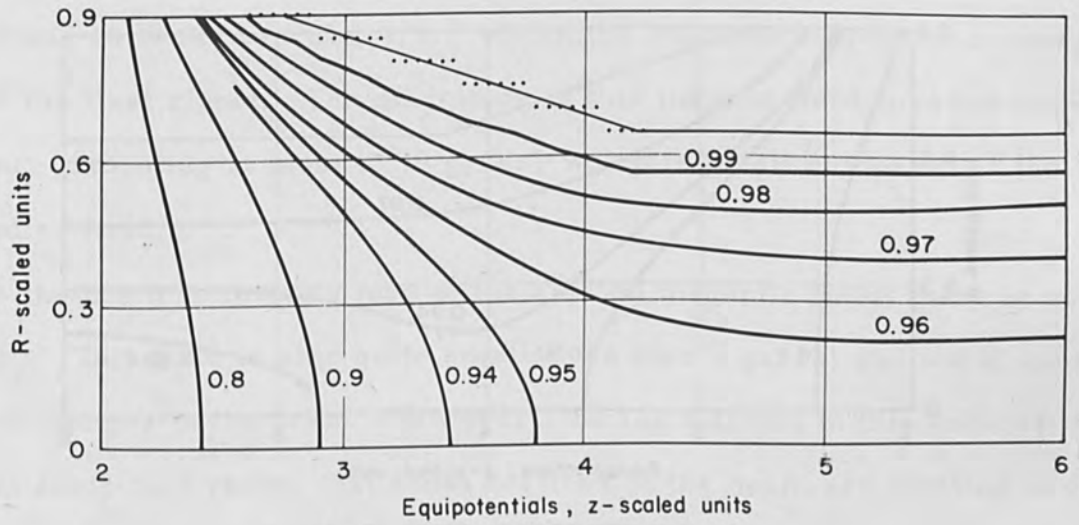

RELATIVISTIC GUN AT 170 Kv

Figure 8 Beam equipotentials, magnetic field and space-charge density at 170 kv.

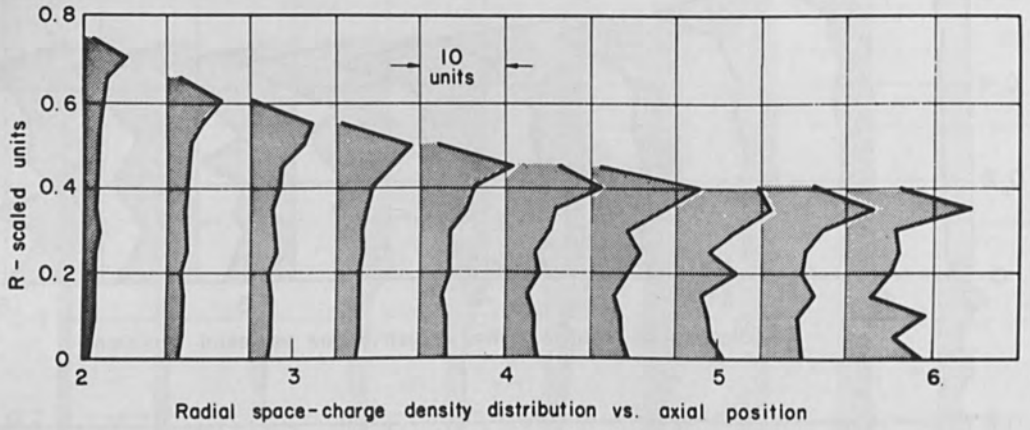

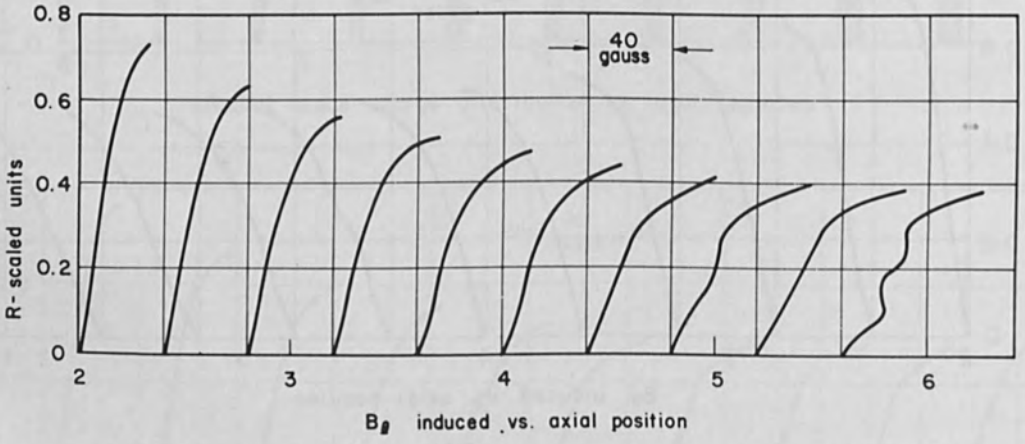

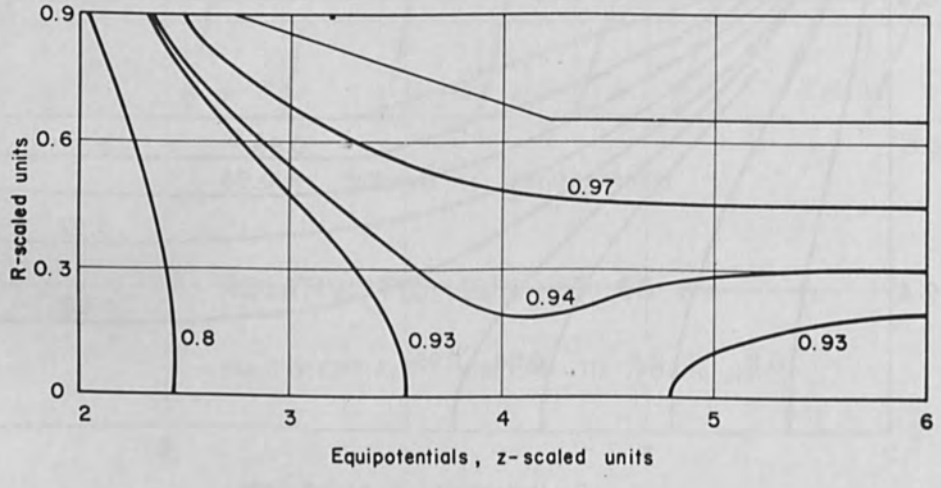

RELATIVISTIC GUN AT 430 Kv

Figure 9 Beam equipotentials, magnetic field and space-charge density at 430 kv.

Nonrelativistic Program

Figure 10 shows the electrodes and beam outline for a gun designed by Frost and Purl[1] combined with a magnetic field added by Kikushima and Johnson.[2] The original gun had a microperveance of 2.2, Kikushima and Johnson obtained a microperveance of 2.4 for the scaled version and the computer program gives a value of 2.5. The outline of the beam is shown as well as the cathode current density distribution as determined by the computer.

Some of the beam details are shown in Figure 11. The bottom section of this drawing is a plot of some representative trajectories starting at the gun exit plane (it should be noted that the radial scale is twice the axial scale). An interesting feature of these trajectories is that the center electrons are moving axially faster than the outer electrons. This is apparently caused by the beam rotation due to the axial magnetic field which causes a greater amount of the outer electrons energy to be involved in circumferential motion.

The irregular fluctuations in the induced B_θ field are caused by irregularities in the current density distribution. These are most easily seen in the region between 7 and 10 of the z-scale, i.e., where the trajectories tend to converge at the end of the first ripple. The magnitude of this induced field does not appear to be significant, amounting at most to 10 gauss, which is small compared to the 7500 gauss applied field.

Since the beam is rotating (due to the applied magnetic field) there is now an induced B_z. This field is also quite small (less than 2 gauss) and would cause no significant changes in the beam. However, the fluctuations in this induced field are significant since they reveal that some sections of the beam are rotating in opposite directions about the axis.

From the cathode out to z = 5 the beam converges faster than the magnetic field, inducing a positive B_z. Just beyond z = 5 the beam starts expanding in its

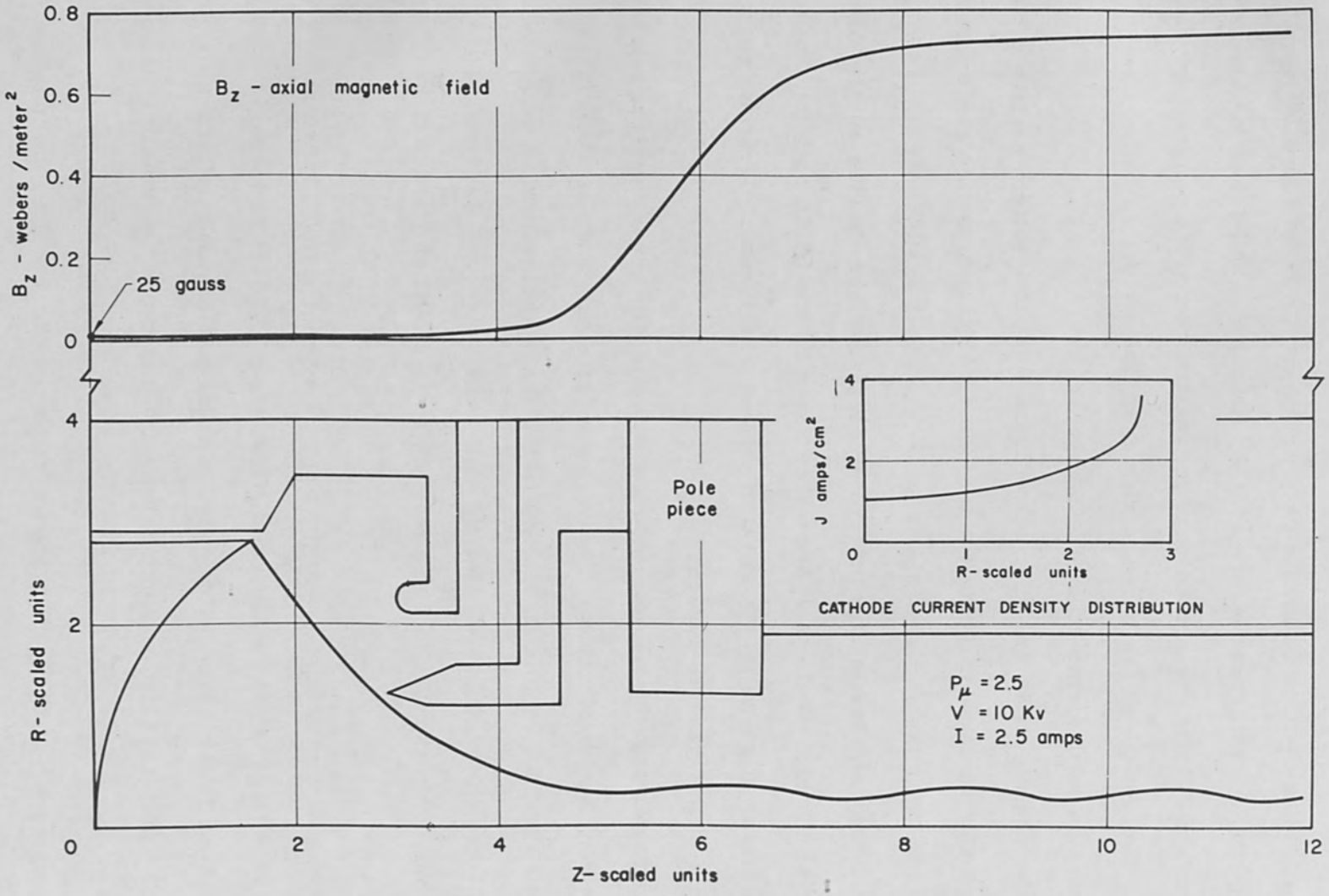

Figure 10 High convergence electron gun in a converging magnetic field.

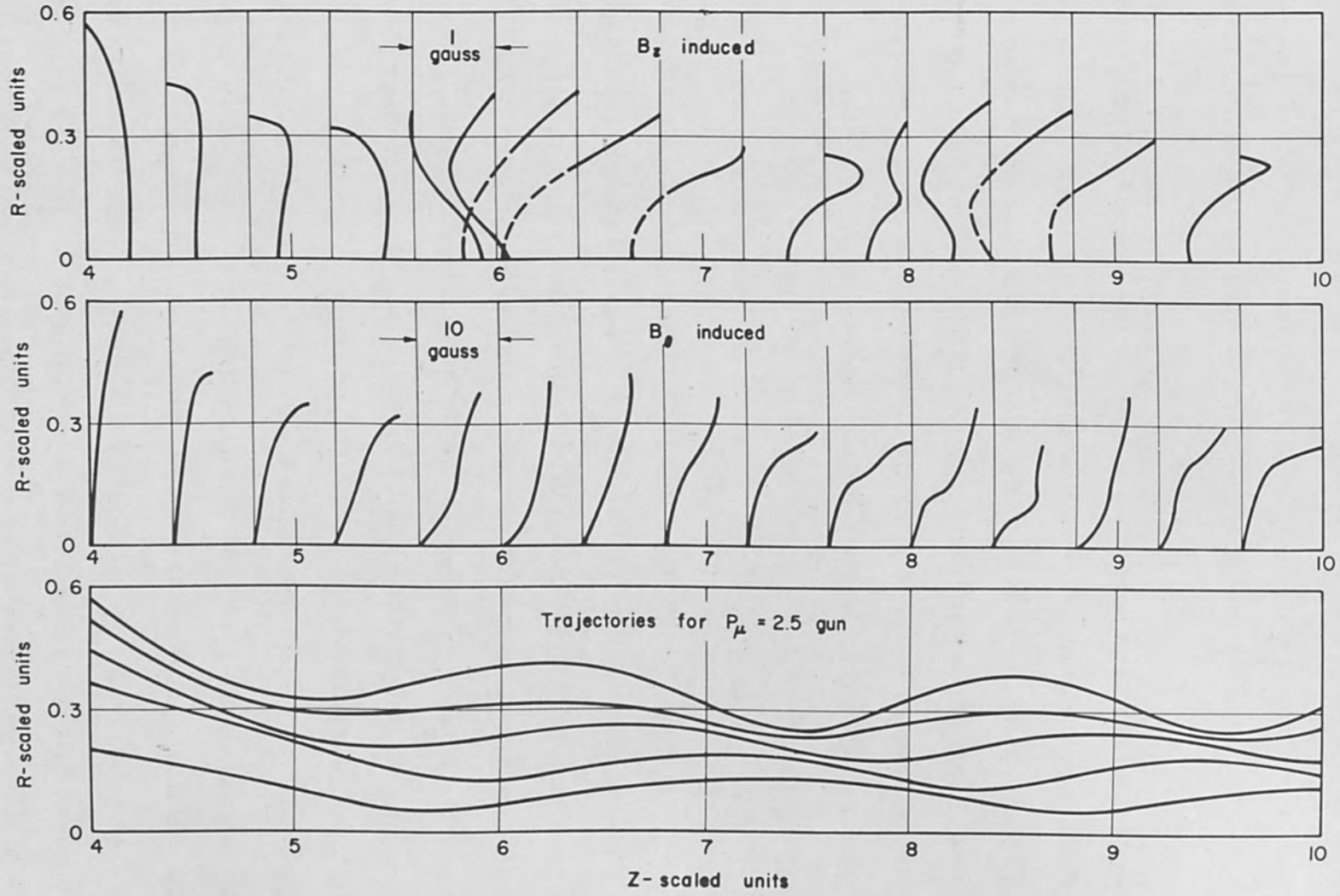

Figure 11 Beam trajectories and induced magnetic fields for high convergence gun.

first ripple while the magnetic field continues to rise so that the electrons move outside to a negative flux linkage. When the magnetic flux within the trajectory becomes greater than the original flux linkage the direction of rotation about the axis reverses (see equation (6))and as a result the induced axial magnetic field reverses.

This reversed field is seen between 5.6 and 7 on the z-scale. For z between 7 and 8, where the outer electrons are converging while the inner electrons are still diverging, the induced B_z is seen to go from negative to positive as one travels out radially from the center of the beam. This requires the inner and outer electrons to be rotating about the axis in opposite directions. How these counterrotating segments would interact is not clear from these results since direct interactions between electrons are not considered by the digital program.

Grid Effects

A modified version of the electrostatically focused, solid-beam program was developed to examine some of the detailed effects of a grid on beam focusing. This program has been employed in the analysis of the structure shown in Figure 12. This structure consists of a round flat cathode, a flat collector and a "Pierce" electrode around the cathode. The grid consists of six rings as shown. Near the axis the innermost grid ring forms a tight loop while the outermost rings simulate essentially straight, parallel wires.

Figure 13 shows the trajectories when the grid is at +1.0 volt and the collector at +100 volts. Between each grid wire there is complete crossing of the trajectories with the ultimate spreading as shown. The actual percentage of current intercepted by the grid is quite small due to the deflecting of the trajectories and is considerably less than the shadow fraction for the grid.

The trajectories with the grid at +5 and +10 volts are shown in Figures 14 and 15. At five volts the trajectories are focused about halfway to the collector and are

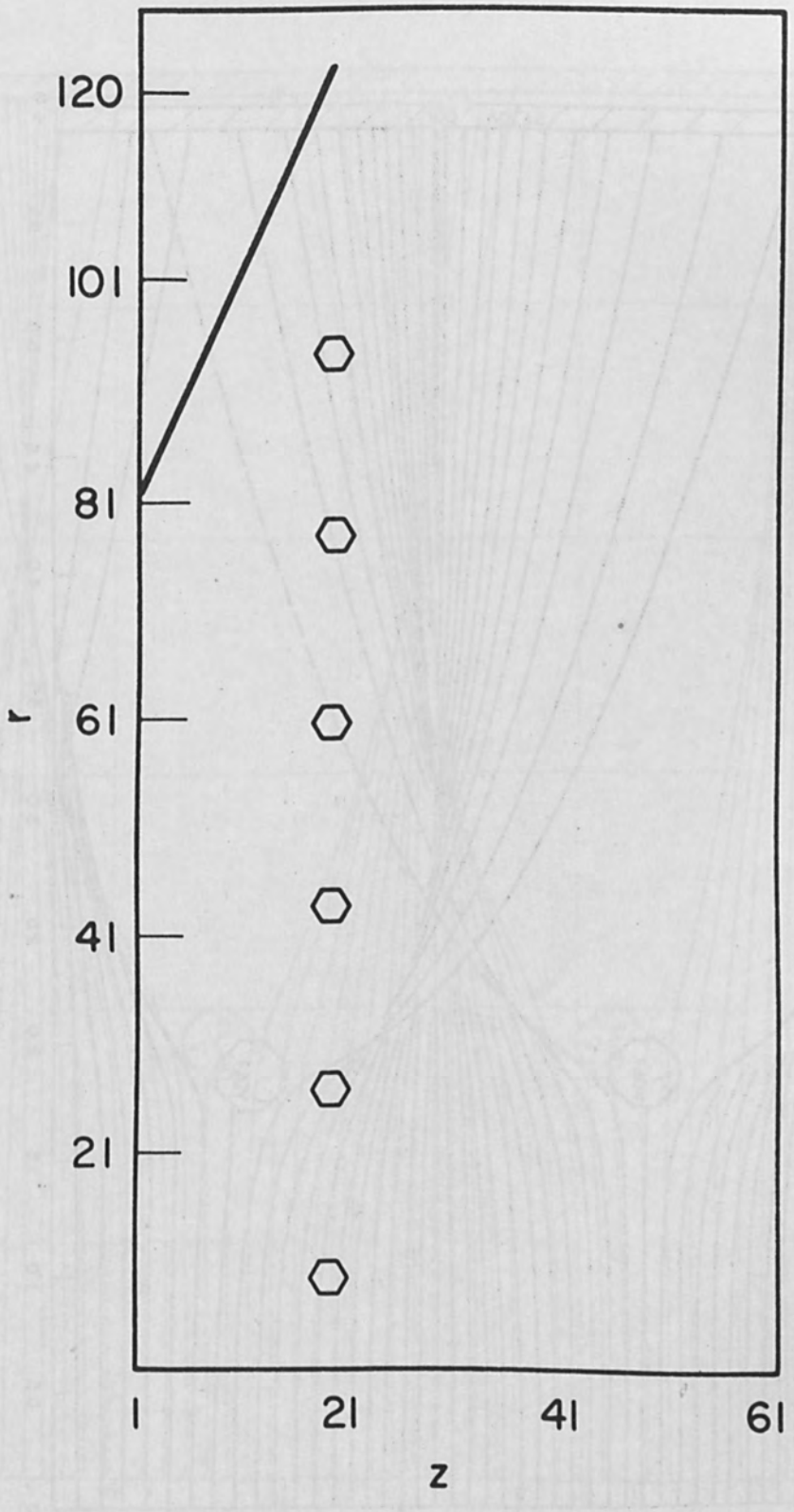

Figure 12 Grid program test geometry.

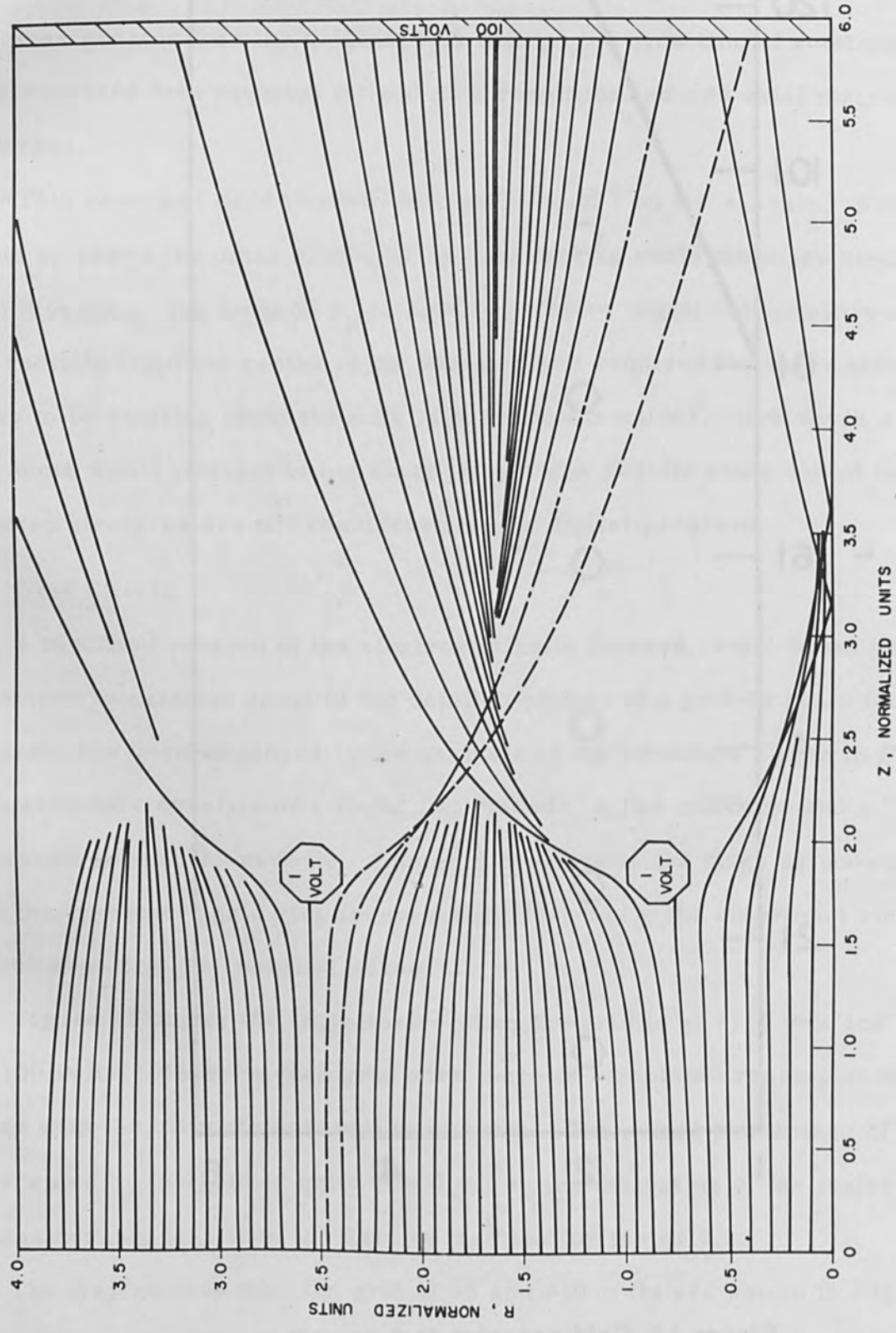

Figure 13 Trajectories through grid at +1.0 volt.

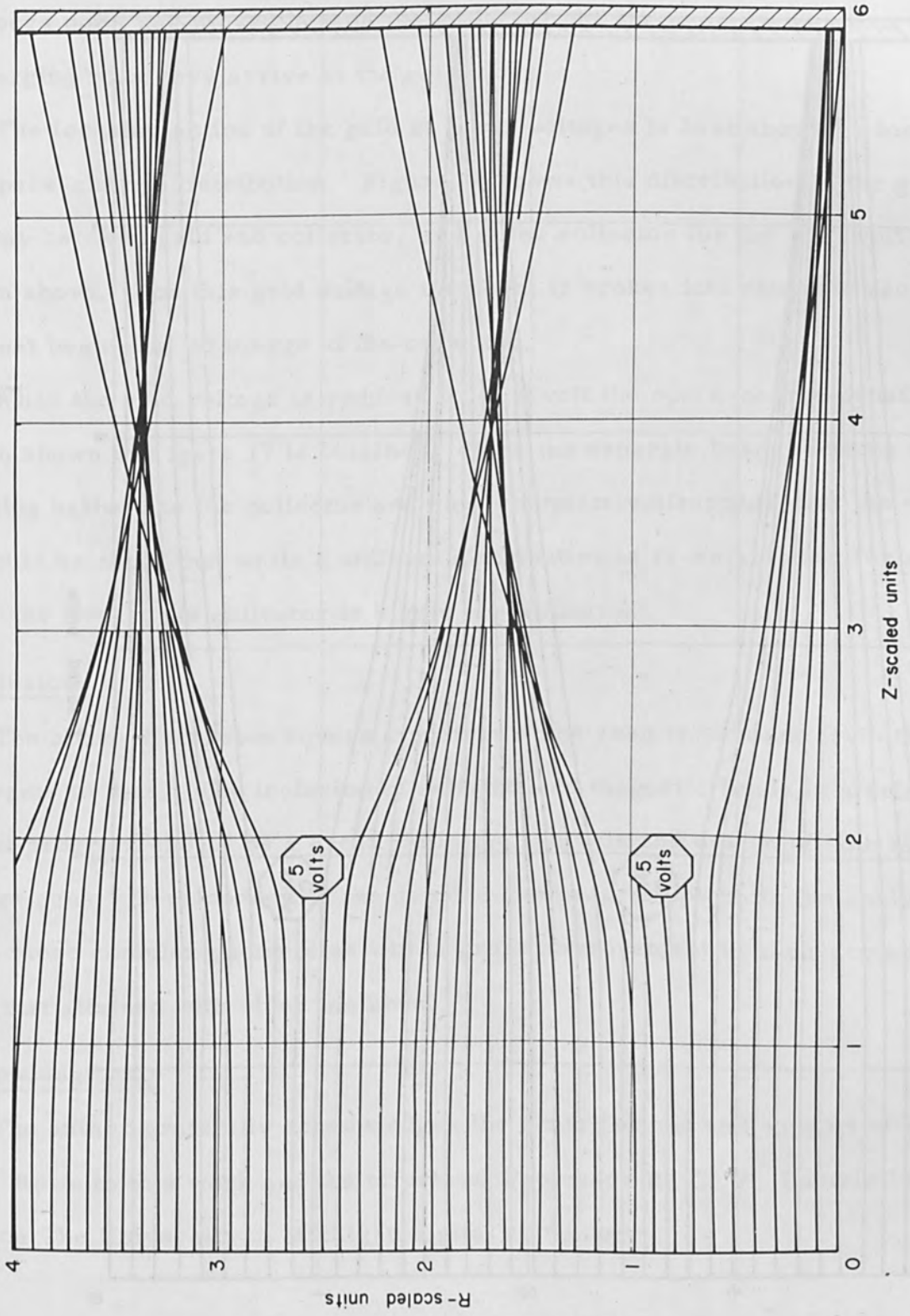

Figure 14 Trajectories through grid at +5 volts.

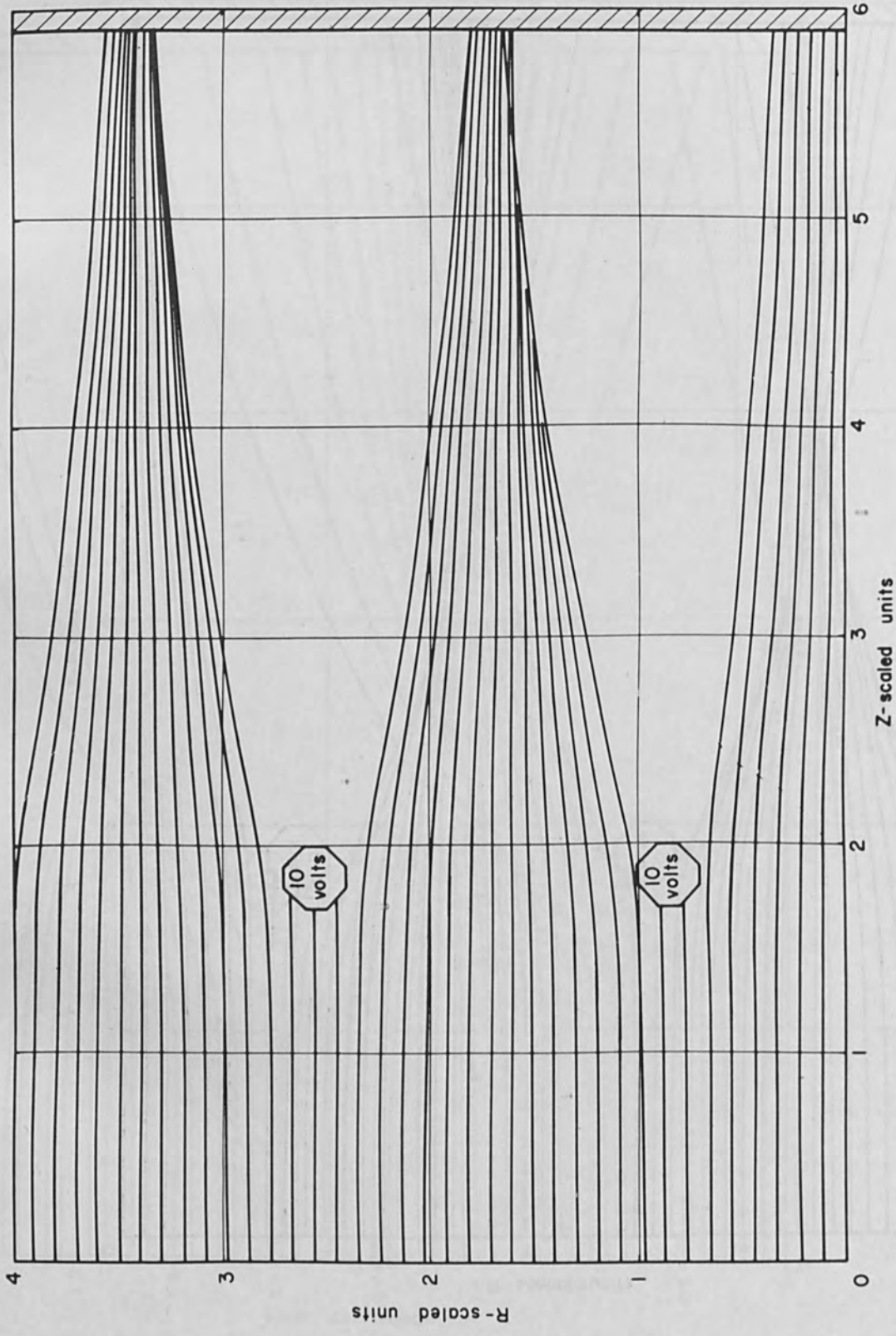

Figure 15 Trajectories through grid at +10 volts.

beginning to spread at the collector but still form separate beams. For ten volts the focus point has moved beyond the collector and the separate sections are still converging when they arrive at the collector.

The focusing action of the grid at lower voltages is best shown by looking at the space-charge distribution. Figure 16 shows this distribution in the grid plane, halfway between grid and collector, and at the collector for the +1.0 volt case shown above. For this grid voltage the beam is broken into separate sections which are just beginning to merge at the collector.

When the grid voltage is reduced to -1.0 volt the space-charge density distribution shown in Figure 17 is obtained. Here the separate beam sections are merging halfway to the collector and have completely disappeared at the collector. It should be noted that while a uniform distribution is re-established for a negative grid, the flow at the collector is highly nonlaminar.

Conclusions

The above discussion covers a portion of the results obtained from the digital programs to date. The inclusion of self-induced magnetic fields in a relativistic digital program should be a great aid in the analysis and design of both high and low voltage guns. Development of the gridded gun program permits the analysis of much more complex geometries with a great improvement in accuracy and detail over that attained with older methods.

Acknowledgments

The author gratefully acknowledges the contributions and support of Professor J. E. Rowe to this work and the efforts of Professor R. C. F. Bartels in providing time on The University of Michigan digital computer.

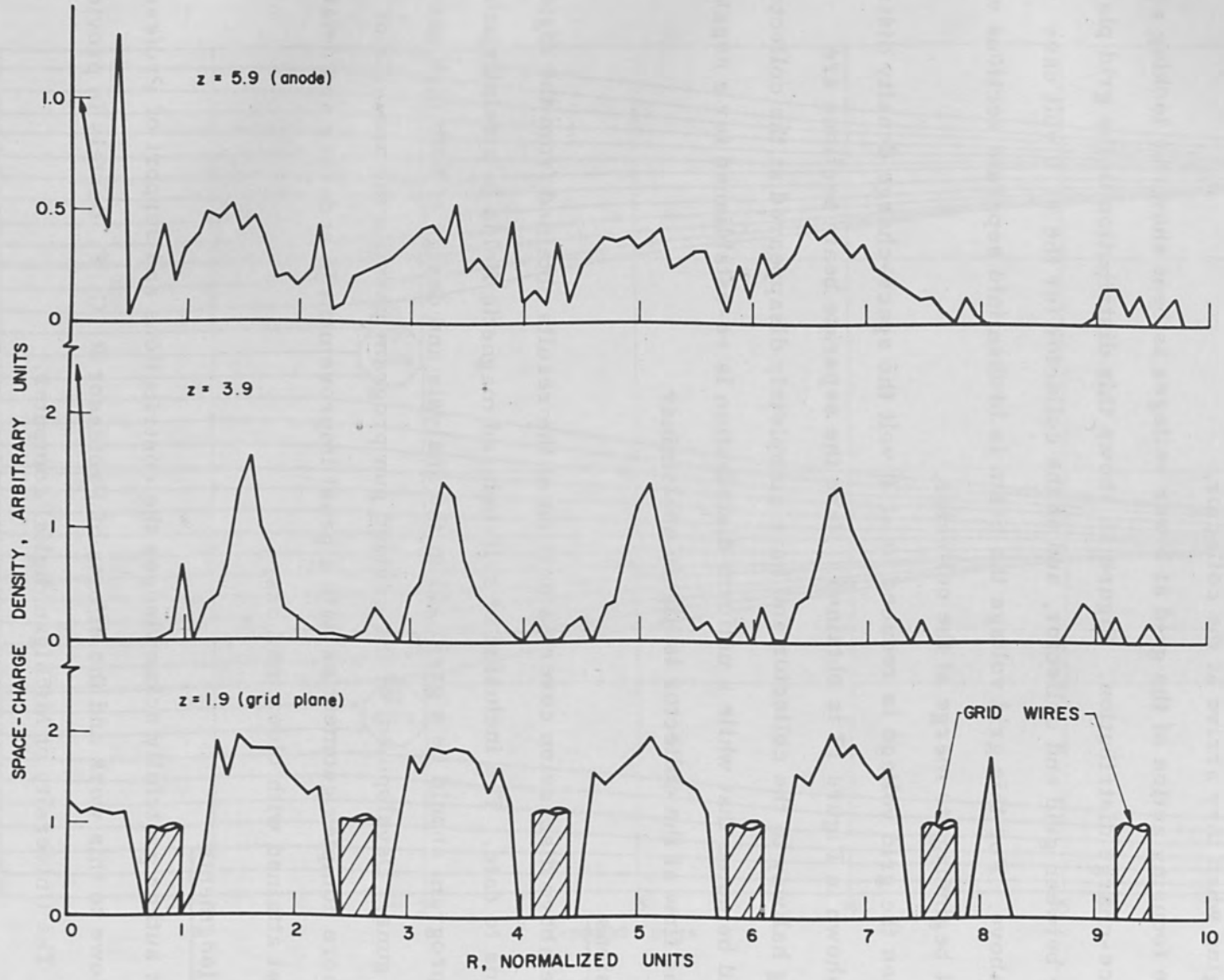

Figure 16 Space-charge density distribution for +1.0 volt on grid.

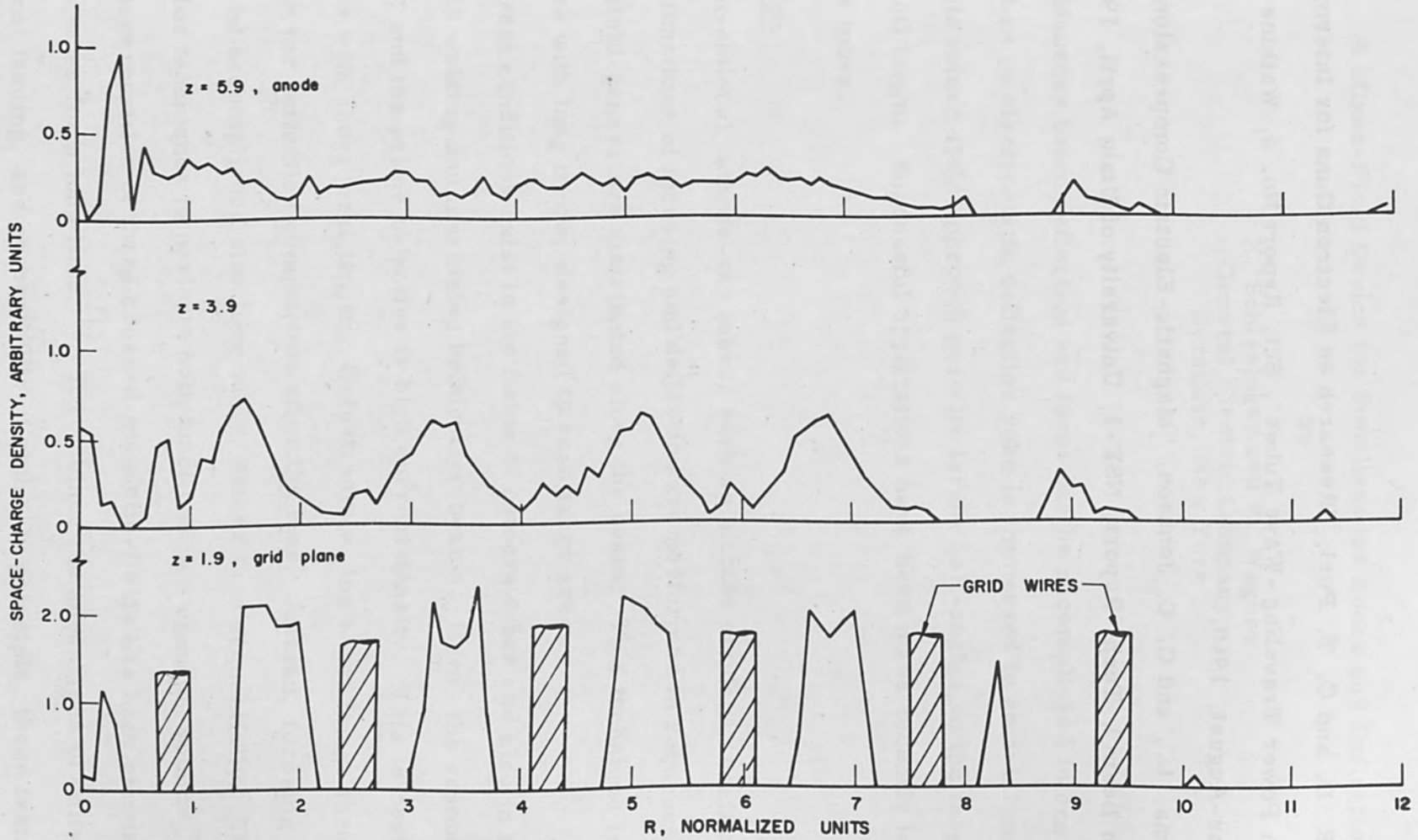

Figure 17 Space-charge density distribution for -1.0 volt on grid.

using this approach are only recently beginning to appear.[2, 3]

If reversibility of the electron path is not required, simultaneous focus and deflection can be realized by a combination of magnetic and electrostatic fields.[4] In this mixed-field category, one approach is particularly attractive. It uses an axial magnetic field for focus and a coaxial deflection-cylinder for scanning. This combination performs in one cylindrical cavity the functions of a "scanning lens", i.e., a lens of short focal length, moving in a plane parallel to target. On this basis, the term "Focus Projection and Scanning", or FPS, suggests itself as a reference for this technique.

Theory of FPS

Since FPS is the combination of an imaging device and a scanner, an analysis of it must account for both aspects of device performance. First, consider the deflection of a filamentary beam.

Beam Deflection Characteristics

Figure 1 shows a cut through a typical FPS system. It starts with an object aperture A, illuminated by a prefocusing gun (a Pierce gun is shown as an example). A beam through A with half-angle α traverses an object drift space a before entering into the FPS cavity ℓ. The latter is bounded by the deflection D and its surrounding focus coil F. For purposes of analysis, F and D are assumed to have equal length. With proper adjustment of voltage V and field B, the cavity can focus an image of A on the screen S within the image distance b.

Figure 1b is a view through the faceplate, looking toward the cathode (-z direction). It is assumed that the magnetic field B points in the direction of flow and that the electric field $\overline{E}$ is uniform in the y direction. (This is no limitation of generality.) The equations of motion then read:

$$\ddot{y} = \eta [E + \dot{x} \overline{B}]$$

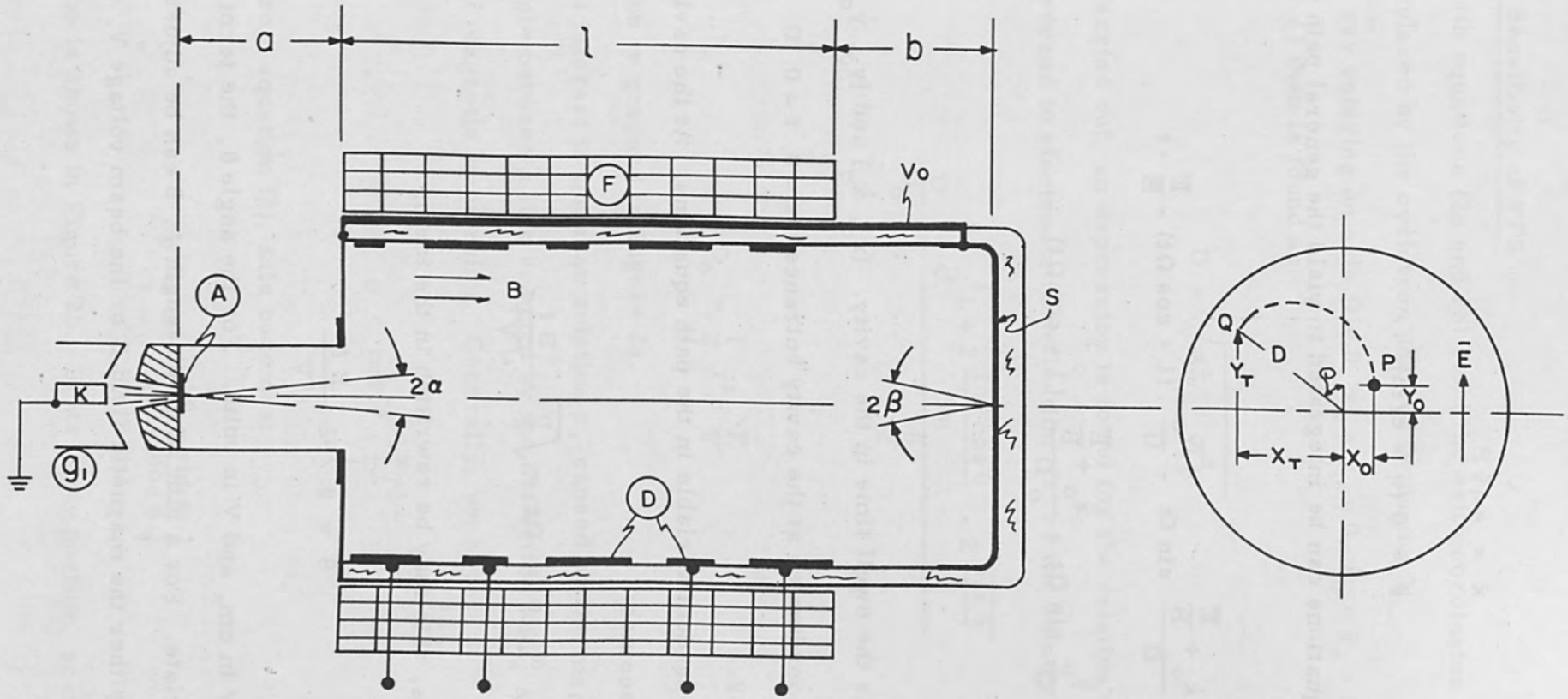

1a. SIDE VIEW

1b. FRONT VIEW

FIGURE 1 TYPICAL F P S SYSTEM

$$\ddot{x} = -\eta \dot{y} B \tag{1}$$

$$\ddot{z} = 0 \quad (\eta = e/m)$$

These simultaneous equations can be integrated to yield the general path equation (2):

$$x = x_o + \frac{\dot{x}_o + \frac{\overline{E}}{B}}{\Omega} \sin \Omega t - \frac{\dot{y}_o}{\Omega} (1 - \cos \Omega t) - \frac{\overline{E}}{B} \cdot t \tag{2a}$$

$$y = y_o + \frac{\dot{y}_o}{\Omega} \sin \Omega t + \frac{\dot{x}_o + \frac{\overline{E}}{B}}{\Omega} (1 - \cos \Omega t) \tag{2b}$$

$$z = \ell \cdot \frac{t}{T} \tag{2c}$$

Here, $T = \frac{\ell}{\sqrt{2\eta V}}$ is the dwell time in the cavity. $(x_o, \dot{x}_o)$ and $(y_o, \dot{y}_o)$ are the position and velocity coordinates at the cavity entrance: $z = 0$, $t = 0$. $\Omega = \eta B$ is the cyclotron frequency.

Ωt is the only independent variable in the path equations. At the cavity output (flight time T), this becomes:

$$\theta = \Omega t = \sqrt{\frac{\eta}{2}} \cdot \frac{B \ell}{\sqrt{V}} \quad . \tag{3a}$$

For practical purposes, this may be rewritten in the form:

$$\theta = 0.292 \frac{B \ell}{\sqrt{V}} \tag{3b}$$

where B is in gauss, ℓ in cm, and V in volts. For the angle θ, the term "cyclotron-phase" seems appropriate. For a tube of given length ℓ, θ can be adjusted experimentally by changing either the magnetic field B or the beam voltage V, or both.

Deflection Sensitivity of FPS

The path equations (2a and 2b) yield the exit coordinates x_T and y_T, respectively, if Ωt is replaced by the cyclotron phase θ (equation 3).

For a ray entering on axis ($t = 0$, $x_o = y_o = 0$, $\dot{x}_o = \dot{y}_o = 0$), deflection at exit ($t = T$, $z = \ell$) then is found as:

$$D = \sqrt{x_T^2 + y_T^2}$$

If this is carried out, an expression is found for the relative deflection sensitivity of FPS, referenced to electrostatic deflection D_o by the same cavity:

$$\frac{D}{D_o} = \frac{\sqrt{1 + 2\,\frac{1 - \cos\theta}{\theta} - 2\,\frac{\sin\theta}{\theta}}}{\frac{\theta}{2}} \qquad (4)$$

where:

$$D_o = \frac{1}{4}\,\ell^2 \cdot \frac{\overline{E}}{V} \qquad (4a)$$

This function is graphed in Figure 2a.

Also of interest is the scan rotation ρ, caused by the magnetic field in FPS. ρ is the angle between a line scanned by the deflection with, and without, the presence of magnetic immersion. Generally, we have:

$$\rho = \tan^{-1}\left(\frac{x_T}{y_T}\right)$$

With data from equation (2), this becomes:

$$\rho = \tan^{-1}\left(\frac{\theta - \sin\theta}{1 - \cos\theta}\right) \qquad (5)$$

This function is shown in Figure 2b. In its early portion, scan-rotation is closely

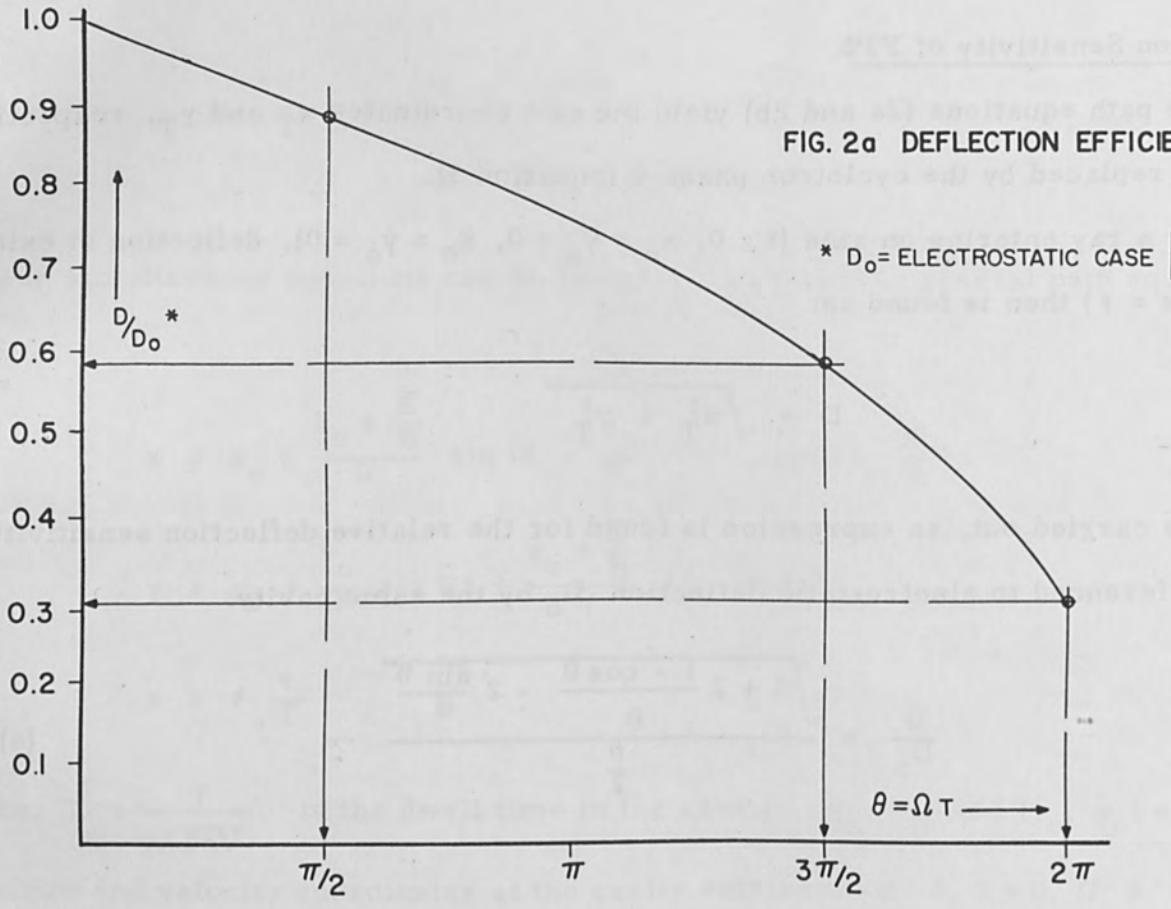

FIG. 2a DEFLECTION EFFICIENCY

* D_o = ELECTROSTATIC CASE [B=0]

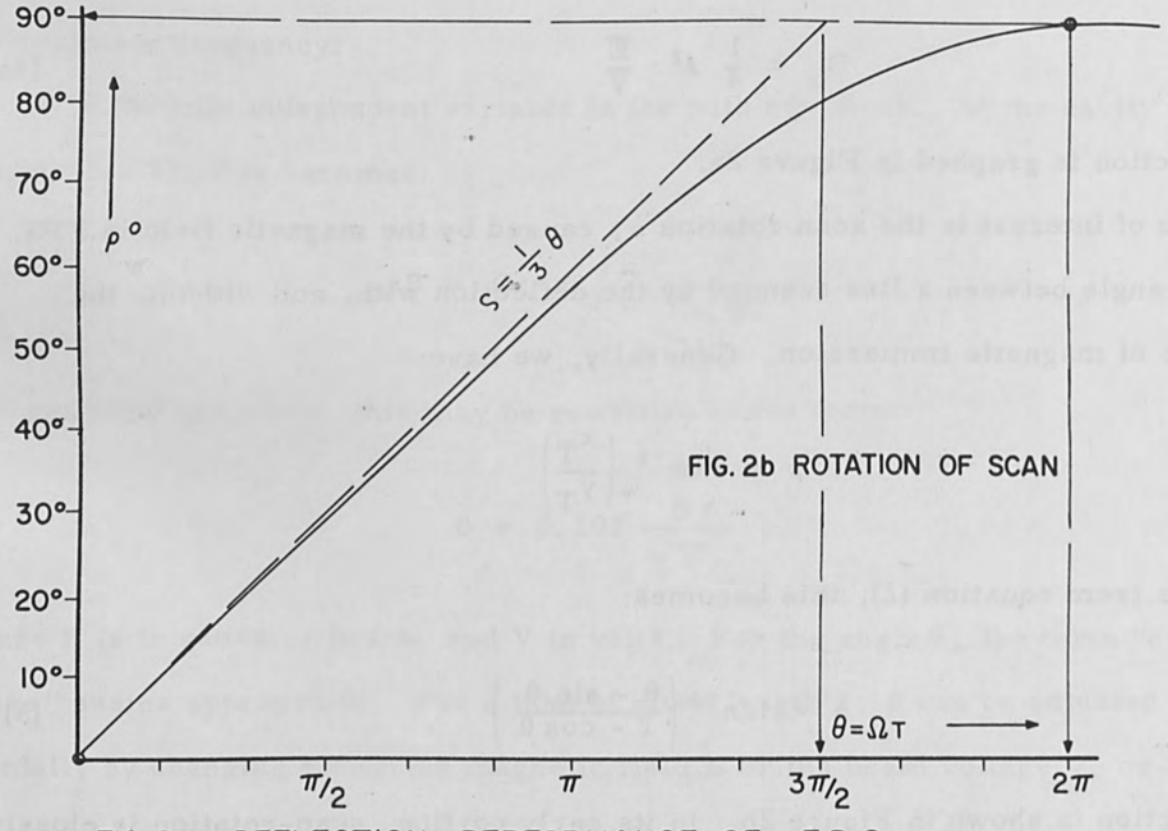

FIG. 2b ROTATION OF SCAN

FIG. 2 DEFLECTION PERFORMANCE OF F P S

approximated by the proportionality:

$$\rho = \frac{1}{3} \cdot \theta \tag{5a}$$

This sets scan-rotation apart from image rotation by the same lens, which is given by:[5]

$$\Phi_c = \frac{1}{2} \cdot \theta \tag{6}$$

While the two angles are never identical, the axes of scan can always be lined up with the coordinates of an image simply by rotating the tube.

Evaluation of Figure 2 is helped by noting that the spring-constant c of a magnetic lens increases with the square of θ:

$$c = \frac{1}{2} \frac{V}{\ell^2} \cdot \theta^2 \tag{7}$$

Hence, the abscissa in Figure 2 defines devices ranging from "weak focusing" (θ in the first and second quadrant) to "strong focusing" (θ in the third and fourth quadrant).

With this in mind, Figure 2 implies that there are roughly two modes to operate FPS:

A. a weak-focusing mode where rotator-action predominates $(0 < \theta < \pi)$

B. a strong-focusing mode where scan-rotation is practically constant $(\pi < \theta < 2\pi)$

In mode A, deflection efficiency is high (>60 per cent); but, in mode B, it drops ultimately to a rather low value (31.8 per cent for $\theta = 2\pi$). Between these two extremes, there is a transition region, with θ in the third quadrant, where deflectability and focusing power both are adequate for most practical applications.

Focusing Aspects of FPS

In an FPS system, the solenoid serves the dual function of:

1. providing magnetic immersion for the deflection.

2. focusing the object aperture on target.

If the FPS-field coil is the only electron lens in the system, then the focusing condition uniquely determines the cyclotron-phase θ occurring in the FPS cavity. This can be shown by Electron Trigonometry[6] in its formulation for magnetic systems. Here, focusing is defined by the following expression:

$$\frac{\theta}{2} + \tan^{-1}\left(\frac{a}{\ell}\cdot\frac{\theta}{2}\right) + \tan^{-1}\left(\frac{b}{\ell}\cdot\frac{\theta}{2}\right) = \pi \qquad (8)$$

This yields θ for any set of object-distance a, image-distance b, and length of cavity ℓ. The system magnification then follows from equation (9):

$$M = \sqrt{\frac{1+\left(\frac{b}{\ell}\cdot\frac{\theta}{2}\right)^2}{1+\left(\frac{a}{\ell}\cdot\frac{\theta}{2}\right)^2}} \qquad (9)$$

For a = b, M is unity for any value of θ; but, for a > b, the system becomes demagnifying, especially for large values of θ. This feature is valuable for the design of high-resolution devices.

Current-Density Gain

FPS is a long-lens device. As such, it has an inherent advantage over a sequential thin-lens system of the same length; it can deliver higher current densities at target. This is illustrated by Figure 3, which shows three non-accelerating gun structures. All have identical image- and object-distances but different lengths of the FPS cavity. The solid lines show the beam profile with FPS, while the dotted lines come straight from a thin Einzel lens assumed to be located at the cavity entrance. Since the half-angle at target is larger with FPS than with the Einzel lens, there should be a potential gain in beam-intensity as given by the law of Helmholtz-Lagrange:

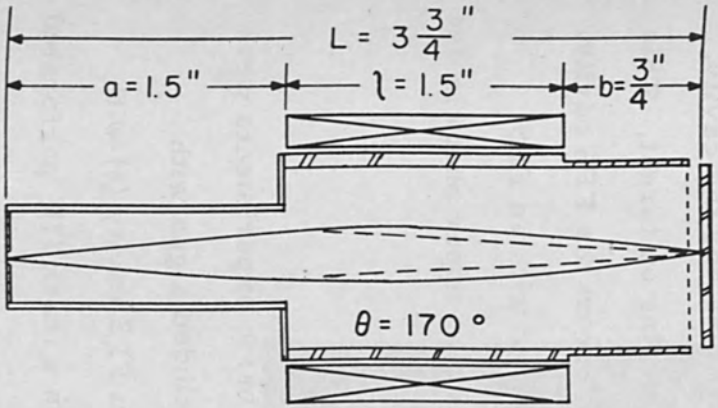

$M_F = 0.70$, $M_E = 1.5$

$G_j = 4.6$

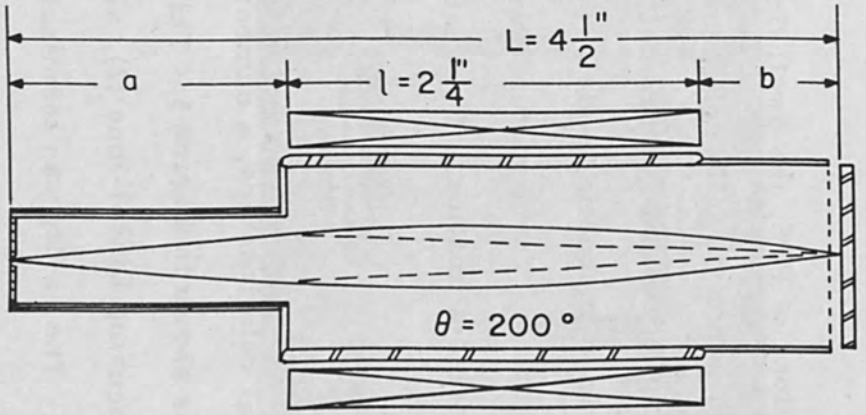

$M_F = 0.75$, $M_E = 2$

$G_j = 7.0$

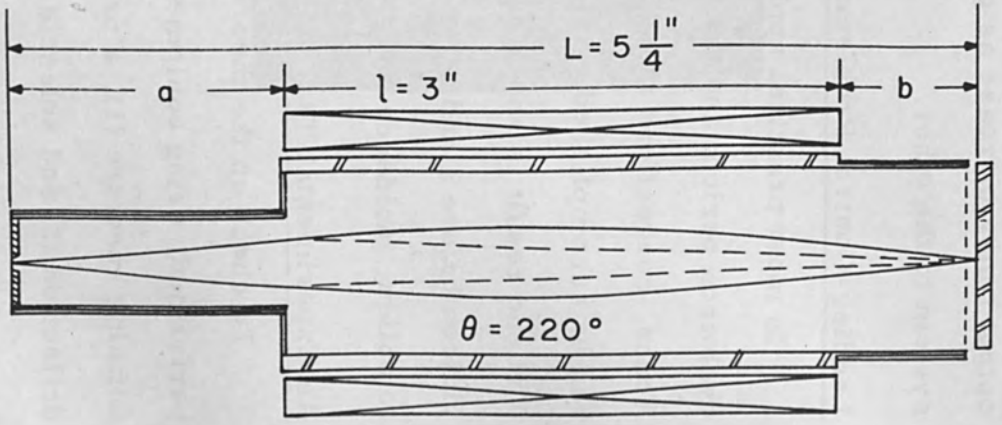

$M_F = 0.80$, $M_E = 2.5$

$G_j = 9.7$

FIG. 3 ANALYSIS OF THREE FPS GUNS

$$g_j = \left(\frac{M_E}{M_F} \right)^2 \qquad (10)$$

where M_E and M_F are the respective values of magnification for the two systems compared. M_E is simply the distance-ratio $(\ell + b)/a$.

Results of the analysis are presented at the margin of Figure 3. It is found that the beam-intensity gains g_j are considerable, especially for long cavities. Since the meaning of g_j includes a gain in "band-merit", i. e., the product $I \cdot N^2$, signal output I may increase as g_j and resolution N by $(\sqrt{g_j})$, in the transition from one system to the other.

Landing-Control Problems

In most practical applications of FPS, the dwell time is shorter than one cyclotron period; and the beam is not yet fully collimated when leaving the cavity. Hence, corrections must be applied later to insure normal landing on target. This can be accomplished by electric or magnetic fields at the exit from the FPS cavity. The end result is shown in Figure 4. These pictures were taken with an FPS vidicon before a and after b post-collimation. The shading in the upper photo is due to oblique incidence on target.

An Experimental Test of FPS

To check on the theoretical relationships, a number of basic experiments were performed, using equipment as shown in Figure 5. This included a gun with defining aperture (1), a pre-focusing Einzel-lens (2), and an FPS cavity (6) with deflection (3) and solenoid (4). The cavity was terminated in a mask (7), perforated by 20-mil holes in a triad-arrangement with 30 mils between centers. The viewing screen (5) was spaced 1" behind the mask. A spiral section (8) permitted post-acceleration without incidental focusing between the 1KV-cavity and the 5KV-screen.

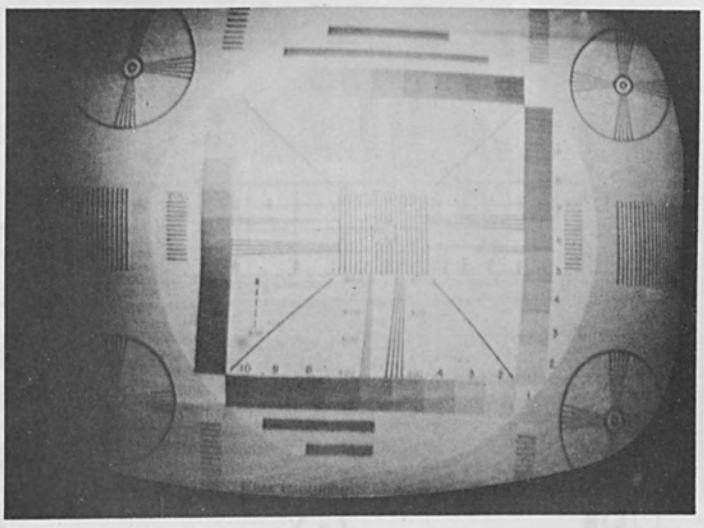

a. previous image

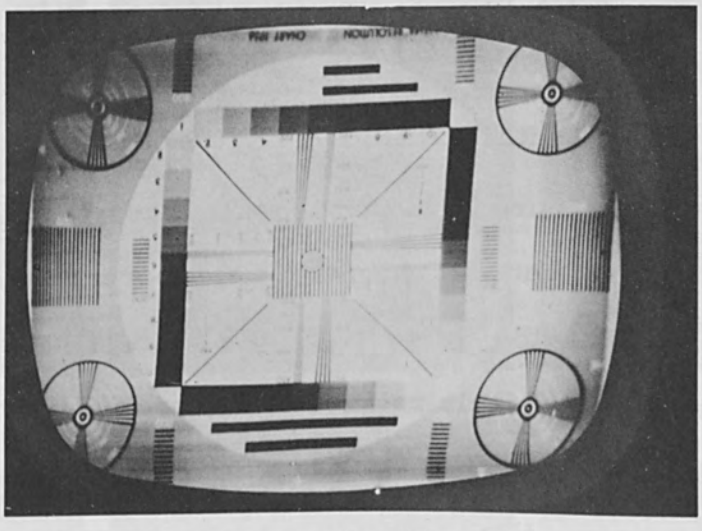

b. present image

FIGURE 4 EFFECT OF ELECTROSTATIC COLLIMATION

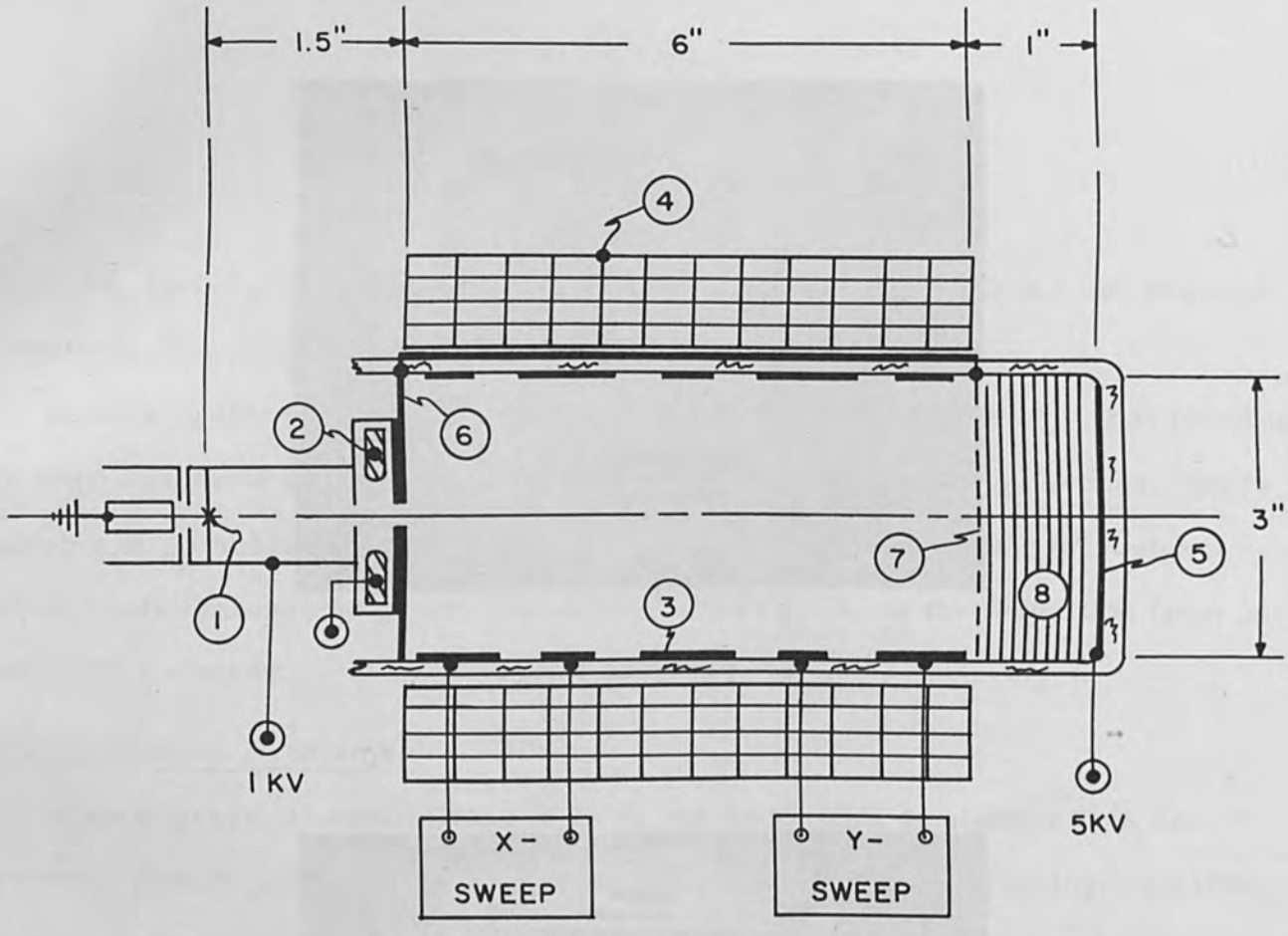

FIGURE 5 BASIC TEST OF F P S

Results are shown in Figure 6, a through c. These photos are taken with constant sweep voltages and with the magnetic field increased in three steps from $\theta = 0$ (Figure 6a) through $\theta = 186°$ (Figure 6b) to $\theta = 320°$ (Figure 6c). In the process, the prefocus lens was progressively relaxed to restore focus. The observed data on deflection and rotation are in good agreement with theory. Other observations included focus performance. Here, we noticed a progressive reduction of spot size and a decrease in the visibility of mesh texture. The mesh can no longer be discerned in Figure 6c, although the definition is at an optimum in that condition. Both of these effects are due to the fact that the equivalent lens of the two-lens system in Figure 5 moves progressively closer to target. This reduces magnification, while the half angle at target increases. Ultimately, in condition (6c), the beam diameter at the mask is so large that it includes more than one mesh-window

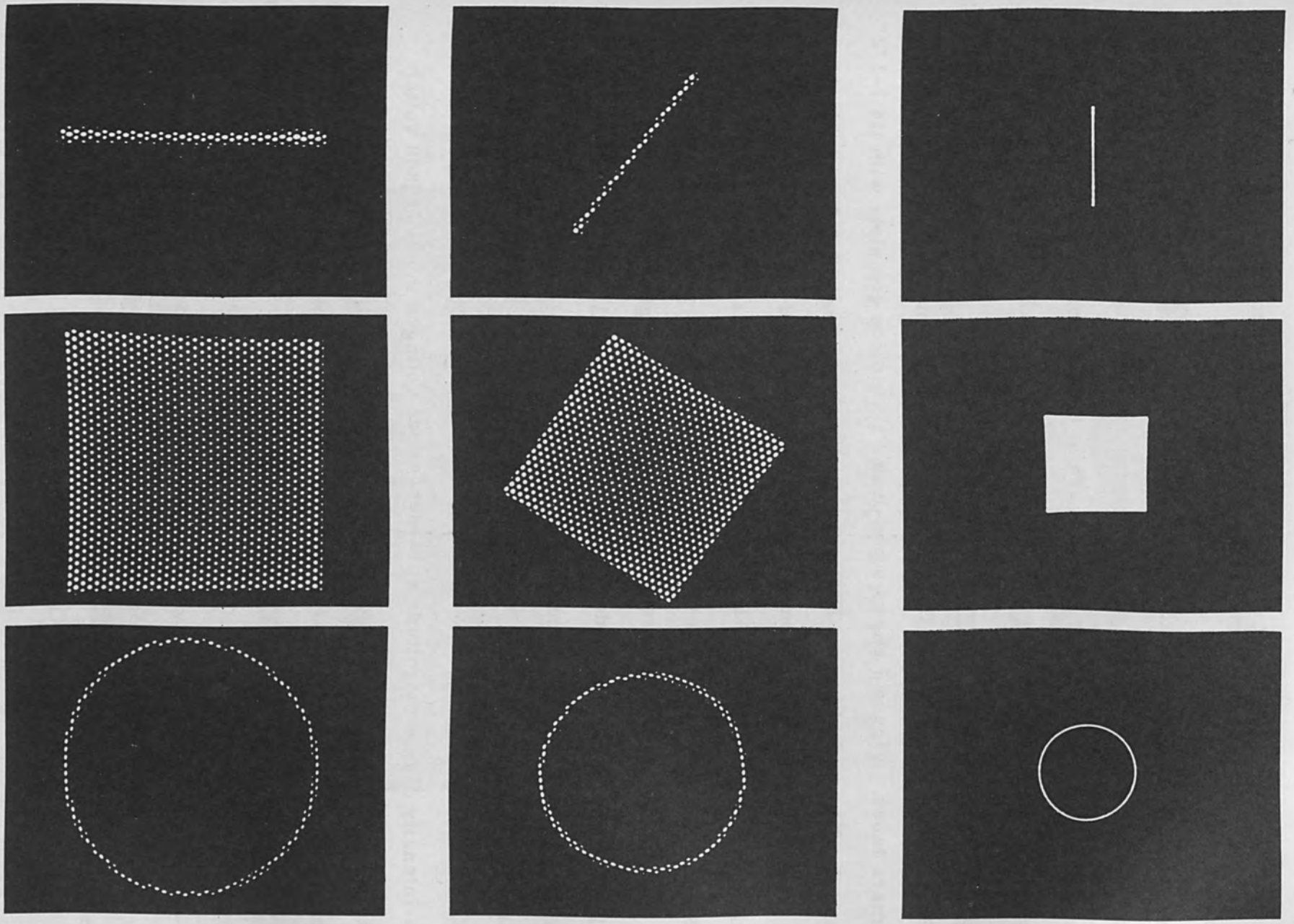

a b c

FIGURE 6 RESULTS OF BASIC TEST

at a time. This condition minimizes incidental beam-intensity modulation due to scanning.

Microscopic examination of Figures 6a to 6c shows the line width to decrease as 1:0.6:0.25. Since the total current reading target remained constant throughout the test, current-density at target increased in the ratio of 1:2.8:16. These are just the intensity gains predicted by the law of Helmholtz-Lagrange.

A Vidicon Using the FPS System

Successful applications of the FPS method have recently been made in the field of camera tubes. Figure 7 shows a one-inch FPS vidicon complete with its 1-1/2" focus coil. Figure 8 shows an FPS vidicon with electrodes printed on the inside of 5/8" glass tubing. Both vidicons have an overall length of 4". The 1" tube has a limiting resolution of over 800 lines; the 1/2" tube has resolved up to 500 lines.

Figure 9 is the photograph of a monitor display taken with the 1" FPS vidicon. This picture was slightly underscanned to facilitate photographic reproduction of small detail. Starting from a defining aperture of 1/2 mil, the FPS optics projects a scanning spot of 0.42 mil, which has a resolution capability of 2400 lines per inch on target.

Current density in this spot is approximately 1.2 amp/cm^2. To generate a beam-intensity of this magnitude at modest anode voltages involved (800 volts) requires an emission density beyond the capabilities of oxide cathodes. A small Pierce gun has been developed for this tube, using an impregnated metal cathode.[7] This emitter runs safely at 0.8 A/cm^2 and is held at a temperature of 1120 °C with a heater power of only 2.7 watts. By contrast, the 1/2" vidicon, shown in Figure 8, uses a conventional oxide cathode with very low heater power (0.3 watt). By comparison, the band-merit of this small tube is only one-third as high as in the larger model.

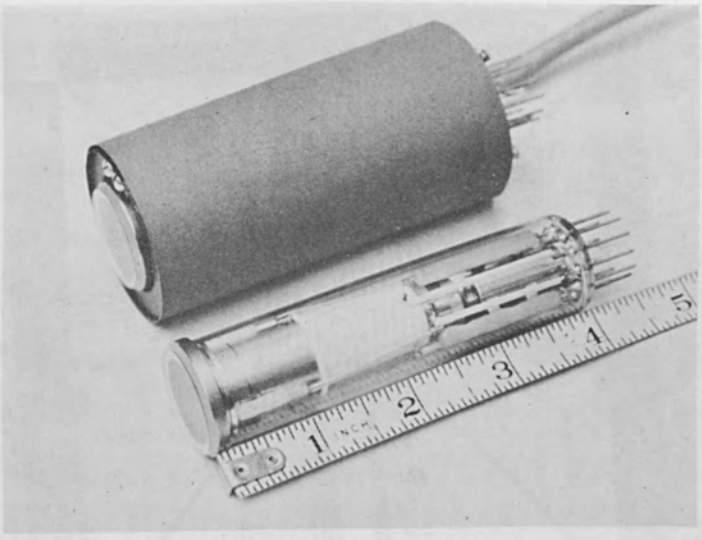

FIGURE 7 1" FPS VIDICON WITH FOCUS COIL

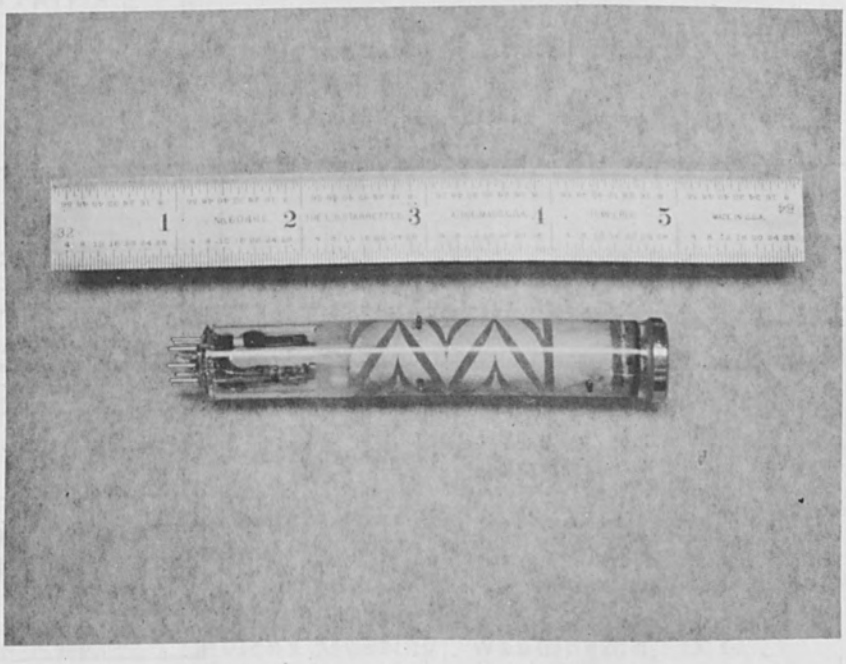

FIGURE 8 1/2" FPS VIDICON

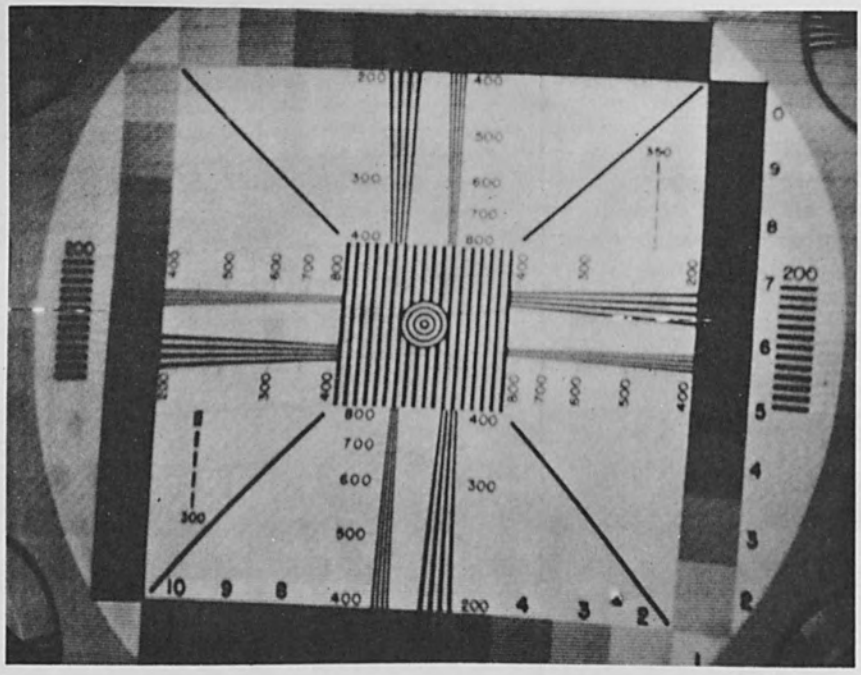

FIGURE 9 PERFORMANCE OF THE 1" FPS VIDICON

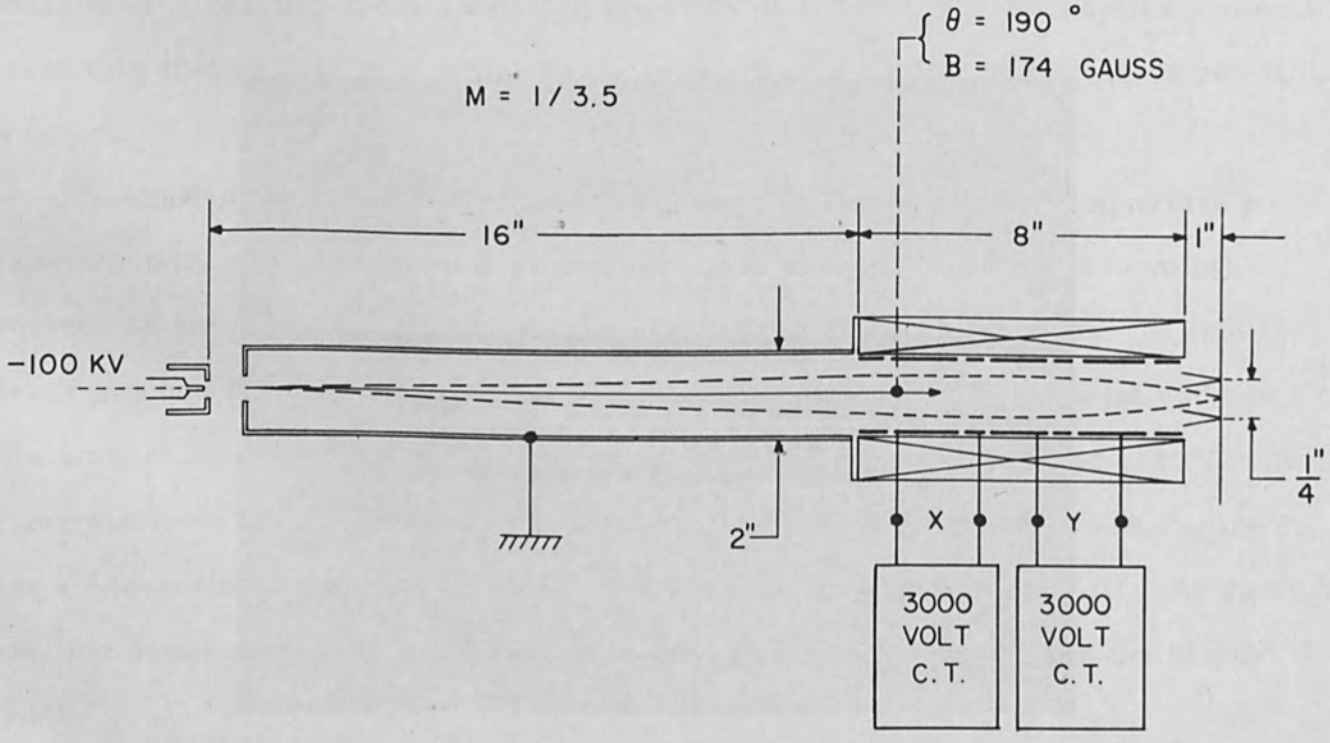

FIGURE 10 FPS - OPTICS FOR ELECTRON BEAM MACHINE

An Application of FPS to Electron-Beam Machining

In line with the objectives of this Conference, a time-limited study has been made to investigate whether FPS might conceivably be applied to an energy-beam apparatus. Figure 10 shows the results of a calculation.

Only a one-lens system has been analyzed; however, El-Kareh has shown in a basic paper[8] that, in actual practice, a separate condensor lens is needed to bridge the enormous gap between load current density (440 A/cm^{-2}) and emission density (1.5 A/cm^{-2}).

The FPS system as shown has an object distance of 16" and a cavity of 8" x 2". For the working distance, one inch has been assumed to be adequate.

Under these conditions, the system of Figure 10 has a demagnification of 1/3.5, i.e., it could image an object of 4.6 mils into a spot of 1.3 mils.

The system will focus a 100 KV beam with a magnetic field of 174 gauss. In a two-inch cavity, deflection by 1/2", or 100-spot-diameters, will require only 3000 volts between opposite terminals. In our experience, insulation of this voltage does not present any particular problems. Besides, a lower deflection voltage is feasible, if the cavity diameter is reduced, until a limit is set by increasing aberrations.

This example may serve to demonstrate that neither deflection voltages nor focusing power will get out of hand if an attempt is made to use FPS in connection with beams of very high energy.

References

1. Zworykin, V. K., and G. A. Morton, "Television", 2nd ed., 1954, John Wiley Part 3, Section 10: TV Pickup Tubes.
2. Macebo, L., "Deflecting Spherical Lens", Lecture presented on November 1, 1965, at the Electron Devices Meeting, Washington, D. C.
3. "An All-Electrostatic Image Orthicon", Pickup Tube Operation, General

Electric Company, Syracuse, New York. To be published.

4. Zworykin, Ramberg, et al, "ElectronOptics and Electron Microscope", John Wiley, New York, 5th printing, 1961, Section 15.6, p 520ff.
5. Spangenberg, K., "Vacuum Tubes", McGraw Hill, 1948, p 398, equation 14.13.
6. Schlesinger, K., "Electron Trigonometry", Proc. IRE, October 1961, pp 1538-49.
7. Levi, R., "Improved Impregnated Cathode", Journal Applied Physics, Vol. 26, No. 5, p 639, May 1955.
8. El-Kareh, A. B., "An Electron-Beam Machine", RCA Review, Vol. 24, No. 1, pp 5-46, March 1963.

Acknowledgements

In connection with the FPS vidicon application, the authors wish to acknowledge that valuable contributions have been made by the following members of the General Electric Pickup Tube Operation: R. Eaton, R. Ney, P. Oakes and I. Saldi. Thanks also are due to Dr. H. J. Hannam, Manger of the Pickup Tube Operation, for his continued interest and permission to publish this paper.

Micro Color Recording, Etching and Machining by Means of High Voltage Ion Beam

by

K. Kanaya, H. Kawakatsu, S. Matsui and H. Yamazaki
Electrotechnical Laboratory
Kamimukodai, Tanashi-machi, Tokyo, Japan

I. Okazaki and K. Tanaka
Japan Electron Optics Laboratory Co. Ltd.
Kamirenjaku, Mitaka-shi, Tokyo, Japan

Abstract

An ion beam device consisting of a hot-cathode discharge ion source, a focusing system and a specimen stage has been designed to be used in applications such as micromachining, surface etching, and color recording. The maximum accelerating voltage and working current are 50 kV and 500 μA, respectively in experiments using argon gas.

Some preliminary experiments have shown that it is possible to produce holes in a thin metal film and to etch the surface of metals without thermal effects by using an ion beam with a high accelerating voltage.

An ion beam with low current density has been used in an attempt to obtain color recordings. The carbon-like layer which is formed as a contaminant on a smooth metal surface being bombarded with ions shows color interference patterns. If a metal surface is uniformly colored with collodion, the color recording of the ion image can be obtained more easily. Accordingly, it is suggested that an ion color microscope can be realized.

Introduction

The kinetic energy of charged particles which have been accelerated can be used for melting, welding, evaporating, and cutting materials.[1] The technology of electron beams has reached a stage of near perfection, as evidenced by the existence of various commercially available electron beam instruments. However,

by using ion beams for such purposes, better performance may be theoretically expected since the ion beam exhibits much shorter wavelength and larger momentum characteristics than the electron beam.[2, 3]

With this in mind we have attempted to obtain a comparative evaluation for the practical use of an ion beam. First, the design and performance of a hot-cathode discharge type ion source[4] and an ion beam focusing system are described. Special attention is given to space charge effects. The ion beam device was tested with argon gas. The maximum accelerating voltage and working current were 50 kV and 500 μA, respectively. Under these conditions some preliminary experiments were tried such as color recording of an ion image, surface etching of a metal, and machining holes in a thin metal sheet.

Design and Performance of Ion Beam Device[5]

Figure 1 shows a cross-section of the complete ion beam device made by the Electrotechnical Laboratory in co-operation with Japan Electron Optics Laboratory Co. Ltd. The arc chamber of the ion source is drilled in a heavy copper cylinder which is arranged within the vacuum seals. On the cathode side of the chamber, a diaphragm of 5 mm diameter acts as an anode for the electron source. The other side of the arc chamber is limited by an "anti-cathode" having an aperture of 3 mm diameter. This provides an outlet for the ion beam. The anode and anti-cathode also act as a pair of pole pieces for the magnet which generates an axial field in the arc chamber. The coil of the magnet is mounted coaxially with the chamber on the outside of the air-tight seals and is energized by direct current.

The electron source unit, which consists of a filament, a Wehnelt cylinder, and a gas inlet, is insulated from the arc chamber by means of a porcelain ring. The electron beam is accelerated by a maximum voltage of 300 V.

In the focusing chamber, the extractor and collection tube are arranged co-axially and insulated from each other by a porcelain insulator. The position of

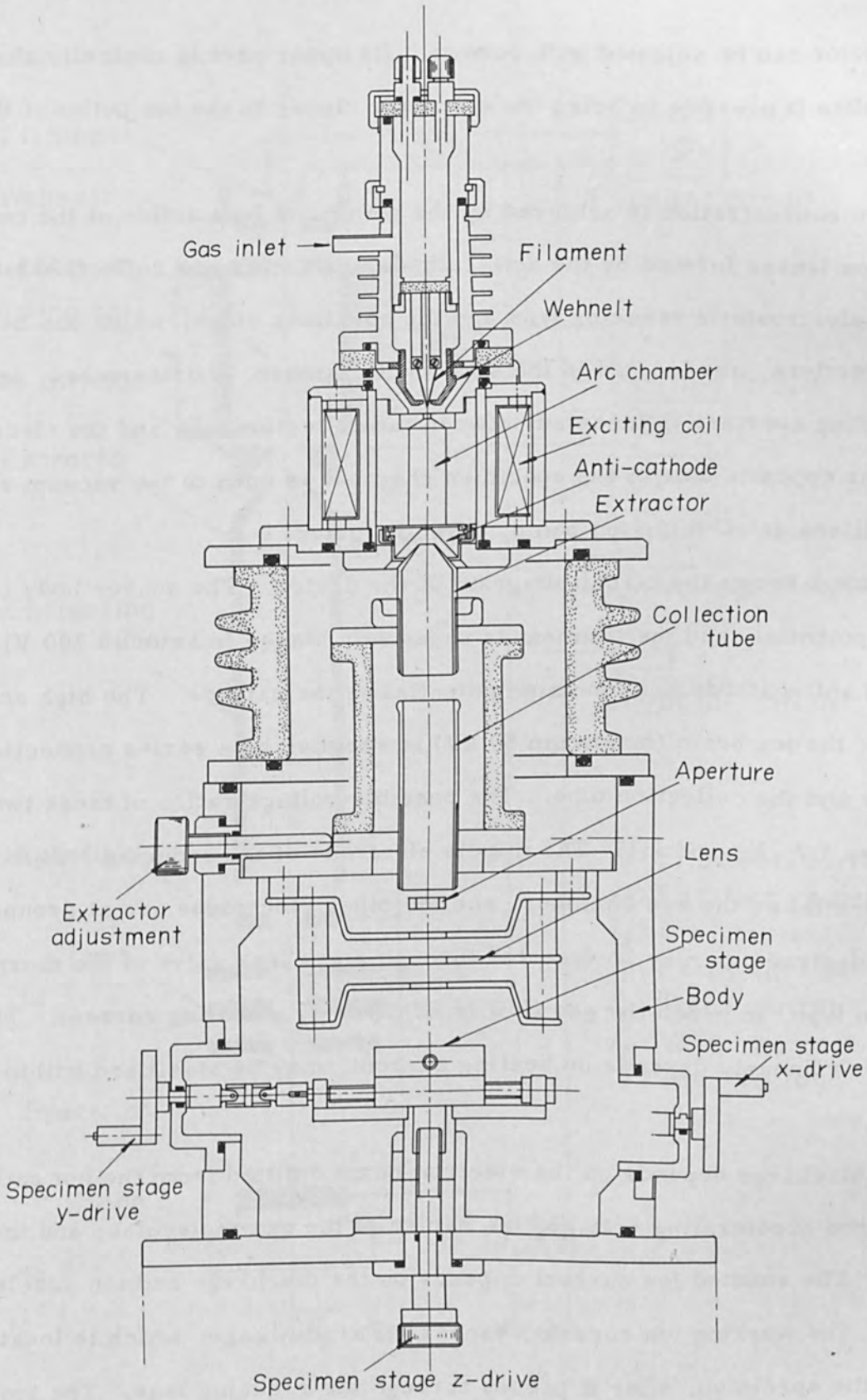

Figure 1 Cross-section of ion beam device.

the extractor can be adjusted with screws. Its upper part is conically shaped which makes it possible to bring the extractor closer to the ion outlet of the anti-cathode.

Beam concentration is achieved by the compound lens action of the two immersion lenses formed by the anti-cathode, extractor and collection tube.

The electrostatic reducing lens and the specimen stage, which can be moved in three directions, are located in the specimen chamber. Furthermore, an adjustable limiting aperture is inserted between the collection tube and the electrostatic lens. The opposite side of the specimen chamber is open to the vacuum system which utilizes an oil diffusion pump, 4" in diameter.

Figure 2 shows the circuit diagram of the device. The source body is at a positive potential, and the filament is negatively biased (maximum 300 V). The insulated anti-cathode has the same potential as the cathode. The high accelerating voltage of the ion beam (maximum 50 kV) is supplied by a series connection of the extractor and the collection tube. The possible voltage ratios of these two electrodes are 3:7, 2:3 and 1:1. The middle electrode of the reducing lens is at the same potential as the arc chamber, and the other electrodes are at ground potential.

The desired gas may be inserted through a gas leak valve of the thermal expansion type, in which the gas flow is adjusted by a heating current. The gas flow, which linearly depends on heating current, may be stabilized within a few seconds.

The discharge depends on the electron beam emitted from the hot cathode, the electron accelerating voltage, the nature of the gas molecules, and the exciting current. The emitted ion current depends on the discharge and ion accelerating voltage. The working ion current reaches a Faraday cage, which is located in the plane of the specimen, after it passes through the reducing lens. The ion current has a maximum value of 500 μA when a total current of 2 mA is used and the

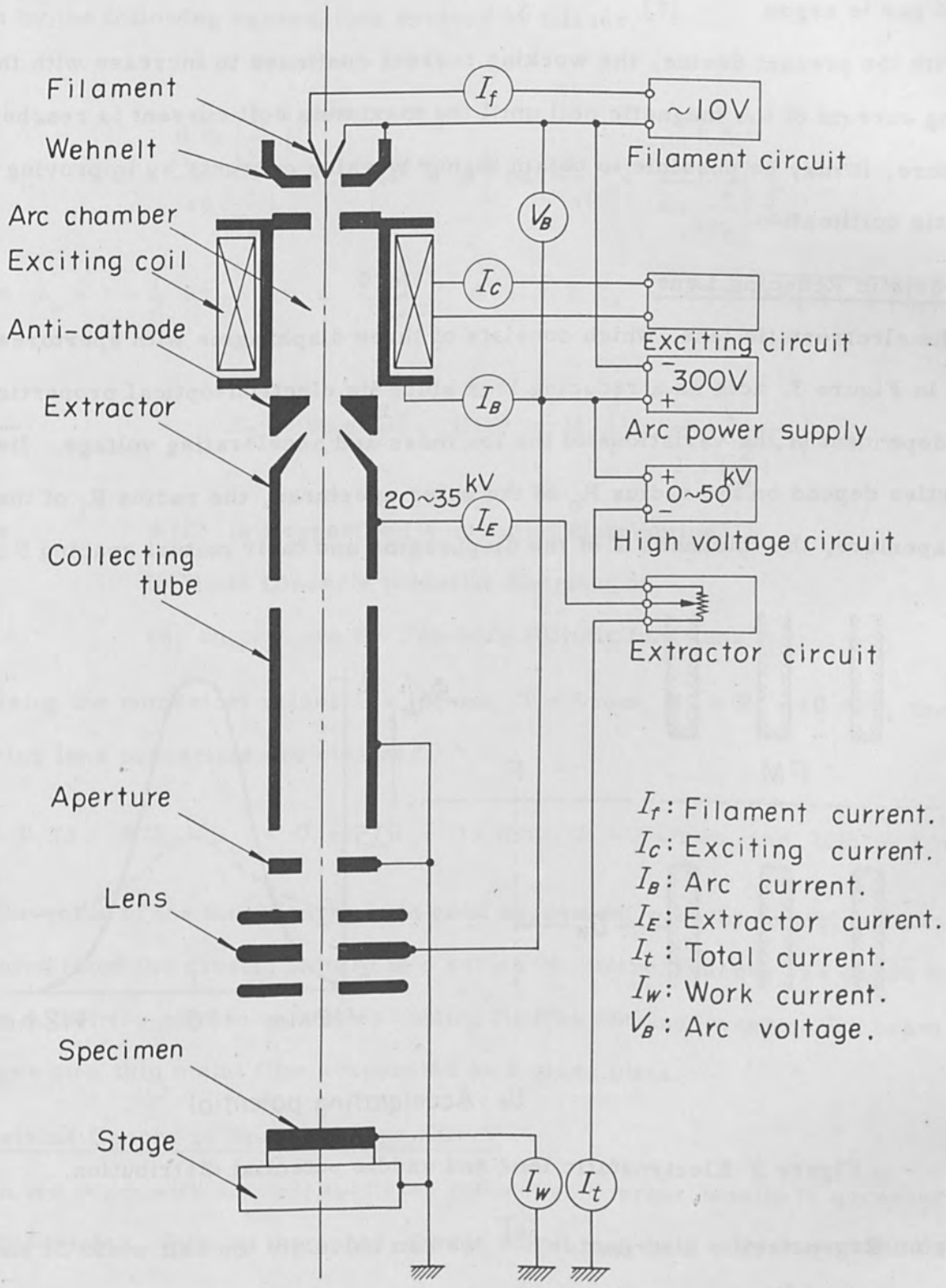

Figure 2 Circuit diagram of the device.

applied gas is argon.

With the present device, the working current continues to increase with the exciting current of the magnetic coil until the maximum coil current is reached. Therefore, it may be possible to obtain higher working currents by improving the magnetic collimation.

Electrostatic Reducing Lens

The electrostatic lens, which consists of three diaphragms with apertures as shown in Figure 3, acts as a reducing lens since its electron-optical properties are independent of the variations of the ion mass and accelerating voltage. Its properties depend on the radius R_o of the outer apertures, the radius R_i of the inner aperture, the thickness T of the diaphragms and their mutual spacing S .

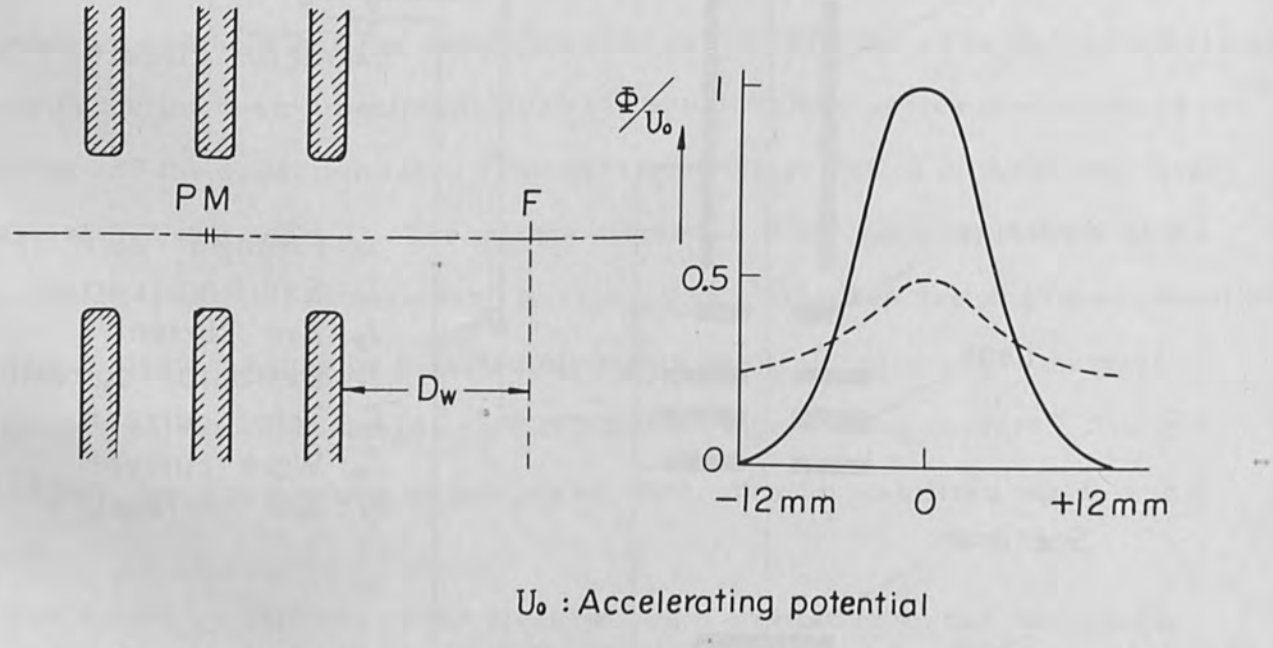

Figure 3 Electrostatic lens and saddle potential distribution.

From Regenstreif's distribution,[6] we can calculate the half width 2d and minimum $U_o(1 - k^2)$ of the potential and using these values, the focal length of the lens and the distance between the principal point P and the mid-plane M are

given by the following expressions derived by Glaser. [7]

$$f = \frac{d\, dn\left(\frac{\pi}{\omega_o}\right)}{sn\left(\frac{\pi}{\omega_o}\right)} \quad , \quad MP = d\left[cs\left(\frac{\pi}{\omega_o}\right) + \frac{dn\left(\frac{\pi}{\omega_o}\right)}{sn\left(\frac{\pi}{\omega_o}\right)} \right],$$

where $\omega_o = 1 - \frac{1}{2} k^2$, $k^2 = \frac{\Phi(o)}{U_o}$, $d = 1.2\, Z_2 \sqrt{\Phi(Z_2)/\Phi(o) - \Phi(Z_2)}$

$$Z_2 = S + \frac{T}{2} \quad , \quad U(Z) = U_o \left(1 - \frac{k^2}{1 + (\frac{Z}{d})^2} \right) .$$

where $\Phi(Z)$ is Regenstreif's potential distribution,

$U(Z)$ is Glaser's potential distribution,

sn, dn, cs are the Jacobian Elliptic functions.

Using the numerical values S = 10 mm, T = 5 mm, $R_o = R_i$ = 10 mm, the following lens properties are obtained:

$k^2 = 0.73$, $\Phi(Z_2)/U_o = 0.36$, d = 13 mm, f = 42 mm and MP = 1 mm.

The value of the focal length is in good agreement with the experimental value estimated from the caustic pattern in a series of different planes, as shown in Figure 4. These patterns show the cutting figures obtained when an ion beam impinges on a thin metal film evaporated on a glass plate.

Aberrations Caused by Space-Charge Effect

An ion beam with a small spot size and a high current density is necessary for micromachining. Hence, the space-charge effect may be a very important limiting factor.

The potential distribution due to space charge is given by

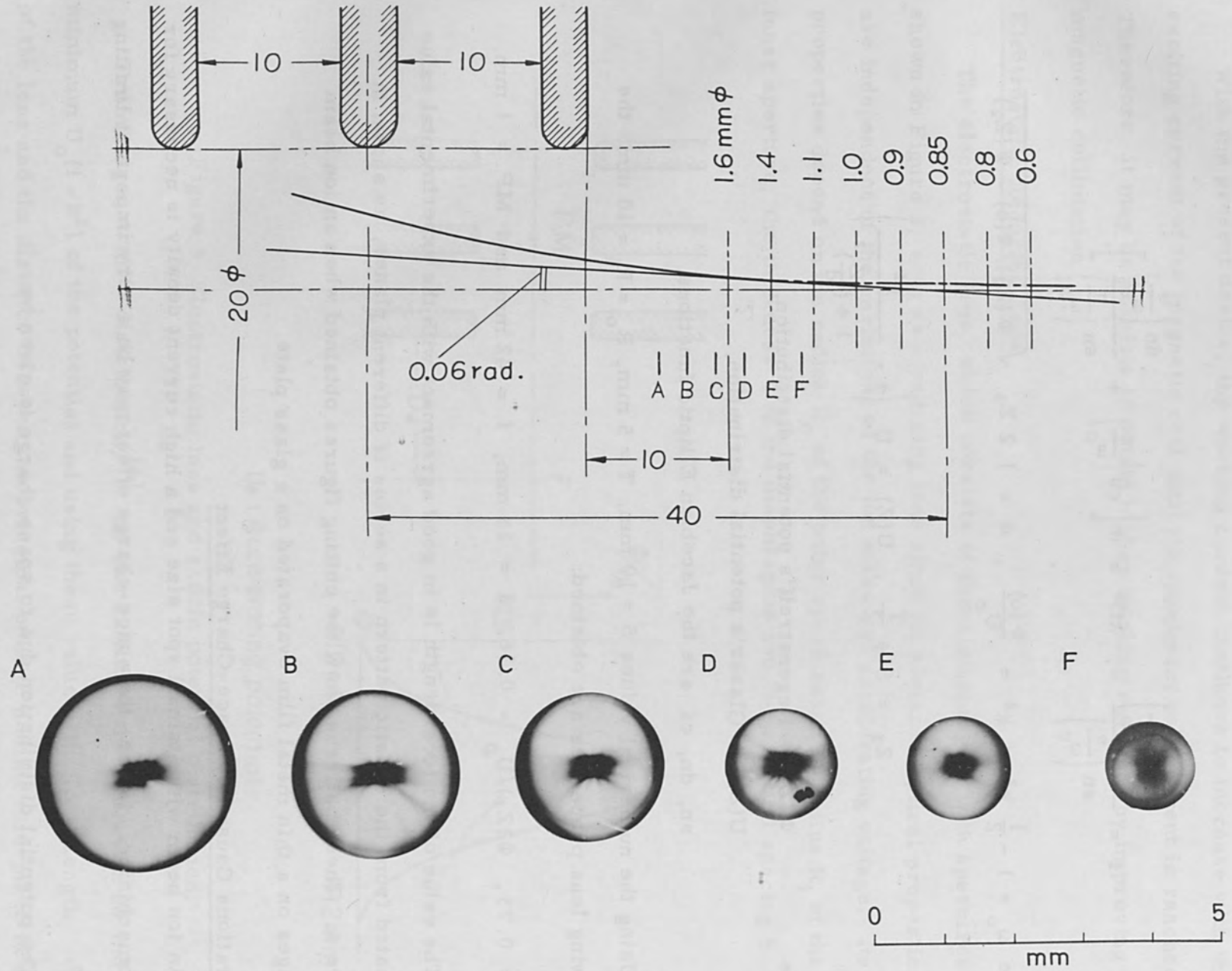

Figure 4 Representation of caustic patterns by focused ion beams.

$$\varphi(r, Z) = - \frac{\rho(Z)}{4\varepsilon_o} r^2 + \ldots\ldots ,$$

where $\rho(Z)$ is the axial space charge distribution and ε_o the permittivity of free space.

Under the assumption that space-charge effects are of the same order as the spherical aberration of the lens system and since the beam paths are determined by the lens, the aberrations caused by space-charge can be calculated by differentiating the eikonal function S with respect to the aperture angle α.

$$\Delta U_s = \partial S / \partial \alpha$$

with $$S = \int \left\{ 1 - \frac{1}{2\Phi} \frac{\rho(Z)}{4\varepsilon_o} r^2 \right\} \left\{ 1 - \frac{1}{2} r'^2 \right\} dZ$$

When an ion beam with radius r_a at the object point Z_a is incident normal to the reducing lens with limiting aperture α_o, and is reduced to $r_a M (M << 1)$ at the focal point $r_b \simeq f$, the aberrations due to space-charge effects for any ray with an angular aperture α are given by

$$-\Delta U_s = \Delta f_i \alpha + B_i \alpha^3$$

$$\Delta f_i = \frac{\sigma_i}{2} \frac{f}{\alpha_o^2} \left(\frac{1}{M} + 1 \right), \quad B_i = \frac{\sigma_i}{2} \frac{f}{\alpha_o^2} ,$$

$$\sigma_i = \frac{f}{2\pi\varepsilon_o} \sqrt{\frac{m_i}{2ne}} \frac{i}{\Phi^{3/2}} ,$$

where m_i is the mass of the ion, n the positive charge in units of e, i the current of the ion beam and Φ the accelerating voltage. The first term gives a negative effect by increasing the focal length, and the second acts as a negative spherical

aberration.

Caustic Pattern Considering Space-Charge Effect

Since the space-charge effect gives both negative defocusing and negative spherical aberrations, the equation of caustic pattern, considering space-charge effect, is given by

$$\left.\begin{aligned} \xi &= (\zeta + \rho_B^2 + 1)\, \rho_B \cos \varphi_B \\ \eta &= (\zeta + \rho_B^2 - 1)\, \rho_B \sin \varphi_B \end{aligned}\right\}$$

with $$3\rho_B^4 + (4\zeta - 2\cos\varphi_B)\rho_B^2 + \zeta^2 - 1 = 0$$

where (ρ_B, φ_B) correspond to coordinates (α, φ_B) of any ray in the aperture plane, and the dimensionless variables ξ, η, ζ are given by

$$\rho_B = \alpha\sqrt{(B - B_i)/N}$$

$$x = \xi\sqrt{N^3/(B - B_i)}\,, \quad y = \eta\sqrt{N^3/(B - B_i)}$$

$$\zeta = (\Delta f - \Delta f_i)/N$$

Here B and N are spherical and astigmatic aberrations of the lens.

If the ion beam passing through the reducing lens is limited by the aperture $\alpha_o = R_B/f$, the radius of minimum confusion at the "crossover point" is expressed by the following formula:

$$r_\ell = \frac{1}{4}(B - B_i)\alpha_o^3 = \frac{1}{4} B \alpha_o^3 - \frac{\sigma_i f}{8} \alpha_o \,,$$

for $$-(\Delta f \pm N) = \frac{3}{4} B \alpha_o^2 - \frac{3}{8}\sigma_i f - \frac{\sigma_i}{2\alpha_o^2} f \left(\frac{1}{M} + 1\right)$$

For the numerical values of i = 150μA, Φ = 30 kV, f = 42 mm, α_o = 0.06 rad., M = 1/8 and B = 400 cm, we obtain r_ℓ = 210μ and Δf_i = 2 cm.

Thus, the obtainable radius of minimum confusion of the ion beam is not limited by space-charge effect, but only by the spherical aberration of the lens. However, the increase of focal length may certainly be caused by the defocusing effect due to space-charge.

Ion Beam Machining and Etching

In order to examine the adaptability of an ion beam for use as a tool such as machining a hole and surface etching, some preliminary experiments were carried out.

Figure 5 shows the micrograph of the cutting pattern produced by the bombardment of an ion beam on a thin evaporated film of Ag about 1000 Å thick. This was obtained with a 20 kV, 100μA beam which was focused by an electrostatic lens. It is evident that the cutting pattern corresponds to the intensity distribution of the caustic pattern caused by the spherical aberration. Special attention is paid to the very sharp resolution of the cutting edge. Figure 6 shows a very small hole cut into a nickel sheet 10μ thick. The thermally affected zone in the neighborhood of the hole cannot be observed.

The absence of detectable thermal effects is probably due to the large momentum of the ion beam.

An etching method using ion beam bombardment with low accelerating voltage and high current[8] has already been used to prepare metal and synthetic fiber samples because the preferential etching patterns due to the orientation of the material appear with only small thermal effects. The experiments of ion beam etching with high voltage and low current were tried in order to ascertain that the thermal effects are smaller. Figure 7 (a), (b) show electronmicrographs of copper surfaces which were etched by ion beam bombardment with a 30 kV, 100 μA/mm^2

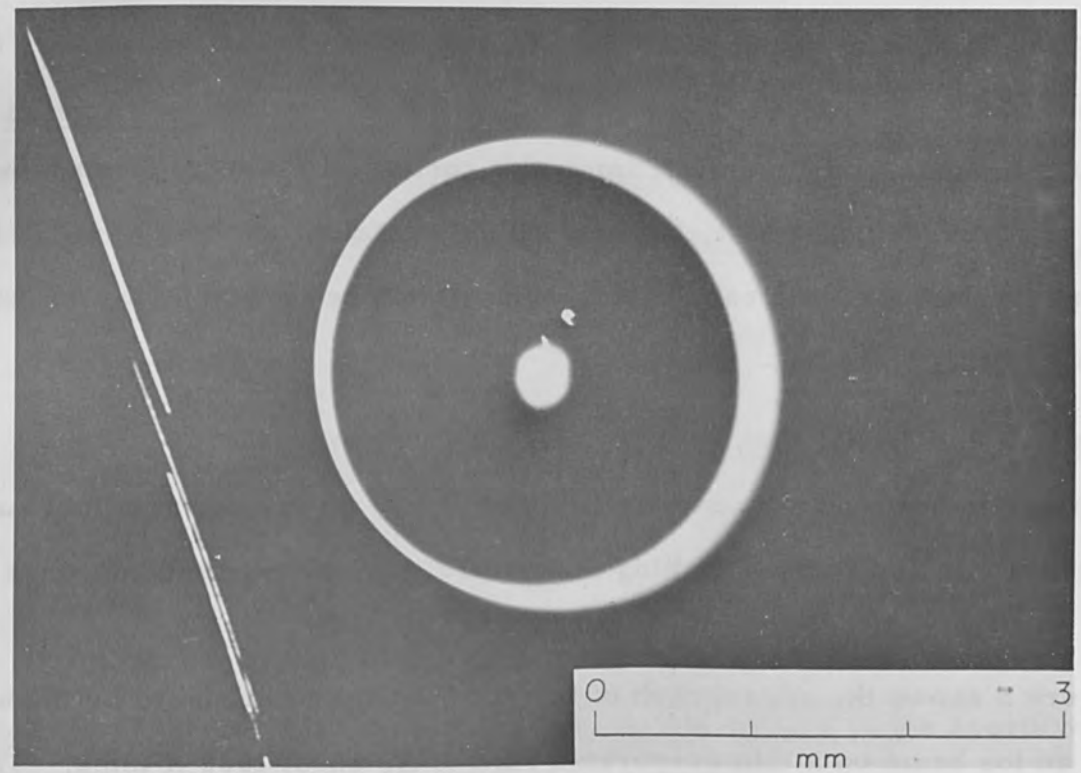

Figure 5 Caustic pattern cut by halo ion beam.

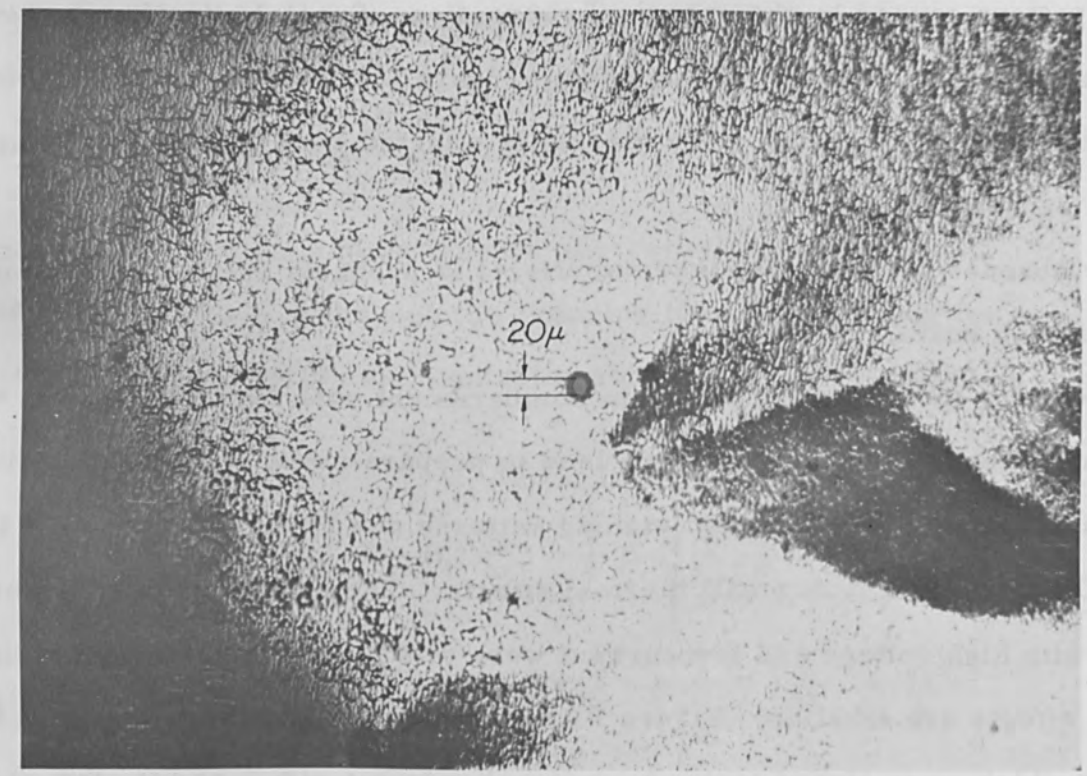

Figure 6 A small hole cut into thin Ni sheet.

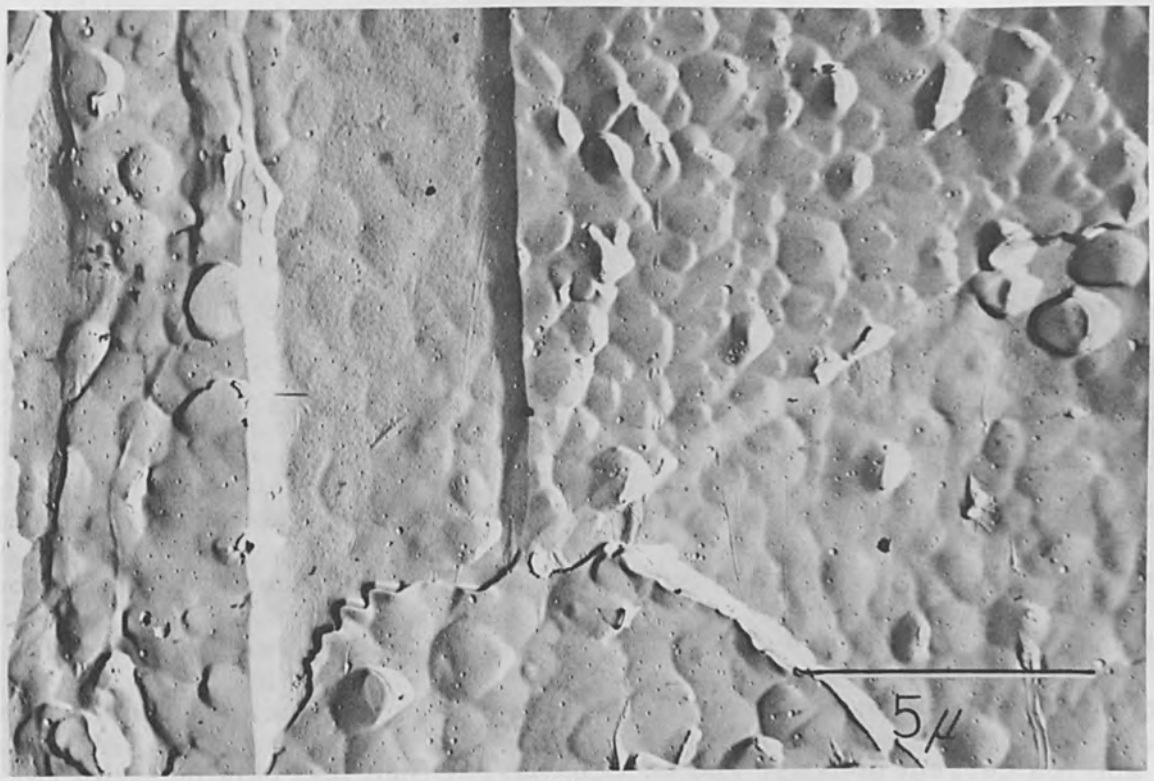

(a)

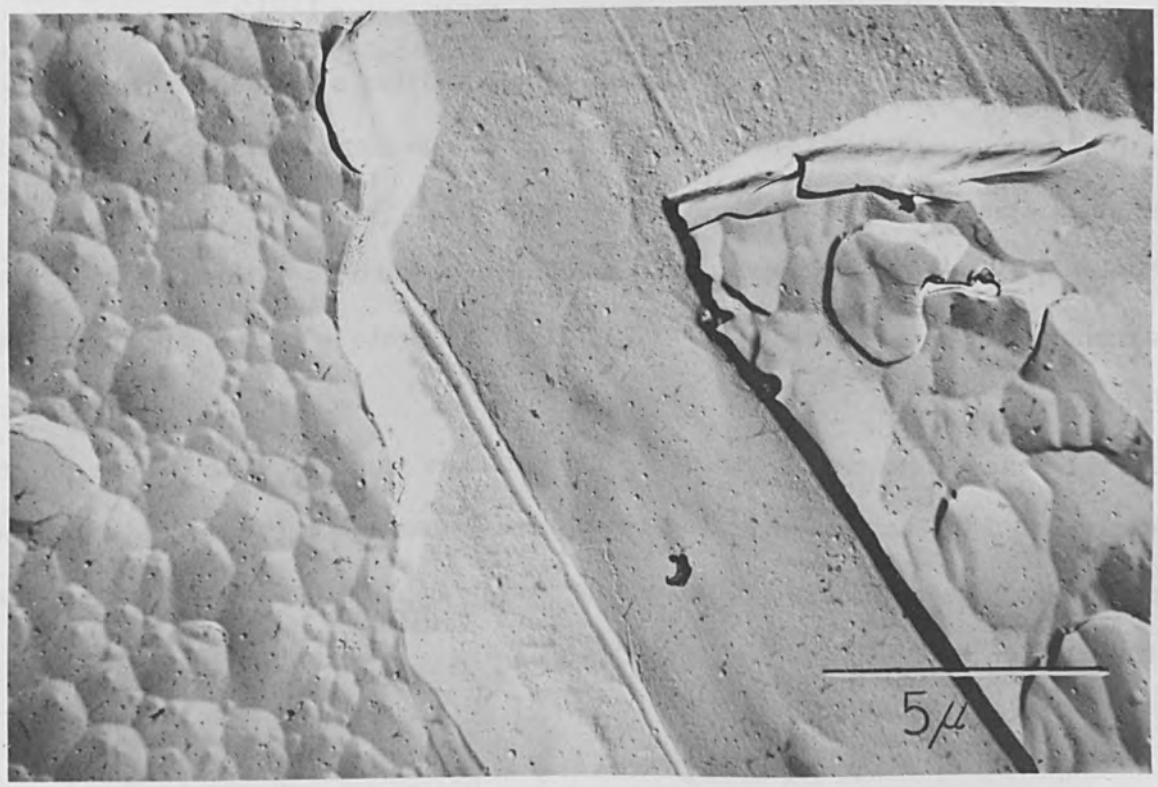

(b)

Figure 7 Copper surfaces etched by ion beam with 30 kV, 100 $\mu A/mm^2$ and (a) 30 sec., (b) 60 sec.

beam and bombardment time (a) 30 sec., and (b) 60 sec. The variation of etching pattern for different crystal orientation can be observed and the grain boundaries appear clearly. However, in these etching patterns, the thermal effects cannot be found.

Accordingly, it is found that the ion beam has a superior adaptability to micro machining and surface etching.

Color Recording

When an ion beam with low current density is directed upon a smooth metal surface in a vacuum, the bombarded part of the surface is covered by a carbon-like contamination layer because of the existence of oil molecules in residual gas. The rate of contamination by the ion beam depends on the residual gas, surface temperature and ion current density, and is much larger than that obtained with an electron beam[9] under the same conditions. Möllenstedt[10] has reported a method of reproducing grids by using the contamination shadow pattern produced by ion bombardment. Furthermore, Speidel[11] has demonstrated color recording of ion images by using the contamination layer.

Figure 8 shows the micrograph of a caustic pattern contaminated by ion beam bombardment for an evaporated Al film, in which various colors appear by light interference.

Let n be the refractive index of the carbon-like contamination layer, n_g that of the metal, and d the thickness of the contamination layer. The relative intensity of reflected light R is expressed by a simple formula, in the cases satisfying the condition that $n = \sqrt{n_g}$ [12] ;

$$R = 4B^2 \cos^2 \frac{\delta}{2} \quad ,$$

with

$$B = \frac{n - 1}{n + 1} \quad , \qquad \delta = \frac{2\pi}{\lambda} \; 2nd \quad .$$

The variation in color is very sensitive to the change in thickness of the contamination layer. Figure 9 shows the thickness distribution estimated by calculations based on the colors observed in Figure 8. Figure 10 shows a reflection micrograph of the shadow pattern of a micro grid on a sheet mesh, which is obtained by ion bombardment of a Ag film evaporated on glass. Figure 11(a) is a reflection micrograph of the colored pattern, in which the variation of color for different current density can be observed. Figure 11(b) is a transmission micrograph of the same pattern as (a), and shows nearly complementary colors in comparison with that in (a).

By using a metal surface uniformly covered by thin collodion film, color recording is more easily performed, and clearer colors appear with shorter exposure of the ion beam. In this case, it is supposed that the interference colors which appear are not due to the thickness of the contamination layer grown on the collodion film, but by the changes in the collodion film which has been partially destroyed by the ion beam.

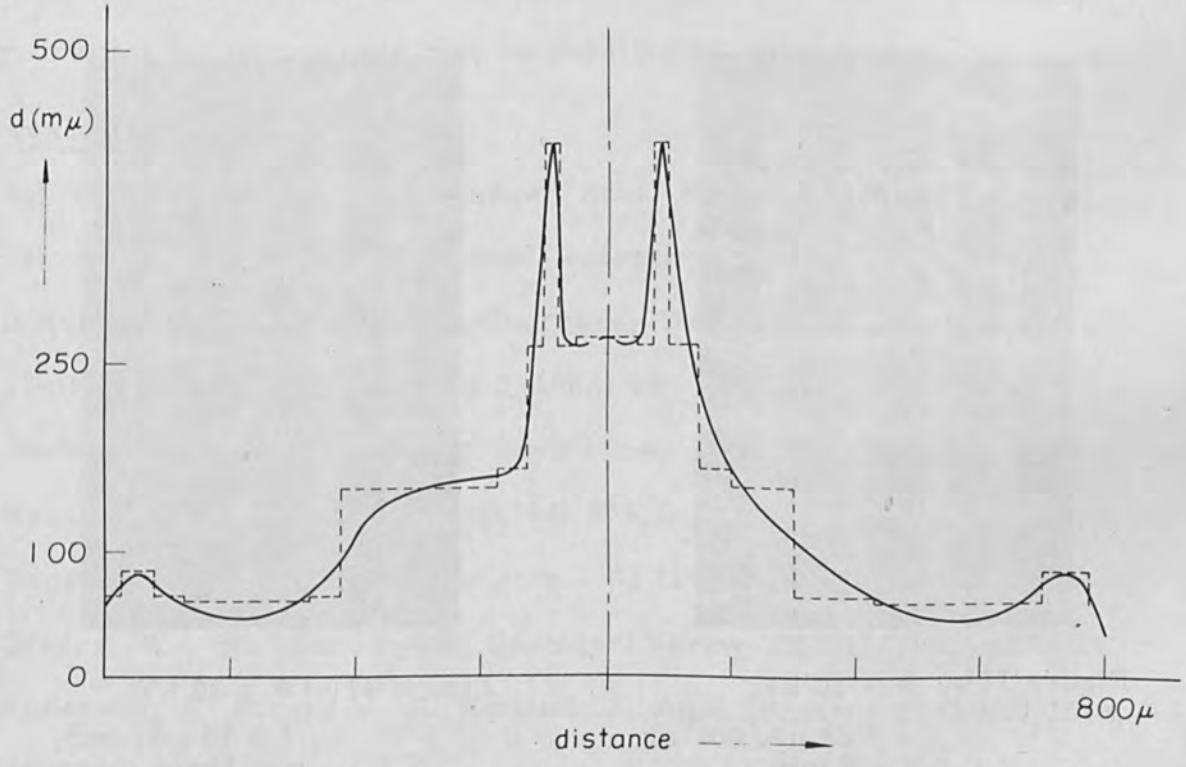

Figure 9 Thickness distribution of caustic pattern in Figure 8.

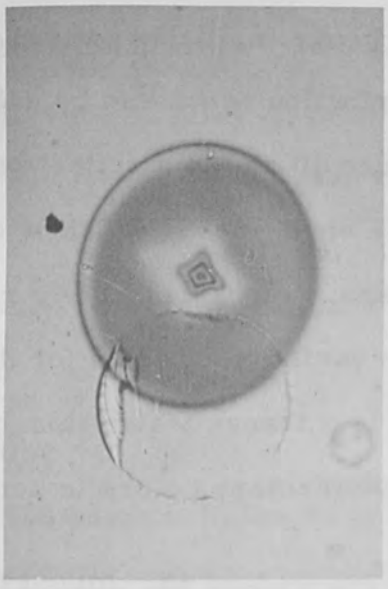

Figure 8 Accelerating voltage $\Phi = 30$ kV, ion density $J = 15$ mA/cm², bombardment time $t = 2$ sec.

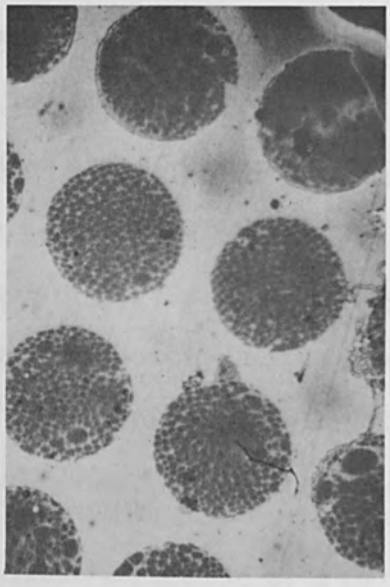

Figure 10 $\Phi = 20$ kV, $J = 50$ μA/cm², $t = 3$ min.

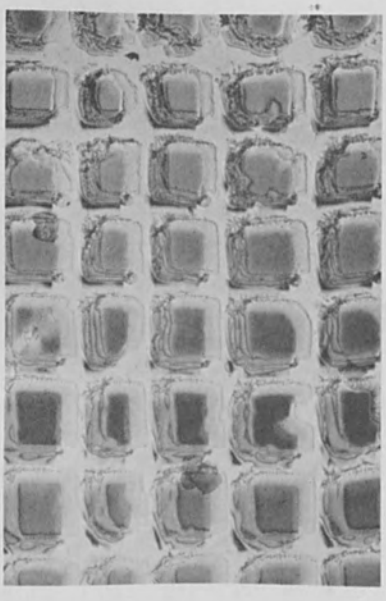

Figure 11(a) $\Phi = 30$ kV, $J = 25$ μA/cm², $t = 5$ min.

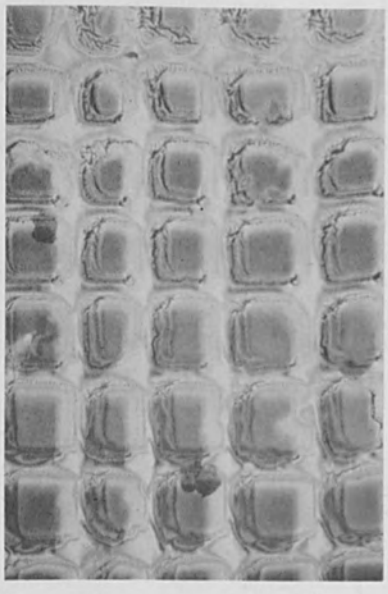

Figure 11(b) $\Phi = 20$ kV, $J = 70$ μA/cm², $t = 2$ min.

Figure 12 shows a more brilliantly colored pattern obtained by such a method. In Figure 13, more detailed variation of color is observed in comparison with Figure 10. Figure 14(a) is a colored pattern of a sheet mesh, and (b) is obtained by evaporating Ag on (a). It shows the change of interference conditions.

Conclusion

In the ion beam device, a stable ion beam can be obtained and focused on the specimen stage by an electrostatic lens. The minimum spot size of the focused beam is not yet limited by space-charge effects, but only by spherical aberration of the lens. However, the focal length of the lens is affected by space-charge.

The most interesting feature of ion beams is that they are suitable for non-thermal processes, but not for applications in which the kinetic energy of the beam is used to melt materials. It has been experimentally shown that ion beams are useful for both micromachining and surface etching.

The images of ion beams can be recorded as colored patterns by a simple treatment and the variation in color is sensitive to the ion current density. Accordingly, a color ion microscope may be possible by improving the ion optics.

References

1. (a) Steigerwald, K. H., Verhandl. deut. Physik.4 (1953) 123.
   (b) Stohr, J. S., Fuel Elements Conference, Paris, Nov. (1957).
2. Schwarz, H., Proc. Vacuum Congress, Washington, Oct. (1961).
3. Jouffery, B., J. Microscopie 2 (1963) 45.
4. Abele, M. and W. Meckbach, Review Sci. Instr. 30 (1959).
5. Kanaya, K., et al., Optik 21 (1964) 399.
6. Regenstreif, E., Ann. Radioelectr., 62 (1951) 51.
7. Glaser, W., Hb. der Physik, Springer-Verlag XXXIII (1956) 379.
8. Anderson, F. R. and V. F. Holland, J. Appl. Physics 31 (1960) 1516.
   34 (1963) 2371.

Figure 12 Φ = 20 kV,
J = 70 $\mu A/cm^2$
t = 2 min.

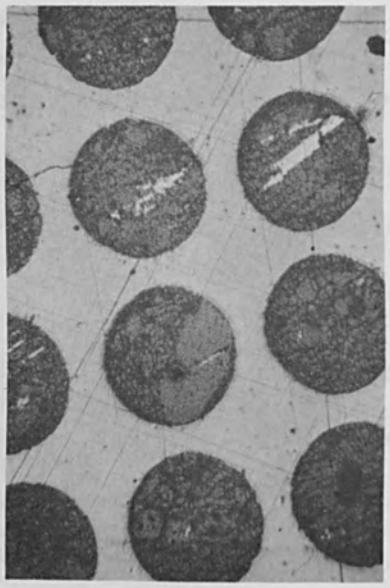

Figure 13 Φ = 20 kV,
J = 70 $\mu A/cm^2$,
t = 1.5 min.

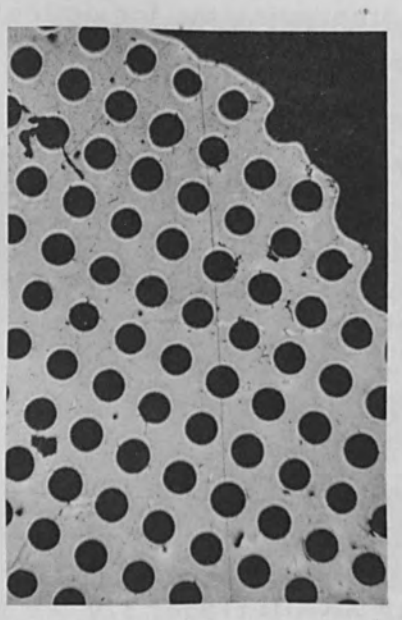

(a)

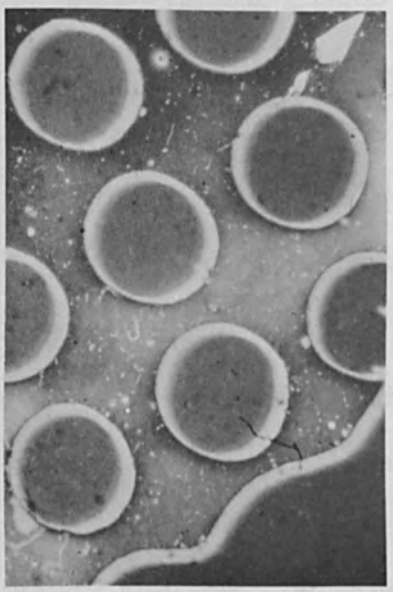

(b)

Figure 14 Φ = 35 kV, J = 100 $\mu A/cm^2$, t = 4 min.

9. Ennos, A. E., Brit. J. Appl. Phys. 4 (1953) 101.

10. Mollenstedt, G., u. R. Speidel, Z. fur angew. Phys. 13 (1961) 231.

11. Speidel, R., Z. fur Physik 154 (1959) 238.

12. Kubota, H., et al., Oyo Buturi (Japanese) 18 (1949) 43.

Electron Beam to Laser Beam: A Direct Conversion

by

C. A. Klein
Raytheon Research Division
Waltham, Massachusetts

Abstract

Recently a direct conversion of electron beam energy into coherent visible or infrared radiation has been achieved. This paper reports on the status of progress in this field, gives an account of the basic physics involved, and explores some of the perspectives opened up by the possibility of constructing electron-beam pumped optical masers.

Introduction

The conversion of electron-beam energy into electromagnetic radiation is currently achieved by means of devices such as the magnetron, the klystron, or the travelling-wave tube, in what is referred to as the microwave industry. For the generation of still higher frequencies, it appears that the interaction of electron beams with plasmas may provide a novel approach in the millimeter and submillimeter-wavelength region. Of greater significance is the fact that, very recently, laser action has been obtained when fast electrons were made to interact with suitable solids. In the following we will be concerned with fundamental aspects of this phenomenon.

Past investigations of ionization processes by fast electrons have shown that, in semiconductors or insulators, about one third of the dissipated energy is transferred to excess carriers and may be reemitted in the form of light. In 1961, Basov[1] suggested that population inversion and, under favorable conditions, laser action could be achieved by this technique. Initial attempts using Ge and GaAs were unsuccessful, but by February 1964 Basov and his co-workers[2] observed line-

narrowing phenomena in irradiated CdS, which they considered as indicative of eventual success. In the meantime, Aigrain's group explored a number of III-V compounds, and in April 1964 reported the first successful operation of an electron-beam pumped (EBP) laser.[3] Shortly later, at the Seventh International Conference on Semiconductor Physics, in Paris, electron-beam pumping was already an active topic of discussion, much of the interest centering around attempts to achieve the required degree of excitation in GaAs. Hence, it is not surprising that during the summer of 1964 U.S. laboratories began initiating vigorous programs on the development of lasers of this type. At the time of this writing, at least three groups have operational EBP lasers made of GaAs.[4, 5, 6]

As illustrated in Figure 1, the "standard" procedure with GaAs is to bombard a surface that was cleaved perpendicular to the two polished faces of a 0.1 to 0.2-mm thick slide of material which constitute resonator-mirror surfaces. The sample

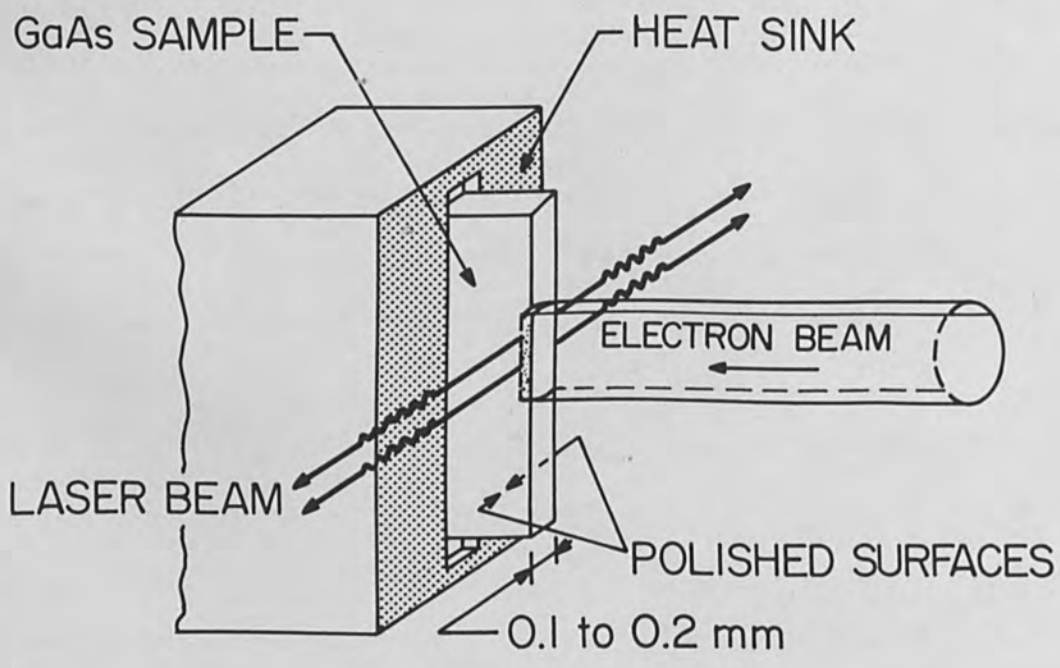

Figure 1 Direct conversion of an electron beam into a laser beam through excitation of a gallium arsenide Fabry-Pérot structure.

is clamped or soldered to a massive heat sink on the cold finger of a liquid-helium or liquid-nitrogen cryostat. An electron gun of the type used for television kinescopes delivers keV electrons (well below the threshold for radiation damage) in pulses of 0.1 to 1 μsec at a repetition rate of about 1000/sec. The light is emitted perpendicular to the polished faces (see Figure 1), and its spatial coherence can be analyzed through an infrared image converter. The angular distribution is found to be similar to that of junction lasers, with a width of the order of 0.1 rad in the plane orthogonal to both the bombarded surface and the "mirrors". This implies a wave penetration of about 5 to 10 μ which, as we shall see later, turns out to be roughly consistent with the effective range of the primary electrons in a typical experiment.

Quantitative work of this nature requires a fair knowledge of the density of electron-hole pairs generated by the electron beam as it penetrates into the active medium. This will be the object of the next section where we will also make a critical evaluation of EBP lasers. Relevant investigations have been concerned mainly with GaAs, and Sec. III reviews the present situation. A short account of work done abroad using other III-V semiconductors and some of the II-VI compounds is presented in Section IV. Solid-state systems such as pink ruby, which may be suitable as EBP laser material, will be considered in Section V. We conclude (Section VI) with a discussion of some unique features of electron-beam devices, an evaluation of the conversion efficiency, and finally, a projection on forthcoming developments and future perspectives.

II. The Excitation Mechanism

As shown in Figure 1, the light wave propagates between the reflecting faces of a Fabry-Pérot cavity. If α designates the rate per unit length at which photon energy is lost to the medium, whereas g characterizes the gain derived from the presence of an inverted population, the wave will grow for $g > \alpha$. To become a laser the system must obey the condition

$$R \exp[(g - \alpha) L] \geq 1 , \qquad (1)$$

where R is the reflectivity of the two cavity planes (32% for a GaAs-air interface), and L their distance. Solving for g, we have

$$g_{th} = \alpha + \ln(1/R)/L . \qquad (2)$$

The gain is related to the rate of spontaneous emission in the excited region, which in turn is determined by the rate of electron-hole pair generation when population inversion is produced by bombardment. Following the usual treatment it can be shown[7] that, in the limit of low temperatures, the pair-generation rate at threshold Z_{th} is proportional to g_{th}, or more precisely,

$$Z_{th} = 3.94 \times 10^{23} [(n^2 E^2 \Delta E)/\eta] [\alpha + \ln(1/R)/L] \text{cm}^{-3} \text{sec}^{-1} \qquad (3)$$

if energies are measured in eV and losses in cm^{-1}. Here, n is the index of refraction, E the photon energy at the peak of the spontaneous emission, ΔE the linewidth at half maximum, and η the internal quantum efficiency.

At this point it ought to be clear why the distribution of electron-hole pairs generated by the primary beam inside the target represents an element of major importance in EBP laser work. Since we may assume that the generated pair density is proportional to the beam energy dissipated per unit volume, reference can be made to the vast body of literature concerned with penetration and scattering of electron beams incident on solid targets. At present, the exact distribution of dissipated electron-beam energy does not appear to be fully understood. This may explain why many calculations still refer to erroneous expressions such as the Thomson-Whiddington square law to approximate range-energy relations. For an excellent bibliography, see reference 8. However, it can be shown that when a monoenergetic (E_o) beam of electrons strikes perpendicular to the surface of a light

crystal such as Si, Ge, or CdS, the number of particles that penetrate to a depth x is

$$N = N_o \exp\left[-(x/bE_o^n)^2 \right] = N_o \exp(-\chi^2) \quad , \tag{4}$$

where b and n are empirical constants characteristic of the crystal. The beam "penetration" is thus left undetermined, but we may consider (see Figure 2) an r.m.s. range

$$R = \sqrt{\overline{x^2}} = bE_o^n \quad . \tag{5}$$

On this basis Makhov[9] shows that the average energy of a primary electron at a point χ below the surface is

$$\overline{E}(\chi) = \frac{E_o}{\exp(-\chi^2)} \int_o^1 \exp\left[-\left(\frac{\chi}{1-\xi^n} \right)^2 \right] d\xi \quad , \tag{6a}$$

and hence that, as a function of depth, the fraction of dissipated beam energy is

$$W(\chi) = 1 - \int_o^1 \exp\left[-\chi^2/(1-\xi^n)^2 \right] d\xi \quad . \tag{6b}$$

An evaluation of (6b) for $n \approx 1.5$, which is typical of data taken at $E_o \lesssim 30$ keV, reveals that more than 80% of the incident energy is absorbed within $0 \leq \chi \leq 1$. Furthermore, in the light of Figure 2 it appears that the distribution of energy losses (the differential energy loss $dW/d\chi$) remains fairly constant over much of this same range.

The primary particles are scattered as a result of collisions with atomic nuclei, core electrons, as well as valence and conduction electrons. They may lose energy by exciting individual atoms to higher energy levels or by entering collective interactions with the valence-electron plasma. In effect, work on characteristic energy losses in solids[10] has demonstrated that the predominant energy-loss

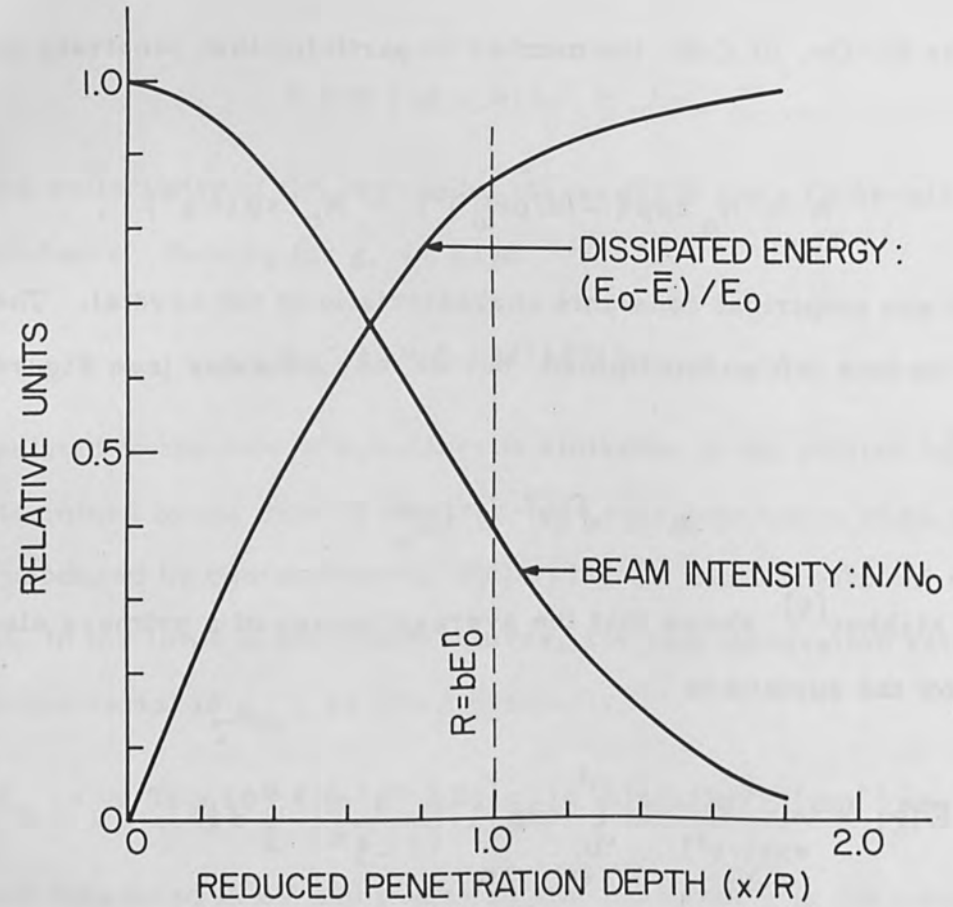

Figure 2 Penetration and energy dissipation of an electron beam impinging on solid material of low or intermediate atomic mass.

mechanism involves the excitation of plasmons. Each plasmon "decays" within about 10^{-15} sec, thus transferring energy from the incident particle to individual valence electrons, more or less in accordance with the pattern outlined in Figure 3. In semiconductors these secondaries "relax" into lowest energy states (the bottom of the conduction band for electrons, the top of the valence band for holes), where they will be available for recombination either through emission of a band-gap photon or through non-radiative processes. Obviously, in this picture the mean energy ε expended to create an electron-hole pair should be an intrinsic property of the solid, in other words, should be independent of the nature or the energy of the incident particle. Following Shockley,[11] it is then easy to see that, for a parabolic band system, one has

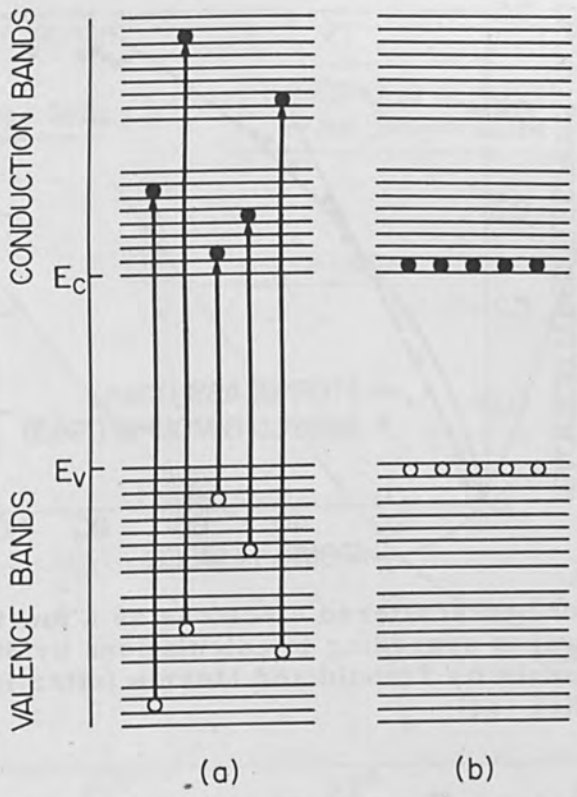

Figure 3 Excitation of electron-hole pairs in a semiconductor: (a) Schematics of transitions induced by fast particles, (b) Relaxation into metastable configurations.

$$\varepsilon = 2.2\, E_G + rE_R \quad , \tag{7}$$

where E_G is the band-gap energy and rE_R the energy dissipated to Raman phonons. If we assume that the energy lost in the initial phonon "burst" is proportional to the plasmon energy, Equation (7) yields ε values that are reasonably compatible with available experimental evidence.[12]

We conclude these considerations by pointing out that the assumption of a uniform rate of pair production throughout the "average penetration depth", d,[13] is justified on the condition that d is taken to designate the r. m. s. range R defined in (5). It follows that an electron beam of density J and potential V produces about $sJV/\varepsilon = Zd$ pairs/cm^2/sec as it is absorbed within the specimen; the factor s accounts for the fraction of backscattered electrons (see Figure 4). Upon incidence on a solid surface, a fraction (1 - s) of the electron beam will be backscattered and

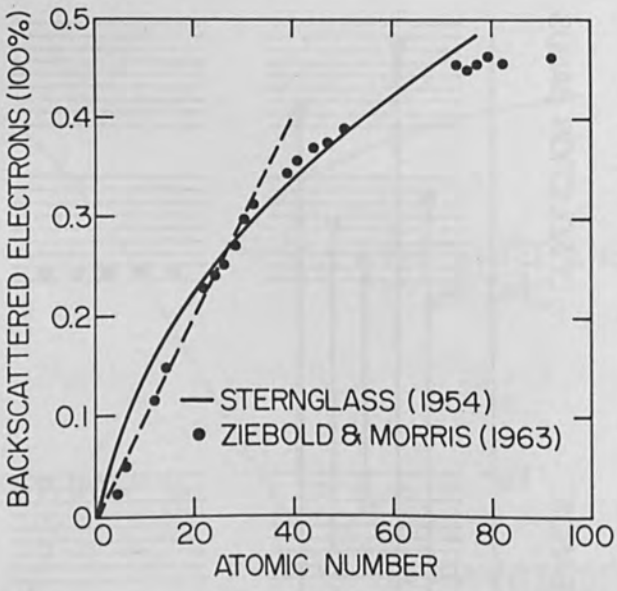

Figure 4 Fraction of backscattered electrons as a function of the atomic number according to calculations by Sternglass and measurements by Ziebold and Morris (after Brown and Ogilvie, Ref. 14).

lost to the excitation process. The amount of backscattering is very nearly independent of the incident energy and depends on the mean atomic number of the target in a known way; recent work by Ziebolt and Morris (quoted in Reference 14 and reproduced in Figure 4) indicates that for atomic numbers Z between 6 and 40 the total backscattering coefficient is about 0.010Z. Thus we may assess the predictions of Equation (3) for the critical pair-generation rate by deriving

$$Z^{*}_{th} = 6.25 \times 10^{25}\ s J_{th} V/(\varepsilon d) \qquad (8)$$

from the beam-current density measured at the threshold for laser action. We use laboratory units. Such a comparison will be made in the next section.

III. EBP GaAs Lasers

For GaAs with donor or acceptor concentrations ranging from $10^{16}/cm^3$ to $10^{20}/cm^3$, Equation (3) yields the two graphs shown in Figure 5. Relevant information on spectral peak position, half width, and efficiency was drawn from Cusano's[15] investigation of cathodoluminescence in gallium arsenide at 77°K.

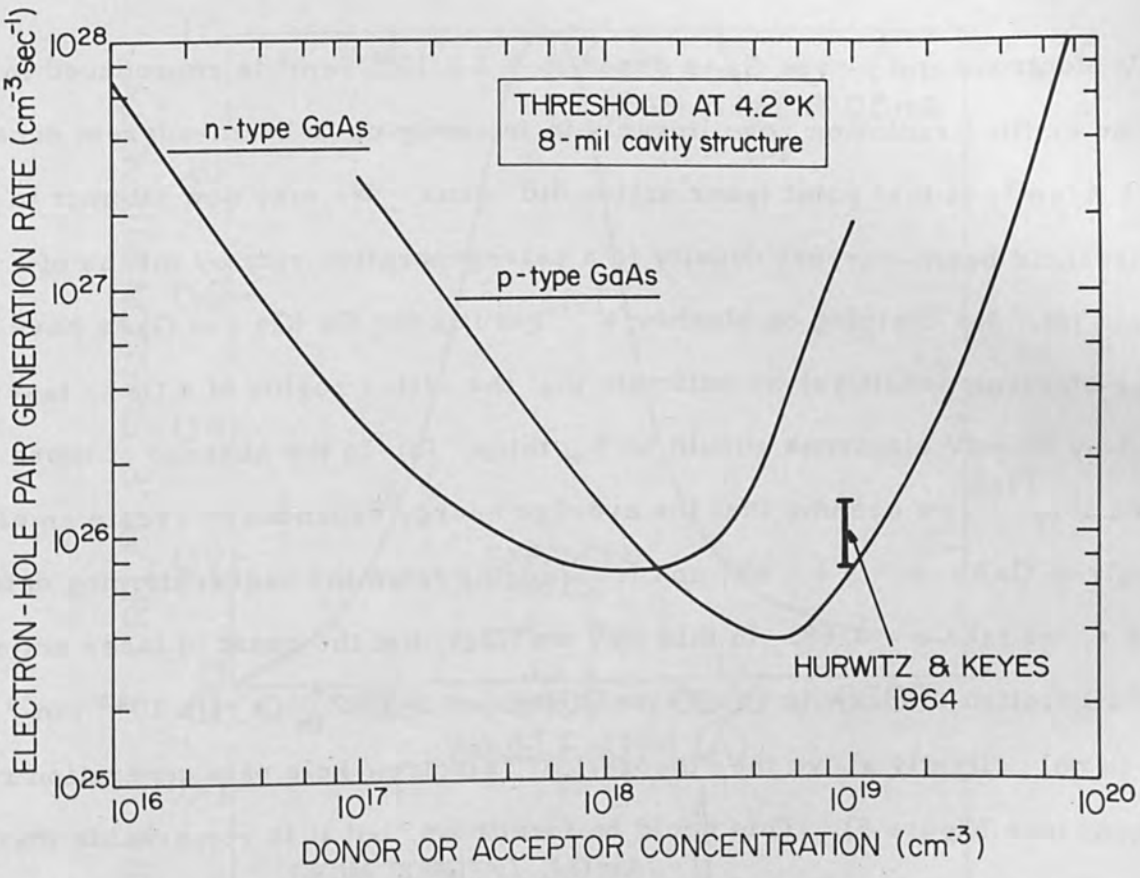

Figure 5 Electron-hole pair generation rate at the threshold for laser action in a conventional Fabry-Pérot cavity of GaAs excited by fast electrons.

The optical cavity was taken as in Hurwitz and Keyes'[4] experiment (L = 0.2 mm). As for the loss term α, since there is evidence that diffraction effects in Fabry-Perot diodes are smaller than anticipated, it was assumed that volume losses are entirely due to free-carrier absorption. On this basis it appears that, with both n- and p-type GaAs, the critical excitation density exhibits a pronounced dependence on the doping level (see Figure 5), which reflects mainly the strong influence of impurities on the efficiency of radiative recombination mechanisms. At very low temperatures, units made of material with 5×10^{18} acceptors/cm^3 should provide an optimum "situation" for achieving laser action by electron-beam bombardment of GaAs.

The broad spontaneous spectrum obtained by Hurwitz and Keyes[4] using

50-keV electrons and p-type GaAs doped to 9.3×10^{18} /cm^3 is reproduced in Figure 6a. The emitted radiation rose linearly in intensity up to beam-current densities of about 1 A/cm^2; at that point laser action did occur. We may now attempt to convert this threshold beam-current density to a pair-generation rate by means of Equation (8). (a) Relying on Makhov's[9] results for Ge (Ge and GaAs have similar electron densities) we estimate that the active region of a GaAs laser excited by 50-keV electrons should be 5 μ thick; (b) In the absence of more specific information,[16] we assume that the average energy expended to create an electron-hole pair in GaAs $\varepsilon = 5 \pm 1$ eV; and (c) Judging from the backscattering data in Figure 4, we take $s = 0.68$. In this way we infer that the onset of laser action in the configuration of Hurwitz and Keyes corresponds to $Z^*_{th} \approx 1 \times 10^{26}$ cm^{-3} sec^{-1}, which is only slightly above the "theoretical" electron-hole pair generation rate at threshold (see Figure 5). This could be fortuitous, but it is remarkable that the discrepancy may also reflect the diffusion of a fraction of the excited minority carriers away from the active region.

Figure 7 illustrates radiative transitions presumed to be associated with laser action in electron-beam pumped GaAs. The peak frequencies agree with transitions involving conduction-band states and acceptor levels (localized or banded) lying about 30 meV above the normal valence-band edge. At the doping concentrations of relevance to the problem on hand, impurity states merge into bands and produce "band-tailing" effects (see Figure 7). Note that we assume suitable n-type material to be compensated.[15] At threshold, we may then deduce the zero-temperature position of the quasi Fermi-level, F_e or F_h, simply from the concentration of injected minority carriers, $Z_{th}\tau$, where τ is the recombination lifetime. To reach threshold at higher temperatures, additional excitation is required. More precisely, with the minority carriers distributed over a broader energy range more electrons (or holes) must be injected to ensure the required amount of gain.[17] In a previous

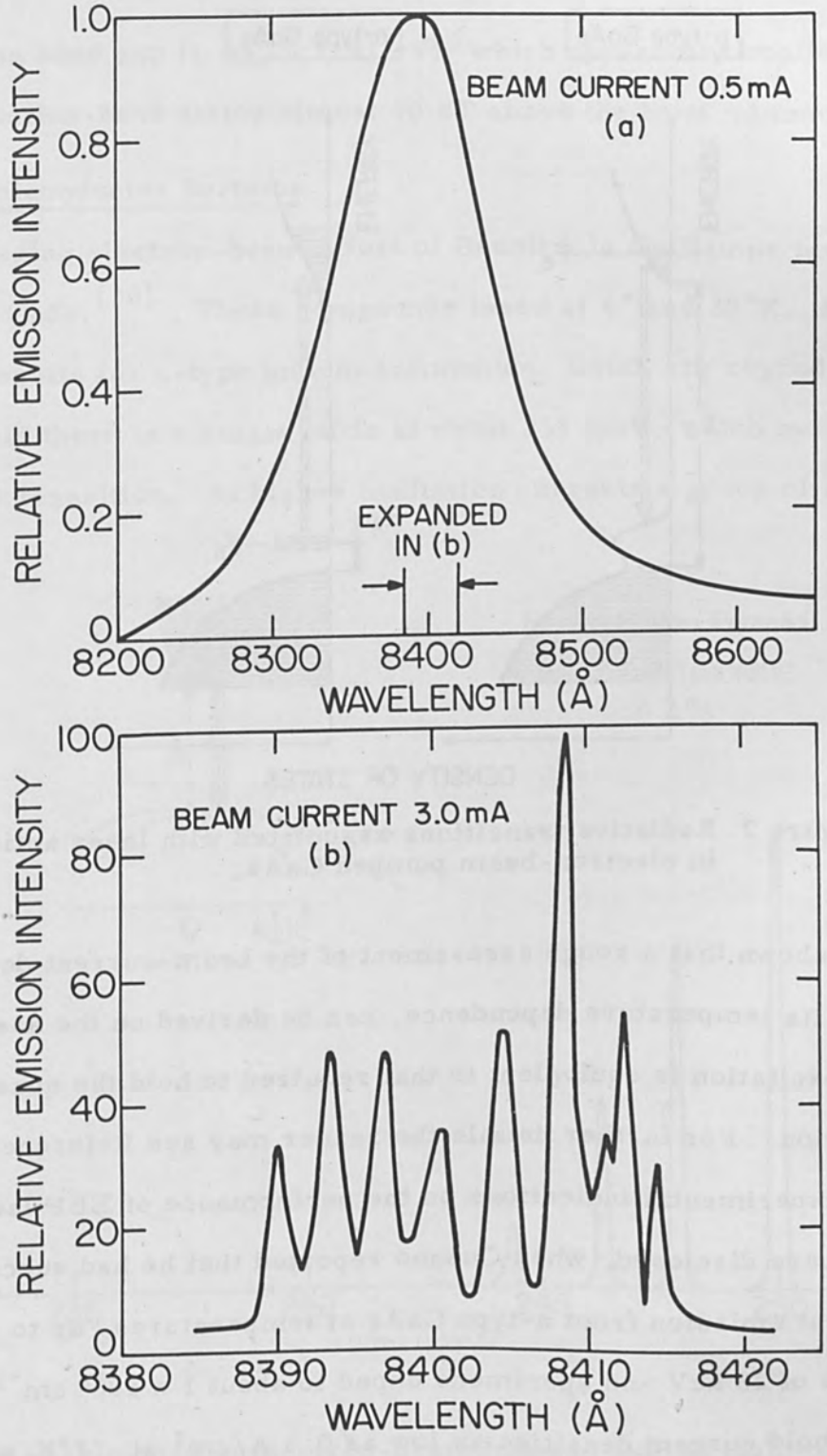

Figure 6 Emission spectrum of electron-beam pumped GaAs at liquid-helium temperature: (a) Spontaneous radiation below threshold, (b) Laser mode structure above threshold (after Hurwitz and Keyes, Ref. 4). Note that the laser spectrum in Fig. 6b was not drawn to the same intensity scale as the much weaker recombination radiation recorded below threshold.

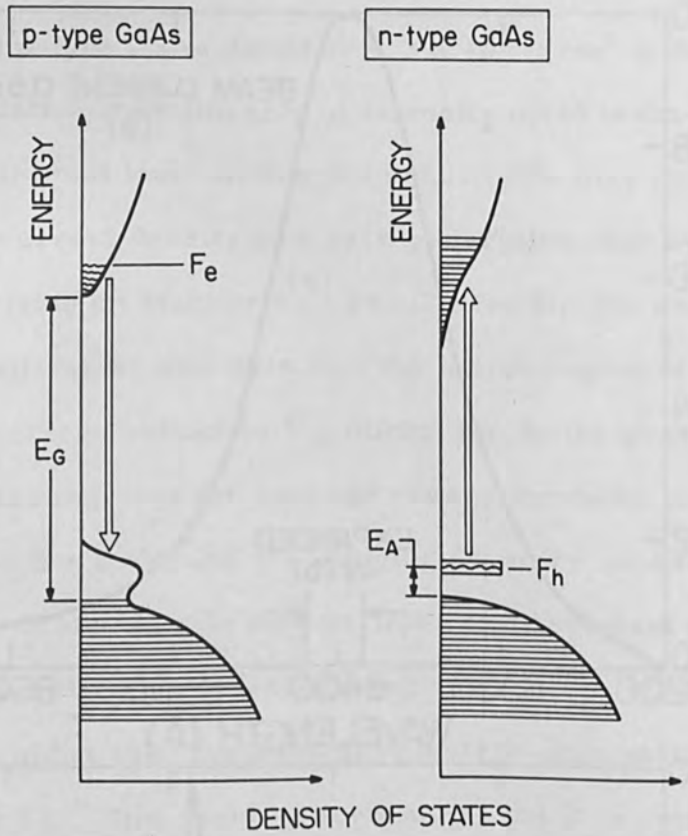

Figure 7 Radiative transitions associated with laser action in electron-beam pumped GaAs.

paper we have shown that a rough assessment of the beam-current density at threshold, and its temperature dependence, can be derived on the assumption that the additional excitation is equivalent to that required to hold the quasi Fermi-level at its 0 °K position. For further details the reader may see Reference 7.

The first experimental indications on the performance of EBP lasers at higher temperatures were disclosed, when Cusano reported that he had succeeded in exciting coherent emission from n-type GaAs at temperatures "up to -40 °C".[18] Using electrons of 28 keV and specimens doped to about 1×10^{18} cm^{-3}, Cusano recorded threshold current densities as low as 0.3 A/cm^2 at 77 °K; as a function of doping he found the threshold variations to be consistent with the pattern predicted in Figure 5. Also worthwhile to be mentioned here is his observation that stimulated emission of heavily doped n-type units occurs at photon energies substantially

greater than the band gap (1.54 vs 1.51 eV), which apparently implies the participation of conduction-band states almost 10 kT above the band minimum.[5]

IV. Other Semiconductor Systems

The pioneering electron-beam effort of Benoît à la Guillaume involved InAs,[3] InSb,[19] and GaSb.[20] These compounds lased at 4° and 20°K. Most remarkable are Benoît's results for n-type indium antimonide, which are reproduced in Figure 8. At threshold there is a single mode at about 235 meV, which corresponds to the intrinsic k = 0 transition. At higher excitation currents a group of regularly spaced

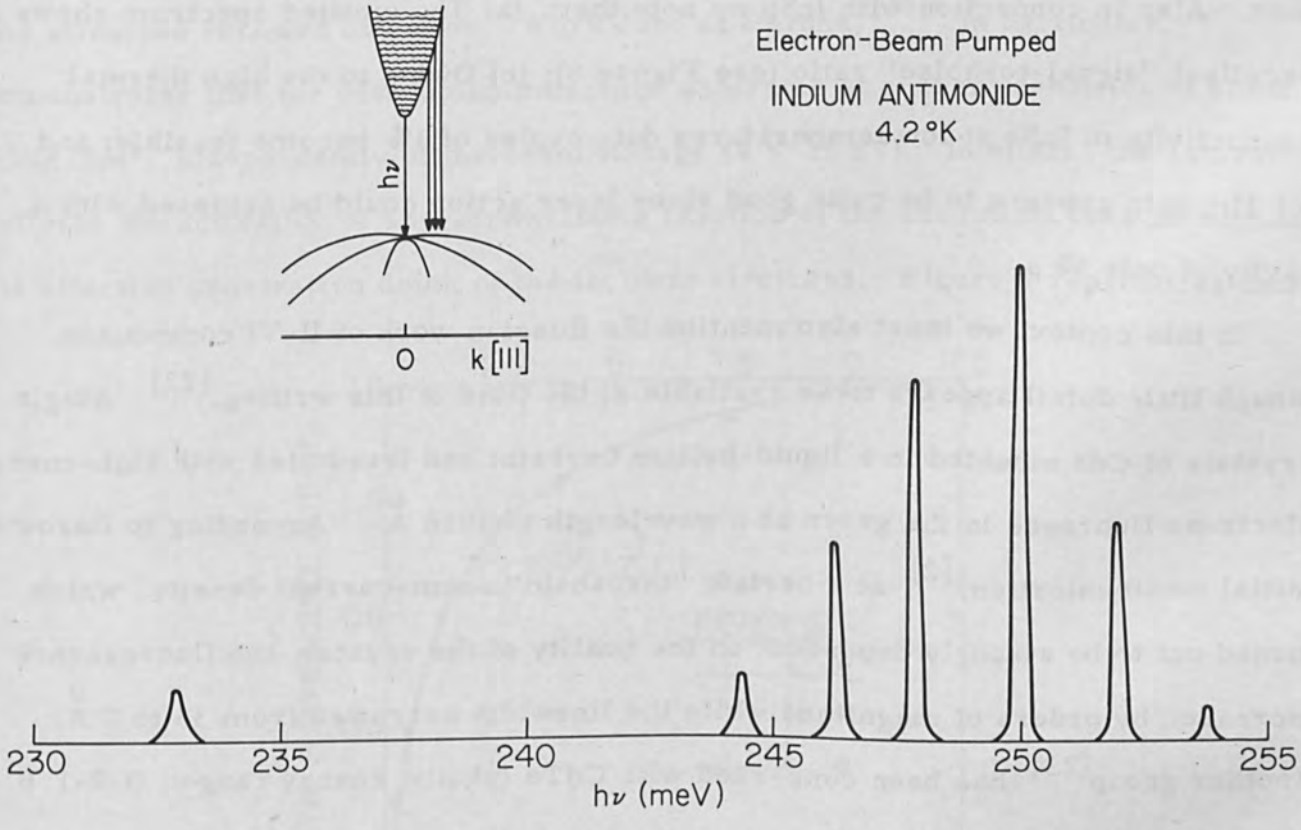

Figure 8 Laser modes in electron-beam pumped InSb at high excitation currents; the inset illustrates the recombination for non-degenerate heavy-hole bands (after Benoît à la Guillaume and Debever, Ref. 18).

modes emerges in the vicinity of 250 meV. Benoît argues that the existence of

these modes is evidence for heavy-hole valence-band maxima that are shifted off the center of the Brillouin zone by spin-orbit interactions, the recombination occurring as shown in inset. If this interpretation were correct, the system would indeed represent a laser configuration involving bands with extrema located at different points in k space. However, it may be objected that a similar $h\nu > E_G$ lasing takes place in electron-beam excited n-type GaAs and is felt to be compatible with a standard band structure, the large momenta of the injected electrons being dissipated at the acceptor impurities.[5] In addition, we may recall that a related proposal was advanced by Nasledov,[21] some time ago, and proved to be premature. Also in connection with InSb we note that: (a) The emitted spectrum shows an excellent "signal-to-noise" ratio (see Figure 8); (b) Owing to the high thermal conductivity of InSb at low temperatures duty cycles of 1% become feasible; and (c) The gain appears to be quite good since laser action could be achieved with a cavity of only 60 μ.

In this context we must also mention the Russian work of II-VI compounds, though little detail appears to be available at the time of this writing.[22] Single crystals of CdS mounted in a liquid-helium cryostat and irradiated with high-energy electrons fluoresce in the green at a wavelength of 4916 Å. According to Basov's initial communication,[2] at a certain "threshold" beam-current density, which turned out to be strongly dependent on the quality of the crystal, the fluorescence increased by orders of magnitude while the linewidth narrowed from 35 to 7 Å. Another group[23] has been concerned with CdTe (photon energy range: 0.7-1.6 eV) and reports that highly efficient vertical transitions occur in this material, which they consider as a leading candidate for EBP laser action in the near infrared. It is interesting that Vavilov's[23] experiment was conducted with electron pulses of 1 MeV and 0.5 mA/cm^2, which would imply that the electron-hole pair generation rate did not exceed 10^{22} cm^{-3} sec^{-1}, thus remaining orders of magnitude below the

presumed threshold value. At this point we wish to point out that, generally speaking, d is proportional to $V^{1.5}$, and hence it should be beneficial to operate at relatively low voltages in dealing with semiconductors [see Equation (8)]. At any rate, I believe it is significant that Benoit did succeed using beams of only 15 kV.

V. Solid State Systems

Ruby ($Al_2O_3: Cr^{3+}$) is known to exhibit intense sharp-line fluorescence under electron-beam bombardment.[24] The spectrum is identical to that emitted under optical excitation and involves predominantly the two familiar red lines at 6934 and 6919 Å (R_1 and R_2, respectively). With the advent of ruby lasers this phenomenon has attracted renewed attention. Work done at Purdue,[23] in particular, demonstrates that the cathodoluminescence saturates at current densities of about 6 mA/cm², independently of the beam voltage (V < 25 kV). In effect, the saturation reflects the activation of an overwhelming fraction of the chromium ions throughout the effective penetration depth of the incident electrons. Figure 9 reproduces data

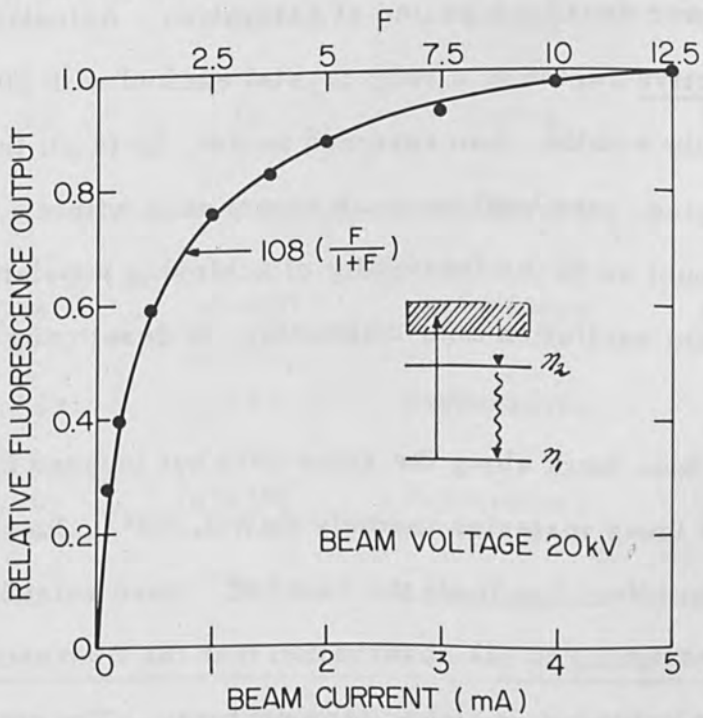

Figure 9 Saturation of the cathodoluminescence in pink ruby at 77°K; the fit is based on the three-level model shown in inset (after Levine and Subramanian, Ref. 23).

of Levine and Subramanian[25] (relative fluorescence output versus beam current) and a fit [108F/(1 + F) vs F] based on the following argument: for a three-level system (see the inset) the spontaneous emission power is given by[26]

$$P_{sp} = (h\nu/\tau)\, n_2 \quad ; \tag{9}$$

the population n_2 can be expressed in terms of the pumping rate A and the total ion concentration n_o

$$n_2 = n_1 (A\tau) = (n_o - n_2)\, F \quad ; \tag{10}$$

thus, it is seen that $P_{sp} \approx F/(1 + F)$, or in other words, "that the observed saturation is a result of the almost total depletion of the ground state".[25] Furthermore, these authors put the absolute fluorescence power density for the R_1 and R_2 lines of their sample in the vicinity of 400 W/cm^3, which is roughly half of the theoretical power density expected at saturation. Actually, we have reasons to believe that the active region of a ruby crystal excited with 20-keV electrons should be substantially smaller than assumed in Ref. 25 (4 μ); the two outputs, measured and predicted, may well be much closer than within a factor 2. Obviously, there can be little doubt as to the feasibility of achieving population inversion in ruby through electron-beam excitation and, ultimately, of developing "solid-state" EBP lasers.

Bisson[27] has done work along the same vein but focused his interest on another conventional laser material, namely $CaWO_4:Nd^{3+}$. Just as with ruby one observes a saturation effect "as if all the ions Nd^{3+} were raised to the excited state".[27] Most intriguing is his observation that the fluorescence output in the 0.8 to 1.1 μ range is enhanced at higher temperatures. The conversion efficiencies however, are low, and Bisson comments that most of the light must be emitted at

other frequencies since little beam energy appears to be dissipated to phonons.

V. Conclusion

The concept of an electron-beam pumped laser has been reduced to practice less than a year ago. Since then, activity in this field has been increasing at a fairly fast

TABLE I. Electron-beam pumped laser materials - the state of the art, Spring 1965.

Material	Wavelength (μ)	Temperature (°K)	Status	Laboratory	Reference
p-GaAs	0.841	4.2	lasing	LL	4
n-GaAs	~0.81	77	lasing	GE	5
InAs	3.00	20	lasing	ENS	3
InSb	4.95	20	lasing	ENS	18
GaSb	1.53	20	lasing	ENS	19
CdS	0.497	4.2	stimulated	LPI	2
CdTe	>0.78	10-300	exploratory	LPI	21
$Al_2O_3:Cr^{3+}$	0.693	77	exploratory	PU	23
$CaWO_4:Nd^{3+}$	1.06	100-300	exploratory	CSF	25
Te	3.72	20	stimulated	ENS	*

* P. Aigrain, private communication (12 January 1965).

rate (see Table I), which makes it difficult to draw "intelligent" conclusions on the state-of-the-art or the future of EBP lasers. Some of their more important features, or rather, features of immediate relevance are:

1. The excitation density. By proper focusing beam-power densities measured in megawatt/cm^2 can be achieved at voltages of 10 to 100 kV, which is well below the threshold for inducing radiation defects in the bulk crystal structure of semiconductors. Such power densities generate enormous numbers of excess carriers in a thin layer of material and thus may yield more intense light pulses than other injection-type devices. Still, it should be kept in mind that beam-current densities exceeding 10 A/cm^2 may cause severe sample erosion even when applied in pulses of less than 1 μsec;[23] since this damage cannot be regarded as an evaporation process due to surface heating, it must involve individual momentum transfers between impacting particles and target atoms, particularly at higher accelerating voltages. Note that Babcock[28] worked with electrons of 125 kV, which could conceivably effect a displacement of surface atoms.

2. The radiating area. Since electron-beam pumping does not involve problems associated with making contacts or junctions, it allows achieving a relatively uniform degree of population inversion over large areas. Large coherently-emitting areas imply small beam angles that are better suited for many contemplated applications of semiconductor lasers. Moreover, we may expect improved wavefront configurations in comparison to those of junction devices which emit, in general, along narrow filaments.

3. The control characteristics. Intensity, shape, and impact point of an electron beam can be controlled instantly and precisely. In addition, by using multiple electron guns unusual beam "geometries" can be achieved. Such remarkable flexibility should result in a growing number of applications for EBP lasers.

To some extent, of course, the future of this device will be determined by its

ultimate conversion efficiency, and much will depend on the feasibility of reducing the various losses. Figures for the percentage of backscattered electrons range up to 50% (see Figure 4), and since they depend quite strongly on the mean atomic number, preference should be given to low-Z material. However, losses due to backscattering are overshadowed by "band-gap losses" because the production of secondaries requires at least twice if not three times the band-gap energy [see equation (7)]. At this stage a factor-of-three loss is almost inevitable. Furthermore, the quantum efficiency η for band-to-band emission can be less than unity. Good laser material must produce the radiation not only efficiently, but also in a narrow spectral range [see equation (3)]. For instance, in GaAs it appears that $\eta \approx 0.6$,[15] and the various loss factors combine to yield a theoretical conversion efficiency of about 12% at low temperatures. In contrast with this result it is interesting to report that, according to Keyes and Quist (quoted in Reference 29), typical current-injection lasers have measured external efficiences of only 2% at 77°K.

In conclusion I wish to mention, as others have done before,[30] that electron-beam pumping is expected to produce laser action in semiconductors or phosphors that do not lend themselves to the preparation of suitable p-n junctions. More specifically, it is reasonable to expect that semiconductor lasers operating in the visible will be made available in the foreseeable future through application of the electron-beam technique. In a similar vein it is reasonable to expect that EBP ruby lasers can be developed along the lines explored at Purdue University.[25] It should be emphasized, however, that the most attractive feature of this or similar "solid-state" devices, namely the ability to modulate the light source, cannot be properly exploited unless means of reducing the critical lifetimes are invented. Finally, since electron-beam pumping eliminates contact-resistance effects and thus eliminates a major element of deleterious heating, it could be that in spite of its low

efficiency this technique may offer significant advantages at the excitation level required to reach threshold around room temperature. In this context further studies concerned with the temperature dependence of the critical electron-hole pair generation rate should be of great help in "optimizing" the selection of EBP laser materials.

Acknowledgments

I am grateful to H. Statz for suggesting work along this line, and I am indebted to J. Lavine for helpful discussions.

References

1. Basov, N. G., Krokhin, O., and J. M. Popov, in Advances in Quantum Electronics, II (Columbia University Press, New York, 1961), p. 498.
2. Basov, N. G., Bogdankevich, O. V., and A. G. Devyatkov, Doklady Akad. Nauk S.S.S.R. 155, 783 (1964).
3. C. Benoît à la Guillaume and J. M. Debever, Solid State Commun. 2, 145 (1964).
4. Hurwitz, C. E., and R. J. Keyes, Appl. Phys. Letters 5, 139 (1964).
5. Cusano, D. A., and J. D. Kingsley, Appl. Phys. Letters 6, 91 (1965).
6. Coleman, P. D., private communication (12 March 1965).
7. Klein, C. A., Raytheon Technical Memorandum T-631 (15 February 1965).
8. Everhart, T. E., Wells, O. C., and R. K. Matta, Proc. IEEE 52, 1642 (1964).
9. Makhov, A. F., Fiz. Tverdogo Tela 2, 2161 (1960).
10. Pines, D., Revs. Modern Phys. 28, 184 (1956).
11. Shockley, W., Czech. J. Phys. B11, 81 (1961).
12. Klein, C. A., submitted for publication (15 March 1965).
13. Klein, C. A., Bull. Am. Phys. Soc. 10, 387 (1965).
14. Brown, D. B., and R. E. Ogilvie, J. Appl. Phys. 35, 2793 (1964).
15. Cusano, D. A., Solid State Commun. 2, 353 (1964).

16. Pfister, H., Z. Naturforsch. 12a, 217 (1957).

17. Laser, G., and F. Stern, Phys. Rev. 133, A553 (1964).

18. Electronic News, Vol. 10 No. 473 (1 February 1965), p. 16.

19. C. Benoît à la Guillaume and J. M. Debever, in Proceedings of the Symposium on Radiative Recombination in Semiconductors, Paris, 27-28 July 1964 (Dunod, Paris, to be published).

20. C. Benoît à la Guillaume and J. M. Debever, Compt. rend. 259, 2200 (1964).

21. Nasledov, D. N., Rogachev, A. A., Ryvkin, S. M., Khartsiev, V. E., and B. V. Tsarenkov, Fiz. Tverdogo Tela 4, 3346 (1962).

22. Proceedings of the Symposium on Radiative Recombination in Semiconductors, Paris, 27-28 July 1964 (Dunod, Paris, 1965).

23. Vavilov, V. S., Nolle, E. L., Egorov, V. D., and S. I. Vintovkin, Fiz. Tverdogo Tela 6, 1406 (1964).

24. Leverenz, H. W., Luminescence of Solids (John Wiley and Sons, New York, 1950).

25. Levine, M. W., and M. Subramanian, Appl. Phys. Letters 6, 87 (1965).

26. Yariv, A., and J. Gordon, Proc. IEEE 51, 4 (1963).

27. Bisson, G., Compt. rend. 258, 4012 (1964).

28. Babcock, R. V., J. Appl. Phys. 35, 3354 (1964).

29. Schlickman, J. J., Fitzgerald, M. E., and R. H. Kingston, Proc. IEEE 52, 1739 (1964).

30. Rediker, R. H., Phys. Today 18 (No. 2), 42 (1965).

A Study of the Formation and the Energy Balance of the Capillary in Electron Beam Deep Penetration Welding

by

W. E. Meyer, W. Scheffels and K. H. Steigerwald
K. H. Steigerwald GmbH.
Munich, Germany

Abstract

The factors affecting the formation of the deep welding capillary are discussed. Calculated values of pressure and temperature are compared in an energy balance with the experimental results.

1. Introduction

If an electron beam of sufficient power density strikes a metal plate, it will first melt the bombarded material, and next will rapidly evaporate the material in the center as it continues to strike the metal. As a result, a hole will be produced.

If the thickness of the plate is less than the diameter of the hole, the surface tension will pull the molten metal at the edge of the hole further outward. The edge thus leaves the beam, cools down rapidly and may in certain cases solidify even before the beam is cut off. As a result a hole is drilled. [1, 2]

If the thickness of the plate exceeds the diameter of the hole, the surface tension will try to pull the edge of the hole inward. The hole will be kept open only by the continuous supply of energy through the beam and will close as soon as the beam is cut off. A permanent hole can be obtained only by special measures, for example by an extremely high power density, sharply decreasing at the edge of the beam or, in certain cases, by the use of a pulsed beam. [3, 4]

Experience gained during recent years has shown that the unstable hole, which closes after the beam has been cut off, is of great importance for welding applications. If local bombardment is not terminated by cutting off the beam but by displacing it laterally (perpendicular to its axis), the hole will follow the beam

through the material. The molten material surrounding the beam causes a weld zone instead of a cut to be formed along the distance covered by the beam. This weld is always narrow, its depth being determined by the depth of the hole. As the power and the power density of the beam are increased, the beam can produce a capillary up to a depth of many centimeters. A narrow, deep weld will then be formed behind the traveling beam, which, for example, can be used for joining the surfaces of two workpieces with a minimum of energy.[5] Figure 1 shows a cross section through a weld obtained in this manner.

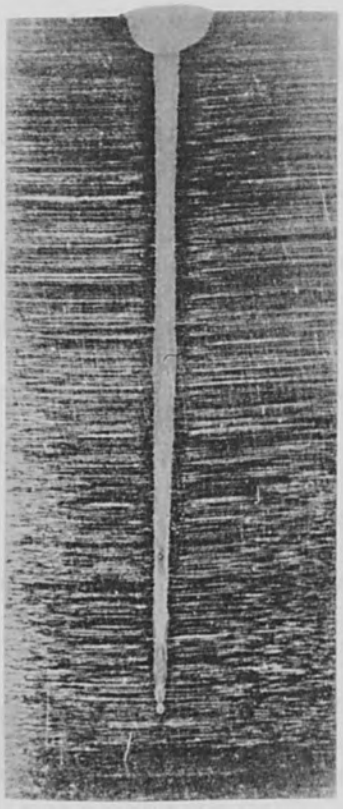

Figure 1 Electron beam deep penetration weld in stainless steel. Depth of penetration 32 mm, welding speed 2 mm/sec, power 3 kW, pulsed beam.

In what follows, a closer study will be made of the physical processes which are of importance for the formation of the capillary and its motion through the material.

2. The Formation of the Capillary

In order to analyze the processes connected with the formation of the capillary we use the following experimental data:

A beam of 130 kV and 12 mA is focused to a diameter of 0.02 cm. In 0.05 sec it will penetrate about 1 cm in steel. From measurements of the evaporation rate[6] and direct pyrometric measurements[7] the temperature at the entrance of the capillary was found to be approximately 2800 °K.

Formation of the capillary can, in principle, be caused by the following processes:

a) Removal of the material by evaporation,

b) Action of the electron pressure on the melt,

c) Action of the vapor pressure on the melt.

A simple estimation shows that in the present case neither evaporation nor the pressure due to electron bombardment are of importance for the formation of the capillary.

The rate of evaporation at 2800 °K is $V = 1.4\ g/cm^2\ sec.$[8] Therefore, in 0.05 sec a quantity of only 2.2×10^{-5} g would evaporate from the entrance of the capillary of 0.02 cm diameter. However, the capillary displaces a quantity of about 120×10^{-5} g.

The pressure due to electron bombardment is given by

$$p_e = j \sqrt{\frac{2U}{e/m_e}}$$

where j is the current density, and U is the accelerating voltage, e and m_e are the charge and mass of the electron respectively. Using the quantities mentioned at the beginning of this section, expressed in the appropriate units, we obtain $p_e = 3.5$ mm

Hg.

In the plane surface of a steel melt, the beam is thus capable of producing a cavity with a radius of curvature of

$$r_K = \frac{2\gamma}{p} \approx 0.7 \text{ cm}$$

where γ is the surface tension of steel assumed to be $\approx$ 1700 dynes/cm measured at melting temperature. [9]

Even if we assume that the surface tension is considerably lower due to the high temperature of the melt, r_K will be sufficiently high, so that with a beam diameter of 0.02 cm the resulting cavity is shallow enough to be neglected.

A considerably greater effect is produced by the vapor pressure at the bombarded area. For $T_o = 2800\,°K$ there results a vapor pressure of $p_o = 170$ mm Hg. [8] The radius r_K of the corresponding cavity thus has about the same magnitude as the radius r_S of the beam, and a hole is formed in the melt. The surface of the melt yielding to the vapor pressure will then tilt with respect to the axis of the beam until the pressure of the surface tension is at every point equal to the vapor pressure produced by the heating effect of the beam.

With the aid of this condition of equilibrium one can determine the pressure in a capillary of a given geometry. A first approximation of this shape is given by the shape of the electron beam penetrating the capillary and the consumption of energy out of the different areas of the capillary.

One question to be studied first is what happens to the material originally filling the capillary space. The experiment shows that the material escapes towards the surface of the plate, forming a bulge as indicated in the right-hand half of Figure 2. The pressure p_R due to the surface tension of the bulge, forces the molten metal towards the axis of the beam. The latter heats the melt to such a degree that the resulting vapor pressure brings about an equilibrium, just as within

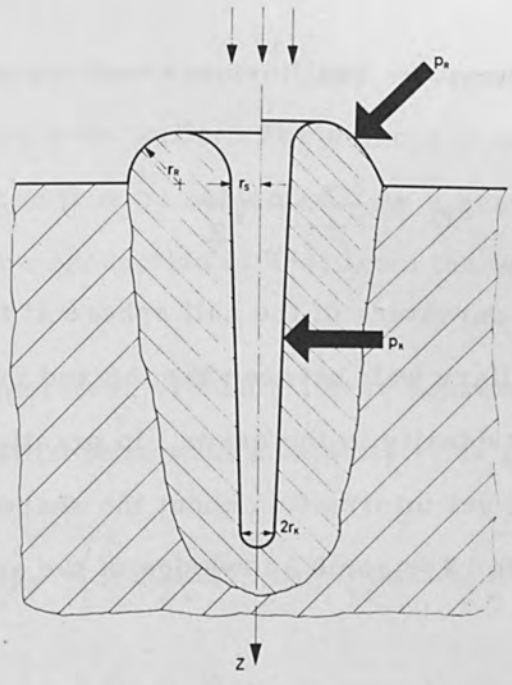

Figure 2 Schematic diagram showing the formation of the capillary in deep penetration welding.

the capillary. The surface of the bulge remaining outside the beam adapts its shape in such a manner that the inward pressure due to its surface tension is the same at every point. It is transferred to the wall of the capillary via the melt and adds to the pressure p_K produced by the surface tension of the capillary.

The pressure p_R can be estimated if, for simplicity, we assume that the material displaced from the capillary forms an annular bulge of semi-circular cross section (Figure 2, left). Equating the volumes of the capillary and the annular bulge we obtain the value 0.02 cm for the radius r_R The pressure $p_R = \frac{\gamma}{r_R}$ with γ for steel equal to 1700 dyne/cm is thus found to be 60 mm Hg.

Taking the aforementioned condition of equilibrium between the vapor pressure on one hand and the pressure produced by the surface tension of capillary aperture and annular bulge on the other, we can write for the pressure at a depth Z of the capillary.

$$p(Z) = \frac{\gamma}{r_S(Z)} + \frac{\gamma}{r_R}$$

At the bottom of the capillary, the equilibrium condition is

$$p_D = \frac{2\gamma}{r_K} + \frac{\gamma}{r_R}$$

where r_K is the radius of curvature of the half sphere at the bottom of the capillary.

The shape of the capillary wall between the top and the bottom depends on the distribution of the current density in the beam. In practice, it will always have an almost conical shape. To get information about the shape of the beam in the capillary it is necessary to have some knowledge of the amount of energy fed by the beam into the capillary.

3. Calculation of the Depth of Penetration

With the aid of an energy balance we shall now calculate the depth of penetration achieved with a laterally moving beam.

The appearance of an electron beam deep penetration weld (Figure 1) suggests that the beam delivers its power approximately uniformly over the entire depth of the capillary, with the exception of the areas at the highest and lowest points. Therefore, we can take as the power supplied per unit length at every point of the capillary

$$q = \frac{I\,U}{D} \quad .$$

Where I is the current, U the voltage and D is the depth of penetration. In principle, a certain portion of this power is used for transporting the material from the front to the rear of the capillary while the beam is moving. This is achieved by an additional heating of the front wall of the capillary. The increased temperature causes both an increased evaporation of the material, which then condenses at the back, as well as a pressure gradient which pushes the molten material from the front around the capillary to the rear. Because only a relatively small amount of

vapor escapes through the opening of the capillary, most of the impinging energy stays in the capillary and heats its walls. The amount of energy to be spent for the transportation of material can thus be neglected. As a result, the power supplied will serve exclusively for the conduction of heat from the wall of the capillary to the material.

The distribution of temperature around a linear source of heat moving in a heat conducting medium in the x-direction with a velocity v, is given by[10]

$$T = T_\infty + \frac{q}{4\lambda} \exp\left(-\frac{\rho c v x}{2\lambda}\right) iH_o^{(1)}\left(\frac{i\rho c v \sqrt{x^2 + y^2}}{2\lambda}\right) ,$$

where T_∞ is the temperature at a large distance from the source, q the power supplied per unit length, λ the thermal conductivity, ρ the density, and c the heat capacity of the material. $H_o^{(1)}(u)$ is Hankel's function.

Let us now compute the heat flow q if the wall of the capillary of radius r_S has the temperature T_o required for keeping the capillary open. Since $\sqrt{x^2 + y^2} = r_S$, the argument $u = \rho c v r_S/2\lambda$ in this case becomes small, and we can write

$$iH_o^{(1)}(u) = \frac{2}{\pi} \ln \frac{1.12}{u} \; ; \; (e^{-u} \approx 1)$$

Thus we obtain for q

$$q = \frac{2\pi\lambda (T_o - T_\infty)}{\ln \frac{2.24\lambda}{\rho c v r_S}} .$$

If we compare this with the power supplied by the electron beam we obtain for the depth of penetration D

$$D = \frac{I U \ln \frac{2.24\lambda}{\rho c v r_S}}{2\pi\lambda (T_o - T_\infty)}$$

The experiment shows that the depth of penetration will hardly vary as long as the velocity is lower than approximately 0.2 cm/sec. Therefore, we can use the experimental data quoted for the capillary in steel in order to check the above formula. With v = 0.2 cm/sec we thus obtain D = 0.98 cm. A value of 0.66 cm is obtained for a welding speed of 1 cm/sec. These values are in good agreement with experiments.

4. An Estimate of the Pressure in the Capillary

The capillary walls receive, at their upper end, the energy from the outer portion of the beam cross-section. At greater depths of the capillary, the portion of the beam cross-section at which the transfer of power takes place increases. The shape of the capillary is defined by the power density distribution in the cross-section of the beam, depending on the condition for pressure equilibrium at the walls of the capillary. The beam cross-section depends on the effects of power exchange between the electrons of the beam, the wall of the capillary and the vapor.

It is difficult to exactly calculate the result of all these effects. Therefore, in order to estimate the shape of the capillary, it seems at present that the best approximation is obtained if we use in the calculation the diameter of the beam at the upper end of the capillary, the depth of the capillary and the energy consumption distribution along the axis of the capillary.

Under these conditions the beam radius r_S at the entrance is taken as the radius of the capillary. At the bottom of the capillary, the radius is approximately 0.3 r_S to 0.5 r_S. With these assumptions the pressure at the bottom of the capillary is approximately 500 mm Hg. In steel, this corresponds to a temperature of approximately 3000 °K.

5. Conclusions

When comparing the above considerations with the results of experiments, allowance has to be made for the fact that the relationship between temperature and

pressure or evaporation rate used here cannot be applied without reservation to alloys. As compared with pure base metal, a component with a relatively high vapor pressure will considerably reduce the temperature required for keeping the capillary open even if the percentage of the component is small.

For calculating the depth of penetration D, attention has to be paid to the temperature dependence of λ, which in some metals is quite considerable.

In any case, however, the above considerations show why the depths of penetration that can be achieved do not only increase with increasing power density, but under constant power density also with the beam power itself.

Theoretical investigations are now underway, which are aimed at a coherent representation of the capillary's geometry and the distribution of pressure and temperature within the capillary as functions of the welding speed and the characteristics of the beam and the material.

References

1. Brüche, E., Zeitschrift für Angewandte Physik 3 (1951), 88.
2. Steigerwald, K. H., Physikalische Verhandlungen 4 (1953), 123.
3. Steigerwald, K. H., 4th International Congress of Electron Microscopy, Springer 1958.
4. Schleich, F., 4th International Congress of Electron Microscopy, Springer, 1958.
5. Steigerwald, K. H., Schweissen und Schneiden 12 (1960), 89.
6. Schwarz, H., Journal of Applied Physics, 35 (1964), 2020.
7. Scheffels, W., Publication in preparation.
8. Honig, R. E., RCA Revue 18 (1957), 23 (1962).
9. Kohl, W. H., Vacuum, 14 (1964), 175.
10. Carslaw, H. S. and J. C. Jaeger, Conduction of Heat in Solids, Oxford 1959, 267.

Welding Electron Optical Systems

by

R. F. Donovan
Hamilton Standard Division
United Aircraft Corporation
Windsor Locks, Connecticut

Abstract

This paper discusses the system aspects of electron beam welding machines. In particular, the major penetration parameters under the control of the machine designer are discussed. The discussion covers the choice of gun design and electron optical system, the resulting image and aberration problems, parameter error analysis and system specifications. Typical theoretical and experimental curves are included. Finally a brief discussion is given pointing out what features one might expect in future electron beam welding machines.